Proceedings
of the International Conference

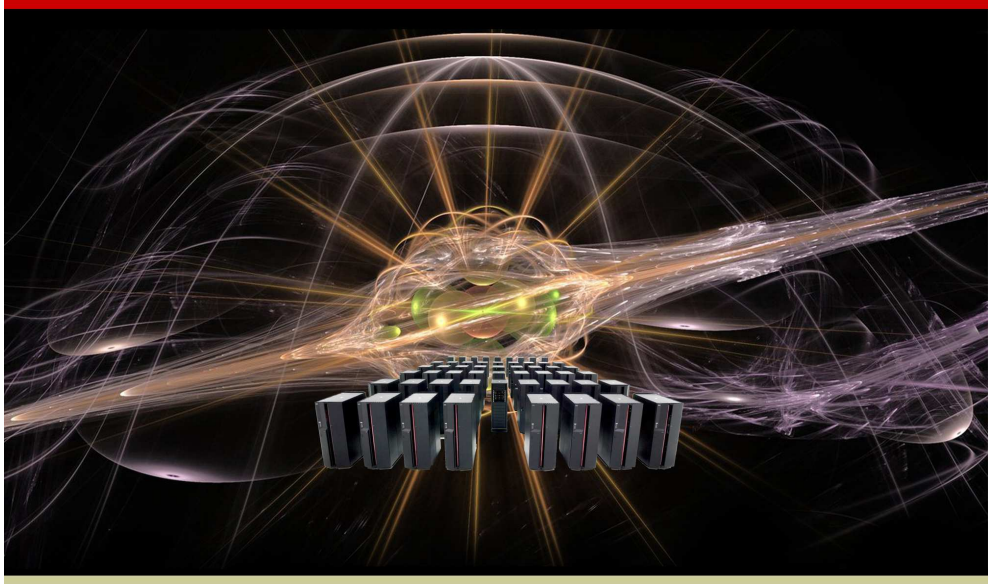

Nuclear Theory
in the Supercomputing Era – 2013

NTSE-2013

Ames, Iowa
May 13–17, 2013

Khabarovsk, 2014

Iowa State University
Pacific National University

NUCLEAR THEORY IN THE SUPERCOMPUTING ERA – 2013 (NTSE-2013)

International Conference

Ames, Iowa, USA, May 13–17, 2013

PROCEEDINGS

Editors A. M. Shirokov and A. I. Mazur

Khabarovsk, Russia
Pacific National University
2014

УДК 539.14
ББК В38я431
N 91

N 91 **Nuclear** Theory in the Supercomputing Era – 2013 (NTSE-2013): International Conference. Ames, Iowa, USA, May 13–17, 2013. Proceedings. Eds. A. M. Shirokov and A. I. Mazur. — Khabarovsk, Russia, Pacific National University, 2014. — 389 p.
ISBN 978-5-7389-1384-6

The primary motivation for the series of International Conference "Nuclear Theory in the Supercomputing Era (NTSE)" was the rapid growth of supercomputers and the impact they, along with theoretical and algorithmic developments, are having on nuclear theory. The first conference in this series, NTSE-2012, was hosted by the Pacific National University, Khabarovsk, Russia in June 18-22, 2012 (http://www.ntse-2012.khb.ru). The second conference, NTSE-2013 (http://www.cpm.iastate.edu/ntse2013), was hosted by the Iowa State University, Ames, Iowa, USA in May 13-17, 2013 and celebrated the 70th birthday of James Vary. The Conference was sponsored by Iowa State University, Ames, Iowa, USA and Pacific National University, Khabarovsk, Russia. These proceedings includes Keynote and Invited talks as well as the Distinguished Lecture of Professor James P. Vary presented at the NTSE-2013 Conference.

The contributions to the NTSE-2013 Proceedings published here, are also available online at http://www.ntse-2013.khb.ru/Proc/.

УДК 539.14
ББК В38я431

ISBN 978-5-7389-1384-6

Preface

The International Conference on Nuclear Theory in the Supercomputing Era — 2013 (NTSE-2013) brought together experts in nuclear theory and high-performance computing in Ames, Iowa from May 13 to May 17, 2013. It was the second conference in a series that focuses on forefront challenges in physics, namely the fundamentals of nuclear structure and reactions, the origin of the strong inter-nucleon interactions from QCD, the nonperturbative regime of relativistic quantum field theory, and computational nuclear physics with leadership class computer facilities to provide forefront simulations leading to new discoveries. During this year's conference, we also celebrated James P. Vary's 70th birthday.

Throughout his career, James has made important contributions to theoretical and computational nuclear physics, mentored more than 30 students and postdocs, and served the science community in a number of elected and appointed positions. He has published a few hundred refereed journal articles, and is a regular invited lecturer at national and international scientific conferences. During his career James has always been involved in international collaborations, and in promoting science in far-flung places.

During the period 1993–2000 James served as Director of the International Institute of Theoretical and Applied Physics (IITAP) and institute patterned after the renowned ICTP in Trieste, Italy. IITAP sponsored more than 1000 international visits, primarily of developing country scientists to the US, with sponsorship from UNESCO, Iowa State University, NSF, DOE as well as corporations and foundations. Many of these projects continue until the present time. The state funding crunch of 2000 and 2001 led to a discontinuance of IITAP operations. However, other universities continue to study the model that IITAP pioneered for multi-lateral support of international scientific projects.

We were very pleased that several of his international collaborators were able to participate in this meeting. We were also very happy to be able to bring together some of James' collaborators from his early career, including his PhD supervisor Joe Ginocchio, his former collaborator as postdocs at MIT, Peter Sauer, and Hans Weidenmüller, his mentor and host on various visits to Heidelberg, Germany.

The conference also welcomed many young scientists, including graduate students in nuclear physics and computational science. All participants together made the conference a great success.

The conference topics,

(1) *Ab initio* nuclear structure;

(2) Microscopic approaches to nuclear reactions;

(3) Origin and properties of the strong interactions;

(4) Light-front quantum field theory; and

(5) Computational science and applied mathematics,

reflect James' research interest and encompass a broad area of fundamental physics and high-performance computing. For each of these topics, a keynote speaker (Gaute Hagen, Jerry Draayer, Petr Návratil, Ruprecht Machleidt, Stan Brodsky, and Esmond Ng) presented an overview of the topic, with an additional keynote talk on Lattice QCD by Martin Savage. George Fai (program manager for nuclear theory at DOE) gave us the view from the DOE nuclear theory office, and the conference concluded with a summary talk by Bruce Barrett. James himself delivered a distinguished

lecture with an overview of his recent research as well as his projections for future directions.

We would like to express our appreciation to all participants of the NTSE-2013 conference, to all contributors to these proceedings, to all members of the Scientific Advisory Committee and to the NTSE-2013 sponsors — Iowa State University and Pacific National University.

The organizing committee:

Bruce Barrett (Co-Chair), University of Arizona
Kristina Launey, Louisiana State University
Pieter Maris (Co-Chair), Iowa State University
Jianwei Qiu, Brookhaven National Laboratory
Joseph Shinar, Iowa State University
Andrey Shirokov (Co-Chair), Moscow State University, Russia
Masha Sosonkina, Old Dominion University
Kirill Tuchin, Iowa State University
Xingbo Zhao, Iowa State University

NTSE-2013 Scientific Advisory Committee:

- **Bruce Barrett (Chair)**, University of Arizona, USA
- **Stanley J. Brodsky**, SLAC-Stanford, USA
- **Ümit Çatalyürek**, The Ohio State University, USA
- **Mark Caprio**, University of Notre Dame, USA
- **David Dean**, Oak Ridge National Laboratory, USA
- **Jerry Draayer**, Louisiana State University, USA
- **John Hiller**, University of Minnesota-Duluth, USA
- **Morten Hjorth-Jensen**, University of Oslo, Norway and Michigan State University, USA
- **Youngman Kim**, Institute for Basic Science, South Korea
- **Ruprecht Machleidt**, University of Idaho, USA
- **Alexander Mazur**, Pacific National University, Russia
- **Petr Navrátil**, TRIUMF, Canada
- **Witek Nazarewicz**, University of Tennessee, USA and Oak Ridge National Laboratory, USA
- **Esmond Ng**, Lawrence Berkeley National Laboratory, USA
- **Giuseppina Orlandini**, University of Trento, Italy
- **W. Erich Ormand**, Lawrence Livermore National Laboratory, USA
- **Takaharu Otsuka**, University of Tokyo, Japan
- **Steve Pieper**, Argonne National Laboratory, USA
- **Wayne Polyzou**, University of Iowa, USA
- **Sophia Quaglioni**, Lawrence Livermore National Laboratory, USA
- **Jianwei Qiu**, Brookhaven National Laboratory, USA
- **Andrey Shirokov**, Moscow State University, Russia
- **Masha Sosonkina**, Old Dominion University, USA
- **James Vary**, Iowa State University, USA

NTSE-2013 Organizing Committee:

- **Bruce Barrett (Co-Chair)**, University of Arizona, USA
- **Kristina Launey**, Louisiana State University, USA
- **Pieter Maris (Co-Chair)**, Iowa State University, USA
- **Jianwei Qiu**, Brookhaven National Laboratory, USA
- **Joseph Shinar**, Iowa State University, USA
- **Andrey Shirokov (Co-Chair)**, Moscow State University, Russia
- **Masha Sosonkina**, Old Dominion University, USA
- **Kirill Tuchin**, Iowa State University, USA
- **Xingbo Zhao**, Iowa State University, USA

Program of International Conference on Nuclear Theory in the Supercomputing Era — 2013 (NTSE-2013)

Sunday, May 12
Memorial Union, 2nd floor, Campanile Room

5:30–6:30pm	*Welcome Reception*

Monday, May 13
All talks are in Memorial Union, 3d floor, Gallery Room

Chair: Bruce Barrett

8:30–8:45am	*Conference opening*
	Keynote talk:
8:45–9:30am	**Gaute Hagen** *Ab Initio* Nuclear Structure — from Light to Medium Weight Nuclei
9:30–10:00am	**David Dean** A Survey of Experimental Challenges to Computational Nuclear Physics
10:00–10:30am	*Coffee break*

Chair: Winfried Leidemann

10:30–11:00am	**Robert B. Wiringa** Quantum Monte Carlo Calculations of Transitions and Reactions
11:00–11:30am	**Steven C. Pieper** Green's Function Monte Carlo Calculations of Carbon
11:30–12:00pm	**Pieter Maris** *Ab Initio* Calculations of p-shell Nuclei with JISP16
12:00–1:30pm	*Lunch break*

Chair: Robert B. Wiringa

	Keynote talk:
1:30–2:15pm	**Jerry P. Draayer** — Unraveling Mysteries of the Strong Interaction — 'Top Down' versus 'Bottom Up' Considerations
2:15–2:45pm	**Tomáš Dytrych** Utilizing Symmetry Coupling Schemes in *Ab Initio* Nuclear Structure Calculations
2:45–3:15pm	*Coffee break*

Chair: Steven C. Pieper

3:15–3:45pm	**Gerald A. Miller** Nuclear Isospin Violation — How It Turned out and Where It Is Going
3:45–4:15pm	**Joseph Carlson** Homogeneous and Inhomogeneous Fermions: Cold Atoms and Neutrons
4:15-4:45pm	**Hans Weidenmüller** Nuclear Excitation by a Strong Zeptosecond Laser Pulse: Theoretical Expectations

Tuesday, May 14
All talks are in Memorial Union, 3d floor, Gallery Room

Chair: Martin Savage

Keynote talk:	
8:30–9:15am	**Stanley J. Brodsky** Light-Front Quantum Chromodynamics
9:15–9:45am	**Heli Honkanen** Modeling Nuclear Parton Distribution Functions
9:45–10:15am	**Dipankar Chakrabarti** Generalized Parton Distributions for the Proton

10:15–10:45am	*Coffee break*

Chair: Morten Hjorth-Jensen

10:45–11:15am	**Vladimir Karmanov** Nonperturbative Calculations in the Light-front Field Theory
11:15–11:45am	**Yang Li** Introduction to Basis Laight-Front Quantization Approach to QCD Bound State Problems
11:45–12:15pm	**Paul Wiecki** Positronium in Basis Light Front Quantization

12:15–1:45pm	*Lunch break*

Chair: Stanley J. Brodsky

Keynote talk:	
1:45–2:30pm	**Martin Savage** Nuclear Forces from Quantum Chromodynamics
2:30-3:00pm	**Kirill Tuchin** Hot Nuclear Matter in Intense Magnetic Field

3:00–3:30pm	*Coffee break*

Chair: Steven C. Pieper

3:30–4:00pm	**Usha Kulshreshtha** Light-front Quantization of Non-Linear Sigma Models
4:00–4:30pm	**Daya Shankar Kulshreshtha** Light-Front Quantization and DLCQ of Large N Scalar QCD_2
4:30–5:00pm	**Xingbo Zhao** Scattering in Time-Dependent Basis Light Front Quantization

Wednesday, May 15
All talks are in Memorial Union, 3d floor, Gallery Room

Chair: Achim Schwenk

Keynote talk:	
8:30–9:15am	**Petr Navrátil** *Ab Initio* Approaches to Nuclear Reactions
9:15–9:45am	**Winfried Leidemann** Recent Results with the Lorentz Integral Transform (LIT) Method
9:45–10:15am	**Jimmy Rotureau** *Ab Initio* Description of Light Nuclei in the Berggren Basis

10:15–10:45am	*Coffee break*

Chair: Jerry P. Draayer

10:45–11:15am	**Andrey Shirokov** Oscillator Basis and Scattering
11:15–11:45am	**Youngman Kim** SuperHeavy Element Studies at RAON
11:45–12:15pm	**George Fai** The View from Germantown

12:15–1:45pm	*Lunch break*

Chair: Takaharu Otsuka

1:45–2:15pm	**John Hill** Studies of Hot Dense Nuclear Matter with the PHENIX Detector at RHIC
2:15–2:45pm	**Jianwei Qiu** The Nucleus: a Laboratory for QCD

2:45–3:15pm	*Coffee break*

Chair: Peter U. Sauer

3:15–3:45pm	**Joseph N. Ginocchio** Relativistic Symmetries in Nuclei and Hadrons
Distinguished lecture:	
3:45–4:45pm	**James P. Vary** Computational Nuclear Physics: Key to Discovery Opportunities

4:45 -6:00pm	*Social Hour; Cash Bar*

6:00 pm	*Group photo and Banquet*

Thursday, May 16
All talks are in Howe Hall, Alliant Energy - Lee Liu Auditorium

Chair: Joseph N. Ginocchio

Keynote talk:	
8:30–9:15am	**Esmond Ng** Challenges in Computational Science at Exascale
9:15–9:45am	**Masha Sosonkina** Accelerating *Ab Initio* Nuclear Physics Calculations with GPUs and Optimization Techniques
9:45–10:15am	**Ümit Çatalyürek** Exploring Intel Xeon Phi and NVidia GPUs for Nuclear Physics Simulations

10:15–10:45am	*Coffee break*

Chair: Mark A. Caprio

10:45–11:15am	**Chao Yang** Computational Techniques for Accelerating Nuclear Configuration Interaction Calculations in MFDn
11:15–11:45am	**George Fann** Adaptive Pseudo-Spectral Method for Solving HFB Equations
11:45–12:15pm	**Hai Ah Nam** Computational Nuclear Physics for Modern Computing Architectures

12:15–1:15pm	*Lunch onsite (covered by the conference fee paid in full)*

Chair: Esmond Ng

1:15–1:45pm	**Takaharu Otsuka** Monte Carlo Shell Model and Shape Phase Transitions in Exotic Nuclei
1:45–2:15pm	**Takashi Abe** Monte Carlo Shell Model Towards *Ab-Initio* Calculations
2:15–2-45pm	**Achim Schwenk** Neutron Matter With Chiral Effective Field Theory: Perturbative and First Quantum Monte Carlo Calculations

2:45–3:15pm	*Coffee break*

Chair: Chao Yang

3:15–3:45pm	**Sidney A. Coon** Infrared and Ultraviolet Cutoffs: Convergence Strategies for Harmonic Oscillator Basis Expansion Methods
3:45–4:45pm	**Thomas Papenbrock** Corrections to Nuclear Energies and Radii in Finite Oscillator Spaces
4:15–4:45pm	**Mark A. Caprio** Convergence of NCCI Calculations for Light p-Shell Nuclei with the Coulomb–Sturmian Basis

5:30pm	*Tour Excursion and Dinner*

Friday, May 17

All talks are in Memorial Union, 3d floor, Gallery Room

Chair: Dick Furnstahl

Keynote talk:	
8:30–9:15am	**Ruprecht Machleidt** Origin and Properties of Strong Inter-Nucleon Interactions
9:15–9:45am	**Evgeny Epelbaum** Nuclear Forces and Light Nuclei from Chiral Effective Field Theory
9:45–10:15am	**Robert Roth** New Horizons in *Ab Initio* Nuclear Structure Theory

10:15–10:45am	*Coffee break*

Chair: Petr Navrátil

10:45–11:15am	**Morten Hjorth-Jensen** Living on the Edge of Stability, the Limits of the Nuclear Landscape
11:15–11:45am	**Wayne Polyzou** Three Nucleon Scattering at Relativistic Energies
11:45–12:15pm	**Peter U. Sauer** Three-Nucleon Forces — Revisited

12:15–1:45pm	*Lunch break*

Chair: Wayne Polyzou

1:45–2:15pm	**Scott Bogner** Shell Model Interactions from the In-Medium Similarity Renormalization Group
2:15–2:45pm	**Dick Furnstahl** High-Resolution Probes of Low-Resolution Nuclei

2:45–3:15pm	*Coffee break*

Chair: Ruprecht Machleidt

3:15–4:00pm	**Bruce Barrett** Conference Summary
4:00pm	*Conference closing*

Contents

Distinguished Lecture of

Professor James P. Vary

Computational Nuclear Physics:
Key To Discovery Opportunities

presented on May 15, 2013 at International Conference

NUCLEAR THEORY
IN THE SUPERCOMPUTING ERA – 2013
(NTSE-2013)

Distinguished Lecture:

Computational Nuclear Physics: Key to Discovery Opportunities

James P. Vary

Department of Physics and Astronomy, Iowa State University, Ames, Iowa 50011, USA

Abstract

The vision of solving the nuclear many-body problem with fundamental interactions tied to QCD via Chiral Perturbation Theory appears to be gaining support. The goals are to preserve the predictive power of the underlying theory, to test fundamental symmetries with the nucleus as laboratory and to develop new understandings of the full range of complex nuclear phenomena. Advances in theoretical frameworks (renormalization and many-body methods) as well as in computational resources (new algorithms and leadership-class parallel computers) signal a new generation of theory and simulations that will yield profound insights into the origins of nuclear shell structure, collective phenomena and complex reaction dynamics. Fundamental discovery opportunities also exist in such areas as physics beyond the Standard Model of Elementary Particles, the transition between hadronic and quark-gluon dominated dynamics in nuclei and signals that characterize dark matter. I will review some recent achievements and present ambitious consensus plans along with their challenges for a coming decade of research that will build new links between theory, simulations and experiment.

Keywords: *Computational Physics, ab initio Nuclear Theory*

1 Introduction

Computational Physics has joined Theoretical and Experimental Physics to form a foundation that supports advances in Physics. According to the recent National Academy Report [1], "High Performance Computing provides answers to questions that neither experiment nor analytic theory can address; hence, it becomes the third leg supporting the field of nuclear physics."

Many of the forefront questions that we address in nuclear physics require advances in theory as well as advances in both computational algorithms and hardware to address. Here are some of my personal favorites for these questions.

1. What controls nuclear saturation?
2. How do the nuclear shell and collective models emerge from the underlying theory?
3. What are the properties of nuclei with extreme neutron/proton ratios?
4. Can we predict useful cross sections that cannot be measured?

Proceedings of International Conference 'Nuclear Theory in the Supercomputing Era — 2013' (NTSE-2013), Ames, IA, USA, May 13–17, 2013. Eds. A. M. Shirokov and A. I. Mazur. Pacific National University, Khabarovsk, Russia, 2014, p. 15.
http://www.ntse-2013.khb.ru/Proc/JPVary.pdf.

5. Can nuclei provide precision tests of the fundamental laws of nature?

6. Can we solve QCD to describe hadronic structures and interactions?

Before I delve into specific issues, let us address a general question: "What is Computational Physics?". I propose that Computational Physics is the field that takes a physics problem through the following stages leading to its solution.

1. Theoretical developments leading to the Problem Statement.

2. Computational hardware and resource assessments.

3. Algorithm developments and/or selections.

4. Software developments and/or selections including validation and verification.

5. Generation of results, analysis of the results and uncertainty quantification.

6. Conclusion with the problem's solution.

There are many prominent examples where computational nuclear physics has become a leading route to discovery. A few examples will suffice:

1. Core-collapse supernova simulation.

2. Hadronic structures and interactions from Lattice QCD.

3. Quark-gluon plasma simulations in Lattice QCD.

4. *Ab initio* nuclear structure and nuclear reactions.

5. Energy density functional simulation of neutron and proton drip lines.

6. Nuclear fission dynamics.

It may be useful to visualize the challenges we face from the long-term perspective of the overarching goal of nuclear physics which I posit as "If the Standard Model of Elementary Particles is correct, we should be able to accurately describe all nuclear processes." For our long-term goal, I propose that we aim to use all the fundamental interactions, including yet-to-be-discovered interactions, to construct a model for the evolution of the entire universe. In my view, the purpose of this international conference is to assess the current progress with theory and the associated supercomputer simulations that highlight our journey along this path.

Since my specific goal here is to address the question of the discovery potential using supercomputer simulations in nuclear theory, I will begin with my particular problem statement: solve the quantum many-body Hamiltonian with strong interactions. Here, I am including both the conventional non-relativistic nuclear many-body Hamiltonian formulation as well as the fully relativistic light-front Hamiltonian approach.

In order to provide one concrete set of examples, I show in Fig. 1 the projected goals of calculating the Nuclear Matrix Elements (NMEs) needed for interpreting experiments on neutrinoless double beta-decay. The goals are laid out along an axis of estimated computational resources needed to perform *ab initio* nuclear structure calculations that retain the predictive power of the underlying microscopic Hamiltonian. The need for reliable NMEs, free from phenomenology and associated uncertainties, to interpret the experimental data is well established [3].

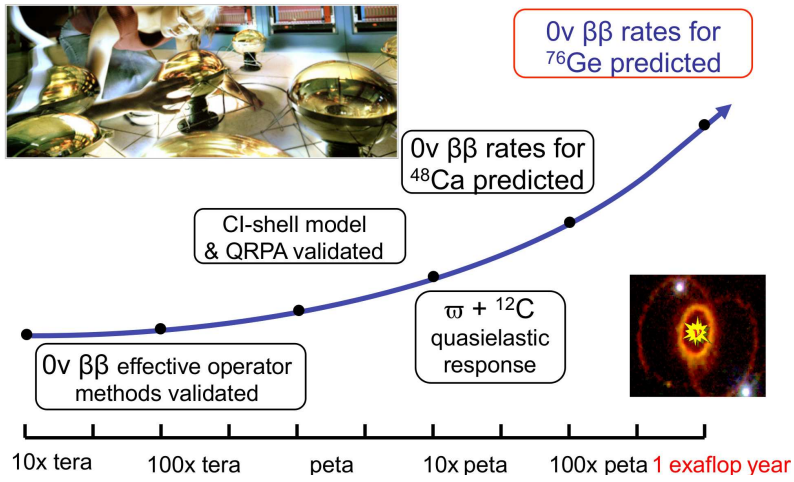

Figure 1: As more computational resources become available (horizontal axis in units of sustained flops × year) we anticipate the indicated research highlights will be achieved under the banner "Nuclei as neutrino physics laboratories" [2].

2 No Core Shell Model

The *ab initio* No Core Shell Model (NCSM) first appeared in Refs. [4,5] where realistic NN interactions, suitably renormalized to a finite Hamiltonian matrix in the harmonic oscillator (HO) basis, were employed to solve for the spectroscopy of ^{12}C in modest basis spaces that were nevertheless sufficient to demonstrate good convergence of the low-lying excitation spectra. Since that time, there has been rapid progress for increasing the basis space in order to address additional observables with increasing precision and to solve for the properties of a wide range of light nuclei. Recent progress has evolved along many semi-independent lines of research aimed at achieving improved accuracy and/or reducing the demands on computational resources.

Fig. 2 displays a snapshot of methods that have appeared that relate in some way

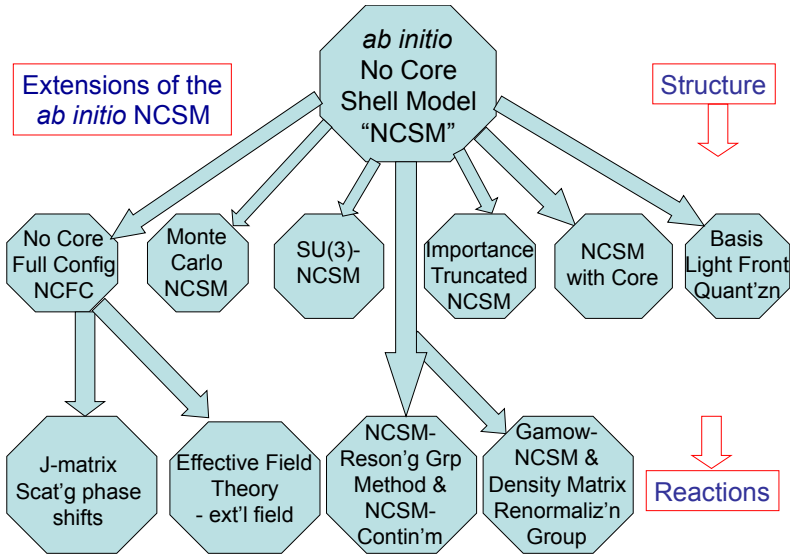

Figure 2: *Ab initio* No Core Shell Model with nuclear structure and nuclear reactions methods based on the NCSM [13]. See the text for additional details.

to the NCSM. At present, some address primarily nuclear structure applications while others address nuclear reactions. I will mention each with a short review.

Ref. [6] introduces the *ab initio* No Core Full Configuration (NCFC) method that adopts the given microscopic strong interaction suitable for an infinite basis space and performs a sequence of increasing finite basis space calculations. The NCFC then features an extrapolation to the infinite basis limit to arrive at the predicted spectra and observables. A significant success of this approach was the accurate prediction of the spectroscopy for the proton-unstable nucleus ^{14}F [7] which was later confirmed by an experiment at Texas A&M University [8]. For a recent review of applications to properties of p-shell see Ref. [9].

The Monte Carlo No Core Shell Model (MCSM) was recently introduced and benchmarked with the NCSM in Ref. [10]. The MCSM has advantageous scaling properties for solving heavier nuclei and is summarized by Abe at this conference [11]. To date, successful benchmark calculations have been performed for p-shell nuclei using the realistic NN interaction, JISP16 [12].

Light nuclei exhibit collective motion and this provides a challenge for the NCSM in a HO basis. This has motivated the development and application of the SU(3)-NCSM as summarized by Draayer [14] and by Dytrych [15] at this conference. In the SU(3)-NCSM one truncates the basis space by including only the leading irreducible representations of SU(3) that are motivated by the collective degrees of freedom dominating the low-lying eigenstates. This approach has led to successful *ab initio* descriptions of collective states in light nuclei with highly truncated basis spaces [16].

Roth and collaborators have introduced the Importance Truncated No Core Shell Model (IT-NCSM) in order to facilitate convergence by sampling larger basis spaces and retaining configurations making significant contributions to the low-lying eigenstates [17–19]. The prospects for this method are very strong and recent developments are presented by Roth at this meeting [20]

The drive to extend the *ab initio* NCSM to heavier nuclei has led to the development of a method that re-introduces the core in order to cut down on the basis space dimensions. Specifically, the *ab initio* Shell Model with a Core method [21, 22] carries out a second renormalization procedure to develop a valence-nucleon Hamiltonian suitable for solving nuclei beyond doubly-magic reference systems. The method is currently being developed for nuclei in the *sd*-shell [23].

Since these Hamiltonian many-body methods have shown great flexibility and applicability, it is natural to seek applications to subfields outside of nuclear structure and nuclear reactions. Not surprisingly, a parallel line of developments has emerged in Hamiltonian light-front field theory with a basis function approach. This has been termed Basis Light-Front Quantization (BLFQ) [24, 25] and several papers at this conference present results from this approach [26–28]. The central theme is that non-perturbative solutions of bound state and scattering problems are achievable in BLFQ and in a time-dependent BLFQ (tBLFQ) [29].

3 No Core Shell Model — applications to reactions

The *ab initio* theory of nuclear reactions has dramatically advanced in recent years based, in part, on the successes of the *ab initio* NCSM. Selected examples are listed on the bottom row of Fig. 2 showing their connections with related no-core structure methods. Space does not permit to review of additional *ab initio* reaction methods based on other *ab initio* structure methods such as the Green's Function Monte Carlo (GFMC) and Coupled Cluster (CC) methods.

The J-matrix inverse scattering approach has been introduced and employed with a HO basis representation to analyze scattering phase shifts and extract resonance

energies and widths from experimental data. One of the main advantages of the J-matrix formalism is that it provides eigenstates directly related to the eigenstates of the NCSM in a given model space and with a given value of the oscillator spacing. In Ref. [30] we discussed the J-matrix inverse scattering technique, extended it for the case of charged colliding particles, and applied it to the analysis of $n-\alpha$ and to $p-\alpha$ scattering. We then compared the J-matrix eigenvalues extracted from experimental phase shifts with the NCSM calculations of ^{5}He and ^{5}Li based on the JISP16 NN interaction and found a remarkably good correlation between J-matrix eigenstates and the NCSM eigenvalues. We anticipate that with improved Hamiltonians that more accurately predict binding energies, the NCSM eigenstates will become predictive components of scattering phase shifts within the J-matrix formalism.

By employing the techniques of EFT and confining our scattering problem to an external HO potential, we may extract the elastic scattering phase shifts as demonstrated in Ref. [31]. An analytic expression that relates the eigenvalues of two interacting particles confined by a HO potential to the scattering phase shift at those energies, analogous to "Lüscher's method" [32,33] allows one to extract the phase shift in the limit that the oscillator length is large compared to the range of nuclear forces. The requirements for demonstrating high accuracy with the NN phase shift application [31] suggests more work is needed to reduce the computational requirements for this method.

Major efforts are underway to develop and apply a hybrid NCSM and Resonating Group Method (RGM) approach called NCSM/RGM [34–36]. The aim is to simultaneously describe both bound and scattering states in light nuclei by combining these two approaches. The goal is to eventually achieve *ab initio* descriptions of scattering and reactions of two light nuclei with three-body breakup channels included [37].

Another major set of efforts aims to develop and apply the Gamow Shell Model (GSM) [38, 39] where a discretized representation of continuum single-particle states are included with conventional bound single-particle states in the many-body basis. The first *ab initio* no core Gamow Shell Model (NCGSM) application has recently appeared [40] and shows great promise for producing *ab initio* descriptions of resonances in light nuclei.

The field of *ab initio* nuclear reaction theory is emerging as a vibrant area of activity with many new ideas showing great promise. For example, direct calculation of microscopic reaction amplitudes in an extended NCSM approach is under intensive investigation [37, 41, 42].

4 Selection of recent results

Since this conference features many excellent talks presenting results from the theoretical approaches that I outlined above as well as from additional *ab initio* approaches, I will select a few examples to illustrate some recent results that complement those discussed by others. The results that I select use realistic interactions from chiral EFT and from inverse scattering.

However, before diving into these results it is also worthwhile to survey the landscape of the research closely related to the *ab initio* approaches, their goals and the computational issues associated with them. This is best illustrated in Fig. 3 that overviews the current research activities in the SciDAC-NUCLEI project [43], a set of collaborations among nuclear theorists, computational scientists and applied mathematicians supported by DOE. Clearly, there is a broad scope of linked research efforts depicted and that scope requires a large set of collaborative enterprises to be successful.

In a recent effort, we examined the properties on $A = 7$ and 8 nuclei in the NCSM [44]. We compared results with chiral NN interaction only [45, 46] and those with chiral NN+NNN interactions [47] (in the local form of Ref. [48]) using $N_{\max} = 8$

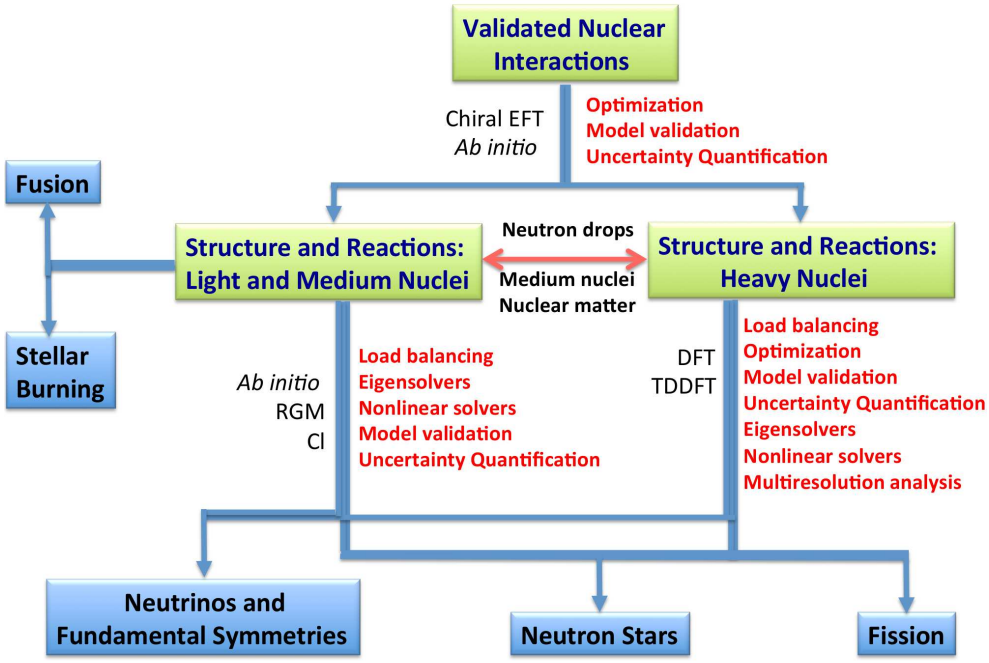

Figure 3: Overview of the workflow of the SciDAC-NUCLEI project [43]. The items in red identify computational and applied mathematics topics related to that particular branch of the workflow. Note that the links extend from fundamental interactions based on QCD at the top to large amplitude nuclear phenomena at the bottom and on the left.

basis spaces. Note that the chiral NN interaction is complete though N3LO while the chiral NNN interaction is complete through N2LO. These are the most advanced chiral interactions available at the present time.

We showed [44] that including the chiral EFT NNN interaction in the Hamiltonian improves overall agreement with experimental binding energies, excitation spectra, transitions and electromagnetic moments. We also predicted states that exhibit sensitivity to including the chiral EFT NNN interaction but are not yet known experimentally.

In order to soften the chiral interactions to render them suitable for the many-body basis spaces currently accessible, we adopted the Okubo–Lee–Suzuki (OLS) [49, 50] renormalization procedure. We review this and alternative renormalization procedures in detail in Ref. [13]. It is worth remarking that the OLS renormalization approach generates induced multi-nucleon interactions that are needed to preserve many-body unitarity. It is our practice to date to retain at most the induced NNN interactions along with the initial NNN interactions. That is, we ignore the induced $4N$ interactions as well as higher-body interactions. While all indirect signs (such as convergence trends) are encouraging, there is a definite need to further investigate this approximation in the future by retaining induced $4N$ interactions.

One should also note there are a number of additional freedoms in the OLS procedure [51, 52] as, indeed, there are in other renormalization procedures. First, there is the choice of the states from the full space calculations with non-vanishing components in the model space. This choice goes into the definition of the similarity transformation and is not unique. Second, there is the additional freedom of a unitary transformation of the resulting effective Hamiltonian within the model space [52]. Third, there is the freedom in the selection of an additional interaction to add and subtract at various stages of the solution of the decoupling equations. The second and third freedom are related. These freedoms remain as opportunities for future

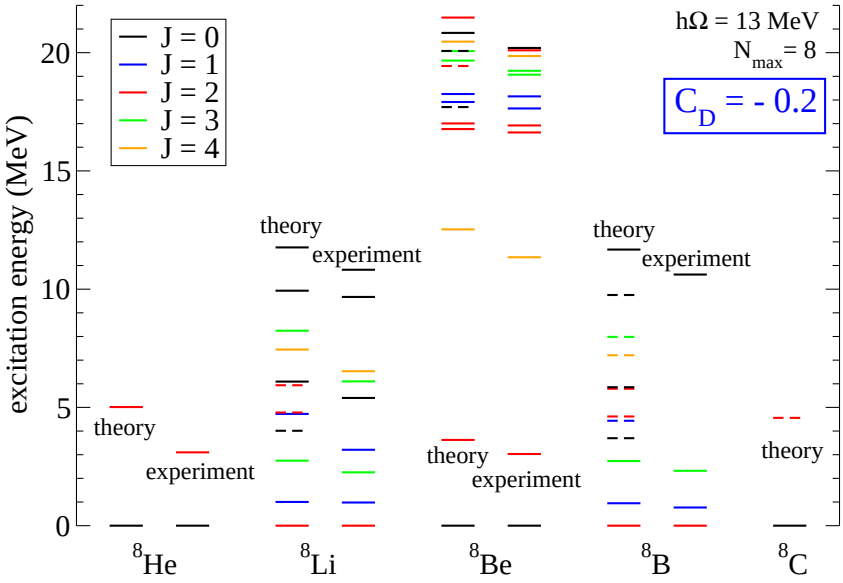

Figure 4: *Ab initio* No Core Shell Model results for $A = 8$ nuclei using chiral $NN + NNN$ interactions in an $N_{\max} = 8$ HO basis with HO energy $\hbar\Omega = 13$ MeV. The solid lines indicate states that are identified both in the theory and the experimental results. The dashed lines indicate additional states predicted by the theory. See the text and Ref. [44] for additional details.

investigations.

While the binding energies are generally close to agreement with experiment, it is easier to view the comparison between theoretical and experimental spectra by lining up the energies of the ground states and displaying just the excitation energies. Therefore, we show in Fig. 4 the excitation spectra of the $A = 8$ nuclei where we compare theory and experiment. For the chiral NNN interaction we adopt the low-energy constants (indicated by $c_D = -0.2$ on the figure) that are tuned to the binding energy and half-life of tritium [53]. The states predicted by the theory, for which there is no apparent experimental counterpart, appear as dashed lines in Fig. 4. Note that these states are in the continuum. We interpret the energies of these states as indications of the resonance widths but we are not able to predict the widths themselves at the present time. We expect that the predictions will be more accurate for the states with narrow widths. We plan to implement the continuum physics in the future and to predict the widths of states appearing above breakup threshold. Among the many options we are considering, several are well-represented here at this meeting [38–41, 54].

In another set of investigations, we have adopted the Similarity Renormalization Group (SRG) [55, 56] approach for decoupling the high momenta components of the inter-nucleon interactions from the low momenta components. As in the OLS renormalization approach mentioned above, this is intended to facilitate convergence of the *ab initio* many-body calculations at the "cost" of calculating induced multi-nucleon interactions and of requiring a corresponding treatment of other operators corresponding to observables that we intend to evaluate with the resulting *ab initio* wavefunctions. We have investigated the detailed predictions and the convergence properties of no-core full configuration calculations with SRG-evolved interactions in p-shell nuclei over a wide range of softening [57, 58]. The dependence on the degree of softening (the SRG resolution scale) allows us to assess convergence properties, to investigate extrapolation techniques, and to infer the role of neglected induced higher-body contributions.

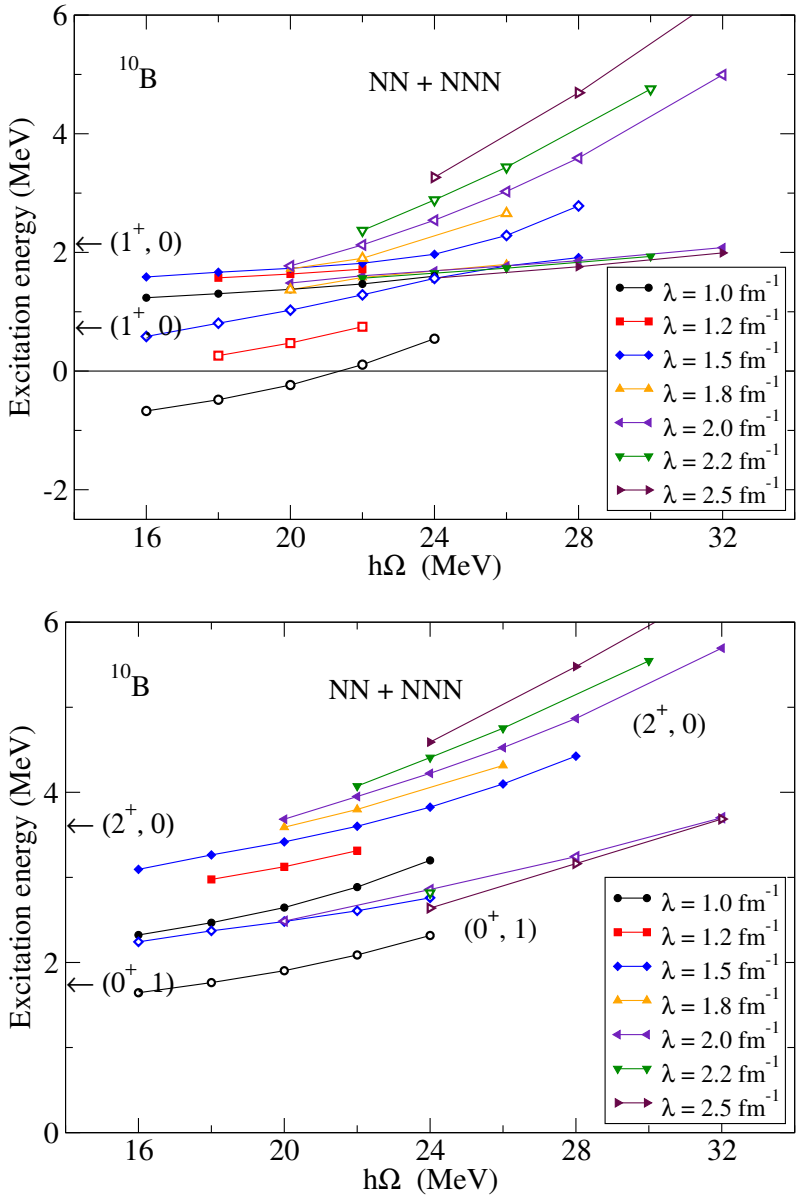

Figure 5: Lowest excited states of ^{10}B as a function of $\hbar\Omega$ for each SRG λ value at $N_{\max} = 8$. The small black arrows on the left shows the experimental values. Each color and shape of the symbol represents a value of λ as defined in the legend. Two excited states are shown in each panel, one with an open symbol and the other with a closed symbol. See Ref. [58] for additional details.

Here, we use the same chiral $NN + NNN$ interaction as in the applications to $A = 7$ and 8 nuclei discussed above using the OLS renormalization. In this case, we are using SRG with a range of evolution scales, λ from 2.5 fm^{-1} down to 1.0 fm^{-1}. This evolution scale dictates the approximate range of momentum transfer retained in the NN T-matrix while preserving the on-shell phase shifts. Generally speaking, we expect induced NNN interactions to increase as we decrease λ. Experience with these chiral $NN+NNN$ interactions indicates non-trivial induced NNN interaction contributions even with $\lambda = 2.5$ fm^{-1}.

Once we adopt the approximation to retain the induced NNN interactions but

to neglect induced $4N$ interactions, it is natural to retain the "bare" chiral NNN interaction defined by the underlying chiral EFT. Figure 5 presents a sample of excited states in ^{10}B relative to the lowest calculated $(3^+, 0)$ state which is the experimental ground state. Note that the ground state spin for ^{10}B has become a highly-cited example of an observable that is sensitive to the inclusion of NNN interactions [59]. Realistic NN interactions, without NNN interactions, tend to predict a ground state spin of $(1^+, 0)$. We see in the upper panel of Fig. 5 that the correct ground state spin is obtained, within the results shown, for all but one value of the SRG λ scale parameter over the range of $\hbar\Omega$ depicted. The spread in the predictions as a function of λ and the dependence on $\hbar\Omega$ are indicators of the role of neglected induced $4N$ and/or higher-body interactions. Thus, with these $N_{\max} = 8$ results in the SRG treatment, it is not reliably established that the NNN interactions produce the correct ground state spin of ^{10}B. Clearly more work is needed to include the induced $4N$ interactions which we expect to produce stronger indication of the fully converged result.

Another feature evident in the upper panel of Fig. 5 is the difference in the trends of two states with the same spin and parity $(1^+, 0)$ in ^{10}B. One state appears to be better converged than the other — that is less reliant on induced 4-body interactions and/or basis space increases. This indicates that these two states have very different structure. A more detailed analysis is needed to disentangle those differences. For example, future work may reveal that the "spin content" of these two states, when decomposed into neutron and proton spin and orbital components as in Ref. [9] for other states in other systems, is distinctively different.

The lower panel of Fig. 5 displays the excitation energy of the $(0^+, 1)$ and $(2^+, 0)$ states compared with experiment. The former appears to be less sensitive to the SRG λ scale parameter, indicating less sensitivity to neglected induced $4N$ interactions. Both states reveal approximately the same dependence on the basis $\hbar\Omega$ indicating approximately the same level of convergence with increasing basis space cutoff $N_{\max}$.

The residual discrepancies between theory based on chiral EFT and experiment, as seen in the results presented here as well as many other results presented at this meeting, are indicators of shortcomings of the present chiral EFT interactions. At present, we use chiral NNN interactions only at N2LO while the NN interactions are at the level of N3LO, which was found important for an accurate description of the NN phase shift data. Thus, we will have consistency once we include the chiral NNN interaction itself at N3LO so that it is at the same order of chiral perturbation theory as the NN interaction. In this context, it is worth noting the large-scale international efforts that are underway to develop and apply these next-generation chiral EFT interactions [60]. Here again, a workflow diagram (see Fig. 6 is useful to illustrate the complexity and diversity of such a project. This workflow indicates the multifaceted challenges and the need for bringing the expertise of many groups into the project to achieve the project goals.

In closing this section with a sample of recent results that help indicate future directions, I will briefly discuss the challenges of clustering phenomena in light nuclei. These phenomena are a particular challenge to the *ab initio* NCSM since clustering implies intermediate range correlations which require large HO basis spaces for accurate descriptions [61,62]. For the Hoyle state, the $(0^+, 0)$ state at 7.66 MeV excitation energy in ^{12}C which is just above the threshold for breakup into three alpha particles, the predominant thinking is that it is dominated by a three-alpha cluster and is the leading resonance for ^{12}C production in astrophysical settings. Many cluster-based models provide successful descriptions of the Hoyle state with the three-alpha configuration. Currently, our hope for extending the *ab initio* NCSM within the HO basis to describe cluster states, like the Hoyle state, is to adopt the SA-NCSM or the MC-NCSM approach discussed above.

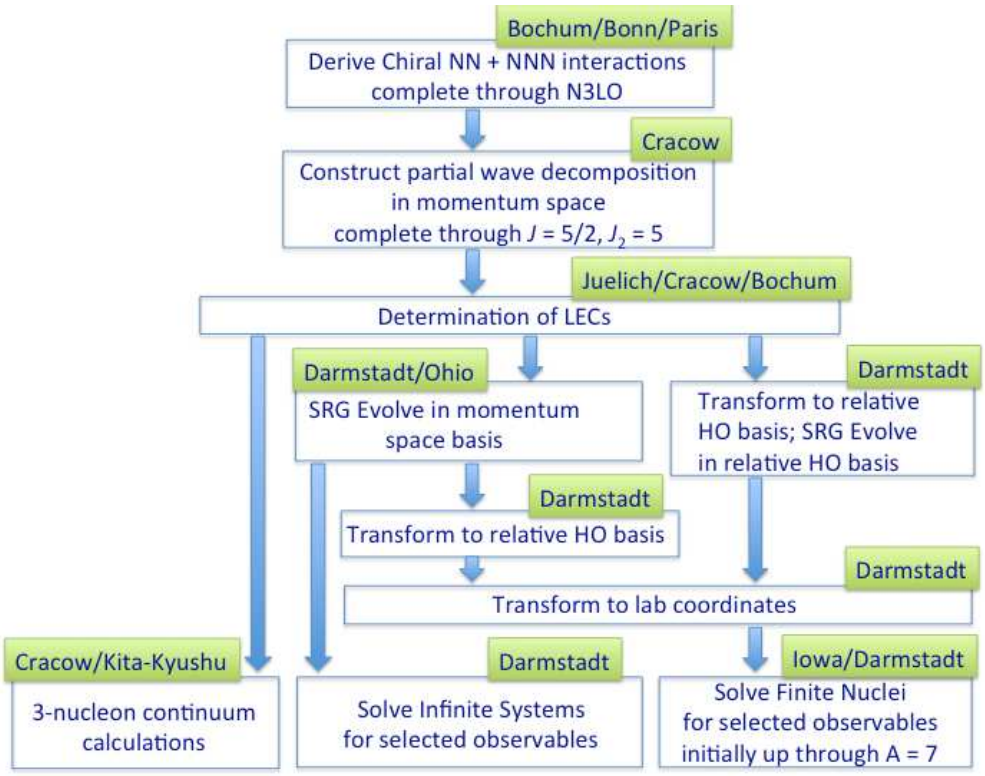

Figure 6: Workflow for the Low Energy Nuclear Physics International Collaboration (LENPIC) showing the development and implementation of the next-generation chiral EFT interactions complete and consistent through Next-to-Next-to-Next-to Leading Order (N3LO). See the text and Ref. [60] for additional details.

5 Reaching for the infinite basis limit

There has been intense recent activity addressing the convergence properties of *ab initio* no-core approaches [63–68]. Clearly, understanding the convergence properties will help us predict results with greater precision using the available computational resources and will help us quantify the uncertainties in these predictions.

While most of this research has focused on extrapolating the ground state energy obtained in a no-core approach within the HO basis to the infinite basis limit, there is also considerable progress in understanding the convergence properties of the root-mean-square (rms) radius. Electromagnetic matrix elements are of particular interest since they are challenging to describe in the HO basis as they are, typically, long-range operators that are sensitive to the asymptotic properties of the nuclear wavefunction. For this reason, the rms radius has served as the initial testing ground for the long-range electromagnetic operators.

For the ground state energy, a simple exponential in $N_{\max}$ at fixed $\hbar\Omega$ has proven to be a useful extrapolation tool [6, 58, 69]. Current thinking implies this is a useful phenomenological extrapolation tool for the ultraviolet (UV) properties but a different functional form, a simple exponential in $\sqrt{N_{\max}}$ is theoretically supported for the infrared (IR) properties [65]. The physical argument for the IR behavior of the wavefunction is appealing — we know from elementary quantum mechanics that the long-range tail of a single-particle wavefunction for a bound state in a finite potential well has an exponential form with a decay constant dictated by the binding energy. The step to the many-body problem involves examining the highest HO single-particle state in the basis and identifying the appropriate exponential tail for that state as it

will dominate the longest range component of the many-body wavefunction. Following, the *ab initio* results through a sequence of many-body cutoffs (i. e. systematically raising the highest HO single-particle state in the basis) allows one to optimize the choice of the constants that go with this exponential in $\sqrt{N_{\max}}$

Let us examine the case of the ground state energy of ^{6}Li calculated in the *ab initio* NCSM with the bare JISP16 interaction [12] as a function of the many-body cutoff $N_{\max}$. This same case was examined in some detail in Refs. [6, 70] and a recent extrapolation has been presented in Ref. [9]. Each of these papers extends the preceding paper either with results calculated at higher $N_{\max}$ values to reduce the uncertainties or with improvements in the uncertainty estimation procedure. Each uses the simple exponential in $N_{\max}$ (i. e. phenomenological form alone) for the fit function. The results are consistent with each other — that is the fall within each others' uncertainty estimates: -31.45 ± 0.05 MeV in Ref. [6] with the maximum $N_{\max} = 14$; -31.49 ± 0.03 MeV in Ref. [70] with the maximum $N_{\max} = 16$; -31.49 ± 0.06 MeV in Ref. [9] with the maximum $N_{\max} = 16$. Note that the experimental ground state energy is -31.994 MeV so JISP16 is clearly underbinding this nucleus by about 0.5 MeV.

A new set of calculations is underway to extend the calculated results to $N_{\max} = 18$ and to further improve the extrapolation procedure by combining both a phenomenological function for the UV and the derived function for the IR. In addition to the ground state energy, extrapolations of the rms radii will be included. The aim is to further reduce the quantified uncertainties by relying on additional theoretical input.

Figure 7 provides an indicator of recent progress in the research on extrapolation methods. Here, I am following the line of developments introduced as "Extrapolation A" in Ref. [6]. In this approach, one identifies the minimum in the ground state energy as a function of $\hbar\Omega$ for each $N_{\max}$ beginning with $N_{\max} = 8$ where one works with increments of 2.5 MeV in $\hbar\Omega$. Then one uses the the 5 consecutive data sets spanning 10 MeV in $\hbar\Omega$ that begin with the $\hbar\Omega$ value below that minimum and extend

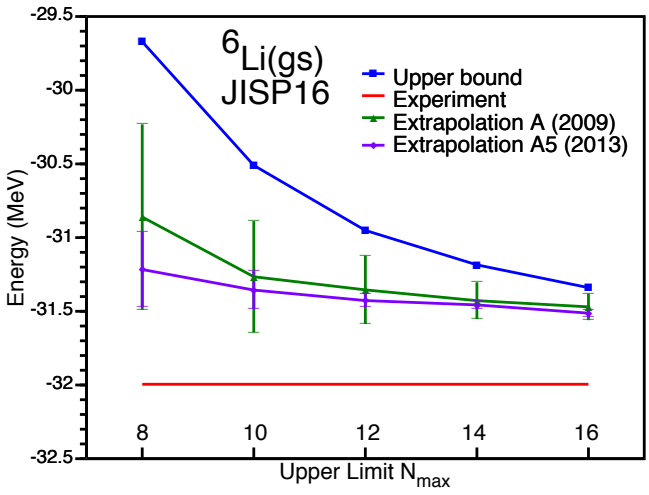

Figure 7: Extrapolations of the *ab initio* No Core Shell Model ground state energy for ^{6}Li using the JISP16 NN interaction [12] as a function of the upper limit on the $N_{\max}$ cutoff of the energies used in the extrapolation. "Extrapolation A (2009)" is the quantity E_∞ from Eq. (1) as reported in Ref. [6]. "Extrapolation A5 (2013)" employs an improved UV + IR functional form using 5 free parameters that is under development. For reference, the variational upper bound (minimum in the ground state energy as a function of $\hbar\Omega$) is shown for each $N_{\max}$ providing a sense of the magnitude of the extrapolation. The A5 extrapolation is -31.51 ± 0.03 MeV at $N_{\max} = 16$. See the text for additional details.

to larger values of $\hbar\Omega$. Results at the 3 increments in $N_{\rm max}$ below that upper limit in $N_{\rm max}$ are also included yielding a total of 20 calculated ground state energies (4 $N_{\rm max}$ values and 5 $\hbar\Omega$ values) for determining the 3 fit parameters of the function:

$$E(N_{\rm max}) = E_\infty + a\exp(-bN_{\rm max}). \quad (1)$$

For Extrapolation A, one then uses Eq. (1) to fit the 4 ground state energies at each of the 5 $\hbar\Omega$ values separately. This determines a spread of the values of E_∞ and half of that spread is defined as the uncertainty in the Extrapolation A result at that upper limit in $N_{\rm max}$. This procedure was tested extensively with JISP16 results for ground state energies of light nuclei and the evaluated uncertainties were found to be consistent with each other with increasing upper limit in $N_{\rm max}$ [6]. This is seen in Fig. 7 by the overlapping error bars of the Extrapolation A points.

Extrapolation A5 builds on the experience with Extrapolation A and includes an additional term to better simulate the IR behavior as motivated by the developments of Refs. [63, 65, 67]. That is, I adopt a 5 parameter function which, for sufficiently large $N_{\rm max}$ can be represented by:

$$E(N_{\rm max}) = E_\infty + a\exp(-bN_{\rm max}) + c\exp\Big(-b\sqrt{N_{\rm max}}\Big). \quad (2)$$

The detailed functional form of the IR term added in Eq. (2) $\Big[\exp\Big(-b\sqrt{N_{\rm max}}\Big)\Big]$ is more involved since it closely follows the forms advocated in Ref. [67]. However, the difference effects mainly the behavior at lower $N_{\rm max}$ and I use Eq. (2) to indicate the primary dependence at large $N_{\rm max}$.

Since two more parameters must now be determined, the procedure defined in Ref. [6] is further extended in several ways. First, I include 5 sets of $N_{\rm max}$ at each of 5 $\hbar\Omega$ values. The range of the $\hbar\Omega$ values is shifted upwards by +5 MeV compared to Extrapolation A as this was found to produce more reliable in tests with ground state energy results in ^{4}He. The need for 5 sets of $N_{\rm max}$ values is clear in order to adequately determine the spread in a manner analogous to the spread determination in Extrapolation A. The data point for Extrapolation A5 at the upper limit $N_{\rm max} = 8$ is a special case as I continue the practice of omitting the $N_{\rm max} = 0$ calculated ground state energies in the fits. For $N_{\rm max} = 8$, the total data set is then only 20 calculated points. The uncertainty assigned to the data point at the upper limit $N_{\rm max} = 8$ for Extrapolation A5 is simply taken to be twice the uncertainty calculated for the next higher data point in Fig. 7.

Note that Extrapolation A and Extrapolation A5 produce results that are consistent with each other — that is they fall within each others' uncertainties. However, both Extrapolation A and Extrapolation A5 produce a noticeable downward drift in the values of E_∞ with increasing upper limit in $N_{\rm max}$. This indicates the need for additional research to develop improved extrapolation forms and procedures.

6 Conclusion and Outlook

Computational physics and forefront simulations have developed rapidly to become one of the key areas of research in nuclear physics, approaching a par with experiment and theory. Many breakthroughs in our understanding of fundamental nuclear processes have emerged from recent advances and any listing would not do justice to the field. In fact, I have generated with the help of colleagues, a list of more than 90 Physical Review Letters to date that have focused on *ab initio* nuclear structure and nuclear reactions. Many of these are joint experiment and theory letters. Therefore, I will simply select examples that specifically focus on the developing bridge provided by chiral EFT between QCD and low-energy nuclear properties. Each of these achievements, indicated in the title, is the focus of a Physical Review Letter that appears below in a chronological sequence.

1. "The three nucleon and four nucleon systems from chiral effective field theory" [71].
2. "Structure of $A = 10-13$ nuclei with two plus three-nucleon interactions from chiral effective field theory" [59].
3. "*Ab Initio* many-body calculations of n-^{3}H, n-^{4}He, p-^{3,4}He, and n-^{10}Be scattering" [34].
4. "Medium-mass nuclei from chiral nucleon-nucleon interactions" [72].
5. "Evolution of nuclear many-body forces with the Similarity Renormalization Group" [73].
6. "Three-nucleon low-energy constants from the consistency of interactions and currents in Chiral Effective Field Theory" [53].
7. "Ground-state and single-particle energies of nuclei around ^{16}O, ^{40}Ca, and ^{56}Ni from realistic nucleon-nucleon forces" [74].
8. "Role of long-range correlations on the quenching of spectroscopic factors" [75].
9. "Lattice effective field theory calculations for $A = 3$, 4, 6, 12 nuclei" [76].
10. "*Ab initio* computation of the ^{17}F proton halo state and resonances in $A = 17$ nuclei" [77].
11. "Constraints on neutron star radii based on chiral effective field theory interactions" [78].
12. "Thermal neutron captures on d and ^{3}He" [79].
13. "*Ab initio* calculation of the Hoyle state" [80].
14. "Origin of the anomalous long lifetime of ^{14}C" [81].
15. "In-medium Similarity Renormalization Group for open-shell nuclei" [82].
16. "Quenching of spectroscopic factors for proton removal in oxygen isotopes" [83].
17. "Similarity-transformed chiral NN+3N Interactions for the *ab initio* description of ^{12}C and ^{16}O" [84].
18. "Measurements of the differential cross sections for the elastic n-^{3}H and n-^{2}H scattering at 14.1 MeV by using an inertial confinement fusion facility" [85].
19. "Chiral two-body currents in nuclei: Gamow–Teller transitions and neutrinoless double-beta decay" [86].
20. "*Ab initio* many-body calculations of the ^{3}H$(d, n)^4$He and ^{3}He$(d, p)^4$He fusion" [87].
21. "First direct mass measurement of the two-neutron halo nucleus ^{6}He and improved mass for the four-neutron halo ^{8}He" [88].
22. "Continuum effects and three-nucleon forces in neutron-rich oxygen isotopes" [89].
23. "Evolution of shell structure in neutron-rich calcium isotopes" [90].
24. "New precision mass measurements of neutron-rich calcium and potassium isotopes and three-nucleon forces" [91].
25. "Medium-mass nuclei with normal-ordered chiral $NN + 3N$ interactions" [92].

26. "Structure and rotations of the Hoyle state" [93].

27. "Three-body forces and proton-rich nuclei" [94].

28. "*Ab initio* description of the exotic unbound ^{7}He nucleus" [95].

29. "Neutron matter at next-to-next-to-next-to-leading order in chiral effective field theory" [96].

30. "Spectroscopy of ^{26}F to probe proton-neutron forces close to the drip line" [97].

31. "The isoscalar monopole resonance of the alpha particle: a prism to nuclear Hamiltonians" [98].

32. "Viability of carbon-based life as a function of the light quark mass" [99].

33. "An optimized chiral nucleon-nucleon interaction at next-to-next-to-leading order" [100].

34. "*Ab initio* calculations of even oxygen isotopes with chiral two- plus three-nucleon interactions" [101].

35. "Quantum Monte Carlo calculations with chiral effective field theory interactions" [102].

36. "Isotopic chains around oxygen from evolved chiral two- and three-nucleon interactions" [103].

37. "First principles description of the giant dipole resonance in ^{16}O" [104].

These are indicators of a broader set of recent achievements that portend the discovery opportunities in computational nuclear physics. Continued close collaboration among nuclear theorists, computational scientists and applied mathematicians will be essential to fully exploit the potential of the rapid growth in computational resources. These collaborations are critical to devising new algorithms and their efficient realizations in order to generate and capitalize upon the full discovery potential. Further close collaboration with experimentalists is needed to fully exploit the predictive power that is emerging along with the opening of new frontier experimental facilities in order to devise and plan critical tests of the theoretical foundations. Joint planning activities will be valuable to efficiently utilize personnel, computational resources and experimental facilities in order to maximize the discovery potential of the field.

I am grateful to my collaborators for discussions and for the joint research accomplishments summarized here. This work was supported in part by the Department of Energy (DOE) under Grant Nos. DE-FG02-87ER40371 and DESC0008485 (SciDAC-3/NUCLEI) and by the National Science Foundation under Grant No. PHY-0904782. Computational resources were provided by the National Energy Research Supercomputer Center (NERSC), which is supported by the Office of Science of the U.S. Department of Energy under Contract No. DEAC02-05CH11231, and by the Oak Ridge Leadership Computing Facility at the Oak Ridge National Laboratory, which is supported by the Office of Science of the U.S. Department of Energy under Contract No. DE-AC05-00OR22725. Additional computational resources were provided by the Argonne Leadership Computing Facility at ANL, which is supported by the DOE Office of Science under Contract DE-AC02-06CH11357. Allocations at the DOE Leadership-class facilities (Argonne and Oak Ridge facilities) is provided by a DOE INCITE award. Finally, I am very grateful to all of you who have organized and/or attended this meeting and for you many generous remarks and warm wishes.

References

[1] *Nuclear physics: Exploring the heart of matter*. National Research Council, National Acad. Sci. Report, 2012, http://www.nap.edu/catalog.php?record_id=13438.

[2] *Scientific grand challenges: Forefront questions in nuclear science and the role of computing at the extreme scale*. Report from the Workshop held January 26–28, 2009, Washington, D.C. U.S. Department of Energy, 2009, http://extremecomputing.labworks.org/nuclearphysics/report.stm.

[3] S. R. Elliott and P. Vogel, Ann. Rev. Nucl. Part. Sci. **52**, 115 (2002), hep-ph/0202264 (2002).

[4] P. Navrátil, J. P. Vary and B. R. Barrett, Phys. Rev. Lett. **84**, 5728 (2000), nucl-th/0004058 (2000).

[5] P. Navrátil, J. P. Vary and B. R. Barrett, Phys. Rev. C **62**, 054311 (2000).

[6] P. Maris, J. P. Vary and A. M. Shirokov, Phys. Rev. C **79**, 014308 (2009), arXiv: 0808.3420 [nucl-th] (2008).

[7] P. Maris, A. M. Shirokov and J. P. Vary, Phys. Rev. C **81**, 021301 (2010), arXiv: 0911.2281 [nucl-th] (2009).

[8] V. Z. Goldberg, B. T. Roeder, G. V. Rogachev, G. G. Chubarian, E. D. Johnson, C. Fu, A. A. Alharbi, M. L. Avila, A. Banu, M. McCleskey, J. P. Mitchell, E. Simmons, G. Tabacaru, L. Trache and R. E. Tribble, Phys. Lett. B **692**, 307 (2010).

[9] P. Maris and J. P. Vary, Int. J. Mod. Phys. E **22**, 1330016 (2013).

[10] T. Abe, P. Maris, T. Otsuka, N. Shimizu, Y. Utsuno and J. P. Vary, Phys. Rev. C **86**, 054301 (2012), arXiv:1204.1755 [nucl-th] (2012).

[11] T. Abe, P. Maris, T. Otsuka, N. Shimizu, Y. Tsunoda, Y. Utsuno and J. P. Vary, *see these Proceedings*, p. 294, http://www.ntse-2013.khb.ru/Proc/Abe.pdf.

[12] A. M. Shirokov, J. P. Vary, A. I. Mazur and T. A. Weber, Phys. Lett. B **644**, 33 (2007).

[13] B. R. Barrett, P. Navratil and J. P. Vary, Progr. Part. Nucl. Phys. **69**, 131 (2013).

[14] J. P. Draayer, T. Dytrych, K. D. Launey, A. C. Dreyfuss, M. C. Ferriss, G. K. Tobin, F. Pan and X. Guan, *see these Proceedings*, p. 47, http://www.ntse-2013.khb.ru/Proc/Draayer.pdf.

[15] T. Dytrych, J. P. Draayer, K. D. Launey, P. Maris, J. P. Vary and D. Langr, *see these Proceedings*, p. 62, http://www.ntse-2013.khb.ru/Proc/Dytrych.pdf.

[16] T. Dytrych, K. D. Launey, J. P. Draayer, P. Maris, J. P. Vary, E. Saule, U. Catalyurek, M. Sosonkina, D. Langr and M. A. Caprio, Phys. Rev. Lett. **111**, 252501 (2013), arXiv:1312.0969 [nucl-th] (2013).

[17] R. Roth and P. Navrátil, Phys. Rev. Lett. **99**, 092501 (2007), arXiv:0705.4069 [nucl-th] (2007).

[18] R. Roth, Phys. Rev. C **79**, 064324 (2009), arXiv:0903.4605 [nucl-th] (2009).

[19] M. K. G. Kruse, Ph.D. Dissertation (*unpublished*) (2012), http://gradworks.umi.com/35/05/3505985.html; *private communication* (2012).

[20] R. Roth, talk at *the Int. Conf. Nucl. Theory in Supercomputing Era — 2013 (NTSE-2013).*

[21] A. F. Lisetskiy, M. K. G. Kruse, B. R. Barrett, P. Navrátil, I. Stetcu and J. P. Vary, Phys. Rev. C **80**, 024315 (2009), arXiv:0906.2829 [nucl-th] (2009).

[22] A. F. Lisetskiy, B. R. Barrett, M. K. G. Kruse, P. Navrátil, I. Stetcu and J. P. Vary, Phys. Rev. C **78**, 044302 (2008), arXiv:0808.2187 [nucl-th] (2008).

[23] E. Dikman, A. F. Lisetskiy, B. R. Barrett, P. Maris, A. M. Shirokov and J. P. Vary, *Ab initio effective interactions for sd-shell valence nucleons* (*in preparation*).

[24] J. P. Vary, H. Honkanen, J. Li, P. Maris, S. J. Brodsky, A. Harindranath, G. F. de Teramond, P. Sternberg, E. G. Ng and C. Yang, Phys. Rev. C **81**, 035205 (2010), arXiv:0905.1411 [nucl-th] (2009).

[25] H. Honkanen, P. Maris, J. P. Vary and S. J. Brodsky, Phys. Rev. Lett. **106**, 061603 (2011), arXiv:1008.0068 [hep-ph] (2010).

[26] Y. Li, P. W. Wiecki, X. Zhao, P. Maris and J. P. Vary, *see these Proceedings*, p. 136, http://www.ntse-2013.khb.ru/Proc/YLi.pdf.

[27] P. Wiecki, Y. Li, X. Zhao, P. Maris and James P. Vary, *see these Proceedings*, p. 146, http://www.ntse-2013.khb.ru/Proc/Wiecki.pdf.

[28] X. Zhao, A. Ilderton, P. Maris and J. P. Vary, *see these Proceedings*, p. 204, http://www.ntse-2013.khb.ru/Proc/Zhao.pdf.

[29] X. Zhao, A. Ilderton, P. Maris and J. P. Vary, Phys. Rev. D **88**, 065014 (2013), arXiv:1303.3273 [nucl-th] (2013).

[30] A. M. Shirokov, A. I. Mazur, J. P. Vary and E. A. Mazur, Phys. Rev. C **79**, 014610 (2009), arXiv:0806.4018 [nucl-th] (2008).

[31] T. Luu, M. J. Savage, A. Schwenk and J. P. Vary, Phys. Rev. C **82**, 034003 (2010), arXiv:1006.0427 [nucl-th] (2010).

[32] M. Lüscher, Commun. Math. Phys. **105**, 153 (1986).

[33] M. Lüscher, Nucl. Phys. B **354**, 531 (1991).

[34] S. Quaglioni and P. Navrátil, Phys. Rev. Lett. **101**, 092501 (2008), arXiv: 0804.1560 [nucl-th] (2008).

[35] S. Quaglioni and P. Navrátil, Phys. Rev. C **79**, 044606 (2009), arXiv:0901.0950 [nucl-th] (2009).

[36] P. Navratil and S. Quaglioni, Phys. Rev. C **83**, 044609 (2011), arXiv:1102.2042 [nucl-th] (2011).

[37] P. Navratil, *see these Proceedings*, p. 211, http://www.ntse-2013.khb.ru/Proc/Navratil.pdf.

[38] J. Rotureau, N. Michel, W. Nazarewicz, M. Ploszajczak and J. Dukelsky, Phys. Rev. Lett. **97**, 110603 (2006), nucl-th/0603021 (2006).

[39] J. Rotureau, *see these Proceedings*, p. 236, http://www.ntse-2013.khb.ru/Proc/Rotureau.pdf.

[40] G. Papadimitriou, J. Rotureau, N. Michel, M. Ploszajczak and B. R. Barrett, Phys. Rev. C (*in press*), arXiv:1301.7140 [nucl-th] (2013).

[41] A. M. Shirokov, in *Proc. Int. Workshop Nucl. Theor. Supercomputing Era (NTSE-2012), Khabarovsk, Russia, June 18–22, 2012*, eds. A. M. Shirokov and A. I. Mazur. Pacific National University, Khabarovsk, 2013, p. 113.

[42] A. M. Shirokov, A. I. Mazur, J. P. Vary and I. A. Mazur, J. Phys. Conf. Ser. **403**, 012021 (2012).

[43] This project is described in the web pages at http://nuclei.mps.ohio-state.edu/.

[44] P. Maris, J. P. Vary and P. Navratil, Phys. Rev. C **87**, 014327 (2013), arXiv: 1205.5686 [nucl-th] (2012).

[45] D. R. Entem and R. Machleidt, Phys. Rev. C **68**, 041001 (2003), nucl-th/0304018 (2003).

[46] R. Machleidt and D. R. Entem, Phys. Rept. **503**, 1 (2011), arXiv:1105.2919 [nucl-th] (2011).

[47] E. Epelbaum, A. Nogga, W. Glöckle, H. Kamada, U. G. Meißner and H. Witała, Phys. Rev. C **66**, 064001 (2002), nucl-th/0208023 (2002).

[48] P. Navrátil, Few-Body Syst. **41**, 117 (2007).

[49] S. Okubo, Progr. Theor. Phys. **12**, 603 (1954).

[50] K. Suzuki and S. Y. Lee, Progr. Theor. Phys. **64**, 2091 (1980).

[51] C. P. Viazminsky and J. P. Vary, J. Math. Phys. **42**, 2055 (2001).

[52] A. G. Negoita, J. P. Vary and S. Stoica, J. Phys. G **37**, 055109 (2010), arXiv: 1003.3428 [nucl-th] (2010).

[53] D. Gazit, S. Quaglioni and P. Navrátil, Phys. Rev. Lett. **103**, 102502 (2009), arXiv:0812.4444 [nucl-th] (2008).

[54] A. M. Shirokov, talk at *the Int. Conf. Nucl. Theory in Supercomputing Era — 2013 (NTSE-2013).*

[55] S. D. Glazek and K. G. Wilson, Phys. Rev. D **48**, 5863 (1993).

[56] F. Wegner, Ann. Phys. (NY) **506**, 77 (1994).

[57] S. K. Bogner, R. J. Furnstahl, P. Maris, R. J. Perry, A. Schwenk and J. P. Vary, Nucl. Phys. A **801**, 21 (2008), arXiv:0708.3754 [nucl-th] (2007).

[58] E. D. Jurgenson, P. Maris, R. J. Furnstahl, P. Navratil, W. E. Ormand and J. P. Vary, Phys. Rev. C **87**, 054312 (2013), arXiv:1302.5473 [nucl-th] (2013).

[59] P. Navrátil, V. G. Gueorguiev, J. P. Vary, W. E. Ormand and A. Nogga, Phys. Rev. Lett. **99**, 042501 (2007), nucl-th/0701038 (2007).

[60] Low-Energy Nuclear Physics International Collaboration (LENPIC); http://www.lenpic.org

[61] M. Chernykh, H. Feldmeier, T. Neff, P. von Neumann-Cosel and A. Richter, Phys. Rev. Lett. **98**, 032501 (2007).

[62] T. Neff, J. Phys. Conf. Ser. **403**, 012028 (2012), arXiv:1210.4093 [nucl-th] (2012).

[63] S. A. Coon, M. I. Avetian, M. K. G. Kruse, U. van Kolck, P. Maris and J. P. Vary, Phys. Rev. C **86**, 054002 (2012), arXiv:1205.3230 [nucl-th] (2012).

[64] S. A. Coon and M. K. G. Kruse, *see these Proceedings*, p. 314, http://www.ntse-2013.khb.ru/Proc/Coon.pdf.

[65] R. J. Furnstahl, G. Hagen and T. Papenbrock, Phys. Rev. C **86**, 031301 (2012), arXiv:1207.6100 [nucl-th] (2012).

[66] R. J. Furnstahl, *see these Proceedings*, p. 371, http://www.ntse-2013.khb.ru/Proc/Furnstahl.pdf.

[67] S. N. More, A. Ekstrom, R. J. Furnstahl, G. Hagen and T. Papenbrock, Phys. Rev. C **87**, 044326 (2013), arXiv:1302.3815 [nucl-th] (2013).

[68] T. Papenbrock, talk at *the Int. Conf. Nucl. Theory in Supercomputing Era — 2013 (NTSE-2013).*

[69] C. Forssén, J. P. Vary, E. Caurier and P. Navrátil, Phys. Rev. C **77**, 024301 (2008), arXiv:0802.1611 [nucl-th] (2008).

[70] C. Cockrell, J. P. Vary and P. Maris, Phys. Rev. C **86**, 034325 (2012), arXiv: 1201.0724 [nucl-th] (2012).

[71] E. Epelbaum, H. Kamada, A. Nogga, H. Witała, W. Glöckle and U.-G. Meißner, Phys. Rev. Lett. **86**, 4787 (2001), nucl-th/0007057 (2000).

[72] G. Hagen, T. Papenbrock, D. J. Dean and M. Hjorth-Jensen, Phys. Rev. Lett. **101**, 092502 (2008), arXiv:0806.3478 [nucl-th] (2008).

[73] E. D. Jurgenson, P. Navrátil and R. J. Furnstahl, Phys. Rev. Lett. **103**, 082501 (2009), arXiv:0905.1873 [nucl-th] (2009).

[74] S. Fujii, R. Okamoto and K. Suzuki, Phys. Rev. Lett. **103**, 182501 (2009), arXiv: 0908.3376 [nucl-th] (2009).

[75] C. Barbieri, Phys. Rev. Lett. **103**, 202502 (2009), arXiv:0909.3040 [nucl-th] (2009).

[76] E. Epelbaum, H. Krebs, D. Lee and U.-G. Meißner, Phys. Rev. Lett. **104**, 142501 (2010), arXiv:0912.4195 [nucl-th] (2009).

[77] G. Hagen, T. Papenbrock and M. Hjorth-Jensen, Phys. Rev. Lett. **104**, 182501 (2010), arXiv:1003.1995 [nucl-th] (2010).

[78] K. Hebeler, J. M. Lattimer, C. J. Pethick and A. Schwenk, Phys. Rev. Lett. **105**, 161102 (2010), arXiv:1007.1746 [nucl-th] (2010).

[79] L. Girlanda, A. Kievsky, L. E. Marcucci, S. Pastore, R. Schiavilla and M. Viviani, Phys. Rev. Lett. **105**, 232502 (2010), arXiv:1008.0356 [nucl-th] (2010).

[80] E. Epelbaum, H. Krebs, D. Lee and U.-G. Meißner, Phys. Rev. Lett. **106**, 192501 (2011), arXiv:1101.2547 [nucl-th] (2011).

[81] P. Maris, J. P. Vary, P. Navrátil, W. E. Ormand, H. Nam and D. J. Dean, Phys. Rev. Lett. **106**, 202502 (2011), arXiv:1101.5124 [nucl-th] (2011).

[82] K. Tsukiyama, S. K. Bogner and A. Schwenk, Phys. Rev. C **85**, 061304 (2012), arXiv:1203.2515 [nucl-th] (2012).

[83] O. Jensen, G. Hagen, M. Hjorth-Jensen, B. A. Brown and A. Gade, Phys. Rev. Lett. **107**, 032501 (2011), arXiv:1104.1552 [nucl-th] (2011).

[84] R. Roth, J. Langhammer, A. Calci, S. Binder and P. Navrátil, Phys. Rev. Lett. **107**, 072501 (2011), arXiv:1105.3173 [nucl-th] (2011).

[85] J. A. Frenje, C. K. Li, F. H. Seguin, D. T. Casey, R. D. Petrasso, D. P. McNabb, P. Navratil, S. Quaglioni, T. C. Sangster, V. Yu. Glebov and D. D. Meyerhofer, Phys. Rev. Lett. **107**, 122502 (2011).

[86] J. Menéndez, D. Gazit and A. Schwenk, Phys. Rev. Lett. **107**, 062501 (2011), arXiv:1103.3622 [nucl-th] (2011).

[87] P. Navrátil and S. Quaglioni, Phys. Rev. Lett. **108**, 042503 (2012), arXiv: 1110.0460 [nucl-th] (2011).

[88] M. Brodeur, T. Brunner, C. Champagne, S. Ettenauer, M. J. Smith, A. Lapierre, R. Ringle, V. L. Ryjkov, S. Bacca, P. Delheij, G. W. F. Drake, D. Lunney, A. Schwenk and J. Dilling, Phys. Rev. Lett. **108**, 052504 (2012), arXiv: 1107.1684 [nucl-ex] (2011).

[89] G. Hagen, M. Hjorth-Jensen, G. R. Jansen, R. Machleidt and T. Papenbrock, Phys. Rev. Lett. **108**, 242501 (2012), arXiv:1202.2839 [nucl-th] (2012).

[90] G. Hagen, M. Hjorth-Jensen, G. R. Jansen, R. Machleidt and T. Papenbrock, Phys. Rev. Lett. **109**, 032502 (2012), arXiv:1204.3612 [nucl-th] (2012).

[91] A. T. Gallant, J. C. Bale, T. Brunner, U. Chowdhury, S. Ettenauer, A. Lennarz, D. Robertson, V. V. Simon, A. Chaudhuri, J. D. Holt, A. A. Kwiatkowski, E. Mané, J. Menéndez, B. E. Schultz, M. C. Simon, C. Andreoiu, P. Delheij, M. R. Pearson, H. Savajols, A. Schwenk and J. Dilling, Phys. Rev. Lett. **109**, 032506 (2012), arXiv:1204.1987 [nucl-ex] (2012).

[92] R. Roth, S. Binder, K. Vobig, A. Calci, J. Langhammer and P. Navrátil, Phys. Rev. Lett. **109**, 052501 (2012), arXiv:1112.0287 [nucl-th] (2011).

[93] E. Epelbaum, H. Krebs, T. A. Lähde, D. Lee and U.-G. Meißner, Phys. Rev. Lett. **109**, 252501 (2012), arXiv:1208.1328 [nucl-th] (2012).

[94] J. D. Holt, J. Menéndez and A. Schwenk, Phys. Rev. Lett. **110**, 022502 (2013), arXiv:1207.1509 [nucl-th] (2012).

[95] S. Baroni, P. Navrátil and S. Quaglioni, Phys. Rev. Lett. **110**, 022505 (2013), arXiv:1210.1897 [nucl-th] (2012).

[96] I. Tews, T. Krüger, K. Hebeler and A. Schwenk, Phys. Rev. Lett. **110**, 032504 (2013), arXiv:1206.0025 [nucl-th] (2012).

[97] A. Lepailleur, O. Sorlin, L. Caceres, B. Bastin, C. Borcea, R. Borcea, B. A. Brown, L. Gaudefroy, S. Grévy, G. F. Grinyer, G. Hagen, M. Hjorth-Jensen, G. R. Jansen, O. Llidoo, F. Negoita, F. de Oliveira, M.-G. Porquet, F. Rotaru, M.-G. Saint-Laurent, D. Sohler, M. Stanoiu and J. C. Thomas, Phys. Rev. Lett. **110**, 082502 (2013), arXiv:1301.5803 [nucl-ex] (2013).

[98] S. Bacca, N. Barnea, W. Leidemann and G. Orlandini, Phys. Rev. Lett. **110**, 042503 (2013), arXiv:1210.7255 [nucl-th] (2012).

[99] E. Epelbaum, H. Krebs, T. A. Lähde, D. Lee and U.-G. Meißner, Phys. Rev. Lett. **110**, 112502 (2013), arXiv:1212.4181 [nucl-th] (2012).

[100] A. Ekström, G. Baardsen, C. Forssén, G. Hagen, M. Hjorth-Jensen, G. R. Jansen, R. Machleidt, W. Nazarewicz, T. Papenbrock, J. Sarich and S. M. Wild, Phys. Rev. Lett. **110**, 192502 (2013), arXiv:1303.4674 [nucl-th] (2013).

[101] H. Hergert, S. Binder, A. Calci, J. Langhammer and R. Roth, Phys. Rev. Lett. **110**, 242501 (2013), arXiv:1302.7294 [nucl-th] (2013).

[102] A. Gezerlis, I. Tews, E. Epelbaum, S. Gandolfi, K. Hebeler, A. Nogga and A. Schwenk, Phys. Rev. Lett. **111**, 032501 (2013), arXiv:1303.6243 [nucl-th] (2013).

[103] A. Cipollone, C. Barbieri and P. Navrátil, Phys. Rev. Lett. **111**, 062501 (2013), arXiv:1303.4900 [nucl-th] (2013).

[104] S. Bacca, N. Barnea, G. Hagen, G. Orlandini and T. Papenbrock, Phys. Rev. Lett. 111, **122502** (2013), arXiv:1303.7446 [nucl-th] (2013).

International Conference

NUCLEAR THEORY IN THE SUPERCOMPUTING ERA – 2013 (NTSE-2013)

KEYNOTE AND INVITED TALKS


Nuclear Theory
in the Supercomputing Era
Computational Nuclear Physics:
Key to Discovery Opportunities
James P. Vary
Iowa State University
IOWA STATE
UNIVERSITY

Ab Initio Calculations of *p*-Shell Nuclei with JISP16

Pieter Maris

Department of Physics and Astronomy, Iowa State University, Ames, IA 50011, USA

Abstract

I present an overview of binding energies and ground state magnetic moments for p-shell nuclei calculated with the phenomenological NN interaction JISP16, and compare with experimental data. I also illustrate how the decomposition of total angular momentum into intrinsic spin and orbital components can provide insights into the structure of states and relationships among states.

Keywords: *Nuclear structure; ab initio; configuration interaction; JISP16*

1 No-Core Full Configuration approach

In the Configuration Interaction (CI) approach to describe quantum many-body systems, the many-body Schrödinger equation

$$H\,\Psi_i(\mathbf{r}_1,\ldots,\mathbf{r}_A) = E_i\,\Psi_i(\mathbf{r}_1,\ldots,\mathbf{r}_A) \tag{1}$$

becomes a large sparse matrix problem with eigenvalues E_i and eigenvectors Ψ_i representing the A-body wavefunctions. For No-Core nuclear structure calculations [1] the wavefunction Ψ of a nucleus consisting of A nucleons is expanded in an A-body basis of Slater determinants Φ_k of single-particle wavefunctions $\phi_{nljm}(\mathbf{r})$,

$$\Psi(\mathbf{r}_1,\ldots,\mathbf{r}_A) = \sum c_k\,\Phi_k(\mathbf{r}_1,\ldots,\mathbf{r}_A), \tag{2}$$

with $\Phi_k(\mathbf{r}_1,\ldots,\mathbf{r}_A) = \mathcal{A}[\phi_{n_1l_1j_1m_1}(\mathbf{r}_1)\,\phi_{n_2l_2j_2m_2}(\mathbf{r}_2)\ldots\phi_{n_Al_Aj_Am_A}(\mathbf{r}_A)]$ and $\mathcal{A}$ is the antisymmetrization operation. Conventionally, one uses a harmonic oscillator (HO) basis for the single-particle wavefunctions, which are labelled by their quantum numbers n, l, j, and m; n and l are the radial and orbital HO quantum numbers (with $N = 2n + l$ the number of HO quanta), j is the total single-particle spin, and m its projection along the z-axis. The many-body basis states Φ_k have well-defined parity, $(-1)^{\sum_A l_i}$, and total spin-projection, $M = \sum_A m_i$, but they do not have a well-defined total spin J. Thus, in two runs (one for each parity), one can obtain the complete low-lying spectrum, including the ground state, even if the spin of the ground state is not known a priori.

The many-body Hamiltonian H in Eq. (1) can be expressed in terms of the relative kinetic energy plus 2-body, 3-body, and, in general, up to A-body interaction terms

$$H = T_{\rm rel} + V_{\rm Coulomb} + V_{NN} + V_{NNN} + \ldots \tag{3}$$

Here I focus on results obtained with the phenomenological 2-body (NN) interaction JISP16. This interaction is constructed from inverse scattering analysis of the neutron-proton phase shifts; subsequently its off-shell behavior is tuned to reproduce the deuteron properties as well as select additional light nuclear properties using

Proceedings of International Conference 'Nuclear Theory in the Supercomputing Era — 2013' (NTSE-2013), Ames, IA, USA, May 13–17, 2013. Eds. A. M. Shirokov and A. I. Mazur. Pacific National University, Khabarovsk, Russia, 2014, p. 37.

http://www.ntse-2013.khb.ru/Proc/Maris.pdf.

phase-shift equivalent unitary transformations [2]. The resulting NN interaction is charge-independent; the only charge dependence comes from the Coulomb interaction $V_{\rm Coulomb}$ in Eq. (3).

A convenient and efficient truncation of the complete (infinite-dimensional) basis is a truncation on the total number of HO quanta of the many-body basis: the basis is limited to many-body basis states with $\sum_A N_i \leq N_0 + N_{\rm max}$. Here, N_i is the number of quanta of each single-particle state; N_0 is the minimal number of quanta for that nucleus; and $N_{\rm max}$ is the truncation parameter. Note that for HO single-particle states, this truncation leads to an exact factorization of the center-of-mass wavefunction and the relative wavefunction [3].

Any CI calculation, using a finite truncation of the complete basis, gives a strict upperbound for the lowest states of each spin and parity for a given nuclear potential. In the No-Core Full Configuration (NCFC) approach [4] one is interested in the convergence with increasing basis space dimensions and thus recover, to within quantifiable uncertainties, results corresponding to the complete basis. In order to do so, one has to address eigenvalue problems for increasingly large matrices, with dimensions of well over a billion. Improved algorithms to construct these matrices and to determine their lowest eigenstates, as well as efficient use of increasing computational resources are critical for the success of this approach [5–10].

The empirical model used for the extrapolation of the (ground state) energies to the complete basis is [4]

$$E(\hbar\omega, N_{\rm max}) = E_\infty + a_{\hbar\omega}\, e^{-b_{\hbar\omega} N_{\rm max}}, \tag{4}$$

where $\hbar\omega$ is the HO energy. I use sets of three consequitive $N_{\rm max}$ values at fixed values of $\hbar\omega$ to estimate the energy in the complete basis. Extrapolations based on calculations up to $N_{\rm max}$ are using results from the $(N_{\rm max}-4)$, $(N_{\rm max}-2)$, and $N_{\rm max}$ bases for the extrapolation, and the difference with the extrapolation of the $(N_{\rm max}-6)$, $(N_{\rm max}-4)$, and $(N_{\rm max}-2)$ bases is used as an estimate of the extrapolation uncertainty. For this extrapolation method one needs results up to at least $N_{\rm max} = 8$.

For consistency, I then check that (1) extrapolations at different $\hbar\omega$ values are within each other's uncertainty estimates; (2) as $N_{\rm max}$ increases, the extrapolations are within the uncertainty estimates of smaller $N_{\rm max}$ values; and (3) numerical uncertainty estimates decrease as $N_{\rm max}$ increases. This is all done at fixed $\hbar\omega$; the final result for E_∞ is the extrapolated result at that $\hbar\omega$ value for which the amount of extrapolation is minimal, i. e. the point where $E(\hbar\omega, N_{\rm max}) - E_\infty$ is minimal. Typically, with JISP16, this is at or slightly above the $\hbar\omega$ value that minimizes the (ground-state) energy in finite bases. The final error estimate is enlarged as necessary in order to get consistent results, such that the central values are within the final numerical error estimate over a 10 MeV range around the variational minimum. (Note that in the original version of this extrapolation [4] we did not make such an adjustment.)

2 Ground state energies with JISP16

This extrapolation method is illustrated in the left panel of Fig. 1 for the ground state of ^{7}Li. As one can see in this figure, the error estimates are minimal around the variational minimum in $\hbar\omega$; furthermore, extrapolations based on the three data points at the largest $N_{\rm max}$ do indeed fall within the error estimates of the previous extrapolations, and do have smaller error estimates. However, there seems to be a systematic $\hbar\omega$ dependence of the extrapolated results suggesting that Eq. (4) is not the correct asymptotic behavior. Indeed, recent studies [11–14] of the effective infrared and ultraviolet cutoffs of a finite HO basis have shown that the asymptotic behavior contains a term that is exponential in $\sqrt{N_{\rm max}}$, in addition to a term that is exponential in $N_{\rm max}$. The uncertainty analysis of these extrapolation methods is still under

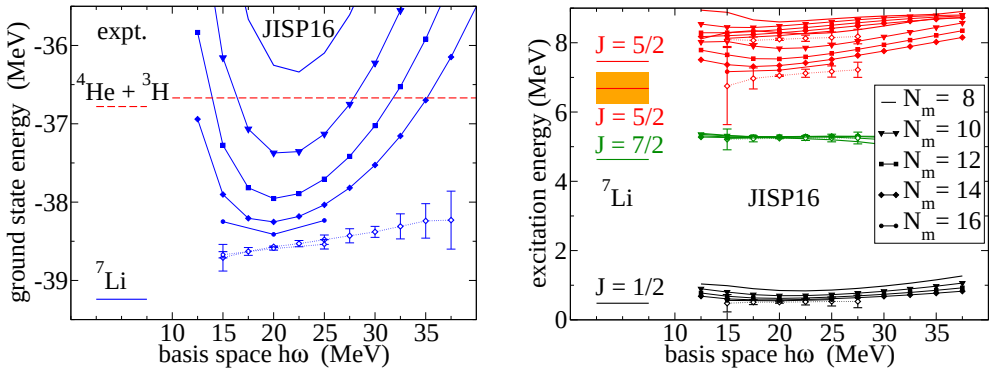

Figure 1: Ground state energy (left) and low-lying spectrum for ^{7}Li (right). Extrapolated energies are depicted with open symbols connected by dotted lines.

investigation; once their uncertainties have been quantified, these extrapolations are likely to become more valuable.

In Fig. 2 I present a summary of ground state energies of light nuclei up to ^{16}O calculated with JISP16 in the NCFC approach [15]. For $A = 3$ and $A = 4$, as well as for ^{6}He and ^{6}Li, our results are in excellent agreement with calculations using the hyperspherical harmonics approach [16, 17]. In recent years, JISP16 has been been used successfully to benchmark novel truncation methods for *ab initio* CI calculations, such as the No-Core Monte Carlo Shell Model [18, 19] and the Symmetry-Adapted No-Core Shell Model [20, 21], as well calculations based on Coulomb–Sturmian single-particle wavefunctions [22] and calculations in a Wood–Saxon basis [23] — each of these methods yields results consistent with the results presented here.

There is a reasonable overall agreement between the calculated and experimental binding energies: for $A = 6$ to 10 JISP16 underbinds slightly, but starting from $A = 12$, JISP16 overbinds the $T = 0$ and $T = \frac{1}{2}$ states by an amount that increases with A, but decreases with T. This trend towards overbinding of the $N = Z$

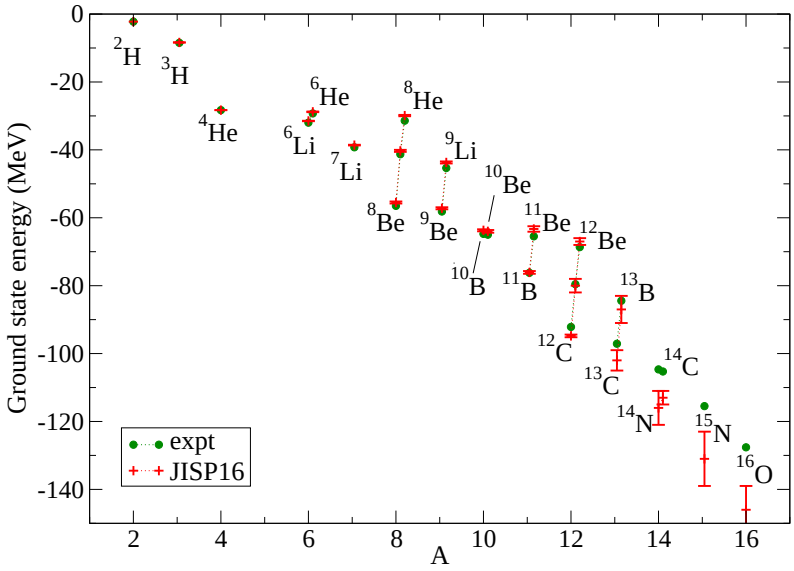

Figure 2: Ground state energy for $A = 2$ to $A = 16$ with JISP16, including numerical uncertainty estimates (only one ground state for each A and T), compared to experimental data.

nuclei starting from ^{12}C has been noted earlier [4], and can be remedied by a further tuning of the off-shell behavior of the NN interaction [24].

3 Excited states

Most known excited states in p-shell nuclei are particle (or cluster) unstable but many have widths less than a few hundred keV. For such narrow states the real part of the S-matrix poles may be well-approximated by the eigenenergies calculated in a HO basis [25]. E. g., for ^{7}Li the first excited state, with $J^\pi = \frac{1}{2}^-$, is below the threshold for ^{4}He plus ^{3}H, but the next excited states state, at about 5 MeV with $J^\pi = \frac{7}{2}^-$, is well above this threshold. Nevertheless, the excitation energy of this state is very well converged, see the right panel of Fig. 1, and one does not really need any extrapolation for the excitation energies of these two lowest excited states [26].

The excitation energies of the two $J^\pi = \frac{5}{2}^-$ states around 7 to 8 MeV however are not as well converged, and do depend on the basis parameters. Even after the exponential extrapolation to a complete basis, the excitation energies shows a systematic dependence on the basis parameter $\hbar\omega$, in particular for the first $J^\pi = \frac{5}{2}^-$ state. This behavior is characteristic for resonances in a pure HO basis, and one might get better converged results using an approach that incorporates continuum states [27–29]. Nevertheless, one can conclude that with JISP16 the excitation energies for the lowest four excited states in ^{7}Li are all within about 10 % to 15 % of the experimental values.

Experimentally, the lowest $J^\pi = \frac{5}{2}^-$ state is broad, whereas the second $J^\pi = \frac{5}{2}^-$ is narrow; not much else is known to distinguish them. Our calculations [26] however indicate that these two states have a very different structure: the first $J^\pi = \frac{5}{2}^-$ has a large negative quadrupole moment, whereas the second has a moderately large positive quadrupole moment. Furthermore, the first $J^\pi = \frac{5}{2}^-$ state has a moderately strong $B(E2)$ transition to the $J^\pi = \frac{3}{2}^-$ ground state, whereas the $B(E2)$ transition from the second $J^\pi = \frac{5}{2}^-$ state is more than an order of magnitude smaller.

In order to get a better understanding of the structure of these (and other) states, one can also look at their spin structure. The contributions to the total spin $\mathbf{J}$ in terms of the nucleon intrinsic spin, $\mathbf{S}$, and orbital motion, $\mathbf{L}$, is given by

$$J = \frac{1}{J+1}\Big(\langle \mathbf{J}\cdot\mathbf{L}_p\rangle + \langle \mathbf{J}\cdot\mathbf{L}_n\rangle + \langle \mathbf{J}\cdot\mathbf{S}_p\rangle + \langle \mathbf{J}\cdot\mathbf{S}_n\rangle\Big). \tag{5}$$

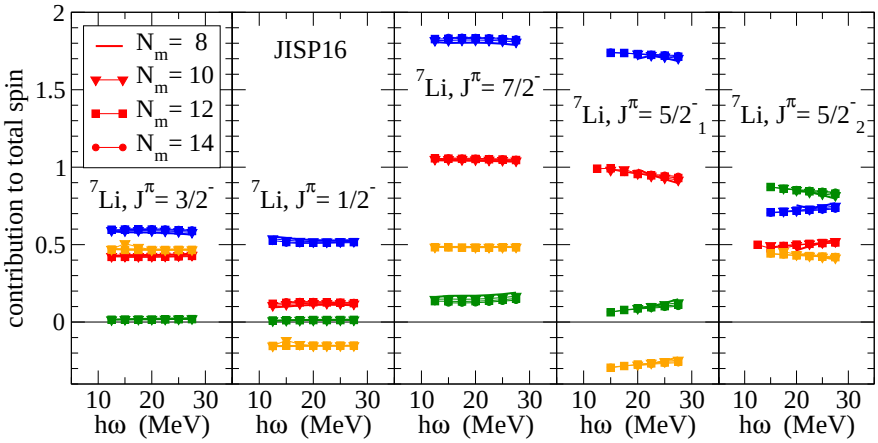

Figure 3: Contribution to the total spin of select states of ^{7}Li from the proton orbital motion (red), neutron orbital motion (blue), proton intrinsic spin (orange), and neutron intrinsic spin (green). Adapted from Ref. [15].

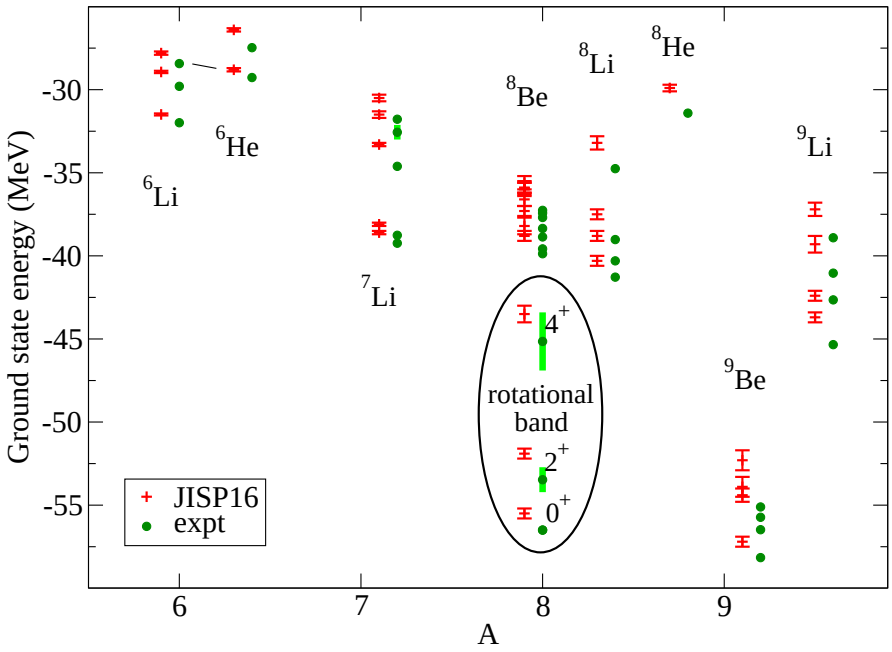

Figure 4: Energies of select low-lying states for $A = 6$ to $A = 9$ with JISP16, including numerical uncertainty estimates, compared to experimental data.

Generally (though not always) these components converge rather quickly. In Fig. 3 these components are shown for the five lowest states in ^{7}Li. Clearly, the first and second $\frac{5}{2}^-$ and $\frac{5}{2}^-$ states have a very different structure, despite being very close in energy: they differ significantly in all their spin components. A closer look at both the quadrupole moments and the spin components of the lowest four states suggests that these states (with $J^\pi = \frac{1}{2}^-$, $\frac{3}{2}^-$, $\frac{5}{2}^-_1$, and $\frac{7}{2}^-$) form a rotational band. Also the $B(E2)$ and $B(M1)$ transition strengths between these states are in qualitative agreement with predictions based on a rotational structure [30].

In Fig. 4 I summarize results for both the ground states and select excited states for $A = 6$ to $A = 9$, after extrapolation to the complete basis. As already noted, JISP16 slightly underbinds these nuclei, but the excitation energies are generally in qualitative agreement with the data, as can be seen in Fig. 4: for most of these nuclei the calculated results (red plusses) seem all to be shifted upwards by a constant (nucleus-dependent) amount, reproducing the experimental spectrum quite well. Also the calculated spin and parity of the states shown in Fig. 4 agrees with the experimentally assigned spin-parity.

4 Beryllium isotopes

It is known that the low-lying states in both ^{8}Be and ^{9}Be are members of rotational bands. Indeed, the excitation energies of the first 2^+ and 4^+ states of ^{8}Be, see Fig. 4, follow the rotational pattern. Although the quadrupole moments themselves are not (yet) converged, the ratio of the quadrupole moments of the first 2^+ and 4^+ states of ^{8}Be are in good agreement with a rotational model, as are their $B(E2)$ transition strength (relative to the intrinsic quadrupole moment) [30].

Starting with ^{8}Be, narrow states of both parities appear in the experimental spectrum; and for ^{11}Be the lowest positive parity state is the ground state, contrary to the expectations based on the shell model, which predicts negative parity ground states for all odd p-shell nuclei. For ^{7}Be through ^{13}Be I performed calculations for

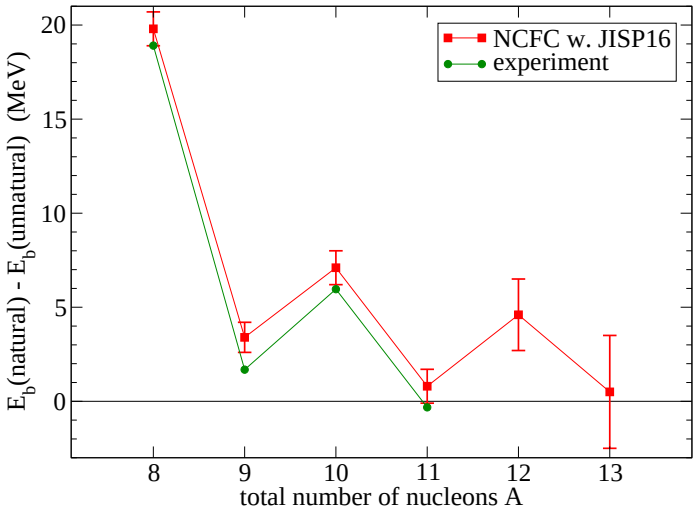

Figure 5: Energy difference between lowest positive and negative parity states for Beryllium isotopes. Adapted from Ref. [31].

both natural and unnatural parity states. Figure 5 shows the difference between the extrapolated binding energy of the lowest natural parity state and the lowest unnatural parity state [31], treating the extrapolation uncertainties as independent. One expect this difference to be positive, but for isotopes with parity inversion it becomes negative. Although JISP16 does not quite reproduce the observed parity inversion for ^{11}Be, parity inversion is within the numerical error estimates for this isotope. Furthermore, over the range of isotopes from ^{8}Be to ^{11}Be the results are in very good qualitative agreement with the data: JISP16 seems to underbind all unnatural parity states by a similar amount of about 1 MeV. Based on these results, I also predict parity inversion for ^{13}Be; experimentally, the parity of the ground state is not confirmed, though likely to be negative [32], which indeed implies parity inversion (^{13}Be has one neutron in the *sd*-shell, so the natural parity is positive).

The negative parity spectrum and positive parity spectrum of ^{9}Be, relative to the lowest state of that parity, is shown in Fig. 6. The excitation energies of the lowest $\frac{5}{2}^-$ and $\frac{7}{2}^-$ states are quite well converged, in contrast to excitation energies of the $\frac{1}{2}^-$, the $\frac{3}{2}^-$, and the second $\frac{5}{2}^-$ states. This difference in convergence rate can be understood by the observation that the ground state forms a rotational band with

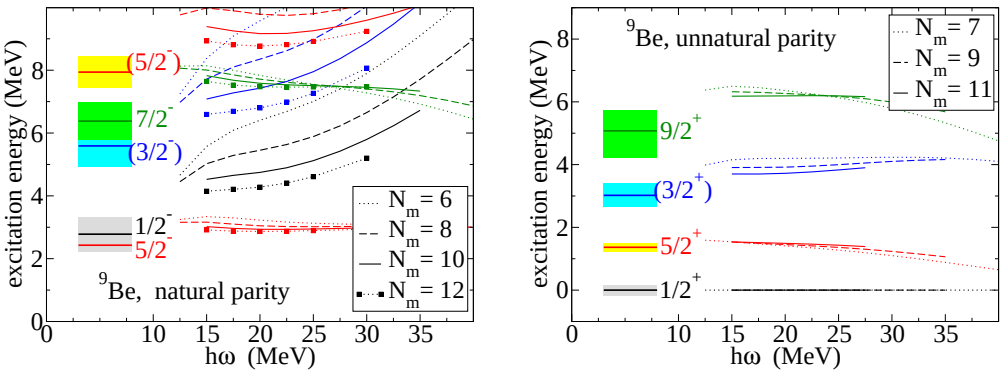

Figure 6: Excitation energies of the lowest excited states of ^{9}Be with negative parity (left) and positive parity (right), relative to the lowest state of that parity.

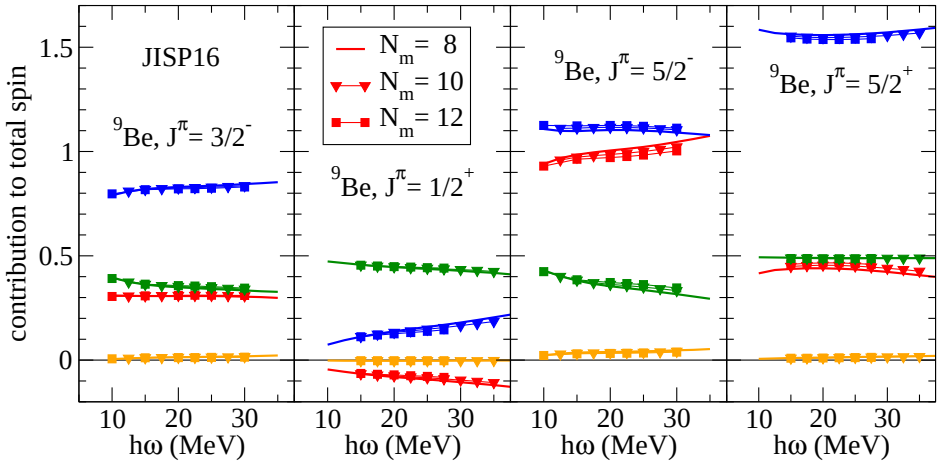

Figure 7: Contribution to the total spin of select states of ^{9}Be from the proton orbital motion (red), neutron orbital motion (blue), proton intrinsic spin (orange), and neutron intrinsic spin (green). Adapted from Ref. [15].

the lowest $\frac{5}{2}^-$ and $\frac{7}{2}^-$ states, and the corresponding wavefunctions have therefore a similar structure, and are likely to converge at a similar rate. The low-lying positive parity states also form a rotational band, and indeed, their excitation energies, relative the $\frac{1}{2}^+$ state, are also quite well converged at $N_{\max} = 11$. Note however that the excitation energy of the positive parity states relative to the (negative parity) ground state are not as well converged, and can only be calculated after extrapolation to the complete basis [15].

In Fig. 7 I show the spin contributions for the lowest two negative parity states and for the lowest two positive parity states of ^{9}Be. In all four states, the contribution from the neutron intrinsic spin is close to $\frac{1}{2}$, and that from the proton intrinsic spin is nearly zero. This is consistent with a cluster configuration of two α-particles and a neutron for these states. The observed spin contributions for the ground state $J^\pi = \frac{3}{2}^-$ suggests that this state is dominated by an α-cluster configuration of two α-particles plus a neutron in a π-orbital, in which the neutron orbital motion contributes one unit to the total angular momentum. The ground state proton and neutron density distributions are consistent with this interpretation as well [31]. On the other hand, the lowest positive parity state, $J^\pi = \frac{1}{2}^+$, is likely to be dominated by two α-particles plus a neutron in a σ-orbital. The $\frac{5}{2}^-$ and $\frac{5}{2}^+$ states can then be interpreted as rotational excitations of these two states, with most of the total angular momentum coming from orbital motion of the nucleons. Indeed, calculations of the quadrupole moments and $B(E2)$ transition strengths of these states are also in agreement with these states forming rotational bands [30].

5 Magnetic moments

Using the canonical 1-body current operator, the magnetic moments in impulse approximation follow from the spin components

$$\mu = \frac{1}{J+1}\Big(\langle \mathbf{J}\cdot\mathbf{L}_p\rangle + 5.586\langle \mathbf{J}\cdot\mathbf{S}_p\rangle - 3.826\langle \mathbf{J}\cdot\mathbf{S}_n\rangle\Big)\mu_0. \tag{6}$$

In Fig. 8 I show results for the magnetic moments of the ground states of p-shell nuclei. Typically, the calculated results are within about $0.3\,\mu$ of the experimental

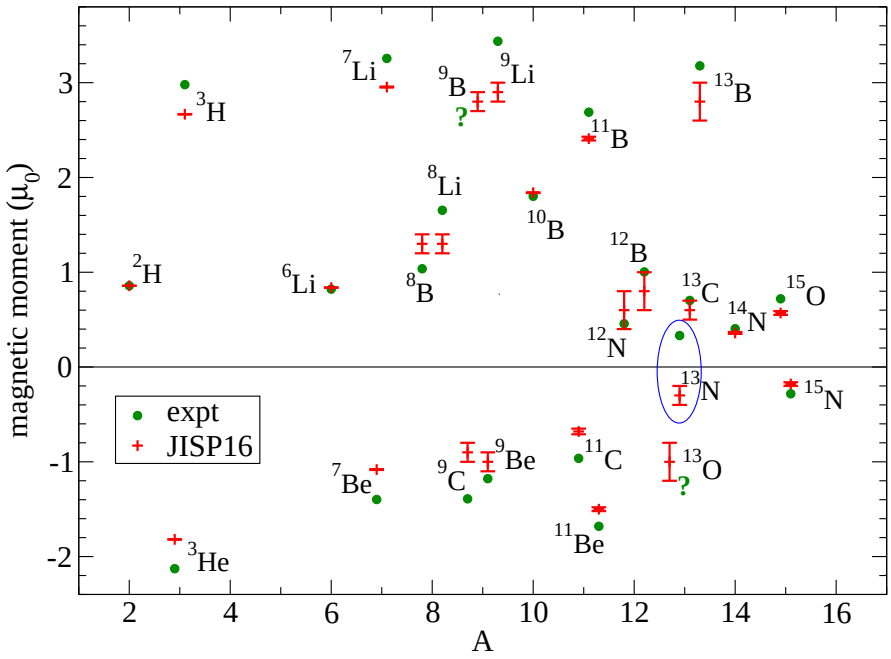

Figure 8: Ground state magnetic moments for $A = 2$ to $A = 16$ with JISP16, including numerical uncertainty estimates, compared to experimental data.

data. This discrepancy is likely due to the omission of 2-body currents; with consistent 2-body currents, one expects to get much better agreement with the data. However, since JISP16 is a purely phenomenological potential, it is not clear how to construct a consistent 2-body current, whereas for a microscopic interaction such as chiral interactions or a phenomenological meson-exchange potential like AV18, one can use consistent meson-exchange currents, and find generally good agreement with the data once meson-exchange currents are included [33, 34].

Some of the largest deviations between the impulse approximation calculations and the experimental data are for the ground states of ^{9}Li and ^{9}C. It is interesting to note that also with AV18 plus IL7 3-body force there is a similarly large discrepancy between impulse approximation calculations and data for these two states. For the AV18 plus IL7 it has been shown that meson-exchange currents contribute $+0.70(2)\,\mu$ and $-0.60(3)\,\mu$ respectively to these magnetic moments, and with these corrections included, the results for ^{9}Li and ^{9}C are in agreement with the data [34]. For other ground state magnetic moments the contribution from meson-exchange currents is of the order of $0.3\,\mu$ or smaller with AV18 plus IL7, and with these corrections included, the calculated magnetic moments are generally closer to the data.

Another surprisingly large discrepancy between the calculated and experimental magnetic moment occurs for ^{13}N. JISP16 gives a negative magnetic moment of about $-0.3(1)\,\mu$, in sharp contrast to the positive experimental value of $+0.322\,\mu$. Note that the calculation for the mirror nucleus, ^{13}C, is in good agreement with the data. It would be interesting to see what one gets with other realistic interactions, and what the meson-exchange contributions are for this case.

Acknowledgements

I would like to thank J. P. Vary, A. M. Shirokov, M. A. Caprio for valuable discussions. This work was supported in part by the National Science Foundation under Grant No. PHY-0904782 and the Department of Energy under Grant Nos. DE-

FG02-87ER40371 and DESC0008485 (SciDAC-3/NUCLEI). A portion of the computational resources were provided by the National Energy Research Scientific Computing Center (NERSC), which is supported by the DOE Office of Science under Contract No. DE-AC02-05CH11231, and by an INCITE award, "Nuclear Structure and Nuclear Reactions", from the DOE Office of Advanced Scientific Computing Research. This research also used resources of the Oak Ridge Leadership Computing Facility at ORNL, which is supported by the DOE Office of Science under Contract DE-AC05-00OR22725, and of the Argonne Leadership Computing Facility at ANL, which is supported by the DOE Office of Science under Contract DE-AC02-06CH11357.

References

[1] B. R. Barrett, P. Navrátil and J. P. Vary, Progr. Part. Nucl. Phys. **69**, 131 (2013) and references therein.

[2] A. M. Shirokov, J. P. Vary, A. I. Mazur and T. A. Weber, Phys. Lett. B **644**, 33 (2007).

[3] M. Moshinsky, Yu. F. Smirnov, *The harmonic oscillator in modern physics.* Harwood Academic Publishers, 1996.

[4] P. Maris, J. P. Vary and A. M. Shirokov, Phys. Rev. C **79**, 014308 (2009).

[5] P. Sternberg, E. G. Ng, C. Yang, P. Maris, J. P. Vary, M. Sosonkina and H. V. Le, *Accelerating configuration interaction calculations for nuclear structure*, in *Proc. 2008 ACM/IEEE conf. on Supercomputing*. IEEE Press, Piscataway, NJ, 2008, p. 15:1.

[6] P. Maris, M. Sosonkina, J. P. Vary, E. G. Ng and C. Yang, Proc. Comput. Sci. **1**, 97 (2010).

[7] H. M. Aktulga, C. Yang, E. G. Ng, P. Maris and J. P. Vary, *Topology-aware mappings for large-scale eigenvalue problems*, in *Euro-Par*, eds. C. Kaklamanis, T. S. Papatheodorou and P. G. Spirakis. Lecture Notes Comput. Sci. **7484**, 830 (2012).

[8] H. M. Aktulga, C. Yang, E. G. Ng, P. Maris and J. P. Vary, *Improving the scalability of symmetric iterative Eigensolver for multi-core platforms*, Concurrency Computat.: Pract. Exper. (2013), DOI: 10.1002/cpe.3129.

[9] C. Yang, H. M. Aktulga, P. Maris, E. Ng and J. Vary, *see these Proceedings*, p. 272, http://www.ntse-2013.khb.ru/Proc/Yang.pdf.

[10] H. Potter, D. Oryspayev, P. Maris, M. Sosonkina, J. Vary, S. Binder A. Calci, J. Langhammer, R. Roth, Ü. Çatalyürek and E. Saule, *see these Proceedings*, p. 263, http://www.ntse-2013.khb.ru/Proc/Sosonkina.pdf.

[11] S. A. Coon, M. I. Avetian, M. K. G. Kruse, U. van Kolck, P. Maris and J. P. Vary, Phys. Rev. C **86**, 054002 (2012).

[12] R. J. Furnstahl, G. Hagen and T. Papenbrock, Phys. Rev. C **86**, 031301 (2012).

[13] S. N. More, A. Ekstrom, R. J. Furnstahl, G. Hagen and T. Papenbrock, Phys. Rev. C **87**, 044326 (2013).

[14] S. A. Coon and M. K. G. Kruse, *see these Proceedings, p.* 314, http://www.ntse-2013.khb.ru/Proc/Coon.pdf.

[15] P. Maris and J. P. Vary, Int. J. Mod. Phys. E **22**, 1330016 (2013).

[16] N. Barnea, W. Leidemann and G. Orlandini, Phys. Rev. C **74**, 034003 (2006).

[17] S. Vaintraub, N. Barnea and D. Gazit, Phys. Rev. C **79**, 065501 (2009).

[18] T. Abe, P. Maris, T. Otsuka, N. Shimizu, Y. Utsuno and J. P. Vary, Phys. Rev. C **86**, 054301 (2012).

[19] T. Abe, P. Maris, T. Otsuka, N. Shimizu, Y. Tsunoda, Y. Utsuno and J. P. Vary, *see these Proceedings, p.* 294, http://www.ntse-2013.khb.ru/Proc/Abe.pdf.

[20] T. Dytrych, K. D. Sviratcheva, C. Bahri, J. P. Draayer and J. P. Vary, Phys. Rev. C **76**, 014315 (2007).

[21] T. Dytrych, J. P. Draayer, K. D. Launey, P. Maris, J. P. Vary and D. Langr, *see these Proceedings, p.* 62, http://www.ntse-2013.khb.ru/Proc/Dytrych.pdf.

[22] M. A. Caprio, P. Maris and J. P. Vary, Phys. Rev. C **86**, 034312 (2012); *see also these Proceedings, p.* 325, http://www.ntse-2013.khb.ru/Proc/Caprio.pdf.

[23] G. Negoita, *PhD thesis*. Iowa State University, 2010, ProQuest 3418277, http://gradworks.umi.com/3418277.pdf.

[24] A. M. Shirokov, V. A. Kulikov, P. Maris, A. I. Mazur, E. A. Mazur and J. P. Vary, EPJ Web Conf. **3**, 05015 (2010).

[25] A. M. Shirokov, A. I. Mazur, J. P. Vary and E. A. Mazur, Phys. Rev. C **79**, 014610 (2009).

[26] C. Cockrell, J. P. Vary and P. Maris, Phys. Rev. C **86**, 034325 (2012).

[27] S. Baroni, P. Navrátil and S. Quaglioni, Phys. Rev. C **87**, 034326 (2013).

[28] G. Papadimitriou, J. Rotureau, N. Michel, M. Ploszajczak and B. R. Barrett, arXiv:1301.7140 [nucl-th] (2013).

[29] J. Rotureau, *see these Proceedings*, p. 236, http://www.ntse-2013.khb.ru/Proc/Rotureau.pdf.

[30] M. A. Caprio, P. Maris and J. P. Vary, Phys. Lett. B **719**, 179 (2013).

[31] P. Maris, J. Phys. Conf. Ser. **402**, 012031 (2012).

[32] G. Audi, O. Bersillon, J. Blachot and A. H. Wapstra, Nucl. Phys. A **624**, 1 (1997).

[33] L. E. Marcucci, M. Pervin, S. C. Pieper, R. Schiavilla and R. B. Wiringa, Phys. Rev. C **78**, 065501 (2008).

[34] S. Pastore, S. C. Pieper, R. Schiavilla and R. B. Wiringa, Phys. Rev. C **87**, 035503 (2013).

NTSE-2013 Keynote Talk:

— Unraveling Mysteries of the Strong Interaction — 'Top Down' versus 'Bottom Up' Considerations

Jerry P. Draayer[a], Tomáš Dytrych[a], Kristina D. Launey[a], Alison C. Dreyfuss[a], Mia C. Ferriss[a], Gregory K. Tobin[a], Feng Pan[b] and Xin Guan[b]

[a] *Department of Physics and Astronomy, Louisiana State University, LA 70803, USA*
[b] *Department of Physics, Liaoning Normal University, Dalian 116029, China*

Abstract

Ab initio theories that build on first principles are essential for understanding nuclear structure at a fundamental level and for providing reliable predictions of short-lived nuclei. While the *ab initio* symmetry-adapted no-core shell model (SA-NCSM) has unveiled a clear symmetry structure that emerges from first principles — an outcome that has only recently become feasible with the advent of high performance computing (HPC) facilities, these symmetries have been long recognized and have been key to successful algebraic models with the cornerstone approaches reviewed here. Utilizing these symmetries, we have found that a fully microscopic no-core symplectic model reproduces characteristic features of the low-lying 0^+ states in ^{12}C and ground-state rotational bands in p and sd-shell nuclei (from Be to Si). Such 'top down' algebraic considerations can hence inform 'bottom up' *ab initio* approaches by exposing emergent properties in terms of simple interaction forms that are likely to dominate nuclear structure.

Keywords: *Ab-initio symmetry-adapted no-core shell model; SU(3) coupling scheme; symplectic Sp(3,R) shell model; Hoyle state*

1 Introduction

The *ab initio* symmetry-adapted no-core shell-model (SA-NCSM), with results that corroborate and are complementary to those enabled within the framework of the no-core shell model[1] (NCSM) [1], and which can be used to facilitate *ab initio* applications to challenging lower *sd*-shell nuclei, reveal that bound states of light nuclei are dominated by high-deformation and low-spin configurations [2]. The applicable symmetries reveal the nature of collectivity in such nuclei and provide a description of bound states in terms of a relatively small fraction of the complete space when the latter is expressed in an $(LS)J$ coupling scheme with the spatial configurations further organized into irreducible representations of SU(3). That SU(3) plays a key role tracks with the seminal work of Elliott [3], and is further reinforced by the fact that SU(3) also underpins the microscopic symplectic model [4, 5], which provides a theoretical framework for understanding deformation-dominated collective phenomena in atomic nuclei [6].

[1] This talk is dedicated to James P. Vary on the occasion of his 70th birthday, and is given in recognition and celebration of his important contributions to nuclear physics, especially for his seminal and sustained leadership in the development of the no-core shell model.

Proceedings of International Conference 'Nuclear Theory in the Supercomputing Era — 2013' (NTSE-2013), Ames, IA, USA, May 13–17, 2013. Eds. A. M. Shirokov and A. I. Mazur. Pacific National University, Khabarovsk, Russia, 2014, p. 47.
http://www.ntse-2013.khb.ru/Proc/Draayer.pdf.

While applications to p-shell and selected heavier nuclei [2, 7–9] illustrate the success of the *ab initio* approach, a very simple algebraic interaction, which reduces to the Elliott SU(3) model [3] in the single-shell limit, augmented by the SU(3) symmetry breaking spin-orbit interaction, reproduces characteristic features of the low-lying 0^+ states in ^{12}C as well as ground-state rotational bands in p and sd-shell nuclei (from Be to Si) [10, 11]. The study of ^{12}C includes the elusive first excited 0^+_2 state, known as the Hoyle state [12] that was predicted based on observed abundances of heavy elements in the universe, and which has attracted much recent attention [13–16]. An implication of the latter is that efforts to reproduce the structure of ^{12}C using a 'bottom up' *ab initio* effective interaction theory may benefit from 'top down' algebraic considerations that serve to expose emergent properties in terms of simple interaction forms that seem to dominate the structure of deformed nuclei, especially the 0^+ states of ^{12}C.

2 Shell models and collectivity-driven models

This section is dedicated to a short review of the major theoretical efforts that underpin development of the SA-NCSM and/or have advanced our understanding of particle- and collectivity-driven phenomena (Table 1). For a complete list of approaches that have made substantial contributions, we refer the reader to the review articles [6, 17, 18] and references therein.

In the 1950s, two simple models of nuclear structure were advanced that are complementary in nature, namely, the independent-particle model of Mayer and Jensen [19], and the collective model of Bohr and Mottelson [20]. The first of these, which is microscopic in nature, recognizes that nuclei can be described by particles independently moving in a mean field, with the harmonic oscillator (HO) potential being a very good first approximation to the average potential experienced by each nucleon in a nucleus. The second of these, which is collective in nature, recognizes that deformed shapes dominate the dynamics. For example, deformed configurations are found to be important even in a nucleus such as ^{16}O, which is commonly treated as spherical in its ground state, but 20% of the latter is governed by deformed shapes; in addition, the lowest-lying excited 0^+ states in ^{16}O and their rotational bands are dominated by large deformation [21]. Bohr and Mottelson offered a simple but important description of nuclei in terms of the deformation of the nuclear surface and associated vibrations and rotations.

The seminal work of Elliott [3, 22] focused on the key role of SU(3), the exact symmetry of the three-dimensional spherical HO. Within a shell-model framework, Elliott's model utilizes an SU(3)-coupled basis that is related via a unitary transformation to the basis used in the conventional shell model. The new feature here is that SU(3) divides the space into basis states of definite $(\lambda\,\mu)$ quantum numbers of SU(3) linked to the intrinsic quadrupole deformation [23–25]. E. g., the simplest cases, $(0\,0)$, $(\lambda\,0)$, and $(0\,\mu)$, describe spherical, prolate, and oblate deformation, respectively. For SU(3)-symmetric interactions, the model can be solved analytically. But regardless whether a simple algebraic interaction is used, such as $H = H_{\rm HO} - \frac{\chi}{2} Q \cdot Q$ (see, e. g., Fig. 1, left), or an SU(3)-symmetry breaking interaction (see, e. g., Fig. 1, right), the results have revealed a striking feature, namely, the dominance of a few most deformed configurations. This has been shown for sd-shell nuclei, such as ^{18}Ne, ^{20}Ne, ^{22}Ne, ^{22}Mg, ^{24}Mg, and ^{28}Si, that have been known to possess a clear collective rotational structure in their low-lying states [22, 26]. It has been also observed in heavier nuclei, where pseudo-spin symmetry and its pseudo-SU(3) complement have been shown to play a similar role in accounting for deformation in the upper pf and lower sdg shells, and in particular, in strongly deformed nuclei of the rare-earth and actinide regions [27].

Table 1: Major cornerstone theories in the development of two classes of nuclear structure models, starting with the Shell Model (SM) and the Collective Model (CM).

Particle Focus	Shape (Collectivity) Focus
Shell Model Goeppert-Mayer & Jensen (1950s) [19] 1963 Nobel Prize: "... for their discoveries concerning nuclear shell structure ..." ∘ Independent-particle model, spherical harmonic oscillator (HO) mean field plus $l\cdot s + l^2$	**Collective Model** Bohr & Mottelson (1950s) [20] 1975 Nobel Prize: "... for the discovery of the connection between collective motion and particle motion in atomic nuclei and the development of the theory of the structure of the atomic nucleus based on this connection ..." ∘ Descriptions in shape variables, β & γ (deformation, rotations, vibrations)
Nilsson Model (1955) [28] ∘ Independent-particle model with a deformed HO mean field plus $l\cdot s + l^2$ **Pairing Model** *Algebraic pairing:* Racah (1940s), Flowers (1950s), Kerman (1960s) [29–31] ∘ SU(2) for like particles (*pp* and *nn* pairs) and Sp(2) for *pp*, *pn*, *nn* pairs *Exact pairing:* ∘ Exact solutions to standard pairing in spherical/deformed mean field (Fig. 2, Guan & Pan (2012) [32]) ∘ *Complementary developments:* *Ab initio* Density Functional Theory (DFT) — first-principle informed, self-consistent mean-field theory plus correlation effects, UNEDF SciDAC Collaboration (2005–Present) [33]	**Elliott SU(3)* Model** (1958) [3] *SU(3) is the symmetry of the 3-D HO Discovery of dominance of a few most deformed configurations (Fig. 1) ∘ Shell model in SU(3)-adapted basis ∘ Valence shell ∘ SU(3)-conserving interactions ∘ SU(3)-breaking interactions: effective, surface-delta (SDI), $l\cdot s + l^2$, **pairing** (Fig. 3a, Vargas & Hirsch (2001) [36]) ∘ *Complementary developments:* Geometric Collective Model — with interactions in terms of β & $\cos 3\gamma$, Greiner (1969) [34] and Interacting Boson Model — algebraic, pairs approximated by bosons, Iachello (1975) [35]
***Ab initio* No-core Shell Model** Vary, Navrátil, Barrett, Maris, ... (2000–Present) [1, 46] First-principle descriptions ($A \leq 16$) ∘ No-core shell model ∘ Realistic interactions (local/nonlocal; NN, NNN, ...) ∘ "Horizontal" cutoff ∘ *Complementary developments:* (2000–Present) GFMC [43], CC method [44], Lattice-EFT [14] (for details, see [45])	**Symplectic Sp(3, $\mathbb{R}$)* Model** Rowe & Rosensteel (1980s) [4] *Sp(3, $\mathbb{R}$) is naturally realized in nuclei (see first-principle findings, Fig. 4 & [2]) Successful reproduction of rotational bands & transition rates without effective charges (Fig. 3b [39] and Section 4) ∘ Shell model in Sp(3, $\mathbb{R}$)-adapted basis (fixed-core & no-core, **NCSpM**) ∘ Schematic and effective interactions, long-range central force ∘ "Vertical" cutoff (by symplectic slices)
Symmetry-Adapted NCSM (SA-NCSM) Dytrych, Draayer, Launey, Maris, Vary, ... (2007–Present) [2] Discovery of emergence of symmetries from first principles (see, e. g., Fig. 4); expanding the reach of *ab initio* models to lower *sd*-shell nuclei ∘ *Ab initio* NCSM with SU(3)-adapted basis (any interaction) ∘ Manage spurious center-of-mass motion ∘ Fully microscopic & equals NCSM if the complete space is included ∘ No effective charges	

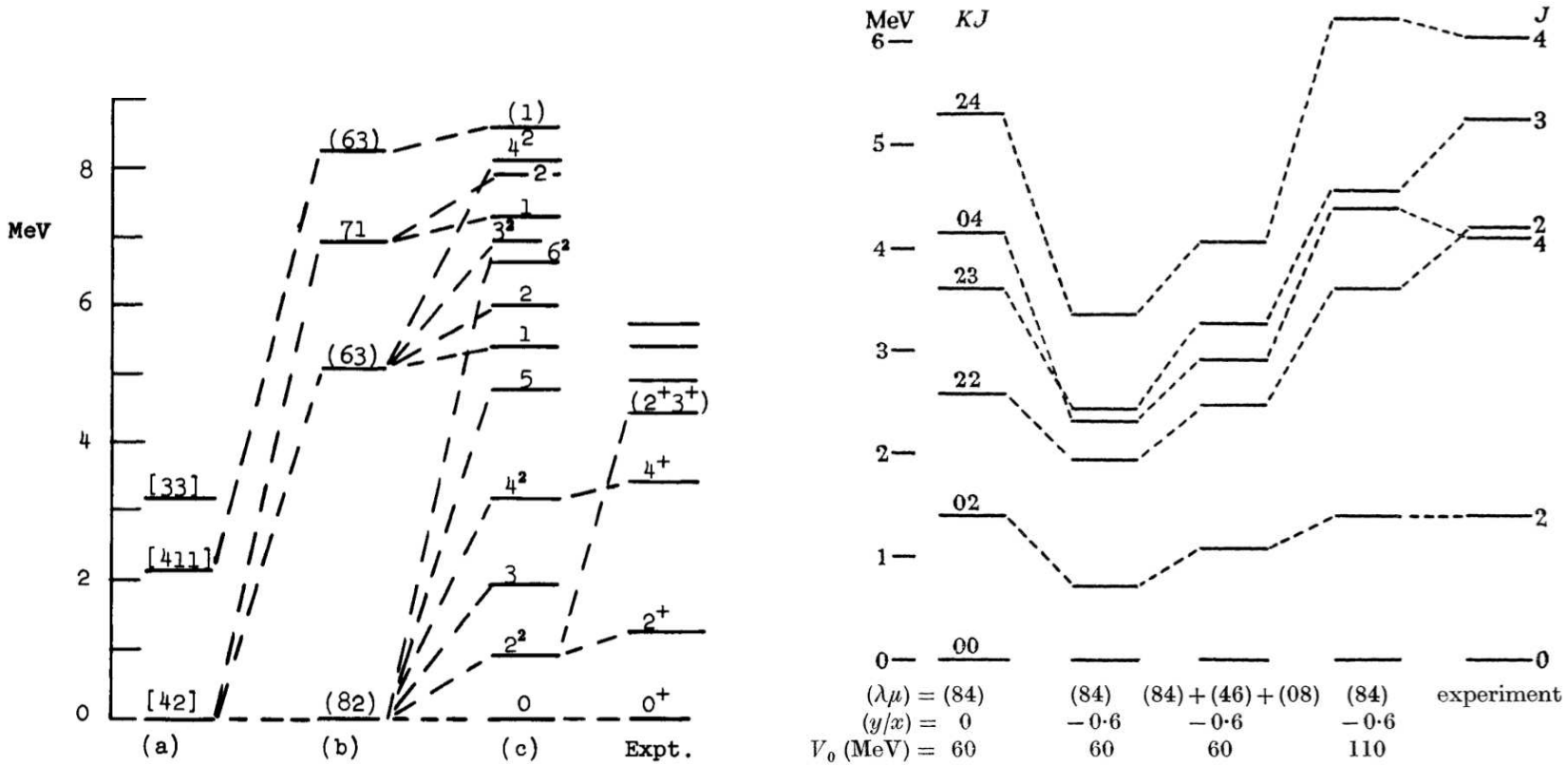

Figure 1: Elliott's SU(3) model applied to *sd*-shell nuclei. Left panel: Spectrum of ^{22}Ne (or ^{22}Mg) (a) with a Majorana potential, (b) with the addition of the second-order SU(3) Casimir invariant, C_2^{su3}, and (c) with the Majorana potential plus an attractive $Q \cdot Q$ interaction [or (b) with the addition of L^2]. Figure taken from [26]. Right panel: Spectrum of ^{24}Mg with a Gaussian central force. Figure taken from [22]. The vertical axis in both figures represents energy in MeV. Note the importance of the most deformed SU(3) configuration (8 2) in ^{22}Ne and (8 4) in ^{24}Mg for reproducing the experimental low-lying states.

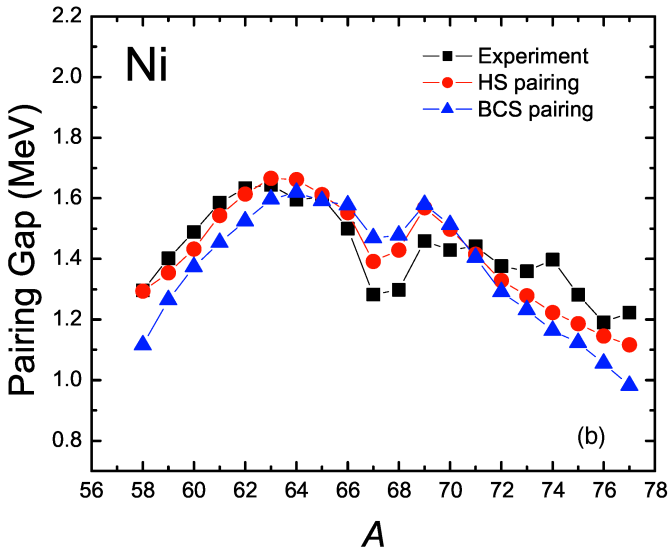

Figure 2: Pairing gaps in MeV as calculated by the exact pairing theory ("HS pairing") and using the BCS approach ("BCS pairing"), and compared to experiment for Ni isotopes, ^{58}Ni to ^{77}Ni, using four j shells, $f_{5/2}$, $p_{1/2}$, $p_{3/2}$, $g_{9/2}$ and $G = 23/A$ MeV. Figure taken from [32].

With an expanding body of experimental evidence that exposed prominent systematic features of nuclei, such as pairing gaps in energy spectra and enhanced electric quadrupole transitions within collective rotational bands, deformation modes were added to the independent-particle model to yield the Nilsson Model (deformed HO mean field) [28]; pairing correlations were taken into account in various algebraic [29–31] and exact pairing models (e. g., see Fig. 2). For the latter, the pairing Hamiltonian includes non-degenerate single-particle energies plus standard pairing and is exactly solvable, for example, yielding solutions for the ground states of Ca, Ni, and Sn isotopes reproducing experimentally observed pairing gaps [32].

As noted in Table 1, a more complete Density Functional Theory (DFT) is a modern derivative theory of this general type, a self-consistent mean-field theory, that can incorporate correlation effects and can accommodate realistic interactions to achieve better predictive capabilities across most of the Chart of the Nuclides. For example, outcomes using this approach generally yield an excellent accounting of binding energies as well as near ground state phenomena across much of the nuclear landscape [33].

Also noted in the Table 1 on the "Shape Focus" side, are two other complementary models that served to inform us of the importance of deformation and pairing; namely, the Geometric Collective Model (GCM) [34] advanced by Greiner and collaborators, and the intriguing Interacting Boson Model (IBM) of Iachello and associates [35]. The latter has offered a bosonic realization of these phenomena in terms of a common overarching U(6) algebraic structure and its physical subgroups, U(5) for pairing modes, SU(3)⊃SO(3) for rotations and O(6)⊃SO(3) for triaxial systems.

The pairing interaction has been microscopically incorporated into the Elliott Model where it breaks the SU(3) symmetry and mixes different $(\lambda\,\mu)$ configurations. It has been shown in Ref. [36] (see also Fig. 3a adapted from [36]) that using an SU(3)-symmetric interaction-plus-pairing yields results close to experiment and to the energies obtained using full *sd*-shell-model calculations [37]. It is remarkable that, even in the presence of pairing, comparable results have been obtained in a truncated model space that includes only about 10 most deformed configurations.

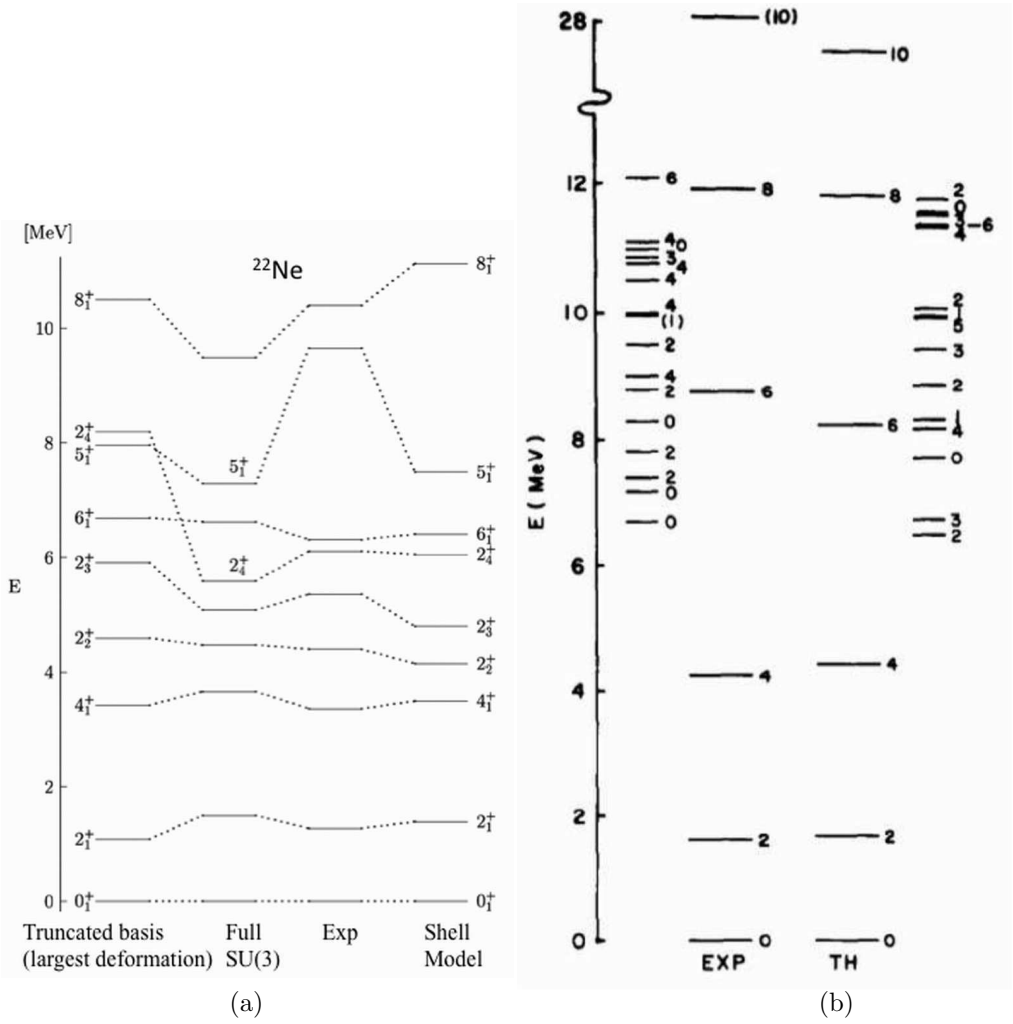

(a) (b)

Figure 3: (a) Elliott's model with a SU(3)-preserving interaction + pairing in the *sd* valence shell for ^{22}Ne. Figure adapted from [36]. (b) Microscopic symplectic model with a set of effective single-particle energies, a $Q\cdot Q$-type interaction+pairing for ^{20}Ne [calculated $B(E2\downarrow)$ transition strengths, not shown in the figure, for $J^\pi = 2^+$, 4^+, 6^+, and 8^+ *without effective charges* fall within the uncertainties of the corresponding experimental measurements]. Figure taken from [39].

Another very significant advance is the microscopic symplectic model [4, 5], developed by Rowe and Rosensteel, which provides a theoretical framework for understanding deformation-dominated collective phenomena in atomic nuclei [6] that involves particle-particle as well as particle-hole excitations across multiple shells. The significance of the symplectic $\mathrm{Sp}(3,\mathbb{R})$ symmetry, the embedding symmetry of SU(3) [$\mathrm{Sp}(3,\mathbb{R})\supset\mathrm{SU}(3)$], for a microscopic description of a quantum many-body system of interacting particles naturally emerges from the physical relevance of its 21 generators, which are directly related to the particle momentum ($p_{s\alpha}$) and coordinate ($r_{s\alpha}$) operators, with $\alpha = x$, y, and z for the 3 spatial directions and s labeling an individual nucleon, and realize important observables. Namely, the many-particle kinetic energy $\sum_{s,\alpha} p_{s\alpha}^2/2m$, the HO potential, $\sum_{s,\alpha} m\Omega^2 r_{s\alpha}^2/2$, the mass quadrupole moment $Q_{(2\mathcal{M})} = \sum_s q_{(2\mathcal{M})s} = \sum_s \sqrt{16\pi/5}\, r_s^2\, Y_{(2\mathcal{M})}(\hat{\mathbf{r}}_s)$ and angular momentum L operators, together with multi-shell collective vibrations and vorticity degrees of freedom for a description from irrotational to rigid rotor flows are all part of this symmetry. Indeed,

the symplectic $\mathrm{Sp}(3,\mathbb{R})$ symmetry underpins the symplectic shell model that provides a microscopic formulation of the Bohr–Mottelson collective model and is a multiple oscillator shell generalization of the successful Elliott SU(3) model. The symplectic model with $\mathrm{Sp}(3,\mathbb{R})$-preserving interactions[2] have achieved a remarkable reproduction of rotational bands and transition rates without the need for introducing effective charges, while only a single $\mathrm{Sp}(3,\mathbb{R})$ configuration is used [6,38]. A shell-model study in a symplectic basis that allows for mixing of $\mathrm{Sp}(3,\mathbb{R})$ configurations due to pairing and non-degenerate single-particle energies above a ^{16}O core [39] has found that using only seven $\mathrm{Sp}(3,\mathbb{R})$ configurations is sufficient to achieve a remarkable reproduction of the ^{20}Ne energy spectrum (Fig. 3b) as well as of $E2$ transition rates without effective charges.

I believe one can safely claim that the summit of the particle-hole, shell model climb, with James Vary leading the pack, has been realized with the development of the no-core shell model (NCSM), which, in principle, can straightforwardly accommodate any type of inter-nucleon interaction. Specifically, for a general problem, the NCSM adopts the intrinsic non-relativistic nuclear plus Coulomb interaction Hamiltonian defined as follows:

$$H = T_{\mathrm{rel}} + V_{NN} + V_{NNN} + \ldots + V_{\mathrm{Coulomb}}, \tag{1}$$

where the V_{NN} nucleon-nucleon and V_{NNN} 3-nucleon interactions are included along with the Coulomb interaction between the protons. The Hamiltonian may include additional terms such as multi-nucleon interactions among more than three nucleons simultaneously and higher-order electromagnetic interactions such as magnetic dipole-dipole terms. It adopts the HO single-particle basis characterized by the $\hbar\Omega$ oscillator strength and retains many-body basis states of a fixed parity, consistent with the Pauli principle, and limited by a many-body basis cutoff $N_{\max}$. The $N_{\max}$ cutoff is defined as the maximum number of HO quanta allowed in a many-body basis state above the minimum for a given nucleus. It divides the space in "horizontal" HO shells and is dictated by particle-hole excitations (this is complementary to the microscopic symplectic model, which divides the space in vertical slices selected by collectivity-driven rules). It seeks to obtain the lowest few eigenvalues and eigenfunctions of the Hamiltonian (1). The NCSM has achieved remarkable descriptions of low-lying states from the lightest s-shell nuclei up through ^{12}C, ^{16}O, and ^{14}F, and is further augmented by several techniques, such as NCSM/RGM [40], Importance Truncation NCSM [41] and Monte Carlo NCSM [42]. This supports and complements results of other first-principle approaches, also shown in Table 1, such as Green's function Monte Carlo (GFMC) [43], Coupled-cluster (CC) method [44], and Lattice Effective Field Theory (EFT) [14] (see also, this proceedings volume [45]). For further details on NCSM, see Vary's distinguished lecture in this proceedings [46].

We have recently explored a fully microscopic no-core symplectic shell model, NCSpM (for details, see Sec. 4) that utilizes a $\mathrm{Sp}(3,\mathbb{R})$-preserving $Q\cdot Q$-type interaction plus a symmetry-breaking $l\cdot s$ interaction. The study has revealed that with a simple interaction and only a few $\mathrm{Sp}(3,\mathbb{R})$ configurations the model can provide a successful description of the ^{12}C Hoyle state and low-lying states in nuclei from Be to Si [10, 11] (including energy spectra, $E2$ transition strengths, quadrupole moments, and matter rms radii). The key to this outcome is the ability of the model to include higher-lying HO shells, thereby making large-$N_{\max}$ calculations feasible.

The next-generation *ab initio* symmetry-adapted no-core shell model (SA-NCSM) [2] combines the first-principle concept of the NCSM with symmetry-guided considerations of the collectivity-driven models. The SA-NCSM has revealed the emergence

[2] An important $\mathrm{Sp}(3,\mathbb{R})$-preserving interaction is $\frac{1}{2}Q\cdot Q = \frac{1}{2}\sum_s q_s\cdot(\sum_t q_t)$, as this realizes the physically relevant interaction of each particle with the total quadrupole moment of the nuclear system.

of clear symmetry patterns from first principles [2] — such as the SU(3) and the symplectic Sp(3, $\mathbb{R}$) symmetries inherent to nuclei, and in addition, have demonstrated the power of using symmetry-dictated subspaces to reach new domains of nuclear structure currently inaccessible by *ab initio* calculations. The model and its recent findings are described in the next section.

3 *Ab initio* SA-NCSM

The *ab initio* symmetry-adapted no-core shell model (SA-NCSM) [2] adopts the first-principle concept and utilizes a many-particle basis that is reduced with respect to the physically relevant SU(3)⊃SO(3) subgroup chain (for a review, see [21]). This allows the full model space to be down-selected to the physically relevant space. The significance of the SU(3) group for a microscopic description of the nuclear collective dynamics can be seen from the fact that it is the symmetry group of the Elliott model [3], and a subgroup of the Sp(3, $\mathbb{R}$) symplectic model [4]. The basis states of the SA-NCSM are based on HO single-particle states and for a given $N_{\max}$, are constructed in the proton-neutron formalism using an efficient construction based on powerful group-theoretical methods. The SA-NCSM basis states are related to the NCSM basis states through a unitary transformation (hence, the SA-NCSM results obtained in a complete $N_{\max}$ space are equivalent to the $N_{\max}$-NCSM results). They are labeled by the SU(3)⊃SO(3) subgroup chain quantum numbers $(\lambda\,\mu)\kappa L$, together with proton, neutron, and total intrinsic spins S_p, S_n, and S. The orbital angular momentum L is coupled with S to the total orbital momentum J and its projection M_J. Each basis state in this scheme is labeled schematically as $|\vec{\gamma}\,(\lambda\,\mu)\kappa L;(S_pS_n)S;JM_J\rangle$. The label κ distinguishes multiple occurrences of the same L value in the parent irrep $(\lambda\,\mu)$, and $\vec{\gamma}$ distinguishes among configurations carrying the same $(\lambda\,\mu)$ and $(S_pS_n)S$ labels.

3.1 Emergence of a simple structure — 'Bottom Up' considerations

The *ab initio* SA-NCSM results for *p*-shell nuclei reveal a dominance of configurations of large deformation (typically large $|\lambda\ -\mu|$) in the $0\hbar\Omega$ subspace. For example, the *ab initio* $N_{\max}=6$ SA-NCSM results with the bare JISP16 realistic interaction [47] for the 0^+ ground state (g. st.), first 2^+ and first 4^+ states of ^{12}C reveal the dominance of the $0\hbar\Omega$ component with the foremost contribution coming from the leading $(0\,4)$ $S=0$ irrep (Fig. 4). Furthermore, we find that important SU(3) configurations are then organized into structures with Sp(3, $\mathbb{R}$) symplectic symmetry, that is, the $(0\,4)$ symplectic irrep gives rise to $(0\,2)$ and $(2\,4)$ configurations in the $2\hbar\Omega$ subspace and so on (see Fig. 4, inset), and those configurations indeed realize the major components of the wavefunction in this subspace. This further confirms the significance of the symplectic symmetry to nuclear dynamics. Similar results are observed for other *p*-shell nuclei. The outcome points to the fact that the relevant model space can be systematically determined by down-selecting to important spin configurations in lower subspaces while expanded to include a limited set of strongly deformed configurations in the higher $N_{\max}$ regime.

In short, the SA-NCSM advances an extensible microscopic framework for studying nuclear structure and reactions that capitalizes on advances being made in *ab initio* methods while exploiting symmetries — exact and partial, known to dominate the dynamics.

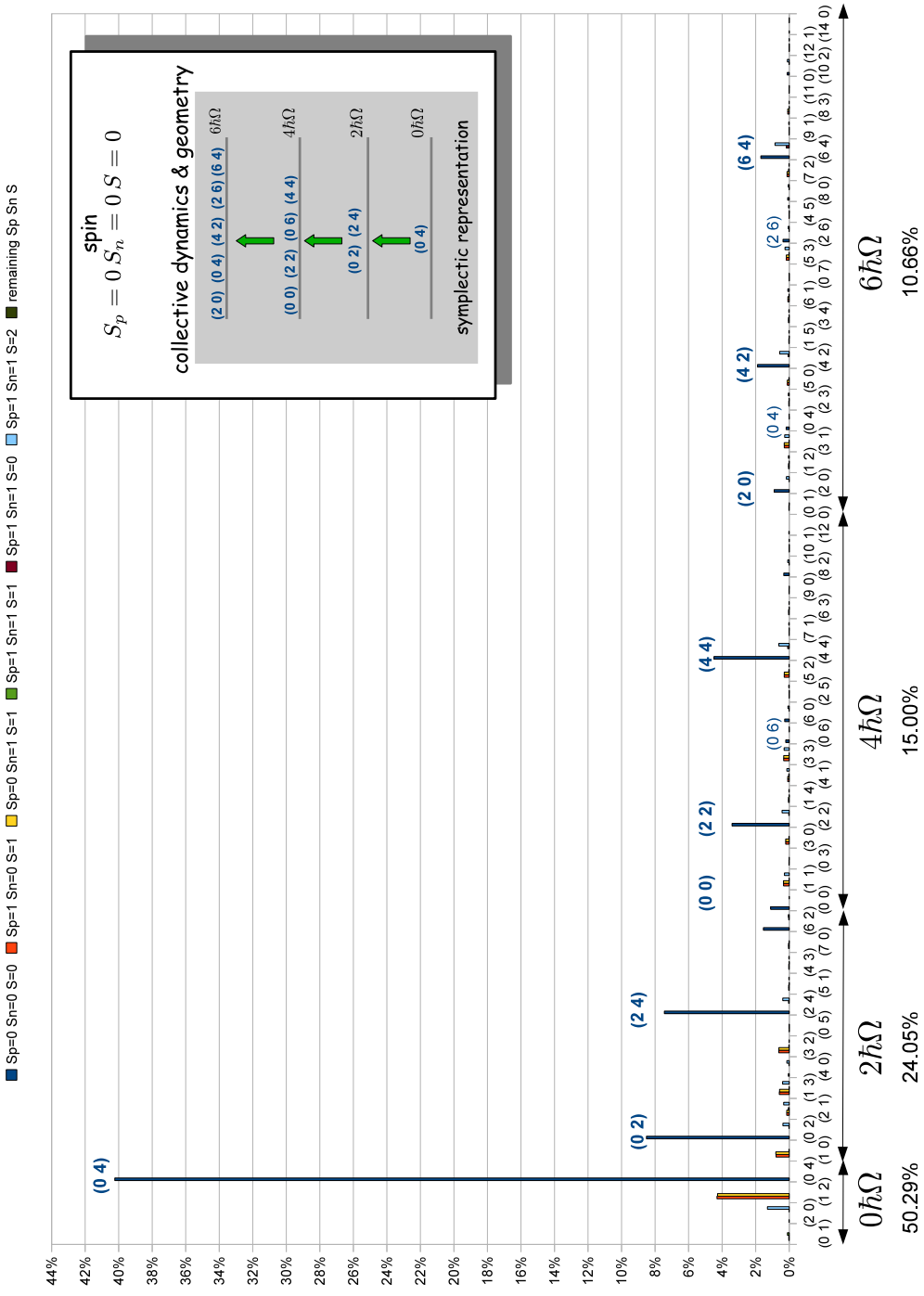

Figure 4: Probability distribution of the lowest calculated 0^+ state for ^{12}C over deformed subspaces labeled by $(\lambda\,\mu)$ for six of the most important spin components $\{S_p, S_n, S\} = \{0,0,0\}, \{1,0,1\}, \{0,1,1\}, \{1,1,1\}, \{1,1,0\}$ and $\{1,1,2\}$. Labels above the columns denote SU(3) quantum numbers of states that belong to the leading $(0\,4)$ symplectic $\mathrm{Sp}(3,\mathbb{R})$ irrep. The wavefunction was obtained using the $N_{\max} = 6$ SA-NCSM with the JISP16 bare interaction and $\hbar\Omega = 10$ MeV.

3.2 Symmetries in realistic nucleon-nucleon interactions

The nucleon-nucleon interaction itself possesses a clear structure when its SU(3) content is studied. This is observed in the decomposition of the NN interaction into $\mathrm{SU}(3) \times \mathrm{SU}(2)_S \times \mathrm{SU}(2)_T$ tensors (isoscalar interactions will be henceforth considered). This is analogous to the unitary transformation of a V_{2b} two-body interaction represented in a m-scheme harmonic oscillator (HO) basis to a JT-coupled basis, which renders V_{2b} as only one $\mathrm{SU}(2)_J \times \mathrm{SU}(2)_T$ tensor of rank $J_0 = 0$ and $T_0 = 0$ (a scalar with respect to rotations in coordinate and isospin space). For example, the scalar interaction part of $(\lambda_0\, \mu_0) = (0\,0)$ does not mix nuclear deformation in analogy to the isoscalar part of an interaction that does not mix isospin values. In addition, the $(\lambda_0\, \mu_0)$ interaction parts with $\lambda_0 = \mu_0$ are almost diagonal, that is, connect configurations within a few shells, while interaction parts with a large difference $|\lambda_0 - \mu_0|$ typically couple low-lying and higher-lying shell-model configurations.

This decomposition organizes the interaction into only a small number of pieces of information that bring forward important physics. In particular, as a measure of the strength or "size" of each interaction tensor, we use its Hilbert–Schmidt norm, which is directly related to the square of the $(\lambda_0\, \mu_0)S_0$ reduced matrix elements. For example, we find a dominance of the $(0\,0)$ scalar part followed by the symplectic-like modes of $(0\,2)$, and equally, the conjugate $(2\,0)$, and then tensors as $(1\,1)$, $(2\,2)$, $(3\,3)$, and etc., which typically dominate for the pairing interaction or contact term (see Fig. 5 for the bare JISP16, which is used for $N_{\max} = 6$ SA-NCSM calculations in Fig. 4). These results, we find, repeat for various realistic bare and renormalized interactions.

4 NCSpM model — 'Top Down' considerations

The no-core symplectic shell model (NCSpM) is a fully microscopic no-core shell model that uses a symplectic $\mathrm{Sp}(3,\mathbb{R})$ basis and $\mathrm{Sp}(3,\mathbb{R})$-preserving interactions. The NCSpM employed within a full model space up through a given $N_{\max}$ coincides with the NCSM for the same $N_{\max}$ cutoff. However, in the case of the NCSpM, the symplectic irreps divide the space into 'vertical slices' that are comprised of basis states of a definite deformation $(\lambda\, \mu)$. Hence, the model space can be reduced to only a few important configurations that are chosen among all possible $\mathrm{Sp}(3,\mathbb{R})$ irreps within the $N_{\max}$ model space. The NCSpM, while selecting the most relevant symplectic configurations, is employed to provide shell model calculations beyond current NCSM limits, namely, up through $N_{\max} = 20$ for ^{12}C, the model spaces we found sufficient for the convergence of results [10].

We employ a very simple Hamiltonian with an effective interaction derived from the long-range expansion of the two-body central nuclear force together with a spin-orbit term,

$$H_{\rm eff} = H_0 + \frac{\chi}{2}\frac{\left(e^{-\gamma Q\cdot Q} - 1\right)}{\gamma} - \kappa \sum_{i=1}^{A} l_i \cdot s_i. \qquad (2)$$

This includes the spherical HO potential, which together with the kinetic energy yields the HO Hamiltonian, $H_0 = \sum_{i=1}^{A}\left(\frac{\mathbf{p}_i^2}{2m} + \frac{m\Omega^2\mathbf{r}_i^2}{2}\right)$, and the $Q\cdot Q$ quadrupole-quadrupole interaction not restricted to a single shell. For the latter term, the average contribution, $\langle Q\cdot Q\rangle_n$, of $Q\cdot Q$ within a subspace of n HO excitations is removed [48], that is, the trace of $Q\cdot Q$ divided by the space dimension for a fixed n. Hence, the large monopole contribution of the $Q\cdot Q$ interaction is removed, which, in turn, helps eliminate the considerable renormalization of the zero-point energy, while retaining the $Q\cdot Q$-driven behavior of the wavefunctions. This Hamiltonian in its zeroth-order approximation (for parameter $\gamma \to 0$) and for a valence shell goes back to the established Elliott model. We take the coupling constant χ to be proportional to $\hbar\Omega$ and,

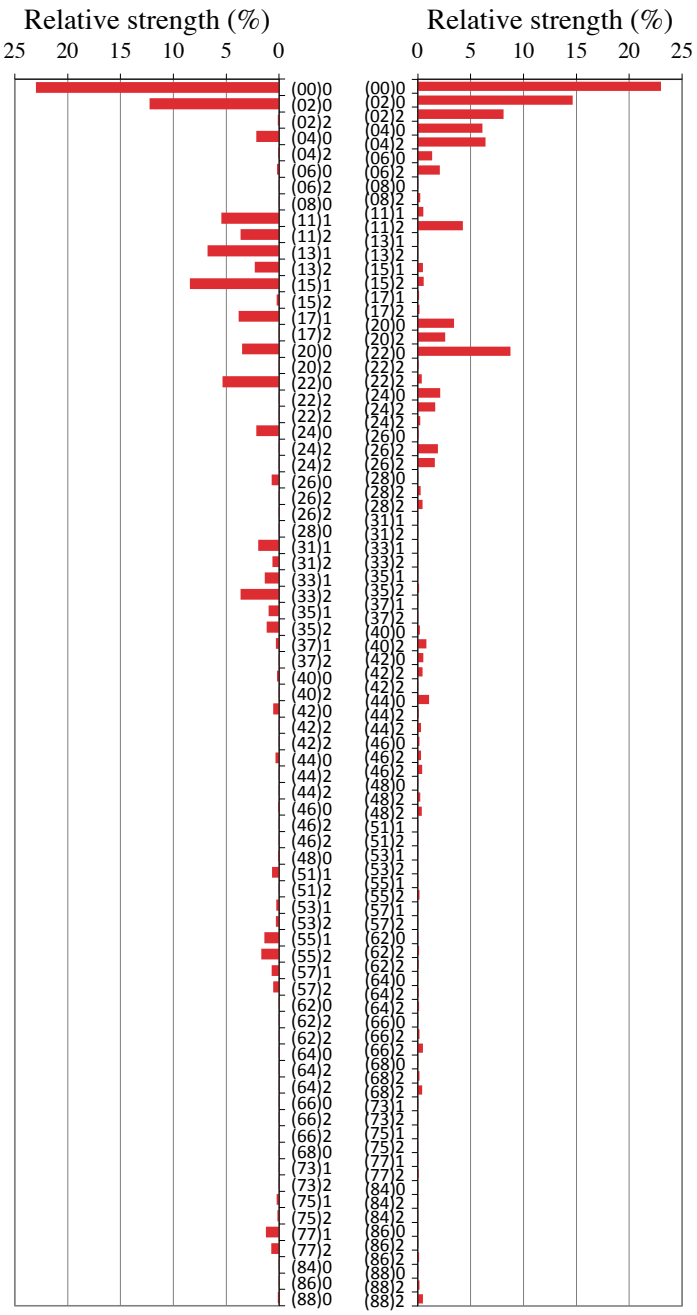

Figure 5: Relative strengths of the $T = 1$ (left) and $T = 0$ (right) bare JISP16 interaction tensors labeled by $(\lambda_0\,\mu_0)S_0$ for $\hbar\Omega = 15$ MeV and $N_{\max} = 6$ for p-shell nuclei.

to leading order, to decrease with the total number of HO excitations, as shown by Rowe [49] based on self-consistent arguments.

As the interaction and the model space are carefully selected to reflect the most relevant physics, the outcome reveals a quite remarkable agreement with the experiment [10]. The low-lying energy spectrum and eigenstates for ^{12}C were calculated using the NCSpM with H of Eq. (2) for $\hbar\Omega = 18$ MeV given by the empirical estimate $\approx 41/A^{1/3} = 17.9$ MeV and for $\kappa \approx 20/A^{2/3} = 3.8$ MeV (see, e. g., [20]). The results are shown for $N_{\max} = 20$, which we found sufficient to yield

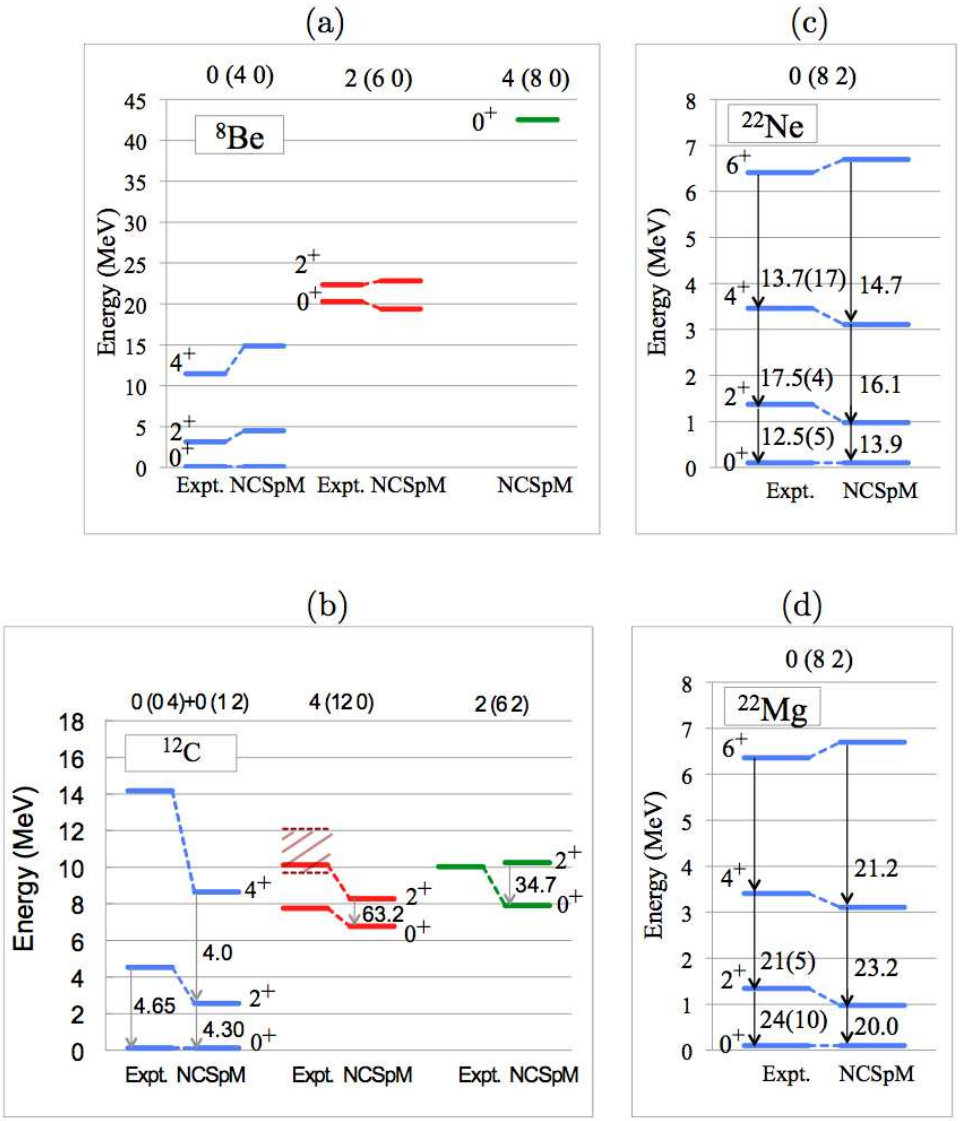

Figure 6: Energy spectra calculated by the NCSpM with $\gamma = -1.71 \times 10^{-4}$ for (a) ^{8}Be in an $N_{\max} = 24$ model space, (b) ^{12}C in an $N_{\max} = 20$ model space, (c) ^{22}Ne and (d) ^{22}Mg in an $N_{\max} = 12$ model space, and compared to experiment ("Expt.").

convergence. This $N_{\max}$ model space is further reduced by selecting the most relevant symplectic irreps, namely, the spin-zero ($S = 0$) $0\hbar\Omega$ 0p-0h (0 4), $2\hbar\Omega$ 2p-2h (6 2), and $4\hbar\Omega$ 4p-4h (12 0) symplectic bandheads together with the $S = 1$ $0\hbar\Omega$ 0p-0h (1 2) and all multiples thereof up through $N_{\max} = 20$ of total dimensionality of 6.6×10^3. In comparison to the experimental energy spectrum (Fig. 6b), the outcome reveals that the lowest 0^+, 2^+, and 4^+ states of the 0p-0h symplectic slices calculated for $\gamma = -1.71 \times 10^{-4}$ closely reproduce the g. st. rotational band, while the calculated lowest 0^+ states of the $4\hbar\Omega$ 4p-4h (12 0) and the $2\hbar\Omega$ 2p-2h (6 2) slices are found to lie close to the Hoyle state and the 10-MeV 0^+ resonance (third 0^+ state), respectively. The model successfully reproduces other observables for ^{12}C that are informative of the state structure, such as mass rms radii, electric quadrupole moments and $B(E2)$ transition strengths (Fig. 6b).

A preponderance of the (0 4) $S = 0$ configuration and also (1 2) $S = 1$ configuration is observed for the ground-state rotational band, thereby indicating an oblate

shape. The Hoyle-state rotational band includes shapes of even larger deformations but prolate, with the largest contribution of (16 0).

While the model includes an adjustable parameter, γ, this parameter only controls the decrease rate of the $Q\cdot Q$ interaction with increasing n. The entire many-body apparatus is fully microscopic and no adjustments are possible. Hence, as γ varies, there is only a small window of possible γ values that, for large enough $N_{\max}$, closely reproduces the relative positions of the three lowest 0^+ states.

The outcome of the present analysis is not limited to ^{12}C. The model we find is also applicable to the low-lying states of other p-shell nuclei, such as ^{8}Be, as well as sd-shell nuclei without any adjustable parameters (Fig. 6). In particular, using the same $\gamma = -1.71 \times 10^{-4}$ as determined here for ^{12}C, we describe selected low-lying states in ^{8}Be in an $N_{\max} = 24$ model space with only 3 spin-zero $0\hbar\Omega$ (4 0), $2\hbar\Omega$ (6 0), and $4\hbar\Omega$ (8 0) symplectic irreps. Furthermore, we have successfully applied the NCSpM without any adjustable parameters to the ground-state rotational band of heavier nuclei, such as ^{20}Ne, ^{22,24}Ne, ^{22,26}Mg, and ^{24,26}Si (see Fig. 6 for ^{22}Ne and ^{22}Mg). This suggests that the fully microscopic NCSpM model has indeed captured an important part of the physics that governs the low-energy nuclear dynamics.

5 Conclusion

Symmetries in atomic nuclei that have been long recognized have been recently utilized and further understood in the framework of the *ab initio* symmetry-adapted no-core shell model SA-NCSM as well as of the microscopic no-core symplectic model NCSpM that combine the shell-model and collectivity-driven concepts. The findings pointed to a remarkable new insight, namely, understanding the mechanism on how such simple structures emerge from a fundamental level.

Symmetry-adapted, no-core shell-model calculations with SU(3) the underpinning symmetry were presented. We showed that employing symmetry considerations is effective in providing an efficient description of low-lying states. This holds promise to significantly enhance the reach of *ab initio* shell models toward heavier nuclear systems as well as to achieve descriptions of collective and cluster phenomena from underlying quark/gluon considerations. In addition, the NCSpM study with a schematic many-nucleon interaction showed how both collective and cluster-like structures emerge out of a no-core shell-model framework, which extended to and took into account essential high-lying shell-model configurations.

Acknowledgments

Our work on the SA-NCSM benefitted greatly from the pioneering work done by James Vary and his colleagues on the NCSM. Special thanks are extended to Pieter Maris for his efforts in sharing the most recent version of the NCSM code with us as well as associated and unpublished software packages for our initial proof-of-principle work and most recent model-to-model comparisons. Interactions with Mark Caprio is also acknowledged, and we thank David J. Rowe and George Rosensteel for useful discussions. This work was supported by the U.S. NSF (0904874), the U.S. DOE (DE-SC0005248), SURA, and Natural Science Foundation of China (11175078, 11375080). We also acknowledge DOE/NERSC and LSU/LONI for providing HPC resources.

References

[1] P. Navrátil, J. P. Vary and B. R. Barrett, Phys. Rev. Lett. **84**, 5728 (2000); Phys. Rev. C **62**, 054311 (2000).

[2] T. Dytrych, K. D. Launey, J. P. Draayer, P. Maris, J. P. Vary, E. Saule, U. Çatalyürek, M. Sosonkina, D. Langr and M. A. Caprio, LSU Preprint PA/NP2013-0005 (2013).

[3] J. P. Elliott, Proc. Roy. Soc. A **245**, 128 (1958).

[4] G. Rosensteel and D. J. Rowe, Phys. Rev. Lett. **38**, 10 (1977).

[5] G. Rosensteel and D. J. Rowe, Ann. Phys. (NY) **126**, 343 (1980).

[6] D. J. Rowe, Rep. Progr. Phys. **48**, 1419 (1985).

[7] P. Maris, A. M. Shirokov and J. P. Vary, Phys. Rev. C **81**, 021301 (R) (2010).

[8] G. Hagen, T. Papenbrock, D. J. Dean and M. Hjorth-Jensen, Phys. Rev. Lett. **101**, 092502 (2008).

[9] S. C. Pieper and R. B. Wiringa Ann. Rev. Nucl. Part. Sci. **51**, 53 (2001).

[10] A. C. Dreyfuss, K. D. Launey, T. Dytrych, J. P. Draayer and C. Bahri, *submitted* (2013); arXiv:1212.2255 [nucl-th] (2012).

[11] K. D. Launey, T. Dytrych, J. P. Draayer, G. K. Tobin, M. C. Ferriss, D. Langr, A. C. Dreyfuss, P. Maris, J. P. Vary and C. Bahri, in *Proc. 5th Int. Conf. "Fission and properties of neutron-rich nuclei", ICFN5*. World Scientific, *to be published*, 2013.

[12] F. Hoyle, Astrophys. J. Suppl. **1**, 121 (1954).

[13] R. B. Wiringa *et al.*, in *INT Program 12-3 "Light nuclei from first principles"*, 2012.

[14] E. Epelbaum, H. Krebs, D. Lee and U.-G. Meissner, Phys. Rev. Lett. **106**, 192501 (2011).

[15] M. Hjorth-Jensen, Physics **4**, 38 (2011).

[16] M. Chernykh, H. Feldmeier, T. Neff, P. Von Neumann-Cosel and A. Richter, Phys. Rev. Lett. **98**, 032501 (2007).

[17] B. R. Barrett, P. Navrátil and J. P. Vary, Progr. Part. Nucl. Phys. **69**, 131 (2013).

[18] J. E. Drut, R. J. Furnstahl and L. Platter, Progr. Part. Nucl. Phys. **64**, 120 (2010).

[19] O. Haxel, J. H. D. Jensen and H. E. Suess, Phys. Rev. **75**, 1766 (1949); M. G. Mayer, *ibid.* **75**, 1969 (1949); *ibid.* **78**, 16 (1950).

[20] A. Bohr and B. R. Mottelson, *Nuclear Structure, Vol. 1.* Benjamin, New York, 1969; *Vol. 2. ibid.*, 1974; B. R. Mottelson, *Nobel Lectures, Physics 1971–1980.* World Scientific, Singapore, 1992.

[21] T. Dytrych, K. D. Sviratcheva, J. P. Draayer, C. Bahri and J. P. Vary, J. Phys. G. **35**, 123101 (2008).

[22] J. P. Elliott and M. Harvey, Proc. Roy. Soc. A **272**, 557 (1963).

[23] G. Rosensteel and D. J. Rowe, Ann. Phys. (NY) **104**, 134 (1977).

[24] Y. Leschber and J. P. Draayer, Phys. Letts. B **190**, 1 (1987).

[25] O. Castaños, J. P. Draayer and Y. Leschber, Z. Phys **329**, 33 (1988).

[26] M. Harvey, Adv. Nucl. Phys. **1**, 62 (1968).

[27] J. P. Draayer, C. Bahri and S. Moszkowski, Phys. Rev. Lett. **68**, 557 (1992).

[28] S. G. Nilsson, Dan. Mat. Fys. Medd. **29**, No 16 (1955).

[29] G. Racah, Phys. Rev. **62**, 438 (1942); *ibid.* **63**, 367 (1943).

[30] B. H. Flowers, Proc. Roy. Soc. (London) A **212**, 248 (1952).

[31] A. K. Kerman, Ann. Phys. (NY) **12**, 300 (1961).

[32] X. Guan, K. D. Launey, M. Xie, L. Bao, F. Pan and J. P. Draayer, Phys. Rev. C **86**, 024313 (2012).

[33] UNEDF SciDAC Collaboration, http://unedf.org/.

[34] J. Eisenberg and W. Greiner, *Nulcear Theory I: Nuclear collective Models*. North-Holland, Amsterdam, 1987; G. Gneuss, U. Mosel and W. Greiner, Phys. Lett. B **30**, 397 (1969).

[35] F. Iachello and A. Arima, *The Interacting Boson Model*. Cambridge University Press, Cambridge, 1987; A. Arima and F. Iachello, Phys. Rev. Lett. **35**, 1069 (1975).

[36] C. E. Vargas, J. G. Hirsch and J. P. Draayer, Nucl. Phys. A **690**, 409 (2001).

[37] B. M. Preedom and B. H. Wildenthal, Phys. Rev. C **6**, 1633 (1972).

[38] C. Bahri and D. J. Rowe, Nucl. Phys. A **662**, 125 (2000).

[39] J. P. Draayer, K. J. Weeks and G. Rosensteel, Nucl. Phys. A **413**, 215 (1984).

[40] S. Quaglioni and P. Navrátil, Phys. Rev. Lett. **101**, 092501 (2008).

[41] R. Roth, J. Langhammer, A. Calci, S. Binder and P. Navrátil, Phys. Rev. Lett. **107**, 072501 (2011).

[42] T. Abe, P. Maris, T. Otsuka, N. Shimizu, Y. Utsuno and J. P. Vary, Phys. Rev. C **86**, 054301 (2012).

[43] S. Pieper, K. Varga and R. B. Wiringa, Phys. Rev. C **66**, 044310 (2002); S. C. Pieper, Nucl. Phys. A **751**, 516c (2005).

[44] M. Włoch, D. J. Dean, J. R. Gour, M. Hjorth-Jensen, K. Kowalski, T. Papenbrock and P. Piecuch, Phys. Rev. Lett. **94**, 212501 (2005); G. Hagen, T. Papenbrock, D. J. Dean and M. Hjorth-Jensen, Phys. Rev. C **82**, 034330 (2010).

[45] *Proc. Int. Conf. Nucl. Theor. Supercomputing Era (NTSE-2013), Ames, IA, USA, May 1–17, 2013*, eds. A. M. Shirokov and A. I. Mazur. Pacific National University, Khabarovsk, 2014 (*see these Proceedings*), http://www.ntse-2013.khb.ru/Proc/.

[46] J. P. Vary, *Computational Nuclear Physics: Key to Discovery Opportunities*, Distinguished Lecture at NTSE-2013, *see these Proceedings*, p. 15, http://www.ntse-2013.khb.ru/Proc/JPVary.pdf.

[47] A. M. Shirokov, J. P. Vary, A. I. Mazur and T. A. Weber, Phys. Lett. B **644**, 33 (2007).

[48] G. Rosensteel and J. P. Draayer, Nucl. Phys. A **436**, 445 (1985).

[49] D. J. Rowe, Phys. Rev. **162**, 866 (1967).

Utilizing Symmetry Coupling Schemes in *Ab Initio* Nuclear Structure Calculations

T. Dytrych[a], J. P. Draayer[a], K. D. Launey[a], P. Maris[b], J. P. Vary[b] and D. Langr[c]

[a] *Department of Physics and Astronomy, Louisiana State University, Baton Rouge, LA 70803, USA*

[b] *Department of Physics and Astronomy, Iowa State University, Ames, IA 50011, USA*

[c] *Department of Computer Systems, Czech Technical University, Prague, Czech Republic*

Abstract

We report on *ab initio* no-core shell model calculations in a symmetry-adapted SU(3)-based coupling scheme that demonstrate that collective modes in p-shell nuclei emerge from first principles. The low-lying states of ^{6}Li, ^{6}He, ^{8}Be, ^{8}B, ^{12}C, and ^{16}O, are shown to exhibit orderly patterns that favor spatial configurations with strong quadrupole deformation and complementary low intrinsic spin values, a picture that is consistent with the nuclear symplectic model. The results also suggest a pragmatic path forward to accommodate deformation-driven collective features in *ab initio* analyses when they dominate the nuclear landscape.

Keywords: *No-core shell model; SU(3) coupling scheme; p-shell nuclei*

1 Introduction

In the last few years, *ab initio* approaches to nuclear structure and reactions have considerably advanced our understanding and capability of achieving first-principle descriptions of p-shell nuclei [1–3]. These advances are driven by the major progress in the development of realistic nuclear potential models, such as J-matrix inverse scattering potentials [4] and two- and three-nucleon potentials derived from meson exchange theory [5] or by using chiral effective field theory [6], and, at the same time, by the utilization of massively parallel computing resources [7–9].

The predictive power that *ab initio* models hold [10, 11] makes them suitable for targeting short-lived nuclei that are inaccessible by experiment but essential to further modeling, for example, of the dynamics of X-ray bursts and the path of nucleosynthesis (see, e. g., Refs. [12, 13]). The main limitation of *ab initio* approaches is inherently coupled with the combinatorial growth in the size of the many-particle model space with increasing nucleon numbers and expansion in the number of single-particle levels in the model space as illustrated in Fig. 1. This points to the need of further major advances in many-body methods to access a wider range of nuclei and experimental observables, while retaining the *ab initio* predictive power.

These considerations motivate us to develop and investigate a novel model, the *ab initio* symmetry-adapted no-core shell model (SA-NCSM) [14], which by taking advantage of symmetries inherent to the nuclear dynamics [15,16] allows one to truncate a model space according to correlations indispensable for modeling important modes of nuclear collective dynamics, thereby overcoming the scale explosion bottleneck of *ab initio* nuclear structure computations.

Proceedings of International Conference 'Nuclear Theory in the Supercomputing Era — 2013' (NTSE-2013), Ames, IA, USA, May 13–17, 2013. Eds. A. M. Shirokov and A. I. Mazur. Pacific National University, Khabarovsk, Russia, 2014, p. 62.

http://www.ntse-2013.khb.ru/Proc/Dytrych.pdf.

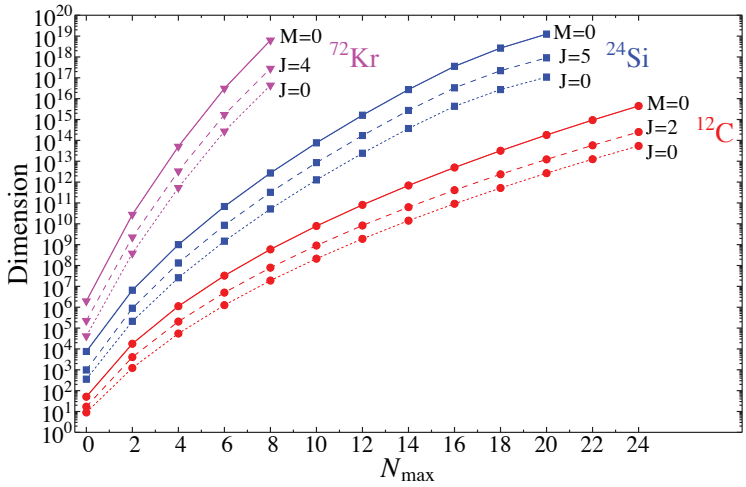

Figure 1: The dimensions of positive parity model spaces as functions of $N_{\max}$ for selected nuclei. Solid curves show the number of basis states with the projection of the total angular momentum $M = 0$. Dashed and dotted curves depict the number of basis states carrying selected values of the total angular momentum J.

2 *Ab initio* calculations in a SU(3)-based coupling scheme

The SA-NCSM joins a no-core shell model (NCSM) theory [2] with a multi-shell, SU(3)-based coupling scheme [15, 17]. Specifically, the many-nucleon basis states of the SA-NCSM are decomposed into spatial and intrinsic spin parts, where the spatial part is further classified according to the SU(3) $\supset$ SO(3) group chain. The significance of the SU(3) group for a microscopic description of the nuclear collective dynamics can be seen from the fact that it is the symmetry group of the successful Elliott model [15], and a subgroup of the physically relevant $\mathrm{Sp}(3,\mathbb{R})$ symplectic model [16], which provides a comprehensive theoretical foundation for understanding the dominant symmetries of nuclear collective motion. The SA-NCSM basis states are labeled as

$$|\vec{\gamma}; N(\lambda\,\mu)\kappa L; (S_p S_n)S; JM\rangle, \tag{1}$$

where N signifies the number of harmonic oscillator quanta with respect to the minimal number for a given nucleus. Quantum numbers S_p, S_n, and S denote proton, neutron, and total intrinsic spins, respectively, and $(\lambda\,\mu)$ represent a set of quantum numbers associated with SU(3) irreducible representations, irreps. The label κ distinguishes multiple occurrences of the same orbital momentum L in the parent irrep $(\lambda\,\mu)$. The L is coupled with S to the total angular momentum J and its projection M. The basis states bring forward important information about nuclear shapes and deformation according to an established mapping [18]. For example, (00), $(\lambda\,0)$ and $(0\,\mu)$ describe spherical, prolate and oblate shapes, respectively. The symbol $\vec{\gamma}$ schematically denotes the additional quantum numbers needed to specify a distribution of nucleon clusters over the major HO shells and their inter-shell coupling. Specifically, in each major HO shell η with degeneracy Ω_η, clusters of protons and neutrons are arranged into antisymmetric $\mathrm{U}(\Omega_\eta) \times \mathrm{SU}(2)_{S_\eta}$ irreps [19], with $\mathrm{U}(\Omega_\eta)$ further reduced with respect to SU(3). The quantum numbers, $\left[f_1, \ldots, f_{\Omega_\eta}\right] \alpha_\eta\, (\lambda_\eta\, \mu_\eta)\, S_\eta$, along with $\mathrm{SU}(3) \times \mathrm{SU}(2)_S$ labels of inter-shell coupling unambiguously determine SA-NCSM basis states (1). Note that a spatial symmetry associated with a Young

shape $\left[f_1,\ldots,f_{\Omega_\eta}\right]$ is uniquely determined by the imposed antisymmetrization and the associated intrinsic spin S_η. A multiplicity index α_η is required to distinguish multiple occurrences of SU(3) irrep $(\lambda_\eta\,\mu_\eta)$ in a given U(Ω_η) irrep. It is important to note that any model space spanned by a complete set of equivalent SU(3) $\times$ SU(2)$_S$ irreps, that is, a space spanned by all configurations carrying a fixed set of $S_p\,S_n\,S$ and $(\lambda\,\mu)$ quantum numbers, permits exact factorization of the center-of-mass motion.

The SA-NCSM implements fast methods for calculating matrix elements of arbitrary (currently up to two-body, but expandable to higher-rank) operators in the symmetry-adapted basis. This facilitates both the evaluation of the Hamiltonian matrix elements and the use of the resulting eigenvectors to evaluate other experimental observables. The underlying principle behind the SA-NCSM computational kernel is an SU(3)-type Wigner–Eckhart theorem, which factorizes interaction matrix elements into the product of SU(3) reduced matrix elements (*rme*) and the associated SU(3) coupling coefficient. The SA-NCSM configurations are constructed by the inter-shell coupling of a sequence of single-shell nucleon clusters arranged into U(Ω) $\times$ SU(2)$_S$, with U(Ω) $\supset$ SU(3), irreps. Therefore, all the multi-shell *rme* are constructed from a set of single-shell *rme* computed in a configuration space of these irreps. This reduces the number of key pieces of information required to the single-shell *rme*, and these track with the number of U(Ω) $\times$ SU(2)$_S$ irreps, with U(Ω) $\supset$ SU(3), that represent building blocks of the SA-NCSM approach. It is therefore significant that their number grows slowly with the increasing nucleon number and $N_{\max}$ cutoff as this allows these key pieces of information to be stored in CPU memory.

3 Structure of nuclear wave functions

The expansion of calculated eigenstates in the physically relevant SU(3) basis unveils salient features that emerge from the complex dynamics of these strongly interacting many-particle systems. To explore the nature of the most important correlations, we analyze the probability distribution across Pauli-allowed $(S_p\,S_n\,S)$ and $(\lambda\,\mu)$ configurations of the four lowest-lying isospin-zero ($T=0$) states of ^{6}Li ($1^+_{\rm gs}$, 3^+_1, 2^+_1, and 1^+_2), the ground-state rotational bands of ^{8}Be, ^{6}He and ^{12}C, the lowest 1^+, 3^+, and 0^+ excited states of ^{8}B, and the ground state of ^{16}O. Results for the ground state of ^{6}Li and ^{8}Be, obtained with the JISP16 and chiral N^{3}LO interactions, respectively, are shown in Figs. 2 and 3. These figures illustrates a feature common to all the low-energy solutions considered; namely, a highly structured and regular mix of intrinsic spins and SU(3) spatial quantum numbers that has heretofore gone unrecognized in other *ab initio* studies, and which, furthermore, does not seem to depend on the particular choice of realistic NN potential.

For a closer look at these results, first consider the spin content. We found that the calculated eigenstates project at a 99% level onto a comparatively small subset of intrinsic spin combinations. For instance, the lowest-lying eigenstates in ^{6}Li are almost entirely realized in terms of configurations characterized by the following intrinsic spin $(S_p\,S_n\,S)$ triplets: $\left(\frac{3}{2}\,\frac{3}{2}\,3\right)$, $\left(\frac{1}{2}\,\frac{3}{2}\,2\right)$, $\left(\frac{3}{2}\,\frac{1}{2}\,2\right)$, and $\left(\frac{1}{2}\,\frac{1}{2}\,1\right)$, with the last one carrying over 90% of each eigenstate. Likewise, the same spin components as in the case of ^{6}Li are found to dominate the ground state and the lowest 1^+, 3^+, and 0^+ excited states of ^{8}B (Table 1). The ground state bands of ^{8}Be, ^{6}He, ^{12}C, and ^{16}O are found to be dominated by many-particle configurations carrying total intrinsic spin of the protons and neutrons equal to zero and one, with the largest contributions due to $(S_p\,S_n\,S) = (0\,0\,0)$ and $(1\,1\,2)$ configurations.

Second, consider the spatial degrees of freedom. Our results show that the mixing of $(\lambda\,\mu)$ quantum numbers, induced by the SU(3) symmetry breaking terms of realistic interactions, exhibits a remarkably simple pattern. One of its key features is the preponderance of a single $0\hbar\Omega$ SU(3) irrep. This so-called leading irrep, according to the established geometrical interpretation of SU(3) labels $(\lambda\,\mu)$ [18], is characterized

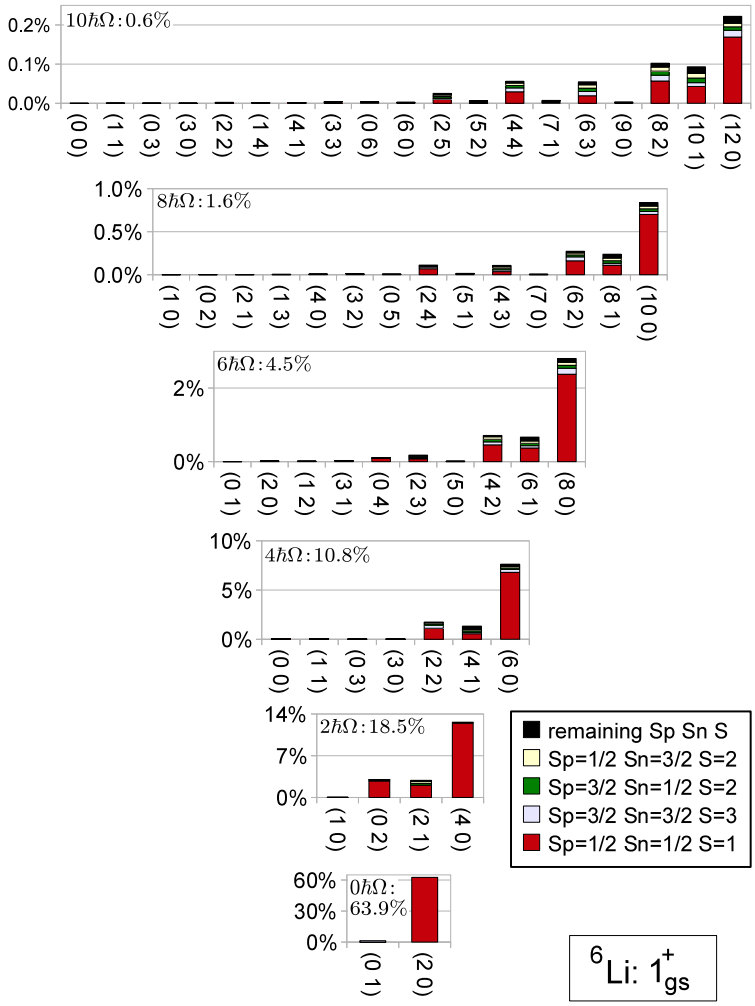

Figure 2: Probability distributions for proton, neutron, and total intrinsic spin components $(S_p\, S_n\, S)$ across the Pauli-allowed $(\lambda\, \mu)$ values (horizontal axis) for the calculated 1^+ ground state of ^{6}Li obtained for $N_{\max} = 10$ and $\hbar\Omega = 20$ MeV with the JISP16 interaction. The total probability for each $N\hbar\Omega$ subspace is given in the upper left-hand corner of each histogram. Adapted from Ref. [14].

by the largest value of the intrinsic quadrupole deformation. For instance, the low-lying states of ^{6}Li project at a 40%–70% level onto the prolate $0\hbar\Omega$ SU(3) irrep $(2\,0)$, as illustrated in Figs. 2 and 3 for the ground state. For the considered states of

Table 1: Probability amplitude of the dominant $(S_p\, S_n\, S)$ spin configuration and the dominant nuclear shapes according to Eq. (2) for the ground state of p-shell nuclei.

Nucleus	$(S_p\, S_n\, S)$	Prob. [%]	$(\lambda_0\, \mu_0)$	Prob. [%]
^{6}Li	$(\frac{1}{2}\,\frac{1}{2}\,1)$	93.26	$(2\,0)$	98.13
^{8}B	$(\frac{1}{2}\,\frac{1}{2}\,1)$	85.17	$(2\,1)$	87.94
^{8}Be	$(0\,0\,0)$	85.25	$(4\,0)$	90.03
^{12}C	$(0\,0\,0)$	55.19	$(0\,4)$	48.44
^{16}O	$(0\,0\,0)$	83.60	$(0\,0)$	89.51

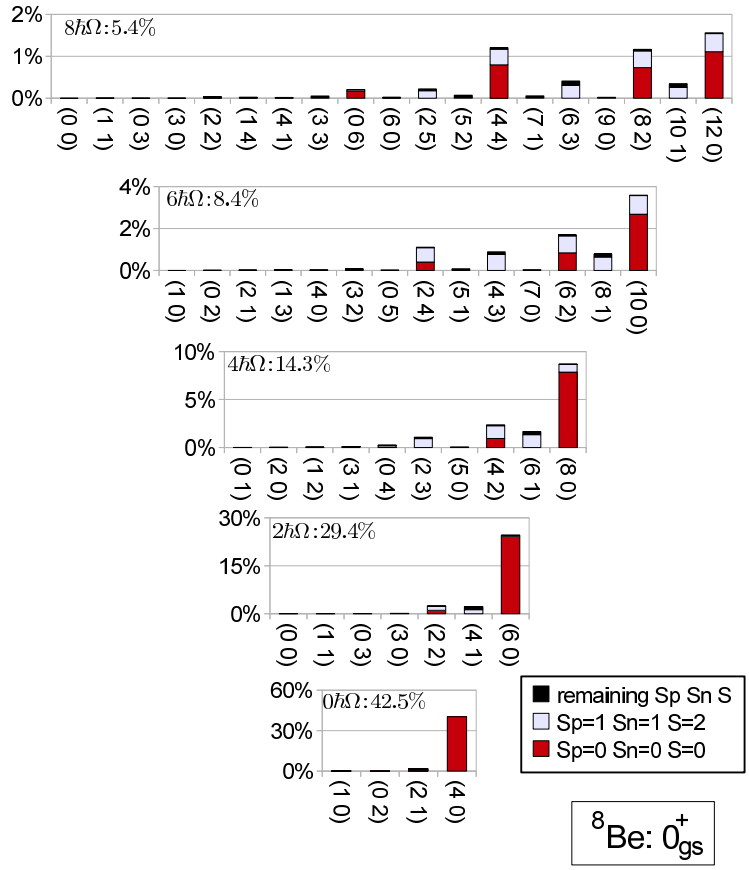

Figure 3: Probability distributions for proton, neutron, and total intrinsic spin components ($S_p\, S_n\, S$) across the Pauli-allowed ($\lambda\, \mu$) values (horizontal axis) for the calculated 0^+ ground state of ^{8}Be obtained for $N_{\max} = 8$ and $\hbar\Omega = 25$ MeV with the chiral N^{3}LO interaction. The total probability for each $N\hbar\Omega$ subspace is given in the upper left-hand corner of each histogram. Adapted from Ref. [14].

^{8}B, ^{8}Be, ^{12}C, and ^{16}O, qualitatively similar dominance of the leading $0\hbar\Omega$ SU(3) irreps is observed — (2 1), (4 0), (0 4), and (0 0) irreps, associated with triaxial, prolate, oblate, and spherical shapes, respectively. The clear dominance of the most deformed $0\hbar\Omega$ configuration within low-lying states of light p-shell nuclei indicates that the quadrupole-quadrupole interaction of the Elliott SU(3) model of nuclear rotations [15] is realized naturally within an *ab initio* framework.

The analysis also reveals that the dominant SU(3) basis states at each $N\hbar\Omega$ subspace ($N = 0, 2, 4, ...$) are typically those with ($\lambda\, \mu$) quantum numbers given by

$$\lambda + 2\mu = \lambda_0 + 2\mu_0 + N \tag{2}$$

where λ_0 and μ_0 denote labels of the leading SU(3) irrep in the $0\hbar\Omega$ ($N = 0$) subspace. We conjecture that this regular pattern of SU(3) quantum numbers reflects the presence of an underlying symplectic Sp$(3, \mathbb{R})$ symmetry of microscopic nuclear collective motion [16] that governs the low-energy structure of both even-even and odd-odd p-shell nuclei. This can be seen from the fact that ($\lambda\, \mu$) configurations that satisfy condition (2) can be determined from the leading SU(3) irrep ($\lambda_0\, \mu_0$) through a successive application of a specific subset of the Sp$(3, \mathbb{R})$ symplectic $2\hbar\Omega$ raising operators. This subset is composed of the three operators, $\hat{A}_{zz}, \hat{A}_{zx}$, and $\hat{A}_{xx}$, that distribute two oscillator quanta in z and x directions, but none in y direction, thereby inducing

SU(3) configurations with ever-increasing intrinsic quadrupole deformation. These three operators are the generators of the $\mathrm{Sp}(2,\mathbb{R}) \subset \mathrm{Sp}(3,\mathbb{R})$ subgroup [20], and give rise to deformed shapes that are energetically favored by an attractive quadrupole-quadrupole interaction [21]. Note that this is consistent with our earlier findings of a clear symplectic $\mathrm{Sp}(3,\mathbb{R})$ structure with the same pattern (2) in *ab initio* eigensolutions for ^{12}C and ^{16}O [22].

Furthermore, there is an apparent hierarchy among states that fulfill condition (2). In particular, the $N\hbar\Omega$ configurations with $(\lambda_0{+}N\ \mu_0)$, the so-called stretched states, carry a noticeably higher probability than the others. For instance, the $(2{+}N\ 0)$ stretched states contribute at the 85% level to the ground state of ^{6}Li, as can be readily seen in Figs. 2 and 3. Moreover, the dominance of the stretched states is rapidly increasing with the increasing many-body basis cutoff $N_{\max}$ as illustrated in Fig. 4. The sequence of the stretched states is formed by consecutive applications of the $\hat{A}_{zz}$ operator, the generator of $\mathrm{Sp}(1,\mathbb{R}) \subset \mathrm{Sp}(2,\mathbb{R}) \subset \mathrm{Sp}(3,\mathbb{R})$ subgroup, over the leading SU(3) irrep. This translates into distributing N oscillator quanta along the direction of the z-axis only and hence rendering the largest possible deformation. The important role of the stretched configurations for the description of the rotational bands in $N = Z$ even-even nuclei was recognized heretofore using a simple microscopic Hamiltonian [23]. In the present study, for the first time, this structure is clearly and simply unveiled within the context of a fully microscopic framework starting from first principles.

4 Efficacy of the SU(3) basis

The observed patterns of intrinsic spin and deformation mixing supports a symmetry-guided basis selection philosophy referenced above. Specifically, one can take advantage of dominant symmetries to refine the definition of the NCSM model space, which is based solely on the $N_{\max}$ cutoff. A SA-NCSM model space, which we denote as $\langle N^{\perp}_{\max}\rangle N^{\top}_{\max}$, can be constructed using a symmetry-guided selection that includes the complete basis up through some $N^{\perp}_{\max} \leq N_{\max}$ along with configurations carrying a restricted set of $(\lambda\,\mu)$ and $(S_p\,S_n\,S)$ quantum numbers in the $N^{\perp}_{\max}$ to $N^{\top}_{\max}$ space. Ultimately, we aim to achieve $N^{\top}_{\max} \geq N_{\max}$, where $N_{\max}$ is the largest value for which complete-space results can be currently calculated. This concept focuses on retaining the most important configurations that support the strong many-nucleon correlations of a nuclear system using the underlying $\mathrm{Sp}(1,\mathbb{R}) \subset \mathrm{Sp}(2,\mathbb{R}) \subset \mathrm{Sp}(3,\mathbb{R})$ symmetry considerations. Within this context, it is important to note that for model spaces truncated according to $(\lambda\,\mu)$ irreps and intrinsic spins $(S_p\,S_n\,S)$, the spurious center-of-mass motion can be factored out exactly, which represents an important advantage of this scheme.

The efficacy of the symmetry-guided concept is illustrated for SA-NCSM results obtained in a model space, which is expanded beyond the complete $N^{\perp}_{\max} = 6$ (or 8) space by relatively few dominant intrinsic spin components and quadrupole deformations that satisfy condition (2). We use selected spaces up through $N^{\top}_{\max} = 12$, which allows a comparison to available results obtained in the complete $N_{\max} = 12$ space and hence, probes the efficacy of the SA-NCSM symmetry-guided model space selection concept. For this analysis, a Coulomb plus bare JISP16 NN interaction for $\hbar\Omega$ values ranging from 17.5 up to 25 MeV is used. SA-NCSM eigenstates are used to determine spectroscopic properties of low-lying $T = 0$ states of ^{6}Li for a $\langle 6\rangle 12$ model space and of the ground-state band of ^{6}He for $\langle 8\rangle 12$. We utilize a complete space of $N^{\perp}_{\max} = 6$ for ^{6}Li and of $N^{\perp}_{\max} = 8$ for ^{6}He, as these spaces seem sufficient to accommodate essential mixing of low-energy HO excitations.

The results indicate that the observables obtained in the symmetry-guided truncated spaces under consideration are excellent approximations to the corresponding complete-space counterparts. In particular, the ground-state binding energies repre-

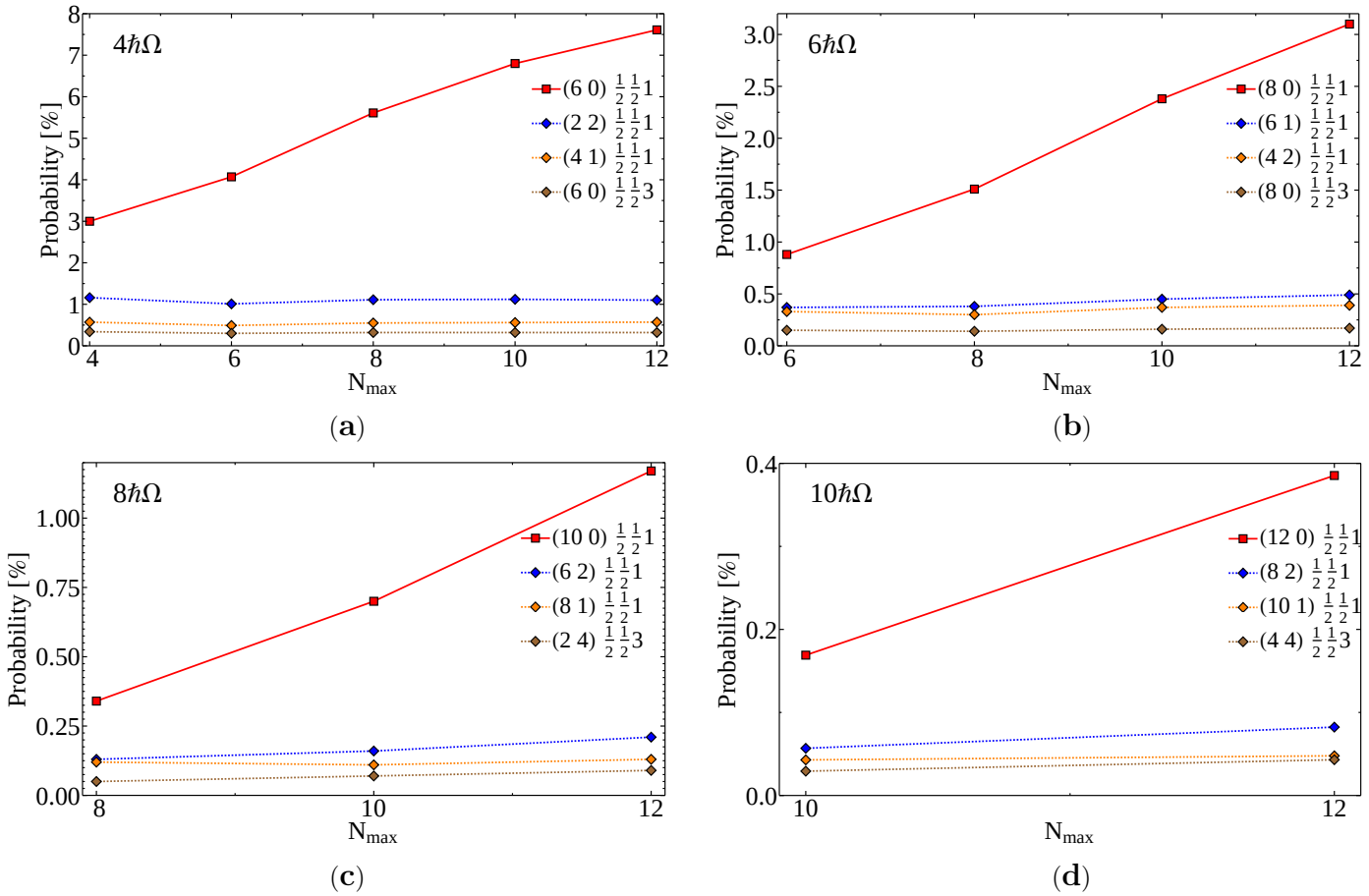

Figure 4: Probabilities of the most important $(\lambda\,\mu)$ $(S_p\,S_n\,S)$ components in ^{6}Li at $4\hbar\Omega$ subspace (a), $6\hbar\Omega$ subspace (b), $8\hbar\Omega$ subspace (c), and $10\hbar\Omega$ subspace as a function of the model space cutoff $N_{\max}$.

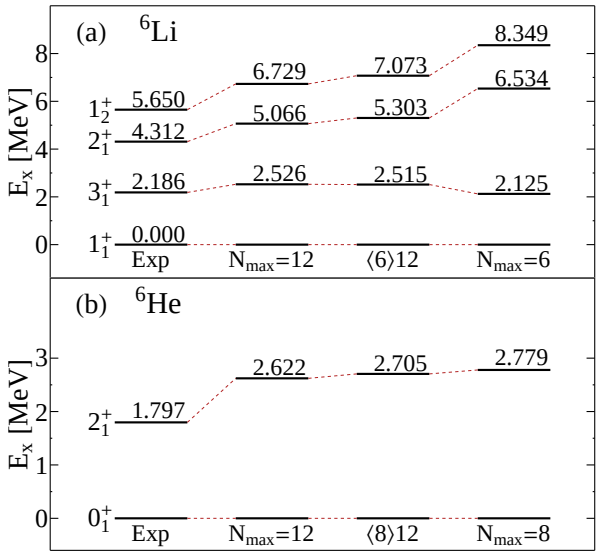

Figure 5: Experimental and theoretical excitation energies: (a) $T = 0$ states of ^{6}Li, and (b) the two lowest-lying states of the halo ^{6}He nucleus. Experimental results [24] are given in the first column. The theoretical results shown are for JISP16 and $\hbar\Omega = 20$ MeV in the complete $N_{\max} = 12$ space (second column), symmetry-guided truncated model space (third column) and the complete $N_{\max} = 6$ or 8 spaces (last column). Note the relatively large change in the calculated excitation spectrum of ^{6}Li when $N_{\max}$ is increased from 6 to 12, and that the $\langle 6\rangle 12$ SA-NCSM results (third column) track the latter closely.

sent from 98% up to 98.7% of the complete-space binding energy in the case of ^{6}Li, and reach over 99% for ^{6}He. Furthermore, the excitation energies differ only by 11 keV to a few hundred keV from the corresponding complete-space results, see Fig. 5, and the agreement with known experimental data is reasonable over a broad range of $\hbar\Omega$ values.

As illustrated in Table 2, the magnetic dipole moments for ^{6}Li agree to within 0.3% for odd-J values, and 5% for $\mu(2_1^+)$. Qualitatively similar agreement is achieved for $\mu(2_1^+)$ of ^{6}He, as shown in Table 3. The results suggest that it may suffice to include all low-lying $\hbar\Omega$ states up to a fixed limit, e. g., $N_{\max}^{\perp} = 6$ for ^{6}Li and $N_{\max}^{\perp} = 8$ for ^{6}He, to account for the most important correlations that contribute to the magnetic dipole moment.

To explore how close one comes to reproducing the important long-range correlations of the complete $N_{\max} = 12$ space in terms of nuclear collective excitations within

Table 2: Magnetic dipole moments μ [μ_N] and point-particle rms matter radii r_m [fm] of $T = 0$ states of ^{6}Li calculated in the complete $N_{\max} = 12$ space and the $\langle 6\rangle 12$ subspace for JISP16 and $\hbar\Omega = 20$ MeV. The experimental value for the 1^+ ground state is known to be $\mu = +0.822\ \mu_N$ [24].

	1_1^+0	3_1^+0	2_1^+0	1_2^+0
	μ			
Full $N_{\max} = 12$	0.838	1.866	0.960	0.336
$\langle 6\rangle 12$	0.840	1.866	1.015	0.337
	rms			
Full $N_{\max} = 12$	2.146	2.092	2.257	2.373
$\langle 6\rangle 12$	2.139	2.079	2.236	2.355

Table 3: Selected observables for the two lowest-lying states of ^{6}He obtained in the complete $N_{\max} = 12$ space and $\langle 8\rangle 12$ model subspace for JISP16 and $\hbar\Omega = 20$ MeV.

	$N_{\max} = 12$	$\langle 8\rangle 12$
$B(E2; 2_1^+ \to 0_1^+)$ [e^2fm^4]	0.181	0.184
$Q(2_1^+)$ [e·fm^2]	−0.690	−0.711
$\mu(2_1^+)$ [μ_N]	−0.873	−0.817
r_m (2_1^+) [fm]	2.153	2.141
r_m (0_1^+) [fm]	2.113	2.110

the symmetry-truncated spaces under consideration, we compared observables that are sensitive to the tails of the wavefunctions; specifically, the point-particle rms matter radii, the electric quadrupole moments and the reduced electromagnetic $B(E2)$ transition strengths that, in addition, could hint at rotational features [25]. As Table 3 clearly shows, the complete-space results for these observables are remarkably well reproduced by the SA-NCSM for ^{6}He in the restricted $\langle 8\rangle 12$ space. Similarly, the $\langle 6\rangle 12$ eigensolutions for ^{6}Li yield results for $B(E2)$ strengths and quadrupole moments that track very closely with their complete $N_{\max} = 12$ space counterparts for all values of $\hbar\Omega$ (Fig. 6). The $B(E2)$ strengths almost double upon increasing the model space from $N_{\max} = 6$ to $N_{\max} = 12$. This result suggests that further expansion of the model space will be needed to reach convergence [26]. The close correlation between the $N_{\max} = 12$ and $\langle 6\rangle 12$ results is nevertheless impressive. In addition to being in agreement, the results reproduce the challenging sign and magnitude of the ground-state quadrupole moment that is measured to be $Q(1^+) = -0.0818(17)$ e·fm^2 [24].

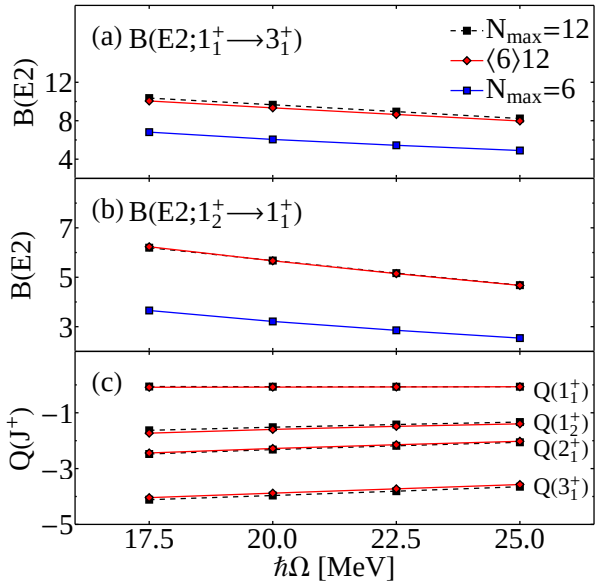

Figure 6: Electric quadrupole transition probabilities in units of e^2fm^4 [(a) and (b), as shown], and quadrupole moments in units of e·fm^2 (c) as a function of $\hbar\Omega$ for $T = 0$ states of ^{6}Li calculated using JISP16 in the complete $N_{\max} = 12$ space (dashed black line), the complete $N_{\max} = 6$ space (solid blue line), and symmetry-truncated $\langle 6\rangle 12$ (solid red line) model spaces. Note that while the $N_{\max} = 6$ results differ considerably from their $N_{\max} = 12$ counterparts, in all cases the latter are nearly indistinguishable from the truncated $\langle 6\rangle 12$ results. Experimentally, $B(E2; 1_1^+ \to 3_1^+) = 25.6(20)$ e^2fm^4 [24].

Finally, the results for the rms matter radii of ^{6}Li, listed in Table 2, agree to within 1%.

The differences between truncated-space and complete-space results are found to be essentially insensitive to the choice of $\hbar\Omega$ and appear sufficiently small as to be inconsequential relative to the residual dependences on $\hbar\Omega$ and on $N_{\max}$ (see Fig. 6). Since the NN interaction dominates contributions from three-nucleon forces (3NFs) in light nuclei, except for selected cases [27–29], we expect our results to be robust and carry forward to planned applications that will include 3NFs.

5 Conclusion

We have developed a novel approach that capitalizes on advances being made in *ab initio* methods while exploiting exact and partial symmetries of nuclear many-body system. Using this approach we have demonstrated that the low-lying eigenstates of ^{6}Li, ^{8}Be, ^{12}C, and ^{16}O, which were obtained using the JISP16 and N^{3}LO NN interaction, exhibit a strong dominance of few intrinsic spin components and carry an intriguingly simple pattern of dominant deformations. The results very clearly underscore the significance of the SU(3) scheme, LS-coupling, and underlying symplectic symmetry in enabling an extension, through symmetry-guided model space reductions, of *ab initio* methods to heavier nuclei beyond ^{16}O.

Acknowledgments

This work was supported in part by the US NSF (OCI-0904874, OCI-0904782, PHY-0904782), the US Department of Energy (DE-SC0005248, DE-SC0008485, DE-FG02-87ER40371), and the Southeastern Universities Research Association. This research used computing resources of the Louisiana Optical Network Initiative, LSU's Center for Computation & Technology, and the National Energy Research Scientific Computing Center, which is supported by the Office of Science of the US Department of Energy under Contract No. DE-AC02-05CH11231.

References

[1] S. C. Pieper, R. B. Wiringa and J. Carlson, Phys. Rev. C **70**, 054325 (2004); K. M. Nollett, S. C. Pieper, R. B. Wiringa, J. Carlson and G. M. Hale, Phys. Rev. Lett. **99**, 022502 (2007).

[2] P. Navrátil, J. P. Vary and B. R. Barrett, Phys. Rev. Lett. **84**, 5728 (2000); Phys. Rev. C **62**, 054311 (2000); S. Quaglioni and P. Navrátil, Phys. Rev. Lett. **101**, 092501 (2008); Phys. Rev. C **79**, 044606 (2009); B. R. Barrett, P. Navrátil and J. P. Vary, Progr. Part. Nucl. Phys. **69**, 131 (2013).

[3] G. Hagen, T. Papenbrock and M. Hjorth-Jensen, Phys. Rev. Lett. **104**, 182501 (2010).

[4] A. M. Shirokov, A. I. Mazur, S. A. Zaytsev, J. P. Vary and T. A. Weber, Phys. Rev. C **70**, 044005 (2004); A. M. Shirokov, J. P. Vary, A. I. Mazur, S. A. Zaytsev and T. A. Weber, Phys. Lett. B **621**, 96(2005); A. M. Shirokov, J. P. Vary, A. I. Mazur and T. A. Weber, Phys. Lett. B **644**, 33 (2007).

[5] R. Machleidt, F. Sammarruca and Y. Song, Phys. Rev. C **53**, R1483 (1996); R. Machleidt, Phys. Rev. C **63**, 024001 (2001).

[6] D. R. Entem and R. Machleidt, Phys. Rev. C **68**, 041001 (2003).

[7] P. Sternberg, E. G. Ng, C. Yang, P. Maris, J. P. Vary, M. Sosonkina and H. V. Le, in *Proc. 2008 ACM/IEEE Conf. on Supercomputing, Austin, November 2008.* IEEE Press, Piscataway, NJ, 2008, p. 15:1.

[8] P. Maris, M. Sosonkina, J. P. Vary, E. G. Ng and C. Yang, Proc. Comput. Sci. **1**, 97 (2010).

[9] H. M. Aktulga, C. Yang, E. N. Ng, P. Maris and J. P. Vary, in *Euro-Par*, eds. C. Kaklamanis, T. S. Papatheodorou and P. G. Spirakis. Lecture Notes Comput. Sci. **7484**, 830 (2012).

[10] P. Maris, A. M. Shirokov and J. P. Vary, Phys. Rev. C **81**, 021301(R) (2010).

[11] V. Z. Goldberg *et al.*, Phys. Lett. B **692**, 307 (2010).

[12] B. Davids, R. H. Cyburt, J. Jose and S. Mythili, Astrophys. J. **735**, 40 (2011).

[13] A. M. Laird *et al.*, Phys. Rev. Lett. **110**, 032502 (2013).

[14] T. Dytrych, K. D. Launey, J. P. Draayer, P. Maris, J. P. Vary, E. Saule, U. Catalyurek, M. Sosonkina, D. Langr and M. A. Caprio, Phys. Rev. Lett., *in press*, arXiv:1312.0969 [nucl-th] (2013).

[15] J. P. Elliott, Proc. Roy. Soc. A **245**, 128 (1958); *ibid.* **245**, 562 (1958); J. P. Elliott and M. Harvey, *ibid.* **272**, 557 (1962).

[16] G. Rosensteel and D. J. Rowe, Phys. Rev. Lett. **38**, 10 (1977).

[17] J. P. Draayer, T. Dytrych, K. D. Launey and D. Langr, Progr. Part. Nucl. Phys. **67**, 516 (2012).

[18] O. Castaños, J. P. Draayer and Y. Leschber, Z. Phys. A **329**, 33 (1988); G. Rosensteel and D. J. Rowe, Ann. Phys. (NY) **104**, 134 (1977); Y. Leschber and J. P. Draayer, Phys. Lett. B **190**, 1 (1987).

[19] J. P. Draayer, Y. Leschber, S. C. Park and R. Lopez, Comput. Phys. Comm. **56**, 279 (1989).

[20] D. R. Peterson and K.T. Hecht, Nucl. Phys. A **344**, 361 (1980).

[21] D. J. Rowe, Rep. Progr. Phys. **48**, 1419 (1985).

[22] T. Dytrych, K. D. Sviratcheva, C. Bahri, J. P. Draayer and J. P. Vary, Phys. Rev. Lett. **98**, 162503 (2007).

[23] F. Arickx, Nucl. Phys. A **268**, 347 (1976).

[24] D. R. Tilley *et al.*, Nucl. Phys. A **708**, 3 (2002).

[25] M. A. Caprio, P. Maris and J. P. Vary, Phys. Lett. B **719**, 179 (2013).

[26] C. Cockrell, J. P. Vary and P. Maris, Phys. Rev. C **86**, 034325 (2012).

[27] B. R. Barrett, P. Navrátil and J. P. Vary, Progr. Part. Nucl. Phys. **69**, 131 (2013).

[28] P. Maris, J. P. Vary, P. Navrátil, W. E. Ormand, H. Nam and D. J. Dean, Phys. Rev. Lett. **106**, 202502 (2011).

[29] P. Maris, J. P. Vary and P. Navrátil, Phys. Rev. C **87**, 014327 (2013).

Nuclear Isospin Violation — How It Turned out and Where It Is Going

Gerald A. Miller

Physics Department, Box 35-1560, University of Washington, Seattle, WA 98195-1560

Abstract

Nuclear isospin violation is reviewed, with emphasis on nucleon-nucleon scattering. The use of the term charge symmetry breaking and its implications are reviewed. Recent work on charge symmetry breaking in the nucleon electromagnetic form factors is outlined.

Keywords: *Charge independence; charge dependent forces; charge symmetry breaking*

1 Introduction

I was very happy to attend this NTSE conference in honor of James P. Vary. I first met James at MIT in the 1970's. I was a graduate student, working with Arthur Kerman and James was a post-doc in the Center for Theoretical Physics.

My Ph. D. project was to understand the formation and decays of double isobaric analog states in the reactions of protons with heavy nuclei. Isobaric analog states are isospin partners (members of the same multiplet) of stable nuclei that are in the continuum. A double analog states differs by two units of T_z from the stable state. My problem was that I could not find a sizable contribution. James made the brilliant suggestion that I should include pairing contributions in ^{210}Po. This enhanced the formation matrix element by a factor of 7. I was able to graduate and I am forever grateful to James Vary.

2 Next steps

Interest in isobaric analog states decayed and the focus changed to isospin violating nucleon-nucleon forces and their consequences in few-body nuclear reactions. It seems appropriate to comment in the present venue that the computational tools discussed at NTSE can lead to a much better treatment of nuclear isospin violations than in the days of my thesis. For example, in my opinion, the computations of the rate for nuclear super allowed beta decay, used to test the unitarity of the CKM matrix, could be improved [1, 2].

A particular focus is charge symmetry (CS) and its breaking. CS is invariance under a rotation in isospin space of π about the y axis. For example, a u quark is rotated into a d quark. CS is broken slightly by the light-quark mass difference and by electromagnetic effects. Isospin invariance or $[H, \vec{T}] = 0$ is invariance under all rotations in isospin space. This invariance is also called charge independence (CI), which refers to invariance amongst states with the same isospin quantum number. Charge symmetry does not imply isospin invariance. Various aspects of charge symmetry and its breaking have been reviewed, see, e. g., [3–6].

Proceedings of International Conference 'Nuclear Theory in the Supercomputing Era — 2013' (NTSE-2013), Ames, IA, USA, May 13–17, 2013. Eds. A. M. Shirokov and A. I. Mazur. Pacific National University, Khabarovsk, Russia, 2014, p. 73.

http://www.ntse-2013.khb.ru/Proc/Miller.pdf.

For example, the mass difference between charged and neutral pions exchanged between nucleons leads to forces that violate CI but not CS. This leads to a difference between ${}^1S_0$ scattering lengths for the np and nn systems. The Henley & Miller classification scheme is reviewed in the Appendix.

In general the size of CSB effects is much smaller than the breaking of isospin invariance, CIB. The scale of CSB is typified by the ratio of the neutron-proton mass difference to the proton mass which is about one part in 1000. This is much smaller than the pion mass difference effect which is one part in 27. The CIB of nucleon-nucleon scattering lengths was discovered well before 1965, but the measurement of their CSB had to wait until about 1979. Thus the expectation is that CSB is a small effect, uncovered only with special effort. The small relative size of CSB effects compared with those of CIB is a consistent with the power counting of of chiral perturbation theory [7].

3 Highlights since 1972

I summarize the progress. Measurements of the $\pi^- d \to nn\gamma$ cross section showed that the ${}^1S_0$ nn force is more attractive than the pp force. As a result the Nolen–Schiffer anomaly was explained. Charge symmetry breaking was observed in np elastic scattering [8–13], the reaction $np \to d\pi^0$ [14], and in the observation of the reaction $dd \to \alpha\pi^0$ [15]. More detail is presented in the reviews mentioned above.

4 Parity violating electron scattering and strangeness electromagnetic nucleon form factors

This subject formed the bulk of the talk. I will only explain the basic idea and an outline of the result here because the subject has already been written up as another conference proceeding [16].

The basic idea is that parity violating (PV) electron-proton scattering is sensitive to nucleon strangeness content [17], and also the value of the weak-mixing angle [18]. So far a convincing signal for strangeness in the nucleon has not been seen.

The relevance of charge symmetry or its breaking to PV electron scattering on the proton arises from the need to relate the amplitude for Z-boson absorption on the proton to measured proton and neutron electromagnetic form factors. This can be done if charge symmetry holds.

The breaking of charge symmetry brings in a correction that cannot be obtained directly from experimental observations [19–21]. The key question is whether the uncertainty in obtaining the correction is large compared to current and projected experimental uncertainties. Experimentalists have stated that charge symmetry is now limiting the ability to push further on the strange form factors because results obtained with improved precision would be hard to interpret cleanly in terms of strangeness or CSB.

We have addressed the question of whether or not CSB really limits the ability to push further. I wrote a paper in 1997 finding that the CSB corrections are less than 1% of the size of the electromagnetic form factors G_E, G_M [20]. When re-expressed in terms of absolute values of charge symmetry breaking form factors, the results were very small of order 2×10^{-3}. This is small enough to ignore.

However, I had ignored the effect of charge symmetry breaking arising from the influence of the neutron-proton mass difference on the pion cloud of the nucleon. This effect was included by Kubis & Lewis [21]. The effects are not small because of a log divergence in the loop integrals. In their resonance-saturation procedure the pion graph is cut off at the mass of the rho meson and rho-omega mixing graphs provide a finite counter term. The resulting effects can be very large and have much uncertainty.

The result, the charge symmetry breaking magnetic form factor ranges between 0.01 and 0.04, or about 10 times larger than my result. There is also a large uncertainty in the results due to lack of knowledge of the ω nucleon strong tensor coupling.

Kubis & Lewis [21] take the strong coupling constants from dispersion analyses of electromagnetic form factors based on vector meson dominance. Such fits are well known to be flexible. The strong coupling constants for omega-nucleon coupling are about seven times larger than used in NN scattering. So there is a conflict.

How can we tell which method (or if either method) is correct? One answer is that the effects of rho-omega mixing in nucleon-nucleon scattering is constrained. It is known to give a medium range class III CSB potential (see the Appendix for terminology) that can account for the scattering length difference between nn and pp systems [4, 22], and a class IV CSB potential that plays an important role in understanding CSB in np scattering. The class III potential accounts for the missing binding energy difference between ^{3}He and ^{3}H [23] and also the Nolen–Schiffer anomaly [24], see the review [5]. The use of the KL coupling constants gives potentials that are rather different than the one [23] needed phenomenologically.

We (student M. Wagman has joined me) have made new calculations of the CSB form factors using relativistic chiral perturbation theory. The use of relativistic chiral perturbation theory leads to finite and convergent results. The preliminary results are that the charge symmetry breaking form factors are very small.

5 Tasks ahead

One should use a model that describes $G_{E,M}$ well in the absence of CSB, and then use those models as a basis for CSB computations. One candidate model is that of Cloet & Miller [25].

More generally, I wish to address a bias. I did a quark *model* calculation. Kubis & Lewis did a chiral perturbation *theory* calculation. One usually thinks that a theory is better than a model. However, if an unconstrained counter term is needed to evaluate the theory, then the model is quite close to a theory.

6 Summary

I obtained small < 0.002 CSB effects in 1998. Kubis & Lewis (KL) obtained a range of about 0.04. However CSB in NN scattering constrains the strong coupling constants used in the KL resonance saturation calculation. The actual size of the CSB effect seems pretty small.

7 Acknowledgments

This work has been partially supported by U.S. DOE Grant No DE-FG02-97ER-41014.

8 Appendix

We review the CSB and CIB terminology of nucleon-nucleon forces [3].

Class (I): Forces which are isospin independent that commute with all components of the isospin operator. Such forces, V_I have an isoscalar form,

$$V_I = a + b\,\vec{\tau}(i)\cdot\vec{\tau}(j), \tag{1}$$

where a and b are Hermitian isospin independent operators and $i \neq j$.

Class (II): Forces which maintain charge symmetry, but break charge independence. These can be written in isotensor form,

$$V_{II} = c\left(\tau_3(i)\tau_3(j) - \vec{\tau}(i)\cdot\vec{\tau}(j)\right). \tag{2}$$

The Coulomb interaction leads to a Class II force as do the effects of the pion mass difference in pion exchange forces. Effects of charge-dependent coupling constants may also lead to such a Class II force.

Class (III): Forces which break both charge independence and charge symmetry, but which are symmetric under the interchange $i \leftrightarrow j$ in isospin space,

$$V_{III} = d\left(\tau_3(i) + \tau_3(j)\right). \tag{3}$$

A Class III force differentiates between nn and pp systems, but does not cause isospin mixing in the two-nucleon system because

$$[V_{III}, T^2] = 0. \tag{4}$$

The effects of ρ^0-ω mixing yields such a force, as does the Coulomb interaction.

Class (IV): Class IV forces break charge symmetry and therefore charge dependence; they cause isospin mixing. These forces take the form

$$V_{IV} = e\left(\vec{\sigma}(i) - \vec{\sigma}(j)\right)\cdot\vec{L}\big(\tau_3(i) - \tau_3(j)\big) + f\left(\vec{\sigma}(i)\times\vec{\sigma}(j)\right)\cdot\vec{L}\big(\tau_3(i)\times\tau_3(j)\big), \tag{5}$$

where $\vec{L}$ is the two-nucleon orbital angular momentum, e and f are Hermitian operators that commute with $\vec{T}$. Such forces give CSB spin-orbit effects that account for the np analyzing power differences [8–13] and contribute to nuclear isospin mixing [26]. Effective field theory [7] tells us that the ordering of the strengths is given by $V_I > V_{II} > V_{III} > V_{IV}$.

References

[1] G. A. Miller and A. Schwenk, Phys. Rev. C **78**, 035501 (2008).

[2] G. A. Miller and A. Schwenk, Phys. Rev. C **80**, 064319 (2009).

[3] E. M. Henley and G. A. Miller, in *Mesons in nuclei, vol. I*, edited by M. Rho and D. Wilkinson. North Holland, Amsterdam, 1979, p. 405.

[4] G. A. Miller, B. M. K. Nefkens and I. Slaus, Phys. Rept. **194**, 1 (1990).

[5] G. A. Miller and W. T. H. van Oers, In *Symmetries and fundamental interactions in nuclei*, edited by W. C. Haxton and E. M. Henley. World Scientific, Singapore, 1995, p. 127.

[6] G. A. Miller, A. K. Opper and E. J. Stephenson, Ann. Rev. Nucl. Part. Sci. **56**, 253 (2006).

[7] U. van Kolck, J. L. Friar and J. T. Goldman, Phys. Lett. B **371**, 169 (1996).

[8] R. Abegg, D. Bandyopadhyay, J. Birchall, E. W. Cairns, H. Coombes, C. A. Davis, N. E. Davison, P. P. J. Delheij *et al.*, Phys. Rev. Lett. **56**, 2571 (1986).

[9] R. Abegg, D. Bandyopadhyay, J. Birchall, E. B. Cairns, G. H. Coombes, C. A. Davis, N. E. Davison, P. P. J. Delheij *et al.*, Phys. Rev. D **39**, 2464 (1989).

[10] R. Abegg, A. R. Berdoz, J. Birchall , J. R. Campbell, C. A. Davis, P. P. J. Delheij, L. Gan, P. W. Green *et al.*, Phys. Rev. Lett. **75**, 1711 (1995).

[11] J. Zhao, R. Abegg, A. R. Berdoz, J. Birchall, J. R. Campbell, C. A. Davis, P. P. J. Delheij, L. Gan *et al.*, Phys. Rev. C **57**, 2126 (1998).

[12] L. D. Knutson, S. E. Vigdor, W. W. Jacobs, J. Sowinski, P. L. Jolivette, S. W. Wissink, C. Bloch, C. Whiddon *et al.*, Phys. Rev. Lett. **66**, 1410 (1991).

[13] S. E. Vigdor, W. W. Jacobs, L. D. Knutson, J. Sowinski, C. Bloch, P. L. Jolivette, S. W. Wissink, R. C. Byrd *et al.*, Phys. Rev. C **46**, 410 (1992).

[14] A. K. Opper, E. J. Korkmaz, D. A. Hutcheon, R. Abegg, C. A. Davis, R. W. Finlay, P. W. Green, L. G. Greeniaus *et al.*, Phys. Rev. Lett. **91**, 212302 (2003).

[15] E. J. Stephenson, A. D. Bacher, C. E. Allgower, A. Gardestig, C. Lavelle, G. A. Miller, H. Nann, J. Olmsted *et al.*, Phys. Rev. Lett. **91**, 142302 (2003).

[16] G. A. Miller, arXiv:1309.0879 [nucl-th] (2013).

[17] D. S. Armstrong and R. D. McKeown, Ann. Rev. Nucl. Part. Sci. **62**, 337 (2012).

[18] D. Androic *et al.* (Qweak Collaboration), arXiv:1307.5275 [nucl-ex] (2013).

[19] V. Dmitrasinovic and S. J. Pollock, Phys. Rev. C **52**, 1061 (1995).

[20] G. A. Miller, Phys. Rev. C **57**, 1492 (1998)

[21] B. Kubis and R. Lewis, Phys. Rev. C **74**, 015204 (2006).

[22] P. C. McNamee, M. D. Scadron and S. A. Coon, Nucl. Phys. A **249**, 483 (1975).

[23] S. A. Coon and R. C. Barrett, Phys. Rev. C **36**, 2189 (1987).

[24] P. G. Blunden and M. J. Iqbal, Phys. Lett. B **198**, 14 (1987).

[25] I. C. Cloet and G. A. Miller, Phys. Rev. C **86**, 015208 (2012).

[26] R. B. Wiringa, S. Pastore, S. C. Pieper and G. A. Miller, arXiv:1308.5670 [nucl-th] (2013).

Nuclear Excitation by a Strong Zeptosecond Multi-MeV Laser Pulse

A. Pálffy and H. A. Weidenmüller

Max-Planck-Institut für Kernphysik, 69023 Heidelberg, Germany

Abstract

Within a few years' time, the "Nuclear Physics Pillar" of ELI (Extreme Light Infrastructure) is expected to produce coherent strong short laser pulses with several MeV energy per photon. We discuss theoretical expectations for the nuclear reactions induced by such pulses with medium-weight and heavy nuclei.

Keywords: *Statistical nuclear theory; compound-nucleus reactions; gamma-induced reactions*

1 Introduction

This work is motivated by recent developments in laser instrumentation. Within a few years' time, coherent laser beams with energies of several MeV per photon and 10^{-19} s length in time are expected to become available for the study of laser-induced nuclear reactions. Three steps are expected to lead towards that goal:

(i) The "Nuclear Physics Pillar" of ELI [1] (Extreme Light Infrastructure) presently under construction in Romania provides a very-high-intensity but otherwise conventional laser beam.

(ii) Passage of that laser beam through an extremely thin diamond-like Carbon foil (about 5 nm thick) ejects a "sheet" of relativistic electrons of several 10 MeV energy.

(iii) That sheet acts like a mirror for the photons of a second (conventional) laser beam. Compton backscattering of the photons produces a coherent laser pulse with several MeV energy per photon and $\approx 10^{-19}$ s length in time.

Recent experiments have shown that passage of a laser beam through a thin Carbon foil does indeed produce electrons with energies of several 10 MeV, see Fig. 1. The production of a very thin sheet of electrons and the coherent backscattering of another laser beam on that sheet are presently under intense investigation [3].

These developments pose a challenge to nuclear theory. What kind of processes do we expect at which rate when a laser beam with coherent photons of several MeV per photon and 10^{-19} s time duration hits a nucleus? What is the difference to the so far widely studied atom-laser interaction?

2 Reaction mechanisms

To answer these questions, we consider a short strong laser pulse with $N = 10^2 - 10^4$ coherent photons per pulse, with a mean photon energy E_L of 5–10 MeV, and with an energy spread σ of 10−50 keV corresponding to a length in time of about 10^{-19} s. Such a pulse seems extremely strong. But comparison with the atomic case shows that for nuclei it is still actually rather weak. In atoms, the electric field strength of a strong

Proceedings of International Conference 'Nuclear Theory in the Supercomputing Era — 2013' (NTSE-2013), Ames, IA, USA, May 13–17, 2013. Eds. A. M. Shirokov and A. I. Mazur. Pacific National University, Khabarovsk, Russia, 2014, p. 78.

http://www.ntse-2013.khb.ru/Proc/Weidenmueller.pdf.

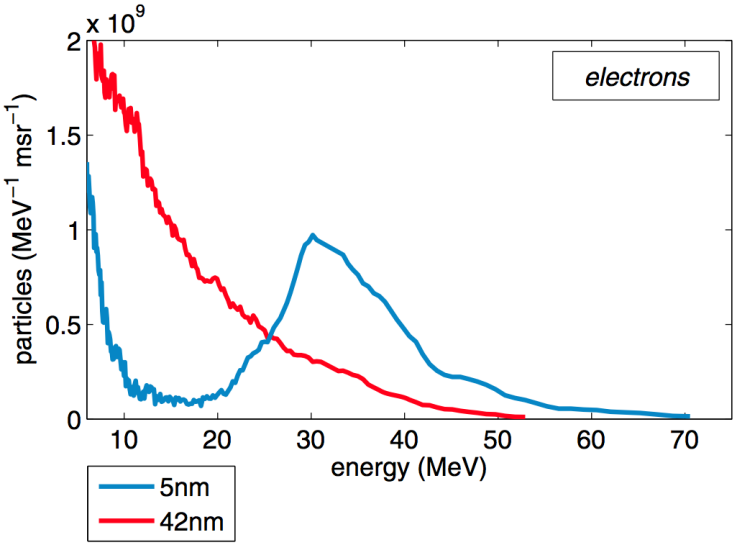

Figure 1: Energy distribution of electrons ejected from two Carbon foils of different thicknesses by a conventional laser beam. Taken from Ref. [2].

laser pulse distorts the nuclear Coulomb potential. Thus, the field strength is of order (eV/ Bohr radius) in magnitude. A corresponding field strength in nuclei would have to be of order (MeV/fm), i. e., about 10 orders of magnitude stronger. That is far more than what is achieved by a laser pulse with the above-mentioned specifications. Thus, even such a strong laser pulse provides only a fairly weak perturbation for nuclei. The difference is due to the fact that nuclei are governed by the strong interaction.

For photons of several MeV energy, the product of wave number and nuclear radius is small compared to unity, and it is justified to consider only dipole absorption, the dominant mode of gamma absorption in nuclei. The dipole width $\Gamma_{\rm dip}$ is strongly energy dependent but, for photon energies of several MeV, has a typical value of several keV. Because of the large number N of photons in the pulse (and since the number N_0 of photons absorbed from the pulse always obeys $N_0 \ll N$) we use the semiclassical approximation throughout the reaction. The characteristic parameter is then $N\Gamma_{\rm dip} \approx 10^2 - 10^4$ keV. The competition between the rate $N\Gamma_{\rm dip}/\hbar$ for dipole absorption and the nuclear relaxation rate $\Gamma_{\rm spr}/\hbar$ (where the spreading width $\Gamma_{\rm spr}$ has a typical value of 5 MeV) defines three regimes for laser-induced nuclear reactions:

(i) The perturbative regime $N\Gamma_{\rm dip} \ll \Gamma_{\rm spr}$. Here, one-step excitation of the Giant Dipole Resonance (GDR) dominates. Double or multiple excitation via absorption of several photons turns out to be unlikely.

(ii) The quasi-adiabatic regime $N\Gamma_{\rm dip} \approx \Gamma_{\rm spr}$. The rates for photon absorption and equilibration are about equal. The nucleus remains close to equilibrium during the entire process. Multiple photon absorption leads to excitation energies up to several 100 MeV. Equilibration is caused by the residual interaction in nuclei. The process seems to have no analogue in laser-atom interactions and constitutes a new regime for the interaction of laser light with matter [4].

(iii) The sudden regime $N\Gamma_{\rm dip} \gg \Gamma_{\rm spr}$. The residual interaction is irrelevant. Nucleons absorb photons individually until their energy exceeds the binding energy whereupon they are ejected. If the laser pulse lasts long enough, the nucleus completely evaporates.

In this paper we discuss processes (i) and (ii).

3 Perturbative regime: collective excitation

In the perturbative regime, excitation of the GDR is the dominant process. In Ref. [5] the GDR and its harmonics were modeled as doorway states coupled to a large number of background states. The latter were described in terms of a random-matrix model. The Brink–Axel hypothesis was used (every excited nuclear state possesses its own GDR). With these assumptions it was shown that in the perturbative regime, the GDR is only singly excited. Multiple photon absorption is an unlikely process.

For an even-even target nucleus the GDR is spread over a large number of states with spin/parity 1^-. In medium-weight and heavy nuclei these have typical spacings of 10 eV. A photon with an energy spread $\sigma \approx 50$ keV excites an entire band of 10^3-10^4 such states coherently. Such coherent excitation precludes the observation of individual excited states. The relevant observable is the decay in time of the compound nucleus. That decay provides information on amplitude correlations that are not available otherwise. For photon energies below (right above) neutron threshold, the decay process is exponential (non-exponential) in time. The non-exponential time dependence is a direct consequence of the Porter–Thomas distribution of neutron decay widths [6]. Examples are shown in Figures 2 and 3, both taken from Ref. [6].

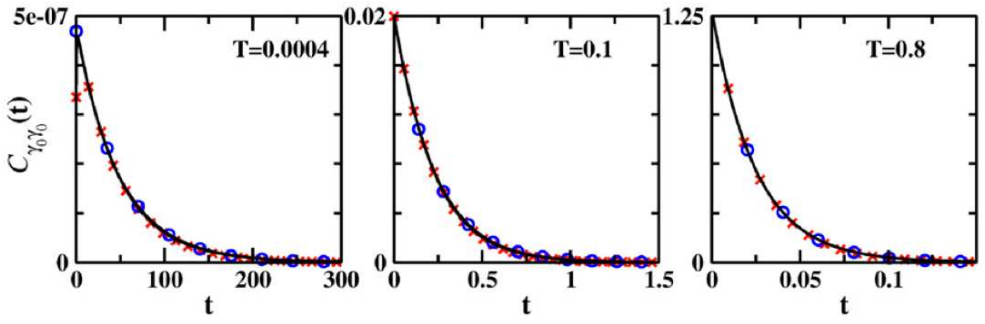

Figure 2: Decay in time of the compound nucleus excited by photon absorption to states below neutron threshold with average level spacing d. Time is in units of h/d. Decay is calculated for 50 gamma decay channels all with the same transmission coefficients T.

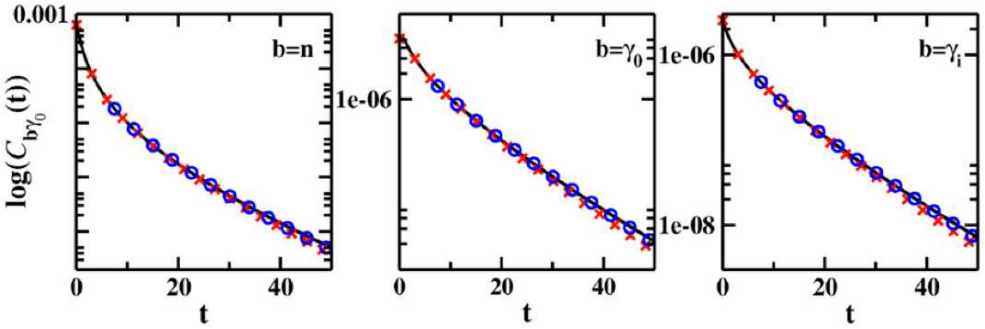

Figure 3: Decay in time of the compound nucleus excited by photon absorption to states right above neutron threshold with average level spacing d. Time is in units of h/d. Decay is calculated for 50 gamma decay channels all with the same transmission coefficients $T_\gamma = 0.0016$ and a single open neutron channel with transmission coefficient $T_\mathrm{n} = 0.4$. The index b denotes the exit channel, the index zero denotes the ground state.

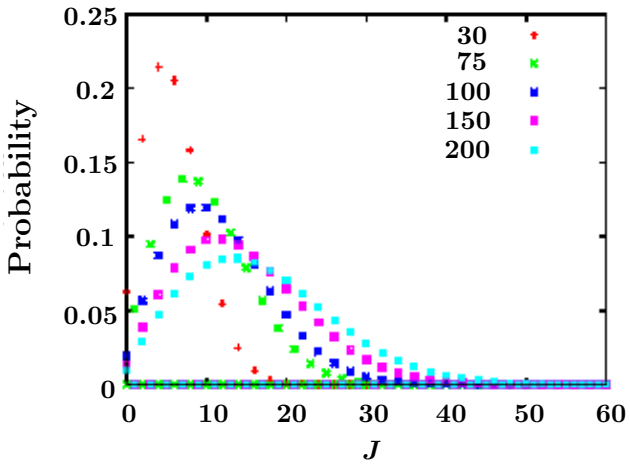

Figure 4: Distribution of spin values in the compound nucleus after absorption of N_0 photons (values in the legend above) versus spin.

4 Quasi-adiabatic regime

The absorption of N_0 dipole photons leads to a slow growth $\propto \sqrt{N_0}$ of the total spin of the compound nucleus, see Fig. 4. Even the absorption of 100 photons of 5 MeV each, producing states 500 MeV above the ground state, on average only leads to spin values around 10. Thus, multiple photon absorption excites states far above the yrast line, a domain of excitation energies hardly explored so far. In view of these small spin values we totally neglect spin in what follows. As is usual for compound-nucleus processes, the reaction is described in terms of rate equations. In addition to the rates $\Gamma_{\rm dip}/\hbar$ for dipole absorption and $\Gamma_{\rm spr}/\hbar$ for internal equilibration, we need the rates for induced gamma emission, for neutron evaporation, and for gamma-induced emission of neutrons and protons. These rates typically depend on nuclear level densities (total density, density of particle-hole states, density of accessible states, etc.). At excitation energies of several 100 MeV above yrast and for medium-weight and heavy nuclei, such level densities are huge (values like 10^{30} or 10^{40} times the mean single-particle level density are easily attained), and the reliable and quick calculation of such densities poses a challenge.

4.1 Level density

In Refs. [7, 8] we have developed a new approach that is specifically tailored to the problem. In short, the total level density is obtained by distributing A non-interacting fermions over a finite number of bound single-particle states defined in terms of a mean-field or a shell-model potential. Here A is the nuclear mass number. For an arbitrary set of single-particle energies, we derive exact analytical expressions for the low moments and low cumulants of the total level density. These are used to determine approximate expressions for the total level density and for particle-hole densities. The Fermi-gas model is used to calculate the density of accessible states.

The resulting total level density (in units of the inverse single-particle level spacing) for p particles distributed over $b = 51$ equally spaced single-particle states is shown in Fig. 5, taken from Ref. [7]. The performance of the approximation used in our approach is shown for several values of p in Fig. 6 (taken from Ref. [7]) by comparison with exact numerical calculations. The agreement is good in the center of the spectrum. Significant differences arise only in the tails. That pattern prevails for all our calculations.

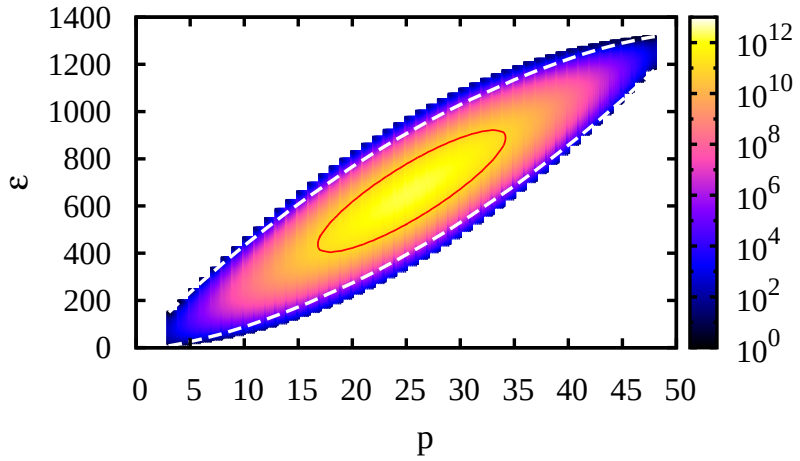

Figure 5: Contour plot of the level density for p particles in $b = 51$ equally spaced single-particle states as a function of energy ε (in units of the single-particle level spacing). Because of the exclusion principle, only states within the colored domain are accessible. The full line depicts the constant level density contour at 10^{11}.

For medium-weight and heavy nuclei, the constant-spacing model is unrealistic. In the calculations reported in Ref. [8] we have, therefore, used smooth single-particle level densities that increase linearly or quadratically with energy. Typical results for the level density for two choices of the single-particle density are shown in Fig. 7, taken from Ref. [8].

In summary, we have developed an analytic, fast-to-implement approach to the calculation of the total level density, and to particle-hole densities. The approach works well for high excitation energies and large particle numbers. It seems desirable, of course, to develop an approximation that is uniformly good in all parts of the spectrum. The huge numbers attained by the nuclear level density (measured in units of the mean single-particle density) preclude such a possibility: for the constant-spacing

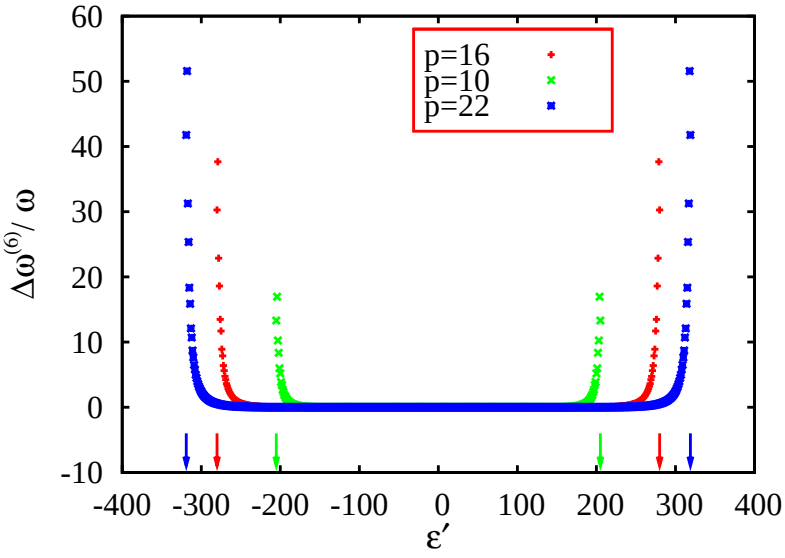

Figure 6: Relative difference between approximate and exact values of the level density for a constant-spacing model with $b = 51$ single-particle states and p fermions.

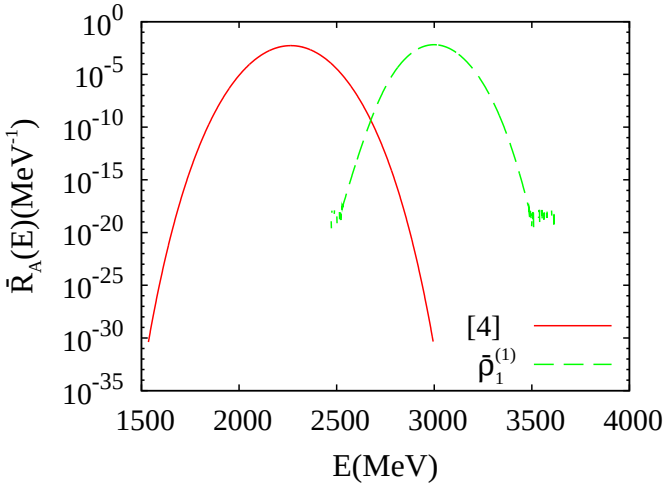

Figure 7: Plot of the normalized level density $R_A(E)$ versus energy E (in MeV) for $A = 100$ particles in $B = 148$ states for the constant-spacing model (full line) and for a smooth single-particle level density that rises linearly with energy (dashed line).

model with 100 particles in 200 single-particle states, the level density ranges over 60 orders of magnitude. That is the accuracy with which exact analytical expressions (if available) would have to be evaluated. This shows that different approximations are needed in different parts of the spectrum.

4.2 Implications for photon-induced reactions

We consider absorption of photons with energy $E_L = 5$ MeV. For clarity we first neglect both neutron evaporation and stimulated nucleon emission. The rate for induced photon emission increases with increasing excitation energy. At the maximum E_0 of the total level density, that rate becomes equal to the rate for photon absorption: excitation beyond E_0 is not possible. The occupation probability of excited nuclear states is nearly stationary and hovers around E_0 while the laser pulse lasts. With E_0 amounting typically to several 100 MeV, excitation of the compound nucleus to energies several 100 MeV above yrast is a novel feature of laser-induced photon absorption.

The picture changes when neutron evaporation is taken into account. The use of the Weisskopf formula and of our results for the total level density shows that the neutron emission becomes competitive with photon absorption only at high excitation energies (several 10 MeV below E_0). The emitted neutrons have predominantly small energies around 10 or 20 MeV and populate highly excited states several 10 MeV below E_0 in the daughter nucleus. These in turn undergo photon absorption and neutron emission, leading to highly excited states in the nucleus having two neutrons less than the target nucleus. In this way, the reaction traverses a chain of nuclei with equal proton numbers and ever decreasing neutron numbers. The reaction terminates after emission of n_0 neutrons where n_0 is determined by the duration in time of the laser pulse. This shows that, depending on the length in time of the laser pulse, laser-induced reactions offer the possibility to generate and study nuclei far off the valley of stability, differing by n_0 neutrons from the target nucleus.

The picture changes once again when emission of nucleons directly induced by photon absorption is taken into account. The emission produces neutrons and protons with nearly equal probabilities. That spreads the distribution of final nuclei, filling the gap between the valley of stability and a nucleus differing by n_0 neutrons from the target nucleus.

5 Conclusions

Coherent laser beams with photon energies around 5 to 10 MeV and pulse lengths of 10^{-19} s are expected to be available within a few years' time. The nuclear reactions induced by such short and intense laser pulses differ from laser-atom reactions in two essential aspects: (i) The nucleus is a strongly interacting system, the laser-nuclear interaction is, therefore, comparatively weak, and (ii) the nucleus may equilibrate, and the excitation of a long-lived compound nucleus at excitation energies several 100 MeV above yrast is possible. That defines a new regime of laser-matter interactions and opens the possibility to study nuclear level densities at such energies.

The competition between the absorption rate for photons and the nuclear equilibration rate defines three regimes. In the perturbative regime, even a strong short laser pulse only leads to single excitation of the GDR. Multiple photon absorption is unlikely. Coherent excitation of a broad band of excited states is observable via the time-decay function. For photon energies larger than neutron threshold, the decay in time is non-exponential. In the quasi-adiabatic regime, about one photon is absorbed per nuclear relaxation time. Up to 100 or more photons may be absorbed, with little angular momentum transfer to the compound nucleus, leading to the large excitation energies above yrast mentioned above. The decay by neutrons and induced emission of neutrons and protons produces a distribution of final nuclei that extends from the valley of stability to a nucleus that differs from the target nucleus by minus n_0 neutrons. Here n_0 is determined by the duration time of the laser pulse. This offers the possibility to study proton-rich nuclei far from the valley of stability.

References

[1] Extreme Light Infrastructure, URL: http://www.extreme-light-infrastructure.eu, 2012.

[2] D. Kiefer *et al.*, Eur. Phys. J. D **55**, 427 (2009).

[3] G. Mourou and T. Tajima, Science **331**, 41 (2011).

[4] A. Di Piazza, C. Müller, K. Z. Hatsagortsyan and C. H. Keitel, Rev. Mod. Phys. **84**, 1177 (2012).

[5] H. A. Weidenmüller, Phys. Rev. Lett. **106**, 122502 (2011).

[6] B. Dietz and H. A. Weidenmüller, Phys. Lett. B **693**, 316 (2010).

[7] A. Pálffy and H. A. Weidenmüller, Phys. Lett. B **718**, 1105 (2013).

[8] A. Pálffy and H. A. Weidenmüller, arXiv:1307.0400 [nucl-th] (2013), Nucl. Phys. A, *submitted*.

NTSE-2013 Keynote Talk:

Light-Front Holographic Quantum Chromodynamics

Stanley J. Brodsky[a], Guy F. de Téramond[b] and Hans Günter Dosch[c]

[a] *SLAC National Accelerator Laboratory, Stanford University, Stanford, CA 94309, USA*
[b] *Universidad de Costa Rica, San José, Costa Rica*
[c] *Institut für Theoretische Physik, Philosophenweg 16, D-6900 Heidelberg, Germany*

Abstract

Light-Front Hamiltonian theory, derived from the quantization of the QCD Lagrangian at fixed light-front time $\tau = x^0 + x^3$, provides a rigorous frame-independent framework for solving nonperturbative QCD. The eigenvalues of the light-front QCD Hamiltonian H_{LF} predict the hadronic mass spectrum, and the corresponding eigensolutions provide the light-front wavefunctions which describe hadron structure. In the case of mesons, the valence Fock-state wavefunctions of H_{LF} for zero quark mass satisfy a single-variable relativistic equation of motion in the invariant variable $\zeta^2 = b_\perp^2 x(1-x)$, which is conjugate to the invariant mass squared $M^2_{q\bar{q}}$. The effective confining potential $U(\zeta^2)$ in this frame-independent "light-front Schrödinger equation" systematically incorporates the effects of higher quark and gluon Fock states. Remarkably, the potential has a unique form of a harmonic oscillator potential if one requires that the chiral QCD action remains conformally invariant. The result is a nonperturbative relativistic light-front quantum mechanical wave equation which incorporates color confinement and other essential spectroscopic and dynamical features of hadron physics.

Anti-de Sitter space in five dimensions plays a special role in elementary particle physics since it provides an exact geometrical representation of the conformal group. Remarkably, gravity in AdS_5 space is holographically dual to frame-independent light-front Hamiltonian theory. Light-front holography also leads to a precise relation between the bound-state amplitudes in the fifth dimension z of AdS space and the variable ζ, the argument of the boost-invariant light-front wavefunctions describing the internal structure of hadrons in physical space-time. The holographic mapping of gravity in AdS space to QCD with a specific "soft-wall" dilaton yields the confining potential $U(\zeta^2)$ which is consistent with conformal invariance of the QCD action and the light-front Schrödinger equation, extended to hadrons with arbitrary spin J. One thus obtains an effective light-front effective theory for general spin which respects the conformal symmetry of the four-dimensional classical QCD Lagrangian. The predictions of the LF equations of motion include a zero-mass pion in the chiral $m_q \to 0$ limit, and linear Regge trajectories $M^2(n, L) \propto n + L$ with the same slope in the radial quantum number n and the orbital angular momentum L. The light-front AdS/QCD holographic approach thus gives a frame-independent representation of color-confining dynamics, Regge spectroscopy, as well as the excitation spectra of relativistic light-quark meson and also baryon bound states in QCD in terms of a single mass parameter.

We also briefly discuss the implications of the underlying conformal template of QCD for renormalization scale-setting and the implications of light-front

Proceedings of International Conference 'Nuclear Theory in the Supercomputing Era — 2013' (NTSE-2013), Ames, IA, USA, May 13–17, 2013. Eds. A. M. Shirokov and A. I. Mazur. Pacific National University, Khabarovsk, Russia, 2014, p. 85.
http://www.ntse-2013.khb.ru/Proc/Brodsky.pdf.

quantization for the value of the cosmological constant.

Keywords: *Quantum chromodynamics; light-front quantization; holography; AdS/QCD correspondence*

1 Introduction

The remarkable advantages of using light-front time $\tau = x^0 + x^3/c$ (the "front form") to quantize a theory instead of the standard time $t = x^0$ (the "instant form") was first demonstrated by Dirac. As Dirac showed [1], the front form has the maximum number of kinematic generators of the Lorentz group, including the boost operator. Thus the description of a hadron at fixed τ is independent of the observer's Lorentz frame, making it ideal for addressing dynamical processes in quantum chromodynamics.

The quantization of QCD at fixed light-front (LF) time — light-front quantization — provides a first-principles method for solving nonperturbative QCD. Given the Lagrangian, one can determine the LF Hamiltonian H_{LF} in terms of the independent quark and gluon fields. The eigenvalues of H_{LF} determine the mass-squared values of both the discrete and continuum hadronic spectra. The eigensolutions determine the LF wavefunctions required for predicting hadronic phenomenology. The LF method is relativistic, has no fermion-doubling, is formulated in Minkowski space, and is frame-independent. The eigenstates are defined at fixed τ within the causal horizon, so that causality is maintained without normal-ordering. In fact, light-front physics is a fully relativistic field theory, but its structure is similar to nonrelativistic atomic physics, and the resulting bound-state equations can be formulated as relativistic Schrödinger-like equations at equal light-front time. Given the frame-independent light-front wavefunctions (LFWFs) $\psi_{n/H}$, one can compute a large range of hadronic observables, starting with form factors, structure functions, generalized parton distributions, Wigner distributions, etc., as illustrated in Fig. 1. For example, the "handbag" contribution [3] to the E and H generalized parton distributions for deeply virtual Compton scattering can be computed from the overlap of LFWFs, automatically satisfy the known sum rules.

Computing hadronic matrix elements of currents is particularly simple in the light-front, since they can be written as an overlap of light-front wave functions (LFWFs) as in the Drell–Yan–West formula [4–6]. For example, a virtual photon couples only to forward-moving $k^+ > 0$ quarks, and only processes with the same number of initial and final partons are allowed. In contrast, if one uses ordinary fixed time t, the hadronic states must be boosted from the hadron's rest frame to a moving frame — an intractable dynamical problem. In fact, the boost of a composite system at fixed time t is only known at weak binding [7, 8]. Moreover, form factors at fixed instant time t require computing off-diagonal matrix elements as well as the contributions of currents arising from fluctuations of the vacuum in the initial state which connect to the hadron wavefunction in the final state. Thus, the knowledge of wave functions alone is not sufficient to compute covariant current matrix elements in the usual instant-form framework.

The gauge-invariant meson and baryon distribution amplitudes which control hard exclusive and direct reactions are the valence LFWFs integrated over transverse momentum at fixed $x_i = k^+/P^+$. The ERBL evolution of distribution amplitudes and the factorization theorems for hard exclusive processes were derived using LF theory [9, 10].

Because of Wick's theorem, light-front time-ordered perturbation theory is equivalent to covariant Feynman perturbation theory. The higher order calculation of the electron anomalous moment at order α^3 and the "alternating denominator method" for renormalizing LF perturbation theory is given in Ref. [11].

Quantization in the light-front provides the rigorous field-theoretical realization

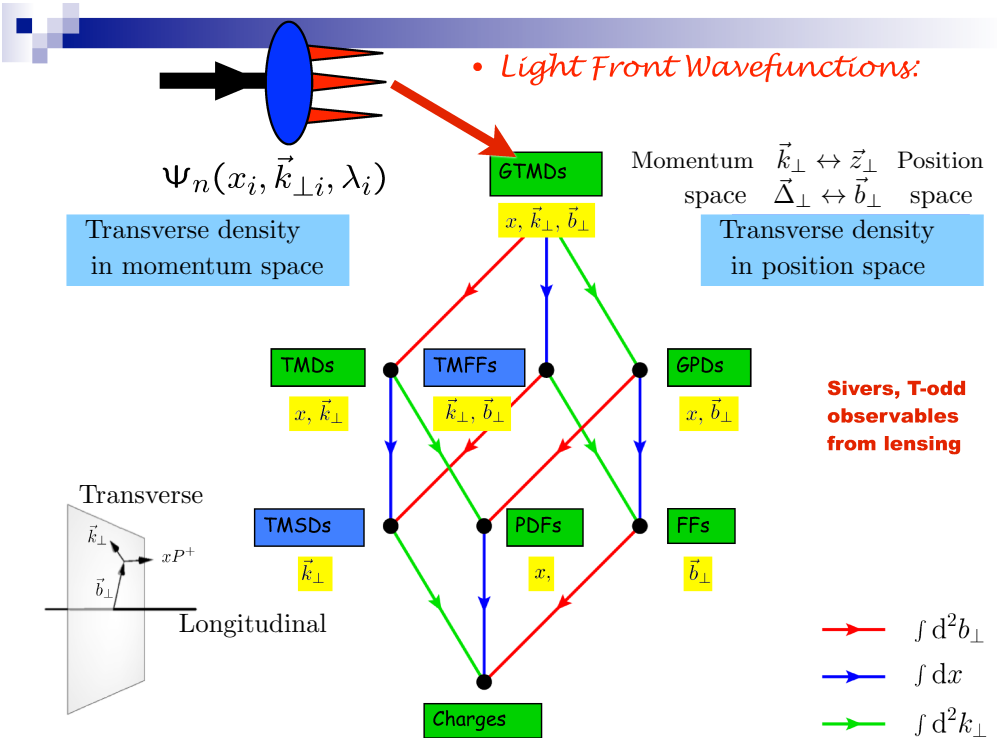

Figure 1: Examples of hadronic observables, including Wigner functions and T-odd observables which are based on overlaps of light-front wavefunctions. Adopted from a figure by F. Lorce and B. Pasquini [2].

of the intuitive ideas of the parton model [12,13] which is formulated at fixed t in the infinite-momentum frame [14, 15]. The same results are obtained in the front form for any frame; e. g., the structure functions and other probabilistic parton distributions measured in deep inelastic scattering are obtained from the squares of the boost invariant LFWFs, the eigensolution of the light-front Hamiltonian. The familiar kinematic variable x_{bj} of deep inelastic scattering becomes identified with the LF fraction at small x.

A measurement in the front form is analogous to taking a flash picture. The image in the resulting photograph records the state of the object as the front of the light wave from the flash illuminates it; in effect, this is a measurement within the spacelike causal horizon ${\Delta x_\mu}^2 \leq 0$. Similarly, measurements such as deep inelastic lepton-proton scattering $\ell H \to \ell' X$, determine the LFWF and structure of the target hadron H at fixed light-front time. For example, the BFKL Regge behavior of structure functions can be demonstrated [16] from the behavior of LFWFs at small x.

One can also prove fundamental theorems for relativistic quantum field theories using the front form, including: (a) the cluster decomposition theorem [17] and (b) the vanishing of the anomalous gravitomagnetic moment for any Fock state of a hadron [18]; one also can show that a nonzero anomalous magnetic moment of a bound state requires nonzero angular momentum of the constituents. Stasto and Cruz-Santiago [19] have shown that the cluster properties [20] of LF time-ordered perturbation theory, together with J^z conservation, can be used to elegantly derive the Parke–Taylor rules for multi-gluon scattering amplitudes. The counting-rule [21] behavior of structure functions at large x and Bloom–Gilman duality have also been derived in LFQCD as well as from holographic QCD [22].

The physics of diffractive deep inelastic scattering and other hard processes where

the projectile hadron remains intact is most easily analysed using LF QCD [23]. The existence of "lensing effects" at leading twist, such as the T-odd "Sivers effect" in spin-dependent semi-inclusive deep-inelastic scattering, was first demonstrated using LF methods [24]. QCD properties such as "color transparency" [25], the "hidden color" of the deuteron LFWF [26], and the existence of intrinsic heavy quarks in the LFWFs of light hadrons [27, 28] can be derived from the structure of hadronic LFWFs. It is also possible to compute jet hadronization at the amplitude level from first principles from the LFWFs [29]. The LFWFs of hadrons thus provide a direct connection between observables and the QCD Lagrangian.

Light-front quantization is thus the natural framework for the description the nonperturbative relativistic bound-state structure of hadrons in quantum chromodynamics. The formalism is rigorous, relativistic and frame-independent. In principle, one can solve nonperturbative QCD by diagonalizing the light-front QCD Hamiltonian H_{LF} directly using the "discretized light-cone quantization" (DLCQ) method [30] which imposes periodic boundary conditions to discretize the k^+ and $k_\perp$ momenta, or the Hamiltonian transverse lattice formulation introduced in Refs. [31–33]. The hadronic spectra and light-front wavefunctions are then obtained from the eigenvalues and eigenfunctions of the Heisenberg problem $H_{LF}|\psi\rangle = M^2|\psi\rangle$, an infinite set of coupled integral equations for the light-front components $\psi_n = \langle n|\psi\rangle$ in a Fock expansion [30]. These nonperturbative methods have the advantage that they are frame-independent, defined in physical Minkowski space-time, and have no fermion-doubling problem. The DLCQ method has been applied successfully in lower space-time dimensions [30], such as QCD(1+1) [34]. It has also been applied successfully to a range of 1+1 string theory problems by Hellerman and Polchinski [35, 36].

Solving the eigenvalue problem using DLCQ is a formidable computational task for a non-abelian quantum field theory in four-dimensional space-time because of the large number of independent variables. Consequently, alternative methods and approximations are necessary to better understand the nature of relativistic bound-states in the strong-coupling regime. One of the most promising methods for solving nonperturbative (3+1) QCD is the "Basis Light-Front Quantization" (BFLQ) method initiated by James Vary [37] and his collaborators. In the BLFQ method one constructs a complete orthonormal basis of eigenstates based on the eigensolutions of the effective light-front Schrödinger equation derived from light-front holography, in the spirit of the nuclear shell model. Matrix diagonalization for BLFQ should converge more rapidly than DLCQ since the basis states have a mass spectrum close to the observed hadronic spectrum.

An extensive review of light-front quantization is given in Ref. [30]. As we shall discuss here, light-front quantized field theory in physical $3 + 1$ space-time has a holographic dual with dynamics of theories in five-dimensional anti-de Sitter space, giving important insight into the nature of color confinement in QCD.

2 What is the origin of the QCD mass scale?

If one sets the masses of the quarks to zero, no mass scale appears explicitly in the QCD Lagrangian. The classical theory thus displays invariance under both scale (dilatation) and special conformal transformations [38]. Nevertheless, the quantum theory built upon this conformal template displays color confinement, a mass gap, as well as asymptotic freedom. A fundamental question is thus how does the mass scale which determines the masses of the light-quark hadrons, the range of color confinement, and the running of the coupling appears in QCD?

A hint to the origin of the mass scale in nominally conformal theories was given in 1976 in a remarkable paper by V. de Alfaro, S. Fubini and G. Furlan (dAFF) [39] in the context of one-dimensional quantum mechanics. They showed that the mass scale which breaks dilatation invariance can appear in the equations of motion without

violating the conformal invariance of the action. In fact, this is only possible if the resulting potential has the form of a confining harmonic oscillator, and the transformed time variable τ that appears in the confining theory has a limited range.

In this contribution to the NTSE meeting we will review how the application of the dAFF procedure, together with light-front quantum mechanics and light-front holographic mapping, leads to a new analytic approximation to QCD — a light-front Hamiltonian and corresponding one-dimensional light-front (LF) Schrödinger and Dirac equations which are frame-independent, relativistic, and reproduce crucial features of the spectroscopy and dynamics of the light-quark hadrons. The predictions of the LF equations of motion include a zero-mass pion in the chiral $m_q \to 0$ limit, and linear Regge trajectories $M^2(n, L) \propto n + L$ with the same slope in the radial quantum number n (the number of nodes) and $L = \max|L^z|$, the internal orbital angular momentum. In fact, we will also show that the effective confinement potential which appears in the LF equations of motion is unique if we require that the chiral QCD action remains conformally invariant.

3 Light-front holography

An important analysis tool for QCD is anti-de Sitter space in five dimensions. In particular, AdS_5 provides a remarkable geometric representation of the conformal group which underlies the conformal symmetry of classical QCD. One can modify AdS space by using a dilaton factor in the AdS action $e^{\varphi(z)}$ to introduce the QCD confinement scale. However, we shall show that if one imposes the requirement that the action of the corresponding one-dimensional effective theory remains conformal invariant, then the dilaton profile $\varphi(z) \propto z^s$ is constrained to have the specific power $s = 2$, a remarkable result which follows from the dAFF construction of conformally invariant quantum mechanics [40]. A related argument is given in Ref. [41] The quadratic form $\varphi(z) = \pm\kappa^2 z^2$ immediately leads to linear Regge trajectories [42] in the hadron mass squared.

A simple way to obtain confinement and discrete normalizable modes is to truncate AdS space with the introduction of a sharp cut-off in the infrared region of AdS space, as in the "hard-wall" model [43], where one considers a slice of AdS space, $0 \le z \le z_0$, and imposes boundary conditions on the fields at the IR border $z_0 \sim 1/\Lambda_{\rm QCD}$. As first shown by Polchinski and Strassler [43], the modified AdS space, provides a derivation of dimensional counting rules [44, 45] in QCD for the leading power-law fall-off of hard scattering beyond the perturbative regime. The modified theory generates the point-like hard behavior expected from QCD, instead of the soft behavior characteristic of extended objects [43]. The physical states in AdS space are represented by normalizable modes $\Phi_P(x, z) = e^{-iP\cdot x}\Phi(z)$, with plane waves along Minkowski coordinates x^μ and a profile function $\Phi(z)$ along the holographic coordinate z. The hadronic invariant mass $P_\mu P^\mu = M^2$ is found by solving the eigenvalue problem for the AdS wave equation.

"Light-front holography" refers to the remarkable fact that dynamics in AdS space in five dimensions is dual to a semiclassical approximation to Hamiltonian theory in physical $3+1$ space-time quantized at fixed light-front time [46]. The correspondence between AdS and QCD, which was originally motivated by the AdS/CFT correspondence between gravity on a higher-dimensional space and conformal field theories in physical space-time [47], has its most explicit and simplest realization as a direct holographic mapping to light-front Hamiltonian theory [46]. For example, the equation of motion for mesons on the light-front has exactly the same single-variable form as the AdS equation of motion; one can then interpret the AdS fifth dimension variable z in terms of the physical variable ζ, representing the invariant separation of the q and $\bar{q}$ at fixed light-front time. There is a precise connection between the quantities that enter the fifth dimensional AdS space and the physical variables of LF theory. The

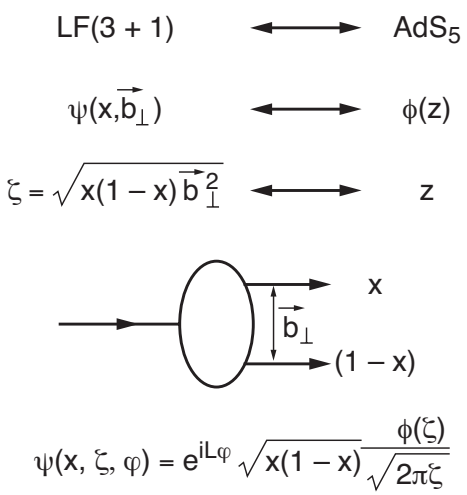

Figure 2: Light-front holography: Mapping between the hadronic wavefunctions of the anti-de Sitter approach and eigensolutions of the light-front Hamiltonian theory derived from the equality of LF and AdS formula for EM and gravitational current matrix elements and their identical equations of motion.

AdS mass parameter μR maps to the LF orbital angular momentum. The formulae for electromagnetic [48] and gravitational [49] form factors in AdS space map to the exact Drell–Yan–West formulae in light-front QCD [50–52].

The light-front holographic principle provides a precise relation between the bound-state amplitudes in AdS space and the boost-invariant LF wavefunctions describing the internal structure of hadrons in physical space-time (see Fig. 2). The resulting valence Fock-state wavefunctions satisfy a single-variable relativistic equation of motion analogous to the eigensolutions of the nonrelativistic radial Schrödinger equation. The quadratic dependence in the effective quark-antiquark potential $U(\zeta^2, J) = \kappa^4\zeta^2 + 2\kappa^2(J-1)$ is determined uniquely from conformal invariance. The constant term $2\kappa^2(J-1) = 2\kappa^2(S+L-1)$ is fixed by the duality between AdS and LF quantization for spin-J states, a correspondence which follows specifically from the separation of kinematics and dynamics on the light-front [53]. The LF potential thus has a specific power dependence-in effect, it is a light-front harmonic oscillator potential. It is confining and reproduces the observed linear Regge behavior of the light-quark hadron spectrum in both the orbital angular momentum L and the radial node number n. The pion is predicted to be massless in the chiral limit [54] — the positive contributions to m_π^2 from the LF potential and kinetic energy is cancelled by the constant term in $U(\zeta^2, J)$ for $J = 0$. This holds for the positive sign of the dilaton profile $\varphi(z) = \kappa^2 z^2$. The LF dynamics retains conformal invariance of the action despite the presence of a fundamental mass scale. The constant term in the LF potential $U(\zeta^2, J)$ derived from LF holography is essential; the masslessness of the pion and the separate dependence on J and L are consequences of the potential derived from the holographic LF duality with AdS for general J and L [40,53]. Thus the light-front holographic approach provides an analytic frame-independent first approximation to the color-confining dynamics, spectroscopy, and excitation spectra of the relativistic light-quark bound states of QCD. It is systematically improvable in full QCD using the basis light-front quantization (BLFQ) method [37] and other methods.

We now give an example of light-front holographic mapping for the specific case of the elastic pion form factor. In the higher-dimensional gravity theory, the hadronic transition amplitude corresponds to the coupling of an external electromagnetic field $A^M(x, z)$, for a photon propagating in AdS space, with an extended field $\Phi_P(x, z)$

describing a meson in AdS is [48]

$$\int d^4x\, dz\, \sqrt{g}\, A^M(x,z)\, \Phi^*_{P'}(x,z) \overleftrightarrow{\partial_M}\, \Phi_P(x,z) \sim (2\pi)^4\, \delta^4(P'-P-q)\, \epsilon_\mu (P+P')^\mu\, F_M(q^2), \quad (1)$$

where the coordinates of AdS_5 are the Minkowski coordinates x^μ and z labeled $x^M = (x^\mu, z)$, with $M = 1, ..., 5$, and g is the determinant of the metric tensor. The expression on the right-hand side of (1) represents the space-like QCD electromagnetic transition amplitude in physical space-time $\langle P'|J^\mu(0)|P\rangle = (P+P')^\mu\, F_M(q^2)$. It is the EM matrix element of the quark current $J^\mu = \sum_q e_q \bar{q}\gamma^\mu q$, and represents a local coupling to pointlike constituents. Although the expressions for the transition amplitudes look very different, one can show that a precise mapping of the matrix elements can be carried out at fixed light-front time [50, 51].

The form factor is computed in the light front formalism from the matrix elements of the plus current J^+ in order to avoid coupling to Fock states with different numbers of constituents and is given by the Drell–Yan–West expression. The form factor can be conveniently written in impact space as a sum of overlap of LFWFs of the $j = 1, 2, ..., n-1$ spectator constituents [55]

$$F_M(q^2) = \sum_n \prod_{j=1}^{n-1} \int dx_j d^2\mathbf{b}_{\perp j} \exp\Big(i\mathbf{q}_\perp \cdot \sum_{j=1}^{n-1} x_j \mathbf{b}_{\perp j}\Big) \times \big|\psi_{n/M}(x_j, \mathbf{b}_{\perp j})\big|^2, \quad (2)$$

corresponding to a change of transverse momentum $x_j\mathbf{q}_\perp$ for each of the $n-1$ spectators with $\sum_{i=1}^n \mathbf{b}_{\perp i} = 0$. The formula is exact if the sum is over all Fock states n.

For simplicity, consider a two-parton bound-state. The $q\bar{q}$ LF Fock state wavefunction for a meson can be written as

$$\psi(x,\zeta,\varphi) = e^{iL\varphi} X(x) \frac{\phi(\zeta)}{\sqrt{2\pi\zeta}}, \quad (3)$$

thus factoring the longitudinal, $X(x)$, transverse, $\phi(\zeta)$, and angular dependence φ. If both expressions for the form factor are to be identical for arbitrary values of Q, we obtain $\phi(\zeta) = (\zeta/R)^{3/2}\Phi(\zeta)$ and $X(x) = \sqrt{x(1-x)}$ [50], where we identify the transverse impact LF variable ζ with the holographic variable z, $z \to \zeta = \sqrt{x(1-x)}\,|\mathbf{b}_\perp|$, where x is the longitudinal momentum fraction and $b_\perp$ is the transverse-impact distance between the quark and antiquark. Extension of the results to arbitrary n follows from the x-weighted definition of the transverse impact variable of the $n-1$ spectator system given in Ref. [50]. Identical results follow from mapping the matrix elements of the energy-momentum tensor [52].

4 The light-front Schrödinger equation: A semiclassical approximation to QCD

It is advantageous to reduce the full multiparticle eigenvalue problem of the LF Hamiltonian to an effective light-front Schrödinger equation which acts on the valence sector LF wavefunction and determines each eigensolution separately [56]. In contrast, diagonalizing the LF Hamiltonian yields all eigensolutions simultaneously, a complex task. The central problem then becomes the derivation of the effective interaction U which acts only on the valence sector of the theory and has, by definition, the same eigenvalue spectrum as the initial Hamiltonian problem. In order to carry out this program one must systematically express the higher Fock components as functionals of the lower ones. This method has the advantage that the Fock space is not truncated, and the symmetries of the Lagrangian are preserved [56].

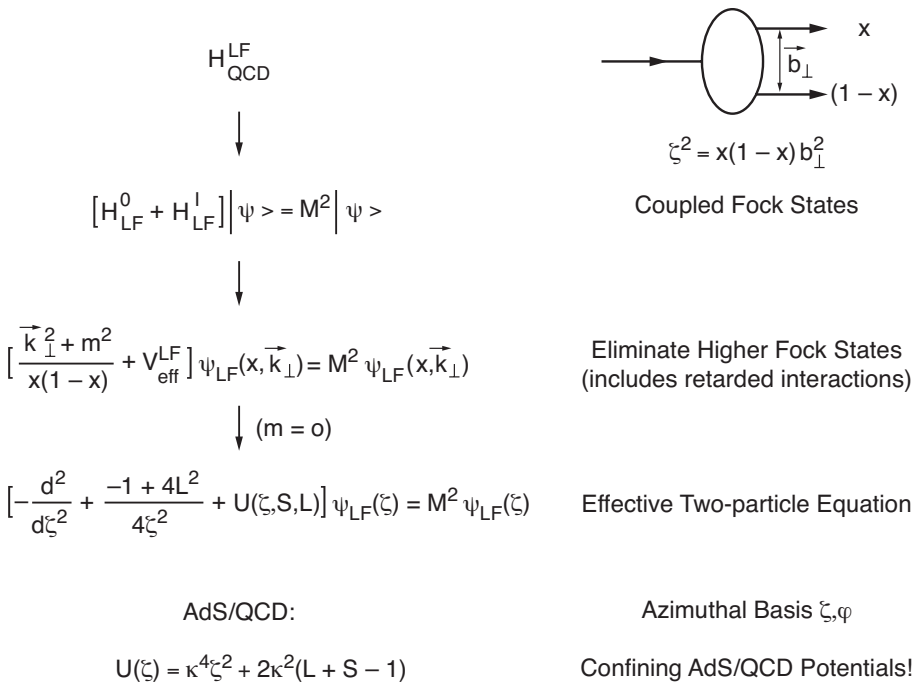

Figure 3: Reduction of the QCD light-front Hamiltonian to an effective $q\bar{q}$ bound state equation. The potential is determined from spin-J representations on AdS_5 space. The harmonic oscillator form of $U(\zeta^2)$ is determined by the requirement that the action remain conformally invariant.

A hadron has four-momentum $P = (P^-, P^+, \mathbf{P}_\perp)$, $P^\pm = P^0 \pm P^3$ and invariant mass $P^2 = M^2$. The generators $P = (P^-, P^+, \vec{P}_\perp)$ are constructed canonically from the QCD Lagrangian by quantizing the system on the light-front at fixed LF time x^+, $x^\pm = x^0 \pm x^3$ [30]. The LF Hamiltonian P^- generates the LF time evolution with respect to the LF time x^+, whereas the LF longitudinal P^+ and transverse momentum $\vec{P}_\perp$ are kinematical generators.

In the limit of zero quark masses the longitudinal modes decouple from the invariant LF Hamiltonian equation $H_{LF}|\phi\rangle = M^2|\phi\rangle$, with $H_{LF} = P_\mu P^\mu = P^- P^+ - \mathbf{P}_\perp^2$. The result is a relativistic and frame-independent light-front wave equation for ϕ [46] (see Fig. 3)

$$\left[-\frac{d^2}{d\zeta^2} - \frac{1-4L^2}{4\zeta^2} + U\left(\zeta^2, J\right)\right]\phi_{n,J,L}(\zeta^2) = M^2\,\phi_{n,J,L}(\zeta^2). \tag{4}$$

This equation describes the spectrum of mesons as a function of n, the number of nodes in ζ, the total angular momentum J, which represent the maximum value of $|J^z|$, $J = \max|J^z|$, and the internal orbital angular momentum of the constituents $L = \max|L^z|$. The variable z of AdS space is identified with the LF boost-invariant transverse-impact variable ζ [50], thus giving the holographic variable a precise definition in LF QCD [46, 50]. For a two-parton bound state $\zeta^2 = x(1-x)b_\perp^2$. In the exact QCD theory U is related to the two-particle irreducible $q\bar{q}$ Green's function.

The potential in the the light-front Schrödinger equation (4) is determined from the two-particle irreducible (2PI) $q\bar{q} \to q\bar{q}$ Greens' function. In particular, the reduction from higher Fock states in the intermediate states leads to an effective interaction $U\left(\zeta^2, J\right)$ for the valence $|q\bar{q}\rangle$ Fock state [56]. A related approach for determining the valence light-front wavefunction and studying the effects of higher Fock states without truncation has been given in Ref. [57].

Unlike ordinary instant-time quantization, the light-front Hamiltonian equations of motion are frame independent; remarkably, they have a structure which matches exactly the eigenmode equations in AdS space. This makes a direct connection of QCD with AdS methods possible. In fact, one can derive the light-front holographic duality of AdS by starting from the light-front Hamiltonian equations of motion for a relativistic bound-state system in physical space-time [46].

5 Effective confinement from the gauge/gravity correspondence

Recently we have derived wave equations for hadrons with arbitrary spin J starting from an effective action in AdS space [53]. An essential element is the mapping of the higher-dimensional equations to the LF Hamiltonian equation found in Ref. [46]. This procedure allows a clear distinction between the kinematical and dynamical aspects of the LF holographic approach to hadron physics. Accordingly, the non-trivial geometry of pure AdS space encodes the kinematics, and the additional deformations of AdS encode the dynamics, including confinement [53].

A spin-J field in AdS_{d+1} is represented by a rank J tensor field $\Phi_{M_1\cdots M_J}$, which is totally symmetric in all its indices. In presence of a dilaton background field $\varphi(z)$ the effective action is [53]

$$S_{\mathit{eff}} = \int d^d x\, dz\, \sqrt{|g|}\, e^{\varphi(z)}\, g^{N_1 N_1'} \cdots g^{N_J N_J'} \times \Big(g^{MM'} D_M\, \Phi^*_{N_1\ldots N_J}\, D_{M'}\, \Phi_{N_1'\ldots N_J'} - \mu^2_{\mathit{eff}}(z)\, \Phi^*_{N_1\ldots N_J}\, \Phi_{N_1'\ldots N_J'} \Big), \quad (5)$$

where D_M is the covariant derivative which includes parallel transport. The effective mass $\mu_{\mathit{eff}}(z)$, which encodes kinematical aspects of the problem, is an *a priori* unknown function, but the additional symmetry breaking due to its z-dependence allows a clear separation of kinematical and dynamical effects [53]. The dilaton background field $\varphi(z)$ in (5) introduces an energy scale in the five-dimensional AdS action, thus breaking conformal invariance. It vanishes in the conformal ultraviolet limit $z \to 0$.

A physical hadron has plane-wave solutions and polarization indices along the $3+1$ physical coordinates $\Phi_P(x,z)_{\nu_1\cdots\nu_J} = e^{iP\cdot x}\Phi_J(z)\epsilon_{\nu_1\cdots\nu_J}(P)$, with four-momentum P_μ and invariant hadronic mass $P_\mu P^\mu = M^2$. All other components vanish identically. The wave equations for hadronic modes follow from the Euler–Lagrange equation for tensors orthogonal to the holographic coordinate z, $\Phi_{zN_2\cdots N_J} = 0$. Terms in the action which are linear in tensor fields, with one or more indices along the holographic direction, $\Phi_{zN_2\cdots N_J}$, give us the kinematical constraints required to eliminate the lower-spin states [53]. Upon variation with respect to $\hat{\Phi}^*_{\nu_1\ldots\nu_J}$, we find the equation of motion [53]

$$\left[-\frac{z^{d-1-2J}}{e^{\varphi(z)}}\, \partial_z \left(\frac{e^{\varphi(z)}}{z^{d-1-2J}}\, \partial_z \right) + \frac{(m\,R)^2}{z^2} \right] \Phi_J = M^2\, \Phi_J, \quad (6)$$

with $(m\,R)^2 = (\mu_{\mathit{eff}}(z)R)^2 - Jz\,\varphi'(z) + J(d-J+1)$, which is the result found in Refs. [46, 58] by rescaling the wave equation for a scalar field. Similar results were found in Ref. [59]. Upon variation with respect to $\hat{\Phi}^*_{N_1\cdots z\cdots N_J}$ we find the kinematical constraints which eliminate lower spin states from the symmetric field tensor [53]

$$\eta^{\mu\nu} P_\mu\, \epsilon_{\nu\nu_2\cdots\nu_J}(P) = 0, \quad \eta^{\mu\nu}\, \epsilon_{\mu\nu\nu_3\cdots\nu_J}(P) = 0. \quad (7)$$

Upon the substitution of the holographic variable z by the LF invariant variable ζ and replacing $\Phi_J(z) = (R/z)^{J-(d-1)/2}\, e^{-\varphi(z)/2}\, \phi_J(z)$ in (6), we find for $d = 4$ the LF

wave equation (4) with effective potential [60]

$$U(\zeta^2, J) = \frac{1}{2}\varphi''(\zeta^2) + \frac{1}{4}\varphi'(\zeta^2)^2 + \frac{2J-3}{2\zeta}\varphi'(\zeta^2), \tag{8}$$

provided that the AdS mass m in (6) is related to the internal orbital angular momentum $L = \max|L^z|$ and the total angular momentum $J^z = L^z + S^z$ according to $(m\,R)^2 = -(2-J)^2 + L^2$. The critical value $L = 0$ corresponds to the lowest possible stable solution, the ground state of the LF Hamiltonian. For $J = 0$ the five dimensional mass m is related to the orbital momentum of the hadronic bound state by $(m\,R)^2 = -4 + L^2$ and thus $(m\,R)^2 \geq -4$. The quantum mechanical stability condition $L^2 \geq 0$ is thus equivalent to the Breitenlohner–Freedman stability bound in AdS [61].

The effective interaction $U(\zeta^2, J)$ is instantaneous in LF time and acts on the lowest state of the LF Hamiltonian. This equation describes the spectrum of mesons as a function of n, the number of nodes in ζ^2, the internal orbital angular momentum $L = L^z$, and the total angular momentum $J = J^z$, with $J^z = L^z + S^z$ the sum of the orbital angular momentum of the constituents and their internal spins. The SO(2) Casimir L^2 corresponds to the group of rotations in the transverse LF plane. The LF wave equation is the relativistic frame-independent front-form analog of the non-relativistic radial Schrödinger equation for muonium and other hydrogenic atoms in presence of an instantaneous Coulomb potential. The LF harmonic oscillator potential could in fact emerge from the exact QCD formulation when one includes contributions from the effective potential U which are due to the exchange of two connected gluons; i. e., "H" diagrams [62]. We notice that U becomes complex for an excited state since a denominator can vanish; this gives a complex eigenvalue and the decay width. The multi gluon exchange diagrams also could be connected to the Isgur–Paton flux-tube model of confinement; the collision of flux tubes could give rise to the ridge phenomena recently observed in high energy pp collisions at RHIC [63].

The correspondence between the LF and AdS equations thus determines the effective confining interaction U in terms of the infrared behavior of AdS space and gives the holographic variable z a kinematical interpretation. The identification of the orbital angular momentum is also a key element of our description of the internal structure of hadrons using holographic principles.

The dilaton profile $\exp\left(\pm\kappa^2 z^2\right)$ leads to linear Regge trajectories [42]. For the confining solution $\varphi = \exp\left(\kappa^2 z^2\right)$ the effective potential is $U(\zeta^2, J) = \kappa^4\zeta^2 + 2\kappa^2(J-1)$ leads to eigenvalues $M^2_{n,J,L} = 4\kappa^2\left(n + \frac{J+L}{2}\right)$, with a string Regge form $M^2 \sim n + L$. A detailed discussion of the light meson and baryon spectrum, as well as the elastic and transition form factors of the light hadrons using LF holographic methods, is given in Ref. [58]. As an example the spectral predictions for the $J = L + S$ light pseudoscalar and vector meson states are compared with experimental data in Fig. 4 for the positive sign dilaton model.

The predictions of the resulting LF Schrödinger and Dirac equations for hadron light-quark spectroscopy and form factors for $m_q = 0$ and $\kappa \simeq 0.5$ GeV are shown in Figs. 4–7 for a dilaton profile $\varphi(z) = \kappa^2 z^2$. A detailed discussion of the computations is given in Ref. [58].

6 Uniqueness of the confining potential

If one starts with a dilaton profile $e^{\varphi(z)}$ with $\varphi \propto z^s$, the existence of a massless pion in the limit of massless quarks determines uniquely the value $s = 2$. To show this, one can use the stationarity of bound-state energies with respect to variation of parameters. More generally, the effective theory should incorporate the fundamental conformal symmetry of the four-dimensional classical QCD Lagrangian in the limit of massless

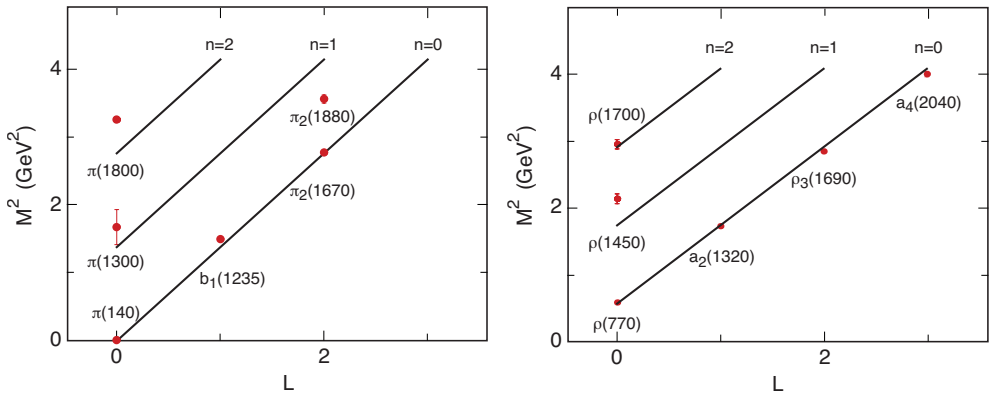

Figure 4: $I = 1$ parent and daughter Regge trajectories for the π-meson family (left) with $\kappa = 0.59$ GeV, and the ρ-meson family (right) with $\kappa = 0.54$ GeV.

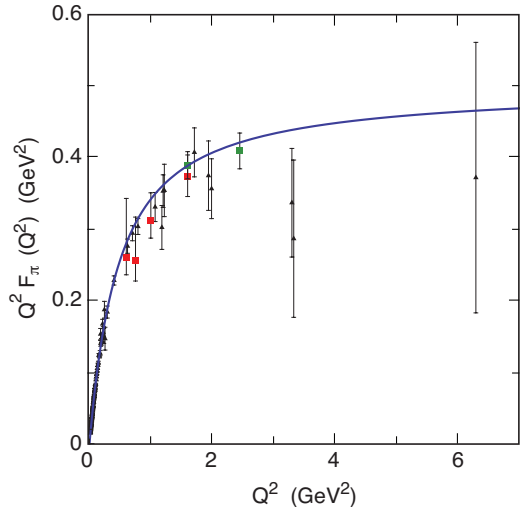

Figure 5: Light-front holographic prediction for the space-like pion form factor.

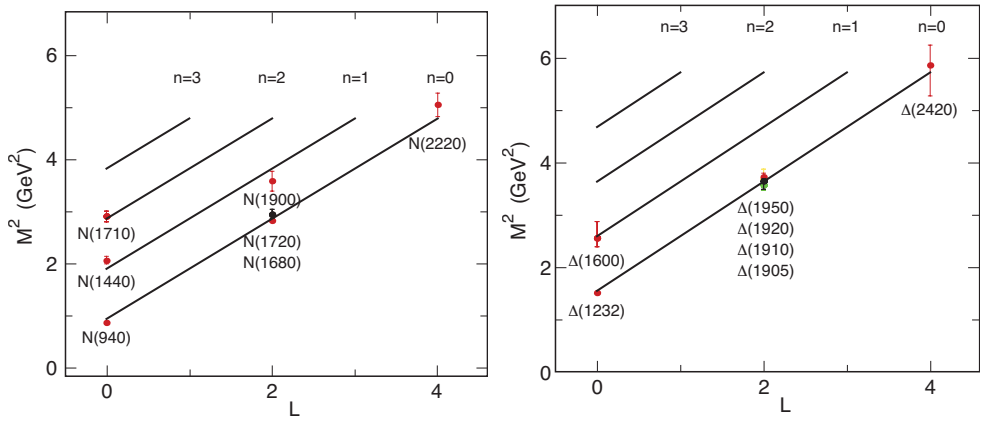

Figure 6: Light front holographic predictions of the light-front Dirac equation for the nucleon spectrum. Orbital and radial excitations for the positive-parity sector are shown for the N (left) and Δ (right) for $\kappa = 0.49$ GeV and $\kappa = 0.51$ GeV respectively. All confirmed positive and negative-parity resonances from PDG 2012 are well accounted using the procedure described in [58].

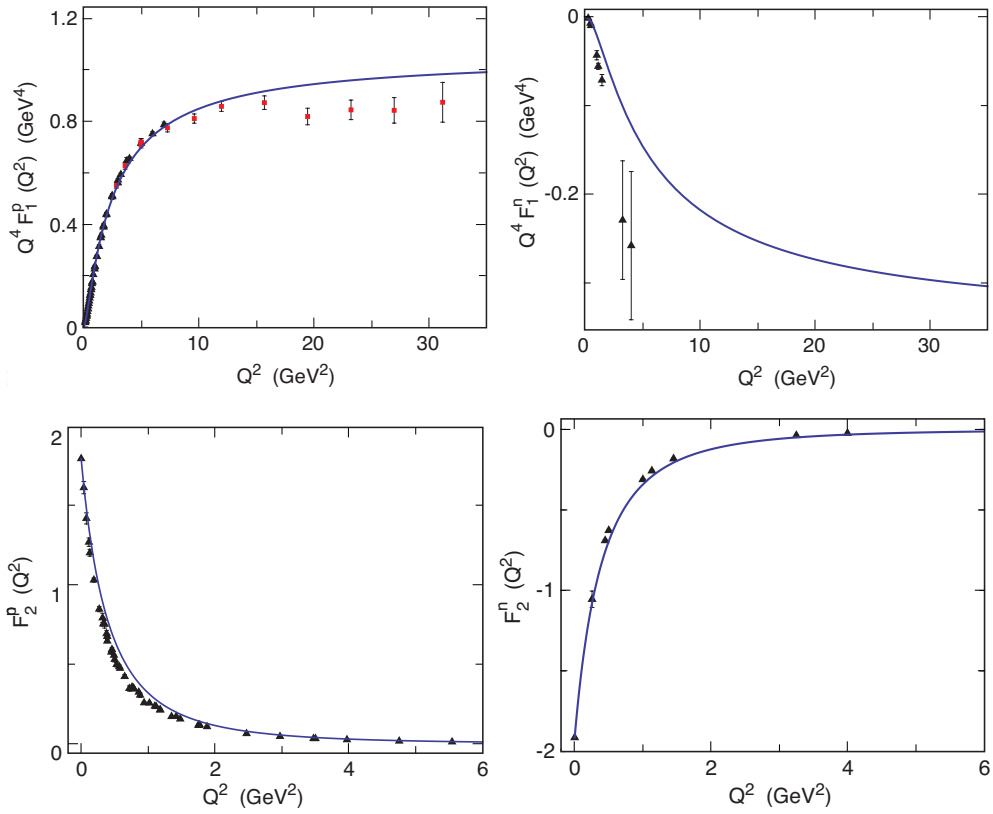

Figure 7: Light-front holographic predictions for the nucleon form factors normalized to their static values.

quarks. To this end we study the invariance properties of a one-dimensional field theory under the full conformal group following the dAFF construction of Hamiltonian operators described in Ref. [39].

One starts with the one-dimensional action $\mathcal{S} = \frac{1}{2}\int dt(\dot{Q}^2 - g/Q^2)$, which is invariant under conformal transformations in the variable t. In addition to the Hamiltonian H_t there are two more invariants of motion for this field theory, namely the dilation operator D and K, corresponding to the special conformal transformations in t. Specifically, if one introduces the the new variable τ defined through $d\tau = dt/(u + v\,t + w\,t^2)$ and the rescaled fields $q(\tau) = Q(t)/(u + v\,t + w\,t^2)^{1/2}$, it then follows that the the operator $G = u\,H_t + v\,D + w\,K$ generates evolution in τ [39]. The Hamiltonian corresponding to the operator G which introduces the mass scale is a linear combination of the old Hamiltonian H_t, D, the generator of dilations, and K, the generator of special conformal transformations. It contains the confining potential $(4uw - v^2)\zeta^2/8$, that is the confining term in (8) for a quadratic dilaton profile and thus $\kappa^4 = (4uw - v^2)/8$. The variable tau is related to the variable t for the case $uw > 0$, $v = 0$ by $\tau = \frac{1}{\sqrt{u\,w}}\arctan\left(\sqrt{\frac{w}{u}}t\right)$, i. e., τ has only a limited range. The finite range of invariant LF time $\tau = x^+/P^+$ can be interpreted as a feature of the internal frame-independent LF time difference between the confined constituents in a bound state. For example, in the collision of two mesons, it would allow one to compute the LF time difference between the two possible quark-quark collisions [40].

7 The Light-Front Vacuum

It is conventional to define the vacuum in quantum field theory as the lowest energy eigenstate of the instant-form Hamiltonian. Such an eigenstate is defined at a single

time t over all space $\vec{x}$. It is thus a causal and frame-dependent. The instant-form vacuum thus must be normal-ordered in order to avoid violations of causality when computing correlators and other matrix elements. In contrast, in the front form, the vacuum state is defined as the eigenstate of lowest invariant mass M. It is defined at fixed light-front time $x^+ = x^0 + x^3$ over all $x^- = x^0 - x^3$ and $\vec{x}_\perp$, the extent of space that can be observed within the speed of light. It is frame-independent and only requires information within the causal horizon.

Since all particles have positive $k^+ = k^0 + k^z > 0$ and + momentum is conserved in the front form, the usual vacuum bubbles are kinematically forbidden in the front form. In fact the LF vacuum for QED, QCD, and even the Higgs Standard Model is trivial up to possible zero modes — backgrounds with zero four-momentum. In this sense it is already normal-ordered. In the case of the Higgs theory, the usual Higgs vacuum expectation value is replaced by a classical $k^+ = 0$ background zero-mode field which is not sensed by the energy momentum tensor [64]. The phenomenology of the Higgs theory is unchanged.

There are thus no quark or gluon vacuum condensates in the LF vacuum — as first noted by Casher and Susskind [65]; the corresponding physics is contained within the LFWFs themselves [66–70], thus eliminating a major contribution to the cosmological constant. In the light-front formulation of quantum field theory, phenomena such as the GMOR relation — usually associated with condensates in the instant form vacuum — are properties of the the hadronic LF wavefunctions themselves. An exact Bethe–Salpeter analysis shows that the quantity that appears in the GMOR relation is the matrix element $\langle 0|\bar{\psi}\gamma_5\psi|\pi\rangle$ for the pion to couple locally to the vacuum via a pseudoscalar operator — not a vacuum expectation value $\langle 0|\bar{\psi}\psi|0\rangle$. In the front-form $\langle 0|\bar{\psi}\gamma_5\psi|\pi\rangle$ involves the pion LF Fock state with parallel q and $\bar{q}$ spin and $L^z = \pm 1$. This pion Fock state automatically appears when the quarks are massive.

The frame-independent causal front-form vacuum is a good match to the "void" — the observed universe without luminous matter. Thus it is natural in the front form to obtain zero cosmological constant from quantum field theory.

8 The Conformal Symmetry Template

In the case of perturbative QCD, the running coupling $\alpha_s(Q^2)$ becomes constant in the limit of zero β-function and zero quark mass, and conformal symmetry becomes manifest. In fact, the renormalization scale uncertainty in pQCD predictions can be eliminated by using the Principle of Maximum Conformality (PMC) [71]. Using the PMC/BLM procedure [72], all non-conformal contributions in the perturbative expansion series are summed into the running coupling by shifting the renormalization scale in α_s from its initial value, and one obtains unique, scale-fixed, scheme-independent predictions at any finite order. One can also introduce a generalization of conventional dimensional regularization, the $\mathcal{R}_\delta$ schemes which illuminates the renormalization scheme and scale ambiguities of pQCD predictions, exposes the general pattern of nonconformal terms, and allows one to systematically determine the argument of the running coupling order by order in pQCD in a form which can be readily automatized [73, 74]. The resulting PMC scales and finite-order PMC predictions are to high accuracy independent of the choice of initial renormalization scale. For example, PMC scale-setting leads to a scheme-independent pQCD prediction [75] for the top-quark forward-backward asymmetry which is within one σ of the Tevatron measurements. The PMC procedure also provides scale-fixed, scheme-independent commensurate scale relations [76], relations between observables which are based on the underlying conformal behavior of QCD such as the generalized Crewther relation [77]. The PMC satisfies all of the principles of the renormalization group: reflectivity, symmetry, and transitivity, and it thus eliminates an unnecessary source of systematic error in pQCD predictions [78].

9 Summary

The triple complementary connection of (a) AdS space, (b) its LF holographic dual, and (c) the relation to the algebra of the conformal group in one dimension, is characterized by a quadratic confinement LF potential, and thus a dilaton profile with the power z^s, with the unique power $s = 2$. In fact, for $s = 2$ the mass of the $J = L = n = 0$ pion is automatically zero in the chiral limit. The separate dependence on J and L leads to a mass ratio of the ρ and the a_1 mesons which coincides with the result of the Weinberg sum rules [79]. One predicts linear Regge trajectories with the same slope in the relative orbital angular momentum L and the LF radial quantum humber n. The AdS approach, however, goes beyond the purely group theoretical considerations of dAFF, since features such as the masslessness of the pion and the separate dependence on J and L are a consequence of the potential (8) derived from the duality with AdS for general high-spin representations.

The QCD mass scale κ in units of GeV has to be determined by one measurement; e. g., the pion decay constant f_π. All other masses and size parameters are then predicted. The running of the QCD coupling is predicted in the infrared region for $Q^2 < 4\kappa^2$ to have the form $\alpha_s(Q^2) \propto \exp\left(\frac{-Q^2}{4\kappa^2}\right)$. As shown in Fig. 8, the result agrees with the shape of the effective charge defined from the Bjorken sum rule [80], displaying an infrared fixed point [80]. In the nonperturbative domain soft gluons are in effect sublimated into the effective confining potential. Above this region, hard-gluon exchange becomes important, leading to asymptotic freedom. The scheme-dependent scale Λ_{QCD} that appears in the QCD running coupling in any given renormalization scheme could be determined in terms of κ.

In our previous papers we have applied LF holography to baryon spectroscopy, space-like and time-like form factors, as well as transition amplitudes such as $\gamma^*\gamma \to \pi^0$, $\gamma^* N \to N^*$, all based on essentially one mass scale parameter κ. Many other applications have been presented in the literature, including recent results by Forshaw and Sandapen [81] for diffractive ρ electroproduction, based on the light-front holo-

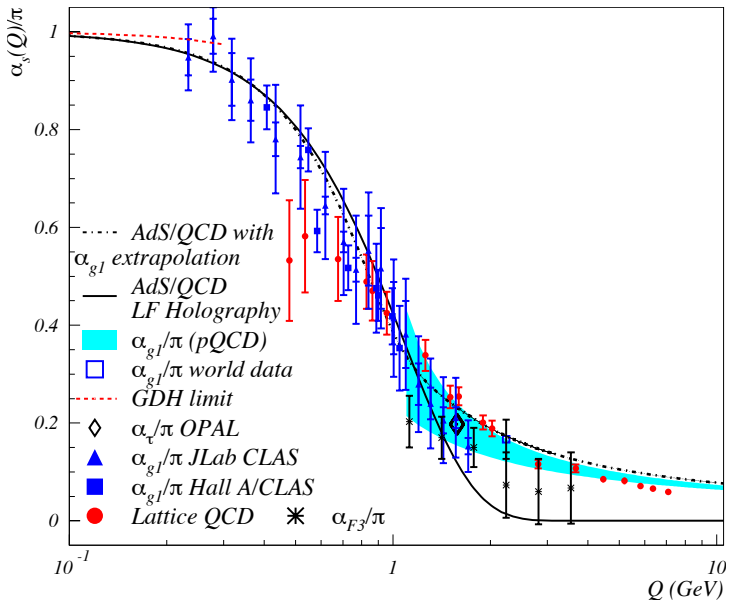

Figure 8: Light-front holographic results for the QCD running coupling from Ref. [80] normalized to $\alpha_s(0)/\pi = 1$. The result is analytic, defined at all scales and exhibits an infrared fixed point.

graphic prediction for the longitudinal ρ LFWF. Other recent applications include predictions for generalized parton distributions (GPDs) [82], and a model for nucleon and flavor form factors [83].

The treatment of the chiral limit in the LF holographic approach to strongly coupled QCD is substantially different from the standard approach based on chiral perturbation theory. In the conventional approach, spontaneous symmetry breaking by a non-vanishing chiral quark condensate $\langle\bar{\psi}\psi\rangle$ plays the crucial role. In QCD sum rules [84] $\langle\bar{\psi}\psi\rangle$ brings in non-perturbative elements into the perturbatively calculated spectral sum rules. It should be noted, however, that the definition of the condensate, even in lattice QCD necessitates a renormalization procedure for the operator product, and it is not a directly observable quantity. In contrast, in Bethe–Salpeter [85] and light-front analyses [86], the Gell Mann–Oakes–Renner relation [87] for m_π^2/m_q involves the decay matrix element $\langle 0|\bar{\psi}\gamma_5\psi|\pi\rangle$ instead of $\langle 0|\bar{\psi}\psi|0\rangle$.

In the color-confining light-front holographic model discussed here, the vanishing of the pion mass in the chiral limit, a phenomenon usually ascribed to spontaneous symmetry breaking of the chiral symmetry, is obtained specifically from the precise cancellation of the LF kinetic energy and LF potential energy terms for the quadratic confinement potential. This mechanism provides a viable alternative to the conventional description of nonperturbative QCD based on vacuum condensates, and it eliminates a major conflict of hadron physics with the empirical value for the cosmological constant [66, 67].

10 Acknowledgments

Invited talk, presented by SJB at the *International Conference on Nuclear Theory in the Supercomputing Era* (NTSE 2013), in honor of James Vary, May 13 – May 17, 2013, Iowa State University, Ames, Iowa. This work was supported by the Department of Energy contract DE–AC02–76SF00515. SLAC-PUB-15735

References

[1] P. A. M. Dirac, Rev. Mod. Phys. **21**, 392 (1949).

[2] C. Lorce and B. Pasquini, Int. J. Mod. Phys. Conf. Ser. **20**, 84 (2012), arXiv:1208.3065 [hep-ph] (2012).

[3] S. J. Brodsky, M. Diehl and D. S. Hwang, Nucl. Phys. B **596**, 99 (2001), hep-ph/0009254 (2000).

[4] S. D. Drell and T. -M. Yan, Phys. Rev. Lett. **24**, 181 (1970).

[5] G. B. West, Phys. Rev. Lett. **24**, 1206 (1970).

[6] S. J. Brodsky and S. D. Drell, Phys. Rev. D **22**, 2236 (1980).

[7] S. J. Brodsky and J. R. Primack, Ann. Phys. (NY) **52**, 315 (1969).

[8] S. J. Brodsky and J. R. Primack, Phys. Rev. **174**, 2071 (1968).

[9] G. P. Lepage and S. J. Brodsky, Phys. Rev. D **22**, 2157 (1980).

[10] A. V. Efremov and A. V. Radyushkin, Phys. Lett. B **94**, 245 (1980).

[11] S. J. Brodsky, R. Roskies and R. Suaya, Phys. Rev. D **8**, 4574 (1973).

[12] R. P. Feynman, Phys. Rev. Lett. **23**, 1415 (1969).

[13] R. P. Feynman, *Photon-hadron interactions*. Reading, Mass., 1972.

[14] S. Fubini and G. Furlan, Physics **1**, 229 (1965).

[15] S. Weinberg, Phys. Rev. **150**, 1313 (1966).

[16] A. H. Mueller, Nucl. Phys. B **415**, 373 (1994).

[17] S. J. Brodsky and C.-R. Ji, Phys. Rev. D **33**, 2653 (1986).

[18] S. J. Brodsky, D. S. Hwang, B.-Q. Ma and I. Schmidt, Nucl. Phys. B **593**, 311 (2001), hep-th/0003082 (2000).

[19] C. A. Cruz-Santiago and A. M. Stasto, Nucl. Phys. B **875**, 368 (2013), arXiv: 1308.1062 [hep-ph] (2013).

[20] F. Antonuccio, S. J. Brodsky and S. Dalley, Phys. Lett. B **412**, 104 (1997), hep-ph/9705413 (1997).

[21] S. J. Brodsky, M. Burkardt and I. Schmidt, Nucl. Phys. B **441**, 197 (1995), hep-ph/9401328 (1994).

[22] T. Gutsche, V. E. Lyubovitskij, I. Schmidt and A. Vega, arXiv:1306.0366 [hep-ph] (2013).

[23] S. J. Brodsky, P. Hoyer, N. Marchal, S. Peigne and F. Sannino, Phys. Rev. D **65**, 114025 (2002), hep-ph/0104291 (2001).

[24] S. J. Brodsky, D. S. Hwang and I. Schmidt, Phys. Lett. B **530**, 99 (2002), hep-ph/0201296 (2002).

[25] S. J. Brodsky and A. H. Mueller, Phys. Lett. B **206**, 685 (1988).

[26] S. J. Brodsky, C.-R. Ji and G. P. Lepage, Phys. Rev. Lett. **51**, 83 (1983).

[27] S. J. Brodsky, P. Hoyer, C. Peterson and N. Sakai, Phys. Lett. B **93**, 451 (1980).

[28] M. Franz, M. V. Polyakov and K. Goeke, Phys. Rev. D **62**, 074024 (2000), hep-ph/0002240 (2000).

[29] S. J. Brodsky, G. F. de Teramond and R. Shrock, AIP Conf. Proc. **1056**, 3 (2008), arXiv:0807.2484 [hep-ph] (2008).

[30] S. J. Brodsky, H.-C. Pauli and S. S. Pinsky, Phys. Rept. **301**, 299 (1998), hep-ph/9705477 (1997).

[31] W. A. Bardeen and R. B. Pearson, Phys. Rev. D **14**, 547 (1976).

[32] M. Burkardt and S. K. Seal, Phys. Rev. D **65**, 034501 (2002), hep-ph/0102245 (2001).

[33] J. Bratt, S. Dalley, B. van de Sande and E. M. Watson, Phys. Rev. D **70**, 114502 (2004), hep-ph/0410188 (2004).

[34] H. C. Pauli and S. J. Brodsky, Phys. Rev. D **32**, 1993 (1985).

[35] S. Hellerman and J. Polchinski, in *The many faces of the superworld*, edited by M. A. Shifman. hep-th/9908202 (1999).

[36] J. Polchinski, Progr. Theor. Phys. Suppl. **134**, 158 (1999), hep-th/9903165 (1999).

[37] J. P. Vary, H. Honkanen, J. Li, P. Maris, S. J. Brodsky, A. Harindranath, G. F. de Teramond, P. Sternberg, E. G. Ng and C. Yang, Phys. Rev. C **81**, 035205 (2010), arXiv:0905.1411 [nucl-th] (2009).

[38] G. Parisi, Phys. Lett. B **39**, 643 (1972).

[39] V. de Alfaro, S. Fubini and G. Furlan, Nuovo Cim. A **34**, 569 (1976).

[40] S. J. Brodsky, G. F. de Teramond and H. G. Dosch, arXiv:1302.4105 [hep-th] (2013).

[41] S. D. Glazek and A. P. Trawinski, arXiv:1307.2059 [hep-ph] (2013).

[42] A. Karch, E. Katz, D. T. Son and M. A. Stephanov, Phys. Rev. D **74**, 015005 (2006), hep-ph/0602229 (2006).

[43] J. Polchinski and M. J. Strassler, Phys. Rev. Lett. **88**, 031601 (2002), hep-th/0109174 (2001).

[44] S. J. Brodsky and G. R. Farrar, Phys. Rev. Lett. **31**, 1153 (1973).

[45] V. A. Matveev, R. M. Muradian and A. N. Tavkhelidze, Lett. Nuovo Cim. **7**, 719 (1973).

[46] G. F. de Teramond and S. J. Brodsky, Phys. Rev. Lett. **102**, 081601 (2009), arXiv:0809.4899 [hep-ph] (2008).

[47] J. M. Maldacena, Adv. Theor. Math. Phys. **2**, 231 (1998), hep-th/9711200 (1997).

[48] J. Polchinski and M. J. Strassler, JHEP **0305**, 012 (2003), hep-th/0209211 (2002).

[49] Z. Abidin and C. E. Carlson, Phys. Rev. D **77**, 095007 (2008), arXiv:0801.3839 [hep-ph] (2008).

[50] S. J. Brodsky and G. F. de Teramond, Phys. Rev. Lett. **96**, 201601 (2006), hep-ph/0602252 (2006).

[51] S. J. Brodsky and G. F. de Teramond, Phys. Rev. D **77**, 056007 (2008), arXiv: 0707.3859 [hep-ph] (2007).

[52] S. J. Brodsky and G. F. de Teramond, Phys. Rev. D **78**, 025032 (2008), arXiv: 0804.0452 [hep-ph] (2008).

[53] G. F. de Teramond, H. G. Dosch and S. J. Brodsky, Phys. Rev. D **87**, 075005 (2013), arXiv:1301.1651 [hep-ph] (2013).

[54] G. F. de Teramond and S. J. Brodsky, Nucl. Phys. Proc. Suppl. **199**, 89 (2010), arXiv:0909.3900 [hep-ph] (2009).

[55] D. E. Soper, Phys. Rev. D **15**, 1141 (1977).

[56] H. C. Pauli, Eur. Phys. J. C **7**, 289 (1999), hep-th/9809005 (1998).

[57] S. S. Chabysheva and J. R. Hiller, Phys. Lett. B **711**, 417 (2012), arXiv:1103.0037 [hep-ph] (2011).

[58] G. F. de Teramond and S. J. Brodsky, arXiv:1203.4025 [hep-ph] (2012).

[59] T. Gutsche, V. E. Lyubovitskij, I. Schmidt and A. Vega, Phys. Rev. D **85**, 076003 (2012), arXiv:1108.0346 [hep-ph] (2011).

[60] G. F. de Teramond and S. J. Brodsky, AIP Conf. Proc. **1296**, 128 (2010), arXiv:1006.2431 [hep-ph] (2010).

[61] P. Breitenlohner and D. Z. Freedman, Ann. Phys. (NY) **144**, 249 (1982).

[62] T. Appelquist, M. Dine and I. J. Muzinich, Phys. Lett. B **69**, 231 (1977).

[63] J. D. Bjorken, S. J. Brodsky and A. S. Goldhaber, arXiv:1308.1435 [hep-ph] (2013).

[64] P. P. Srivastava and S. J. Brodsky, Phys. Rev. D **66**, 045019 (2002), hep-ph/0202141 (2002).

[65] A. Casher and L. Susskind, Phys. Rev. D **9**, 436 (1974).

[66] S. J. Brodsky and R. Shrock, Proc. Nat. Acad. Sci. **108**, 45 (2011), arXiv:0905.1151 [hep-th] (2009).

[67] S. J. Brodsky, C. D. Roberts, R. Shrock and P. C. Tandy, Phys. Rev. C **82**, 022201 (2010), arXiv:1005.4610 [nucl-th] (2010).

[68] L. Chang, I. C. Cloet, J. J. Cobos-Martinez, C. D. Roberts, S. M. Schmidt and P. C. Tandy, arXiv:1301.0324 [nucl-th] (2013).

[69] L. Chang, C. D. Roberts and S. M. Schmidt, arXiv:1308.4708 [nucl-th] (2013).

[70] S. D. Glazek, Acta Phys. Polon. B **42**, 1933 (2011), arXiv:1106.6100 [hep-th] (2011).

[71] S. J. Brodsky and L. Di Giustino, Phys. Rev. D **86**, 085026 (2012), arXiv:1107.0338 [hep-ph] (2011).

[72] S. J. Brodsky, G. P. Lepage and P. B. Mackenzie, Phys. Rev. D **28**, 228 (1983).

[73] M. Mojaza, S. J. Brodsky and X. -G. Wu, Phys. Rev. Lett. **110**, 192001 (2013), arXiv:1212.0049 [hep-ph] (2012).

[74] S. J. Brodsky, M. Mojaza and X. -G. Wu, arXiv:1304.4631 [hep-ph] (2013).

[75] S. J. Brodsky and X. -G. Wu, Phys. Rev. D **85**, 114040 (2012), arXiv:1205.1232 [hep-ph] (2012).

[76] S. J. Brodsky and H. J. Lu, Phys. Rev. D **51**, 3652 (1995), hep-ph/9405218 (1994).

[77] S. J. Brodsky, G. T. Gabadadze, A. L. Kataev and H. J. Lu, Phys. Lett. B **372**, 133 (1996), hep-ph/9512367 (1995).

[78] X. -G. Wu, S. J. Brodsky and M. Mojaza, Progr. Part. Nucl. Phys. **72**, 44 (2013), arXiv:1302.0599 [hep-ph] (2013).

[79] S. Weinberg, Phys. Rev. Lett. **18**, 507 (1967).

[80] S. J. Brodsky, G. F. de Teramond and A. Deur, Phys. Rev. D **81**, 096010 (2010), arXiv:1002.3948 [hep-ph] (2010).

[81] J. R. Forshaw and R. Sandapen, Phys. Rev. Lett. **109**, 081601 (2012), arXiv:1203.6088 [hep-ph] (2012).

[82] A. Vega, I. Schmidt, T. Gutsche and V. E. Lyubovitskij, Phys. Rev. D **83**, 036001 (2011), arXiv:1010.2815 [hep-ph] (2010).

[83] D. Chakrabarti and C. Mondal, arXiv:1307.7995 [hep-ph] (2013).

[84] M. A. Shifman, A. I. Vainshtein and V. I. Zakharov, Nucl. Phys. B **147**, 385 (1979).

[85] P. Maris, C. D. Roberts and P. C. Tandy, Phys. Lett. B **420**, 267 (1998), nucl-th/9707003 (1997).

[86] S. J. Brodsky, C. D. Roberts, R. Shrock and P. C. Tandy, Phys. Rev. C **85**, 065202 (2012), arXiv:1202.2376 [nucl-th] (2012).

[87] M. Gell-Mann, R. J. Oakes and B. Renner, Phys. Rev. **175**, 2195 (1968).

Modeling Nuclear Parton Distribution Functions

H. Honkanen[a], M. Strikman[a] and V. Guzey[b]

[a] *The Pennsylvania State University, 104 Davey Lab, University Park, PA 16802, USA*
[b] *National Research Center "Kurchatov Institute", Petersburg Nuclear Physics Institute (PNPI), Gatchina, 188300, Russia*

Abstract

The presence of nuclear medium and collective phenomena which involve several nucleons modify the parton distribution functions of nuclei (nPDFs) compared to those of a free nucleon. These modifications have been investigated by different groups using global analyses of high energy nuclear reaction world data resulting in modern nPDF parametrizations with error estimates, such as EPS09(s), HKN07 and nDS. These phenomenological nPDF sets roughly agree within their uncertainty bands, but have antiquarks for large-x and gluons for the whole x-range poorly constrained by the available data. In the kinematics accessible at the LHC this has negative impact on the interpretation of the heavy-ion collision data, especially for the $p+A$ benchmarking runs. The EMC region is also sensitive to the proper definition of x, where the nuclear binding effects have to be taken into account, and for heavy nuclei one also needs to take into account that a fraction of the nucleus momentum is carried by the equivalent photons which modifies the momentum sum rule. We study how these effects affect the predictions for the nuclear modification ratios at the LHC kinematics using a model where we combine theoretical input for the leading twist nuclear shadowing (the FGS model) and the EKS98s/EPS09s nPDF set where the spatial dependence is formulated as a power series of the nuclear thickness functions T_A.

Keywords: *Nuclear parton distribution function; LHC; impact parameter; EMC region*

1 Proper definition of x

Nuclear parton distribution functions (nPDFs) are usually defined for each parton flavor in terms of nuclear modifications $R_i^A(x,Q^2)$ and the corresponding free proton PDF $f_i^p(x,Q^2)$ such that

$$f_i^A(x,Q^2) \equiv R_i^A(x,Q^2)\, f_i^p(x,Q^2), \tag{1}$$

where the Bjorken $x = A\,Q^2/(2q\cdot p_A)$, with $0 \le x \le A$. In the collider frame, x is simply the fraction of the nucleus momentum scaled by the factor A. However, since these nPDF sets are built "on top" of proton PDF sets, the tail $1 \le x \le A$ is usually ignored.

Phenomenological parametrizations for nuclear modifications, such as EKS98 [1], EPS09 [2], HKN07 [3], DSZS [4], nCTEQ [5], etc., are largely based on deep inelastic scattering (DIS) data, which are given as a function of $x_p = Q^2/(2q_0 m_p)$, which is independent of the target mass. The difference between x_p and x thus originates from

Proceedings of International Conference 'Nuclear Theory in the Supercomputing Era — 2013' (NTSE-2013), Ames, IA, USA, May 13–17, 2013. Eds. A. M. Shirokov and A. I. Mazur. Pacific National University, Khabarovsk, Russia, 2014, p. 104.
http://www.ntse-2013.khb.ru/Proc/Honkanen.pdf.

the nuclear binding (see Refs. [6, 7][1]),

$$x_p = x\,(1\,+r_x^A), \tag{2}$$

where

$$r_x^A = \frac{1}{m_p}\big((m_n - m_p)N/A - \epsilon_A\big) < 0. \tag{3}$$

As an example, the nuclear binding energy $\epsilon_A \approx 7.88\,(7.68)$ MeV for Pb (C).

In addition to the nuclear binding energy, the fraction of nucleus momentum carried by equivalent photons has to be taken into account in high energy heavy nuclear collisions. The fraction of the nucleus momentum carried by the photons is found to be [7]

$$\eta_\gamma(^{12}\mathrm{C}) = 0.11\%, \quad \eta_\gamma(^{208}\mathrm{Pb}) = 0.7\%. \tag{4}$$

Since the gluon nPDFs are least constrained by the DIS and DY data, presence of the photons in the momentum sum rule mostly affects the overall momentum carried by gluons. The effect of the equivalent photon field can be taken into account by rescaling the gluons after Eq. (2) has been applied to satisfy

$$\sum_i \int_0^1 \mathrm{d}x\, x\, f_i^A(x, Q^2) = 1 - \eta_\gamma(A). \tag{5}$$

To apply the "conventional" nPDFs given as a function of x_p for the calculation of the nuclear effects in the ultra-relativistic heavy ion collisions where x is used, one has to translate to the "conventional" nPDFs, given as a function of x_p, by taking into account the difference between x_p and x which from now on we explicitly call $x_{\rm shift}$, as follows:

$$x_{\rm shift}\, f_i^A(x_{\rm shift}, Q^2) = \begin{cases} \frac{x_p}{1+r_x^A}\, f_i^A\big(\frac{x_p}{1+r_x^A}, Q^2\big), & i = q, \bar{q} \\ g_{\rm scale}\, \frac{x_p}{1+r_x^A}\, f_i^A\big(\frac{x_p}{1+r_x^A}, Q^2\big), & i = g \end{cases}, \tag{6}$$

where the scaling factor for gluons, $g_{\rm scale}$, is determined via Eq. (5). Note that for a free proton, $x = x_p = x_{\rm shift}$. It follows from Eq. (6) that while the fraction of the nucleus momentum carried by quarks is invariant with respect to the $x_p \to x_{\rm shift}$ conversion, the amount of the nucleus momentum carried by gluons, $\eta_g \equiv \int_0^1 dx_{\rm shift}\; x_{\rm shift}\, g_A(x_{\rm shift}, Q^2)$, decreases by the factor of $g_{\rm scale} = \frac{\eta_g - \eta_\gamma(A)}{\eta_g}$ with the rescaling.

2 Theoretically motivated nPDF model

In this work we combine a small-x theoretical model for the leading twist nuclear shadowing, the FGS model [6], with the phenomenological EKS98/EPS09 nPDF set. The FGS model is based on the generalization of the Gribov–Glauber multiple scattering formalism and QCD factorization theorems. Using the picture of high energy scattering in the laboratory frame[2] and the notion of cross section fluctuations of energetic projectiles, multiple interactions are modeled using the effective x-dependent and flavor-dependent rescattering cross section $\sigma^i_{\rm soft}(x, Q^2)$, which controls the strength of the resulting nuclear shadowing. In Ref. [6], based on the phenomenological analysis of cross section fluctuations in virtual photons, two models were suggested: model 1 (here referred to as FGS1) and model 2 (FGS2) corresponding to the upper and lower bounds on the predicted nuclear shadowing, respectively. Both models were built on top of CTEQ5 PDFs [8] (given as a function of x_p), and we will use this set for the combined model as well. In this paper, we will work in LO.

[1] In Ref [7] there is a sign error in the corresponding formula, Eq. (20). For detailed discussion, see the revised version of [7].

[2] The equivalent picture can be formulated in the nucleus fast frame [6].

Table 1: The percentage of nucleus momentum carried by the gluons.

	EKS98		FGS1+EKS98		FGS2+EKS98	
	Pb	C	Pb	C	Pb	C
x_p:	43.98	42.61	44.20	42.58	44.30	42.62
$x_{\rm shift}$:	43.58	42.54	43.81	42.52	43.91	42.56

In the following the initial scale sea quark and gluon ($Q_0^2 = 2.5$ GeV^2) nuclear modifications for the region $10^{-4} \leq x \leq 0.01$, where data practically do not constrain nPDFs, are taken from the FGS1 and FGS2 parametrizations; for $0.03 \leq x \leq 1.0$, the nuclear modifications are taken from the EKS98 parametrization [1] (which in this region is very similar to the newer set EPS09 [2]). For the valence quarks, the nuclear modifications are taken from EKS98 for the whole x-range. The two parametrizations are combined by performing polynomial interpolation between them, and [after being corrected for the difference in the argument according to Eq. (2)] the gluons are rescaled as in Eq. (6). The resulting scaling factor at $Q_0^2 = 2.5$ GeV^2 for the gluons is $g_{\rm scale} \sim 0.984$ ($g_{\rm scale} \sim 0.997$) for Pb (C) nucleus. (The change in the scaling factor is $\sim 0.4\%$ at $Q^2 = 10000^2$ GeV^2, so in practice a uniform scaling factor can be used for any scale.) Consequently the amount of the momentum carried by the gluons decreases by 0.88% (0.14%) for Pb (C). The fraction of the momentum carried by the gluons for each model is listed in Table 1 (41.80% for the proton in CTEQ5L).

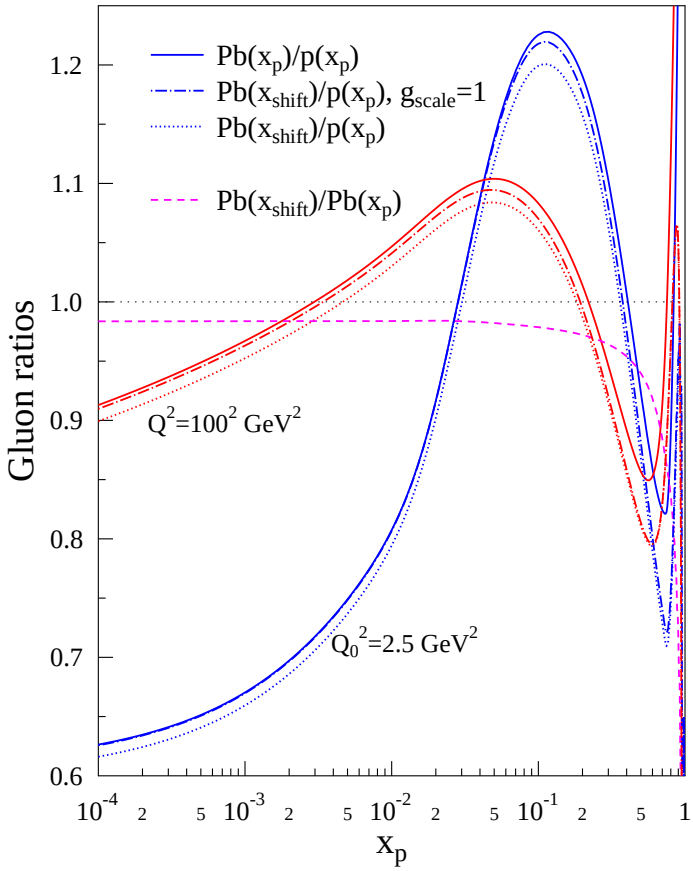

Figure 1: Gluon ratio for Pb($x_{\rm shift}$)/Pb(x_p) at $Q_0^2 = 2.5$ GeV^2 and for Pb/p at $Q_0^2 = 2.5$ GeV^2 and $Q^2 = 100^2$ GeV^2 for EKS98.

In Fig. 1 we show how changing the definition of x affects the EKS98 gluon modification ratio Pb/p at the initial scale $Q_0^2 = 2.5$ GeV^2 and how this effect evolves up to the higher scale $Q^2 = 100^2$ GeV^2. In this work we use the QCDNUM DGLAP evolution code [9]. At the initial scale the original EKS98 gluon modification ratio $x_p\, G^{\rm Pb}(x_p)/x_p\, G^p(x_p)$ (solid line) is first modified setting $g_{\rm scale} = 1$ in Eq. (6) (dotted-dashed line). As a result, the gluon modification ratio is only essentially modified at the EMC-region, $x_p > 0.5$, where the (n)PDFs are decreasing rapidly. For the full conversion with $g_{\rm scale} \sim 0.98$ (dotted line), the gluon nPDF is naturally scaled down over the whole x_p-range. When evolved up to $Q^2 = 100^2$ GeV^2, the differences persist and spread towards smaller values of x_p. Using $x_{\rm shift}$ instead of x_p obviously affects gluons for the whole x_p-range due to the rescaling (and at higher scales also the sea quarks via the DGLAP evolution), but for all the parton flavors the most prominent effect sets in at the EMC-region, where the parton distribution functions change quickly. As seen from above, the gluon ratio Pb($x_{\rm shift}$)/Pb(x_p) (dashed line) is < 1 for the whole x_p-range.

Note in passing that even for the valence quark distributions, the experimental information on the EMC effect in the region where the leading twist contribution dominates is very limited as the higher twist effects give a large (dominant?) contribution to the eA scattering cross section for $x \geq 0.5$ in the SLAC and JLab kinematics. Hence, to date, practically no data on the quark modification for $x \geq 0.5$ in the scaling region is available for heavy nuclei such as, e. g., lead.

In Fig. 2 we show the gluon ratio (Pb/d) for the combined models FGS1+EKS98 (dotted-dashed) and FGS2+EKS98 (dotted), together with the EKS98 (solid) gluon

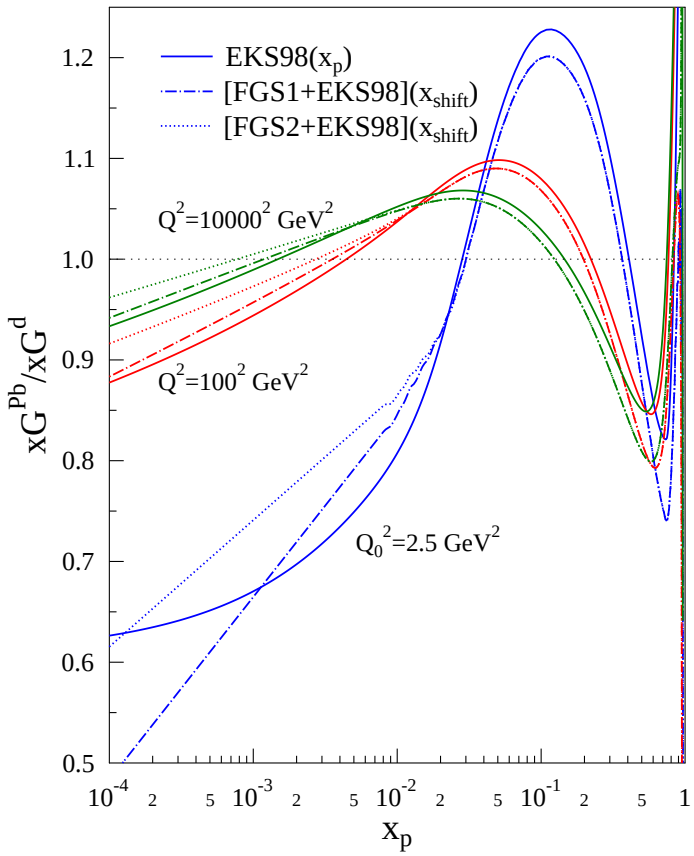

Figure 2: Gluon ratios for Pb/d at $Q_0^2 = 2.5$, 100^2 and 10000^2 GeV^2 for EKS98, and the combination model FGS1(2)+EKS98.

modification. At the initial scale above $x_p > 0.01$, the difference between the models originates only from the different definition of x; below $x_p \leq 0.01$, the two FGS nuclear shadowing models span a region considerably smaller than the error band of EPS09 gluons (see Ref. [2] for details). When evolved up to $Q^2 = 10000^2$ GeV^2, a relevant scale in the LHC kinematics, it is evident that processes which are sensitive to the EMC-region are also sensitive to the proper definition of x.

3 Consequences for the LHC

In order to understand the sensitivity of the LHC kinematics to the EMC effect, we study inclusive π^0 production in $p + \mathrm{Pb}$ collisions, which schematically can be expressed as

$$\sigma^{p+\mathrm{Pb}\to\pi^0+X} = \sum_{i,j,k=q,\bar{q},g} f_i^p(x_1,Q^2) \otimes f_j^{\mathrm{Pb}}(x_2,Q^2) \otimes \hat{\sigma}^{ij\to k+X}(x_1,x_2,Q^2) \otimes D_{k\to\pi^0}(z,\mu_F^2), \quad (7)$$

where the factorization and renormalization scales have been set equal (see, e. g., Ref. [10] for the formulae and details). In this work, we choose $\mu_F = p_T$ (the outgoing pion transverse momentum) and $Q = q_T$ (partonic transverse momentum).

In Fig. 3 we show the LO invariant cross section $E\,d^3\sigma/dp^3$ for $p + \mathrm{Pb} \to \pi^0 + X$ at $p_T = 3.0$, 10.0 and 100.0 GeV as a function of x_2 [the momentum fraction carried

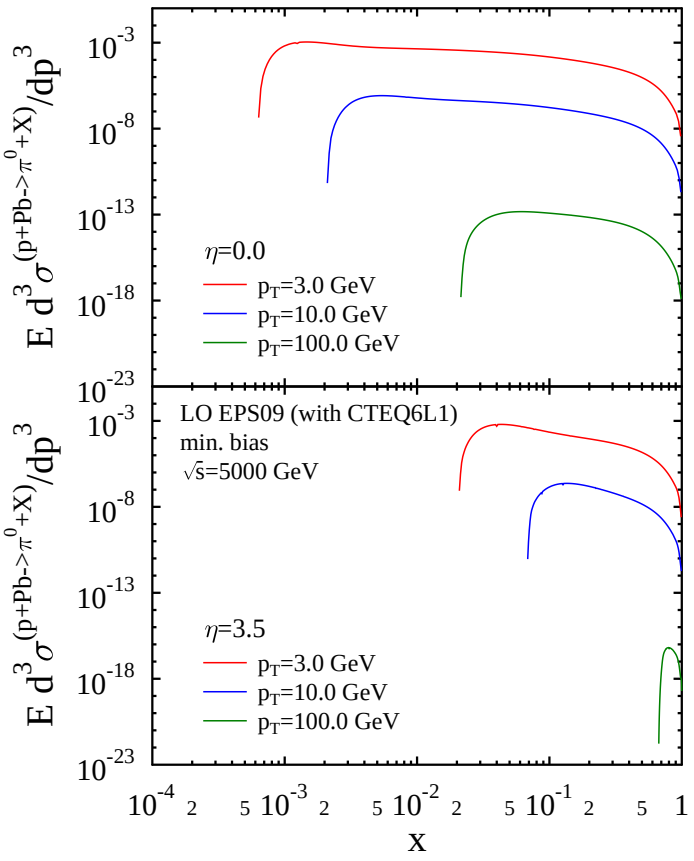

Figure 3: The x-distribution for the minimum bias π^0 production at the LHC at $\eta = 0$ and $\eta = 3.5$ for different p_T.

by the parton in Pb, without conversion given in Eq. (6)]. The results have been computed with the EPS09 nuclear modifications [2], CTEQ6L PDFs [11] and DSS fragmentation functions [12]. Working in LO the overall normalization of the spectra is not fixed, but the x_2-distribution and the relative normalization are not affected by this. The upper panel shows the mid-rapidity and the lower panel — the forward rapidity (at the LHC, the Pb rapidity is positive) π^0 production. For each p_T value studied, the mid-rapidity production peaks at an order of magnitude smaller values of x_2 than the forward rapidity results, and remains significant over a wider range of x_2. In the forward direction the pion production is concentrated on a rather narrow x_2-range, making it a more sensitive probe of nuclear effects. In particular, at high-p_T, the pions are produced exclusively from the EMC-region, making them also sensitive to the definition of x_2.

Figures 4 and 5 show the FGS1(2)+EKS98 results for the minimum bias nuclear modification ratio,

$$R^{\pi^0}_{p\mathrm{Pb}}(p_T,\eta) = \frac{d^3\sigma^{p\mathrm{Pb}}/dp^3}{d^3\sigma^{pp}/dp^3}, \tag{8}$$

at the LHC at $\sqrt{s} = 5500$ GeV. For comparison, the EKS98 results with the CTEQ5L

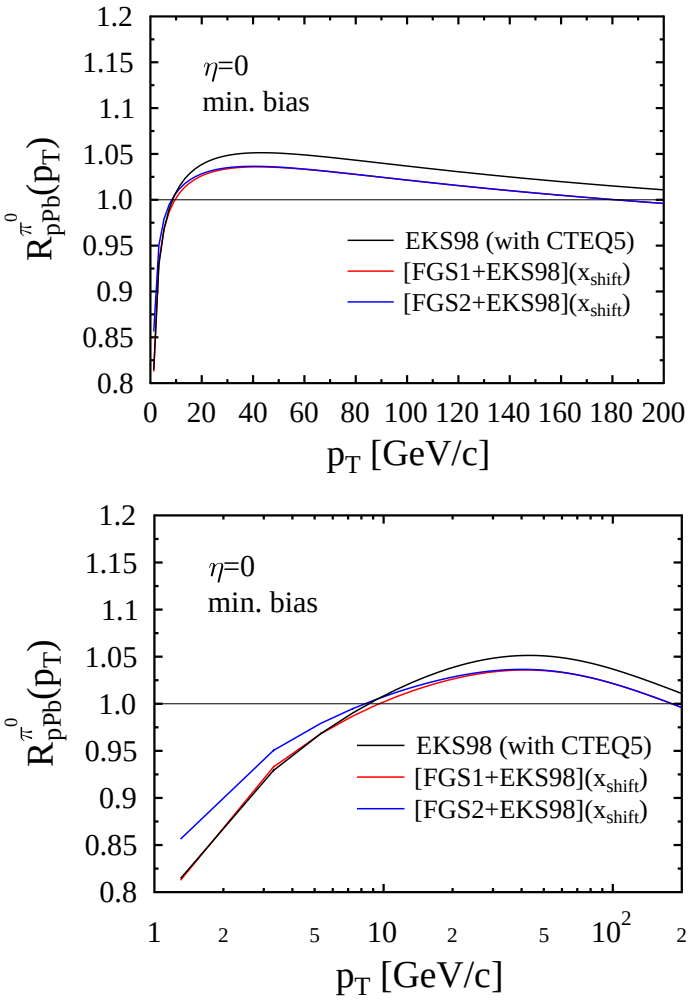

Figure 4: Minimum bias FGS1(2)+EKS98 results for $R^{\pi^0}_{p\mathrm{Pb}}(p_T)$ for the LHC at $\sqrt{s} = 5500$ GeV and $\eta = 0.0$. For comparison, the EKS98 grid result with CTEQ5L PDFs is also shown. Upper panel on linear scale, lower panel on logarithmic scale.

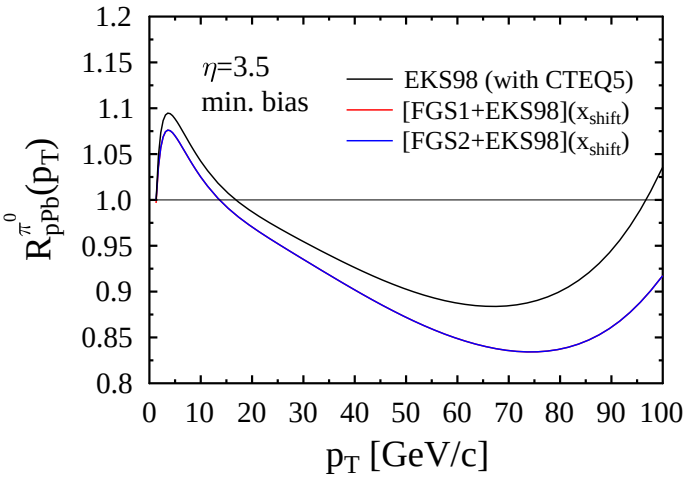

Figure 5: Minimum bias FGS1(2)+EKS98 results for $R^{\pi^0}_{p\rm Pb}$ for the LHC at $\sqrt{s} = 5500$ GeV and $\eta = 3.5$. For comparison, the EKS98 grid result with CTEQ5L PDFs is also shown. The FGS1+EKS98 and FGS2+EKS98 curves are indistinguishable.

PDFs are also shown. In the mid-rapidity (Fig. 4) the difference between the EKS98 and FGS+EKS98 results remain within a few %. As can be seen from Fig. 3 (upper panel), up to $p_T \sim 100$ GeV, the pion spectra mostly originate from the gluon distribution dominated x-range below the EMC-region. Therefore the differences between the models are caused both by the different assumptions about shadowing (see the lower panel where the small-p_T part is shown on a logarithmic scale) and the scaling of the gluon distribution with $g_{\rm scale} < 1$. The difference between the models remain moderate even above $p_T > 100$ GeV.

As seen from Fig. 5, the situation is drastically different in the forward rapidity pion production. Above $p_T \sim 10$ GeV, the two FGS-models are indistinguishable, but start to deviate from the EKS98 result as p_T increases. This sizable effect is caused by the correction to the x-definition alone.

Until now we have discussed the minimum bias results, where the impact parameter dependence of the nuclear effects has been spatially averaged. In the FGS model the transverse position $\mathbf{s}$ dependence is naturally built in as functions of $T_A(\mathbf{s})$ since the nuclear shadowing is first calculated for fixed $\mathbf{s}$ and next the integral over $\mathbf{s}$ is taken. In the EKS98s/EPS09s model [13], the EKS98 and EPS09 nPDF parametrizations were also assumed to have spatial dependence as a power series of $T_A(\mathbf{s})$. With the centrality classes modeled using the optical Glauber model, the EPS09s results were found to be consistent with the mid-rapidity PHENIX $R^{\pi^0}_{d\rm Au}$ centrality systematics [14]. However, as already seen in Fig. 5, the proper definition of x has a major effect on the LHC predictions at forward rapidity. In Fig. 6 we applied the procedure described in Ref. [13] to $R^{\pi^0}_{p\rm Pb}$ at $\eta = 3.5$ for a selection of different centrality classes, and compared the EKS98s results (with CTEQ6L PDFs) with and without the x-corrections. Irrespective of the centrality, the correction causes a clear, measurable effect.

For an impact parameter dependent theoretically motivated nPDF model it is also important to pay special attention to the EMC region for another reason. In Ref. [15] the magnitude of the EMC effect was shown to be linearly related to the short range correlations (SRC) scale factor measured from electron inclusive scattering at $x \geq 1$. Consequently the impact parameter dependence of the EMC effect should be proportional to the local density [16] and the EMC effect thus should be strongest in the center of the nucleus. We will address this issue in Ref. [17], where a full NLO

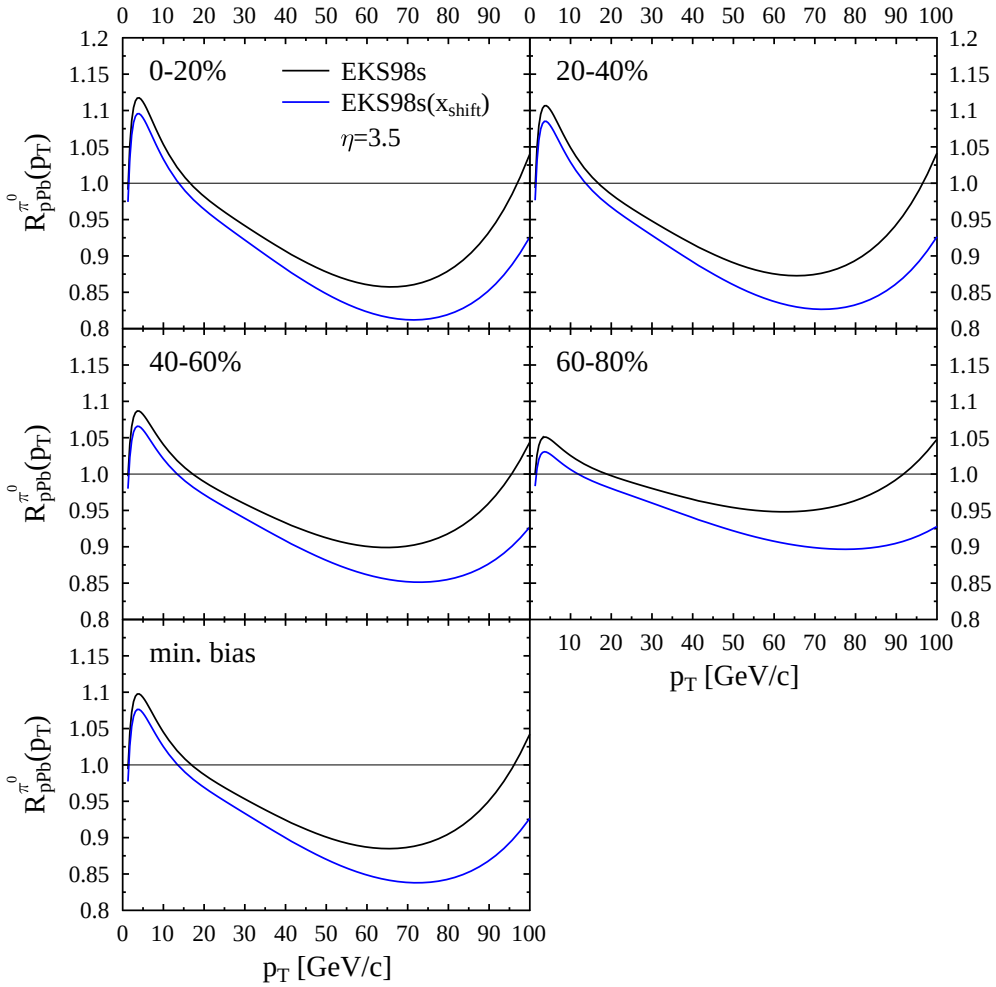

Figure 6: $R^{\pi^0}_{p\mathrm{Pb}}$ for the LHC at $\sqrt{s} = 5500$ GeV and $\eta = 3.5$ for the EKS98 (with CTEQ6L1) results computed with x_p and x_{shift}. The different centrality classed are computed as in [13]. The FGS1+EKS98 and FGS2+EKS98 curves are indistinguishable.

impact parameter dependent nPDF set will be released.

This work was supported in part by US DOE Contract No DE-FG02-93ER40771.

References

[1] K. J. Eskola, V. J. Kolhinen and C. A. Salgado, Eur. Phys. J. C **9**, 61 (1999), hep-ph/9807297 (1998).

[2] K. J. Eskola, H. Paukkunen and C. A. Salgado, JHEP **0904**, 065 (2009), arXiv:0902.4154 [hep-ph] (2009).

[3] M. Hirai, S. Kumano and T. -H. Nagai, Phys. Rev. C **76**, 065207 (2007), arXiv:0709.3038 [hep-ph] (2007).

[4] D. de Florian and R. Sassot, Phys. Rev. D **69**, 074028 (2004), hep-ph/0311227 (2003).

[5] K. Kovarik, I. Schienbein, F. I. Olness, J. Y. Yu, C. Keppel, J. G. Morfin, J. F. Owens and T. Stavreva, Phys. Rev. Lett. **106**, 122301 (2011), arXiv:1012.0286 [hep-ph] (2010).

[6] L. Frankfurt, V. Guzey and M. Strikman, Phys. Rept. **512**, 255 (2012), arXiv:1106.2091 [hep-ph] (2011).

[7] L. Frankfurt and M. Strikman, Int. J. Mod. Phys. E **21**, 1230002 (2012), arXiv:1203.5278 [hep-ph] (2012).

[8] H. L. Lai *et al.* (CTEQ Collaboration), Eur. Phys. J. C **12**, 375 (2000), hep-ph/9903282 (1999).

[9] M. Botje, Comput. Phys. Commun. **182**, 490 (2011), arXiv:1005.1481 [hep-ph] (2010).

[10] K. J. Eskola and H. Honkanen, Nucl. Phys. A **713**, 167 (2003), hep-ph/0205048 (2002).

[11] J. Pumplin, D. R. Stump, J. Huston, H. L. Lai, P. M. Nadolsky and W. K. Tung, JHEP **0207**, 012 (2002), hep-ph/0201195 (2002).

[12] D. de Florian, R. Sassot and M. Stratmann, Phys. Rev. D **75**, 114010 (2007), hep-ph/0703242 [hep-ph] (2007).

[13] I. Helenius, K. J. Eskola, H. Honkanen and C. A. Salgado, JHEP **1207**, 073 (2012), arXiv:1205.5359 [hep-ph] (2012).

[14] S. S. Adler *et al.* (PHENIX Collaboration), Phys. Rev. Lett. **98**, 172302 (2007), nucl-ex/0610036 (2006).

[15] L. B. Weinstein, E. Piasetzky, D. W. Higinbotham, J. Gomez, O. Hen and R. Shneor, Phys. Rev. Lett. **106**, 052301 (2011), arXiv:1009.5666 [hep-ph] (2010).

[16] L. L. Frankfurt and M. I. Strikman, Phys. Rept. **160**, 235 (1988).

[17] H. Honkanen, M. Strikman and V. Guzey, *work in progress*.

A Study of Generalized Parton Distributions for the Proton in AdS/QCD

Dipankar Chakrabarti and Chandan Mondal

Department of Physics, Indian Institute of Technology Kanpur, Kanpur-208016, India

Abstract

We have evaluated the generalized parton distributions (GPDs) from the electromagnetic form factors of the nucleons. The light front wave functions of the nucleons are obtained from soft wall model in AdS/QCD. We have considered a quark model with SU(6) spin-flavor symmetry. The GPDs in impact parameter space are compared with a phenomenological model.

Keywords: *Parton distributions; AdS/QCD; soft wall model; form factor; light front wave function*

1 Introduction

Generalized parton distributions (GPDs) encode more informations about the hadron than the ordinary parton distributions (PDFs). The GPDs are functions of three variables namely, longitudinal momentum fraction x of the quark or gluon, square of the total momentum transferred (t) and the skewness ζ which represents the longitudinal momentum transferred in the process and contain lot more informations about the nucleon structure and spin compared to the ordinary PDFs which are functions of x only. There are many good review articles on the GPDs [1]. The GPDs appear in the exclusive processes like Deeply Virtual Compton Scattering (DVCS) or vector meson productions and are expressed as off-forward matrix elements of bilocal light front currents. The GPDs reduce to the ordinary parton distributions in the forward limit and their first moments are related to the form factors and provide interesting informations about the spin and orbital angular momentum of the constituents as well as the spatial structure of the nucleons. Being off-forward matrix elements, the GPDs have no probabilistic interpretation. But for zero skewness, the Fourier transforms of the GPDs with respect to the transverse momentum transfer ($\Delta_\perp$) give the impact parameter dependent GPDs which satisfy the positivity condition and can be interpreted as distribution functions [2]. The impact parameter dependent GPDs provide us the information about partonic distributions in the impact parameter or the transverse position space for a given longitudinal momentum (x). The impact parameter $b_\perp$ gives the separation of the struck quark from the center of momentum. In the $t \to 0$ limit, Ji sum rule [3] relates the moment of the GPDs to the angular momentum contribution to the nucleon by the quark or gluon. Lot of experiments measured DVCS as well as vector meson production cross sections to gain informations about the GPDs [4]. Experiments will also be done in JLAB in near future.

Using AdS/QCD, one can extract the light front wave functions (LFWF) for the hadrons and thus provides an interesting way to calculate the GPDs. Polchinski and Strassler [5] first used the AdS/CFT duality to address the deep inelastic scattering. The AdS/QCD for meson and baryon sectors have been developed by several groups [6–8]. So far this method has been successfully applied to describe many hadron

Proceedings of International Conference 'Nuclear Theory in the Supercomputing Era — 2013' (NTSE-2013), Ames, IA, USA, May 13–17, 2013. Eds. A. M. Shirokov and A. I. Mazur. Pacific National University, Khabarovsk, Russia, 2014, p. 113.

http://www.ntse-2013.khb.ru/Proc/Chakrabarti.pdf.

properties, e. g., hadron mass spectrum, parton distribution functions, meson and nucleon form factors, structure functions, etc. [9–11]. Recently it has been shown that the results for ρ meson electroproduction calculated with the light front wave functions derived from AdS/QCD are in agreement with experimental data [12]. Studies of the nucleon form factors with higher Fock sectors have been done in Ref. [13]. Vega *et al.* [14] proposed a prescription to extract GPDs from the form factors in AdS/QCD and they have done the GPD calculations using both the hard and soft wall models in AdS/QCD. Here we provide the results for GPDs using the LFWFs obtained from the AdS/QCD [15]. We use the formula for the nucleon form factors in the light front quark model with SU(6) spin flavor symmetry and compare the GPDs in the impact parameter space with a phenomenological model of the GPDs for the proton. The GPDs are related to the Dirac and Pauli form factor by sum rules and thus it is possible to extract the flavor form factors, i. e., individual quark contributions to the nucleon form factors. Recently, the flavor form factors calculated from the GPDs in this model are shown to agree remarkably with the experimental data [16].

2 GPDs in AdS/QCD

For the extraction of the nucleon wavefunctions in AdS/QCD we follow Brodsky and Teramond [6, 11]. We know that the AdS/CFT correspondence relates a gravitationally interacting theory in anti de Sitter space AdS_{d+1} with a conformal gauge theory in d-dimensions residing at the boundary. Since QCD is not a conformal theory, one needs to break the conformal invariance of the above duality to generate a bound state spectrum and to relate with QCD. There are two models in the literature to do so. One is the hard wall model in which the conformal symmetry is broken by introducing a boundary at $z_0 \sim 1/\Lambda_{QCD}$ in the AdS direction where the wavefunction is made to vanish. While in the soft wall model, the conformal invariance is broken by introducing a confining potential in the action of a Dirac field propagating in AdS_{d+1} space.

We will consider the soft model in this paper. The relevant action in soft model is written as [11]

$$S = \int d^4x\, dz\, \sqrt{g}\Big(\frac{i}{2}\bar{\Psi}\, e_A^M\, \Gamma^A\, D_M\, \Psi - \frac{i}{2}(D_M\bar{\Psi})\, e_A^M\, \Gamma^A\, \Psi - \mu\, \bar{\Psi}\, \Psi - V(z)\, \bar{\Psi}\, \Psi\Big), \quad (1)$$

where $e_A^M = (z/R)\, \delta_A^M$ is the inverse vielbein and $V(z)$ is the confining potential, R is the AdS radius. The corresponding Dirac equation in AdS is given by

$$i\Big(z\, \eta^{MN}\, \Gamma_M\, \partial_N + \frac{d}{2}\, \Gamma_z\Big)\Psi - \mu\, R\, \Psi - R\, V(z)\, \Psi = 0. \quad (2)$$

With z identified as the light front transverse impact variable ζ which gives the separation of the quark and gluonic constituents in the hadron, it is possible to extract the lightfront wavefunctions for the hadron. In $d = 4$ dimensions, $\Gamma_A = \{\gamma_\mu, -i\gamma_5\}$. The form of the confining potential in the meson sector can be determined by introducing a dilaton background profile of the form $\phi(z) = e^{\pm\kappa^2 z^2}$. It generates an effective linear confining potential of $U(\zeta) = (R/\zeta)V(\zeta) = \kappa^2\zeta$ in the light front Dirac equation. For the baryon sector, the dilaton profile can be scaled away by redefinition of the fields [11]. In the baryon sector, the linear confining potential same as the meson sector is put in by hand. The nucleon wavefunctions in the soft wall model are given by [11]

$$\psi_+(z) = \frac{\sqrt{2}\kappa^2}{R^2}\, z^{7/2}\, e^{-\kappa^2 z^2/2}, \quad (3)$$

$$\psi_-(z) = \frac{\kappa^3}{R^2}\, z^{9/2}\, e^{-\kappa^2 z^2/2}. \quad (4)$$

The Dirac and Pauli form factors for the nucleons are related to the GPDs by the sum rules [17]

$$\begin{aligned} F_1^p(t) &= \int_0^1 dx \left[\frac{2}{3}H_v^u(x,t) - \frac{1}{3}H_v^d(x,t)\right], \\ F_1^n(t) &= \int_0^1 dx \left[\frac{2}{3}H_v^d(x,t) - \frac{1}{3}H_v^u(x,t)\right], \\ F_2^p(t) &= \int_0^1 dx \left[\frac{2}{3}E_v^u(x,t) - \frac{1}{3}E_v^d(x,t)\right], \\ F_2^n(t) &= \int_0^1 dx \left[\frac{2}{3}E_v^d(x,t) - \frac{1}{3}E_v^u(x,t)\right]. \end{aligned} \tag{5}$$

Here x is the fraction of the light cone momentum carried by the active quark and the GPDs for valence quark q are defined as $H_v^q(x,t) = H^q(x,0,t) + H^q(-x,0,t)$; $E_v^q(x,t) = E^q(x,0,t) + E^q(-x,0,t)$. The GPDs at $-x$ for quark are equal to the GPDs at x for antiquark with a minus sign.

A quark model with SU(6) spin-flavor symmetry is constructed by weighting the different Fock components in the nucleon state by the charge and spin-projections of the quarks as dictated by the symmetry [11]. The Dirac form factors for the nucleons in this model are given by

$$F_1^p(Q^2) = R^4 \int \frac{dz}{z^4}\, V(Q^2,z)\, \psi_+^2(z) \tag{6}$$

$$F_1^n(Q^2) = -\frac{1}{3}R^4 \int \frac{dz}{z^4}\, V(q^2,z)\, (\psi_+^2(z) - \psi_-^2(z)). \tag{7}$$

The Pauli form factors requires non-minimal electromagnetic coupling as proposed by Abidin and Carlson [10] and are given by

$$F_2^{p/n}(Q^2) \sim \int \frac{dz}{z^3}\, \psi_+(z)\, V(Q^2,z)\, \psi_-(z). \tag{8}$$

The normalization conditions are given by $F_1^{p/n}(0) = e_{p/n}$, where $e_{p/n}$ represents the electric charge of proton/neutron and $F_2^{p/n}(0) = \kappa_{p/n}$ where $\kappa_{p/n}$ is the anomalous magnetic moment of the proton/neutron. Using the the above mentioned wavefunctions ψ_+ and ψ_-, the Pauli form factors fitted to the static values are rewritten as

$$F_2^{p/n}(Q^2) = \kappa_{p/n} R^4 \int \frac{dz}{z^4}\, V(Q^2,z)\, \psi_-^2(z). \tag{9}$$

The bulk-to-boundary propagator for soft wall model is given by

$$V(Q^2,z) = \Gamma\left(1 + \frac{Q^2}{4\kappa^2}\right) U\left(\frac{Q^2}{4\kappa^2}, 0, \kappa^2 z^2\right), \tag{10}$$

where $U(a,b,z)$ is the Tricomi confluent hypergeometric function given by

$$\Gamma(a)\, U(a,b,z) = \int_0^\infty e^{-zx}\, x^{a-1} (1+x)^{b-a-1}\, dx. \tag{11}$$

The above propagator can be written in a simple integral form [11, 18]

$$V(Q^2,z) = \kappa^2 z^2 \int_0^1 \frac{dx}{(1-x)^2}\, x^{Q^2/(4\kappa^2)}\, e^{-\kappa^2 z^2 x/(1-x)}. \tag{12}$$

We use the integral form of the bulk-to-boundary propagator in the formulas for the form factors in AdS space to extract the GPDs using the formulas in Eq. (5). In

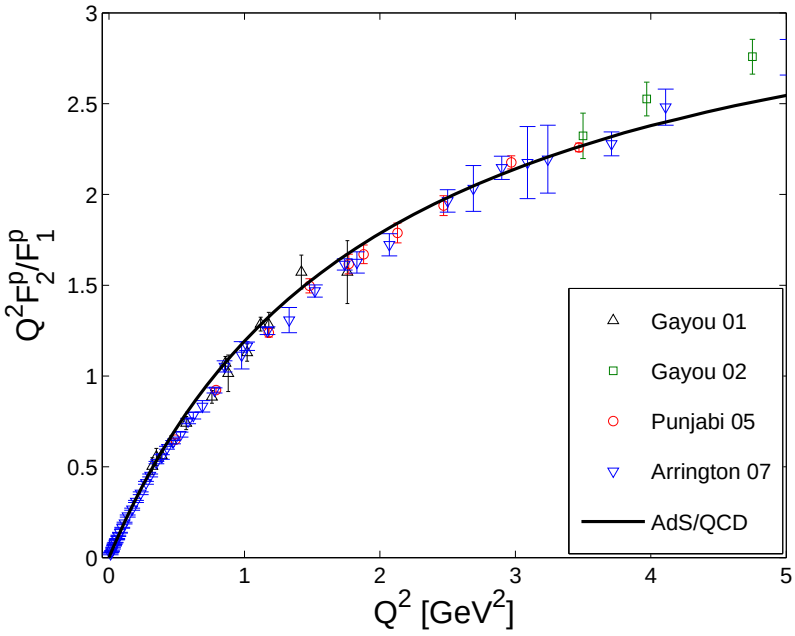

Figure 1: The ratio of the Pauli and Dirac form factors for the proton multiplied by $Q^2 = -t$. The experimental data are taken from Refs. [19–22].

Fig. 1, we show the fit of our result with the experimental proton form factor data. We found that the best fit to the form factors obtained for $\kappa = 0.4066$ GeV. All the calculations and plots presented here are done with this fixed value of κ.

In Figs. 2 (a) and (b) we have shown the GPD $H(x,t)$ as functions of x for different $-t$ values for up and down quarks. Except the fact that it falls off faster for d quark as x increases, the overall nature is the same for both u and d quarks. Similarly in Figs. 3 (a) and (b) we have shown the GPD $E(x,t)$ as a function of x for different $-t$ for u and d quark. Unlike $H(x,t)$, the fall off of the GPD $E(x,t)$ with increasing x is similar for both u and d quark.

3 GPDs in impact parameter space

GPDs in transverse impact parameter space are defined as [23]:

$$H(x,b) = \frac{1}{(2\pi)^2}\int d^2\Delta\; e^{-i\Delta^\perp\cdot b^\perp} H(x,t),$$
$$E(x,b) = \frac{1}{(2\pi)^2}\int d^2\Delta\; e^{-i\Delta^\perp\cdot b^\perp} E(x,t). \tag{13}$$

The transverse impact parameter $b = |b_\perp|$ is a measure of the transverse distance between the struck parton and the center of momentum of the hadron and satisfies $\sum_i x_i b_i = 0$, where the sum is over the number of partons. An estimate of the size of the bound state can be obtained from the relative distance between the struck parton and the centre of momentum of the spectator system and is given by $\frac{b}{1-x}$ [17]. However as the spatial extension of the spectator system is not available from the GPDs, exact estimation of the nuclear size is not possible. In Figs. 4 (a) and (b), we have shown the behavior of $H^{u/d}(x,b)$ in the impact parameter space for fixed values of x and the similar plots for the GPD $E^{u/d}(x,b)$ are shown in Fig. 5.

We compare the AdS/QCD results for the GPDs in impact parameter space with those obtained from a phenomenological model for proton [24]. The GPDs in this

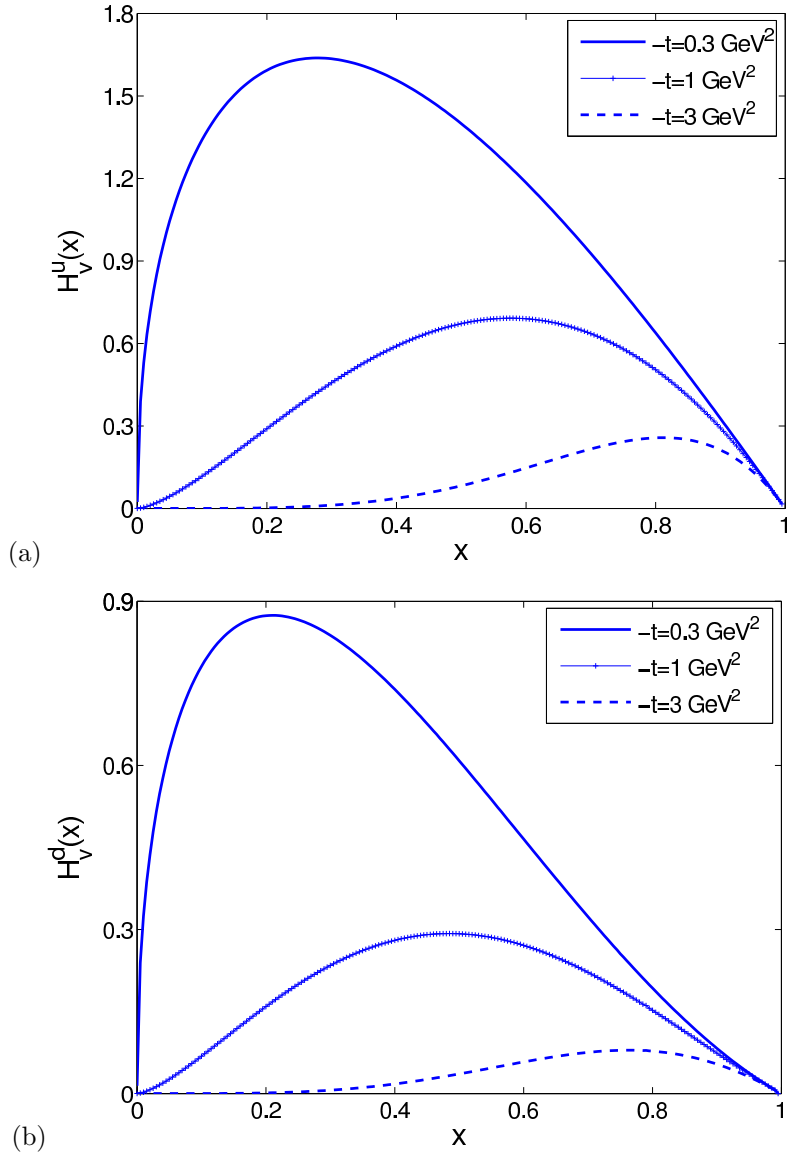

Figure 2: Plots of (a) $H^u(x,t)$ vs x for fixed values of $-t$. (b) same as in (a) but for d quark.

model are given by

$$H^q(x,t) = G^{\lambda^q}_{M_x^q}(x,t)\, x^{-\alpha^q - \beta_1^q (1-x) p_1 t}, \tag{14}$$

$$E^q(x,t) = \kappa_q G^{\lambda^q}_{M_x^q}(x,t)\, x^{-\alpha^q - \beta_2^q (1-x) p_2 t}, \tag{15}$$

where the first part is derived from spectator model and modified by Regge term to have proper behavior at low x. κ_q in the above equation is the quark contribution to the anomalous magnetic moment. The parameters are fixed by fitting the form factors. The details of the functional forms and the values of the parameters can be found in Ref. [24]. The impact parameter dependent GPDs from this model have been studied in Ref. [25]. One should remember here that the valence GPDs we have considered here in AdS/QCD are not exactly the same as GPDs in this model and so exact agreement is not expected. But one should expect that the valence GPDs will dominate the overall behavior for the proton GPDs and thus it is interesting to

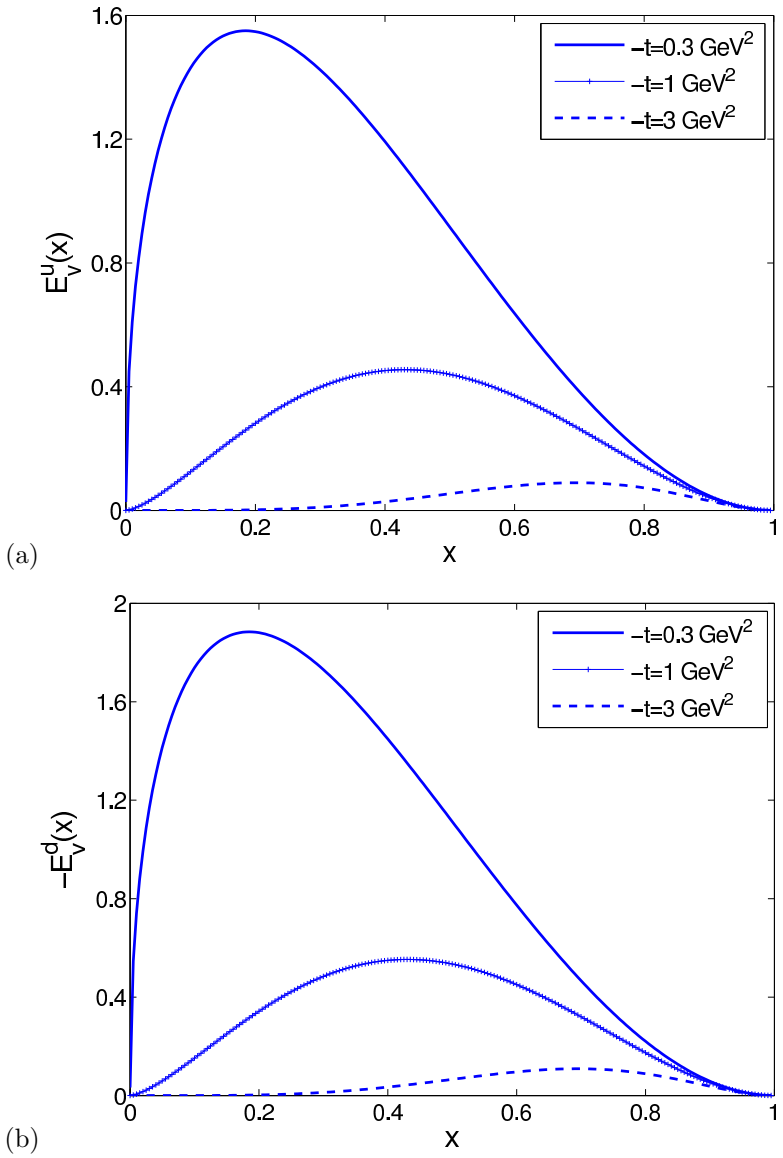

Figure 3: Plots of (a) $H^u(x,t)$ vs x for fixed values of $-t$. (b) same as in (a) but for d quark.

compare and contrast the GPDs from these two models.

In Fig. 6 we have compared the impact parameter dependent proton GPD $H(x,b)$ from AdS/QCD with the model mentioned above, for both u and d quarks. The GPDs are fatter in the AdS/QCD compared to the model when plotted against x, while in the impact parameter space they look almost same except the difference in the magnitudes. In Fig. 7 we have compared the two models for the proton GPD $E(x,b)$. The behavior in x for u quark is quite different in the two models while they agree better for d quark and again the GPDs from AdS/QCD are fatter compared to the other model. In the model, the behavior of $E(x,b)$ for u and d quarks is quite different when plotted against x for fixed values of impact parameter b whereas in the AdS/QCD, it shows almost same behavior for both u and d quarks. As a result, the GPD E in both models agrees better in impact parameter space for the d quark than for the u quark. It is interesting to note that in both cases, at small values of impact parameter b, the the GPD $H(x,b)$ is larger for u quark than for d quark whereas the

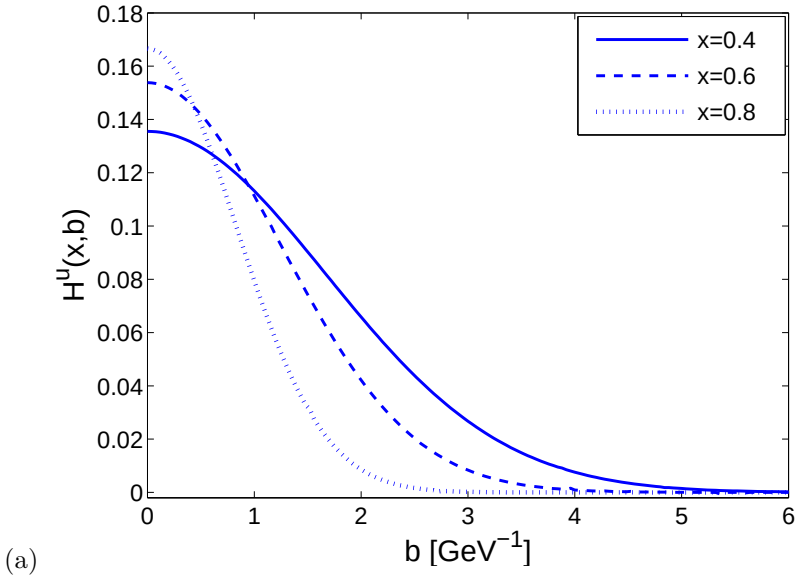

(a)

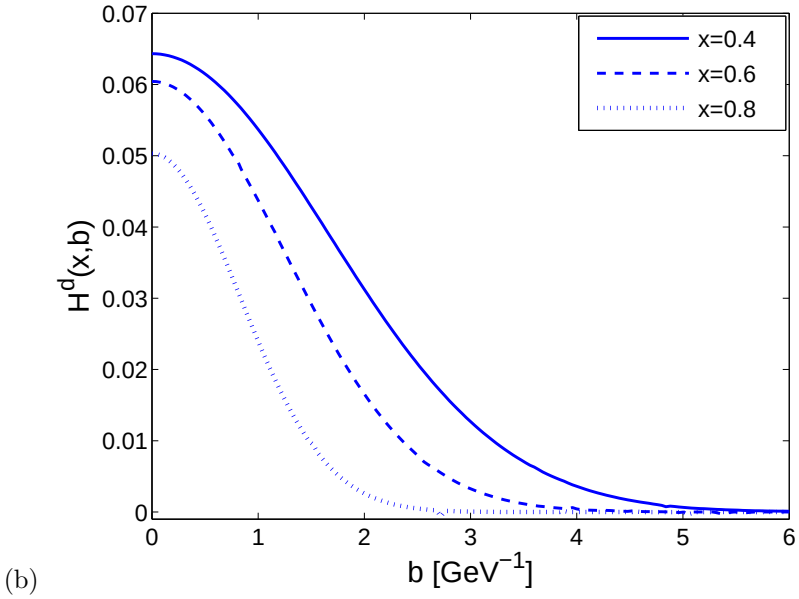

(b)

Figure 4: Plots of (a) $H^u(x,t)$ vs b for fixed values of x. (b) same as in (a) but for d quark.

magnitude of the GPD $E(x,b)$ is marginally larger for d quark than the same for u quark and thus it is interesting to check with other models whether this is a model independent result.

4 Conclusions

The main results of this work are the GPDs calculated in a quark model with SU(6) spin-flavor symmetry in AdS/QCD. The light front wave functions for the nucleons are evaluated from AdS/QCD. The parameter κ in the model is fixed by fitting the experimental data on proton form factors. The Pauli form factors require non-minimal electromagnetic coupling and are fitted to their static values. It was shown [11] that the electromagnetic form factors for proton and neutron calculated by using the

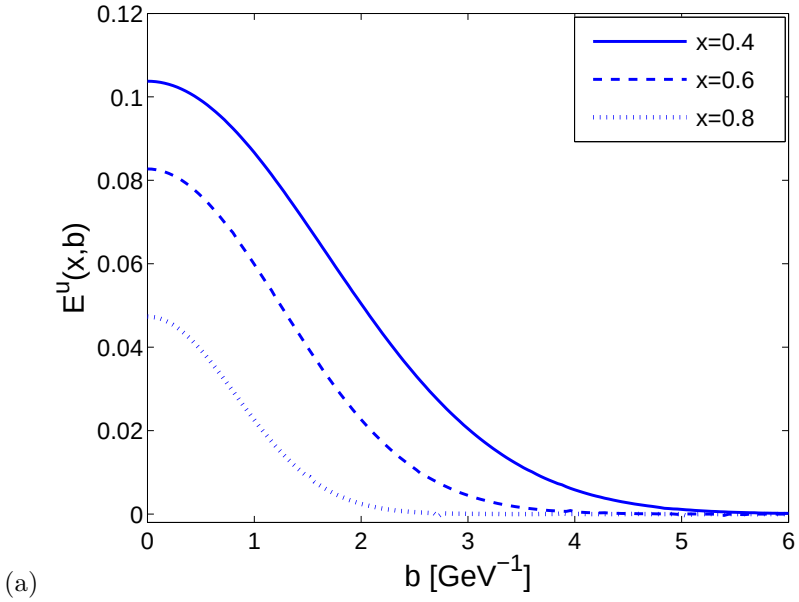

(a)

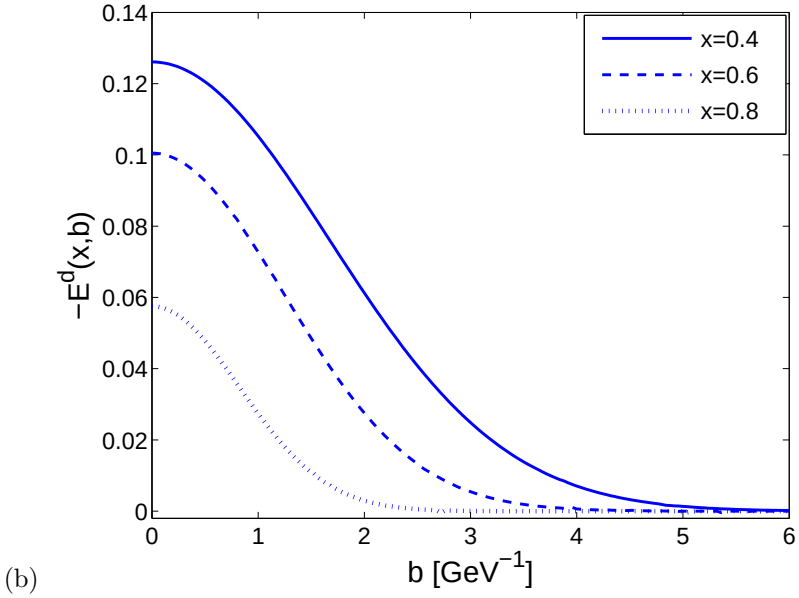

(b)

Figure 5: Plots of (a) $E^u(x,t)$ vs b for fixed values of x. (b) same as in (a) but for d quark.

AdS/QCD wave functions fit well with the experimental results. The Dirac and Pauli form factors for the nucleons are given by the first moments of the GPDs weighted with proper charge factors. Using these sum rules for the GPDs and exploiting the integral representation of the bulk-to-boundary propagator in AdS space we evaluate the GPDs for both up and down quarks. The Fourier transform of the GPDs with respect to the transverse momentum transferred give the GPDs in the impact parameter space. Though the GPDs don't have any density interpretation, the impact parameter dependent GPDs for zero skewness are positive definite and related with the charge and magnetization densities of the nucleons. We have compare the impact parameter dependent GPDs in the model with the GPDs obtained from a phenomenological model. It is found that the GPDs from AdS/QCD are fatter than the other model when compared the behaviors in x space for both u and d quarks. In

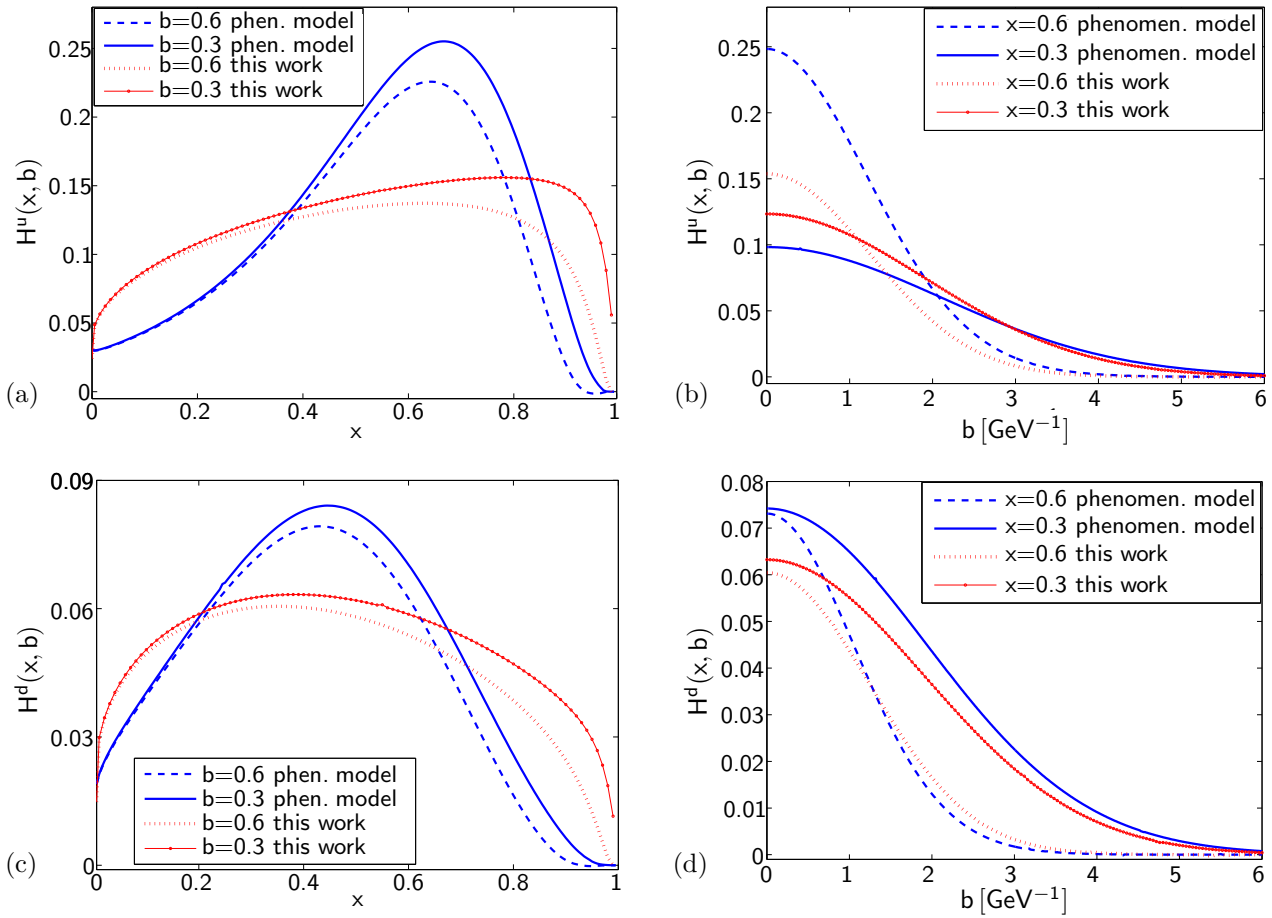

Figure 6: Plots of (a) $H^u(x,b)$ vs x for fixed values of $b = |b_\perp|$. (b) $H^u(x,b)$ vs b for fixed values of x. (c) same as in (a) but for d quark and (d) same as in (b) but for d quark.

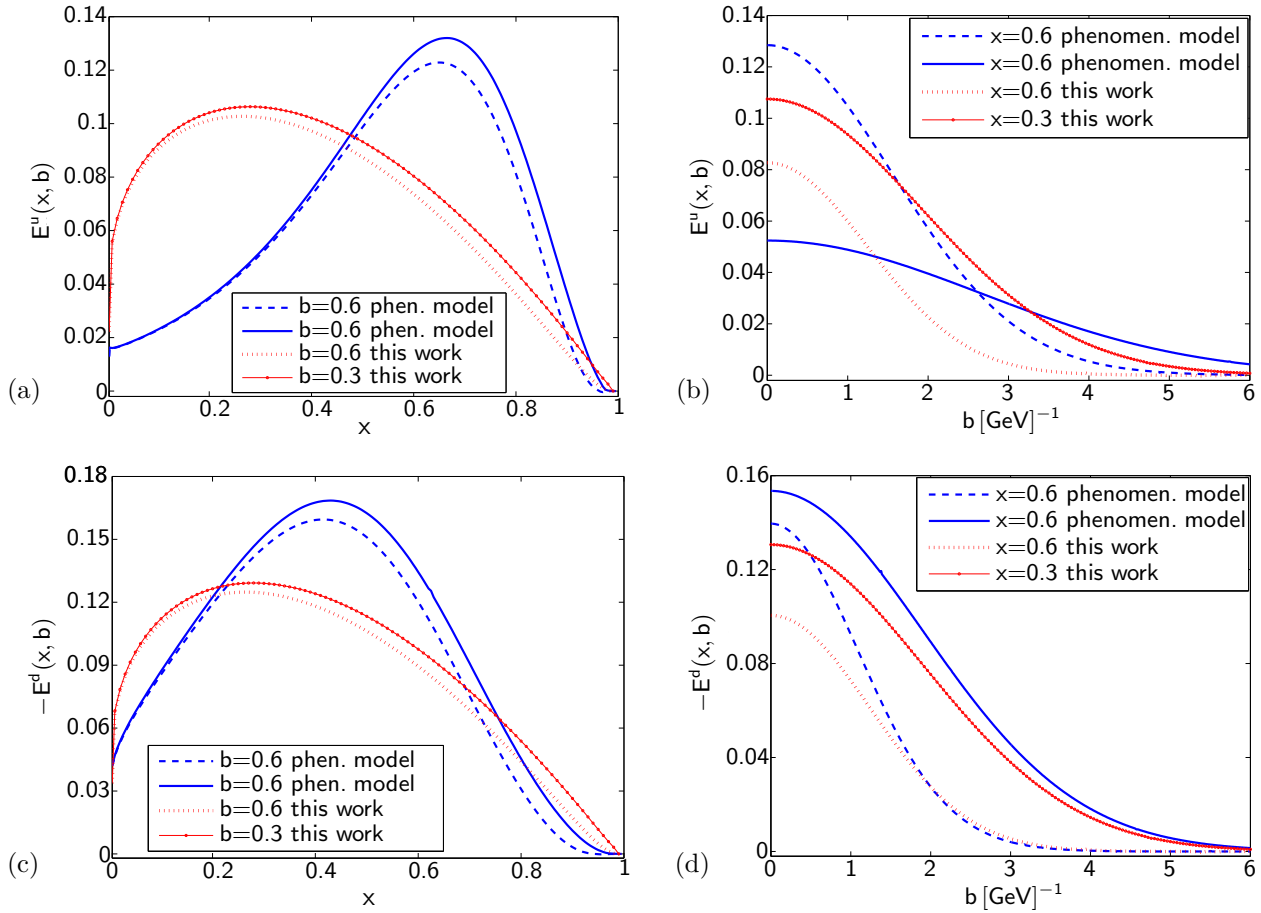

Figure 7: Plots of (a) $E^u(x,b)$ vs x for fixed values of $b = |b_\perp|$. (b) $E^u(x,b)$ vs b for fixed values of x. (c) same as in (a) but for d quark and (d) same as in (b) but for d quark.

the AdS/QCD we have only valence GPDs and as we expect that major contributions to proton GPDs should come from valence quarks, it is interesting to note that their behaviors in impact parameter space are quite similar to the phenomenological model for GPDs.

References

[1] For reviews on generalized parton distributions and DVCS, see M. Diehl, Phys. Rept. **388**, 41 (2003); A. V. Belitsky and A. V. Radyushkin, *ibid.* **418**, 1 (2005); K. Goeke, M. V. Polyakov and M. Vanderhaeghen, Progr. Part. Nucl. Phys. **47**, 401 (2001).

[2] M. Burkardt, Int. J. Mod. Phys. A **18**, 173 (2003).

[3] X. Ji, Phys. Rev. Lett. **78**, 610 (1997).

[4] C. Adloff *et al.* (H1 Collaboration), Eur. Phys. J. C **13**, 371 (2000); C. Adloff *et al.* (H1 Collaboration), Phys. Lett. B **517**, 47 (2001); N. d'Hose, E. Burtin, P. A. M. Guichon and J. Marroncle (COMPASS Collaboration), Eur. Phys. J. A **19**, Suppl. 1, 47 (2004); J. Breitweg *et al.* (ZEUS Collaboration), Eur. Phy. J. C **6**, 603 (1999); S. Chekanov *et al.* (ZEUS Collaboration), Phys. Lett. B **573**, 46 (2003); A. Airapetian *et al.* (HERMES Collaboration), Phys. Rev. Lett. **87**, 182001 (2001); S. Stepanyan *et al.* (CLAS Collaboration), *ibid.* **87**, 182002 (2001).

[5] J. Polchinski and M. J. Strassler, JHEP **0305**, 012 (2003).

[6] S. J. Brodsky and G. F. de Téramond, Phys. Lett. B **582**, 211 (2004); Phys. Rev. Lett. **94**, 201601 (2005); *ibid.* **96**, 201601 (2006); Phys. Rev. D **77**, 056007 (2006); Phys. Rev. Lett. **102**, 081601(2009).

[7] H. Forkel, M. Beyer and T. Frederico, Int. J. Mod. Phys. E **16**, 2794 (2007); W. de Paula, T. Frederico, H. Forkel and M. Beyer, Phys. Rev. D **79**, 75019 (2009).

[8] A. Vega, I. Schmidt, T. Branz, T. Gutsche and V. E. Lyubovitskij, Phys. Rev. D **80**, 055014 (2009).

[9] S. J. Brodsky and G. F. de Téramond, Phys. Rev. D **77**, 056007 (2008); *ibid.* **78**, 025032 (2008); *ibid.* **83**, 036011(2011); *ibid.* **85**, 096004 (2012).

[10] Z. Abidin and C. E. Carlson, Phys. Rev. D **77**, 095007(2008); *ibid.* **77**, 115021(2008); *ibid.* **79**, 115003 (2009).

[11] S. J. Brodsky and G. F. de Téramond, arXiv:1203.4125 [hep-ph] (2012).

[12] J. R. Forshaw and R. Sandapen, Phys. Rev. Lett. **109**, 081601 (2012).

[13] T. Gutsche, V. E. Lyubovitskij, I. Schmidt and A. Vega, Phys. Rev. D **86**, 036007 (2012).

[14] A. Vega, I. Schimdt, T. Gutsche and V. E. Lyubovitskij, Phys. Rev. D **83**, 036001 (2011); *ibid.* **85**, 096004 (2012).

[15] D. Chakrabarti and C. Mondal, arXiv:1307.5128 [hep-ph] (2013).

[16] D. Chakrabarti and C. Mondal, arXiv:1307.7995 [hep-ph] (2013).

[17] M. Diehl, T. Feldman, R. Jacob and P. Kroll, Eur. Phys. J. C **39**, 1 (2005).

[18] H. R. Grigoryan and A. V. Radyushkin, Phys. Rev. D **76**, 095007 (2007).

[19] O. Gayou *et al.*, Phys. Rev. C **64**, 038202 (2001).

[20] O. Gayou *et al.*, Phys. Rev. Lett. **88**, 092301 (2002).

[21] V. Punjabi *et al.*, Phys. Rev. C **71**, 055202 (2005).

[22] J. Arrington, W. Melnitchouk and J. A. Tjon, Phys. Rev. C **76**, 03205 (2007).

[23] M. Burkardt, Phys. Rev. **D 72**, 094020 (2005).

[24] S. Ahmad, H. Honkanen, S. Liuti and S. Taneja, Phys. Rev. D **75**, 094003 (2007).

[25] D. Chakrabarti, R. Manohar and A. Mukherjee, Phys. Lett. B **682**, 428 (2010).

Nonperturbative Calculations in the Light-Front Field Theory

V. A. Karmanov

Lebedev Physical Institute, Leninsky Prospect 53, 119991 Moscow, Russia

Abstract

A nonperturbative approach to field theory based on the decomposition of the state vector in Fock components, and on the covariant formulation of light-front dynamics, together with the Fock sector dependent renormalization scheme, is briefly reviewed. The approach is applied to the calculation, in the framework of three-body Fock space truncation, of the fermion electromagnetic form factors in the Yukawa model (in particular, of anomalous magnetic moment). Once the renormalization conditions are properly taken into account, the anomalous magnetic moment does not depend on the regularization scale when the latter is much larger than the physical masses.

Keywords: *Light-front dynamics; Yukawa model; non-perturbative renormalization; electromagnetic form factors*

1 Introduction

In the quantum field theory, due to the particle creation and annihilation, the number of particles in a system is not fixed and the state vector is a superposition of the states (Fock sectors) with different numbers of particles:

$$|p\rangle = \sum_{n=1}^{\infty} \int \psi_n(k_1, \ldots, k_n, p)\, |n\rangle\, D_k. \tag{1}$$

ψ_n is the n-body wave function and D_k is an integration measure. In the cases when we can expect that the decomposition (1) converges rapidly enough, we can make truncation, that is replace the infinite sum in (1) by a finite one. Then, substituting the truncated state vector in the eigenvector equation

$$H\,|p\rangle = M\,|p\rangle,$$

we obtain a system of integral equations of finite dimension for the Fock components ψ_n which can be solved numerically. With the decomposition (1), the normalization condition for the state vector $\langle p'|p\rangle = 2\,p_0\,\delta^{(3)}(\mathbf{p}' - \mathbf{p})$ writes as

$$\sum_{n}^{\infty} I_n = 1, \tag{2}$$

where I_n is the contribution of the n-body Fock sector to the norm.

In this way we do not require the smallness of the coupling constant. The approximate (truncated) solution is non-perturbative. This is the basis of a non-perturbative approach which we developed, together with J.-F. Mathiot and A. V. Smirnov, in a series of papers [1–5] (see for review [6]).

Proceedings of International Conference 'Nuclear Theory in the Supercomputing Era — 2013' (NTSE-2013), Ames, IA, USA, May 13–17, 2013. Eds. A. M. Shirokov and A. I. Mazur. Pacific National University, Khabarovsk, Russia, 2014, p. 125.

http://www.ntse-2013.khb.ru/Proc/Karmanov.pdf.

The main difficulty on this way is to ensure cancellation of infinities. In a perturbative approach, for a renormalizable field theory, this cancellation is obtained as a by-product after renormalization in any fixed order of coupling constant. For the cancelation it is important to take into account the complete set of graphs in a given order. Omitting some of these graphs destroys the cancellation and the infinities survive after renormalization. Namely that happens after the truncation: though the truncated solution can be decomposed in infinite series in terms of the coupling constant, it does not contain the complete set of perturbative graphs in any given order. Therefore the standard renormalization scheme does not eliminate the infinities. To provide cancellation of infinities, the sector-dependent renormalization scheme has been proposed [7]. This scheme, in which the values of the counter terms are precised from sector to sector according to unambiguously formulated rules, was developed in detail in Ref. [3] and applied to calculation of electromagnetic form factors in Refs. [4, 5]. Below we will give its brief review and present some results obtained in this approach.

We discuss the convergence of the decomposition (1) in Section 2. The sector dependent renormalization scheme is briefly described in Section 3. It is applied to calculation of anomalous magnetic moment of fermion in Yukawa model. The antifermion degrees of freedom are taken into account in Section 4. The results are summarized in Section 5.

2 On convergence of the Fock decomposition

We work in the light-front dynamics (LFD) [8–10], more precisely, in its explicitly covariant version [8, 9]. In four-dimensional space, the state vector (1) is defined on the light-front plane of a general orientation $\omega\cdot x = 0$, where ω is an arbitrary four-vector restricted by the condition $\omega^2 = 0$ [8, 9]. The traditional form of LFD [10] is recovered by using $\omega = (1, 0, 0, -1)$.

As mentioned, the truncation of the Fock decomposition can be efficient if the decomposition (1) converges rapidly enough. The convergence depends, of course, on the nature of a system under consideration. If this system is dominated by a finite number of degrees of freedom (like hadrons in quark models), then the decomposition (1) is determined with a good accuracy by a finite number of the components. Notice that these "degrees of freedom", e. g., quarks as basis of decomposition (1), may be some effective dressed constituents.

The convergence of the Fock decomposition was estimated [11] in the explicitly solvable Wick–Cutkosky model [12]. This model corresponds to spineless massive particles with equal masses m interacting by spineless massless exchange. One can find the two-body Bethe–Salpeter amplitude. The requirement for the electromagnetic form factor $F(Q^2 = 0) = 1$ fixes the normalization of the Bethe–Salpeter amplitude. On the other hand, projecting the Bethe–Salpeter amplitude on the light-front plane, we find the two-body Fock component of the state vector (1). Its normalization integral is not unity but gives the two-body contribution to the full normalization. One can also estimate the valence three-body contribution. We chose the parameters maximally unfavorable for dominance of a few-body sector. Namely, the coupling constant is very strong, $\alpha = 2\pi$, that corresponds to the limiting case when the binding energy in the Wick–Cutkosky model, $E_b = -2m$, compensates the full mass of the system. The strong coupling constant increases contributions of higher orders, i. e., of many-body components. In addition, since the exchange particles are massless, they can be easy created. The result for different contributions [11] is given in Table 1.

We see that even in this unfavorable case, the Fock states with 2 and 3 particles contribute 90% to the normalization integral. This would give the 10% accuracy in calculation of observables, say, of the electromagnetic form factor.

Table 1: Contributions of the Fock sectors with the number of particles $n = 2$, $n = 3$ and $n \geq 4$ ($I_{n\geq 4} = \sum_{n=4}^{\infty} I_n$) to the full normalization integral $I = \sum_{n=2}^{\infty} I_n = 1$ of the state vector for $M = 0$ ($\alpha = 2\pi$).

I_2	I_3	$I_{n\geq 4}$	$I_2 + I_3 + I_{n\geq 4}$
0.643	0.257	0.100	1

3 Fock sector dependent renormalization scheme

We will find the state vector of the Yukawa model Hamiltonian containing the fermion field ψ and the scalar field ϕ with the interaction vertex $g_0\bar{\psi}\psi\phi$. For regularization, we include in the Hamiltonian the Pauli–Villars fields (one fermion and one boson), which, after that, appear in the basis of decomposition (1). Since our formalism is explicitly covariant, the spin structure of the wave function ψ_n is easy found. It should incorporate the ω-dependent components. Therefore the spin structure of the two-body component in the Yukawa model reads:

$$\bar{u}(k_1)\,\Gamma_2 u(p) = \bar{u}(k_1)\left[b_1 + \frac{M\,\not{\omega}}{\omega\cdot p}\,b_2\right]u(p). \tag{3}$$

where $\not{\omega} = \omega_\mu\gamma^\mu$. The coefficients b_1 and b_2 are scalar functions determined by dynamics. In LFD they depend on well-known variables $k_\perp$, x: $b_{1,2} = b_{1,2}(k_\perp, x)$.

System of equations for the Fock components in the truncation $N = 3$ is graphically shown in Fig. 1. One can exclude the three-body component and obtain a reduced system of equations which includes the one- and two-body components only. It is shown in Fig. 2. In comparison to the equations of Fig. 1, we included in the equations of Fig. 2 another counter term Z_ω discussed below in this section. Namely this reduced system of eight equations for two two-body spin components, for physical and Pauli–Villars fermions and bosons ($2 \times 2 \times 2 = 8$), was solved numerically. It contains also a one-body component Γ_1, but it is a constant which can be found from the normalization condition. The limit of the fermion Pauli–Villars mass $m_1 \to \infty$ was taken analytically, whereas the limit of the boson Pauli–Villars mass $\mu_1 \to \infty$ was taken numerically.

The renormalization condition, as always, means that one should express the bare coupling constant g_0 and the fermion mass counter term δm via the physical coupling

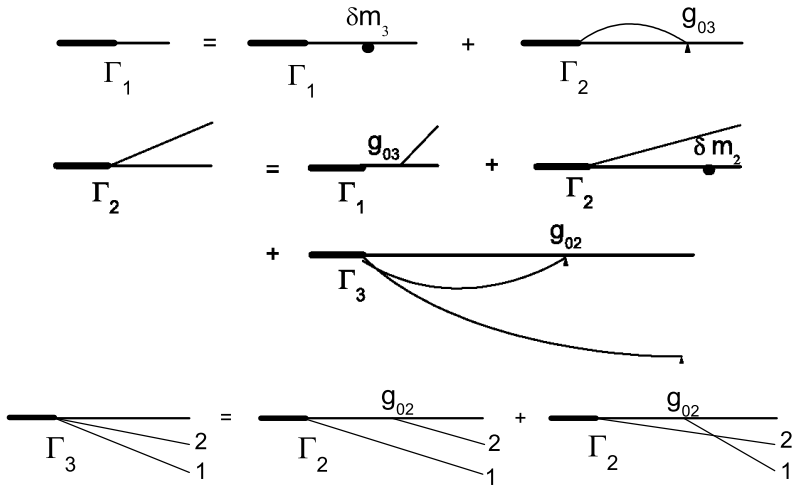

Figure 1: System of equations for the Fock components in the truncation $N = 3$.

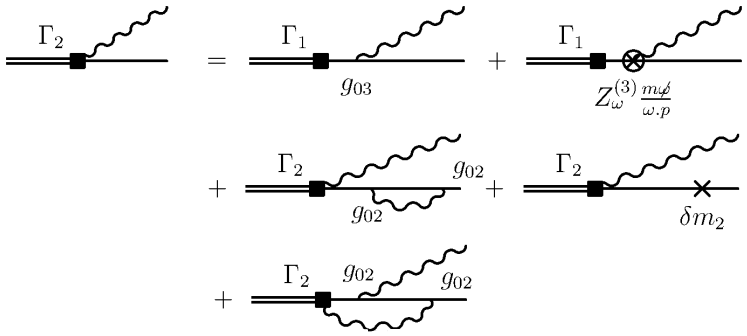

Figure 2: Equation for the two-body component.

constant and mass. In perturbation theory, as mentioned, this leads, as a by-product, to cancellation of infinities. In the non-perturbative approach the strategy is, in principle, the same, however, because of truncation, the infinities are not cancelled. Therefore we use the sector-dependent renormalization scheme [3]. The fermion mass counter term δm, and the bare coupling constant g_0, are thus extended to a sequence:

$$g_0 \rightarrow g_{0l}, \tag{4}$$

$$\delta m \rightarrow \delta m_l, \tag{5}$$

The index l runs through the Fock sectors with $l = 1, 2, ..., N$. The quantities g_{0l} and δm_l are calculated by solving the systems of equations for the vertex functions in the $N = 1$, $N = 2$, $N = 3$, ... approximations successively. That is, we start with the first non-trivial case $N = 2$ and find g_{02}, δm_2. In the case $N = 3$, the parameters g_0, δm_0 may appear in two ways. Namely: (*i*) Via the two-body sector which enters the three-body equations, as it happens, for example, in the last line in Fig. 1. In this case we use for them already found values of g_{02} and δm_2. (*ii*) Via the one-body sector which also enters the three-body equations, as it happens, for example, in the first line in Fig. 1. Then these parameters are the new ones: g_{03}, δm_3, which did not appear in the previous $N = 2$ truncation. They are found from the renormalization conditions in the three-body sector. This procedure continues for increasing N. As an example, system of equations for the next $N = 4$ truncation is shown in Fig. 3.

The renormalization condition for the coupling constant g_0 is a relation between the two-body components Γ_2 (containing g_0) and the physical coupling constant g. In order to fix this relationship, one needs to take into account the normalization factors of the external legs of the two-body vertex function. These normalization factors do

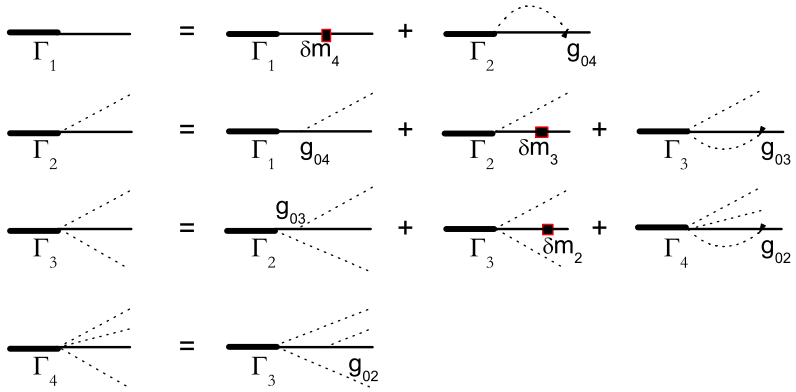

Figure 3: System of equations for the Fock components in the truncation $N = 4$.

also depend on the order of truncation of the Fock space. In the Yukawa model, this relationship reads [6]:

$$\Gamma_2^{(N)}(s_2 = M^2) = g\sqrt{I_1^{(N-1)}}. \tag{6}$$

Here $\Gamma_2^{(N)}$ is the two-body Fock component found in the truncation N whereas $I_1^{(N-1)}$ is the one-body normalization integral (for the fermion state) calculated in the previous $N-1$ truncation. We omit the corresponding boson factor since we do not consider here fermion loops and the boson self-energy (quenched approximation).

The condition (6) has an important consequence: the two-body vertex function, depending according to Eq. (3) on ω, at the value $s_2 = M^2$ should be independent of the orientation ω of the light-front plane. With the spin decomposition (3), this implies that the component b_2 at $s_2 = M^2$ should be identically zero:

$$b_2^{(N)}(s_2 = M^2) \equiv 0. \tag{7}$$

If Eq. (7) is satisfied, Eq. (6), in the quenched approximation, turns into

$$b_1^{(N)}(s_2 = M^2) \equiv g\sqrt{I_1^{(N-1)}}. \tag{8}$$

While the property (7) is automatically fulfilled in the case of the two-body Fock space truncation provided one uses a rotationally invariant regularization scheme [6], this is not guaranteed for higher order truncations. The ω-dependence of the off-shell vertex Γ_2, Eq. (3), is allowed even for the exact solution, but it must completely disappear on the energy shell. Because of approximations, the latter does not happen automatically.

Another consequence of the truncation of the Fock space is the fact that the components $b_{1,2}(s_2 = M^2)$ are not constants. Indeed, $b_{1,2}$ depend on two kinematical variables $k_\perp, x$. The on-shell condition

$$s_2 \equiv \frac{k_\perp^2 + m^2}{1-x} + \frac{k_\perp^2 + \mu^2}{x} = M^2 \tag{9}$$

can be used to fix one of the two variables, say $k_\perp$, in the non-physical domain (for $M = m$):

$$k_\perp = k_\perp^*(x) \equiv i\sqrt{x^2 m^2 + (1-x)\mu^2}, \tag{10}$$

so that $b_{1,2}(s_2 = M^2) \equiv b_{1,2}(k_\perp^*(x), x)$ depends on x, whereas the conditions (7) and (8) should be valid identically, i. e. for any value of x.

In order to enforce the condition (7), we introduce an appropriate counterterm which depends explicitly on the four-vector ω. It is shown by cross in the first line of Fig. 2. It originates from the following additional term introduced in the interaction Hamiltonian:

$$\delta H_\omega^{int} = -Z_\omega \bar{\psi}' \frac{m \not{\omega}}{i\omega\cdot\partial} \psi' \varphi', \tag{11}$$

where Z_ω is just the new counterterm, $\psi'(\varphi')$ is the fermion (scalar boson) field being a sum of the corresponding physical and Pauli–Villars components: $\psi' = \psi + \psi_{PV}$ and similarly for φ'; $1/(i\omega\cdot\partial)$ is the reversal derivative operator. The enforcement of the condition (7) for any x by an appropriate choice of the counterterm Z_ω implies that Z_ω should *a priori* depend on x, i. e. $Z_\omega = Z_\omega(x)$. It induces also an unique dependence of $g_{0N} = g_{0N}(x)$ as a function of the kinematical variable x.

The fact that, in order to satisfy the renormalization conditions, the bare parameters must depend on the kinematical variable x, is crucial to obtain results which are finite after the renormalization procedure in the truncated Fock space. The stability of our results relative to the value of the regularization scale, if the latter reasonably exceeds the physical masses, is confirmed numerically with high precision (see Fig. 4 below).

At first glance, the x-dependence of the bare parameters seems unusual. However, it is a natural consequence of the truncation. Of course, the bare parameters in the fundamental non-truncated Hamiltonian are true constants. After truncation, the initial Hamiltonian is replaced by a finite matrix which acts now in a finite Fock space. But it turns out that the modification of the Hamiltonian is not restricted to a simple truncation. Indeed, to preserve the renormalization conditions, the bare parameters in this *finite* matrix become x-dependent. This x-dependence cannot be derived from the initial Hamiltonian. It appears only after the Fock space truncation.

Our truncated Hamiltonian with the x-dependent bare parameters is a self-consistent approximation to the initial fundamental Hamiltonian. One expects that the approximation becomes better when the number of Fock components increases. At the same time, the x-dependence of the bare parameters should become weaker. An indication of this behavior, when one adds the antifermion contribution, is found in Ref. [5] and is demonstrated below in Section 4. We emphasize that there is no any ambiguity in finding the bare parameters, in spite of their x-dependence. These functions of x are completely fixed by the renormalization conditions.

Using this scheme, in the three-body truncation (up to 1 fermion + 2 bosons), we calculated [4, 5] the fermion electromagnetic form factors $F_1(Q^2)$ and $F_2(Q^2)$. In all computations, we used the physical particle masses $m = 0.938$ and $\mu = 0.138$ reflecting the characteristic nuclear physics mass scales. Each physical quantity was calculated for three values of the physical coupling constant $\alpha = g^2/4\pi = 0.5$, 0.8, and 1.0.

The value $F_2(0)$ is the anomalous magnetic moment (AMM). It is shown in Fig. 4 as a function of the Pauli–Villars boson mass μ_1. Each of the two- and three-body Fock sector contributions to the AMM essentially depends on μ_1, while their sum is stable as μ_1 becomes large enough. Note that using x-dependent bare parameters removes μ_1-dependence of the AMM observed in Ref. [4] already for $\alpha \sim 0.5$, even for larger coupling constants.

As it was explained, we took the limit $m_1 \to \infty$ analytically and then the limit of large μ_1 numerically. For a test of stability of our calculations, we compare in Table 2 the numerical results for AMM obtained in two different orders of limits of large Pauli–Villars masses. The AMM is considered as a function of the Pauli–Villars mass which is kept finite (m_1, if the limit $\mu_1 \to \infty$ has been taken, and vice versa). For convenience of the comparison, we took the same sets of finite mass values for Pauli–Villars boson and fermion.

If each of the finite Pauli–Villars masses is much larger than all physical masses, the values of the AMM, obtained in both limits, coincide within the computational accuracy (about 0.2%), as it should be if the renormalization procedure works properly. We can thus choose any convenient order of the infinite Pauli–Villars mass limits. Since the equations for the Fock components are technically simpler in the

Table 2: The anomalous magnetic moment calculated for $\alpha = 0.8$ in the two different limits of the Pauli–Villars masses.

Pauli–Villars mass kept finite (μ_1 or m_1)	AMM when $m_1 \to \infty$	AMM when $\mu_1 \to \infty$
5	0.1549	0.1454
10	0.1641	0.1630
25	0.1690	0.1704
50	0.1702	0.1715
100	0.1706	0.1716
250	0.1708	0.1714
500	0.1709	0.1713

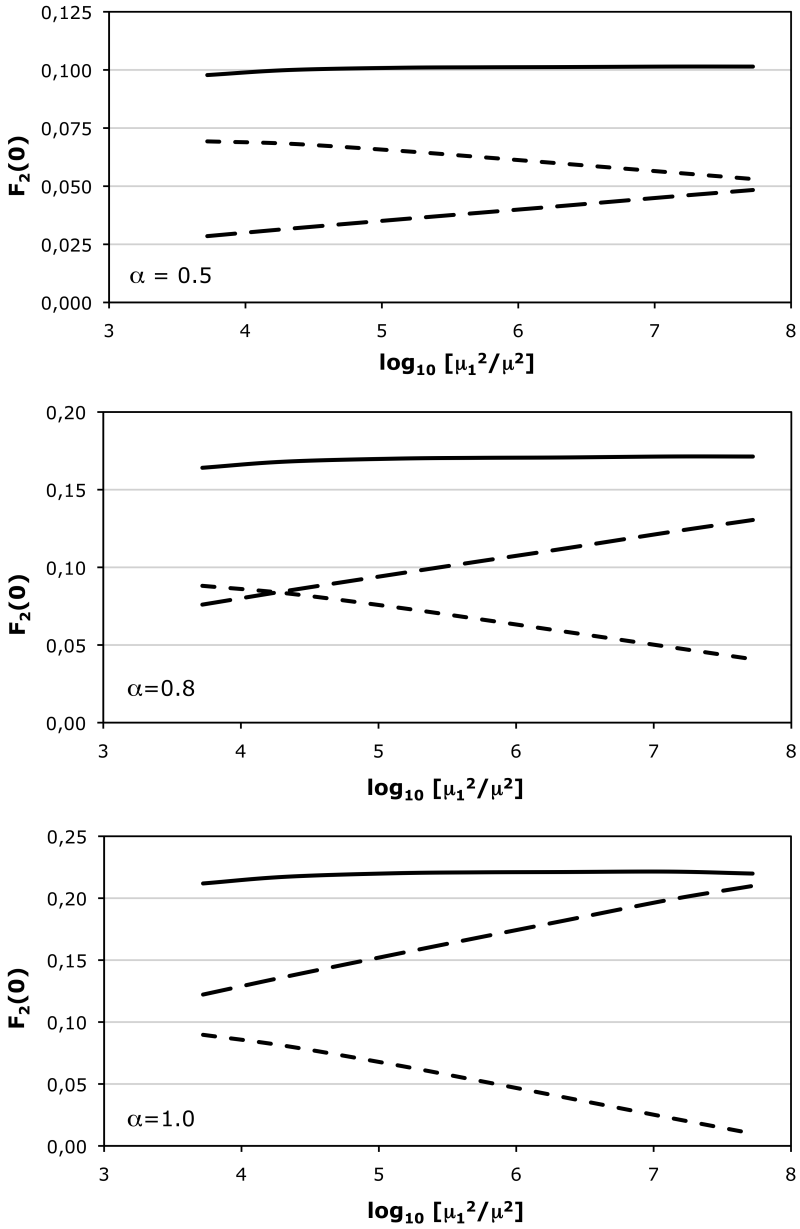

Figure 4: The anomalous magnetic moment in the Yukawa model as a function of the Pauli–Villars mass μ_1, for three different values of the coupling constant, $\alpha = 0.5$ (upper plot), 0.8 (middle plot) and $\alpha = 1.0$ (lower plot). The dashed and long-dashed lines are, respectively, the two- and three-body contributions, while the solid line is the total result.

limit $m_1 \to \infty$, we continue to work with the vertex functions and the electromagnetic vertex taken in this limit. The independence of physical results of the order in which the infinite Pauli–Villars mass limit is taken and, hence, on the way we use to get rid of the bare parameters, is a strong evidence of the self-consistency of our renormalization scheme.

The AMM of electron was calculated non-perturbatively, in the $N = 2$ truncation and with the oscillator basis, in Ref. [13] (see Ref. [14] for the review).

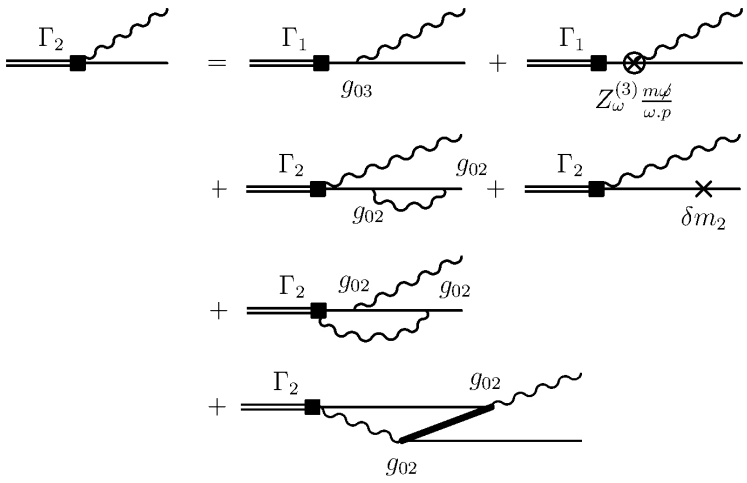

Figure 5: Graphical representation of the equation for the two-body vertex function including the contribution of antifermion d.o.f. in the quenched approximation.

4 Antifermion degrees of freedom

We extend the Fock decomposition of the fermion state vector by introducing the antifermion d.o.f. In the lowest (also three-body) approximation this corresponds to adding the $ff\bar{f}$ Fock sector to those previously introduced (f, fb, and fbb). In the three-body approximation, this new Fock component is easily expressed through the two-body component, as the fbb one. As a result, we obtain a closed (matrix) equation for the two-body vertex function, as given, in the quenched approximation, by Fig. 5. It differs from the equation in the $f + fb + fbb$ approximation, shown in Fig. 2, by an additional term on the right-hand side (the last diagram in Fig. 5).

It turns out that the antifermion contribution makes a week influence on values of form factors, but these values are now obtained with the parameters $g_{03}(x), Z_\omega(x)$ which are much more flat functions of x than without the antifermion.

In Figs. 6 and 7 these bare parameters are shown as a function of x, each for $\alpha = 0.5$, 0.8, and 1.0, at a typical value $\mu_1 = 100$. In Fig. 6 the relative value of g'_{03} with respect to its mean value $\bar{g}'_{03}$ over the interval $0 \le x \le 1$ is shown, i. e. we plot the quantity

$$\delta g'_{03}(x) = [g'_{03}(x) - \bar{g}'_{03}]/\bar{g}'_{03},$$

where $\bar{g}'_{03} = \int_0^1 g'_{03}(x)\,dx$. The "prime" indicates that $g'_{03}(x)$ and $Z'_\omega(x)$ include some factors precised in Ref. [5]. For comparison, we show also in these plots the same functions calculated without antifermion contributions. The most interesting fact is that the function $g'_{03}(x)$, which exhibits strong x-dependence in the $f + fb + fbb$ approximation, becomes almost a constant if the $ff\bar{f}$ Fock sector is included. Concerning the function $Z'_\omega(x)$, it shows a similar tendency as well, with a bit stronger x-dependency than $g'_{03}(x)$. In addition, the magnitude of $Z'_\omega(x)$ is reasonably smaller than that calculated in the $f + fb + fbb$ truncated Fock space.

5 Conclusion

We have developed a non-perturbative approach to field theory based on the Fock decomposition and its truncation. It includes also the non-perturbative renormalization. The approach is applied to calculations of electromagnetic form factors in the Yukawa model. Truncating the Fock space up to the three-body sector fbb and then including $ff\bar{f}$, we calculated anomalous magnetic moment of fermion. It is rather

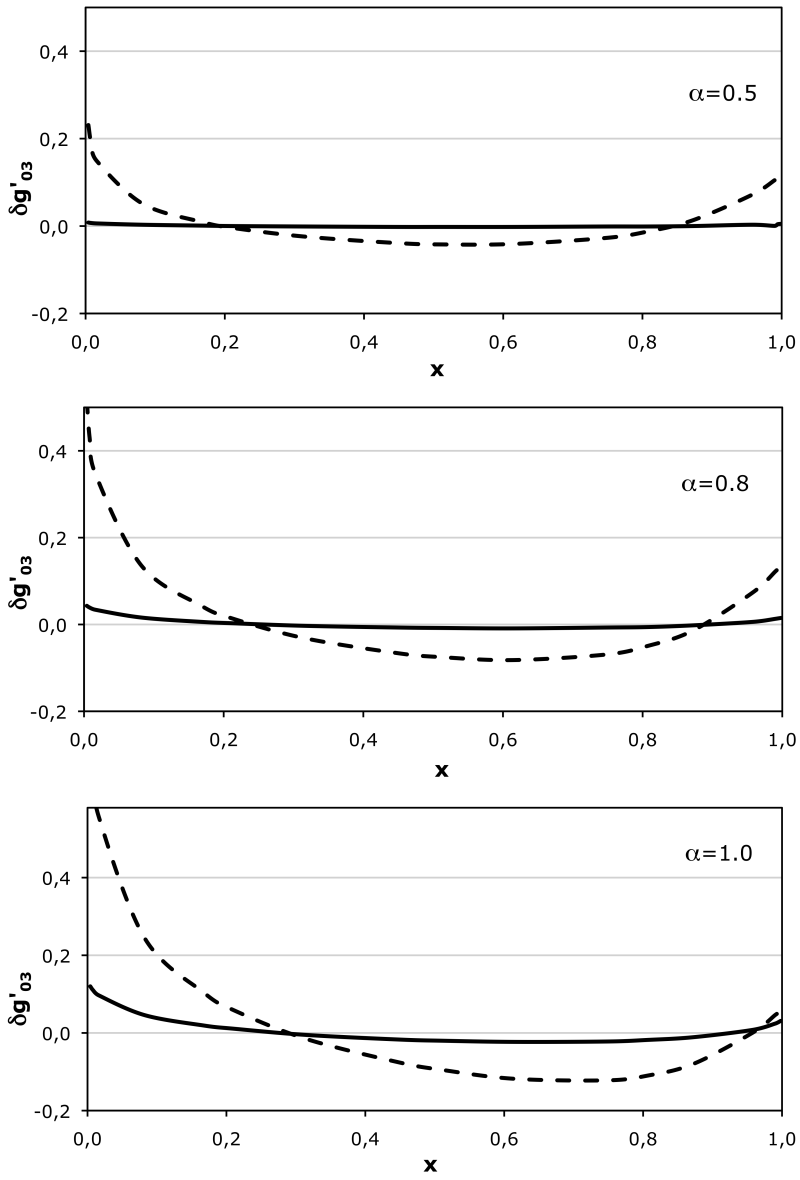

Figure 6: x-dependence of the bare coupling constant g'_{03} calculated for $\mu_1 = 100$ relatively to its mean value over the interval $x \in [0, 1]$ for $\alpha = 0.5$ (upper plot), $\alpha = 0.8$ (middle plot) and $\alpha = 1.0$ (lower plot). The solid (dashed) lines correspond to the results obtained with (without) the $ff\bar{f}$ Fock sector contribution.

stable relative to the increase of the regulator — the Pauli–Villars meson mass μ_1, that indicates that in this way we find the convergent results. Due to the truncation, the bare parameters in the truncated Hamiltonian depend on the kinematical variable x. This dependence becomes weaker when the $ff\bar{f}$ sector is included.

The numerical results for the $N = 3$ truncation presented above were obtained by a laptop. In order to go further, one should certainly use supercomputers which open wide perspectives for the non-perturbative calculations in the field theory. This can make an alternative to the lattice calculations. For a review of this field, applications to the light-front Hamiltonian dynamics and the results of *ab initio* calculations in nuclear physics see Refs. [14, 15]. It would be very important, as the next step, to carry out calculations for the four-body truncation (to solve the equations shown in

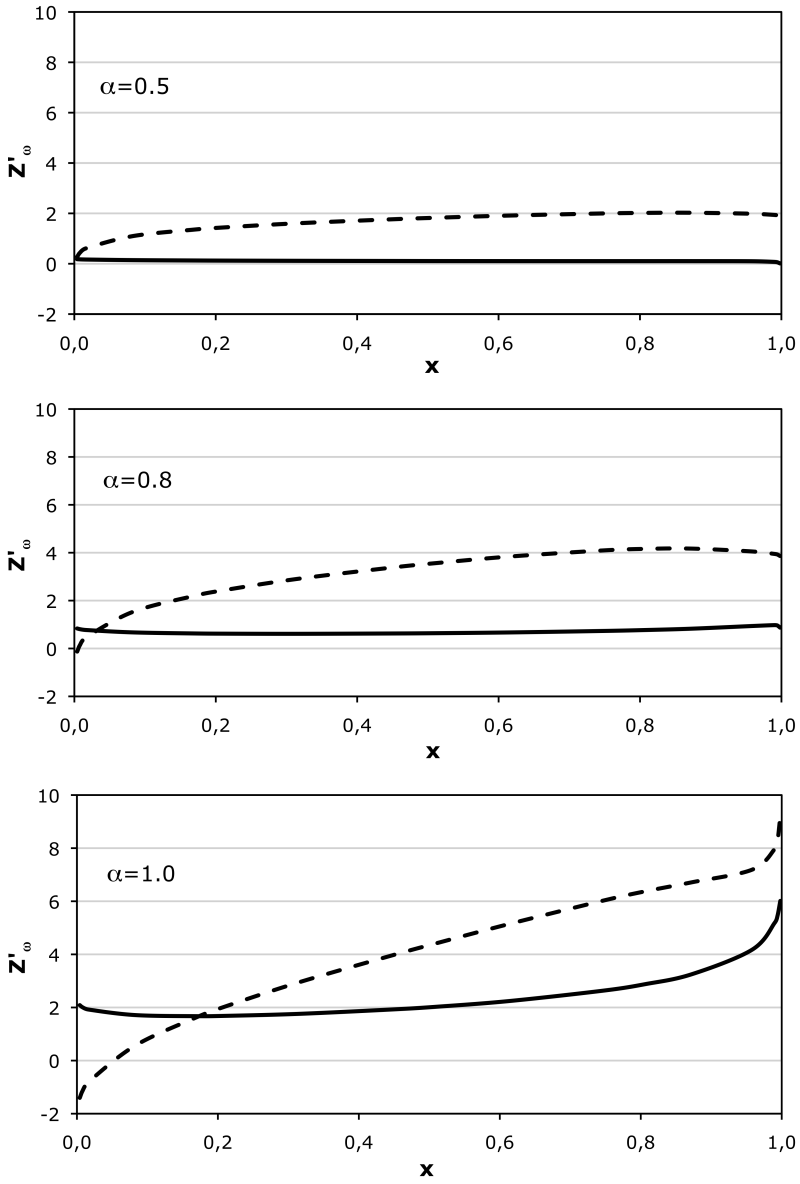

Figure 7: The same as Fig. 6 but for the x-dependence of the counterterm Z'_ω.

Fig. 3) in order to check a possible convergence relative to the number of incorporated Fock sectors. From the Yukawa model which serves as a testing area for development of methods, one should go over to a realistic field theory.

References

[1] V. A. Karmanov, J.-F. Mathiot and A. V. Smirnov, Phys. Rev. D **69**, 045009 (2004).

[2] V. A. Karmanov, J.-F. Mathiot and A. V. Smirnov, Phys. Rev. D **75**, 045012 (2007).

[3] V. A. Karmanov, J.-F. Mathiot and A. V. Smirnov, Phys. Rev. D **77**, 085028 (2008).

[4] V. A. Karmanov, J.-F. Mathiot and A. V. Smirnov, Phys. Rev. D **82**, 056010 (2010).

[5] V. A. Karmanov, J.-F. Mathiot and A. V. Smirnov, Phys. Rev. D **86**, 085006 (2012).

[6] J.-F. Mathiot, A. V. Smirnov, N. A. Tsirova and V. A. Karmanov, Few-Body Syst. **49**, 183 (2011).

[7] R. J. Perry, A. Harindranath and K. G. Wilson, Phys. Rev. Lett. **65**, 2959 (1990).

[8] V. A. Karmanov, Zh. Eksp. Teor. Fiz. **71**, 399 (1976) [Sov. Phys. JETP **44**, 210 (1976)].

[9] J. Carbonell, B. Desplanques, V. A. Karmanov and J.-F. Mathiot, Phys. Rept. **300**, 215 (1998).

[10] S. J. Brodsky, H. Pauli and S. S. Pinsky, Phys. Rept. **301**, 299 (1998).

[11] Dae Sung Hwang and V. A. Karmanov, Nucl. Phys. B **696**, 413 (2004).

[12] G. C. Wick, Phys. Rev. **96**, 1124 (1954); R. E. Cutkosky, *ibid.* **96**, 1135 (1954).

[13] X. Zhao, H. Honkanen, P. Maris, J. P. Vary and S. J. Brodsky, Few-Body Syst. **52**, 339 (2012).

[14] J. P. Vary, Few-Body Syst. **52**, 331 (2012).

[15] J. P. Vary, *Computational Nuclear Physics: Key to Discovery Opportunities*, Distinguished Lecture at NTSE-2013, *see these Proceedings*, p. 15, http://www.ntse-2013.khb.ru/Proc/JPVary.pdf.

Introduction to Basis Light-Front Quantization Approach to QCD Bound State Problems

Yang Li, Paul W. Wiecki, Xingbo Zhao, Pieter Maris and James P. Vary

Department of Physics and Astronomy, Iowa State University, Ames, IA 50011

Abstract

Basis Light-Front Quantized Field Theory (BLFQ) is an *ab initio* Hamiltonian approach that adopts light-cone gauge, light-front quantization and state-of-the-art many-body methods to solve non-perturbative quantum field theory problems. By a suitable choice of basis, BLFQ retains the underlying symmetries to the extent allowed within light-front coordinates. In this talk, we outline the scheme for applying BLFQ to QCD bound state problems. We adopt a 2D harmonic oscillator with 1D plane wave basis that corresponds to the AdS/QCD soft-wall solution. Exact treatment of the symmetries will be discussed.

Keywords: *Light-front; harmonic oscillator basis; QCD; non-perturbative; symmetry*

1 Introduction

Solving bound state problems arising in quantum chromodynamics (QCD) is the key to understand a series of important questions in physics. The solutions will provide consistent descriptions of the structure of mesons, baryons and also particles with "exotic" quanta beyond the scope of the constituent quark model. One salient challenge is to predict the spin content of the baryons. Furthermore, it could also help to explain the nature of confinement and dynamical chiral symmetry breaking. QCD bound states are strong coupling non-perturbative solutions that cannot be generated from perturbation theory. Among various non-perturbative methods, light-front Hamiltonian quantization within a basis function approach has shown significant promise by capitalizing on both the advantages of light-front dynamics as well as the recent theoretical and computational achievements in quantum many-body theory. We begin with an overview of the light-front quantum field theory. We will then introduce the Basis Light-Front Quantized Field Theory (BLFQ) and its application to bound state problems in quantum field theory.

2 Light-front quantum field theory

The idea of quantization on a light-front surface was first considered by Paul Dirac in 1949 in his famous investigation of forms of relativistic dynamics [1]. Light-front quantum field theory is quantized on a light-front plane $x^+ \equiv x^0 + x^3 = 0$ and evolves according to light-front time x^+. It is convenient to define light-front variables $x^\pm = x^0 \pm x^3$, $\boldsymbol{x}^\perp = (x^1, x^2)$, where x^+ is the light-front time, x^- is the longitudinal coordinate. The light-front momentum $p^\pm = p^0 \pm p^3$, $\boldsymbol{p}^\perp = (p^1, p^2)$, where the p^+ is the longitudinal momentum and $p_+ = \frac{1}{2}p^-$ is the light-front energy. For

Proceedings of International Conference 'Nuclear Theory in the Supercomputing Era — 2013' (NTSE-2013), Ames, IA, USA, May 13–17, 2013. Eds. A. M. Shirokov and A. I. Mazur. Pacific National University, Khabarovsk, Russia, 2014, p. 136.

http://www.ntse-2013.khb.ru/Proc/YLi.pdf.

positive energy states, p^+ and p^- are positive. An important consequence of this is that the light-front vacuum state is trivial [2, 3].

Let $M^{\mu\nu}$, P^μ be the generators of the Poincaré symmetry. $J^k = \frac{1}{2}\epsilon^{ijk}M^{ij}$, $K^i = M^{0i}$, $(i,j,k = 1,2,3)$ are the equal-time angular momentum and boost generators respectively. The light-front rotation and boost generators are $F^- \equiv M^{12} = J^3$, $F^i \equiv \varepsilon^{ij}M^{j-} = J^i + \varepsilon^{ij}K^j$, $(i,j = 1,2)$ and $E^- \equiv \frac{1}{2}M^{+-} = K^3$, $E^i \equiv M^{+i} = K^i + \varepsilon^{ij}J^j$, $(i,j = 1,2)$. According to Dirac, in light-front dynamics the number of kinematic operators of the Poincaré algebra is maximal: $\{P^+, \boldsymbol{P}^\perp, E^-, \boldsymbol{E}^\perp, F^-\}$. The kinematic feature of the the light-front boost generators E^-, $\boldsymbol{E}^\perp$ provides convenience in evaluating matrix elements of certain experimental observables where the initial and final states differ by a boost. Note however that the total angular momentum operator is dynamic in light-front dynamics.

Irreducible representations can be identified with mutually commuting operators or compatible operators. It is customary to take the set of compatible operators as $\{P^2, W^2, P^+, \boldsymbol{P}^\perp, \mathcal{J}^3\}$, where $W^\mu = -\frac{1}{2}\varepsilon^{\mu\nu\kappa\lambda}M_{\nu\kappa}P_\lambda$ is the Pauli–Lubanski vector, $\mathcal{J}^3 \equiv \frac{W^+}{P^+} = J^3 + \varepsilon^{ij}\frac{E^iP^j}{P^+}$ is the longitudinal projection of the light-front spin [3]. Note that in relativistic dynamics, the total angular momentum operator $\boldsymbol{J}^2 = J_1^2 + J_2^2 + J_3^2$ is generally different from the total spin operator[1] $\boldsymbol{\mathcal{J}}^2 = \mathcal{J}_1^2 + \mathcal{J}_2^2 + \mathcal{J}_3^2 = -W^2/P^2$ [3, 4]. In light-front dynamics, $P^2 \equiv P_\mu P^\mu$, $W^2 \equiv W_\mu W^\mu$ are dynamical. They have to be diagonalized simultaneously at $x^+ = 0$:

$$P^2\,|\mathscr{M},\mathcal{J}\rangle = \mathscr{M}^2\,|\mathscr{M},\mathcal{J}\rangle, \tag{1a}$$

$$W^2\,|\mathscr{M},\mathcal{J}\rangle = -\mathscr{M}^2\mathcal{J}(\mathcal{J}+1)\,|\mathscr{M},\mathcal{J}\rangle. \tag{1b}$$

It is conventional to call P^2 the "light-cone Hamiltonian", $H_{\rm LC} \equiv P^2$. It is convenient to express this light-cone Hamiltonian in terms of kinetic energy and potential energy, $H_{\rm LC} = H_{\rm LC}^{(0)} + V_{int}$. The kinetic energy, $H_{\rm LC}^{(0)}$, resembles the non-relativistic kinetic energy,

$$H_{\rm LC}^{(0)} = 2P^+P_+^{(0)} - \boldsymbol{P}^{\perp\,2} = \sum_a \frac{\boldsymbol{p}_a^{\perp\,2} + m_a^2}{x_a} - \boldsymbol{P}^{\perp\,2}, \tag{2}$$

where "a" represents the quark or gluon constituent and $\boldsymbol{P}^\perp = \sum_a \boldsymbol{p}_a^\perp$ is the total transverse Center-of-Mass (CM) momentum while $x_a = \frac{p_a^+}{P^+}$ is the longitudinal momentum fraction carried by each constituent.

The triviality of the Fock space vacuum provides a strong appeal for the Fock space representation of the quantum field theory [2]. The Fock space expansion of an eigenstate in a plane-wave basis reads,

$$\begin{aligned}|\Psi;P\rangle = \sum_{n=0}^{\infty}\sum_{\sigma_1,\cdots\sigma_n}\int \frac{{\rm d}^3k_1}{(2\pi)^3 2k_1^+}\,\theta(k_1^+)\cdots\frac{{\rm d}^3k_n}{(2\pi)^3 2k_n^+}\,\theta(k_n^+)\\ \times 2P^+(2\pi)^3\,\delta^3(k_1+\cdots+k_n-P)\,\Psi_n^{\sigma_1,\cdots,\sigma_n}(k_1,\cdots,k_n)\,a_{\sigma_1}^\dagger(k_1)\cdots a_{\sigma_n}^\dagger(k_n)\,|0\rangle,\end{aligned} \tag{3}$$

where ${\rm d}^3k = {\rm d}^2k^\perp{\rm d}k^+$, $\delta^3(p_1-p_2) = \delta(p_1^+-p_2^+)\,\delta^2(\boldsymbol{p}_1^\perp-\boldsymbol{p}_2^\perp)$ and $\Psi_n^{\sigma_1,\cdots,\sigma_n}(k_1,k_2,\cdots,k_n)$ is called the light-front wavefunction (LFWF). LFWFs are boost-invariant, namely frame independent, following the boost-invariance of the light-cone Hamiltonian and the pure kinematic character of the light-front boosts. In practice, a non-perturbative diagonalization of the Hamiltonian can only be achieved in a finite-truncated Fock space. The Tamm–Dancoff approximation (TDA) introduces a truncation based on Fock sectors. The rationale of the TDA is founded on the success of the constituent quark model, according to which the hadrons can be approximated by a few particles as in the leading Fock space representation [6]. However, there are also new challenges

[1] Note that the total spin $\mathcal{J}$ is the observable quantity quoted as "J" in the Particle Data Group compilations [5].

in light-front TDA. Fock sector truncation breaks rotational symmetry. As a result, the total spin $\mathcal{J}$ in a truncated calculation is no longer a good quantum number.

3 Basis light-front quantized field theory

BLFQ is an *ab initio* Hamiltonian approach to light-front quantum field theory that adopts a complete set of orthonormal single-particle basis functions for field expansions resulting in Fock space basis states $|\phi_i\rangle$ expressed in terms of these single-particle basis states [7]. In the Fock space basis, the Hamiltonian and eigenstates become,

$$H_{ij} = \langle\phi_i|\, H_{\rm LC}\, |\phi_j\rangle, \quad |\Psi\rangle = \sum_i c_i\, |\phi_i\rangle. \tag{4}$$

The system of equations (1a) is reformulated as a standard eigenvalue problem,

$$\sum_j H_{ij} c_j = \lambda c_i, \tag{5}$$

which is then truncated and solved numerically. The full field theory is restored in the continuum limit and the complete Fock sectors limit of the Hamiltonian many-body dynamics.

In principle, the choice of the basis functions is arbitrary but subject to the conditions of completeness and orthonormality. Basis functions preserving the kinematic symmetries can dramatically reduce the dimensionality of the problem for a specific accuracy. Basis functions emulating the correct asymptotic behavior of the solution can accelerate the convergence. BLFQ adopts a light-front basis comprised of plane-wave functions in the longitudinal direction and 2D harmonic oscillator (HO) functions in the transverse direction. The transverse HO basis states are generated by the following operator [8],

$$P_+^{\rm HO} = \sum_a \frac{\boldsymbol{p}_a^{\perp\,2}}{2p_a^+} + \frac{\Omega^2}{2} p_a^+ \boldsymbol{r}_a^{\perp\,2}, \tag{6}$$

where $\boldsymbol{r}_a^\perp \equiv \boldsymbol{x}_a^\perp = -\frac{\boldsymbol{E}_a^\perp}{p_a^+}$ (at $x^+ = 0$) is the transverse position operator[2]. The adoption of the BLFQ basis exploits known similarity between light-front dynamics and non-relativistic dynamics, and is consistent with the recent development of the AdS/QCD [9, 10]. In momentum space, the single-particle basis functions are given in terms of the generalized Laguerre polynomials L_n^α by

$$\begin{aligned}\left\langle p^+, \boldsymbol{p}^\perp | n, m, x\right\rangle &= \mathcal{N} e^{{\rm i}m\theta} \left(\tfrac{\rho}{\sqrt{x}}\right)^{|m|} e^{-\frac{\rho^2}{2x}}\, L_n^{|m|}(\rho^2/x)\, \delta(p^+ - xP^+) \\ &\equiv \frac{1}{\sqrt{x}}\, \Psi_n^m\left(\tfrac{\boldsymbol{p}^\perp}{\sqrt{x}}\right) 2\pi 2p^+ \delta(p^+ - xP^+), \quad \rho = \frac{|\boldsymbol{p}^\perp|}{\sqrt{P^+\Omega}}, \quad \theta = \arg \boldsymbol{p}^\perp, \end{aligned} \tag{7}$$

which are associated with the HO eigenvalues $E_{n,m} = (2n + |m| + 1)\Omega$. x is the longitudinal momentum fraction. We can identify the HO energy scale parameter $b = \sqrt{P^+\Omega}$ comparing with $b = \sqrt{M\Omega}$ used in the non-relativistic HO basis [11–13]. The orthonormality of the basis functions reads

$$\langle n, m, x | n', m', x'\rangle = 2\pi 2x\, \delta(x - x')\, \delta_{n,n'}\, \delta_{m,m'}. \tag{8}$$

To introduce a finite truncation, BLFQ selects a particular finite subset of the basis space. In the longitudinal direction, we confine the longitudinal coordinate $-\mathsf{L} \le x^- \le +\mathsf{L}$ with *periodic boundary condition* for bosons and *anti-periodic boundary condition* for fermions. Thus the longitudinal momentum p^+ is discretized as,

$$p^+ = \frac{2\pi k}{\mathsf{L}}, \quad k = \begin{cases} 0, 1, 2, 3, \cdots & \text{for bosons,} \\ \frac{1}{2}, \frac{3}{2}, \frac{5}{2}, \frac{7}{2}, \cdots & \text{for fermions,} \end{cases} \tag{9}$$

[2]Recall the transverse light-front boost at $x^+ = 0$: $E^i = M^{+i} = x^+ P^i - x^i P^+ = -x^i P^+$.

where L is the length of the longitudinal box. We omit the zero-modes for the bosons in the calculations that follow. In the transverse direction, we select the Fock space basis states by

$$\sum_a (2n_a + |m_a| + 1) \leq \mathcal{N}_{\max}. \tag{10}$$

Let $\mathcal{P}$ denote the projection operator for the truncated basis space. Then for a basis state $|\alpha\rangle \equiv |n_1, m_1, x_1, n_2, m_2, x_2, \cdots\rangle$, $\mathcal{P}\,|\alpha\rangle = \theta(\mathcal{N}_{\max} - N_\alpha)\,|\alpha\rangle$ where $N_\alpha = \sum_a (2n_a + |m_a| + 1)$. The continuum limit is achieved by taking $\mathsf{L} \to \infty$, $\mathcal{N}_{\max} \to \infty$.

A symmetry may be broken by the basis truncation. For example, let A be a conserved operator and $[H_{\rm LC}, A] = 0$. Then in the truncated basis space, the commutator becomes

$$[\mathcal{P}H_{\rm LC}\mathcal{P}, \mathcal{P}A\mathcal{P}] = \mathcal{P}\,[[\mathcal{P}, H_{\rm LC}], [\mathcal{P}, A]]\,\mathcal{P}.$$

For the transverse truncation, the commutation relation survives if $[A, P^{\rm HO}_+] = 0$. The proof is as following: $[A, P^{\rm HO}_+] = 0 \;\Rightarrow\; A\,|\alpha\rangle = \sum_{\alpha'} C_{\alpha'} \delta_{N_\alpha, N_{\alpha'}}\,|\alpha'\rangle$. Then

$$\begin{aligned}
\mathcal{P}A\,|\alpha\rangle &= \mathcal{P}\sum_{\alpha'} C_{\alpha'}\,\delta_{N_\alpha,N_{\alpha'}}\,|\alpha'\rangle = \sum_{\alpha'} C_{\alpha'}\,\delta_{N_\alpha,N_{\alpha'}}\,\theta(\mathcal{N}_{\max} - N_{\alpha'})\,|\alpha'\rangle \\
&= \theta(\mathcal{N}_{\max} - N_\alpha)\sum_{\alpha'} C_{\alpha'}\,\delta_{N_\alpha,N_{\alpha'}}\,|\alpha'\rangle = A\mathcal{P}\,|\alpha\rangle\,, \\
\Rightarrow \quad & [\mathcal{P}, A] = 0, \\
\Rightarrow \quad & [\mathcal{P}H_{\rm LC}\mathcal{P}, \mathcal{P}A\mathcal{P}] = 0.
\end{aligned}$$

Among all generators of the Poincaré symmetry, a complete set of compatible operators (including the Hamiltonian) is particularly useful for solving Eq. (5), as the Hamiltonian is block diagonal with respect to the mutual eigenstates. A distinguishing feature of the BLFQ basis with the finite truncation is that it preserves the set of compatible kinematic operators. We define $P^{\rm CM}_+ = \frac{1}{2P^+}\Big(\boldsymbol{P}^{\perp\,2} + \Omega^2 \boldsymbol{E}^{\perp\,2}\Big) = \frac{1}{2P^+}\boldsymbol{P}^{\perp\,2} + \frac{\Omega^2}{2}P^+\boldsymbol{R}^{\perp\,2}$. With some effort, one can show that $\{H_{\rm LC}, P^+, P^{\rm CM}_+, J^3, \mathcal{J}^3\}$ is a set of mutually commuting operators and $[P^+, P^{\rm HO}_+] = [J^3, P^{\rm HO}_+] = [P^{\rm CM}_+, P^{\rm HO}_+] = [\mathcal{J}^3, P^{\rm HO}_+] = 0$, where $\mathcal{J}^3 = J^3 + \frac{\varepsilon^{ij}}{P^+}E^i P^j = J^3 - \varepsilon^{ij}R^i P^j$. Therefore in the finite basis space the truncated operators,

$$\{\mathcal{P}H_{\rm LC}\mathcal{P}, \mathcal{P}P^+\mathcal{P}, \mathcal{P}P^{\rm CM}_+\mathcal{P}, \mathcal{P}J^3\mathcal{P}, \mathcal{P}\mathcal{J}^3\mathcal{P}\}, \tag{11}$$

still form a set of compatible operators.

For simplicity, we will omit the projection operator when there is no danger of confusion. For example, the compatible operators in the finite-truncated basis space will be denoted as $\{H_{\rm LC}, P^+, P^{\rm CM}_+, J^3, \mathcal{J}^3\}$. The compatible operators allow us to further fix the total longitudinal momentum and the angular momentum projection of the system from the kinematic construction:

$$\begin{aligned}
P^+ = \frac{2\pi\mathcal{K}}{\mathsf{L}} \quad &\Rightarrow \quad \sum_a k_a = \mathcal{K}; \\
J^3 = M_j \quad &\Rightarrow \quad \sum_a (m_a + \sigma_a) = M_j,
\end{aligned} \tag{12}$$

where σ_a is the spin projection of the a-th constituent. Due to the boost invariance, the light-cone Hamiltonian depends on the longitudinal momentum fractions $x_a = \frac{k_a}{\mathcal{K}}$ instead of p^+_a. Therefore, for a fixed L, the continuum limit is also achieved by taking $\mathcal{K} \to \infty$, $\mathcal{N}_{\max} \to \infty$.

We also take advantage of the internal symmetries to fix the charge $Q = \sum_a Q_a$, baryon number $B = \sum_a B_a$, color projection and the total color, that is, color configurations are restricted to color-singlet configurations.

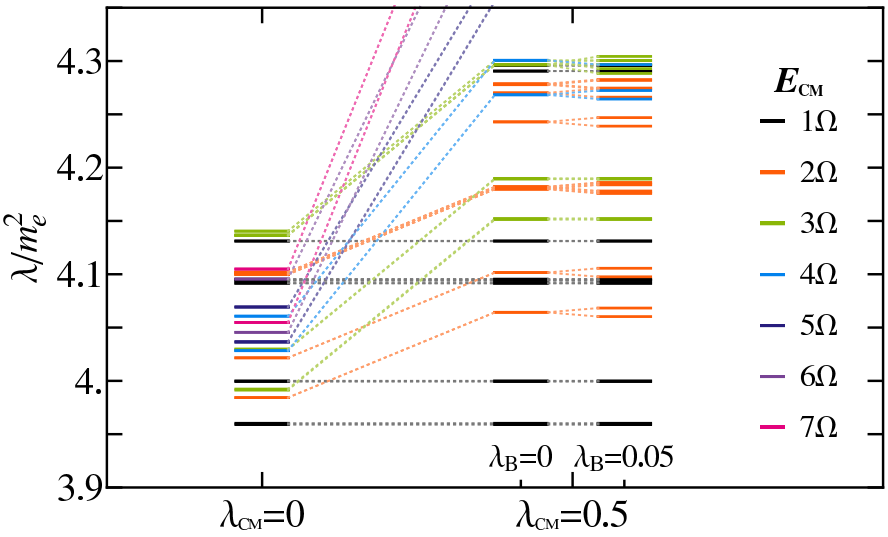

Figure 1: Using Lagrange multiplier method to lift the CM excitations. The calculation is performed in the Fock sectors $|e^+e^-\rangle$ and $|e^+e^-\gamma\rangle$ with $M_j = 0$, $\mathcal{K} = \mathcal{N}_{\max} = 8$, $\sqrt{P^+\Omega} = 0.3m_e$ (See Section 4 for details). The vertical axis shows the eigenvalues of the light-cone Hamiltonian $H_{\rm LC}$. States with different $E_{\rm CM}$ are colored differently. We show spectra with the lowest 50 states for three cases: $\lambda_{\rm CM} = 0$, $\lambda_{\rm B} = 0$; $\lambda_{\rm CM} = 0.5$, $\lambda_{\rm B} = 0$ and $\lambda_{\rm CM} = 0.5$, $\lambda_{\rm B} = 0.05$. In the last case, degeneracies caused by CM excitations are lifted.

Let HO states $|N, M\rangle$ be the mutual eigenstates of $P_+^{\rm CM}$ and $L^3 \equiv J^3 - \mathcal{J}^3 = R^1P^2 - R^2P^1$ associated with the eigenvalues $E_{\rm CM} = E_{N,M} \equiv (2N + |M| + 1)\Omega$ and M, respectively. Then the eigenvalue $\mathcal{M}_j$ of the light-front spin projection $\mathcal{J}^3$ can be expressed in terms of the eigenvalues of J^3 and L^3 as $\mathcal{M}_j = M_j - M$. The eigenstates of P^2 can be identified with the eigenvalues of the compatible operators as $|\mathscr{M}^2, \frac{2\pi\mathcal{K}}{L}, E_{N,M}, M_j, \mathcal{M}_j\rangle$. They can also be identified in terms of N, M as $|\mathscr{M}, \mathcal{K}, \mathcal{M}_j, N, M\rangle \equiv |\varphi_{\rm intr}\rangle \otimes |\Phi_{\rm CM}\rangle$, where $|\varphi_{\rm intr}\rangle = |\mathscr{M}, \mathcal{K}, \mathcal{M}_j\rangle$, $|\Phi_{\rm CM}\rangle = |N, M\rangle$. Therefore, the finite BLFQ basis admits an exact factorization of the center-of-mass motion [14].

The light-cone Hamiltonian $H_{\rm LC} = H_{\rm LC}^{(0)} + V_{int}$ only acts on the intrinsic part of the wavefunction. So different CM states are degenerate. It is useful to introduce Lagrange multipliers in the Hamiltonian [15]:

$$P_+ \to P_+ + \lambda_{\rm CM}(P_+^{\rm CM} - \Omega) + \lambda_{\rm B}\Omega L^3, \tag{13}$$

where $\lambda_{\rm CM} > 0$ and $|\lambda_{\rm B}| < \lambda_{\rm CM}$. The eigenvalues of the light-cone Hamiltonian become $\lambda = \mathscr{M}^2 + 2\lambda_{\rm CM}(2N + |M|)P^+\Omega + 2\lambda_{\rm B}MP^+\Omega$. The CM excitations are driven to high energy with sufficiently large $\lambda_{\rm CM}$. Fig. 1 shows the use of Lagrange multipliers to lift the degeneracies of the states in a numerical calculation of a positronium model.

To separate the CM part and the intrinsic part in the basis functions in single-particle coordinates, we introduce the generalized 2D Talmi–Moshinsky (TM) transformation [16],

$$\Psi_{n_1}^{m_1}\left(\frac{\boldsymbol{p}_1}{\sqrt{x_1}}\right)\Psi_{n_2}^{m_2}\left(\frac{\boldsymbol{p}_2}{\sqrt{x_2}}\right) =$$

$$\sum_{NMnm} (NMnm|n_1m_1n_2m_2)|_\xi\, \delta_{\varepsilon_1+\varepsilon_2,E+\epsilon}\, \delta_{M+m,m_1+m_2}\, \Psi_N^M\left(\frac{\boldsymbol{p}_1+\boldsymbol{p}_2}{\sqrt{x_1+x_2}}\right)\Psi_n^m\left(\frac{\boldsymbol{p}}{\sqrt{x}}\right), \tag{14}$$

where $\varepsilon_i = 2n_i + |m_i| + 1, E = 2N + |M| + 1$, $\epsilon = 2n + |m| + 1$, $\xi = \arctan\sqrt{\frac{x_2}{x_1}}$, $x = \sqrt{\frac{x_1 x_2}{x_1+x_2}}$ and $\boldsymbol{p} = \frac{x_2}{x_1+x_2}\,\boldsymbol{p}_1 - \frac{x_1}{x_1+x_2}\,\boldsymbol{p}_2$ is the intrinsic momentum. The sum is finite due to the Kronecker delta $\delta_{E_1+E_2,E+\varepsilon}$. The coefficients $(NMnm|n_1m_1n_2m_2)|_\xi$ are called the generalized 2D TM coefficients. They can be computed analytically within a closed form (See appendix A).

4 Basis light-front quantization applied to QED

In recent applications to QED, Honkanen *et al.* and Zhao *et al.* calculated the electron anomalous magnetic moment and obtained high precision results [11, 12]. Here we present an application of BLFQ to a highly regularized model of positronium in the Fock sectors $|e^-e^+\rangle$ and $|e^-e^+\gamma\rangle$ which complements the treatment of positronium presented in Ref. [13].

We adopt a light-cone gauge $A^+ = 0$ for QED. The light-front QED interactions are shown in Fig. 2 which include the $e \to e\gamma$ vertex,

$$P_+^{(e\to e\gamma)} = g\int \mathrm{d}x_+\mathrm{d}^2x^\perp\ \bar\psi(x)\,\gamma_\mu\,\psi(x)\,A^\mu(x)\Big|_{x^+=0}, \tag{15}$$

and two instantaneous vertices,

$$\begin{aligned} P_+^{(e\gamma\to e\gamma)} &= \tfrac{1}{2}g^2\int \mathrm{d}x_+\mathrm{d}^2x^\perp\ \bar\psi(x)\,\gamma_\mu\,A^\mu(x)\frac{\gamma^+}{\mathrm{i}\partial^+}\gamma_\nu\,A^\nu(x)\,\psi(x)\Big|_{x^+=0},\\ P_+^{(ee\to ee)} &= \tfrac{1}{2}g^2\int \mathrm{d}x_+\mathrm{d}^2x^\perp\ \bar\psi(x)\,\gamma^+\,\psi(x)\frac{1}{(\mathrm{i}\partial^+)^2}\bar\psi(x)\,\gamma^+\,\psi(x)\Big|_{x^+=0}. \end{aligned} \tag{16}$$

In this model, we take the coupling constant $\alpha = \frac{g^2}{4\pi} = 0.2$ and the basis energy scale $b = \sqrt{P^+\Omega} = 0.3m_e$, where $m_e = 0.511$ MeV is the mass of the electron. We adopt a regulator for the light-front small-x singularity, $\frac{1}{(x_1-x_2)^2} \to \frac{1}{(x_1-x_2)^2+\varepsilon}$ with $\varepsilon = 0.01$ [8, 17]. We then construct the light-cone Hamiltonian matrix $H_{\rm LC}^{\rm (pos)}$. Fig. 3 shows the number of nonzero matrix elements compared to the total number of matrix elements. The Hamiltonian matrix is a large sparse matrix. We diagonalize the matrix with the Lanczos method implemented by the ARPACK software [18], which is particularly suitable for solving large sparse matrix eigenvalue problems.

We obtain the positronium spectrum directly from the diagonalization. Fig. 4(a) shows the positronium bound-state spectrum for light-front spin projections $\mathcal{M}_j =$ 0, 1, 2 from the numerical calculations with $\mathcal{N}_{\rm max} = \mathcal{K} = 12$, $M_j = 0, 1, 2, 3$; $\lambda_{\rm CM} = 5$, $\lambda_{\rm B} = 0$. Some of the states in the figure are nearly degenerate. We have put a label n to the left of each bar to indicate the existence of n states around each bar in Fig. 4(a). In the light-front TDA, the total spin $\mathcal{J}$ is only approximate. We can identify the total spin by counting the approximate degeneracy of particles with

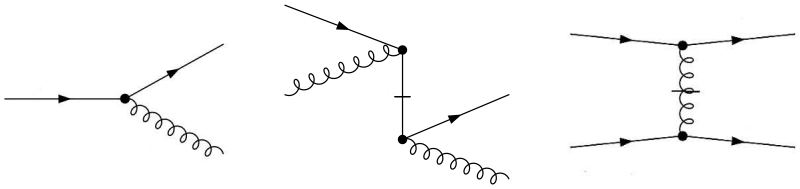

(a) $e \to e\gamma$ vertex (b) $e\gamma \to e\gamma$ vertex (c) $ee \to ee$ vertex

Figure 2: The relevant light-front QED vertices for positronium in the Fock sectors $|e^-e^+\rangle$ and $|e^-e^+\gamma\rangle$.

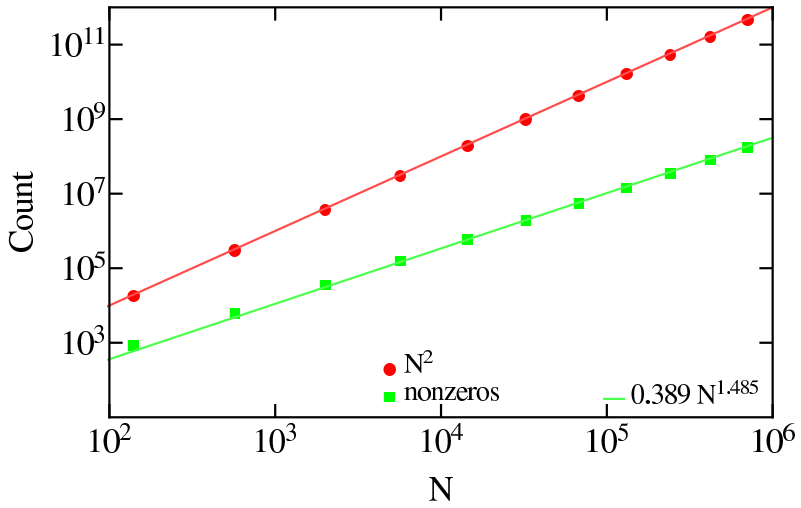

Figure 3: The sparsity of the light-cone Hamiltonian matrix $H_{\rm LC}^{\rm (pos)}$. The horizontal axis is the dimensionality N of the basis space. The square dots show the number of nonzero matrix elements. A power-law fitting suggests the number of nonzero elements is proportional to $\sim N^{1.485}$.

different $\mathcal{M}_j$ [3]. Fig. 4(b) shows the states with $\mathcal{M}_j = 0$ identified by their total spin $\mathcal{J}$. The energy splitting between the singlet state ($\mathcal{J} = 0, \mathcal{M}_j = 0$) and the triplet state ($\mathcal{J} = 1, \mathcal{M}_j = 0$) is the fine splitting [shown in Fig. 4(a)]. The non-relativistic quantum mechanics gives a fine splitting for the ground state $E_{\rm triplet} - E_{\rm singlet} = \frac{1}{3}\alpha^4 m_e \simeq 5.33 \times 10^{-4} m_e$ [19]. In our calculation, the fine splitting is $2.77 \times 10^{-4} m_e$, which is the correct order of magnitude and is reasonable given that we have a relativistic treatment (important for strong coupling) and our implementation of regulators.

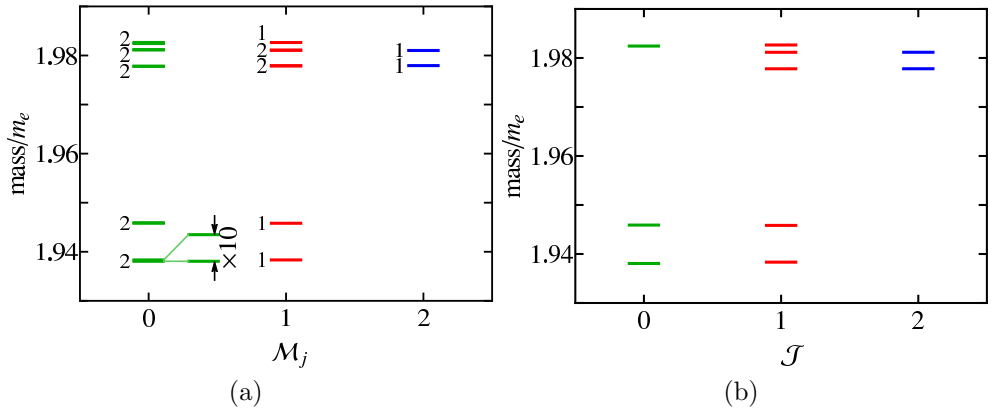

Figure 4: The positronium spectrum for (a) spin projection $\mathcal{M}_j = 0, 1, 2$; (b) total spin $\mathcal{J} = 0$, 1, 2, $\mathcal{M}_j = 0$ identified from plot (a). For $\mathcal{M}_j = 3$, there is no state within the range of the plot. The numbers to the left of the bars in plot (a) label the multiplicity of the states around each bar. Plot (a) also shows the fine splitting between the lowest $\mathcal{J} = 0$, $\mathcal{M}_j = 0$ and $\mathcal{J} = 1$, $\mathcal{M}_j = 0$ states. The total spin $\mathcal{J}$ in plot (b) is obtained by counting the approximate degeneracy of states with different $\mathcal{M}_j$.

5 Conclusions and outlook

We have introduced the Basis Light-Front Quantization (BLFQ) approach to the QCD bound-state problem and analyzed the symmetries of the finite basis space. BLFQ converts the field theory problem into a form where we can take advantage of the recent advances in quantum many-body problems and the state-of-the-art methods developed for large sparse matrix eigenvalue problem. The compatible operators provide a means to identify states. We have shown the exact factorization of the center-of-mass motion in the finite basis space. They also allow us to reduce the dimensionality of the problem dramatically for a given level of accuracy, as we have demonstrated in the positronium model. BLFQ has retained the kinematic symmetries of the underlying Hamiltonian. We also introduced a generalized 2D Talmi–Moshinsky transformation to relate internal motions to a fixed coordinate system. Finally we have applied BLFQ to QED and obtained the positronium bound-state spectrum.

To obtain physical results, one must perform renormalization. There are three types of divergences existing in the light-front quantized field theory: the ultraviolet divergence, the infrared divergence and the spurious small-x divergence. Various schemes have been developed to address these issues (see, for example, Refs. [13, 17, 20, 21]).

As a non-perturbative *ab initio* Hamiltonian approach to QFT, BLFQ requires major computational efforts. Thanks to the rapid advances in supercomputing, we foresee promising applications of BLFQ to understanding the structure of QCD bound states.

6 Acknowledgement

The authors thank S. J. Brodsky, H. Honkanen and D. Chakrabarti, V. Karmanov, A. El-Hady, C. Yang and E. G. Ng for fruitful discussions. This work was supported in part by the Department of Energy under Grant Nos. DE-FG02-87ER40371 and DESC0008485 (SciDAC-3/NUCLEI) and by the National Science Foundation under Grant No. PHY-0904782. A portion of the computational resources were provided by the National Energy Research Scientific Computing Center (NERSC), which is supported by the DOE Office of Science.

Appendix A: Talmi-Moshinsky transformation

Consider the exponential generating function of the 2D HO wavefunctions $\Psi_n^m(\boldsymbol{q})$,

$$e^{-\frac{1}{2}\boldsymbol{q}^2+2\boldsymbol{q}\cdot\boldsymbol{z}-\boldsymbol{z}^2} = \sum_{n=0}^{\infty}\sum_{m=-\infty}^{\infty} \frac{(-1)^n}{\sqrt{4\pi(n+|m|)!n!}}\,\Psi_n^m(\boldsymbol{q})\,e^{-\mathrm{i}m\theta}\,z^{2n+|m|}, \tag{17}$$

where $\boldsymbol{q}=\frac{\boldsymbol{p}}{\sqrt{x}}$, $z=|\boldsymbol{z}|/\sqrt{P^+\Omega}$, $\theta=\arg\boldsymbol{z}$. If we define

$$\begin{aligned} \boldsymbol{Q} &= \boldsymbol{q_1}\cos\xi+\boldsymbol{q_2}\sin\xi, \quad \boldsymbol{q} = \boldsymbol{q_1}\sin\xi-\boldsymbol{q_2}\cos\xi,\\ \boldsymbol{Z} &= \boldsymbol{z_1}\cos\xi+\boldsymbol{z_2}\sin\xi, \quad \boldsymbol{z} = \boldsymbol{z_1}\sin\xi-\boldsymbol{z_2}\cos\xi, \end{aligned} \tag{18}$$

where $\xi=\arctan\sqrt{\frac{x_2}{x_1}}$, $\boldsymbol{Q}=\frac{\boldsymbol{p}_1+\boldsymbol{p}_2}{\sqrt{x_1+x_2}}$, $\boldsymbol{q}=\frac{x_2\boldsymbol{p}_1-x_1\boldsymbol{p}_2}{\sqrt{x_1x_2(x_1+x_2)}}$, then there exists an identity

$$\begin{aligned} &\left(-\tfrac{1}{2}\boldsymbol{q}_1^2+2\boldsymbol{q}_1\cdot\boldsymbol{z}_1-\boldsymbol{z}_1^2\right)+\left(-\tfrac{1}{2}\boldsymbol{q}_2^2+2\boldsymbol{q}_2\cdot\boldsymbol{z}_2-\boldsymbol{z}_2^2\right)\\ &\qquad=\left(-\tfrac{1}{2}\boldsymbol{Q}^2+2\boldsymbol{Q}\cdot\boldsymbol{Z}-\boldsymbol{Z}^2\right)+\left(-\tfrac{1}{2}\boldsymbol{q}^2+2\boldsymbol{q}\cdot\boldsymbol{z}-\boldsymbol{z}^2\right). \end{aligned} \tag{19}$$

Thanks to Eq.(17),

$$\sum_{n_1,m_1,n_2,m_2} \frac{(-1)^{n_1+n_2}\,\Psi_{n_1}^{m_1}(\boldsymbol{q_1})\,\Psi_{n_2}^{m_2}(\boldsymbol{q_2})}{4\pi\sqrt{(n_1+|m_1|)!n_1!(n_2+|m_2|)!n_2!}}\,e^{-\mathrm{i}m_1\theta_1-\mathrm{i}m_2\theta_2}\,z_1^{2n_1+|m_1|}\,z_2^{2n_2+|m_2|}$$

$$=\sum_{N,M,n,m}\frac{(-1)^{N+n}\,\Psi_N^M(\boldsymbol{Q})\,\Psi_n^m(\boldsymbol{q})}{4\pi\sqrt{(N+|M|)!N!(n+|m|)!n!}}\,e^{-\mathrm{i}M\Theta-\mathrm{i}m\theta}\,Z^{2N+|M|}\,z^{2n+|m|}, \quad (20)$$

where $z_i=|\boldsymbol{z}_i|$, $Z=|\boldsymbol{Z}|$, $z=|\boldsymbol{z}|$, $\theta_i=\arg\boldsymbol{z}_i$, $\Theta=\arg\boldsymbol{Z}$, $\theta=\arg\boldsymbol{z}$. We can express Z, z, $e^{\mathrm{i}\Theta}$, $e^{\mathrm{i}\theta}$ in terms of z_1, z_2, $e^{\mathrm{i}\theta_1}$, e^{θ_2} and identify the corresponding coefficients.

$$\Psi_{n_1}^{m_1}(\boldsymbol{q}_1)\,\Psi_{n_2}^{m_2}(\boldsymbol{q}_2)$$
$$\equiv\sum_{NMnm}(NMnm|n_1m_1n_2m_2)|_\xi\;\delta_{\varepsilon_1+\varepsilon_2,E+\epsilon}\,\delta_{m_1+m_2,M+m}\,\Psi_N^M(\boldsymbol{Q})\,\Psi_n^m(\boldsymbol{q}),$$

where $E=2N+|M|+1$, $\epsilon=2n+|m|+1$, $\varepsilon_i=2n_i+|m_i|+1$ and the coefficients are

$$(N_1M_1N_2M_2|n_1m_1n_2m_2)|_\xi$$
$$=(-1)^{N_1-n_1-n_2+\frac{1}{2}(|M_2|-M_2)}\,(\sin\xi)^{2n_2+|m_2|}\,(\cos\xi)^{2n_1+|m_1|}$$
$$\times\sqrt{\frac{(n_1+|m_1|)!(n_2+|m_2|)!n_1!n_2!}{(N_1+|M_1|)!(N_2+|M_2|)!N_1!N_2!}}\sum_{\gamma_1=0}^{v_1}\sum_{\gamma_2=0}^{v_2}\sum_{\beta_1=0}^{\gamma_1}\sum_{\beta_2=0}^{\gamma_2}\sum_{\beta_3=0}^{V_2}\sum_{\beta=0}^{M_2}(-\tan\xi)^{\beta_1-\beta_2+\beta+M_2}$$
$$\times\binom{M_1}{\chi}\binom{M_2}{\beta}\binom{V_2}{\beta_1,\beta_2,\beta_3,\beta_4}\binom{v_1+v_2-V_2}{\gamma_1-\beta_1,\gamma_2-\beta_2,v_1-\gamma_1-\beta_3,\beta_5}, \quad (21)$$

where $v_i=n_i+\frac{1}{2}(m_i-|m_i|)$, $V_i=N_i+\frac{1}{2}(M_i-|M_i|)$, $i=1,2$, $\chi=v_1-v_2+m_1+\gamma_2-\gamma_1-\beta$, $\xi=\arctan\sqrt{\frac{x_2}{x_1}}$. The multinomial coefficients $\binom{n}{m_1,m_2,\cdots,m_k}=\frac{n!}{m_1!m_2!\cdots m_k!}$ satisfy $m_1+m_2+\cdots+m_k=n$, $0\le m_i\le n$, $i=1,2,\ldots,k$. So, $\beta_4=V_2-\beta_1-\beta_2-\beta_3$, $\beta_5=v_2-\gamma_2-\beta_4$. The generalized binomial coefficients satisfy $\binom{n}{m}=\frac{n(n-1)\cdots(n-m+1)}{m!}$, $m\ge0$ and $\binom{n}{0}=1$.

References

[1] P. A. M. Dirac, Rev. Mod. Phys. **21**, 392 (1949).

[2] Robert J. Perry, A. Harindranath and K. G. Wilson, Phys. Rev. Lett. **65**, 2959 (1990).

[3] S. J. Brodsky, H.-C. Pauli and S. S. Pinsky, Phys. Rept. **301**, 299 (1998).

[4] N. N. Bogolubov, A. A. Logunov, I. T. Todorov, *Introduction to axiomatic quantum field theory.* W. A. Benjamin, Advanced Book Program, Reading, Mass., 1975.

[5] J. Beringer *et al.* (Particle Data Group), Phys. Rev. D **86**, 010001 (2012) and 2013 partial update for the 2014 edition, URL: http://pdg.lbl.gov.

[6] K. G. Wilson, T. S. Walhout, A. Harindranath, W.-M. Zhang, R. J. Perry and S. D. Głazek, Phys. Rev. D **49**, 6720 (1994).

[7] J. P. Vary, H. Honkanen, J. Li, P. Maris, S. J. Brodsky, A. Harindranath, G. F. de Téramond, P. Sternberg, E. G. Ng and C. Yang, Phys. Rev. C **81**, 035205 (2010), arXiv:0905.1411 [nucl-th] (2009).

[8] P. Maris, P. W. Wiecki, Y. Li, X. Zhao and J. P. Vary, Acta Phys. Polon. Supp. **6**, 321 (2013).

[9] S. J. Brodsky and G. F. de Téramond, Phys. Rev. Lett. **96**, 201601 (2006).

[10] G. F. de Téramond and S. J. Brodsky, Phys. Rev. D **77**, 056007 (2008), arXiv:0707.3859 [hep-ph] (2007).

[11] H. Honkanen, P. Maris, J. P. Vary and S. J. Brodsky, Phys. Rev. Lett. **106**, 061603 (2011).

[12] X. Zhao, H. Honkanen, P. Maris, J. P. Vary and S. J. Brodsky, Few-body Syst. **52**, 339 (2012); arxiv:1110.0553 [hep-ph] (2011).

[13] P. W. Wiecki, Y. Li, X. Zhao, P. Maris and J. P. Vary, *see these Proceedings*, p. 146, http://www.ntse-2013.khb.ru/Proc/Wiecki.pdf.

[14] M. A. Caprio, P. Maris and J. P. Vary, Phys. Rev. C **86**, 034312 (2012).

[15] D. H. Gloeckner and R. D. Lawson, Phys. Lett. B **53**, 313 (1974).

[16] I. Talmi, Helv. Phys. Acta **25**, 185 (1952); M. Moshinsky, Nucl. Phys. **13**, 104 (1959).

[17] V. A. Karmanov, J.-F. Mathiot and A. V. Smirnov, Phys. Rev. D **82**, 056010 (2010); arXiv:1006.5640 [hep-th] (2010).

[18] R. B. Lehoucq, D. C. Sorensen and C. Yang, *ARPACK users guide: Solution of large scale eigenvalue problems by implicitly restarted Arnoldi methods*. SIAM, Philadelphia, PA, 1998.

[19] D. Griffiths, *Introduction to elementary particles, 2nd revised ed.* Wiley, Weinheim, 2008.

[20] S. K. Bogner, R. J. Furnstahl and R. J. Perry, Phys. Rev. C **75**, 061001(R) (2007).

[21] S. D. Głazek and K. G. Wilson, Phys. Rev. D **48**, 5863 (1993); **49**, 4214 (1994).

Positronium in Basis Light-Front Quantization

Paul W. Wiecki, Yang Li, Xingbo Zhao, Pieter Maris and James P. Vary

Department of Physics and Astronomy, Iowa State University, Ames, Iowa 50011, USA

Abstract

We present a calculation of the mass spectrum of positronium within the framework of the recently developed Basis Light-Front Quantization approach to non-perturbative quantum field theory. In this calculation, we employ a two-body effective interaction for the photon exchange, neglecting self-energy effects. We demonstrate the cancellation of Light-Front small-x divergences within our non-perturbative approach. The resulting spectrum is compared to both non-relativistic quantum mechanics and previous work in Discretized Light-Cone Quantization.

Keywords: *Light-front dynamics; non-perturbative; bound state; positronium*

1 Introduction

The *ab initio* calculation of hadron mass spectra and other hadron observables remains an outstanding theoretical question. Recent observations of "tetraquark" states in the quarkonium spectrum point to the pressing need for theoretical methods which can address such systems. In the current "supercomputing era", the computational tools necessary for such large-scale calculations are now readily available.

The recently developed Basis Light-Front Quantization (BLFQ) [1] approach is a promising tool for tackling hadron problems. BLFQ combines the well-known advantages of Light-Front Dynamics [2, 3] with modern developments in *ab initio* nuclear structure calculations, such as the No-Core Shell Model (NCSM) [4]. The similarity of the Light-Front Hamiltonian formulation to non-relativistic quantum mechanics allows the quantum field theoretical bound state problem to be formulated as large, sparse matrix eigenvalue problem. State-of-the-art methods developed for NCSM calculations can then brought to bear on the hadron problem.

BLFQ has so far been applied to the problem of a free electron in QED. Honkanen [5] and Zhao [6] calculated Schwinger's electron anomalous magnetic moment to high precision within the BLFQ approach. More recently, BLFQ has been applied to time-dependent problems in non-perturbative quantum field theory, such as non-linear Compton scattering [7].

Here, we present the first application of BLFQ to a bound state problem, using the positronium system as a test case. We develop a two-body effective interaction that acts only on the two-particle sector of the basis. Our calculation is thus equivalent to a ladder truncation on the Light Front.

Proceedings of International Conference 'Nuclear Theory in the Supercomputing Era — 2013' (NTSE-2013), Ames, IA, USA, May 13–17, 2013. Eds. A. M. Shirokov and A. I. Mazur. Pacific National University, Khabarovsk, Russia, 2014, p. 146.

http://www.ntse-2013.khb.ru/Proc/Wiecki.pdf.

2 Basis Light-Front Quantization

In BLFQ, hadron observables are calculated by solving the equation

$$P^\mu P_\mu |\Psi\rangle = M^2 |\Psi\rangle, \tag{1}$$

where P^μ is the energy-momentum 4-vector operator. Using Light-Cone Gauge, the operator P^2 can be constructed. This operator plays the role of the Hamiltonian in NCSM calculations, and is often referred to as the "Light-Cone Hamiltonian" $H_{LC} \equiv P^2$ [2]. One can then calculate the matrix elements of this operator in a basis to produce a matrix, which can be diagonalized to find the mass eigenvalues (squared) and Light-Front amplitudes. The approach is thus non-perturbative. Since the basis is infinite dimensional, it must be truncated for the problem to be tractable on a computer. Three separate truncations are made in BLFQ.

The first is truncation on the number of Fock sectors. Since we are solving a quantum field theory, the basis must, in principle, contain "sectors" with all possible numbers and species of particles that can be generated by the interactions within P^2. The operator P^2 contains terms which change particle number and thus couples the sectors. For example, the "physical" positronium state, could be expressed schematically as

$$\left|e^+e^-\right\rangle_{\text{phys}} = a\left|e^+e^-\right\rangle + b\left|e^+e^-\gamma\right\rangle + c\left|e^+e^-\gamma\gamma\right\rangle + d|\gamma\rangle + f\left|e^+e^-e^+e^-\right\rangle + \cdots . \tag{2}$$

In order to have a finite basis, then, we must truncate the Fock sectors at some point. This truncation will be made by physical considerations. For the moment we restrict ourselves to the $|e^+e^-\rangle$ and $|e^+e^-\gamma\rangle$ sectors. This should be sufficient for generating the Bohr spectrum of positronium. We do not yet make any attempt to examine the limit of increasing the number of Fock sectors.

Secondly, we need a truncation on the Light-Front longitudinal modes. We discretize the longitudinal momentum by putting our system in a longitudinal box of length L and applying periodic boundary conditions (BCs). Specifically, we choose periodic BCs for bosons and anti-periodic BCs for fermions. Thus

$$p^+ = \frac{2\pi}{L} j, \tag{3}$$

where j is an integer for bosons, or a half-integer for fermions. For bosons, we exclude the "zero modes", i. e. $j \neq 0$. In the many-body basis, we select the value of the total longitudinal momentum $P^+ = \sum_i p_i^+$, where the sum is over particles. We then parameterize this using a dimensionless variable $K = \sum_i j_i$ such that $P^+ = \frac{2\pi}{L} K$. For a given particle i, the longitudinal momentum fraction x is defined as

$$x_i = \frac{p_i^+}{P^+} = \frac{j_i}{K}. \tag{4}$$

Due to the positivity of longitudinal momenta on the Light Front [8], fixing K serves as a Fock space cutoff and makes the number of longitudinal modes finite [9]. It is easy to see that K determines our "resolution" in the longitudinal direction, and thus our resolution on parton distribution functions. Real physics corresponds to the limit $K \to \infty$.

Finally, in the Light-Front transverse direction we employ a 2D Harmonic Oscillator (HO) basis. That is, the basis functions are the eigenfunctions of the potential $V = \frac{1}{2} M \Omega^2 \mathbf{r}^2$. Each value of the *oscillator energy parameter* $b = \sqrt{M\Omega}$ determines a unique complete basis. Convergence rates depend upon b but the final converged results should not. The basis is made finite by restricting the number of allowed oscillator quanta according to

$$\sum_i (2n_i + |m_i| + 1) \leq N_{\max}, \tag{5}$$

where n and m are the radial and orbital quantum numbers of the 2D Harmonic Oscillator, respectively. Of course, real physics is obtained in the continuum limit of $N_{\max} \to \infty$. Furthermore, we use an M-scheme basis. That is, our many-body basis states have a well-defined value of

$$M_J = \sum_i (m_i + s_i), \tag{6}$$

where s is the helicity. These basis states do not, however, have a well-defined value of total J.

Since our basis is constructed in single-particle coordinates, the center-of-mass (CM) motion of the system is contained in our solutions. This problem is also faced in NCSM calculations. The use of the HO basis combined with the $N_{\max}$ truncation is a great advantage here since it allows for the exact factorization of the wavefunction into "intrinsic" and "CM" components, even within a truncated basis. The CM motion can then be removed from the low-lying spectrum by introducing a Lagrange multiplier proportional to H_{CM} (also known as the Lawson term) to the Hamiltonian [10]. The extra term essentially makes CM excitations very costly energetically and thus forces the CM part of the wavefunction to be the ground state of CM motion. In this way, spurious CM excitations are removed from the spectrum of interest.

It is important to note that, in NCSM calculations, the exact factorization only happens if the isoscalar kinetic energy is used. That is, the proton and neutron mass are treated as the same. On the Light Front, the kinetic energy can be written as

$$P^+P^- = \sum_i \frac{\mathbf{p}_i^2 + m^2}{x_i}. \tag{7}$$

Comparing to the non-relativistic form $\sum_i \frac{\mathbf{p}_i^2}{2m}$ we see that, on the Light Front, the longitudinal momentum fraction x is analogous to mass. Thus the equivalent to using the isoscalar kinetic energy in the NCSM is for the particles to have *equal longitudinal momentum splitting*. For two fermions, this situation corresponds to $K = 1$ (similarly $K = \frac{3}{2}$ for three fermions). Indeed, in initial applications of BLFQ it was found that CM factorization only occurred when the total longitudinal momentum was split equally among the constituents. In order to generalize the factorization, the following alternate coordinates were introduced [11]:

$$\begin{aligned} \mathbf{q} &\equiv \frac{\mathbf{p}}{\sqrt{x}}, \\ \mathbf{s} &\equiv \sqrt{x}\,\mathbf{r}. \end{aligned} \tag{8}$$

When the Hamiltonian is expressed in these coordinates, exact CM factorization is obtained for all eigenstates even in a basis with arbitrary distributions of longitudinal momenta as well as an arbitrary numbers of sectors. An illustration of the exact CM factorization in BLFQ is given in Refs. [11, 12].

3 Two-Body effective interaction

We truncate the Fock space to include only $|e^+e^-\rangle$ and $|e^+e^-\gamma\rangle$ states. We wish to formulate an effective potential acting only in the $|e^+e^-\rangle$ space that includes the effects generated by the $|e^+e^-\gamma\rangle$ space. In the formalism of effective potentials, we consider the P space to be the $|e^+e^-\rangle$ space and Q space to be the $|e^+e^-\gamma\rangle$ space. Let $\mathcal{P}$ be the operator that projects onto the P space, and $\mathcal{Q}$ be the operator that projects onto the Q space.

We choose the Bloch form of the effective Hamiltonian. The Bloch form of the effective Hamiltonian has several advantages compared to the traditional Tamm–Dancoff effective Hamiltonian used in previous studies of positronium on the Light

Front [13]. The Bloch effective Hamiltonian has only unperturbed energies in the energy denominators, as opposed to an energy eigenvalue which then needs to be found in a self-consistent manner. The Bloch Hamiltonian is also automatically Hermitian. The Bloch Hamiltonian is given by:

$$\langle f|H_{\rm eff}|i\rangle = \langle f|\mathcal{P}H\mathcal{P}|i\rangle + \frac{1}{2}\sum_n \langle f|\mathcal{P}H\mathcal{Q}|n\rangle\langle n|\mathcal{Q}H\mathcal{P}|i\rangle\left[\frac{1}{\epsilon_i-\epsilon_n}+\frac{1}{\epsilon_f-\epsilon_n}\right]. \quad (9)$$

Here, $H = H_{LC} = P^2$ is the Light-Cone Hamiltonian introduced above. States i and f are states in P space ($|e^+e^-\rangle$), while state n is in the Q space ($|e^+e^-\gamma\rangle$). ϵ_i is the unperturbed energy of state i, etc. Note that if $i = f$ this reduces to the usual formula from second-order energy shift in perturbation theory. Furthermore, note that, due to the definition of H_{LC}, both the "Hamiltonian" and the "energy" have mass-squared dimensions. The mass eigenvalues are thus the square root of the eigenvalues of H_{LC}. The derivation of (9), based on a perturbative expansion of the Okubo–Lee–Suzuki effective Hamiltonian [14–19], is given in Ref. [20].

$\mathcal{P}H\mathcal{P}$ is the part of the Hamiltonian that acts within the two-particle space. It contains two pieces. First, it contains the two-particle kinetic energy. Secondly, it contains the Light-Front instantaneous photon exchange interaction. Thus it can be expressed as

$$\mathcal{P}H\mathcal{P} = \mathcal{P}\left(H_0 + H_{\rm inst}\right)\mathcal{P}. \quad (10)$$

The instantaneous photon exchange interaction $H_{\rm inst}$ contains a singularity of the form $\frac{1}{(x_1-x_1')^2}$, where x_1 (x_1') is the longitudinal momentum fraction of the incoming (outgoing) fermion. This singularity is not physical and must be cancelled.

Since we are interested in primarily the effects of repeated photon exchange, we will only include those combinations of terms in $\mathcal{P}H\mathcal{Q}$ and $\mathcal{Q}H\mathcal{P}$ which generate the photon exchange. We neglect the combinations which result in the photon being emitted and absorbed by the same fermion. That is, we do not incorporate the fermion self-energy, and therefore no fermion mass renormalization is necessary in this model. In addition, we work with unit-normalized eigenstates and a fixed value of the coupling constant.

In Light-Front S-matrix perturbation theory $i = f$. In momentum space, the sum in (9) reduces to a sum over the polarization states of the photon:

$$\sum_\lambda \epsilon_\mu\left(k,\lambda\right)\epsilon_\nu^*\left(k,\lambda\right) = -g_{\mu\nu} + \frac{k_\mu\eta_\nu + k_\nu\eta_\mu}{k^\kappa\eta_\kappa}, \quad (11)$$

where $\eta^\mu = \left(\eta^+,\eta^-,\eta^\perp\right) = (0,2,\mathbf{0})$ is a unit null vector. The second term in (11) generates a term identical to the instantaneous photon exchange term of the Light-Front Hamiltonian, but opposite in sign. That is, a piece of the second term on the RHS of (9) cancels the instantaneous exchange piece [$H_{\rm inst}$ in (10)] of the first term on the RHS of (9), leaving the effective interaction free of Light-Front small-x divergences [2, 8].

In our non-perturbative calculation $i \neq f$ and the cancellation of small-x singularities does not occur in general. This leaves the effective potential with an unphysical singularity, and the resulting interaction is unstable with increasing K. The numerical calculation, as a result, does not converge to a finite number in the continuum limit.

To cure this pathology, we introduce a counterterm of the form

$$\langle f|H_{\rm ct}|i\rangle = -\sum_n \langle f|\mathcal{P}H\mathcal{Q}|n\rangle\,\langle n|\mathcal{Q}H\mathcal{P}|i\rangle\left[\frac{(a-b)^2}{2ab\,(a+b))}\right], \quad (12)$$

where $a = \epsilon_i - \epsilon_n$ and $b = \epsilon_f - \epsilon_n$. The resulting effective potential is

$$\langle f|H_{\rm eff}^{\rm new}|i\rangle = \langle f|(H_{\rm eff}+H_{\rm ct})|i\rangle = \langle f|\mathcal{P}H\mathcal{P}|i\rangle + \sum_n \frac{\langle f|\mathcal{P}H\mathcal{Q}|n\rangle\langle n|\mathcal{Q}H\mathcal{P}|i\rangle}{\frac{1}{2}[(\epsilon_i-\epsilon_n)+(\epsilon_f-\epsilon_n)]}. \quad (13)$$

In this form the cancellation of the instantaneous diagram does occur, and $H_{\rm eff}^{\rm new}$ is free of unphysical Light-Front small-x singularities. We note that our choice of counterterm is equivalent to the prescription used in previous work in Light-Front effective potentials [13].

By substituting in the terms from the LFQED Hamiltonian, along with the free-field momentum-space mode expansions, the effective potential can be easily derived, and the cancellation of the instantaneous diagram verified. The sum over intermediate states is performed in momentum space, before translating the result back to the HO basis.

The result, after canceling the instantaneous interaction, is

$$\begin{aligned}\langle f|H_{\rm eff}^{\rm new}|i\rangle = \langle f|PH_0P|i\rangle + \alpha\frac{\delta_{x_1+x_2}^{x_1'+x_2'}}{K}\sqrt{x_1x_2x_1'x_2'}\int\frac{d^2q_1}{(2\pi)^2}\frac{d^2q_2}{(2\pi)^2}\frac{d^2q_1'}{(2\pi)^2}\frac{d^2q_2'}{(2\pi)^2}\\ \times\frac{\Psi_{n_1}^{m_1}(q_1)\,\Psi_{n_2}^{m_2}(q_2)\,\Psi_{n_1'}^{m_1'*}(q_1')\,\Psi_{n_2'}^{m_2'*}(q_2')\,\bar u(1')\,\gamma^\mu\,u(1)\,\bar v(2)\,\gamma_\mu\,v(2')}{\frac{x_1-x_1'}{2}[(\epsilon_i-\epsilon_n)+(\epsilon_f-\epsilon_n)]}\\ \times(2\pi)^2\,\delta^{(2)}\Big(\sqrt{x_1}q_1+\sqrt{x_2}q_2-\sqrt{x_1'}q_1'-\sqrt{x_2'}q_2'\Big), \quad (14)\end{aligned}$$

where u and v are the 4-component Dirac spinors and

$$\begin{aligned}\epsilon_i-\epsilon_n &= \frac{x_1q_1^2+m^2}{x_1}-\frac{x_1'q_1'^2+m^2}{x_1'}-\frac{\left(\sqrt{x_1}q_1-\sqrt{x_1'}q_1'\right)^2+\mu^2}{x_1-x_1'},\\ -(\epsilon_f-\epsilon_n) &= \frac{x_2q_2^2+m^2}{x_2}-\frac{x_2'q_2'^2+m^2}{x_2'}-\frac{\left(\sqrt{x_2}q_2-\sqrt{x_2'}q_2'\right)^2+\mu^2}{x_2-x_2'}.\end{aligned} \quad (15)$$

(μ is a fictitious photon mass; see below.) The integral is evaluated using repeated 2D Talmi–Moshinsky (TM) transformations [21]. With the help of these TM transformations, the integral can be reduced down to a single 2D integral, which is evaluated numerically. The details of the calculation will be presented elsewhere [22].

The effective potential $H_{\rm eff}^{\rm new}$ has one remaining singularity we have not yet discussed. In the event that $x_1 = x_1'$ and $\mu = 0$, the integrations diverge in the low transverse-momentum limit. The singularity thus corresponds to the case where the photon has zero momentum. The exact same singularity was found within the context of a Bloch Hamiltonian on the Light Front in Ref. [20]. The integral has no singularity if $\mu \neq 0$. This is why we have introduced μ as a regulator for this physical infrared divergence. Thus, in addition to examining the limits $K \to \infty$ and $N_{\rm max} \to \infty$, we must also consider the limit $\mu \to 0$.

4 Numerical results

In non-relativistic Quantum Mechanics, the hyperfine splitting between the $^1S_0$ and $^3S_1$ states of positronium scales as α^4, where α is the fine structure constant. At physical coupling, the expected hyperfine splitting and even the binding energy are then uncomfortably small relative to the precision of our numerical integrals. Since we would like to use the hyperfine splitting to test our BLFQ results, we use a large coupling of $\alpha = 0.3$ to exaggerate both the binding energy and the hyperfine splitting. We then compare our results not to experiment, but to the predictions of

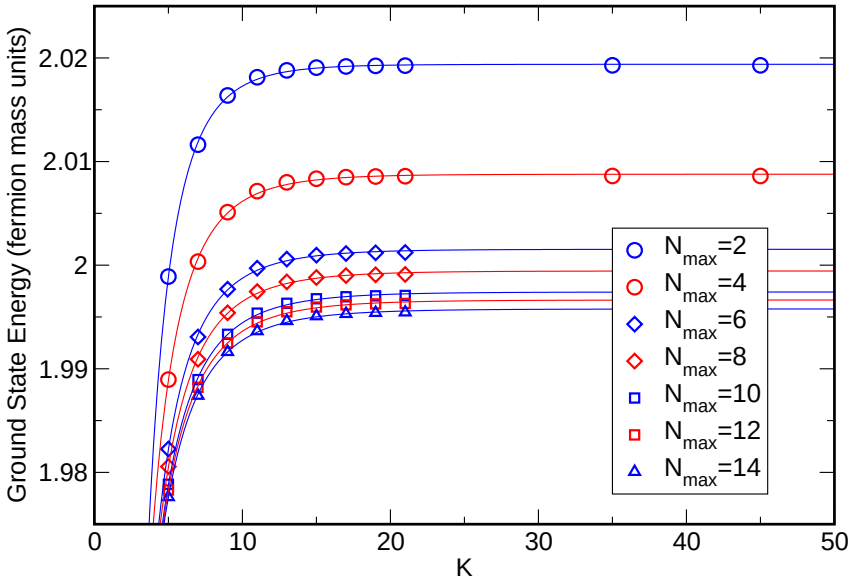

Figure 1: Convergence of the ground state energy with respect to K for various values of $N_{\max}$. The parameters used are $\alpha = 0.3$, $b = 0.5\, m_f$ and $\mu = 0.1\, m_f$. Ground state energy below 2 fermion mass units represents a bound state.

non-relativistic Quantum Mechanics at this unphysical value of α. This value of α also allows a direct comparison to the Discretized Light-Cone Quantization (DLCQ) results of Ref. [13].

The numerical results were obtained using the Hopper Cray XE6 at NERSC. ScaLAPACK software [23] was used for the diagonalization. In this particular implementation of BLFQ, the resulting matrix is quite dense. However, in future applications involving multiple Fock sectors, the matrix will be extremely sparse.

Figure 1 shows the convergence of the ground state energy as a function of K for various values of $N_{\max}$. In this plot, the basis energy parameter is chosen to be $b = 0.5\, m$, where m is the fermion mass. We also take $\mu = 0.1\, m$. The same plot made with a different value of μ would look qualitatively similar, but with differing absolute energies. The ground state energy is also expressed in fermion mass units. Thus a ground state energy below 2 indicates a bound state. The ground state energy is seen to converge rapidly with increasing K. The fitting function used to make the extrapolations is

$$E = a + be^{-c\sqrt{K}}. \tag{16}$$

The parameter a is taken to be the result at infinite K for a given $N_{\max}$.

We can then plot these extrapolated values as a function of $N_{\max}$. The result is shown in Fig. 2. The four curves represent different values of our infrared regulator μ. The ground state energy shows a converging trend as a function of $N_{\max}$, although the convergence is slow. In addition, the binding becomes deeper as we decrease the infrared cutoff μ. For each μ, the curve is fit to the function

$$E = a + be^{-c\sqrt{N_{\max}}}. \tag{17}$$

The value of a is then taken to be the ground state energy in the limit $K \to \infty$ and $N_{\max} \to \infty$ for a given value of μ.

Next we must examine the limit $\mu \to 0$. The results for the limit $K \to \infty$ and $N_{\max} \to \infty$ are plotted as a function of $\sqrt{\mu}$ in Fig. 3 as the circles. A linear fit is obtained. The diamonds represent values for the first excited state, calculated in

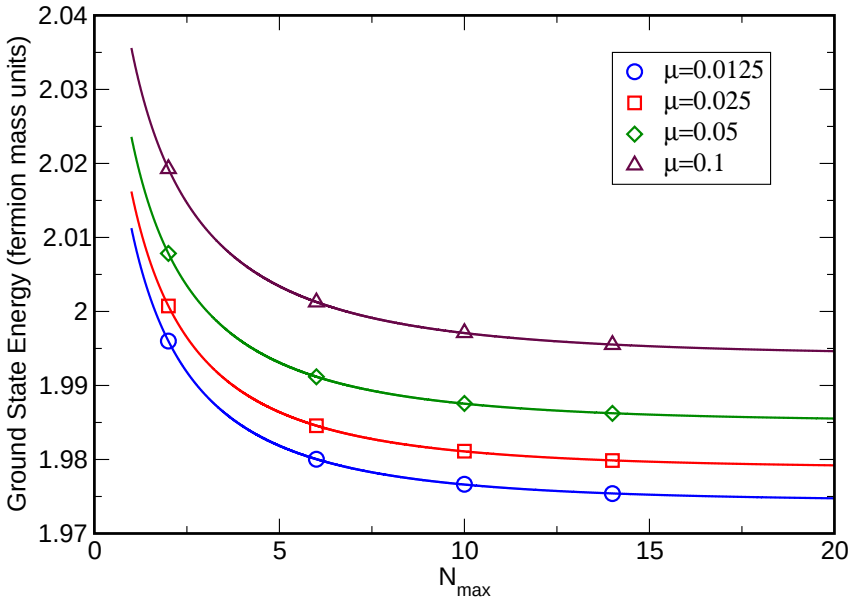

Figure 2: Convergence of the ground state energy with respect to $N_{\max}$ for various values of infrared regulator μ ($\alpha = 0.3$ and $b = 0.5 m_f$). Each point has already been extrapolated to the $K \to \infty$ limit as shown in Fig. 1.

exactly the same fashion as the ground state curve. We will compare the splitting between these states to the expected hyperfine splitting.

While we cannot yet calculate the total angular momentum of these states, our identification of the ground state being a $J = 0$ state and the first excited state being a $J = 1$ state is strongly suggested by the following argument. When we do

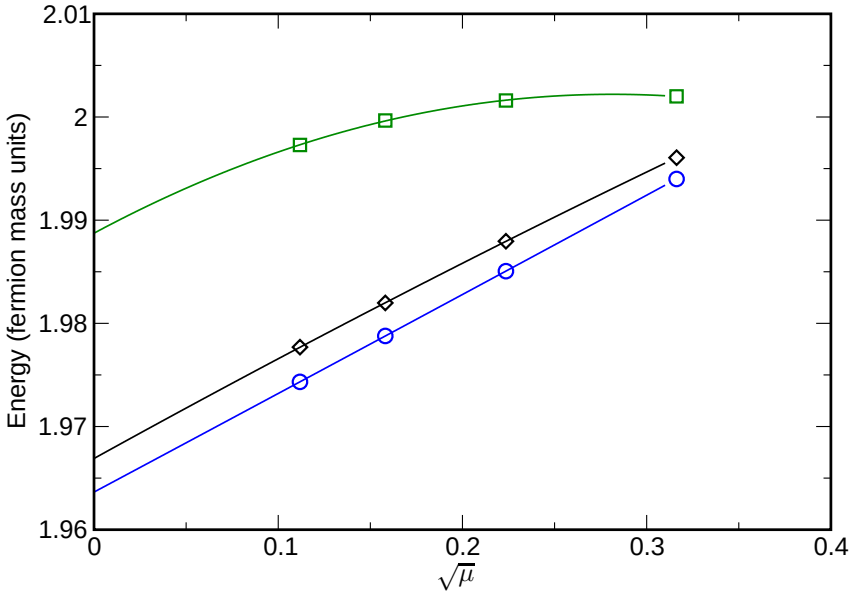

Figure 3: Converged (with respect to $N_{\max}$ and K) spectrum as a function of $\sqrt{\mu}$ for $\alpha = 0.3$. Lowest line is the ground state of $M_J = 0$ sector, middle line is the ground state of $M_J = \pm 1$ sector and upper line is the ground state of $M_J = \pm 2$ sector.

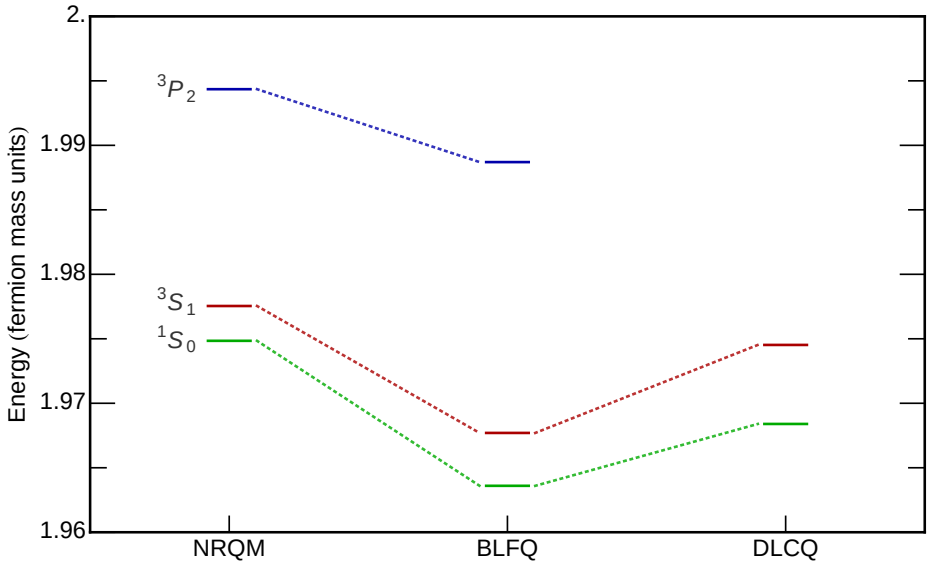

Figure 4: Comparison of BLFQ results to other methods. Quantum Mechanics results are from Ref. [24]. Results reported for DLCQ (Ref. [13]) are the result of a Padé extrapolation of a non-converging trend (see Outlook). Dotted lines are only to guide the eye; we have not calculated total J for these states in BLFQ (see text).

the calculation for $M_J = 0$, we see these two states. If we then do the calculation at $M_J = \pm 1$, the lower state disappears and the remaining state is nearly (but not identically) degenerate with the higher state in the $M_J = 0$ calculation. Furthermore, both states have disappeared at $M_J = \pm 2$. This suggests that our ground state has $J = 0$ and the first excited state has $J = 1$, but we cannot yet prove this statement.

The squares in Fig. 3 represent the ground state of our $M_J = \pm 2$ calculation. This state disappears when we go up to $M_J = \pm 3$. This again suggests that this state has $J = 2$, but we cannot yet prove it. We will then compare this state to the lowest $J = 2$ state of the postironium system, which is the $^3P_2$ state. The curve is fit to a second order polynomial.

The intercepts of the curves in Fig. 3 with the vertical axis (at $\mu = 0$) thus represent the energies in the limit $K \to \infty$, $N_{\max} \to \infty$ and $\mu \to 0$ and can be compared to the predictions of non-relativistic Quantum Mechanics, and other non-perturbative schemes. This comparison is made in Fig. 4. The BLFQ results are seen to be qualitatively similar to the NRQM expectations, but with a significant overbinding. The hyperfine splitting is well reproduced. The BLFQ results are also compared to the DLCQ results of Ref. [13]. Those authors also find an overall overbinding, and a hyperfine splitting of the correct order of magnitude. They do not report a numerical result for the $J = 2$ state.

5 Summary and outlook

We have calculated the spectrum of the positronium system in the non-perturbative Basis Light-Front Quantization approach. Instead of tackling the problem directly with a dynamical photon, we have introduced a two-body effective interaction, which implements the effects of photon exchange, but not the fermion self-energy. Thus no mass renormalization was necessary in this calculation. The final converged results

agree qualitatively with the expectations of NRQM and previous work in DLCQ, with a tendency toward overbinding.

We note that previous authors [13, 25] who have worked on ladder truncation of positronium on the Light Front have seen a slight dependence on the ultraviolet cutoff of the theory. These authors claim that the divergence they see will be cancelled when crossed ladder graphs are included in the interaction kernel. While currently we see no evidence of such a divergence, we accept that it is present and believe that we are simply not yet at high enough $N_{\max}$ to be sensitive to it. These issues will be explored in future work.

Our two-body effective potential model should also be applicable to heavy quarkonia if we include a confining potential, such as the one motivated by "soft wall" AdS/QCD [26–28]. The effective interaction implemented here could then be interpreted as providing a first correction to the basic AdS/QCD spectrum.

Implementation of the problem with one or more dynamical photons in the basis requires the implementation of a non-perturbative renormalization scheme, such as the Fock Sector dependent scheme of Karmanov *et al.* [29]. In addition, the cancellation of unphysical Light-Front singularities would need to occur numerically within the matrix diagonalization, and not analytically as is done here. The full potential of BLFQ will be realized only when these difficulties are overcome.

Acknowledgements

We thank Stanley J. Brodsky, Heli Honkanen and Dipankar Chakrabarti for fruitful discussions. This work was supported in part by the Department of Energy under Grant Nos. DE-FG02-87ER40371 and DESC0008485 (SciDAC-3/NUCLEI) and by the National Science Foundation under Grant No. PHY-0904782. A portion of the computational resources were provided by the National Energy Research Scientific Computing Center (NERSC), which is supported by the Office of Science of the U.S. Department of Energy under Contract No. DE-AC02-05CH11231.

References

[1] J. P. Vary *et al.*, Phys. Rev. C **81**, 035205 (2010).

[2] S. J. Brodsky, H.-C. Pauli and S. S. Pinsky, Phys. Rept. **301**, 299 (1998).

[3] W.-M. Zhang and A. Harindranath, Phys. Rev. D **48**, 4868 (1993).

[4] P. Navrátil, J. P. Vary and B. R. Barrett, Phys. Rev. Lett. **84**, 5728 (2000).

[5] H. Honkanen, P. Maris, J. P. Vary and S. J. Brodsky, Phys. Rev. Lett. **106**, 061603 (2011).

[6] X. Zhao, H. Honkanen, P. Maris, J. P. Vary and S. J. Brodsky, Few-Body Syst. **52**, 339 (2011).

[7] X. Zhao, A. Ilderton, P. Maris and J. P. Vary, Phys. Rev. D **88**, 065014 (2013).

[8] A. Harindranath, *Light Front QCD: Lecture notes*, Saha Institute of Nuclear Physics, Kolkata (2005).

[9] K. Hornbostel, S. J. Brodsky and H.-C. Pauli, Phys. Rev. D **41**, 3814 (1990).

[10] D. H. Gloeckner and R. D. Lawson, Phys. Lett. B **53**, 313 (1974).

[11] P. Maris, P. W. Wiecki, Y. Li, X. Zhao and J. P. Vary, Acta Phys. Polon. Suppl. **6**, 321 (2013).

[12] Y. Li, P. W. Wiecki, X. Zhao, P. Maris and J. P. Vary, *see these Proceedings*, p. 136, http://www.ntse-2013.khb.ru/Proc/YLi.pdf.

[13] M. Krautgärtner, H. C. Pauli and F. Wölz, Phys. Rev. D **45**, 3755 (1992).

[14] S. Okubo, Progr. Theor. Phys. **12**, 603 (1954).

[15] K. Suzuki and S.Y. Lee, Progr. Theor. Phys. **64**, 2091 (1980).

[16] K. Suzuki, Progr. Theor. Phys. **68**, 246 (1982).

[17] K. Suzuki and R. Okamoto, Progr. Theor. Phys. **70**, 439 (1983).

[18] K. Suzuki, Progr. Theor. Phys. **68**, 1999 (1982).

[19] K. Suzuki and R. Okamoto, Progr. Theor. Phys. **92**, 1045 (1994).

[20] D. Chakrabarti and A. Harindranath, Phys. Rev. D **64**, 105002 (2001).

[21] L. Chaos-Cador and E. Ley-Koo, Int. J. Quantum Chem. **97**, 844 (2004).

[22] P. W. Wiecki, Y. Li, X. Zhao, P. Maris and J. P. Vary, *in preparation.*

[23] L. S. Blackford *et al.*, *ScaLAPACK Users' Guide*, Society for Industrial and Applied Mathematics, Philadelphia, 1997.

[24] H. A. Bethe and E. E. Salpeter, *Quantum Mechanics of One- and Two-Electron Atoms*, Springer, Heidelberg, 1957.

[25] M. Mangin-Brinet, J. Carbonell and V.A. Karmanov, Phys. Rev. C **68**, 055203 (2003).

[26] A. Karch, E. Katz, D. T. Son and M. A. Stephanov, Phys. Rev. D **74**, 015005 (2006).

[27] J. Erlich, E. Katz, D. T. Son and M. A. Stephanov, Phys. Rev. Lett. **95**, 261602 (2005).

[28] G. F. de Teramond and S. J. Brodsky, Phys. Rev. Lett. **102**, 081601 (2009).

[29] V. A. Karmanov, J.-F. Mathiot and A. V. Smirnov, Phys. Rev. D **77**, 085028 (2008).

NTSE-2013 Keynote Talk:

Nuclear Forces from Lattice Quantum Chromodynamics

Martin J. Savage

Institute for Nuclear Theory, Box 351550, Seattle, WA 98195-1550, USA

Abstract

A century of coherent experimental and theoretical investigations have uncovered the laws of nature that underly nuclear physics. The standard model of strong and electroweak interactions, with its modest number of input parameters, dictates the dynamics of the quarks and gluons — the underlying building blocks of protons, neutrons, and nuclei. While the analytic techniques of quantum field theory have played a key role in understanding the dynamics of matter in high energy processes, they encounter difficulties when applied to low-energy nuclear structure and reactions, and dense systems. Expected increases in computational resources into the exa-scale during the next decade will provide the ability to numerically compute a range of important strong interaction processes directly from QCD with quantifiable uncertainties using the technique of lattice QCD. These calculations will refine the chiral nuclear forces that are used as input into nuclear many-body calculations, including the three- and four-nucleon interactions. I discuss the state-of-the-art lattice QCD calculations of quantities of interest in nuclear physics, progress that is expected in the near future, and the impact upon nuclear physics.

Keywords: *Nuclear forces; lattice QCD*

1 Introduction

A nucleus is at the heart of every atom, and loosely speaking, is a collection of protons and neutrons that interact pairwise, with much smaller, but significant, three-body interactions. We are fortunate to know that the underlying laws governing the strong interactions result from a quantum field theory called quantum chromodynamics (QCD). It is constructed in terms of quark and gluon fields with interactions determined by a local SU(3) gauge-symmetry and, along with quantum electrodynamics (QED), underpins all of nuclear physics when the five relevant input parameters, the scale of strong interactions $\Lambda_{\rm QCD}$, the three light-quark masses m_u, m_d and m_s, and the electromagnetic coupling α_e, are set to their values in nature. It is remarkable that the complexity of nuclei emerges from "simple" gauge theories with just five input parameters. Perhaps even more remarkable is that nuclei resemble collections of nucleons and not collections of quarks and gluons. By solving QCD, we are expecting to predict, with arbitrary precision, nuclear processes and the properties of multi-baryon systems.

The fine-tunings observed in the structure of nuclei, and in the interactions between nucleons, are peculiar and fascinating aspects of nuclear physics. For the values

Proceedings of International Conference 'Nuclear Theory in the Supercomputing Era — 2013' (NTSE-2013), Ames, IA, USA, May 13–17, 2013. Eds. A. M. Shirokov and A. I. Mazur. Pacific National University, Khabarovsk, Russia, 2014, p. 156.

http://www.ntse-2013.khb.ru/Proc/Savage.pdf.

of the input parameters that we have in our universe, the nucleon-nucleon (NN) interactions are fine-tuned to produce unnaturally large scattering lengths in both s-wave channels [described by non-trivial fixed-points in the low-energy effective field theory (EFT)], and the energy levels in the ^{8}Be-system, ^{12}C and ^{16}O are in "just-so" locations to produce enough ^{12}C to support life, and the subsequent emergence and evolution of the human species. At a fundamental level it is important for us to determine the sensitivity of the abundance of ^{12}C to the light-quark masses and to ascertain the degree of their fine-tuning.

Being able to solve QCD for the lightest nuclei, using the numerical technique of lattice QCD (LQCD), would allow for a partial unification of nuclear physics. It would be possible to "match" the traditional nuclear physics techniques — the solution of the quantum many-body problem for neutrons and protons using techniques such as No-Core Shell Model (NCSM), Green's Function Monte Carlo (GFMC), and others, to make predictions for the structure and interactions of nuclei for larger systems than can be directly calculated with LQCD. By placing these calculations on a fundamental footing, reliable predictions with quantifiable uncertainties can then be made for larger systems.

2 Chiral nuclear forces

During the 1990's, the nuclear forces were systematized by the hierarchy emerging from the spontaneously broken chiral symmetries of QCD. The resulting small expansion parameters are powers of the external momenta and powers of the light-quark masses normalized to the scale of chiral symmetry breaking, as pioneered by Weinberg, first in the meson sector and then the multi-nucleon sector [1–3]. In addition to generating nuclear forces that are consistent with QCD, this construction provides the calculational advantage of parametric estimates of the systematic uncertainty introduced by the truncation of the nuclear interactions at a given order in the expansion. The actual ordering of contributions remains a subject of debate even today, with Weinberg's chiral expansion of the potential having its peculiar difficulties, as does the KSW expansion of scattering amplitudes [4, 5]. Calculations are being performed at a sufficiently high order where the size of truncation errors is quite small. Weinberg's ordering of operators based upon a chiral expansion of the n-body potentials between nucleons has been carried out to N^{3}LO, which includes contributions to the three-body (starting at N^{2}LO) and the leading four-body interactions (starting at N^{3}LO) (for a recent review see Ref. [6]).

During the last several years, nuclear structure calculations have been performed with the chiral nuclear forces, leading to both postdictions and predictions for nuclei to a given order in the expansion, and compared with experiment, e. g., see Fig. 1. The nuclear forces that are presently used in such calculations are constrained by experimental measurements of NN scattering and light nuclei. As the desired precision increases, which requires working to higher orders in the expansion, the number of required experimental constraints increases. Eventually, there are too few experimental constraints to practically reduce the systematic uncertainty below some level in any given calculation. However, LQCD calculations are expected to provide a way to constrain the nuclear forces beyond what is possible with experiment, and hence to further reduce the systematic uncertainties in nuclear structure calculations. Beyond providing direct calculations of important quantities, LQCD calculations of the light nuclei and nuclear forces can

1. verify experimental constraints and/or reduce the uncertainties in the constraints imposed by experiment,

2. constrain components of the nuclear forces that are inaccessible to experiment,

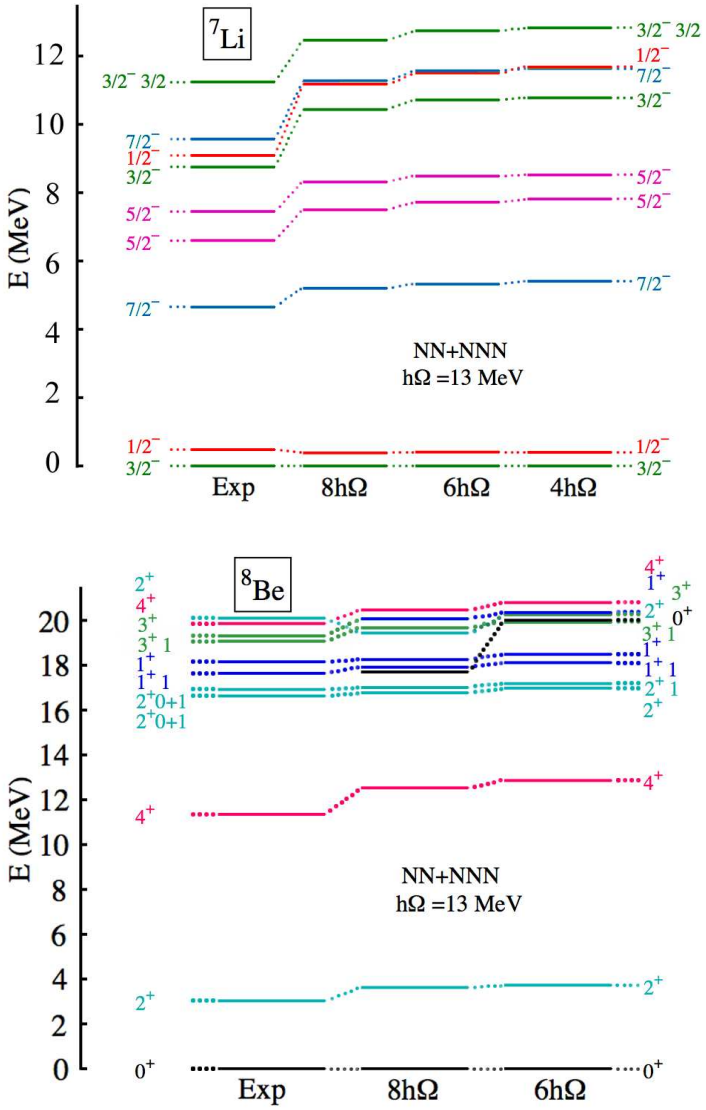

Figure 1: NCSM calculations of lowest-lying levels in ^{7}Li and ^{8}B using chiral nuclear forces [7]. Image is reproduced with the permission of P. Maris.

for instance the light-quark mass dependences which dictates some of the multi-pion vertices, and multi-neutron forces,

3. constrain counterterms at higher orders in the expansion to further reduce the systematic uncertainties.

3 Lattice QCD

LQCD is a technique in which space-time is discretized into a four-dimensional grid and the QCD path integral over the quark and gluon fields at each point in the grid is performed in Euclidean space-time using Monte Carlo methods. A LQCD calculation of a given quantity will deviate from its value in nature because of the finite volume of the space-time (with $L^3 \times T$ lattice points) over which the fields exist, and the finite separation between space-time points (the lattice spacing, b). However, such deviations can be systematically removed by performing calculations in multiple vol-

umes with multiple lattice spacings, and extrapolating using the theoretically known functional dependences on each. Supercomputers are needed for such calculations due to the number of space-time points and the Monte Carlo evaluation of the path integral over the dynamical fields. In order for a controlled continuum extrapolation, the lattice spacing must be small enough to resolve structures induced by the strong dynamics, encapsulated by $b\Lambda_\chi \ll 1$ where Λ_χ is the scale of chiral symmetry breaking. Further, in order to have the hadron masses, and also the scattering observables, exponentially close to their infinite-volume values, the lattice volume must be large enough to contain the lightest strongly interacting particle, encapsulated by $m_\pi L \gtrsim 2\pi$ where m_π is the mass of the pion and L is the extent of the spatial dimension of the cubic lattice volume (this, of course, can be generalized to non-cubic volumes). Effective field theory (EFT) descriptions of these observables exist for $b\Lambda_\chi \lesssim 1$ [the Symanzik action and its translation into chiral perturbation theory (χPT) and other frameworks] and $m_\pi L \gtrsim 2\pi$ (the p-regime of χPT and other frameworks). The low-energy constants in the appropriate EFT are fit to the results of the LQCD calculations, which are then used to take the limit $b \to 0$ and $L \to \infty$. Computational resources devoted to LQCD calculations are becoming sufficient to be able to perform calculations at the physical values of the light quark masses in large enough volumes and at small enough lattice spacings to be relevant, but the majority of present day calculations are performed with pion masses of $m_\pi \gtrsim 200$ MeV. Therefore, most calculations require the further extrapolation of $m_q \to m_q^{\rm phys}$, but do not yet include strong isospin breaking or electromagnetism. In principle, the gauge-field configurations that are generated in LQCD calculations can be used to calculate an enormous array of observables, spanning the range from particle to nuclear physics. In practice, this is becoming less common, largely due to the different scales relevant to particle physics and to nuclear physics. Calculations of quantities involving the pion with a mass of $m_\pi \sim 140$ MeV are substantially different from those of, say, the triton with a mass of $M(^3\mathrm{H}) \sim 3$ GeV, and with the typical scale of nuclear excitations being $\Delta E \sim 1$ MeV. Present day dynamical LQCD calculations of nuclear physics quantities are performed with $m_\pi \sim 400$ MeV, lattice spacings of $b \sim 0.1$ fm and volumes with spatial extent of $L \sim 4$ fm.

LQCD calculations are approached in the same way that experimental efforts use detectors to measure one or more quantities — the computer is equivalent to the accelerator and the algorithms, software stack, and parameters of the LQCD calculation(s) are the equivalent of the detector. The parameters, such as lattice spacing, quark masses and volume, are selected based upon available computational resources, and simulations of the precision of the calculation(s) required to impact the physical quantity of interest, i. e. simulations of the LQCD Monte Carlos are performed. The size of the computational resources required for cutting edge calculations are such that you only get "one shot at it". A typical work-flow of a LQCD calculation consists of three major components. The first component is the production of an ensemble of gauge-field configurations which contain statistically independent samplings of the gluon fields resulting from the LQCD action. The production of gauge-fields requires the largest partitions on the leadership class computational facilities, typically requiring $\gtrsim$ 128K compute cores. Present-day calculations have $n_f = 0$, 2, 2+1, 3, 2+1+1 dynamical light-quark flavors and use the Wilson, $\mathcal{O}(b)$-improved-Wilson, staggered (Kogut–Susskind), domain-wall or overlap discretizations, each of which have their own "features". It is the evaluation of the light-quark determinant (the determinant of a sparse matrix with dimensions $\gtrsim 10^8 \times 10^8$) that consumes the largest fraction of the resources. Roughly speaking, $\gtrsim 10^4$ Hybrid Monte Carlo (HMC) trajectories are required to produce an ensemble of 10^3 decorrelated gauge fields, but in many instances this is an under estimate. For observables involving quarks, a second component of production is the determination of the light-quark propagators on each of the configurations. The light-quark propagator from a given source point (an example of which

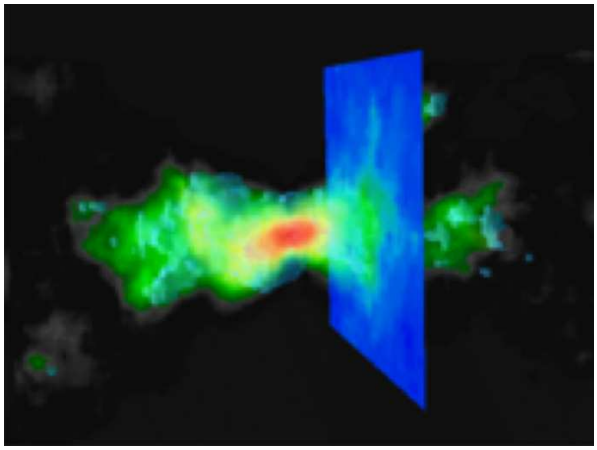

Figure 2: An example of (the real part of one component of) a light-quark propagator. The (blue) "wall" corresponds to the anti-periodic boundary conditions imposed in the time direction. Image is reproduced with the permission of R. Gupta.

is shown in Fig. 2) is determined by an iterative inversion of the quark two-point function, using the conjugate-gradient (CG) algorithm or variants thereof such as BiCGSTAB, or the most recently developed multi-grid (MG). During the last couple of years, the propagator production codes have been ported to run on GPU machines in parallel. GPU's can perform propagator calculations faster than standard CPU's by an order of magnitude, and have led to a major reduction in the statistical uncertainties in many calculations. There have been numerous algorithm developments that have also reduced the resources required for propagator production, such as the implementation of deflation techniques and the use of multi-grid methods. The third component of a LQCD calculation is the production of correlation functions from the light-quark propagators. This involves performing all of the Wick contractions that contribute to a given quantity. The number of contractions required for computing a single hadron correlation function is small. However, to acquire long plateaus in the effective mass plots (EMPs) that persist to short times, Lüscher–Wolff type methods involve the computation of a large number of correlation functions resulting from different interpolating operators, and the number of contractions can become large. In contrast, the naive number of contractions required for a nucleus quickly becomes astronomically large ($\sim 10^{1500}$ for uranium), but symmetries in the contractions, and new algorithms (e. g. Ref. [8]) greatly reduce the number of operations that must be performed. A further consequence of the hierarchy of mass scales is that there is an asymptotic signal-to-noise problem in nuclear correlation functions. The ratio of the mean value of the correlation function to the variance of the sample from which the mean is evaluated degrades exponentially at large times. However, this is absent at short and intermediate times and the exponential degradation of the signal-to-noise in the correlation functions can be avoided.

4 Cold nuclear physics with lattice QCD

Capability computing resources provided by leadership class computing facilities are used to produce ensembles of gauge-field configurations, while capacity computing resources, both those operated by USQCD and elsewhere are used to perform observable-dependent calculations of correlation functions using these configurations. Thus the capability resources enable a multitude of physics calculations to be accomplished with the capacity resources. In the area of cold nuclear physics there is currently a

well-defined set of goals, and a program in place to accomplish these goals, as described in one of the 2013 USQCD Whitepapers [9]: **Hadron Structure**, **Hadron Spectroscopy**, **Hadronic Interactions, Nuclear Forces and Nuclei**, and **Fundamental Symmetries**.

4.1 The spectra and structure of the hadrons

Before calculations of nuclei can be sensibly undertaken, the mass and structure of the nucleon must be reproduced in LQCD calculations. The spectrum of the lowest-lying hadrons calculated with LQCD is shown in Fig. 3, from which we observe that indeed LQCD is postdicting all of the light-hadron masses within uncertainties. Beyond its mass, one property of the nucleon that is well known experimentally is the forward-matrix element of the isovector axial current, g_A. Significant effort has been put into calculating g_A with LQCD, a summary of which is shown in Fig. 4, but the extrapolated LQCD value has consistently been smaller than the experimental value. With calculations beginning to be performed at the physical pion mass, the community is focused on understanding and quantifying the systematic uncertainties in these calculations.

A central element of the physics program at JLab is to determine the excited spectra of mesons and baryons, including searching for exotic states that are beyond the naive nonrelativistic quark model of hadrons, but arise naturally in QCD. A critical component of this program is the LQCD calculations of the spectra. They will play a central role in interpreting and understanding the experimental measurements. The spectra of such states is complicated by the presence of open multi-hadron channels and significant formal developments remain to be put in place before rigorous statements about the spectra can be made. Calculations at unphysical pion masses have been performed by the JLab LQCD group, examples of which are shown in Fig. 5, and remarkable progress has been made in the identification of states in these calculations. The aim is to have LQCD predict the exotic spectra of hadrons before, or at the same time as, the GlueX experiment at JLab runs, targeting the 2018 milestone HP15.

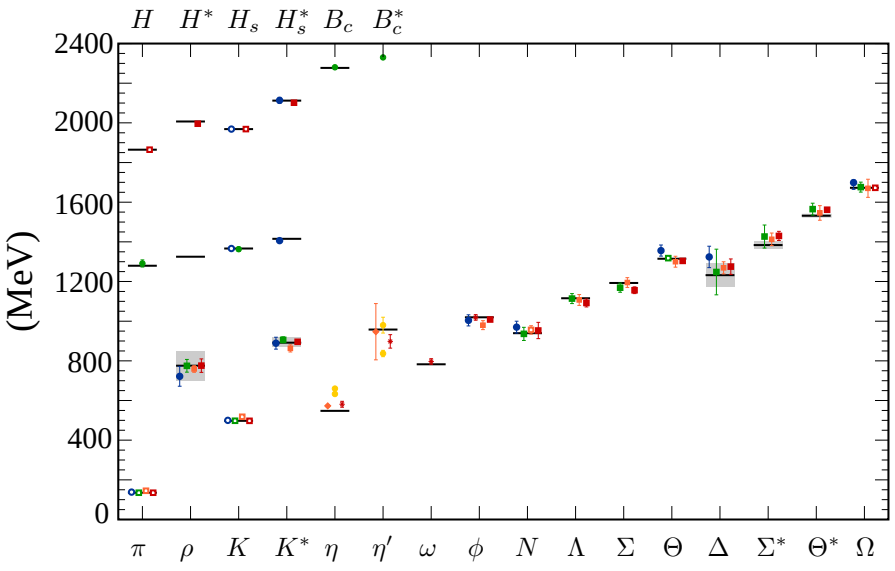

Figure 3: A summary of the low-lying hadron masses calculated with LQCD [10,11]. Image is reproduced with the permission of A. Kronfeld.

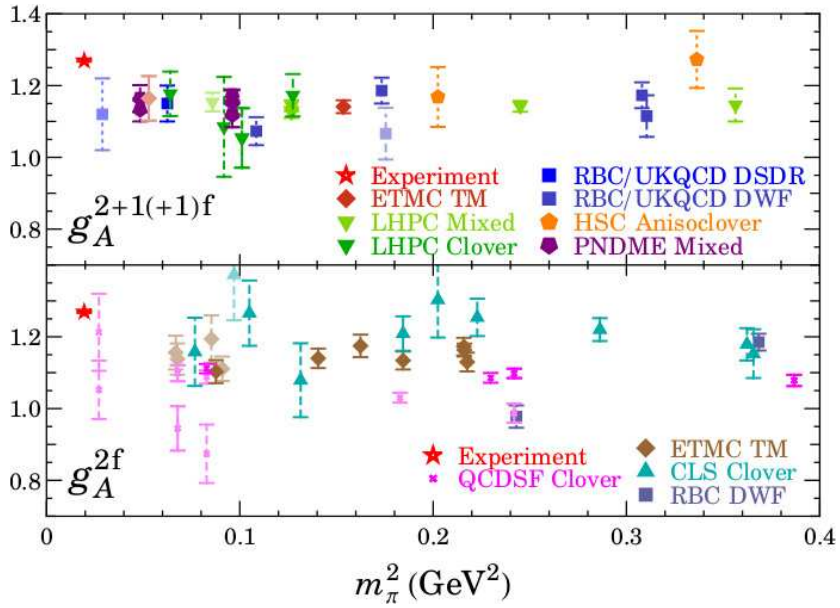

Figure 4: A summary of LQCD calculations of g_A [12]. Image is reproduced with the permission of H.-W. Lin.

4.2 Meson-meson scattering

Multi-hadron LQCD calculations are significantly more challenging than single-hadron calculations for a number of reasons, and systems involving baryons are even more challenging. Meson-meson systems are the simplest multi-hadron systems, and impressive progress has been made in the recent past, particularly when the LQCD calculations are combined with χPT. There is little or no signal-to-noise problem in such calculations and therefore highly accurate LQCD calculations of stretched-isospin states can be performed with modest computational resources. Moreover, the EFTs which describe the low-energy interactions of pions and kaons, including lattice-spacing and finite-volume effects, have been developed to non-trivial orders in the chiral expansion. The $I = 2$ pion-pion ($\pi^+\pi^+$) scattering length serves as a benchmark calculation with an accuracy that can only be aspired to in other systems. The scattering lengths for $\pi\pi$ scattering in the s-wave are uniquely predicted at LO in χPT [14]:

$$m_{\pi^+} a_{\pi\pi}^{I=0} = 0.1588, \quad m_{\pi^+} a_{\pi\pi}^{I=2} = -0.04537. \tag{1}$$

While experiments do not directly provide stringent constraints on the scattering lengths, a determination of s-wave $\pi\pi$ scattering lengths using the Roy equations has reached a remarkable level of precision [15, 16]:

$$m_{\pi^+} a_{\pi\pi}^{I=0} = 0.220 \pm 0.005, \quad m_{\pi^+} a_{\pi\pi}^{I=2} = -0.0444 \pm 0.0010. \tag{2}$$

The Roy equations [17] use dispersion theory to relate scattering data at high energies to the scattering amplitude near threshold. At present, LQCD can compute $\pi\pi$ scattering only in the $I = 2$ channel with precision as the $I = 0$ channel contains disconnected diagrams which require large computational resources. It is of great interest to compare the precise Roy equation predictions with LQCD calculations, and Fig. 6 summarizes theoretical and experimental constraints on the s-wave $\pi\pi$ scattering lengths [16]. This is clearly a strong-interaction process for which theory has somewhat out-paced the challenging experimental measurements.

Mixed-action $n_f = 2 + 1$ LQCD calculations, employing domain-wall valence quarks on a rooted staggered sea and combined with mixed-action χPT, have

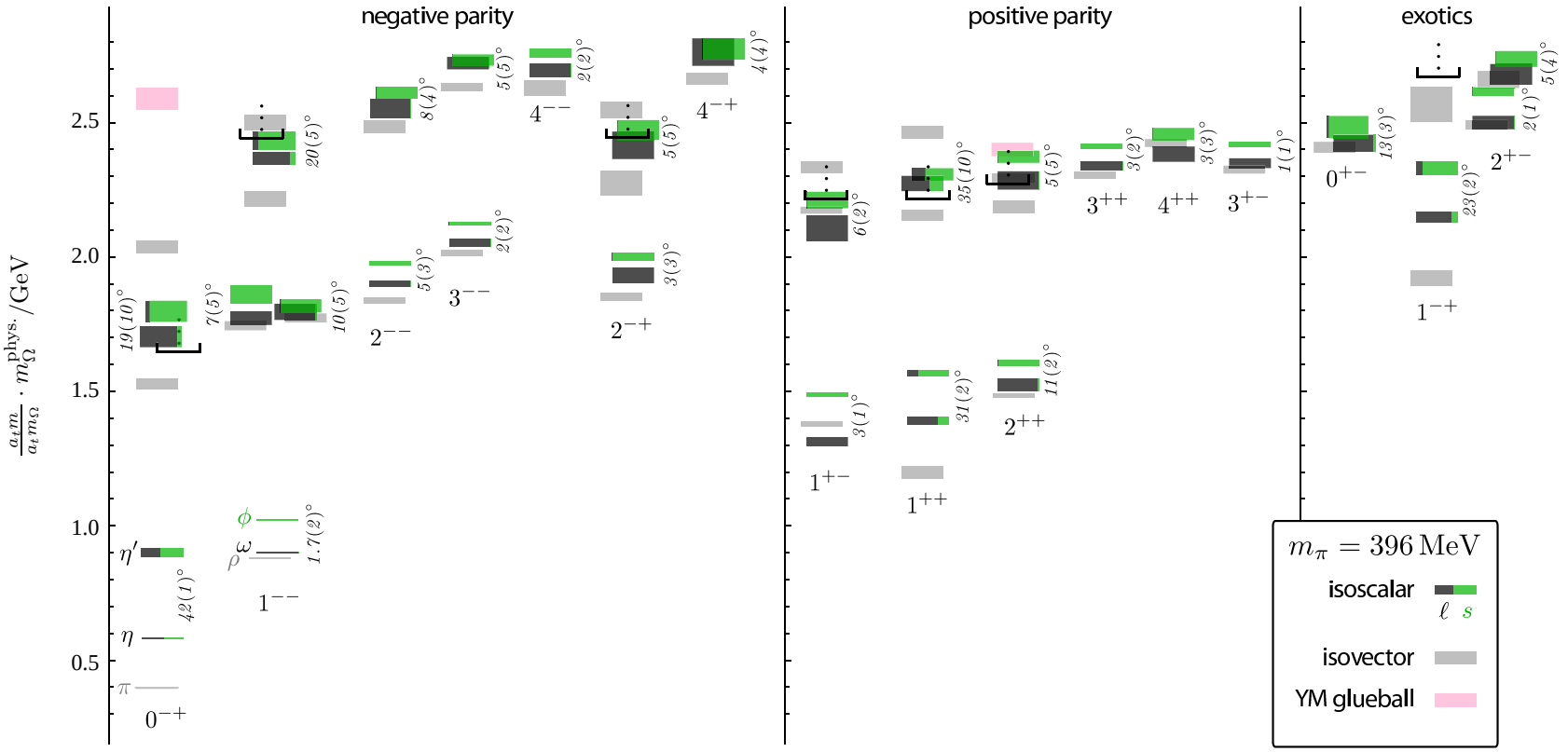

Figure 5: The spectra of isoscalar mesons calculated at $m_\pi \sim 396$ MeV by the JLab LQCD group [13] Image is reproduced with the permission of R. Edwards.

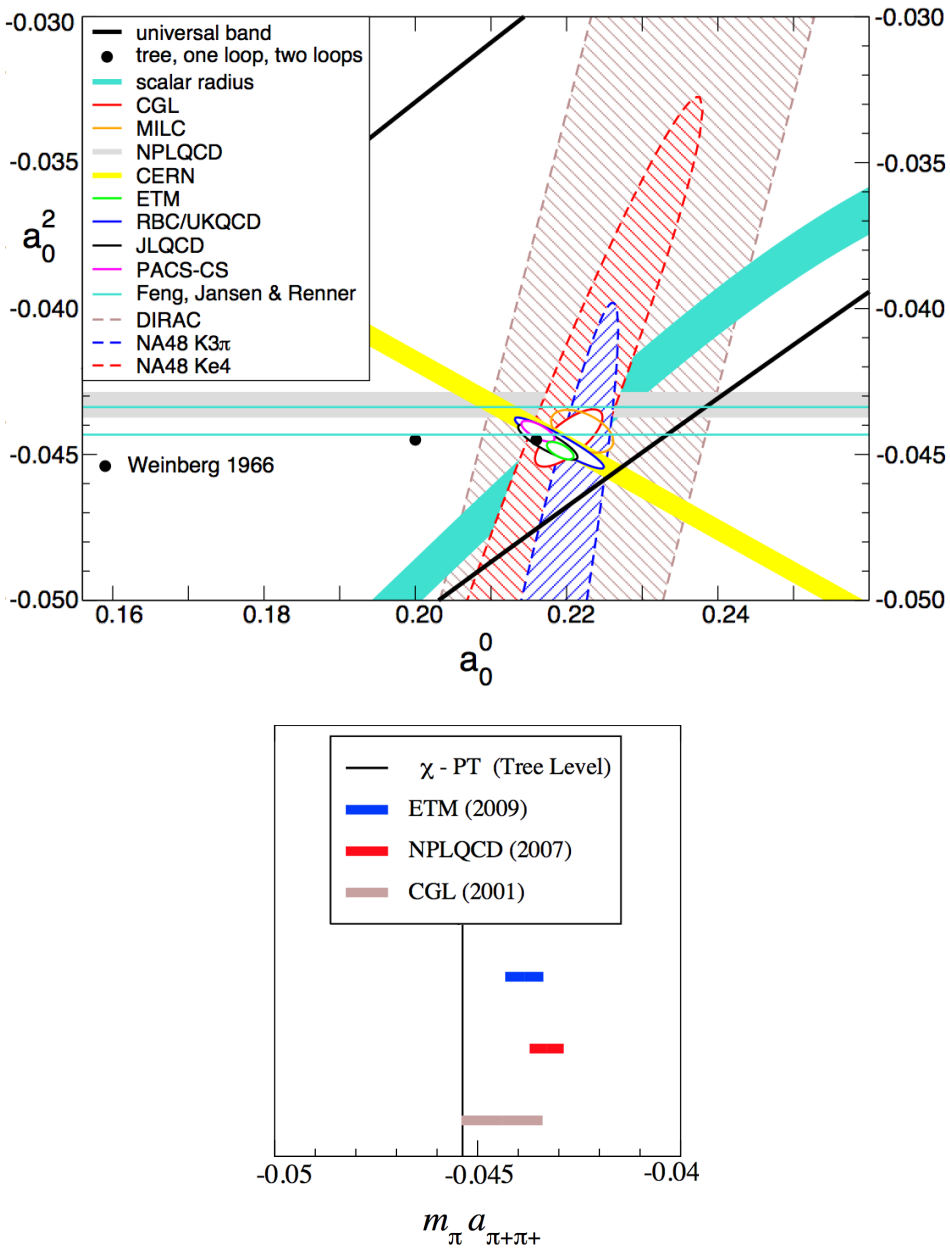

Figure 6: Constraints on threshold s-wave $\pi\pi$ scattering [16]. Image in the upper panel is reproduced with the permission of H. Leutwyler.

predicted [18]

$$m_{\pi^+} a_{\pi\pi}^{I=2} = -0.04330 \pm 0.00042 \tag{3}$$

at the physical pion mass. The agreement between this result and the Roy equation determination is a striking confirmation of the lattice methodology, and a powerful demonstration of the constraining power of chiral symmetry in the meson sector. However, LQCD calculations at one or more smaller lattice spacings, and with different discretizations, are required to verify and further refine this calculation. The ETM collaboration has performed a $n_f = 2$ calculation of the $I = 2$ $\pi\pi$ scattering length [19], producing a result extrapolated to the physical pion mass of

$$m_{\pi^+} a_{\pi\pi}^{I=2} = -0.04385 \pm 0.00028 \pm 0.00038. \tag{4}$$

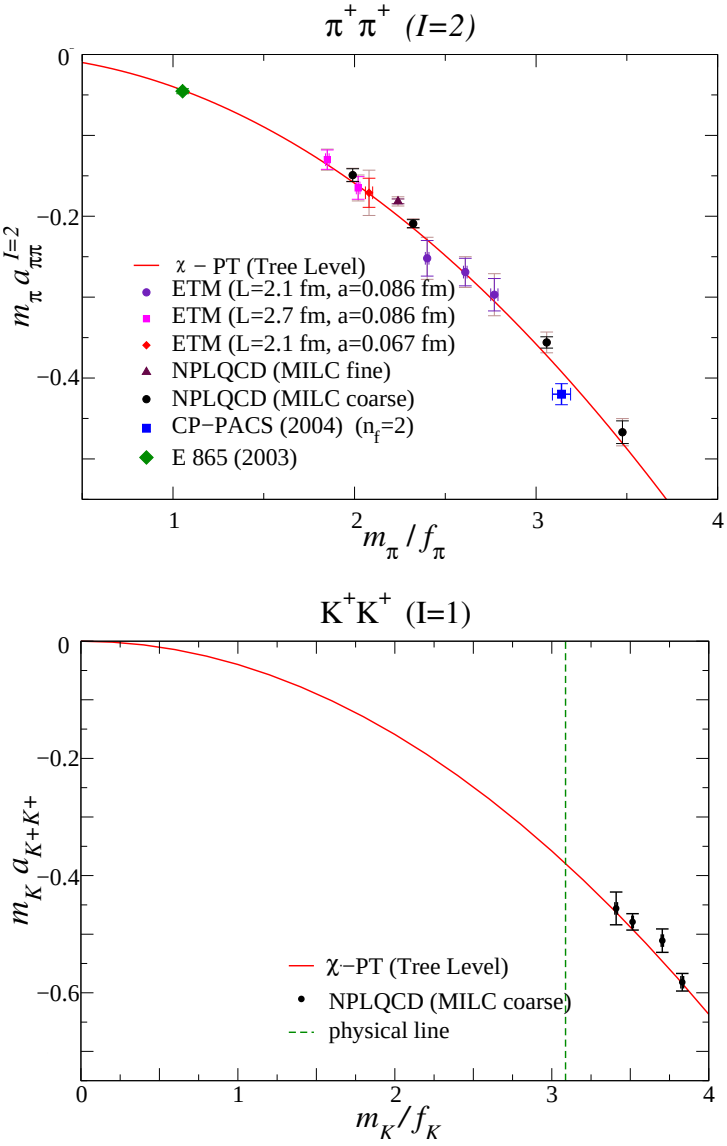

Figure 7: $m_{\pi^+}a_{\pi^+\pi^+}$ vs m_{π^+}/f_{π^+} (upper panel) and $m_{K^+}a_{K^+K^+}$ vs m_{K^+}/f_{K^+} (lower panel). The solid (red) curves are the current algebra predictions.

It is interesting to compare the pion mass dependence of the meson-meson scattering lengths to the current algebra predictions. In Fig. 7 (upper panel) one sees that the $I = 2$ $\pi\pi$ scattering length is consistent with the current algebra result up to pion masses that are expected to be at the edge of the chiral regime in the two-flavor sector. While in the two-flavor theory one expects fairly good convergence of the chiral expansion and, moreover, one expects that the effective expansion parameter is small in the channel with maximal isospin, the LQCD calculations clearly imply a degree of cancellation between chiral logs and counterterms. However, as one sees in Fig. 7 (lower panel), the same phenomenon occurs in K^+K^+ where the chiral expansion is governed by the strange quark mass and is therefore expected to be much more slowly converging. This remarkable conspiracy between chiral logs and counterterms for the meson-meson scattering lengths remains mysterious.

LQCD calculations of the meson-meson scattering phase-shifts are much less advanced than of the scattering length. This is because the calculation of the phase

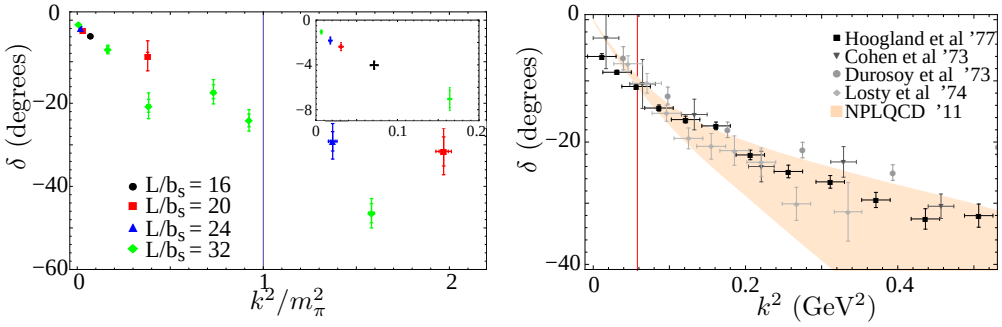

Figure 8: The $\pi^+\pi^+$ scattering phase-shift. The left panel shows the results of the LQCD calculations below the inelastic threshold ($|\mathbf{k}|^2 = 3m_\pi^2$) at a pion mass of $m_\pi \sim 390$ MeV [22]. The vertical (blue) line denotes the start of the t-channel cut. The shaded region in the right panel shows the results of the LQCD calculation extrapolated to the physical pion mass using NLO χPT, while the points and uncertainties corresponds to the existing experimental data. The vertical (red) line corresponds to the inelastic threshold.

shift, $\delta(E)$, at a given energy, E, requires a LQCD calculation of the two-meson correlation function at the energy E. Generally speaking, a given calculation can determine the lowest few two-hadron energy eigenvalues for a given momentum of the center-of-mass, and that multiple lattice volumes will allow for additional values of E at which to determine $\delta(E)$. The first serious calculation of the s-wave ($l = 0$) $I = 2$ $\pi\pi$ phase-shift was done by the CP-PACS collaboration with $n_f = 2$ at a relatively large pion mass [20], and more recently two groups have performed calculations at lower pion masses [21, 22], the results of which are shown in Fig. 8. Further, in some nice work by the Hadron Spectrum Collaboration (HSC), the first efforts have been made to extract the d-wave ($l = 2$) $I = 2$ $\pi\pi$ phase shift [21]. One of the more exciting recent results is the mapping out of the ρ-resonance at $m_\pi \sim 390$ MeV from the $\pi^+\pi^0$ energy-levels using Lüscher's method, as shown in Fig. 9 [23].

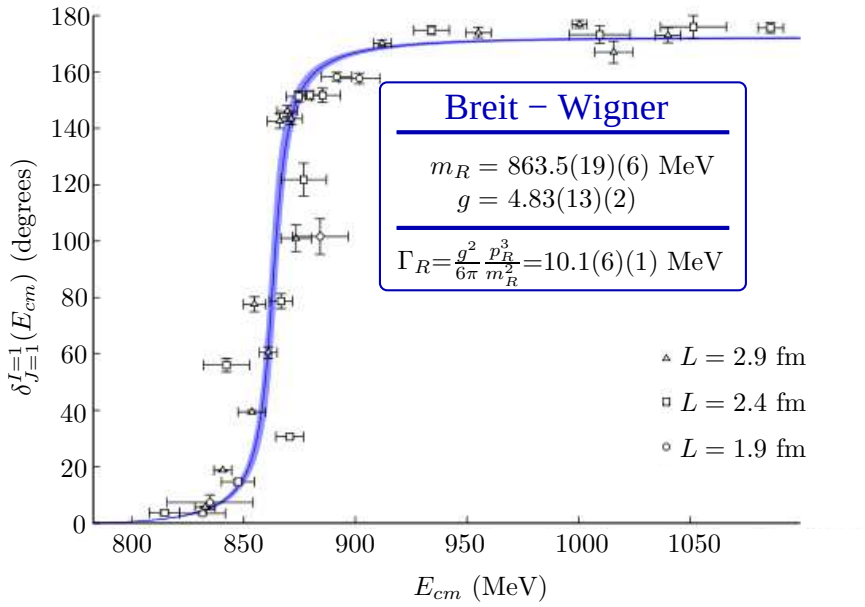

Figure 9: The ρ-resonance at a pion mass of $m_\pi \sim 390$ MeV [23]. Image is reproduced with the permission of R. Edwards.

4.3 Nuclear interactions

Calculations of the nucleon-nucleon scattering lengths have been successfully underway for the last decade [24–37] for a range of pion masses. Recently, LQCD calculations have been performed at $m_\pi \sim 800$ MeV that also provide the effective ranges [38], the results of which are shown in Fig. 10. Also shown are fits to the effective range expansion (ERE), including the shape parameter. The scattering length and effective range in the $^3S_1$ channel determined from the NLO fit to the ERE are

$$\begin{aligned} m_\pi a^{(^3S_1)} &= 7.45^{+0.57+0.71}_{-0.53-0.49}\,, & m_\pi r^{(^3S_1)} &= 3.71^{+0.28+0.28}_{-0.31-0.35}\,, \\ a^{(^3S_1)} &= 1.82^{+0.14+0.17}_{-0.13-0.12}\ \text{fm}, & r^{(^3S_1)} &= 0.906^{+0.068+0.068}_{-0.075-0.084}\ \text{fm}. \end{aligned} \tag{5}$$

The shape parameter obtained from the NNLO fit to the ERE expansion is: $Pm_\pi^3 = 2^{+5+5}_{-6-6}$. An interesting aspect of this result is that the ratio of scattering length to effective range, a measure of the naturalness of the system, is ∼2, which is to be compared with ∼3 at the physical quark masses. This leads one to speculate that

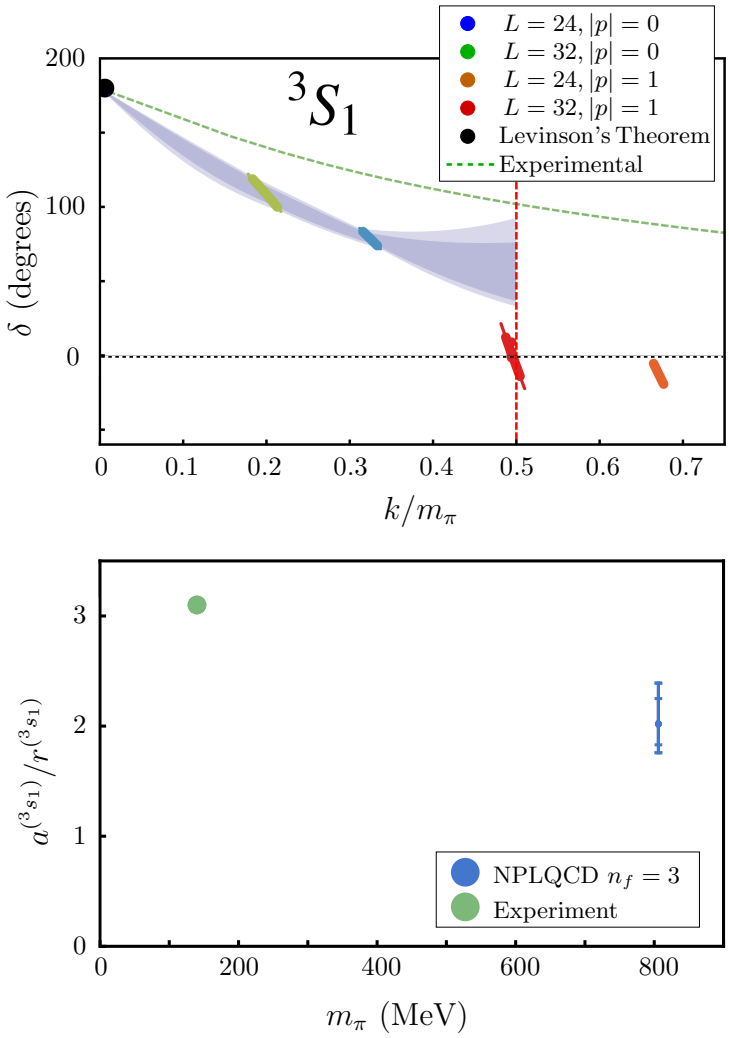

Figure 10: The upper panel shows the NN scattering phase shift in the $^3S_1$ channel extracted from LQCD calculations at the SU(3) symmetric point, including the fit to the ERE at N^{2}LO. The lower panel shows the ratio of the scattering length to effective range, a quantity that is a measure of the naturalness of the system.

the deuteron might be unnatural over a large range of quark masses and not just close to the physical values, indicating that it is not finely tuned. This speculation requires precise calculations at lighter quark masses to determine if this is, in fact, the situation.

4.4 Nuclei

Perhaps some of the most important LQCD calculations of late are those of the ground states of the light nuclei, including the deuteron, ^{3}He, ^{4}He and light hypernuclei. Fig. 11 shows the binding energy of the deuteron, ^{3}He and ^{4}He [34, 36, 37] as a function of the pion mass. Not only is it exciting to see nuclei emerge from QCD for a range of the light-quark masses, such calculations are crucial in dissecting and refining the chiral nuclear forces. However, it is clear that calculations at lighter pion masses are required, including at the physical pion mass. A summary of the energy-levels at the flavor SU(3) symmetry point found in the s-shell nuclei and hypernuclei [36] is shown in Fig. 12. These energy levels are elements of SU(3) irreps which allowed, in some cases, e. g., the H-dibaryon, the hypertriton and ${}^{\ \ 4}_{\Lambda\Lambda}$He, for distinct energy levels with the same spin and parity to be determined. Such calculations will become somewhat more complicated at lighter quark masses when the up and down quarks are not degenerate with the strange quark.

The calculations of NPLQCD and those of Yamazaki *et al.* are already shedding light on how the ground-state energies of the light nuclei approach their values at the physical light-quark masses. They are all bound at the heavier light-quark masses and become less bound as the quarks become lighter. In the case of the dineutron, which is bound at $m_\pi \sim 800$ MeV, it becomes unbound at some intermediate value of the pion mass, giving rise to a neutron-neutron system with an infinite scattering length.

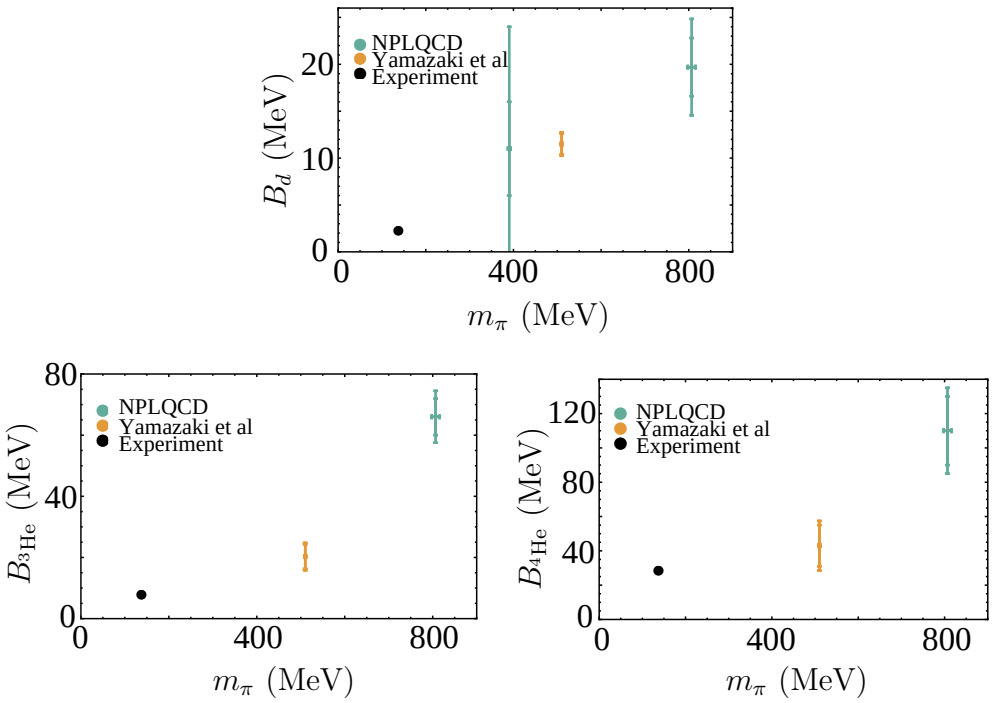

Figure 11: The deuteron (upper panel), ^{3}He (lower left panel) and ^{4}He (lower right panel) binding energies from $n_f = 2 + 1$ LQCD calculations [34, 36, 37].

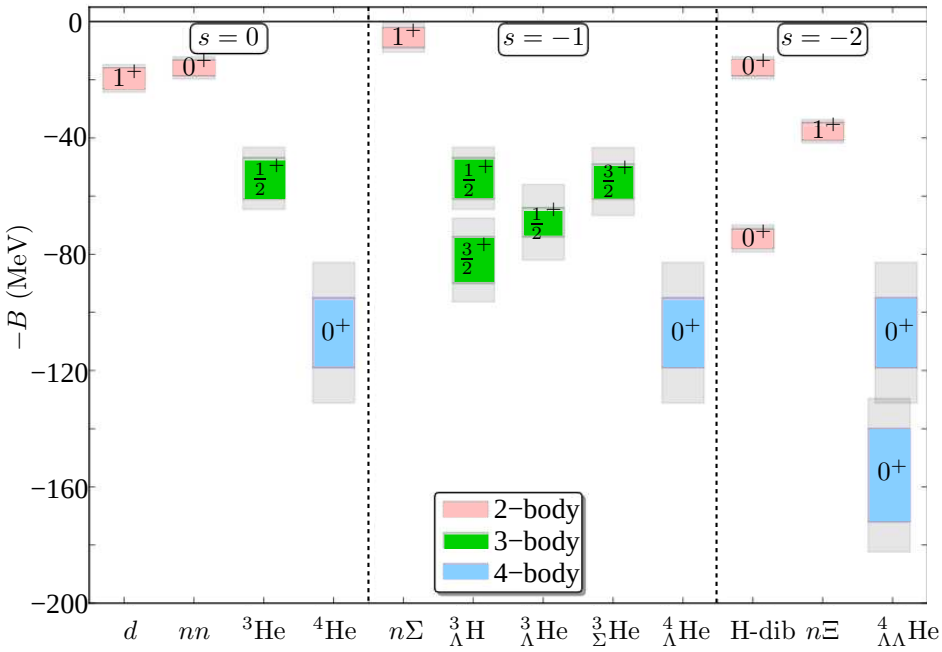

Figure 12: A compilation of the energy levels in light nuclei and hypernuclei in the limit of flavor SU(3) symmetry (with spin and parity J^π) calculated by NPLQCD [36] at a pion mass of $m_\pi \sim 800$ MeV.

One of the interesting aspects of the nuclear forces to explore is the tensor interaction, responsible for the mixing between the S-wave and D-wave channels in the deuteron channel. There is a series of LQCD calculations that can be performed that will permit an extraction of the SD mixing parameter, ϵ_1, using Lüscher's method [39–41], see Ref. [42].

4.4.1 Roadblocks of the past

It is important to understand how a few of the past roadblocks to progress in this area have been recently overcome. One of the roadblocks of the past was/is the "signal-to-noise problem" that afflicts states other than the pion. This problem is seen most simply in the single-nucleon correlation function, generated with a three-quark source and a three-quark sink. The variance of this correlation function is dictated by a 3-quark 3-anti-quark source and a 3-quark 3-anti-quark sink, which overlaps with both the $N\overline{N}$ and 3π intermediate states (and all others with the appropriate quantum numbers). At large times, the variance correlation function is dominated by the 3π intermediate state, while the single nucleon correlation function is dominated by the single nucleon, giving rise to an exponentially degrading signal. However, at intermediate times, the behavior of the "signal-to-noise" is determined by the overlap of the variance sinks and sources onto the intermediate hadronic states. The momentum projection onto single nucleon blocks, that NPLQCD is currently using, provides a volume suppression of the 3π intermediate state compared to the $N\overline{N}$ state. Thus, there is an intermediate time interval in which the signal-to-noise ratio is not exponentially degrading. It is in this time interval, dubbed the "Golden Window", that plateaus for the low-lying energy levels in light nuclei can be identified. Unfortunately, the window shrinks as the number of nucleons is increased, and so further developments will be required to go to much larger nuclei.

A second roadblock that inhibited progress in LQCD calculations of nuclei was the number of Wick contractions required to form a correlation function. A system con-

taining N_u up quarks and N_d down quarks requires $N_u!N_d!$ Wick contractions, which is a rapidly growing number as one moves beyond the nucleon. It was recognized that recursion relations relating the Wick contractions in systems with N mesons can be related to those with $N-1$ mesons [43]. Further, somewhat more sophisticated algorithms [8, 44] have been developed for the multi-baryon systems that greatly reduce the computing resources required to perform the contractions. These have led to very efficient calculations of the s-shell nuclei and hypernuclei, moving beyond the s-shell requires extensions of these works, and new ideas are required to calculate heavier nuclei.

4.5 The bridge between LQCD and nuclear structure

One of the points of discussion that came up during this presentation was how to optimally couple the results of LQCD calculations to nuclear structure calculations. Given the expertise in the nuclear structure community, it makes little sense for LQCD theorists to "go it alone" and attempt to calculate the entire periodic table. It makes much more sense for the LQCD theorists to produce sets of quantities that can be handed to the nuclear structure theorists who use them in their machinery to determine the periodic table. The question is what are the optimal quantities to pass along from LQCD.

It seems that the minimal set of quantities that could be passed along are the energy eigenvalues for a given system. LQCD calculations of the energy spectrum of an A-nucleon system could be performed in multiple lattice volumes, with multiple lattice spacings and at multiple light-quark masses, and handed to the the nuclear structure theorists who in turn reproduce the energies by tuning the chiral interactions. These tuned interactions are then used to calculate processes in the continuum. This methodology was used to calculate the $n\Sigma^-$ interactions at the physical pion mass using χPT [45]. The chiral interactions were tuned to reproduce the finite-volume energy levels determined in a series of LQCD calculations, and then used to calculate the scattering phase shift at the physical pion mass. Progress in this direction is starting to be made, as demonstrated in recent calculations by Nir Barnea and collaborators [46], by using the ground state energies of the deuteron, dineutron and ^{3}He at $m_\pi \sim 800$ MeV to reproduce the ^{4}He ground state using the pionless EFT.

5 Summary and final comments

I have summarized the rapid progress that is being made in developing LQCD into a reliable calculational tool for low-energy nuclear physics. It holds the promise to directly connect the structure and properties of nuclei with QCD, and to enable a refinement of the chiral nuclear forces that are used as input into nuclear structure calculations. At present, the ground states of the s-shell nuclei and hypernuclei are being calculated at unphysically heavy light-quark masses, but within the next few years, such calculations at $m_\pi \sim 140$ MeV will be performed (if hardware and software resources increase as expected). Within the next five years, the spectrum and interactions of the lightest nuclei and hypernuclei will be postdicted or predicted with fully-quantified uncertainties.

It is worth emphasizing that the LQCD effort in the US relies heavily on SciDAC funding to support the scientists who develop and optimize the software to run on the rapidly evolving computational hardware, e. g., GPU-accelerated compute nodes that comprise Titan at ORNL, or the BG/Qs at ANL and LLNL. Further, the effort requires ongoing access to both capability computing resources on leadership-class computing facilities, and capacity computing obtained from NERSC, XSEDE, through

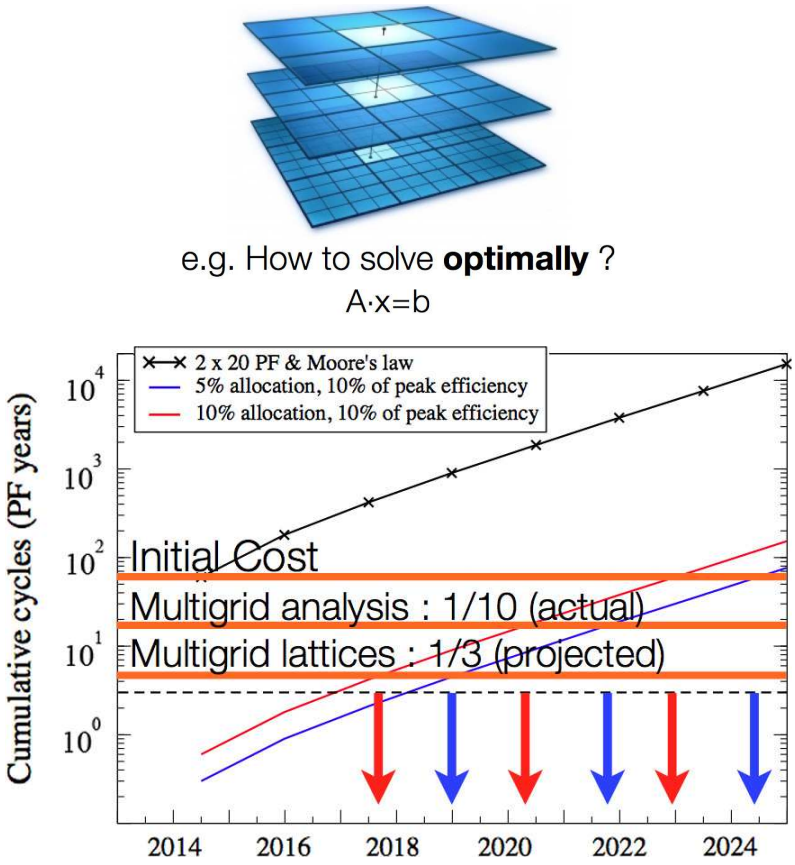

Figure 13: Multigrid is a recent algorithmic development to be implemented in LQCD calculations [47]. The horizontal (orange) cost estimates (that I have added to the original figure) provide one example of what is possible for a given production scenario. Parts of this image [48] are reproduced with the permission of B. Joo.

USQCD and at local compute clusters. Ongoing software (see Fig. 13) and hardware support are critical to progress in this area.

Ideally, one would start with a LQCD calculation and predict all of the quantities of interest in low-energy nuclear physics. Presently, we are not in a position to do this, even if significantly more computing resources were provided to the program. While Lüscher provided the formalism to relate the two-body S-matrix directly to two-particle energy levels inside a cubic volume with the fields subject to periodic boundary conditions [39, 40], which has since been understood and generalized to the two-nucleon systems, e. g. Ref. [41], such formalism is complicated to apply in coupled-channels systems [49–51]. Further, the formalism is not in place for the three- and higher-body sectors, but progress is being made in such systems [52, 53].

In closing, great progress is being made to reliably determine and refine the nuclear forces directly from QCD using lattice QCD.

Happy Birthday James: *James Vary is one of the first nuclear theorists I met when I arrived in the United States to enter the PhD program at Caltech in the mid 1980's. I recall James taking the time to talk physics with me during his stay. His detailed knowledge of, and passion for, important problems of the day left a lasting impression on me. Despite having been able to chat with, and even collaborate with, James since that time, when I learned that this conference was in part to celebrate James's 70th birthday, I was taken aback as it seems like yesterday that he was in his*

early 40's (and I was in my early 20's), and he has retained the same passion and energy for science. I should also add that James is responsible for me remembering the value of ħc! Happy 70$^{\text{th}}$*!!*

References

[1] S. Weinberg, Phys. Lett. B **251**, 288 (1990).

[2] S. Weinberg, Nucl. Phys. B **363**, 3 (1991).

[3] S. Weinberg, Phys. Lett. B **295**, 114 (1992), hep-ph/9209257 (1992).

[4] D. B. Kaplan, M. J. Savage and M. B. Wise, Phys. Lett. B **424**, 390 (1998), nucl-th/9801034 (1998).

[5] D. B. Kaplan, M. J. Savage and M. B. Wise, Nucl. Phys. B **534**, 329 (1998), nucl-th/9802075 (1998).

[6] E. Epelbaum and U.-G. Meissner, Ann. Rev. Nucl. Part. Sci. **62**, 159 (2012), arXiv:1201.2136 [nucl-th] (2012).

[7] P. Maris, J. P. Vary and P. Navrátil, Phys. Rev. C **87**, 014327 (2013), arXiv: 1205.5686 [nucl-th] (2012).

[8] W. Detmold and K. Orginos, Phys. Rev. D **87**, 114512 (2013), arXiv:1207.1452 [hep-lat] (2012).

[9] http://www.usqcd.org/collaboration.html#2013Whitepapers

[10] A. S. Kronfeld, Ann. Rev. Nucl. Part. Sci. **62**, 265 (2012), arXiv:1203.1204 [hep-lat] (2012).

[11] A. S. Kronfeld, arXiv:1209.3468 [physics.hist-ph] (2012).

[12] H.-W. Lin, PoS LATTICE 2012, 013 (2012), arXiv:1212.6849 [hep-lat] (2012).

[13] J. J. Dudek, R. G. Edwards, B. Joo, M. J. Peardon, D. G. Richards and C. E. Thomas, Phys. Rev. D **83**, 111502 (2011), arXiv:1102.4299 [hep-lat] (2011).

[14] S. Weinberg, Phys. Rev. Lett. **17**, 616 (1966).

[15] G. Colangelo, J. Gasser and H. Leutwyler, Nucl. Phys. B **603**, 125 (2001), hep-ph/0103088 (2001).

[16] H. Leutwyler, PoS CONFINEMENT8, 068 (2008), arXiv:0812.4165 [hep-ph] (2008).

[17] S. M. Roy, Phys. Lett. B **36**, 353 (1971).

[18] S. R. Beane, T. C. Luu, K. Orginos, A. Parreno, M. J. Savage, A. Torok and A. Walker-Loud, Phys. Rev. D **77**, 014505 (2008), arXiv:0706.3026 [hep-lat] (2007).

[19] X. Feng, K. Jansen and D. B. Renner, Phys. Lett. B **684**, 268 (2010), arXiv:0909.3255 [hep-lat] (2009).

[20] T. Yamazaki *et al.* (CP-PACS Collaboration), Phys. Rev. D **70**, 074513 (2004), hep-lat/0402025 (2004).

[21] J. J. Dudek, R. G. Edwards, M. J. Peardon, D. G. Richards and C. E. Thomas, Phys. Rev. D **83**, 071504 (2011), arXiv:1011.6352 [hep-ph] (2010).

[22] S. R. Beane *et al.* (NPLQCD Collaboration), arXiv:1107.5023 [hep-lat] (2011).

[23] J. J. Dudek, R. G. Edwards and C. E. Thomas, Phys. Rev. D **87**, 034505 (2013), arXiv:1212.0830 [hep-ph] (2012).

[24] M. Fukugita, Y. Kuramashi, H. Mino, M. Okawa and A. Ukawa, Phys. Rev. Lett. **73**, 2176 (1994), hep-lat/9407012 (1994).

[25] M. Fukugita, Y. Kuramashi, M. Okawa, H. Mino and A. Ukawa, Phys. Rev. D **52**, 3003 (1995), hep-lat/9501024 (1995).

[26] S. R. Beane, P. F. Bedaque, K. Orginos and M. J. Savage, Phys. Rev. Lett. **97**, 012001 (2006), hep-lat/0602010 (2006).

[27] S. R. Beane *et al.* (NPLQCD Collaboration), Phys. Rev. D **81**, 054505 (2010), arXiv:0912.4243 [hep-lat] (2009).

[28] N. Ishii, S. Aoki and T. Hatsuda, Phys. Rev. Lett. **99**, 022001 (2007), nucl-th/0611096 (2006).

[29] S. Aoki, T. Hatsuda and N. Ishii, Comput. Sci. Dis. **1**, 015009 (2008), arXiv: 0805.2462 [hep-ph] (2008).

[30] S. Aoki, T. Hatsuda and N. Ishii, Progr. Theor. Phys. **123**, 89 (2010), arXiv: 0909.5585 [hep-lat] (2009).

[31] T. Yamazaki, Y. Kuramashi and A. Ukawa, arXiv:1105.1418 [hep-lat] (2011).

[32] T. Yamazaki, Y. Kuramashi and A. Ukawa, Phys. Rev. D **81**, 111504 (2010), arXiv:0912.1383 [hep-lat] (2009).

[33] P. de Forcrand and M. Fromm, Phys. Rev. Lett. **104**, 112005 (2010), arXiv: 0907.1915 [hep-lat] (2009).

[34] S. R. Beane *et al.* (NPLQCD Collaboration), Phys. Rev. D **85**, 054511 (2012), arXiv:1109.2889 [hep-lat] (2011).

[35] T. Inoue *et al.* (HAL QCD Collaboration), Nucl. Phys. A **881**, 28 (2012), arXiv: 1112.5926 [hep-lat] (2011).

[36] S. R. Beane, E. Chang, S. D. Cohen, W. Detmold, H. W. Lin, T. C. Luu, K. Orginos, A. Parreno, M. J. Savage and A. Walker-Loud, arXiv:1206.5219 [hep-lat] (2012).

[37] T. Yamazaki, K. -I. Ishikawa, Y. Kuramashi and A. Ukawa, Phys. Rev. D **86**, 074514 (2012), arXiv:1207.4277 [hep-lat] (2012).

[38] S. R. Beane, E. Chang, S. D. Cohen, W. Detmold, P. Junnarkar, H. W. Lin, T. C. Luu, K. Orginos, A. Parreno, M. J. Savage and A. Walker-Loud, Phys. Rev. C **88**, 024003 (2013), arXiv:1301.5790 [hep-lat] (2013).

[39] M. Lüscher, Commun. Math. Phys. **105**, 153 (1986).

[40] M. Lüscher, Nucl. Phys. B **354**, 531 (1991).

[41] R. A. Briceno, Z. Davoudi and T. C. Luu, Phys. Rev. D **88**, 034502 (2013), arXiv:1305.4903 [hep-lat] (2013).

[42] R. A. Briceno, Z. Davoudi, T. Luu and M. J. Savage, arXiv:1309.3556 [hep-lat] (2013).

[43] W. Detmold and M. J. Savage, Phys. Rev. D **82**, 014511 (2010), arXiv:1001.2768 [hep-lat] (2010).

[44] T. Doi and M. G. Endres, Comput. Phys. Commun. **184**, 117 (2013), arXiv: 1205.0585 [hep-lat] (2012).

[45] S. R. Beane, E. Chang, S. D. Cohen, W. Detmold, H.-W. Lin, T. C. Luu, K. Orginos, A. Parreno, M. J. Savage and A. Walker-Loud, Phys. Rev. Lett. **109**, 172001 (2012), arXiv:1204.3606 [hep-lat] (2012).

[46] N. Barnea, *Nuclear physics with heavy pions — EFT for LQCD*, a talk presented at the *Institute for Nuclear Theory*, July 31, 2013.

[47] J. C. Osborn, R. Babich, J. Brannick, R. C. Brower, M. A. Clark, S. D. Cohen and C. Rebbi, PoS LATTICE 2010, 037 (2010), arXiv:1011.2775 [hep-lat] (2010).

[48] B. Joo, *Computational Challenges in Cold QCD*, a talk at the *Computational Nucl. Phys. Meeting*, Washington, D.C., July 23–24, 2012.

[49] M. T. Hansen and S. R. Sharpe, Phys. Rev. D **86**, 016007 (2012), arXiv:1204.0826 [hep-lat] (2012).

[50] R. A. Briceno and Z. Davoudi, Phys. Rev. D **87**, 094507 (2013), arXiv:1212.3398 [hep-lat] (2012).

[51] P. Guo, J. Dudek, R. Edwards and A. P. Szczepaniak, Phys. Rev. D **88**, 014501 (2013), arXiv:1211.0929 [hep-lat] (2012).

[52] R. A. Briceno and Z. Davoudi, arXiv:1204.1110 [hep-lat] (2012).

[53] K. Polejaeva and A. Rusetsky, Eur. Phys. J. A **48**, 67 (2012), arXiv:1203.1241 [hep-lat] (2012).

Hot Nuclear Matter in Intense Magnetic Field

Kirill Tuchin

Department of Physics and Astronomy, Iowa State University, Ames, IA 50011

Abstract

Collision of two relativistic heavy ions produces highly intense electromagnetic field. Exact solution of Maxwell equations indicates that the field strength reaches $\sim m_\pi^2$ at RHIC and $\sim 10 m_\pi^2$ at LHC. Moreover, time-evolution of this field in electrically conducting nuclear matter is much slower than in vacuum. This fact has many important phenomenological consequences, two of which are discussed in detail: J/ψ dissociation in background magnetic field and synchrotron photon radiation by quark-gluon plasma.

Keywords: *Heavy-ion collisions; magnetic field; synchrotron radiation, J/ψ production*

1 Origin of magnetic field

Electromagnetic field of two relativistic heavy-ions can be estimated using elementary arguments. Suppose that each ion has radius R, electric charge Ze and collide at impact parameter $\boldsymbol{b}$. According to the Biot and Savart law they create magnetic field that in the center-of-mass frame has magnitude $B \sim \gamma Zeb/R^3$ and directed perpendicular to the collision plane, where $\gamma = \sqrt{s_{NN}}/2m_N$ is the Lorentz factor. At RHIC heavy-ions are collided at 200 GeV per nucleon, hence $\gamma = 100$. Using $Z = 79$ for Gold and $b \sim R_A \approx 7$ fm we estimate $eB \approx m_\pi^2 \sim 10^{18}$ G. To appreciate how strong is this field, compare it with the following numbers: the strongest magnetic field created on Earth in a form of electromagnetic shock wave is $\sim 10^7$ G, magnetic field of a neutron star is estimated to be $10^{10}-10^{13}$ G, that of a magnetar up to 10^{15} G.

It has been known for a long time that classical electrodynamics breaks down at the critical (Schwinger) field strength $F = m_e^2/e$. In cgs units the corresponding magnetic field is 10^{13} G. Because $m_\pi/m_e = 280$, electromagnetic fields created at RHIC and LHC are well above the critical value. This offers a unique opportunity to study the super-strong electromagnetic fields in laboratory. In the next section I present a classical solution to the problem of electromagnetic field in heavy-ion collisions. I then consider two phenomenological applications: Lorentz ionization of J/ψ in Section 3, and synchrotron photon radiation in Section 4.

2 Solution of Maxwell equations

In relativistic heavy-ion collisions, production of valence quarks in the central rapidity region – the baryon stopping – is suppressed. Hence Z valence quarks of each nucleus continue to travel after heavy-ion collision along the straight lines in opposite directions. These valence quarks carry total electric charge $2Ze$ that creates electromagnetic field in the interaction region. Unlike the valence quarks, gluons and sea quarks are produced mostly in the central rapidity region, i. e. in a plane perpendicular to the collision axis. It has been suggested by Landau long ago [1, 2] that

Proceedings of International Conference 'Nuclear Theory in the Supercomputing Era — 2013' (NTSE-2013), Ames, IA, USA, May 13–17, 2013. Eds. A. M. Shirokov and A. I. Mazur. Pacific National University, Khabarovsk, Russia, 2014, p. 175.

http://www.ntse-2013.khb.ru/Proc/Tuchin.pdf.

high multiplicity events in heavy-ion collisions can be effectively described using relativistic hydrodynamics. In particular, matter produced in heavy-ion collisions can be characterized by a few transport coefficients. This approach has enjoyed a remarkable phenomenological success (see, e. g., Ref. [3]). Since sea quarks carry electric charge, electromagnetic field created by valence quarks depends on the permittivity ϵ, permeability μ and conductivity σ of the produced matter.

Consider electromagnetic field created by a point charge e moving along the positive z-axis with velocity v. It is governed by Maxwell equations:

$$\boldsymbol{\nabla}\cdot\boldsymbol{B}=0, \qquad \boldsymbol{\nabla}\times\boldsymbol{E}=-\frac{\partial\boldsymbol{B}}{\partial t}, \tag{1}$$

$$\boldsymbol{\nabla}\cdot\boldsymbol{D}=e\,\delta(z-vt)\,\delta(\boldsymbol{b}), \qquad \boldsymbol{\nabla}\times\boldsymbol{H}=\frac{\partial\boldsymbol{D}}{\partial t}+\sigma\boldsymbol{E}+ev\hat{\boldsymbol{z}}\,\delta(z-vt)\,\delta(\boldsymbol{b}), \tag{2}$$

where $\boldsymbol{r}=z\hat{\boldsymbol{z}}+\boldsymbol{b}$ (such that $\boldsymbol{b}\cdot\hat{\boldsymbol{z}}=0$) is the position of the observation point. Introducing Fourier transforms of field components

$$\boldsymbol{E}(t,\boldsymbol{r})=\int_{-\infty}^{\infty}\frac{d\omega}{2\pi}\int_{-\infty}^{\infty}\frac{dk_z}{2\pi}\int\frac{d^2k_\perp}{(2\pi)^2}\,e^{-i\omega t+ik_zz+i\boldsymbol{k}_\perp\cdot\boldsymbol{b}}\,\boldsymbol{E}_{\omega\boldsymbol{k}}, \qquad \text{etc.,} \tag{3}$$

we can write the solution as follows:

$$\boldsymbol{H}_{\omega\boldsymbol{k}}=-2\pi iev\,\frac{\boldsymbol{k}\times\hat{\boldsymbol{z}}}{\omega^2\tilde{\epsilon}\mu-\boldsymbol{k}^2}\,\delta(\omega-k_zv), \quad \boldsymbol{E}_{\omega\boldsymbol{k}}=-2\pi ie\,\frac{\omega\mu v\hat{\boldsymbol{z}}-\boldsymbol{k}/\epsilon}{\omega^2\tilde{\epsilon}\mu-\boldsymbol{k}^2}\,\delta(\omega-k_zv), \tag{4}$$

where $\tilde{\epsilon}=\epsilon+i\sigma/\omega$ and ϵ, μ are functions of ω that depend on matter properties.

Later time dependence of electromagnetic field is determined by a singularity of Eq. (4) in the plane of complex ω that has smallest imaginary part. To obtain a conservative estimate of the matter effect we assume that the leading singularity is determined by electrical conductivity. Therefore, we adopt a simple model $\epsilon=\mu=1$, i. e. neglect polarization and magnetization response of nuclear matter, but take into account its finite electrical conductivity. Plugging (4) into Eq. (3) we take first trivial k_z-integral. Integration over ω for positive values of $x_-=t-z/v$ is done by closing the integration contour over the pole in the lower half-plane of complex ω. In the relativistic limit $\gamma=1/\sqrt{1-v^2}\gg1$ the result is [4,5]

$$\boldsymbol{H}(t,\boldsymbol{r})=H(t,\boldsymbol{r})\hat{\boldsymbol{\phi}}=\frac{e}{2\pi\sigma}\hat{\boldsymbol{\phi}}\int_0^\infty\frac{J_1(k_\perp b)\,k_\perp^2}{\sqrt{1+\frac{4k_\perp^2}{\gamma^2\sigma^2}}}\exp\left\{\frac{1}{2}\sigma\gamma^2x_-\left(1-\sqrt{1+\frac{4k_\perp^2}{\gamma^2\sigma^2}}\right)\right\}dk_\perp, \tag{5}$$

$$E_z(t,\boldsymbol{r})=\frac{e}{4\pi}\int k_\perp\,J_0(k_\perp b)\,\frac{1-\sqrt{1+\frac{4k_\perp^2}{\gamma^2\sigma^2}}}{\sqrt{1+\frac{4k_\perp^2}{\gamma^2\sigma^2}}}\exp\left\{\frac{1}{2}\sigma\gamma^2x_-\left(1-\sqrt{1+\frac{4k_\perp^2}{\gamma^2\sigma^2}}\right)\right\}dk_\perp, \tag{6}$$

$$\boldsymbol{E}_\perp(t,\boldsymbol{r})=H(t,\boldsymbol{r})\hat{\boldsymbol{r}}, \tag{7}$$

where $\hat{\boldsymbol{r}}$ and $\hat{\boldsymbol{\phi}}$ are unit vectors of polar coordinates in transverse plane x,y. Electromagnetic field is a function of $\boldsymbol{r}-\boldsymbol{r}'$, where $\boldsymbol{r}$ and $\boldsymbol{r}'=vt\hat{\boldsymbol{z}}$ are the positions of the observation point and the moving charge correspondingly. In fact, it depends only on distances $z-vt=-vx_-$ and b.

Equations (5)–(7) have two instructive limits depending on the value of parameter $\gamma\sigma b$ that appears in the exponents once we notice that $k_\perp\sim1/b$. If $\gamma\sigma b\ll1$, then, after a simple integration, Eqs. (5)–(7) reduce to the boosted Coulomb potential in free space:

$$\boldsymbol{E}=\frac{e\gamma}{4\pi}\frac{\boldsymbol{b}-vx_-\hat{\boldsymbol{z}}}{(b^2+\gamma^2v^2x_-^2)^{3/2}}, \qquad \boldsymbol{H}=\frac{e\gamma}{4\pi}\frac{v\hat{\boldsymbol{\phi}}}{(b^2+\gamma^2v^2x_-^2)^{3/2}}. \tag{8}$$

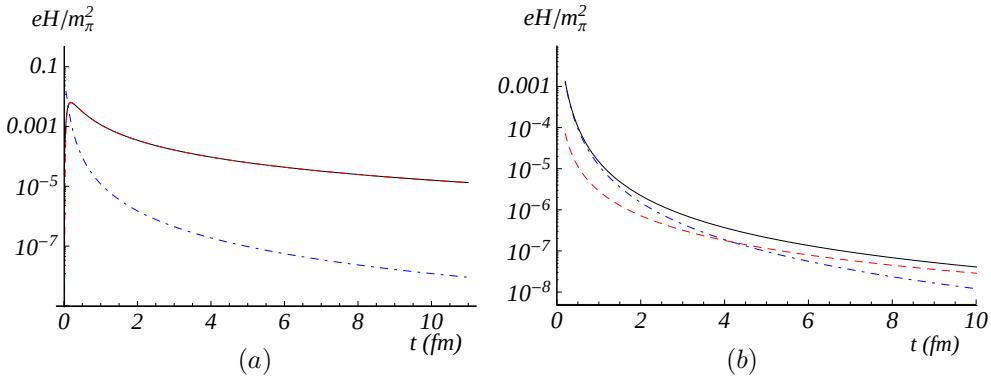

Figure 1: Time evolution of magnetic field created by a point unit charge at $z = 0$, $b = 7.4$ fm, $\gamma = 100$ and (a) $\sigma = 5.8$ MeV, (b) $\sigma = 0.01$ MeV. Black solid line is numerical computation of Eq. (5), red dashed line is "diffusion" approximation (9), blue dash-dotted line is a solution in free space.

This is the solution discussed in Ref. [6]. In the opposite limit $\gamma\sigma b \gg 1$, we expend the square root in Eqs. (5), (6) and derive

$$E_r = H_\phi = \frac{e}{2\pi}\frac{b\sigma}{4x_-^2}e^{-\frac{b^2\sigma}{4x_-}}, \qquad E_z = -\frac{e}{4\pi}\frac{x_- - b^2\sigma/4}{\gamma^2 x_-^3}e^{-\frac{b^2\sigma}{4x_-}}. \tag{9}$$

This is the solution suggested in Ref. [7]. Notice that the electromagnetic field in Eq. (8) drops as $1/x_-^3$ at late times, whereas in conducting matter only as $1/x_-^2$. At RHIC $\gamma = 100$, $\sigma \approx 5.8$ MeV [8–10]. For $b = 7$ fm we estimate $\gamma\sigma b = 19$, hence the field is given by the "diffusive" solution (9). This argument is augmented by numerical calculation presented in Fig. 1. In Fig. 1(a) we plot the result of numerical integration in Eq. (5) for $\sigma \approx 5.8$ MeV and compare it with the asymptotic solutions (8) and (9). It is seen that solution (9) completely overlaps with the exact solution at all times, except at $t < 0.1$ fm (not seen in the figure). To illustrate what happens at $\gamma\sigma b \ll 1$, we plotted in Fig. 1(b) the same formulas as in Fig. 1(a) calculated at artificially reduced conductivity $\sigma \approx 0.01$ MeV. One can clearly observe that at early time matter plays little role in the field time-evolution which follows Eq. (8), whereas at later time Foucault currents eventually slow down magnetic field decline, which then follows Eq. (9).

To obtain the total electromagnetic field of two colliding ions one needs to sum over all electric charges, which can be approximated by convolution (5)–(7) with nuclear densities. The resulting time dependence of total magnetic field is shown in Fig. 2.

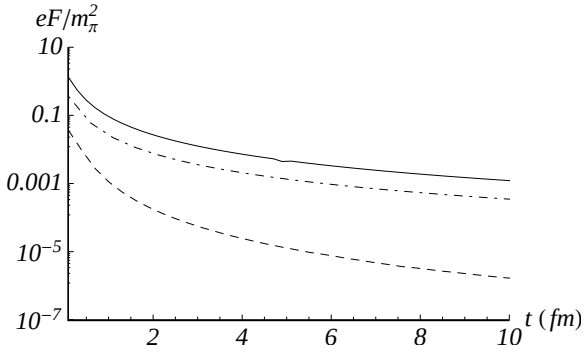

Figure 2: Time dependence of total electromagnetic magnetic field F at mid-rapidity $z = 0$, $\gamma = 100$, $B = 7$ fm, $t = 2$ fm. Solid line: $F = H_y$ at $x = y = 0$, dashed line $F = -H_x$ at $x = y = 1$ fm, dashed-dotted line $F = -E_y$ at $x = y = 1$ fm.

As expected late time dependence of all components is the same and governed by Eq. (9).

Transverse coordinate structure of electromagnetic field was investigated in Ref. [4] were it was observed that the space variation of H_y is mild. Other transverse components vary more significantly as they are required to vanish at either $x = 0$ or $y = 0$ by symmetry. When averaged over the transverse plane, only H_y component survives. In the following section we will consider phenomenological effect of constant magnetic field $\boldsymbol{B} = B\hat{\boldsymbol{y}} = H_y\hat{\boldsymbol{y}}$.

3 J/ψ in magnetic field

Strong magnetic field created in heavy-ion collisions generates a number of remarkable effects on quarkonium production.

1. *Lorentz ionization.* Consider quarkonium traveling with constant velocity in magnetic field in the laboratory frame. In quarkonium comoving frame, we find mutually orthogonal electric and magnetic fields given by Eqs. (10). In the presence of electric field quark and antiquark have a finite probability to tunnel through the potential barrier thereby causing quarkonium dissociation. We discuss this effect at length below.

2. *Zeeman effect.* Magnetic field lifts degeneration of quarkonium states with respect of the total angular momentum projection J_y. The corresponding splitting is of the order $\Delta M = \frac{eB_0}{2m} g J_y$, where $J_y = -J, -J+1, \dots, J$, m is quark mass and g is Landé factor. For example, J/ψ state with spin $S = 1$, orbital angular momentum $L = 0$ and total angular momentum $J = 1$ has $g \approx 2$ and splits into three states with $J_y = \pm 1, 0$ with mass difference $\Delta M = 0.15$ GeV at $eB_0 = 15 m_\pi^2$. Thus, the Zeeman effect leads to the emergence of new quarkonium states in plasma.

3. *Distortion of the quarkonium potential* in magnetic field. This effect arises in higher order perturbation theory and becomes important at field strengths of order $B \sim 3\pi m^2/e^3$ [11]. This is $3\pi/\alpha$ times stronger than the critical Schwinger's field. Therefore, this effect can be neglected at the present collider energies.

In this section I focus on Lorentz ionization, which contributes to J/ψ suppression in heavy-ion collisions [12, 13]. Before we proceed to analytical calculations it is worthwhile to discuss the physics picture in more detail in two reference frames: the quarkonium proper frame and the lab frame. In the quarkonium proper frame the potential energy of, say, antiquark (with $e < 0$) is a sum of its potential energy in the binding potential and its energy in the electric field $-eEx$, where x is the electric field direction. Since $|e|Ex$ becomes large and negative at large and negative x (far away from the bound state) and because the quarkonium potential has finite radius, this region opens up for the motion of the antiquark. Thus there is finite quantum mechanical probability to tunnel through the potential barrier formed on one side by the vanishing quarkonium potential and on the other by increasing absolute value of the antiquark energy in electric field. Of course, the total energy of antiquark (not counting its mass) is negative after tunneling. However, its kinetic energy grows proportionally to eEx as it goes away. By picking up a light quark out of vacuum it can hadronize into a D-meson.

If we now go to the reference frame where $E = 0$ and there is only magnetic field B (we can always do so since $E < B$), then the entire process looks quite different. An energetic quarkonium travels in external magnetic field and decays into quark-antiquark pair that can late hadronize into D-mesons. This happens in spite

of the fact that J/ψ mass is smaller than masses of two D-mesons due to additional momentum $e\boldsymbol{A}$ supplied by the magnetic field. Similarly, a single photon can decay into electron-positron pair in external magnetic field.

Consider a J/ψ traveling with velocity $\boldsymbol{V}$ in constant magnetic field $\boldsymbol{B}_0$ (subscript 0 indicates the laboratory frame). Let $\boldsymbol{B}$ and $\boldsymbol{E}$ be magnetic and electric fields in the comoving frame, and let subscripts $\parallel$ and $\perp$ denote field components parallel and perpendicular to $\boldsymbol{V}$ correspondingly. Then,

$$E_\parallel = 0, \qquad \boldsymbol{E}_\perp = \gamma_L \boldsymbol{V} \times \boldsymbol{B}_0, \tag{10a}$$

$$B_\parallel = \frac{\boldsymbol{B}_0 \cdot \boldsymbol{V}}{V}, \qquad \boldsymbol{B}_\perp = \gamma_L \frac{(\boldsymbol{V} \times \boldsymbol{B}_0) \times \boldsymbol{V}}{V^2}, \tag{10b}$$

where $\gamma_L = (1 - V^2)^{-1/2}$. Clearly, in the comoving frame $\boldsymbol{B} \cdot \boldsymbol{E} = 0$. We choose y and x axes of the comoving frame such that $\boldsymbol{B} = B\hat{\boldsymbol{y}}$ and $\boldsymbol{E} = E\hat{\boldsymbol{x}}$. A convenient gauge choice is $\boldsymbol{A} = -Bx\,\hat{\boldsymbol{z}}$ and $\varphi = -Ex$. The relative strength of electric and magnetic fields in comoving frame is $\rho = E/B$. This parameter is always in the range $0 \le \rho \le 1$ because $B^2 - E^2 = B_0^2 \ge 0$. When J/ψ moves perpendicularly to the magnetic field $\boldsymbol{B}_0$, $\rho = V$.

The force binding q and $\bar{q}$ in J/ψ is short-range in the sense that $(M\varepsilon_b)^{1/2} R \ll 1$, where ε_b and M are binding energy and mass of J/ψ and R is the nuclear force range. This approximation enables us to calculate the dissociation probability w with exponential accuracy regardless of the precise form of the J/ψ wave function. This is especially important since solutions of the relativistic two-body problem for quarkonium are not readily available.

It is natural to study quarkonium ionization in the comoving frame [12]. Quark energy ε_0 ($\varepsilon_0 < m$) in electromagnetic field can be written as

$$\varepsilon_0 = \sqrt{m^2 + (\boldsymbol{p} - e\boldsymbol{A})^2} + e\varphi = \sqrt{m^2 + (p_z + eBx)^2 + p_x^2 + p_y^2} - eEx. \tag{11}$$

In terms of ε_0, quarkonium binding energy is $\varepsilon_b = m - \varepsilon_0$. Ionization probability of quarkonium equals its tunneling probability through the potential barrier. The later is given by the transmission coefficient

$$w = e^{-2\int_0^{y_1} \sqrt{-p_y^2}\, dy} \equiv e^{-f}. \tag{12}$$

In the non-relativistic approximation one can also calculate the pre-exponential factor, which appears due to the deviation of the quark wave function from the quasi-classical approximation. The result of the calculation reads [12]:

$$\begin{aligned} \frac{f}{m^2} = {} & \frac{\sqrt{-\epsilon_0^2 + 1 + q^2}\,(\epsilon_0 E - qB)}{e(B^2 - E^2)} \\ & - \frac{(\epsilon_0 E - qB)^2 - (B^2 - E^2)(-\epsilon_0^2 + 1 + q^2)}{e(B^2 - E^2)^{3/2}} \\ & \times \ln\left\{ \frac{\epsilon_0 E - qB + \sqrt{(B^2 - E^2)(-\epsilon_0^2 + 1 + q^2)}}{\sqrt{(\epsilon_0 E - qB)^2 - (B^2 - E^2)(\epsilon_0^2 + 1 + q^2)}} \right\}, \end{aligned} \tag{13}$$

where $\epsilon_0 = \varepsilon_0/m$ and $q = p_z/m$.

For different q's function $w = e^{-f}$ gives the corresponding ionization probabilities. The largest probability corresponds to smallest f, which occurs at momentum q_m determined by equation [14]

$$\frac{\partial f(q_m)}{\partial q_m} = 0. \tag{14}$$

Using Eq. (13) we find [12]

$$\frac{\rho(\epsilon_0 - \rho q_m)}{1 - \rho^2} \ln\left\{ \frac{\epsilon_0 \rho - q_m + \sqrt{1 - \rho^2}\,\sqrt{-\epsilon_0^2 + 1 + q_m^2}}{\sqrt{(\epsilon_0 - \rho q_m)^2 - 1 + \rho^2}} \right\} = \frac{\sqrt{-\epsilon_0^2 + 1 + q_m^2}}{\sqrt{1 - \rho^2}}. \tag{15}$$

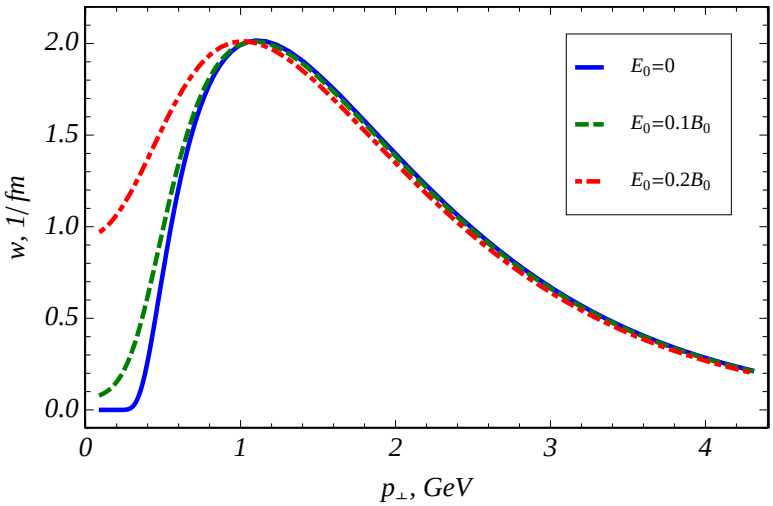

Figure 3: Dissociation rate of J/ψ at $eB_0 = 15m_\pi^2$, $\phi = \pi/2$ (in the reaction plane), $\eta = 0$ (midrapidity) as a function of J/ψ transverse momentum in the Lab frame $p_\perp$.

This is an implicit equation for the extremal momentum $q_m = q_m(\epsilon_0, \rho)$. Substituting q_m into Eq. (13) one obtains $f = f(\epsilon_0, \rho)$, which by means of Eq. (12) yields the ionization probability. The quasi-classical approximation that we employed in this section is valid inasmuch as $f(q_m) \gg 1$.

In the non-relativistic approximation we get a familiar result

$$f(q_m) = \frac{2m^2(2\epsilon_b)^{3/2}}{3eE}\, g(\gamma), \tag{16}$$

where $g(\gamma)$ is the Keldysh function

$$g(\gamma) = \frac{3\tau_0}{2\gamma}\left[1 - \frac{1}{\gamma}\left(\frac{\tau_0^2}{\gamma^2} - 1\right)^{1/2}\right], \tag{17}$$

and $\gamma = \frac{\sqrt{2\epsilon_b}}{\rho}$ is the adiabaticity parameter.

It is shown in Ref. [12] that the non-relativistic limit provides a very good approximation to the dissociation rate. It also allows one to calculate the pre-exponential factor [14–16]. The final result is depicted in Fig. 3 [13]. We also show the dissociation rate of J/ψ for several values of the electric field $\boldsymbol{E}_0$ possibly induced by the Chiral Magnetic Effect [6]. Note, that typical size of the medium traversed by a J/ψ in magnetic field can be estimated very conservatively as a few fm. Therefore, $w \sim 0.3$–0.5 fm^{-1} corresponds to complete destruction of J/ψ's. This means that in the magnetic field of strength $eB_0 \sim 15m_\pi^2$ all J/ψ's with $p_\perp \gtrsim 0.5$ GeV are destroyed independently of the strength of E_0.

Angular distribution of J/ψ's was discussed in detail in Ref. [13]. In the absence of electric field $\boldsymbol{E}_0$, the dissociation probability peaks in the direction perpendicular to the direction of magnetic field $\boldsymbol{B}_0$, i. e. in the reaction plane. Dissociation rate vanishes in the $\boldsymbol{B}_0$ direction. The shape of the azimuthal distribution strongly depends on quarkonium velocity: while at low V the strongest dissociation is in the direction of the reaction plane, at higher V the maximum shifts towards small angles around the $\boldsymbol{B}_0$ direction.

4 Synchrotron radiation

As a second example, consider electromagnetic radiation by quark and anti-quarks in plasma. QGP is transparent to the emitted electromagnetic radiation because its absorption coefficient is suppressed by α^2. Electromagnetic radiation by quarks and antiquarks of QGP moving in external magnetic field originates from two sources: (i) synchrotron radiation and (ii) quark and antiquark annihilation. It is argued in Ref. [17] that contribution of annihilation channel is negligible, hence we focus on synchrotron radiation. In strong magnetic field it is essential to account for quantization of fermion spectra. Indeed, spacing between the Landau levels is of the order eB/ε (ε being quark energy), while their thermal width is of the order T. Spectrum quantization is negligible only if $eB/\varepsilon \ll T$ which is barely the case at RHIC and certainly not the case at LHC (at least during the first few fm's of the evolution).

Synchrotron radiation is a process of photon γ radiation by a fermion f with electric charge $e_f = z_f e$ in external magnetic field B: $f(e_f, j, p) \to f(e_f, k, q) + \gamma(\boldsymbol{k})$, where $\boldsymbol{k}$ is the photon momentum, p, q are the momentum components along the magnetic field direction and indices j, $k = 0, 1, 2, ...$ label the discrete Landau levels in the reaction plane. The Landau levels are given by

$$\varepsilon_j = \sqrt{m^2 + p^2 + 2je_fB}, \qquad \varepsilon_k = \sqrt{m^2 + q^2 + 2ke_fB}. \tag{18}$$

In constant magnetic field only momentum component along the field direction is conserved. Thus, the conservation laws for synchrotron radiation read

$$\varepsilon_j = \omega + \varepsilon_k, \qquad p = q + \omega\cos\theta, \tag{19}$$

where ω is the photon energy and θ is the photon emission angle with respect to the magnetic field. Spectral intensity of angular distribution of synchrotron radiation by a fermion in the j'th Landau state is given by [18]

$$\frac{dI^j}{d\omega d\Omega} = \sum_f \frac{z_f^2\alpha}{\pi}\,\omega^2 \sum_{k=0}^{j} \Gamma_{jk}\left\{|\mathcal{M}_\perp|^2 + |\mathcal{M}_\parallel|^2\right\}\delta(\omega - \varepsilon_j + \varepsilon_k), \tag{20}$$

where $\Gamma_{jk} = (1+\delta_{j0})(1+\delta_{k0})$ accounts for the double degeneration of all Landau levels except the ground one. The squares of matrix elements $\mathcal{M}$, which appear in Eq. (20) can be found in Ref. [18] (our notations follow Ref. [19]).

In the context of heavy-ion collisions the relevant observable is the differential photon spectrum. For ideal plasma in equilibrium each quark flavor gives the following contribution to the photon spectrum:

$$\frac{dN^{\rm synch}}{dtd\Omega d\omega} = \sum_f \int_{-\infty}^{\infty} dp\,\frac{e_fB(2N_c)V}{2\pi^2} \sum_{j=0}^{\infty}\sum_{k=0}^{j} \frac{dI^j}{\omega d\omega d\Omega}\,(2-\delta_{j,0})\,f(\varepsilon_j)\,[1-f(\varepsilon_k)], \tag{21}$$

where $2N_c$ accounts for quarks and antiquarks each of N_c possible colors, and $(2-\delta_{j,0})$ sums over the initial quark spin. Index f indicates different quark flavors. V stands for the plasma volume. $f(\varepsilon)$ is a statistical factor. The δ-function appearing in Eq. (20) yields a constraint on the quark's momentum

$$p_\pm^* = \Big\{\cos\theta\,(m_j^2 - m_k^2 + \omega^2\sin^2\theta) \\ \pm\sqrt{\left[(m_j+m_k)^2 - \omega^2\sin^2\theta\right]\left[(m_j-m_k)^2 - \omega^2\sin^2\theta\right]}\Big\}\Big/(2\omega\sin^2\theta), \tag{22}$$

where $m_j^2 = m^2 + 2je_fB$, $m_k^2 = m^2 + 2ke_fB$. Inspection of Eq. (22) reveals that this equation has a real solution only in two cases

$$\text{(i) } m_j - m_k \geq \omega\sin\theta, \qquad \text{or} \qquad \text{(ii) } m_j + m_k \leq \omega\sin\theta. \tag{23}$$

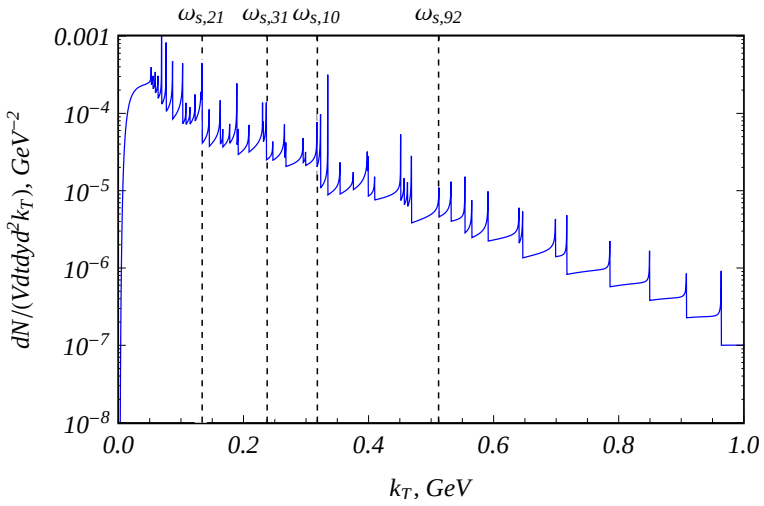

Figure 4: Spectrum of synchrotron radiation by u quarks at $eB = m_\pi^2$, $y = 0$, $\phi = \pi/3$: contribution of 10 lowest Landau levels $j \leq 10$; several cutoff frequencies are indicated. Adopted from Ref. [17].

The first case is relevant for the synchrotron radiation while the second one for the one-photon pair annihilation. Accordingly, allowed photon energies in the $j \to k$ transition satisfy

$$\omega \leq \omega_{s,jk} \equiv \frac{m_j - m_k}{\sin\theta} = \frac{\sqrt{m^2 + 2je_fB} - \sqrt{m^2 + 2ke_fB}}{\sin\theta}\,. \tag{24}$$

No synchrotron radiation is possible for $\omega > \omega_{s,jk}$ (see Fig. 4). In particular, when $j = k$, $\omega_{s,jk} = 0$, i. e. no photon is emitted. The reason is clearly seen in the frame where $p = 0$: since $\varepsilon_j \geq \varepsilon_k$, constraints (18) and (19) hold only if $\omega = 0$.

Substitution of (20) into Eq. (21) yields the spectral distribution of the synchrotron radiation rate per unit volume

$$\frac{dN^{\rm synch}}{Vdtd\Omega d\omega} = \sum_f \frac{2N_c z_f^2 \alpha}{\pi^3}\, e_f B \sum_{j=0}^{\infty}\sum_{k=0}^{j} \omega(1+\delta_{k0})\,\vartheta(\omega_{s,ij}-\omega) \int dp \sum_{\pm} \frac{\delta(p - p_\pm^*)}{\left|\frac{p}{\varepsilon_j} - \frac{q}{\varepsilon_k}\right|}$$
$$\times \left\{|\mathcal{M}_\perp|^2 + |\mathcal{M}_\parallel|^2\right\} f(\varepsilon_j)[1 - f(\varepsilon_k)], \tag{25}$$

where ϑ is the step-function.

The natural variables to study the synchrotron radiation are the photon energy ω and its emission angle θ with respect to the magnetic field. However, in high energy physics particle spectra are traditionally presented in terms of rapidity y (which for photons is equivalent to pseudo-rapidity) and transverse momentum $k_\perp$. $k_\perp$ is a projection of three-momentum $\boldsymbol{k}$ onto the transverse plane. These variables are not convenient to study electromagnetic processes in external magnetic field. In particular, they conceal the azimuthal symmetry with respect to the magnetic field direction. The change of variables is performed using formulas

$$\omega = k_\perp \cosh y, \qquad \cos\theta = \frac{\sin\phi}{\cosh y}\,. \tag{26}$$

Because $dy = dk_z/\omega$ the photon multiplicity in a unit volume per unit time reads

$$\frac{dN^{\rm synch}}{dV\,dt\,d^2k_\perp dy} = \omega\frac{dN^{\rm synch}}{dV\,dt\,d^3k} = \frac{dN^{\rm synch}}{dV\,dt\,\omega d\omega d\Omega} \tag{27}$$

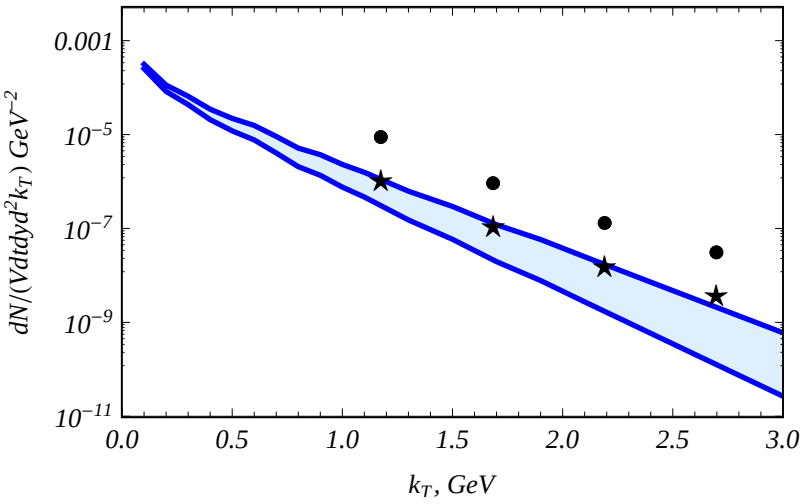

Figure 5: Azimuthal average of the synchrotron radiation spectrum of u, d, s quarks and their corresponding antiquarks compared to the experimental data from Ref. [20] divided by $Vt = 25\pi$ fm^4 (dots) and $Vt = 9 \times 25\pi$ fm^4 (stars); $eB = m_\pi^2$, $y = 0$. Lower line: $T = 200$ MeV, upper line: $T = 250$ MeV. Adopted from Ref. [17].

Figure 4 displays the spectrum of synchrotron radiation by u quarks as a function of $k_\perp$ at fixed ϕ [17]. At midrapidity $y = 0$, Eq. (26) implies that $k_\perp = \omega$. Contribution of d and s quarks is qualitatively similar. At $eB \gg m^2$, quark masses do not affect the spectrum much. The main difference stems from the difference in electric charge. In Fig. 4 only the contributions of the first ten Landau levels are displayed. The cutoff frequencies $\omega_{s,jk}$ can be clearly seen and some of them are indicated on the plot for convenience.

In order to compare the photon spectrum produced by synchrotron radiation to the photon spectrum measured in heavy-ion collisions, the u, d and s quarks contributions must be summed up. Furthermore, the experimental data from Ref. [20] should be divided by Vt, where t is the magnetic field relaxation time. The volume of the plasma can be estimated as $V = \pi R^2 t$ with $R \approx 5$ fm being the nuclear radius. The results are plotted in Fig. 5. It is seen that synchrotron radiation gives a significant contribution to the photon production in heavy-ion collisions at low k_T's. This is the region where conventional models of photon production fail to explain the experimental data.

5 Summary

High intensity and long life-time of electromagnetic field produced in relativistic heavy ion collisions indicate its phenomenological significance. In this presentation I discussed only two examples. It is clear however that the electromagnetic field changes the very structure of quark-gluon plasma and leaves hardly any observable unaffected. The ongoing experimental programs at RHIC and LHC can shed more light on the properties of hot nuclear matter in intense electromagnetic field.

References

[1] L. D. Landau, Izv. Akad. Nauk Ser. Fiz. **17**, 51 (1953).

[2] S. Z. Belenkij and L. D. Landau, Nuovo Cim. Suppl. **3S10**, 15 (1956) [Usp. Fiz. Nauk **56**, 309 (1955)].

[3] P. F. Kolb and U. W. Heinz, in *Quark gluon plasma 3*, eds. R. C. Hwa and X.-N. Wang. World Scientific, Singapore, 2004, p. 634, nucl-th/0305084 (2003).

[4] K. Tuchin, arXiv:1305.5806 [hep-ph] (2013).

[5] K. Tuchin, Adv. High Energy Phys. **2013**, 490495 (2013), arXiv:1301.0099 [hep-ph] (2013).

[6] D. E. Kharzeev, L. D. McLerran and H. J. Warringa, Nucl. Phys. A **803**, 227 (2008).

[7] K. Tuchin, Phys. Rev. C **82**, 034904 (2010); Erratum: *ibid.* **83**, 039903 (2011).

[8] H. T. Ding, A. Francis, O. Kaczmarek, F. Karsch, E. Laermann and W. Soeldner, arXiv:1012.4963 [hep-lat] (2010).

[9] G. Aarts, C. Allton, J. Foley, S. Hands and S. Kim, Phys. Rev. Lett. **99**, 022002 (2007), arXiv:hep-lat/0703008 (2007).

[10] A. Amato, G. Aarts, C. Allton, P. Giudice, S. Hands and J. -I. Skullerud, arXiv:1307.6763 [hep-lat] (2013).

[11] B. Machet and M. I. Vysotsky, Phys. Rev. D **83**, 025022 (2011), arXiv:1011.1762 [hep-ph] (2010).

[12] K. Marasinghe and K. Tuchin, Phys. Rev. C **84**, 044908 (2011), arXiv:1103.1329 [hep-ph] (2011).

[13] K. Tuchin, Phys. Lett. B **705**, 482 (2011), arXiv:1105.5360 [nucl-th] (2011).

[14] V. S. Popov, B. M. Karnakov and V. D. Mur, Phys. Lett. A **250**, 20 (1998).

[15] V. S. Popov, B. M. Karnakov and V. D. Mur, Phys. Lett. A **229**, 306 (1997).

[16] V. S. Popov, B. M. Karnakov and V. D. Mur, JETP **86**, 860 (1998).

[17] K. Tuchin, Phys. Rev. C **87**, 024912 (2013), arXiv:1206.0485 [hep-ph] (2012).

[18] A. A. Sokolov and I. M. Ternov, *Synchrotron radiation*. Pergamon Press, Oxford, 1968.

[19] M. G. Baring, Mon. Not. R. Ast. Soc. **235**, 57, (1988).

[20] A. Adare *et al.* (PHENIX Collaboration), Phys. Rev. Lett. **104**, 132301 (2010).

Light-Front Quantization of Non-Linear Sigma Models

Usha Kulshreshtha[1]

Department of Physics, Kirori Mal College, University of Delhi, Delhi-110007, India
Department of Physics and Astronomy, Iowa State University, Ames, Iowa

Abstract

A study of a class of the non-linear sigma models and gauged non-linear sigma models is presented. The canonical structure, constrained dynamics and the instant-form and light-front quantization of these models is reviewed and studied.

Keywords: *Quantum electrodynamics; quantum chromodynamics; non-linear sigma models; instant-form quantization; light-front quantization*

1 Introduction

In this talk, a study of the non-linear sigma models (NLSM) [1–9] and a class of gauged non-linear sigma models (GNLSM) is presented [7, 8]. The canonical structure and constraint quantization [10–18] of these models is studied using the instant-form and light-front dynamics [17,18]. The instant-form (IF) quantization (IFQ) and light-front (LF) quantization (LFQ) of these models is reviewed and studied.

In this talk, we consider a class of non-linear sigma models [1–6] and gauged non-linear sigma models [1–9]. We first review a class of NLSM [1–9] including their canonical structure and constrained dynamics, and then study their IFQ and LFQ [17, 18] using the Hamiltonian [10], path integral [11–13] and Becchi–Rouet–Stora and Tyutin (BRST) [14–16] formulations.

Using the above methods, we study a class of NLSM and GNLSM in one-space one-time dimensions ($2D$). We study their canonical structure and constraint quantization in the IFQ and LFQ, using Dirac's Hamiltonian formulation and the path integral and BRST formulations. Our studies also involve a construction of gauge-invariant (GI) field theories from the gauge-non-invariant (GNI) field theories using the Stueckelberg formalism and other methods. We could recover the physical contents of the original GNI theories from the corresponding newly constructed GI theories under some special non-trivial gauge-fixing conditions (GFC).

A few points about the IF and LF dynamics are in order. In the IF quantization of field theories, one studies the theory on the hyper surfaces defined by the IF time: $t = x^0 = constant$ [17, 18]. On the other hand, in the LFQ [17, 18] of field theories, one studies the theory on the hyper surfaces of the LF defined by the light-cone (LC) time: $\tau = x^+ = (x^0 + x^1)/\sqrt{2} = constant$.

The LFQ [17,18] has several advantages over the IFQ [17,18]. The LF theory, e. g., has more kinematical generators than the corresponding IF theory and the removal of constraints by Dirac's method gives fewer independent dynamical variables in the

[1]Dedicated to Prof. James Vary on his Seventieth Birthday.

Proceedings of International Conference 'Nuclear Theory in the Supercomputing Era — 2013' (NTSE-2013), Ames, IA, USA, May 13–17, 2013. Eds. A. M. Shirokov and A. I. Mazur. Pacific National University, Khabarovsk, Russia, 2014, p. 185.
http://www.ntse-2013.khb.ru/Proc/UKulshreshtha.pdf.

LFQ than in the IFQ. In LFQ there is no conflict with the microcausality principle. In the LFQ of gauge theories, the transverse degrees of freedom of the gauge field can be immediately identified as the dynamical degrees of freedom, as a result, the LFQ remains very economical in displaying the relevant degrees of freedom leading directly to the physical Hilbert space. Also, because the LF coordinates are not related to the conventional instant-form coordinates by a finite Lorentz transformation, the descriptions of the same physical result may be different in IF and LF dynamics. The advantages of the LFQ over the IFQ are reviewed in Ref. [18]. Use of both the IF and LF gives a rather complete dynamics of the system. A study of such theories could be used to test several interesting ideas in field theories.

Further the product of two Fermi fields at the same space-time point is highly singular and leads to regularization ambiguities. In order to take care of these regularization ambiguities one introduces a regularization parameter which appears in the coefficient of the mass term of the U(1) gauge field A^μ. This regularization scheme is often referred to as the standard regularization.

The O(N) nonlinear sigma models in $2D$, where the field sigma is a real N-component field, provide a laboratory for the various nonperturbative techniques, e. g., $1/N$-expansion, operator product expansion, and the low energy theorems. These models are characterized by features like renormalization and asymptotic freedom common with that of quantum chromodynamics and exhibit a nonperturbative particle spectrum, have no intrinsic scale parameter, possess topological charges, and are very crucial in the context of conformal and string field theories where they appear in the classical limit.

The Hamiltonian formulation of the gauge-non-invariant O(N)-NLSM in $2D$ has been studied in Refs. [2, 3, 6] and its two GI versions have been studied in Ref. [6] in the IFQ using the Hamiltonian and BRST formulations. The LFQ of this theory has been studied by us in Ref. [9], using the Hamiltonian, path integral and BRST formulations.

The IFQ of the gauged non-linear sigma model has been studied by us in Ref. [7], and its LFQ has been studied in Ref. [8], using the Hamiltonian and BRST formulations. We now proceed to study these models in some details in the following.

2 The non-linear sigma models

The O(N)-NLSM in one-space one-time dimensions is defined by the action [1–6]:

$$\begin{aligned} S &= \int \mathcal{L}(\sigma_k, \lambda)\, d^2x, \\ \mathcal{L} &= \left[\frac{1}{2}\partial_\mu \sigma_k \partial^\mu \sigma_k + \lambda(\sigma_k^2 - 1)\right]. \end{aligned} \tag{1}$$

Here $\sigma_k(x,t)$ (with $k = 1, 2, \ldots, N$) is a multiplet of N real scalar fields in two-dimensions, and $\lambda(x,t)$ is another scalar field. The vector field $\sigma(x,t)$ maps the two-dimensional space-time into the N-dimensional internal manifold whose coordinates are $\sigma_k(x,t)$. In the above equation, the first term corresponds to a massless boson (which is equivalent to a massless fermion), and the second term is the usual term involving the nonlinear constraint $(\sigma_k^2 - 1)$ and the auxiliary field. Also $\mu = 0,\ 1$ for the IFQ and $\mu = +,\ -$ for LFQ.

2.1 Instant-form quantization

In the IFQ, the action of the theory reads [1–6]:

$$\begin{aligned} S &= \int \mathcal{L}(\sigma_k, \lambda)\, dx^0 dx^1, \\ \mathcal{L} &= \left[\frac{1}{2}(\partial_0\sigma_k\partial_0\sigma_k - \partial_1\sigma_k\partial_1\sigma_k) + \lambda(\sigma_k^2 - 1)\right]. \end{aligned} \tag{2}$$

This model is seen to possess a set of four constraints [1–6]:

$$\begin{aligned} \chi_1 &= p_\lambda \approx 0, \\ \chi_2 &= (\sigma_k^2 - 1) \approx 0, \\ \chi_3 &= 2\sigma_k\pi_k \approx 0, \\ \chi_4 &= \left(2\pi_k^2 + 4\lambda\sigma_k^2 + 2\sigma_k\partial_1\partial_1\sigma_k\right) \approx 0. \end{aligned} \tag{3}$$

Here p_λ and π_k denote the momenta canonically conjugate respectively to λ and σ_k. Also, χ_1 is a Primary constraint and χ_2, χ_3 and χ_4 are the secondary Gauss law constraints. The symbol $\approx$ here denotes a weak equality in the sense of Dirac, and it implies that these constraints hold as strong equalities only on the reduced hypersurface of the constraints and not in the rest of the phase space of the classical theory (and similarly one can consider it as a weak operator equality for the corresponding quantum theory). The canonical Hamiltonian density of the theory is [6]:

$$\mathcal{H}_c = \left[\frac{1}{2}(\pi_k^2 + \partial_1\sigma_k\partial_1\sigma_k) - \lambda(\sigma_k^2 - 1)\right]. \tag{4}$$

After including the primary constraint in the canonical Hamiltonian density with the help of the Lagrange multiplier field u which is treated as a dynamical field, the total Hamiltonian density of the theory is [6]:

$$\mathcal{H}_T = \left[\frac{1}{2}(\pi_k^2 + \partial_1\sigma_k\partial_1\sigma_k) - \lambda(\sigma_k^2 - 1) + p_\lambda u\right]. \tag{5}$$

The Hamilton's equations of motion which preserve the constraints of the theory could now be obtained using this total Hamiltonian density and are omitted here for the sake of brevity [6]. Also the matrix of the Poisson brackets among the constraints χ_i is non-singular. The theory possesses a vector gauge anomaly at the classical level, implying that the theory describes a gauge-non-invariant theory. However, it is possible to construct gauge-invariant models corresponding to this GNI theory using the techniques of constraint quantization. It is also possible to recover the physical contents of the original GNI theory from the newly constructed GI versions. One can also study the instant-form quantization and light-front quantization of these models (cf. Refs. [6] and [9]).

The Dirac quantization procedure in the IF Hamiltonian formulation leads to the non-vanishing equal-time commutation relations for this theory as [2, 6]:

$$\begin{aligned} [\pi_l(x,t), \pi_m(y,t)] &= \frac{-i}{\sigma_k^2}\left[\sigma_l(x)\,\pi_m(y) - \pi_l(x)\,\sigma_m(y)\right]\delta(x-y), \\ [\sigma_l(x,t), \pi_m(y,t)] &= i\left[\delta_{lm} - \frac{\sigma_l(x)\,\sigma_m(y)}{\sigma_k^2}\right]\delta(x-y). \end{aligned} \tag{6}$$

This model is seen to possess a set of (four) second-class constraints implying that it describes a gauge-non-invariant theory. However it is possible to construct gauge-invariant models corresponding to this GNI theory using the techniques of constrained

dynamics. One can also recover the physical contents of the original GNI theory from the newly constructed GI versions. Further, it is also possible to study this theory using the LFQ, where the theory becomes GI, as has been done by us in Ref. [9].

In the path integral formulation [11–14], the transition to quantum theory is made by writing the vacuum to vacuum transition amplitude for the theory called the generating functional $Z[J_k]$ for the present theory, in the presence of the external sources J_k it could be written as:

$$Z[J_k] = \int [d\mu]\ \exp\biggl\{ i \int d^2x \left[J_k \Phi^k + p_\lambda \partial_0 \lambda + \pi_k \partial_0 \sigma_k + \Pi_u \partial_0 u - \mathcal{H}_T \right] \biggr\}. \tag{7}$$

Here, the phase space variables of the theory are $\Phi^k \equiv (\lambda, \sigma_k, u)$ with the corresponding respective canonical conjugate momenta $\Pi_k \equiv (p_\lambda, \pi_k, \Pi_u)$. The functional measure $[d\mu]$ of the generating functional $Z[J_k]$ is obtained as:

$$\begin{aligned}[d\mu] = \bigl[16\sigma_k^2\sigma_k^2\,\delta(x-y)\bigr][d\sigma_k][d\lambda][du][d\pi_k][dp_\lambda]d\Pi_u]\,\delta[p_\lambda \approx 0]\delta\bigl[(\sigma_k^2-1)\approx 0\bigr] \\ \times\,\delta\bigl[(2\sigma_k\pi_k)\approx 0\bigr]\delta\bigl[(2\pi_k^2 + 4\lambda\sigma_k^2 + 2\sigma_k\partial_1\partial_1\sigma_k)\approx 0\bigr].\end{aligned} \tag{8}$$

2.2 Light-front quantization

In the LFQ the action of this theory reads [9]:

$$\begin{aligned} S &= \int \mathcal{L}(\sigma_k, \lambda)\, dx^+ dx^-, \\ \mathcal{L} &= \bigl[\partial_+\sigma_k\partial_-\sigma_k + \lambda(\sigma_k^2 - 1)\bigr]. \end{aligned} \tag{9}$$

This model is seen to possess a set of three constraints:

$$\begin{aligned} \psi_1 &= p_\lambda \approx 0, \\ \psi_2 &= (\pi_k - \partial_-\sigma_k) \approx 0, \\ \psi_3 &= (\sigma_k^2 - 1) \approx 0. \end{aligned} \tag{10}$$

Here p_λ and π_k denote the momenta canonically conjugate respectively to λ and σ_k. Also, ψ_1 and ψ_2 here are primary constraints and ψ_3 is the secondary Gauss law constraint. These constraints form a set of first-class constraints, implying that the theory describes a GI theory. The theory is indeed seen to be invariant under the gauge transformations [9]:

$$\begin{aligned} &\delta\sigma_k = \beta(x^+, x^-), \quad \delta\pi_k = \partial_-\beta(x^+, x^-), \quad \delta v = \partial_+\beta(x^+, x^-), \\ &\delta\lambda = \delta u = \delta\pi_k = \delta\pi_u = \delta\pi_v = 0, \end{aligned} \tag{11}$$

where the gauge parameter $\beta \equiv \beta(x^+, x^-)$ is a function of its arguments. The canonical Hamiltonian density of the theory is [9]:

$$\mathcal{H}_c = \bigl[-\lambda(\sigma_k^2 - 1)\bigr]. \tag{12}$$

After including the primary constraints in the canonical Hamiltonian density with the help of the Lagrange multiplier fields u and v which are to be treated as dynamical fields, the total Hamiltonian density of the theory is:

$$\mathcal{H}_T = \bigl[-\lambda(\sigma_k^2 - 1) + p_\lambda u + (\pi_k - \partial_-\sigma_k)v\bigr]. \tag{13}$$

3 Gauge-invariant non-linear sigma models

3.1 Model-A

In Ref. [6], we have constructed and studied a gauge-invariant non-linear sigma model using the Stueckelberg mechanism. In constructing the gauge-invariant model corresponding to the above gauge-non-invariant model, we enlarge the Hilbert space of the theory and introduce a new field θ, called the Stueckelberg field, through the following redefinition of fields [6]:

$$\sigma_k \to \Sigma_k = \sigma_k - \theta, \qquad \lambda \to \Lambda = \lambda + \partial_0\theta. \tag{14}$$

Performing the changes in to the Lagrangian density of the above theory, we obtain the modified Lagrangian density $\mathcal{L}^I$ (ignoring the total space and time derivatives) as [6]

$$\mathcal{L}^I = \mathcal{L} + \mathcal{L}^S \tag{15}$$

with

$$\mathcal{L}^S = \Big[\frac{1}{2}(\partial_0\theta)^2 - \frac{1}{2}(\partial_1\theta)^2 - \partial_0\sigma_k\,\partial_0\theta + \partial_1\sigma_k\,\partial_1\theta + \partial_0\theta(\sigma_k^2 - 1) - (\lambda + \partial_0\theta)\theta(2\sigma_k - \theta)\Big], \tag{16}$$

where $\mathcal{L}^S$ is the appropriate Stueckelberg term corresponding to $\mathcal{L}^I$ and in fact, one can easily see that it is possible to recover the physical contents of the original gauge-non-invariant theory under some special gauge choice. This gauge-invariant theory is seen to possess a set of three constraints:

$$\begin{aligned} \eta_1 &= p_\lambda \approx 0, \\ \eta_2 &= \big[\pi_\theta + \pi_k - (\sigma_k^2 - 1) + \theta(2\sigma_k - \theta)\big] \approx 0, \\ \eta_3 &= \big[(\sigma_k^2 - 1) - \theta(2\sigma_k - \theta)\big] \approx 0, \end{aligned} \tag{17}$$

where η_1 and η_2 are primary constraints and η_3 is the secondary Gauss-law constraint of the theory. Here, p_λ, π_θ, π_k are the momenta canonically conjugate respectively to the variables λ, θ and σ_k. The canonical Hamiltonian density of the theory is [6]:

$$\mathcal{H}_c = \Big[\frac{1}{2}\pi_k^2 + \frac{1}{2}(\partial_1\,\sigma_k)^2 + \frac{1}{2}(\partial_1\theta)^2 - \partial_1\sigma\partial_1\theta - \lambda(\sigma_k^2 - 1) + \lambda\theta(2\sigma_k - \theta)\Big]. \tag{18}$$

The total Hamiltonian density corresponding to this gauge-invariant theory obtained after including in the canonical Hamiltonian density of the theory the primary constraints of the theory with the help of Lagrange multiplier fields is:

$$\mathcal{H}_T = \Big[\frac{1}{2}\pi_k^2 + \frac{1}{2}(\partial_1\sigma_k)^2 + \frac{1}{2}(\partial_1\theta)^2 - \partial_1\sigma\,\partial_1\theta - \lambda(\sigma_k^2 - 1) + \lambda\theta(2\sigma_k - \theta) + p_\lambda u + [\pi_\theta + \pi_k - (\sigma_k^2 - 1) + \theta(2\sigma_k - \theta)]v\Big]. \tag{19}$$

The set of constraints of the theory is first-class, implying that the theory is gauge-invariant. The theory is indeed seen to be invariant under the following gauge-transformations:

$$\begin{aligned} &\delta\sigma_k = \beta(x^0, x^1), \qquad \delta\lambda = -\delta\theta = -\partial_0\beta(x^0, x^1), \\ &\delta p_\lambda = \delta\pi_\theta = \delta\pi_k = 0, \end{aligned} \tag{20}$$

where the gauge parameter $\beta \equiv \beta(x^0, x^1)$ is a function of its arguments. From this gauge-invariant theory, it is however, possible to recover the physical contents of the original gauge-non-invariant theory under some special gauge-fixing conditions. For this we go to a special gauge given by $\theta = 0$, and accordingly choose the gauge-fixing conditions of the theory as [7]:

$$\begin{aligned} \zeta_1 &= (2\sigma_k \pi_k - \pi_\theta - \pi_k) \approx 0, \\ \zeta_2 &= (2\pi_k^2 + 4\lambda\sigma_k^2 + 2\sigma_K + \partial_1\partial_1\sigma_k) \approx 0, \\ \zeta_3 &= \theta \approx 0. \end{aligned} \tag{21}$$

As studied in details in Ref. [6], it is easy to see that the above set of gauge-fixing conditions reproduces precisely the quantum system described by the original gauge-non-invariant theory. The above set of gauge-fixing conditions in fact translates the gauge-invariant version of the theory into the gauge-non-invariant one. The physical Hilbert spaces of the two theories are just the same [6].

3.2 Model-B

In Ref. [6], we have studied another gauge-invariant non-linear sigma model (constructed by Mitra and Rajaraman in Refs. [4, 5], using their procedure of gauge-invariant reformulation). This model is defined by the total Hamiltonian density

$$\mathcal{H}_T = \left[\frac{1}{2}\pi_k^2 + \frac{1}{2}(\partial_1\sigma_k)^2 - \lambda(\sigma_k^2 - 1) + p_\lambda u - \eta(\sigma_k\pi_k)\right], \quad \eta \equiv \eta(x^\mu) := \left[\frac{\sigma_k\pi_k}{2\sigma_k^2}\right], \tag{22}$$

and its corresponding second-order Lagrangian density [6]

$$\mathcal{L} = \left[\frac{1}{2}\partial_\mu\sigma_k\,\partial^\mu\sigma_k + \lambda(\sigma_k^2 - 1) + \eta(2\sigma_k\,\partial_0\sigma_k\right]. \tag{23}$$

This model possesses a set of two constraints:

$$\begin{aligned} \chi_1 &= p_\lambda \approx 0, \\ \chi_2 &= (\sigma_k^2 - 1) \approx 0. \end{aligned} \tag{24}$$

Here p_λ and π_k denote the momenta canonically conjugate respectively to λ and σ_k. Also, χ_1 is a primary constraint and χ_2 is the secondary Gauss law constraint. Here the remaining two secondary constraints of the original gauge-non-invariant theory have been truncated using the method of Mitra–Rajaraman [7, 8] for the gauge-invariant reformulation of the corresponding original gauge-non-invariant theory. It is important to note here that this method is applicable only to those theories which possess a chain of constraints following from a single constraint. The constraints which have thus been truncated could now be imposed on the original theory as gauge-fixing conditions for the quantization of the gauge-invariant theory under gauge-fixing. The above gauge-invariant theory is indeed seen to be invariant under the gauge-transformations [6]:

$$\delta\eta = \beta(x^0, x^1), \quad \delta\pi_k = 2\sigma_k\beta(x^0, x^1), \quad \delta\lambda = \partial_0\beta(x^0, x^1), \quad \delta\sigma_k = \delta p_\lambda = 0, \tag{25}$$

where the gauge parameter $\beta \equiv \beta(x^0, x^1)$ is a function of its arguments.

4 The gauged non-linear sigma models

In Refs. [7, 8], we have constructed and studied a gauged non-linear sigma model and studied its quantization using the IFQ [7] and LFQ [8]. The GNLSM with the

standard regularization in one-space one-time dimensions is defined by the action [7]:

$$\begin{aligned} S &= \int \mathcal{L}(\sigma_k, \lambda, A^\mu)\, d^2x, \\ \mathcal{L} &= \left[\frac{1}{2}\,\partial_\mu\sigma_k\,\partial^\mu\sigma_k + \lambda(\sigma_k^2 - 1) - \frac{1}{4}F_{\mu\nu}F^{\mu\nu} - eA_\mu\,\partial^\mu\sigma_k + \frac{1}{2}ae^2A_\mu A^\mu\right]. \end{aligned} \tag{26}$$

In the above equation, the first term corresponds to a massless boson (which is equivalent to a massless fermion), the second term is the usual term involving the nonlinear constraint and the auxiliary field λ, the third term is the kinetic energy term of the electromagnetic vector-gauge field $A^\mu(x,t)$, the fourth term represents the coupling of the sigma field to the electromagnetic field, and the last term is the mass term for the vector gauge field $A^\mu(x,t)$. Here e is the coupling constant that couples the massless fermion(or equivalently the boson) with the U(1) gauge field A^μ. This theory is a well known gauge-invariant theory, possessing a set of first-class constraints. Here we have constructed a gauged version of the usual NLSM by introducing the U(1) gauge field A^μ into the theory. We have also included the mass term for the U(1) gauge-field A^μ into the above Lagrangian, defined by $[\mathcal{L}_m = \frac{1}{2}ae^2A_\mu A^\mu]$, where a is the standard regularization parameter. The modified resulting theory then describes the gauged NLSM (GNLSM) with the standard regularization. This theory is seen to be GI and has been studied in details using the IFQ in Ref. [7], and its LFQ has been studied in Ref. [8].

4.1 Instant-form quantization

The GNLSM with the standard regularization is defined by the action (with $\mu, \nu = 0,\ 1$ for IFQ) [7]:

$$\begin{aligned} S &= \int \mathcal{L}(\sigma_k, \lambda, A^\mu)\, d^2x, \\ \mathcal{L} &= \left[\frac{1}{2}(\partial_0\sigma_k\,\partial_0\sigma_k - \partial_1\sigma_k\,\partial_1\sigma_k) + \lambda(\sigma_k^2 - 1) - e(A_0\partial_0\sigma_k - A_1\partial_1\sigma_k)\right. \\ &\qquad \left. + \frac{1}{2}(\partial_0A_1 - \partial_1A_0)^2 + \frac{1}{2}ae^2(A_0^2 - A_1^2)\right]. \end{aligned} \tag{27}$$

This model is seen to possess a set of five constraints as follows:

$$\begin{aligned} \varphi_1 &= \Pi_0 \approx 0, \\ \varphi_2 &= p_\lambda \approx 0, \\ \varphi_3 &= (\partial_1 E - e\Pi_k) \approx 0, \\ \varphi_4 &= (\sigma_k^2 - 1) \approx 0, \\ \varphi_5 &= (2\sigma_k\Pi_k + 2eA_0\sigma_k) \approx 0. \end{aligned} \tag{28}$$

Here p_λ, π_k, Π_0 and $E = \Pi^1$ denote the momenta canonically conjugate respectively to λ, σ_k, A_0 and A_1. Also, φ_1 and φ_2 are primary constraints and φ_3, φ_4 and φ_5 are the secondary Gauss law constraints. Further, these constraints form a set of first-class constraints, implying that the theory possesses the gauge symmetry and is invariant under the following gauge-transformations [7]:

$$\begin{aligned} &\delta\sigma_k = e\beta(x^0, x^1), \quad \delta\lambda = -\delta A_0 = -\partial_0\beta(x^0, x^1), \quad \delta A_1 = \partial_1\beta(x^0, x^1), \\ &\delta\pi_k = \delta E = \delta\Pi_0 = \delta p_\lambda = \delta\Pi_u = \delta\Pi_v = 0, \\ &\delta u = -\delta v = \partial_0\partial_0\beta(x^0, x^1), \end{aligned} \tag{29}$$

where the gauge parameter $\beta \equiv \beta(x^0, x^1)$ is a function of its arguments. The canonical Hamiltonian density of the theory is [7]:

$$\mathcal{H}_c = \Big[\frac{1}{2}\big[\pi_k^2 + E^2 + (\partial_1\sigma_k)^2 + e^2A_0^2\big] - \frac{1}{2}e^2\big(A_0^2 - A_1^2\big) + E\partial_1 A_0 + eA_0\pi_k - eA_1\partial_1\sigma_k - \lambda\big(\sigma_k^2 - 1\big)\Big]. \quad (30)$$

After including the primary constraints in the canonical Hamiltonian density with the help of the Lagrange multiplier fields u and v which are to be treated as dynamical fields, the total Hamiltonian density of the theory is:

$$\mathcal{H}_T = \Big[\frac{1}{2}\big[\pi_k^2 + E^2 + (\partial_1\sigma_k)^2 + e^2A_0^2\big] + E\partial_1 A_0 + eA_0\pi_k - \frac{1}{2}e^2\big(A_0^2 - A_1^2\big) - eA_1\partial_1\sigma_k - \lambda\big(\sigma_k^2 - 1\big) + \Pi_0 u + p_\lambda v\Big]. \quad (31)$$

4.2 Light-front quantization

The GNLSM with the standard regularization is defined by the action with $\mu, \nu = +, -$ for LFQ) [8]:

$$S = \int \mathcal{L}(\sigma_k, \lambda, A^\mu)\, dx^+ dx^-,$$

$$\mathcal{L} = \Big[(\partial_+\sigma_k)(\partial_-\sigma_k) + \lambda\big(\sigma_k^2 - 1\big) - e\big(A^-\partial_-\sigma_k + A^+\partial_+\sigma_k\big) + \frac{1}{2}\big(\partial_+A^+ - \partial_-A^-\big)^2 + ae^2\big(A^+A^-\big)\Big]. \quad (32)$$

This model is seen to possess a set of five constraints:

$$\begin{aligned}
\xi_1 &= \Pi^+ \approx 0,\\
\xi_2 &= p_\lambda \approx 0,\\
\xi_3 &= \big(\pi_k - \partial_-\sigma_k + eA^+\big) \approx 0,\\
\xi_4 &= \big(\partial_-\Pi^- + e\partial_-\sigma_k, +e^2A^+\big) \approx 0,\\
\xi_5 &= \big(\sigma_k^2 - 1\big) \approx 0.
\end{aligned} \quad (33)$$

Here p_λ, π_k, Π^+ and Π^- denote the momenta canonically conjugate respectively to λ, σ_k, A^- and A^+. Also, ξ_1, ξ_2 and ξ_3 here are primary constraints and ψ_4 and ψ_5 are the secondary Gauss law constraints. These constraints form a set of first-class constraints, implying that the theory describes a GI theory. The theory is indeed seen to be invariant under the gauge transformations [8]:

$$\begin{aligned}
&\delta\sigma_k = e\beta(x^+, x^-), \quad \delta\lambda = -\delta A^- = -\partial_+\beta(x^+, x^-), \quad \delta A^+ = \partial_-\beta(x^+, x^-),\\
&\delta\pi_k = \delta\Pi^+ = \delta\Pi^- = \delta p_\lambda = \delta\pi_k = \delta\Pi_u = \delta\Pi_v = \delta\Pi_w = 0,\\
&\delta u = -\delta v = \partial_+\partial_+\beta(x^+, x^-), \qquad \delta w = e\partial_+\beta(x^+, x^-),
\end{aligned} \quad (34)$$

where the gauge parameter $\beta \equiv \beta(x^0, x^1)$ is a function of its arguments. The canonical Hamiltonian density of the theory is [8]:

$$\mathcal{H}_c = \big[-\lambda(\sigma_k^2 - 1)\big]. \quad (35)$$

After including the primary constraints in the canonical Hamiltonian density with the help of the Lagrange multiplier fields u, v and w which are treated as dynamical fields, the total Hamiltonian density of the theory is:

$$\mathcal{H}_T = \big[-\lambda(\sigma_k^2 - 1) + \Pi^+ u + p_\lambda v + (\pi_k - \partial_- \sigma_k + eA^+)w\big]. \tag{36}$$

Also, in the usual Hamiltonian and path integral formulations of a GI theory under some GFC, one necessarily destroys the gauge invariance of the theory by fixing the gauge (which converts a set of first-class constraints into a set of second-class constraints, implying a breaking of gauge invariance under gauge-fixing). In order to achieve the quantization of a GI theory such that the gauge-invariance of the theory is maintained even under gauge-fixing one goes to a more generalized procedure called BRST formulation.

For the BRST quantization of a GI theory, one enlarges the phase space of the classical theory or the Hilbert space of the corresponding quantum theory of the GI theory by introducing the Faddeev–Popov fermionic ghost and anti-ghost fields and the Nakanishi–Lautrup bosonic ghost field into the first-order Lagrangian density or the action of the theory. One thus rewrites the GI system as a quantum system which possesses a generalized gauge-invariance called the BRST symmetry. In the BRST formulation, one thus embeds a GI theory into a BRST-invariant system, and the quantum Hamiltonian of the system which includes the gauge-fixing contribution commutes with the BRST charge operator Q as well as with the anti-BRST charge operator $\bar{Q}$, and the new symmetry of the quantum system (the BRST symmetry) which replaces the gauge-invariance is maintained even under the gauge-fixing and hence projecting any state onto the sector of BRST and anti-BRST invariant states, yields a theory which is isomorphic to the original gauge-invariant theory.

5 Acknowledgments

Author thanks the University Grants Commission (UGC), New Delhi, India, **for the award of a "Full Travel Grant"** for attending the International Conference on "Nuclear Theory in the Supercomputing Era — 2013 (NTSE-2013)", held at the Iowa State University, Ames, Iowa, USA, from May 13–17, 2013, where this work was presented as an Invited Talk. She also thanks Prof. James Vary for his kind hospitality at the ISU, Ames, Iowa, during the Summer of 2013, where this work was completed. She also thanks the Organizers of NTSE-2013 for providing an excellent and a very welcoming environment and hospitality during the conference. She thanks Prof. James Vary for several fruitful and educative discussions. This work was supported in part by the Department of Energy under Grant No. DE-FG02-87ER40371.

References

[1] J. Schwinger, Ann. Phys. (NY) **2**, 407 (1958).

[2] J. Maharana, Phys. Lett. B **128**, 411 (1983).

[3] J. Maharana, Ann. Inst. H. Poincaré A **XXXIX**, 193 (1983).

[4] P. Mitra and R. Rajaraman, Ann. Phys. (NY) **203**, 137 (1990).

[5] P. Mitra and R. Rajaraman, Ann. Phys. (NY) **203**, 157 (1990).

[6] U. Kulshreshtha, D. S. Kulshreshtha and H. J. W. Müller-Kirsten, Helv. Phys. Acta **66**, 752 (1993).

[7] U. Kulshreshtha, Int. J. Theor. Phys. **40**, 491 (2001).

[8] U. Kulshreshtha, Int. J. Theor. Phys. **40**, 1561 (2001).

[9] U. Kulshreshtha and D. S. Kulshreshtha, Int. J. Theor. Phys. **41**, 1941 (2002).

[10] P. A. M. Dirac, Can. J. Math. **2**, 129 (1950).

[11] P. Sanjanovic, Ann. Phys. (NY) **100**, 227 (1976).

[12] U. Kulshreshtha and D. S. Kulshreshtha, Phys. Lett. B **555**, 255 (2003).

[13] U. Kulshreshtha and D. S. Kulshreshtha, Eur. Phys. J. C **29**, 453 (2003).

[14] C. Becchi, A. Rouet and A. Stora, Phys. Lett. B **52**, 344 (1974).

[15] V. Tyutin, Report No. FIAN-39 (1975) (*unpublished*).

[16] D. Nemeschansky, C. Preitschopf and M. Weinstein, Ann. Phys. (NY) **183**, 226 (1988).

[17] P. A. M. Dirac, Rev. Mod. Phys. **21**, 392 (1949).

[18] S. J. Brodsky, H. C. Pauli and S. S. Pinsky, Phys. Rept. **301**, 299 (1998).

LFQ of Large N Scalar QCD_2 with a Higgs Potential

Usha Kulshreshtha[a,c], Daya Shankar Kulshreshtha[b,c,1] and James Vary[c]

[a] *Department of Physics, Kirori Mal College, University of Delhi, Delhi-110007, India*
[b] *Department of Physics and Astrophysics, University of Delhi, Delhi-110007, India*
[c] *Department of Physics and Astronomy, Iowa State University, Ames, Iowa 50011, USA*

Abstract

Recently Grinstein, Jora and Polosa have studied a model of large N scalar quantum chromodynamics in one-space one-time dimension. This model admits a Bethe–Salpeter equation describing the discrete spectrum of $q\bar{q}$ bound states. They consider the gauge fields in the adjoint representation of SU(N) and the scalar fields in the fundamental representation. The model is asymptotically free and linearly confining. The model provides a good framework for the description of a large class of tetraquark (diquark-antidiquark) states. Recently we have studied the light-front quantization of this model *without* a Higgs potential. In the present work, we study the light-front Hamiltonian, path integral and BRST formulations of this model in the presence of a Higgs potential.

Keywords: *Quantum chromodynamics (QCD); tetraquark states; diquark-antidiquark states; light-front quantization; Hamiltonian quantization; path integral quantization; BRST quantization*

1 Introduction

Study of multiquark states has been a subject of wide interest for a rather long time [1–15]. Their interpretation remains a challenging task and a number of phenomenological models [1–15] have been proposed to understand various experimental observations. Various possibilities of understanding the hadron structure different from the usual mesons and baryons [3,4] have been considered in the literature rather widely [1–15]. Some of these states find a rather more natural interpretation in terms of four quark states or tetraquark states [3–15]. By now it is widely perceived that not only the heavier states like the X, Y, Z states have an exotic structure which find more natural explanation as tetraquark states or diquark-antidiquark ($Q\bar{Q}$) states [3–15], but even the light scalar mesons are also most likely the lightest particles with an exotic structure also to be understood as $Q\bar{Q}$ or tetraquark states (because they cannot be classified as standard $q\bar{q}$ mesons) [1–14].

Very recently 't Hooft, Isidori, Maini, Polosa and Riquer [13] and others [2–5], have shown how one could explain the decays of the light scalar mesons by assuming a dominant $Q\bar{Q}$ structure for the lightest scalar mesons, where the diquark (Q) is being taken to be a spin zero antitriplet color state [1–5]. Further, Grinstein,

[1] Speaker at the Conference.

Proceedings of International Conference 'Nuclear Theory in the Supercomputing Era — 2013' (NTSE-2013), Ames, IA, USA, May 13–17, 2013. Eds. A. M. Shirokov and A. I. Mazur. Pacific National University, Khabarovsk, Russia, 2014, p. 195.
http://www.ntse-2013.khb.ru/Proc/DSKulshreshtha.pdf.

Jora and Polosa [14] have studied a model of large N scalar quantum chromodynamics (QCD) [1–15] in one-space one-time dimensions. Their model admits [14] a Bethe–Salpeter equation describing the discrete spectrum of $q\bar{q}$ bound states [1–5]. It is important to emphasize here that in the first approximation, the nonet formed by $f_0(980)$, $a_0(980)$, $\kappa(900)$, $\sigma(500)$ is interpreted as the lowest $Q\bar{Q}$ multiplet [14], and the decuplet of scalar mesons with masses above 1 GeV, formed by $f_0(1370)$, $f_0(1500)$, $f_0(1710)$, $a_0(1450)$, $K_0(1430)$ and possibly containing the lowest glueball, is interpreted as the lowest $q\bar{q}$ scalar multiplet [12–14]. The work of Grinstein *et al.* [14] is seen to further support this hypothesis. In the work of Grinstein *et al.* [14], the gauge fields have been considered in the adjoint representation of SU(N) and the scalar fields in the fundamental representation. The theory is asymptotically free and linearly confining and different aspects of this theory have been studied by several authors in various contexts [14].

In a recent paper we have studied [15] the light-front (LF) quantization (LFQ) of this theory [with a mass term for the complex scalar (diquark) field but without the Higgs potential], under appropriate LC gauge-fixing conditions. In the present work, we study the LF Hamiltonian [16], path integral [17–19] and BRST [20–22] formulations of this theory [14] in the presence of a Higgs potential on the LF (i. e., on the hyperplanes defined by the equal light-cone (LC) time $\tau = x^+ = (x^0 + x^1)/\sqrt{2} = constant$ [23–27]. The LF theory is seen to be gauge-invariant (GI) possessing a set of first-class constraints.

In our earlier work involving the LFQ of this theory [15], the theory was considered with a mass term for the complex scalar (diquark) field *but without a Higgs potential*, whereas we now study this theory *in the presence of the Higgs potential*. The motivation for doing this is to study the aspects related to the spontaneous symmetry breaking in the theory. Also, because the theory is GI, we also study its BRST quantization under appropriate BRST LC gauge-fixing. Actually, in the Hamiltonian and path integral quantization of a theory under some gauge-fixing conditions the gauge-invariance of the theory necessarily gets broken because the procedure of gauge-fixing converts the set of first-class constraints of the theory into a set of second-class ones. In view of this, in order to achieve the quantization of a GI theory, such that the gauge-invariance of the theory is maintained even under gauge-fixing, one of the possible ways is go to a more generalized procedure called the BRST quantization, where the extended gauge symmetry called the BRST symmetry is maintained even under gauge-fixing.

2 Some basics of the theory

In this section we consider the instant-form (IF) quantization (IFQ) of this model of large N scalar QCD in the presence of a Higgs potential, studied by Grinstein, Jora and Polosa [without a Higgs potential but with a mass term for the complex scalar (diquark) field ϕ] [14]. We absorb the mass term for the complex scalar (diquark) field ϕ in the definition of our Higgs potential. The bosonized action of the theory that we study is defined (suppressing the color indices) by the action:

$$S = \int \mathcal{L}(\phi, \phi^\dagger, A^\mu)\, d^2x, \tag{1a}$$

$$\mathcal{L} = \left[-\frac{1}{4} F_{\mu\nu} F^{\mu\nu} + \partial_\mu \phi^\dagger \partial^\mu \phi + \left[i\rho(\phi A^\mu \partial_\mu \phi^\dagger - \phi^\dagger A_\mu \partial^\mu \phi) + \rho^2 \phi^\dagger \phi A_\mu A^\mu \right] - V(|\phi|^2) \right], \tag{1b}$$

$$V(|\phi|^2) = V(\phi^\dagger\phi) = \big[\mu^2(\phi^\dagger\phi) + \frac{\lambda}{6}(\phi^\dagger\phi)^2\big], \quad |\phi|^2 = (\phi^\dagger\phi), \quad \phi_0 \neq 0, \tag{1c}$$

$$F^{\mu\nu} = (\partial^\mu A^\nu - \partial^\nu A^\mu), \quad \rho = \frac{g}{\sqrt{N}}, \quad (-\mu^2 > 0\ ,\ \lambda > 0), \tag{1d}$$

$$g^{\mu\nu} = g_{\mu\nu} := \begin{pmatrix} 1 & 0 \\ 0 & -1 \end{pmatrix}, \quad \mu,\ \nu = 0,\ 1 \qquad \text{(IFQ)}, \tag{1e}$$

$$g^{\mu\nu} = g_{\mu\nu} := \begin{pmatrix} 0 & 1 \\ 1 & 0 \end{pmatrix}, \quad \mu,\ \nu = +,\ - \qquad \text{(LFQ)}. \tag{1f}$$

In the above Lagrangian density of the theory, the first term represents the kinetic energy of the gluon field, the second term represents the kinetic energy term for the scalar absorbed (diquark) field, the third term represents the interaction term for the scalar (diquark) field with the gluon field (the color indices have again been suppressed) and the last term represents the Higgs potential which is kept rather general, without making any specific choice for the parameters μ^2 and λ. However, they are chosen such that the potential remains a double well potential with the vacuum expectation value $\phi_0 = \langle 0|\phi(x)|0\rangle \neq 0$, so as to allow the spontaneous symmetry breaking in the theory. Also, the mass term for the scalar (diquark) field has been absorbed in the definition of the Higgs potential. The values $\mu^2 = m^2$ and $\lambda = 0$ reproduce the theory of Grinstein, Jora and Polosa [14]. For obtaining the gauged theory under our present investigation, we have used the gauging prescription: $\partial_\mu \to D_\mu = (\partial_\mu + i\rho A_\mu)$ (where the color indices are being suppressed) (it is to be noted here that our work of Ref. [15] uses a different gauging prescription).

Also, in order to remain consistent with the work of Grinstein, Jora and Polosa [14], we have ignored the gluon self coupling term in our considerations (just like the work of Ref. [25]).

3 Instant-form quantization

In the instant-form quantization of the theory (with the metric tensor $g_{\mu\nu} = g^{\mu\nu} = diag(+1, -1)$; $\mu, \nu = 0, 1$), the theory is seen to possess a set of three constraints:

$$\begin{aligned} &\psi_1 = \Pi^0 \approx 0, \qquad \psi_2 = \big[\partial_1 E + i\rho(\phi\pi - \phi^\dagger\pi^\dagger)\big] \approx 0, \\ &\psi_3 = \big[2\rho^2 A_0\pi^\dagger\phi^\dagger + i\rho A_1(\phi\partial_1\phi^\dagger + \phi^\dagger\partial_1\phi)\big] \approx 0, \end{aligned} \tag{2}$$

where the constraint ψ_1 is a primary constraint and the constraints ψ_2 and ψ_3 are the secondary Gauss-law constraints. Also, here π, $\pi^\dagger$, Π^0 and $E = \Pi^1$ are the momenta canonically conjugate respectively to ϕ, $\phi^\dagger$, A_0 and A_1 (here, $A_0 \equiv A_0^a\tau^a$, $A_1 \equiv A_1^a\tau^a$, $\Pi^0 \equiv \Pi^{0a}\tau^a$, $E \equiv E^a\tau^a$). The symbol $\approx$ here denotes a weak equality in the sense of Dirac [16]. Further, these constraints are easily seen to form a set of second-class constraints because the matrix of the Poisson brackets among these constraints is a non-singular matrix implying that the theory is gauge-non-invariant. The canonical Hamiltonian density of this theory is:

$$\begin{aligned} \mathcal{H}_c = \Big[&\frac{1}{2}(E)^2 - A_0\,\partial_1 E + \pi^\dagger\pi + \partial_1\phi^\dagger\partial_1\phi + \rho^2 A_1^2\phi^\dagger\phi \\ &- i\rho A_0(\phi\pi - \phi^\dagger\pi^\dagger) - i\rho A_1(\phi^\dagger\partial_1\phi - \phi\,\partial_1\phi^\dagger) + \mu^2(\phi^\dagger\phi) + \frac{\lambda}{6}(\phi^\dagger\phi)^2\Big]. \end{aligned} \tag{3}$$

After including the primary constraint ψ_1 in the canonical Hamiltonian density with the help of the Lagrange multiplier field u, the total Hamiltonian density becomes:

$$\begin{aligned} \mathcal{H}_T = \Big[&\Pi^0 u + \frac{1}{2}(E)^2 - A_0\,\partial_1 E + \pi^\dagger\pi + \partial_1\phi^\dagger\partial_1\phi + \rho^2 A_1^2\phi^\dagger\phi \\ &- i\rho A_0(\phi\pi - \phi^\dagger\pi^\dagger) - i\rho A_1(\phi^\dagger\partial_1\phi - \phi\,\partial_1\phi^\dagger) + \mu^2(\phi^\dagger\phi) + \frac{\lambda}{6}(\phi^\dagger\phi)^2\Big]. \end{aligned} \tag{4}$$

The Hamilton's equations of motion of the theory that preserve the constraints of the theory in the course of time could be obtained from the total Hamiltonian density and are omitted here for the sake of brevity. The matrix $R_{\alpha\beta}$ of the Poisson brackets among the set of these constraints ψ_i with $(i = 1, 2, 3)$ is seen to be singular, implying that the set of these constraints ψ_i is first-class and that the theory under consideration is gauge-invariant. Consequently the theory is seen to possess the local vector gauge symmetry defined by the local vector gauge transformations:

$$\delta\phi = i\rho\beta\phi, \quad \delta\phi^\dagger = -i\rho\beta\phi^\dagger, \quad \delta A_0 = \partial_0\beta, \quad \delta A_1 = \partial_1\beta, \tag{5}$$

where $\beta \equiv \beta(x_0, x_1)$ is an arbitrary function of its arguments. This theory could now be quantized under some appropriate gauge-fixing conditions, e. g., under the time-axial or temporal gauge: $A_0 \approx 0$. The details of this IFQ are however, outside the scope of the present work [what actually happens is that one of the matrix elements of the matrix $R_{\alpha\beta}$ involves a linear combination of a Dirac distribution function $\delta(x^1-y^1)$ and its first derivative and finding its inverse is a rather non-trivial task]. We now proceed with the LFQ of this theory in the next section.

4 Light-front Hamiltonian and path integral quantization

For the LFQ, the bosonized action of the theory (suppressing the color indices) in LF coordinates $x^\pm := (x^0 \pm x^1)/\sqrt{2}$ reads:

$$S = \int \mathcal{L}\, dx^+ dx^-, \tag{6a}$$

$$\mathcal{L} = \Big[\frac{1}{2}(\partial_+ A^+ - \partial_- A^-)^2 + (\partial_+\phi^\dagger\partial_-\phi + \partial_-\phi^\dagger\partial_+\phi) - \mu^2(\phi^\dagger\phi) - \frac{\lambda}{6}(\phi^\dagger\phi)^2 + i\rho A^+(\phi\,\partial_+\phi^\dagger - \phi^\dagger\partial_+\phi) + i\rho A^-(\phi\,\partial_-\phi^\dagger - \phi^\dagger\partial_-\phi) + 2\rho^2\phi^\dagger\phi\, A^+A^-\Big]. \tag{6b}$$

In the work of Ref. [14], the authors have studied the above action, after implementing the gauge-fixing condition (GFC) $A^+ \approx 0$ "strongly" in the above action. In contrast to this, we propose to study the theory defined by the above action, following the standard Dirac quantization procedure [16] and we do not fix any gauge at this stage. We instead consider this GFC ($A^+ \approx 0$) as one of the gauge constraints [16] which becomes strongly equal to zero only on the reduced hyper surface of the constraints and remains non-zero in the rest of the phase space of the theory and we do not set it strongly equal to zero in above equation.

We like to emphasize here that one of the salient features of Dirac quantization procedure [16] is that in this quantization the GFC's should be treated on par with other gauge-constraints of the theory which are only weakly equal to zero in the sense of Dirac [16], and they become strongly equal to zero only on the reduced hyper surface of the constraints of the theory and not in the rest of the phase space of the classical theory (in the corresponding quantum theory these weak equalities become the weak operator equalities).

Another thing to be noted here is that we have introduced the Higgs potential in our present work and we have absorbed the mass term for the scalar (diquark) field in the definition of our Higgs potential. This LF theory is seen to possess a set of four constraints:

$$\chi_1 = \Pi^+ \approx 0, \quad \chi_2 = [\pi - \partial_-\phi^\dagger + i\rho A^+\phi^\dagger] \approx 0, \quad \chi_3 = [\pi^\dagger - \partial_-\phi - i\rho A^+\phi] \approx 0,$$
$$\chi_4 = [\partial_-\Pi^- + i\rho(\phi\,\partial_-\phi^\dagger - \phi^\dagger\partial_-\phi) + 2\rho^2\phi^\dagger\phi\, A^+] \approx 0, \tag{7}$$

where the constraints χ_1, χ_2 and χ_3 are primary constraints and the constraint χ_4 is the secondary Gauss-law constraint, which is obtained by demanding that the primary constraint χ_1 be preserved in the course of time. The preservation of χ_2, χ_3 and χ_4, for all times does not give rise to any further constraints. The theory is thus seen to possess only four constraints χ_i (with $i = 1, 2, 3, 4$). Also, here π, $\pi^\dagger$, Π^+ and Π^- are the momenta canonically conjugate respectively to ϕ, $\phi^\dagger$, A^- and A^+ (here, $A^+ \equiv A^{+a}\tau^a$, $A^- \equiv A^{-a}\tau^a$, $\Pi_0 \equiv \Pi_{0a}\tau^a$, $E \equiv E^a\tau^a$). Now, the constraints χ_2, χ_3 and χ_4 could however, be combined into a single constraint:

$$\eta = \left[\partial_- \Pi^- + i\rho(\phi\,\pi - \phi^\dagger \pi^\dagger)\right] \approx 0, \tag{8}$$

and with this modification, the new set of constraints of the theory could be written as:

$$\Omega_1 = \chi_1 = \Pi^+ \approx 0, \qquad \Omega_2 = \eta = \left[\partial_- \Pi^- + i\rho(\phi\pi - \phi^\dagger \pi^\dagger)\right] \approx 0. \tag{9}$$

Further, the matrix of the Poisson brackets among the constraints Ω_i, with $i = 1, 2$ is seen to be a singular matrix implying that the set of constraints Ω_i is first-class and that the theory under consideration is gauge-invariant. The canonical Hamiltonian density for this LF theory is:

$$\mathcal{H}_c = \Bigg[\frac{1}{2}(\Pi^-)^2 + \Pi^-(\partial_- A^-) + \mu^2(\phi^\dagger\phi) + \frac{\lambda}{6}(\phi^\dagger\phi)^2 - i\rho A^-(\phi\,\partial_-\phi^\dagger - \phi^\dagger\partial_-\phi) - 2\rho^2\phi^\dagger\phi\, A^+A^-\Bigg]. \tag{10}$$

After including the primary constraints χ_1, χ_2 and χ_3 in the canonical Hamiltonian density $\mathcal{H}_c$ with the help of the Lagrange multiplier fields u, v and w, the total Hamiltonian density could be written as:

$$\mathcal{H}_T = \Bigg[(\Pi^+)u + (\pi - \partial_-\phi^\dagger + i\rho A^+\phi^\dagger)v + (\pi^\dagger - \partial_-\phi - i\rho A^+\phi)w + \mu^2(\phi^\dagger\phi) + \frac{\lambda}{6}(\phi^\dagger\phi)^2 + \frac{1}{2}(\Pi^-)^2 + \Pi^-\partial_- A^- - i\rho A^-(\phi\,\partial_-\phi^\dagger - \phi^\dagger\partial_-\phi) - 2\rho^2\phi^\dagger\phi\, A^+A^-\Bigg]. \tag{11}$$

The Hamilton's equations of motion of the theory that preserve the constraints of the theory in the course of time could be obtained from the total Hamiltonian density. Also, the divergence of the vector gauge current density of the theory is seen to vanish, implying that the theory possesses at the classical level a local vector-gauge symmetry. The action of the theory is indeed seen to be invariant under the local vector gauge transformations:

$$\begin{aligned}
&\delta\phi = -i\rho\beta\phi, \quad \delta\phi^\dagger = i\rho\beta\phi^\dagger, \quad \delta A^- = \partial_+\beta, \quad \delta A^+ = \partial_-\beta,\\
&\delta\pi = \left[\rho^2\beta\phi^\dagger A^+ + i\rho\beta\partial_-\phi^\dagger\right], \quad \delta\pi^\dagger = \left[\rho^2\beta\phi A^+ - i\rho\beta\partial_-\phi\right],\\
&\delta u = \delta v = \delta w = \delta\Pi^+ = \delta\Pi^- = \delta\Pi_u = \delta\Pi_v = \delta\Pi_w = 0,
\end{aligned} \tag{12}$$

where $\beta \equiv \beta(x^+, x^-)$ is an arbitrary function of its arguments and Π_u, Π_v and Π_w are the momenta canonically conjugate to the Lagrange multiplier fields u, v and w respectively, which are treated here as dynamical fields.

The theory could now be quantized, e. g., under the GFC's: $\zeta_1 = A^+ \approx 0$, $\zeta_2 = A^- \approx 0$, where the gauge $A^+ \approx 0$ represents the LC time-axial or temporal gauge and the gauge $A^- \approx 0$ represents the LC Coulomb gauge and both of these gauges are physically important gauges. The matrix $R_{\alpha\beta}$ of the Poisson brackets

among the set of constraints Ω_i with $i = 1, 2$ is seen to be nonsingular with the determinant given by

$$\Big[\big|\big|\det(R_{\alpha\beta})\big|\big|\Big]^{\frac{1}{2}} = \Big[\big[\delta^{'}(x^- - y^-)\big]\big[\delta(x^- - y^-)\big]\Big]. \tag{13}$$

Finally, following the Dirac quantization procedure in the Hamiltonian formulation, the non-vanishing equal light-cone-time commutators of the theory, under the GFC's $A^+ \approx 0$ and $A^- \approx 0$ are obtained as:

$$\big[\phi(x^+, x^-), \pi(x^+, y^-)\big] = i\delta(x^- - y^-), \tag{14}$$

$$\big[\phi^\dagger(x^+, x^-), \pi^\dagger(x^+, y^-)\big] = i\delta(x^- - y^-), \tag{15}$$

$$\big[\phi(x^+, x^-), \Pi^-(x^+, y^-)\big] = \frac{1}{2}\rho\phi\epsilon(x^- - y^-), \tag{16}$$

$$\big[\phi^\dagger(x^+, x^-), \Pi^-(x^+, y^-)\big] = -\frac{1}{2}\rho\phi^\dagger\epsilon(x^- - y^-), \tag{17}$$

$$\big[\pi(x^+, x^-), \Pi^-(x^+, y^-)\big] = \frac{1}{2}\rho\pi\epsilon(x^- - y^-), \tag{18}$$

$$\big[\pi^\dagger(x^+, x^-), \Pi^-(x^+, y^-)\big] = -\frac{1}{2}\rho\pi^\dagger\epsilon(x^- - y^-), \tag{19}$$

$$\big[\Pi^-(x^+, x^-), \phi(x^+, y^-)\big] = \frac{1}{2}\rho\phi\epsilon(x^- - y^-), \tag{20}$$

$$\big[\Pi^-(x^+, x^-), \phi^\dagger(x^+, y^-)\big] = -\frac{1}{2}\rho\phi^\dagger\epsilon(x^- - y^-), \tag{21}$$

$$\big[\Pi^-(x^+, x^-), \pi(x^+, y^-)\big] = -\frac{1}{2}\rho\pi\epsilon(x^- - y^-), \tag{22}$$

$$\big[\Pi^-(x^+, x^-), \pi^\dagger(x^+, y^-)\big] = \frac{1}{2}\rho\pi^\dagger\epsilon(x^- - y^-). \tag{23}$$

The first-order Lagrangian density $\mathcal{L}_{I0}$ of the theory is:

$$\mathcal{L}_{I0} = \bigg[\frac{1}{2}(\Pi^-)^2 + \partial_+\phi^\dagger\partial_-\phi + \partial_-\phi^\dagger\partial_+\phi + 2\rho^2\phi^\dagger\phi A^+A^- - \mu^2\phi^\dagger\phi$$
$$- i\rho A^-(\phi^\dagger\partial_-\phi - \phi\partial_-\phi^\dagger) - i\rho A^+(\phi^\dagger\partial_+\phi - \phi\,\partial_+\phi^\dagger) - \frac{\lambda}{6}(\phi^\dagger\phi)^2\bigg]. \tag{24}$$

In the path integral formulation [17–19], the transition to quantum theory is made by writing the vacuum to vacuum transition amplitude for the theory called the generating functional $Z[J_k]$. For the present theory, under the GFC's $\zeta_1 = A^+ \approx 0$ and $\zeta_2 = A^- \approx 0$ and in the presence of the external sources J_k, it reads:

$$Z[J_k] = \int [d\mu] \exp\bigg[i\int d^2x \Big(J_k\Phi^k + \pi\partial_+\phi + \pi^\dagger\partial_+\phi^\dagger + \Pi^+\partial_+A^-$$
$$+ \Pi^-\partial_+A^+ + \Pi_u\partial_+u + \Pi_v\partial_+v + \Pi_w\partial_+w - \mathcal{H}_T\Big)\bigg]. \tag{25}$$

Here, the phase space variables of the theory are $\Phi^k \equiv (\phi, \phi^\dagger, A^-, A^+, u, v, w)$ with the corresponding respective canonical conjugate momenta: $\Pi_k \equiv (\pi, \pi^\dagger, \Pi^+, \Pi^-, \Pi_u, \Pi_v, \Pi_w)$. The functional measure $[d\mu]$ of the generating functional $Z[J_k]$ under the above gauge-fixing is obtained as:

$$[d\mu] = [\delta'(x^- - y^-)\,\delta(x^- - y^-)][d\phi][d\phi^\dagger][dA^+][dA^-][du][dv][dw]$$
$$\times [d\pi][d\pi^\dagger][d\Pi^-][d\Pi^+][d\Pi_u][d\Pi_v][d\Pi_w]\,\delta[\Pi^+ \approx 0]\,\delta[A^- \approx 0]$$
$$\times \delta\big[\big(\partial_-\Pi^- + i\rho(\phi\pi - \phi^\dagger\pi^\dagger)\big) \approx 0\big]\,\delta[A^+ \approx 0]. \tag{26}$$

5 Light-front BRST quantization

For the BRST formulation of the model, we rewrite the theory as a quantum system that possesses the generalized gauge invariance called BRST symmetry. For this, we first enlarge the Hilbert space of our gauge-invariant theory and replace the notion of gauge-transformation, which shifts operators by c-number functions, by a BRST transformation, which mixes operators with Bose and Fermi statistics. We then introduce new anti-commuting variable c and $\bar{c}$ (Grassmann numbers on the classical level and operators in the quantized theory) and a commuting variable b such that [20–22]:

$$\begin{aligned}
&\hat{\delta}\phi = -i\rho c\phi, \quad \hat{\delta}\phi^\dagger = i\rho c\phi^\dagger, \quad \hat{\delta}A^- = \partial_+ c, \quad \hat{\delta}A^+ = \partial_- c,\\
&\hat{\delta}\pi = \big[\rho^2 c\,\phi^\dagger A^+ + i\rho\, c\,\partial_-\phi^\dagger\big], \quad \hat{\delta}\pi^\dagger = \big[\rho^2 c\,\phi A^+ - i\rho\, c\,\partial_-\phi\big],\\
&\hat{\delta}u = \hat{\delta}v = \hat{\delta}w = \hat{\delta}\Pi^+ = \hat{\delta}\Pi^- = \hat{\delta}\Pi_u = \hat{\delta}\Pi_v = \hat{\delta}\Pi_w = 0,\\
&\hat{\delta}c = 0, \quad \hat{\delta}\bar{c} = b, \quad \hat{\delta}b = 0,
\end{aligned} \tag{27}$$

with the property $\hat{\delta}^2 = 0$. We now define a BRST-invariant function of the dynamical phase space variables of the theory to be a function f such that $\hat{\delta}f = 0$. Now the BRST gauge-fixed quantum Lagrangian density $\mathcal{L}_{BRST}$ for the theory could be obtained by adding to the first-order Lagrangian density $\mathcal{L}_{I0}$, a trivial BRST-invariant function, e. g., as follows:

$$\begin{aligned}
\mathcal{L}_{BRST} = \Big[&\frac{1}{2}(\Pi^-)^2 + \partial_+\phi^\dagger\partial_-\phi + \partial_-\phi^\dagger\partial_+\phi - i\rho A^-(\phi^\dagger\partial_-\phi - \phi\,\partial_-\phi^\dagger)\\
&- \frac{\lambda}{6}(\phi^\dagger\phi)^2 - \mu^2\phi^\dagger\phi + 2\rho^2\phi^\dagger\phi A^+A^- - i\rho A^+(\phi^\dagger\partial_+\phi - \phi\,\partial_+\phi^\dagger) + \hat{\delta}\big[\bar{c}(\partial_+A^- + \frac{1}{2}b)\big]\Big].
\end{aligned} \tag{28}$$

The last term in the above equation is the extra BRST-invariant gauge-fixing term. After one integration by parts, the above equation could now be written as:

$$\begin{aligned}
\mathcal{L}_{BRST} = \Big[&\frac{1}{2}(\Pi^-)^2 + \partial_+\phi^\dagger\partial_-\phi + \partial_-\phi^\dagger\partial_+\phi - i\rho A^-(\phi^\dagger\partial_-\phi - \phi\partial_-\phi^\dagger) - \mu^2\phi^\dagger\phi - \frac{\lambda}{6}(\phi^\dagger\phi)^2\\
&+ 2\rho^2\phi^\dagger\phi A^+A^- - i\rho A^+(\phi^\dagger\partial_+\phi - \phi\,\partial_+\phi^\dagger) + \partial_+A^- + \frac{1}{2}b^2 + (\partial_+\bar{c})(\partial_+c)\Big].
\end{aligned} \tag{29}$$

The Euler–Lagrange equation obtained by the variation of $\mathcal{L}_{BRST}$ with respect to $\bar{c}$ implies $\partial_+\partial_+c = 0$. We thus define the bosonic momenta in the usual manner so that $\Pi^+ := b$ but for the fermionic momenta with directional derivatives we set $\Pi_c := \partial_+\bar{c}$ and $\Pi_{\bar{c}} := \partial_+c$, implying that the variable canonically conjugate to c is $\partial_+\bar{c}$ and the variable conjugate to $\bar{c}$ is ∂_+c. The quantum BRST Hamiltonian density of the theory is:

$$\begin{aligned}
\mathcal{H}_{BRST} = \Big[&\frac{1}{2}(\Pi^-)^2 + \Pi^-(\partial_-A^- - 2\rho^2\phi^\dagger\phi A^+A^- + \mu^2\phi^\dagger\phi + \frac{\lambda}{6}(\phi^\dagger\phi)^2\\
&- i\rho A^-(\phi\,\partial_-\phi^\dagger - \phi^\dagger\partial_-\phi) - \frac{1}{2}(\Pi^+)^2 + \Pi_c\Pi_{\bar{c}}\Big].
\end{aligned} \tag{30}$$

The BRST charge operator of the present theory is:

$$Q = \int dx^-\Big[ic\partial_-\Pi^- - \rho c(\phi\pi - \phi^\dagger\pi^\dagger) - i\partial_+c\Pi^+\Big]. \tag{31}$$

The theory is seen to possess negative norm states in the fermionic sector. The existence of these negative norm states as free states of the fermionic part of $\mathcal{H}_{\mathcal{BRST}}$ is,

however, irrelevant to the existence of physical states in the orthogonal subspace of the Hilbert space. The Hamiltonian is also invariant under the anti-BRST transformation given by:

$$\bar{\delta}\phi = i\rho\bar{c}\phi, \quad \bar{\delta}\phi^\dagger = -i\rho\bar{c}\phi^\dagger, \quad \bar{\delta}A^- = -\partial_+\bar{c}, \quad \bar{\delta}A^+ = -\partial_-\bar{c}, \tag{32}$$

$$\bar{\delta}\pi = \left[-\rho^2\bar{c}\,\phi^\dagger A^+ - i\rho\,\bar{c}\,\partial_-\phi^\dagger\right], \quad \bar{\delta}\pi^\dagger = \left[-\rho^2\bar{c}\phi A^+ + i\rho\bar{c}\partial_-\phi\right], \tag{33}$$

$$\bar{\delta}u = \bar{\delta}v = \bar{\delta}w = \bar{\delta}\Pi^+ = \bar{\delta}\Pi^- = \bar{\delta}\Pi_u = \bar{\delta}\Pi_v = \bar{\delta}\Pi_w = 0, \tag{34}$$

$$\bar{\delta}c = -b, \quad \bar{\delta}\bar{c} = 0, \quad \bar{\delta}b = 0, \tag{35}$$

with generator or anti-BRST charge

$$\bar{Q} = \int dx^- \left[-i\,\bar{c}\,\partial_-\Pi^- - \rho\,\bar{c}\,(\phi\pi - \phi^\dagger\pi^\dagger) + i\,\partial_+\bar{c}\,\Pi^+\right]. \tag{36}$$

We also have

$$\partial_+ Q = [Q, H_{BRST}] = 0, \qquad \partial_+\bar{Q} = [\bar{Q}, H_{BRST}] = 0 \tag{37}$$

with $H_{BRST} = \int dx^-\,\mathcal{H}_{BRST}$, and we further impose the dual condition that both Q and $\bar{Q}$ annihilate physical states, implying that

$$Q|\psi\rangle = 0 \quad \text{and} \quad \bar{Q}|\psi\rangle = 0. \tag{38}$$

The states for which the constraints of the theory hold, satisfy both of these conditions and are in fact, the only states satisfying both of these conditions. Now, because $Q|\psi\rangle = 0$, the set of states annihilated by Q contains not only the set of states for which the constraints of the theory hold but also additional states for which the constraints of the theory do not hold in particular. This situation is, however, easily avoided by additionally imposing on the theory, the dual condition: $Q|\psi\rangle = 0$ and $\bar{Q}|\psi\rangle = 0$. Thus by imposing both of these conditions on the theory simultaneously, one finds that the states for which the constraints of the theory hold satisfy both of these conditions and, in fact, these are the only states satisfying both of these conditions because in view of the conditions on the fermionic variables c and $\bar{c}$ one cannot have simultaneously c, $\partial_+ c$ and $\bar{c}$, $\partial_+\bar{c}$ applied to $|\psi\rangle$ to give zero. Thus the only states satisfying $Q|\psi\rangle = 0$ and $\bar{Q}|\psi\rangle = 0$ are those that satisfy the constraints of the theory and they belong to the set of BRST-invariant as well as to the set of anti-BRST-invariant states. Here, the new extended gauge symmetry which replaces the gauge invariance is maintained (even under the BRST gauge-fixing) and hence projecting any state onto the sector of BRST and anti-BRST invariant states yields a theory which is isomorphic to the original GI theory.

6 Acknowledgments

Author thanks the Department of Science and Technology (DST), New Delhi, India, **for the award of a Full Travel Grant** for attending the International Conference on Nuclear Theory in the Supercomputing Era — 2013 (NTSE-2013), held at the Iowa State University, Ames, Iowa, USA, on May 13–17, 2013, where this work was presented as an "Invited Talk". He also thanks the Organizers of NTSE-2013 for providing a very warm and excellent environment and hospitality during the conference. This work was supported in part by the Department of Energy under Grant No. DE-FG02-87ER40371. Last but not least, the authors thank Prof. Stan Brodsky for a very fruitful collaboration on this subject and for several crucial clarifications and for his invaluable continuous guidance, support and motivations throughout the course of this work.

References

[1] R. L. Jaffe, Phys. Rev. D **15**, 267 (1977).

[2] R. L. Jaffe, Phys. Rev. D **15**, 281 (1977).

[3] R. L. Jaffe and F. Wilczek, Phys. Rev. Lett. **91**, 232003 (2003).

[4] G. 't Hooft, Nucl. Phys. B **75**, 461 (1974).

[5] A. D. Polosa, in *Proc. Int. Workshop on Charm Phys. (Charm 2007), 5–8 Aug., 2007, Ithaca, New York*, eds. H. Mahlke and J. Napolitano. eConf C070805, 36 (2007).

[6] L. Maiani, A. D. Polosa and V. Riquer, Phys. Rev. Lett. **99**, 182003 (2007).

[7] L. Maiani, F. Piccinini, A. D. Polosa and V. Riquer, Phys. Rev. D **71**, 014028 (2005).

[8] L. Maiani, A. D. Polosa and V. Riquer, New J. Phys. **10**, 073004 (2008).

[9] L. Maiani, F. Piccinini, A. D. Polosa and V. Riquer, Phys. Rev. Lett. **93**, 212002 (2004).

[10] I. Bigi, L. Maiani, F. Piccinini, A. D. Polosa and V. Riquer, Phys. Rev. D **72**, 114016 (2005).

[11] L. Maiani, F. Piccinini, A. D. Polosa and V. Riquer, PoS HEP2005, 105 (2006).

[12] A. D. Polosa, Nucl. Phys. B Proc. Suppl. **181-182**, 175 (2008).

[13] G. 't Hooft, G. Isidori, L. Maiani, A. D. Polosa and V. Riquer, Phys. Lett. B **662**, 424 (2008).

[14] B. Grinstein, R. Jora and A. D. Polosa, Phys. Lett. B **671**, 440 (2009).

[15] U. Kulshreshtha, D. S. Kulshreshtha and J. P. Vary, Phys. Lett. B **708**, 195 (2012).

[16] P. A. M. Dirac, Can. J. Math **2**, 129 (1950).

[17] P. Sanjanovic, Ann. Phys. (NY) **100**, 227 (1976).

[18] U. Kulshreshtha and D. S. Kulshreshtha, Phys. Lett. B **555**, 255 (2003).

[19] U. Kulshreshtha and D. S. Kulshreshtha, Eur. Phys. Jour. C **29**, 453 (2003).

[20] C. Becchi, A. Rouet and A. Stora, Phys. Lett. B **52**, 344 (1974).

[21] V. Tyutin, Report No. FIAN-39 (1975) (*unpublished*).

[22] D. Nemeschansky, C. Preitschopf and M. Weinstein, Ann. Phys. (NY) **183**, 226 (1988).

[23] P. A. M. Dirac, Rev. Mod. Phys. **21**, 392 (1949).

[24] S. J. Brodsky, H. C. Pauli and S. S. Pinsky, Phys. Rept. **301**, 299 (1998).

[25] P. P. Srivastava and S. J. Brodsky, Phys. Rev. D **64** 045006 (2001).

[26] P. P. Srivastava and S. J. Brodsky, Phys. Rev. D **61**, 025013 (2000).

[27] P. P. Srivastava and S. J. Brodsky, Phys.Rev. D **66**, 045019 (2002).

Non-Perturbative Time-Dependent Quantum Field Evolution

Xingbo Zhao[a], Anton Ilderton[b], Pieter Maris[a] and James P. Vary[a]

[a] *Department of Physics and Astronomy, Iowa State University, Ames, Iowa 50011, USA*
[b] *Department of Applied Physics, Chalmers University of Technology, SE-412 96 Gothenburg, Sweden*

Abstract

We present a nonperturbative, first-principles numerical approach for time-dependent problems in the framework of quantum field theory. In this approach the time evolution of quantum field systems is treated in real time and at the amplitude level. As a test application, we apply this method to QED and study photon emission from an electron in a strong time-dependent external field. Coherent superposition of electron acceleration and photon emission is observed in the nonperturbative regime.

Keywords: *Non-perturbative; time-dependent; strong field; quantum electrodynamics; light-front dynamics*

1 Introduction

Solving time-dependent problems in quantum field theory is desired for a wide range of applications. One important area is in scattering processes. Simulating scattering processes as time-dependent processes at the amplitude level opens up possibilities for handling complicated scenarios from first-principles. Typical examples include: 1) The asymptotic states cannot be well-defined. For example, long range forces exist between the colliding particles; another example is parton collisions in the deconfined medium created in relativistic heavy-ion collisions. 2) The scattering processes occur in the presence of time-dependent background fields, which are typically encountered in strong field laser physics as well as in relativistic heavy-ion physics. In the former case, time-dependent electromagnetic fields are provided by laser beams, and in the latter case, colliding nuclei create strong and time-dependent (color-)electromagnetic fields. 3) One is interested in the explicit time evolution of quantum field amplitudes during scattering processes, which could shed light on, e. g., the mechanism of hadronization in QCD.

To address time-dependent processes at the amplitude level, one first needs a stationary state description for stable particles participating in the time-dependent process in terms of quantum field amplitudes. This was achieved by the previously constructed Basis Light-front Quantization (BLFQ) [1, 2]. The BLFQ adopts the light-front quantization and the Hamiltonian framework, see Ref. [3] for a review on the light-front dynamics. It solves for the (boost-invariant) light-front amplitudes for both bound states and scattering states by diagonalizing the light-front Hamiltonian of the quantum field system. Recently, the efforts of applying BLFQ to positronium systems have been initiated [4, 5].

Proceedings of International Conference 'Nuclear Theory in the Supercomputing Era — 2013' (NTSE-2013), Ames, IA, USA, May 13–17, 2013. Eds. A. M. Shirokov and A. I. Mazur. Pacific National University, Khabarovsk, Russia, 2014, p. 204.
http://www.ntse-2013.khb.ru/Proc/Zhao.pdf.

In this paper, we introduce an extension of the BLFQ to the time-dependent regime, which is called the *time-dependent* Basis Light-Front Quantization (tBLFQ) [6, 7]. Based on the stationary amplitudes obtained in BLFQ, tBLFQ evaluates the time-evolution of quantum field configurations by explicitly solving the time-dependent Schrödinger equation. This approach provides a natural framework for addressing scattering problems from a time-dependent perspective.

In this work, we illustrate tBLFQ through an application to strong field laser physics. Specifically, we study the "nonlinear Compton scattering" (nCs) process [8,9], in which an electron is excited by a background laser field and emits a photon. This paper is organized as follows: in Section 2, we introduce our model for the background laser field; in Section 3 we discuss the formalism of tBLFQ; in Section 4 we give a brief review on BLFQ which is employed to construct basis states for tBLFQ; in Section 5 we conduct a sample calculation for the nCs process and present the numerical results. Finally we conclude and provide our outlook for future work in Section 6.

2 Background field

We model the laser background as a classical field (i. e., we neglect back reaction on the laser). We consider a longitudinal periodic electric field pointing in the 3-direction with profile,

$$E^3(x^+, x^-) = -E_0^3 \sin(l_- x^-)\,\Theta(x^+)\,\Theta(\Delta x^+ - x^+), \tag{1}$$

where E_0^3 is the peak amplitude and l_- is the frequency. The theta functions impose a finite light-front time duration on the field. An appropriate gauge potential is

$$\mathcal{A}^-(x^+, x^-) = \frac{E_0^3}{l_-}\cos(l_- x^-)\,\Theta(x^+)\,\Theta(\Delta x^+ - x^+). \tag{2}$$

The dependence on x^+ and x^- makes this particularly suitable to a light-front treatment.

3 Quantum evolution

In tBLFQ, we calculate the evolution of quantum field configurations at the amplitude level. For the nCs process, the Hamiltonian P^- contains two parts, $P^-_{\rm QED}$ which is the *full* interacting light-front Hamiltonian of QED, and interactions $V(x^+)$ introduced by the external field, so

$$P^-(x^+) = P^-_{\rm QED} + V(x^+)\,. \tag{3}$$

Both the QED Hamiltonian P^-_{QED} and the external field interaction $V(x^+)$ may induce transitions on the quantum field amplitudes over time. In the nCs process, we are, however, mostly interested in transitions induced by the external field $V(x^+)$. Therefore, we adopt an interaction picture, in which the light-front QED Hamiltonian P^-_{QED} serve as the "main" part of the Hamiltonian and the external field interaction $V(x^+)$ as the "interaction" part. In this interaction picture, the quantum field amplitude evolves according to

$$i\frac{\partial}{\partial x^+}|\psi; x^+\rangle_I = \frac{1}{2}V_I(x^+)|\psi; x^+\rangle_I, \tag{4}$$

where $|\psi; x^+\rangle_I = e^{iP^-_{QED}x^+/2}|\psi; x^+\rangle$ is the quantum field amplitude in the interaction picture, and the "interaction Hamiltonian in the interaction picture" V_I evolves in time according to

$$V_I(x^+) = e^{\frac{i}{2}P^-_{\rm QED}x^+}V(x^+)\,e^{-\frac{i}{2}P^-_{\rm QED}x^+}. \tag{5}$$

The solution to (4) can be formally written in terms of a time-ordered ($\mathcal{T}_+$) series as

$$|\psi; x^+\rangle_I = \mathcal{T}_+ \, e^{-\frac{i}{2}\int_{x_0^+}^{x^+} V_I \, dx^+} |\psi; x_0^+\rangle_I, \tag{6}$$

where $|\psi; x_0^+\rangle_I$ is the initial quantum field amplitude at light-front time x_0^+. In the nCs process, this initial state corresponds to a single physical electron.

To implement this solution numerically, we need to specify a basis for the quantum field amplitudes $|\psi; x^+\rangle_I$ as well as the external field interaction $V_I(x^+)$. Eq. (5) suggests that the most convenient basis is what comprises the eigenstates of the light-front QED Hamiltonian, P^-_{QED}. We denote this basis as $|\beta\rangle$, which can be found by solving the eigenvalue problem for P^-_{QED},

$$P^-_{QED}|\beta\rangle = P^-_\beta \, |\beta\rangle, \tag{7}$$

where P^-_β is the eigenvalue (light-front energy) for the eigenstate $|\beta\rangle$. In tBLFQ, we employ the previously constructed BLFQ [1,2] to solve this eigenvalue problem. More details will be shown in the next section.

In terms of the basis states $|\beta\rangle$, the quantum field state $|\psi; x^+\rangle$ is represented as

$$|\psi; x^+\rangle_I = \sum_\beta c_\beta(x^+)|\beta\rangle, \tag{8}$$

where $c_\beta(x^+) = \langle\beta|\, \psi; x^+\rangle$ is the amplitude in the basis $|\beta\rangle$. The initial state in the nCs process — a physical electron — is an eigenstate of P^-_{QED} and thus can be trivially expressed in this basis.

With both the quantum field configuration and the interaction term in the Hamiltonian represented in the basis $|\beta\rangle$, Eq. (6) can be realized as a series of matrix-vector multiplications acting on an initial state vector. To make the numerical calculation feasible, in this step, we make two approximations: "time-step discretization" and "basis truncation": the former is to decompose the time-evolution operator in Eq. (6) into small but finite steps in light-front time x^+, with the step size δx^+,

$$\mathcal{T}_+ e^{-\frac{i}{2}\int_{x_0^+}^{x^+} V_I \, dx^+} |\psi(x_0^+)\rangle_I \to \left[1 - \tfrac{i}{2} V_I(x_n^+)\delta x^+\right] \cdots \left[1 - \tfrac{i}{2} V_I(x_1^+)\delta x^+\right] |\psi(x_0^+)\rangle_I, \tag{9}$$

and the latter is to keep the basis dimensionality finite. In tBLFQ, the basis truncation is performed in the basis state ($|\beta\rangle$) construction stage in BLFQ, which will be introduced in the next section. "Basis truncation" and "time-step discretization" are the only two approximations in tBLFQ.

4 Basis construction

In this section we present a brief review of BLFQ [1, 2] and explain the procedure of constructing the tBLFQ basis $|\beta\rangle$ through solving the eigenvalue problem of P^-_{QED} in BLFQ. For more details, see Ref. [6].

Since quantum field systems generally have large numbers of degrees-of-freedom, to mitigate the computational burden, it is important to choose an efficient basis for the eigenvalue problem. The idea in BLFQ is that an efficient basis should capture the symmetries of the underlying dynamics, so that in such a basis the Hamiltonian exhibits a block-diagonal structure. Each block is associated with a group of quantum numbers corresponding to the symmetries captured by the basis. Thus, the Hamiltonian can be diagonalized block by block, and in practice, we can selectively diagonalize only those blocks with desired quantum numbers.

Specifically for the light-front QED Hamiltonian $P^-_{\rm QED}$, the BLFQ basis, denoted as $|\alpha\rangle$, captures the following three symmetries: 1) Translational symmetry in the x^- direction; 2) Rotational symmetry in the transverse plane; 3) Lepton number conservation. These three symmetries correspond to three conserved operators. These are the longitudinal momentum P^+, longitudinal projection of angular momentum J^3, and charge, or net fermion number Q, respectively. The BLFQ basis states $|\alpha\rangle$ are chosen to be the eigenstates of these three operators: $\{P^+, J^3, Q\}|\alpha\rangle = \{2\pi K/L, M_j, N_f\}|\alpha\rangle$ (L is the length of the longitudinal "box" in which we embed our system, see below). These eigenvalues divide the BLFQ basis states $|\alpha\rangle$ into multiple "segments". Each segment consists of the basis states $|\alpha\rangle$ sharing the same group of eigenvalues.

BLFQ basis states $|\alpha\rangle$ are constructed in terms of a Fock sector expansion. Each Fock particle has helicity, longitudinal momentum $p^+ = 2\pi k/L$ (the sum of k, in each state, must equal K, which implicitly imposes basis truncation on the longitudinal degree of freedom), and two transverse degrees of freedom. The latter are described in terms of the radial quantum number, n, and the angular quantum number, m, of the eigenstates of a 2D-harmonic oscillator (2D-HO). This choice of basis, motivated by applications to QCD, is suitable for describing the confining interaction. This choice is supported by the success of the AdS/QCD approach to hadron spectroscopy [10], where a similar basis is adopted.

In summary, a complete specification of a BLFQ basis requires 1) the segment specifiers K, M_j, and N_f, 2) two truncation parameters, namely the choice of Fock sectors to retain, and the transverse truncation parameter $N_{\rm max}$, the maximum total number of oscillator quanta $2n + |m|$ for the Fock states and 3) the "box length" L in the longitudinal direction and a scale parameter $b = \sqrt{M\Omega}$ for the 2D-HO wave functions, where M and Ω are the mass and frequency of the 2D-HO.

Specifically for the nCs processes, the initial state is a single physical electron. Since the external field interaction $V(x^+)$ conserves net fermion number and does not excite transverse degrees of freedom, we only need to prepare eigenstates of P^-_{QED} in segments of different K. The K's in these segments are equally spaced by the longitudinal momentum quantum number of the background field $k_{\rm las} = Ll_-/\pi$. In each segment, we truncate the Fock sectors to the lowest two sectors, $|e\rangle$ and $|e\gamma\rangle$. We take $L = 2\pi\,\mathrm{MeV}^{-1}$, so the value of $k(K)$ can be read as the longitudinal momentum in units of MeV, and $b = 0.511\,\mathrm{MeV}$, which matches the natural scale in QED set by the physical electron mass m_e.

In our constructed BLFQ basis $|\alpha\rangle$, P^-_{QED} manifests as a block-diagonal numerical matrix. Each block is associated with a distinct K. Then, upon diagonalizing P^-_{QED} block by block (see Ref. [11] for sector-dependent renormalization, and Refs. [12, 13] for applications), we obtain the eigenvalues P^-_β and the associated eigenstates $|\beta\rangle$ in the basis $|\alpha\rangle$,

$$|\beta\rangle = \sum_\alpha |\alpha\rangle\langle\alpha|\,\beta\rangle. \tag{10}$$

These eigenstates $|\beta\rangle$ are the basis states used in tBLFQ. For each basis state, the invariant mass M_β relates to its eigenvalue P^-_β as: $M^2_\beta = P^+_\beta P^-_\beta - P^2_{\perp,\beta}$, where P^+_β and $P_{\perp,\beta}$ are the longitudinal and transverse momentum for $|\beta\rangle$, respectively. The ground states (with the lowest invariant mass in each segment) are interpreted as the physical electron states and the excited states are interpreted as the electron-photon scattering states.

5 Numerical results

In this section we carry out a sample numerical calculation for the nCs process. A basis consisting of three segments with $K = \{K_i, K_i{+}k_{\rm las}, K_i{+}2k_{\rm las}\}$ is chosen for

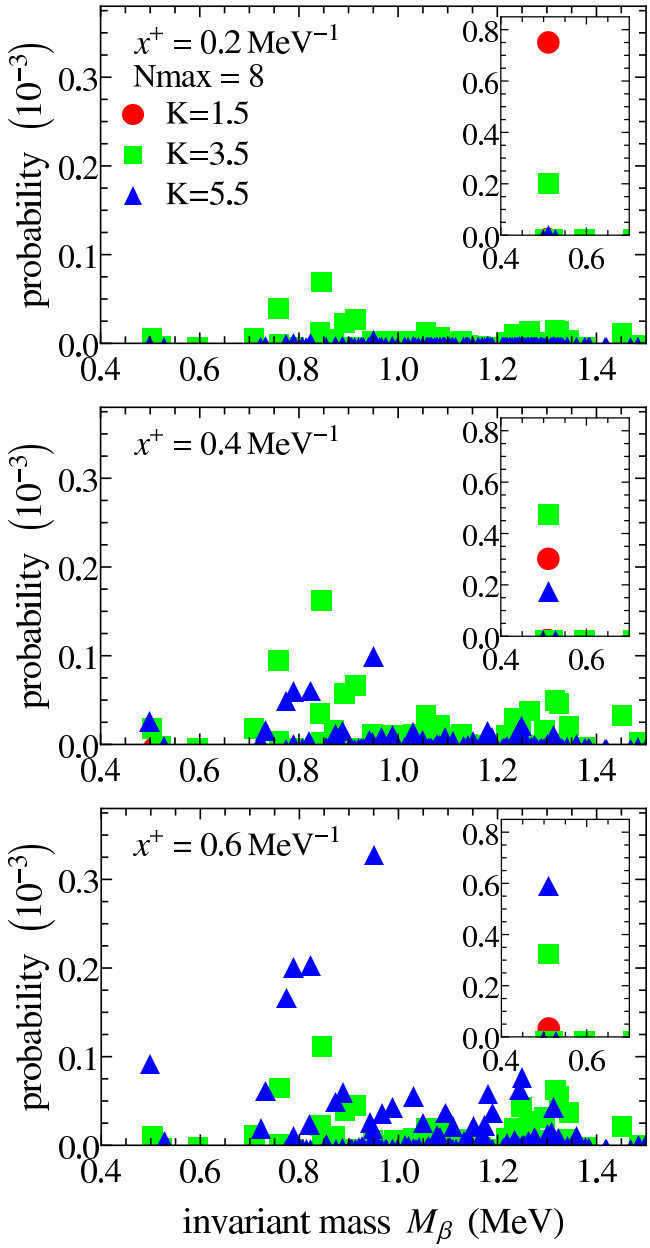

Figure 1: Time evolution of the system at (from top to bottom) $x^+ = 0.2$, 0.4, 0.6 MeV^{-1}, with the background field switched on at $x^+ = 0$. Each dot represents a tBLFQ basis state $|\beta\rangle$, an eigenstate of QED. Horizontal axis: the invariant mass of the state M_β. Vertical axis: the probability of finding the state $|\beta\rangle$ in units of 10^{-3}. The inset panels show, at normal scale, the (much larger) probabilities of finding the single physical electron states (in the $K = 1.5$, 3.5, 5.5 segments), with invariant mass $M_\beta = m_e$.

this calculation. In each segment we retain *both* the single electron (ground) and electron-photon (excited) states. The initial state for our process is a single (ground state) electron in the $K = K_i$ segment. This basis allows for the ground state to be excited twice by the background (from the segment with $K = K_i$ through to segment with $K_i + 2k_{\mathrm{las}}$). In this calculation, we take $K_i = 1.5$ and $N_{\mathrm{max}} = 8$, with $a_0 = 10$, $k_{\mathrm{las}} = 2$ and $L = 2\pi\ \mathrm{MeV}^{-1}$. We present the evolution of the electron system in Fig. 1,

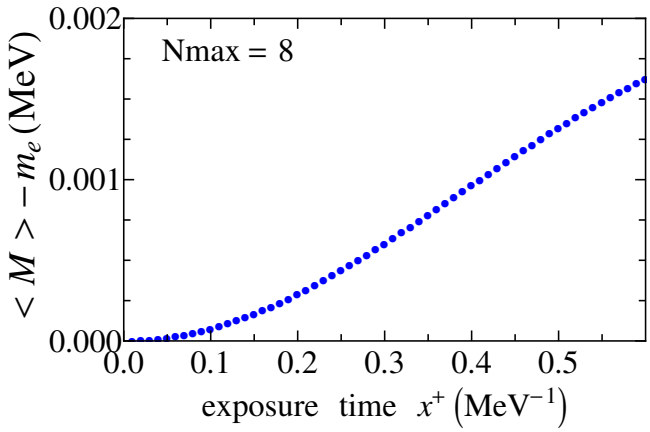

Figure 2: The average invariant mass of the electron-photon system evolves as a function of exposure time. The vertical axis is the difference between the average invariant mass of the electron-photon system and that of a single physical electron.

at increasing (top to bottom) light-front times. As time evolves, Fig. 1 shows how the background causes transitions from the ground state in the $K = 1.5$ segment to other eigenstates of P^-_{QED}. Both the single electron states and electron-photon states are populated; the former represent the acceleration of the electron by the background, while the latter represent the process of radiation. At times $x^+ = 0.2\ \mathrm{MeV}^{-1}$, the single electron state in the $K = 3.5$ segment becomes populated while the probability for finding the initial state begins to drop. The populated electron-photon states begin forming a peak structure. The location of the peak is around the invariant mass of 0.8 MeV, roughly consistent with the expected value of $M_{\mathrm{pk1}} = \sqrt{P_i^-(K_i + k_{\mathrm{las}})} = 0.78\,\mathrm{MeV}$, where $P_i^- = \frac{m_e^2}{K_i} \sim 0.17\,\mathrm{MeV}$ is the light-front energy of the initial single electron state with $K = 3.5$.

As time evolves, the probability of finding the electron in its initial (ground) state continues to decrease. Single electron states with successively higher K dominate the system. It also becomes possible to find electron-photon states of higher K and invariant mass, following the absorption of more energy from the background field as time evolves (see the second and third rows of Fig. 1).

As the state $|\psi; x^+\rangle$ encodes all the information of the system, other observables can be constructed out of $|\psi; x^+\rangle$. As an example, the evolution of the average invariant mass $\langle M\rangle \equiv \sum_\beta M_\beta \langle\beta|\psi\rangle^2$ of the system as a function of exposure time is displayed in Fig. 2. The approximately linear increase of the invariant mass up to an exposure time of 0.6 MeV^{-1} indicates the fact that photons are created as the background field pumps energy into the system.

6 Conclusion and outlook

In this paper, we review a recently constructed nonperturbative framework for time-dependent problems in quantum field theory. It is called "time-dependent BLFQ" (tBLFQ). Adopting the light-front dynamics and Hamiltonian formalism, tBLFQ provides the evolution of quantum field amplitudes through the light-front Schrödinger equation. Given the light-front Hamiltonian of the system, and an initial state as input, the quantum field amplitudes of the system at any subsequent time can be evaluated. The entire calculation is performed nonperturbatively with basis truncation and time-step discretization being the only two approximations.

As a generic method for time-dependent problems in quantum field theory, the

tBLFQ method can be applied to both first-principles and effective Hamiltonians, where the time-dependence arises either from the background fields or from using non-stationary initial states. In this work we apply the tBLFQ method to strong field laser physics and specifically study the nonlinear Compton scattering process, in which an electron is accelerated by a background field and emits a photon. The numerical calculation reveals a coherent superposition of electron acceleration and photon-emission processes in the nonperturbative regime.

As a next step, we plan to apply this method to relativistic heavy-ion collisions in which the medium of the colliding nuclei can be modeled as a dissipative background field. For example, the energy loss of the produced quark and gluon jets in this evolving background field can be predicted. Another application is the hadronization process in QCD.

We acknowledge valuable discussions with K. Tuchin, H. Honkanen, S. J. Brodsky, P. Hoyer, P. Wiecki and Y. Li. This work was supported in part by the Department of Energy under Grant Nos. DE-FG02-87ER40371 and DESC0008485 (SciDAC-3/NUCLEI) and by the National Science Foundation under Grant No PHY-0904782. A. I. is supported by the Swedish Research Council, contract 2011-4221.

References

[1] J. P. Vary *et al.*, Phys. Rev. C **81**, 035205 (2010), arXiv:0905.1411 [nucl-th] (2009).

[2] H. Honkanen, P. Maris, J. P. Vary and S. J. Brodsky, Phys. Rev. Lett. **106**, 061603 (2011), arXiv:1008.0068 [hep-ph] (2010).

[3] S. J. Brodsky, H.-C. Pauli and S. S. Pinsky, Phys. Rept. **301**, 299 (1998), hep-ph/9705477 (1997).

[4] P. W. Wiecki, Y. Li, X. Zhao, P. Maris and J. P. Vary, *see these Proceedings*, p. 146, http://www.ntse-2013.khb.ru/Proc/Wiecki.pdf.

[5] Y. Li, P. W. Wiecki, X. Zhao, P. Maris and J. P. Vary, *see these Proceedings*, p. 136, http://www.ntse-2013.khb.ru/Proc/YLi.pdf.

[6] X. Zhao, A. Ilderton, P. Maris and J. P. Vary, Phys. Rev. D **88**, 065014 (2013), arXiv:1303.3273 [nucl-th] (2013).

[7] X. Zhao, A. Ilderton, P. Maris and J. P. Vary, Phys. Lett. B **726**, 856 (2013), arXiv:1309.5338 [nucl-th] (2013).

[8] A. I. Nikishov and V. I. Ritus, Zh. Eksp. Teor. Fiz. **46**, 776 (1963); **46**, 1768 (1964).

[9] A. Di Piazza, C. Muller, K. Z. Hatsagortsyan and C. H. Keitel, Rev. Mod. Phys. **84**, 1177 (2012), arXiv:1111.3886 [hep-ph] (2011).

[10] G. F. de Teramond and S. J. Brodsky, Phys. Rev. Lett. **102**, 081601 (2009), arXiv:0809.4899 [hep-ph] (2008).

[11] V. A. Karmanov, J.-F. Mathiot and A. V. Smirnov, Phys. Rev. D **77**, 085028 (2008); **86**, 085006 (2012), arXiv:1204.3257 [hep-th] (2012).

[12] S. S. Chabysheva and J. R. Hiller, Ann. Phys. (NY) **325**, 2435 (2010), arXiv:0911.3686 [hep-ph] (2009).

[13] X. Zhao, H. Honkanen, P. Maris, J. P. Vary and S. J. Brodsky, *in preparation.*

NTSE-2013 Keynote Talk:

Ab Initio Approaches to Nuclear Reactions

Petr Navrátil

TRIUMF, 4004 Wesbrook Mall, Vancouver, BC V6T 2A3, Canada

Abstract

The exact treatment of nuclei starting from the constituent nucleons and the fundamental interactions among them has been a long-standing goal in nuclear physics. In addition to the complex nature of nuclear forces, one faces the quantum-mechanical many-nucleon problem governed by an interplay between bound and continuum states. In recent years, significant progress has been made in *ab initio* nuclear structure and reaction calculations based on input from QCD employing Hamiltonians constructed within chiral effective field theory. In this contribution, we first present a brief overview of recent achievements of various *ab initio* nuclear reaction approaches and then focus on the newly developed techniques, the no-core shell model with continuum (NCSMC) capable of describing simultaneously both bound and scattering states in light nuclei.

Keywords: *Ab initio calculations; low-energy nuclear reactions, resonances, halo nuclei*

1 Introduction

One of the central goals of nuclear physics is to come to a basic understanding of the structure and dynamics of nuclei, quantum many-body systems exhibiting bound states, unbound resonances, and scattering states, all of which can be strongly coupled. *Ab initio* (i. e., from first principles) approaches attempt to achieve such a goal for light nuclei. Over the past fifteen years, efficient techniques such as the Green's function Monte Carlo (GFMC) [1], *ab initio* NCSM [2], Coupled Cluster Method (CCM) [3–5] or nuclear lattice effective field theory (EFT) [6] have greatly advanced our understanding of bound-state properties of light nuclei starting from realistic nucleon-nucleon (NN) and three-nucleon ($3N$) interactions. On the other hand, a fully-developed fundamental theory able to address a large range of nuclear scattering and nuclear reaction properties is still missing, particularly for processes involving more than four nucleons overall. Better still, achieving a realistic *ab initio* description of light nuclei requires abandoning the "traditional" separated treatment of discrete states and scattering continuum in favor of a unified treatment of structural and reaction properties. The development of such a unified fundamental theory of light nuclei is key to refining our understanding of the underlying forces across the nuclear landscape: from the well-bound nuclei to the exotic nuclei at the boundaries of stability that have become the focus of the next generation experiments with rare-isotope beams, to the low-energy fusion reactions that represent the primary energy-generation mechanism in stars, and could potentially be used for future energy generation on earth.

In this contribution, we present a brief overview of the emerging field of *ab initio* calculations of nuclear reactions in Section 2. In Section 3, we describe the recently

Proceedings of International Conference 'Nuclear Theory in the Supercomputing Era — 2013' (NTSE-2013), Ames, IA, USA, May 13–17, 2013. Eds. A. M. Shirokov and A. I. Mazur. Pacific National University, Khabarovsk, Russia, 2014, p. 211.

http://www.ntse-2013.khb.ru/Proc/Navratil.pdf.

introduced *ab initio* many-body approach to nuclear bound and continuum states, the no-core shell model with continuum (NCSMC) that combines the resonating-group method (RGM) [7] with the *ab initio* no-core shell model (NCSM) [8]. In Section 4, we discuss recent applications of the NCSMC to the description of ^{7}He resonances, we investigate the $3N$ interaction effects in the nucleon-^{4}He scattering, we highlight the introduction of the three-body clusters in the description of ^{6}He, and present preliminary study of the continuum effects in the low-lying resonances of ^{9}Be. Conclusions are given in Section 5.

2 *Ab initio* approaches to nuclear reactions

Because of their importance nuclear reactions attract much attention, and there have been many interesting new developments in the recent past. In this section we will give a brief and non-exhaustive overview of the theoretical efforts devoted to *ab initio* approaches to nuclear reactions, and in particular scattering of light nuclei.

By *ab initio* approaches we mean methods, in which all the nucleons involved in the process are treated as active degrees of freedom, and the antisymmetrization of the many-body wave functions is treated exactly. Further, the NN interactions among all participating nucleons are realistic, i. e., describe accurately NN scattering and the deuteron. Finally, the approximations used in the calculations should be controllable in a sense that it should be feasible to arrive at or to extrapolate to an exact result with a specified uncertainty. We note that, in general, the $3N$ force that provides a realistic description of the three-nucleon system should also be considered in *ab initio* calculations.

In the three- and four-nucleon sectors there has been remarkable progress over the past decade: the Faddeev [9], Faddeev–Yakubovsky (FY) [10, 11], Alt, Grassberger and Sandhas (AGS) [12, 13], hyperspherical harmonics (HH) [14], Lorentz integral transform (LIT) methods [15–17], RGM [18], etc., are among the best known of several numerically exact techniques able to describe reactions observables starting from realistic NN and in some cases also $3N$ forces.

Going beyond four nucleons there are fewer *ab initio* or *ab initio* inspired methods able to describe reactions observables starting from realistic forces. Only very recently the Green's function Monte Carlo (GFMC) [19], the no-core shell model combined with the resonating group method (NCSM/RGM) [20,21] and the fermionic molecular dynamics [22] have made steps in this direction.

Among the recent developments in the $A = 4$ scattering and reaction calculations we highlight the new capability to include properly the Coulomb interaction in momentum space [12, 13] and to include the three-nucleon interaction in the p-^{3}H Faddeev–Yakubovsky configuration space calculations [11]. A benchmark for the n-^{3}H low-energy elastic cross section calculation has been performed by the FY, AGS and HH methods using different NN potentials [23]. The main conclusion of this work is the failure of the existing NN forces to reproduce the n-^{3}H total cross section. Remarkable recent results are the p-^{3}He scattering calculations performed using the hyperspherical harmonic basis, which demonstrated that the new NN plus $3N$ interactions derived within chiral effective field theory (EFT) reduce noticeably the discrepancy observed for the A_y observable [24]. Further, with the same Hamiltonian, the low-energy total n-^{3}H cross section calculated by the HH method was found in improved agreement with the data [25].

In a ground-breaking development, the AGS method has been generalized to calculations of the n-^{3}H scattering above the four-nucleon breakup threshold [26]. This allowed to calculate the elastic cross section of 14.1 MeV neutrons. This is in particular important as such high-energy neutrons are produced in the deuteron-triton fusion.

The first *ab initio* scattering calculation for a system with $A > 4$ was performed within the GFMC approach. The n-α low-lying $J^\pi = 3/2^-$ and $1/2^-$ P-wave resonances as well as the $1/2^+$ S-wave non-resonant scattering below 5 MeV center of mass (c.m.) energy were obtained using the AV18 NN potential with and without the three-nucleon force, chosen to be either the Urbana IX or the Illinois-2 model [19]. The results of these calculations revealed sensitivity to the inter-nucleon interaction, and in particular to the strength of the spin-orbit force. New developments of the GFMC applications to nuclear reactions include calculations of spectroscopic overlaps for light nuclei [27] and calculations of the asymptotic normalization constants (ANC) by integral relations with the variational Monte Carlo (VMC) wave functions [28].

The FMD approach has been applied quite successfully to the description of the radiative capture cross section (S-factor) of the ^{3}He(α,γ)^{7}Be reaction important for astrophysics. The FMD calculations describe new experimental data both at low energy (below 100 keV) as well as at high energy (from 1 MeV to 2.5 MeV) [29].

As an interesting theoretical development to the many-body scattering, we mention the approach based on the variational description of continuum states in terms of integral relations [30] that may be used to directly apply the bound-state many-body techniques to scattering. A variation of this approach has been explored in the $A = 5$ scattering in Ref. [31]. Further, the use of bound-state methods to calculate scattering properties with possible applications for lattice calculations has been investigated in Ref. [32].

There are also some recent attempts to describe the nuclear scattering in an effective field theory approach. In particular, the pionless EFT combined with the RGM was successfully applied to three- and four-nucleon bound state and scattering calculations [33].

In a big jump in mass number, we note that the ^{17}F low-lying states were recently investigated within the coupled-cluster (CC) approach with the Gamow–Hartree–Fock basis that incorporates effects of the continuum [34]. The calculation resulted in a good description of the $1/2^+$ proton halo state in ^{17}F. It was shown that the continuum effects are essential to obtain these results and that the proton halo state single-particle energy is not affected by short-range correlations in the nuclear interactions.

The CC theory has been recently combined with the LIT method to calculate the photodisintegration of ^{4}He and, in particular, the giant dipole resonance in ^{16}O [35].

Using the Gamow–Hartree–Fock basis, the CCM was used for the first time to calculate *ab initio* elastic proton scattering on a nucleus as heavy as ^{40}Ca [36]. Elastic scattering of a nucleon on a target nucleus can be computed from the one-nucleon overlap functions. These are calculated within the CC theory. The obtained cross sections at low-energy for elastic proton scattering on ^{40}Ca were found in a fair agreement with experiment.

As a completely new development, *ab initio* calculations of nuclear scattering and reactions on the lattice has been explored in Ref. [37]. Adiabatic projection method was implemented and tested in elastic fermion-dimer scattering in lattice effective field theory. Such calculation corresponds to neutron-deuteron scattering in the spin-quartet channel at leading order in pionless effective field theory. The method adapts features of the resonating group method [7] in a similar fashion as in the NCSM/RGM approach [38] discussed in the subsequent sections.

3 No-core shell model with continuum

In this section we briefly overview the newly introduced approach to nuclear bound and continuum states, the no-core shell model with continuum [39, 40]. This approach adopts an extended model space that, in addition to the continuous binary-cluster $(A-a, a)$ NCSM/RGM states, with $A-a$ and a nucleons in the heavier and

the lighter cluster, respectively, encompasses also square-integrable NCSM eigenstates of the complete A-nucleon system. Such eigenstates introduce in the trial wave function short- and medium-range A-nucleon correlations that in the binary-cluster NCSM/RGM formalism have to be treated by including a large number of excited states of the clusters.

3.1 NCSM

The *ab initio* NCSM is a nuclear-structure technique appropriate for the description of bound states or for approximations of narrow resonances. Nuclei are considered as systems of A non-relativistic point-like nucleons interacting through realistic internucleon interactions. Translational invariance as well as angular momentum and parity of the system under consideration are conserved. The many-body wave function is cast into an expansion over a complete set of antisymmetric A-nucleon harmonic oscillator (HO) basis states containing up to $N_{\max}$ HO excitations above the lowest possible configuration:

$$|\Psi_A^{J^\pi T}\rangle = \sum_{N=0}^{N_{\max}} \sum_i c_{Ni} \, |ANiJ^\pi T\rangle. \tag{1}$$

Here, N denotes the total number of HO excitations of all nucleons above the minimum configuration, $J^\pi T$ are the total angular momentum, parity and isospin, and i additional quantum numbers. The sum over N is restricted by parity to either an even or odd sequence. The basis is further characterized by the frequency Ω of the HO well and may depend on either Jacobi relative or single-particle coordinates. In the former case, the wave function does not contain the center of mass (c.m.) motion, but antisymmetrization is complicated. In the latter case, antisymmetrization is trivially achieved using Slater determinants, but the c.m. degrees of freedom are included in the basis. The HO basis within the $N_{\max}$ truncation is the only possible one that allows an exact factorization of the c.m. motion for the eigenstates, even when working with single-particle coordinates and Slater determinants. Calculations performed with the two alternative coordinate choices are completely equivalent.

Square-integrable energy eigenstates expanded over the $N_{\max}\hbar\Omega$ basis, $|ANiJ^\pi T\rangle$, are obtained by diagonalizing the intrinsic Hamiltonian, $\hat{H} = \hat{T}_{\rm int} + \hat{V}$,

$$\hat{H} \, |A\lambda J^\pi T\rangle = E_\lambda \, |A\lambda J^\pi T\rangle, \tag{2}$$

where $\hat{T}_{\rm int}$ is the internal kinetic energy operator and $\hat{V}$ is the NN or NN+3N interaction. We note that with the HO basis sizes typically used ($N_{\max}$∼10−14), the $|A\lambda J^\pi T\rangle$ eigenstates lack correct asymptotic behavior for weakly-bound states and always have incorrect asymptotic behavior for resonances.

3.2 NCSM/RGM

In the NCSM/RGM [38, 41], the ansatz of Eq. (1) for the A-nucleon wave function is replaced by an expansion over antisymmetrized products of binary-cluster channel states $|\Phi_{\nu r}^{J^\pi T}\rangle$ and wave functions of their relative motion

$$|\Psi_A^{J^\pi T}\rangle \;\; = \;\; \sum_\nu \int dr \, r^2 \frac{\gamma_\nu(r)}{r} \hat{\mathcal{A}}_\nu |\Phi_{\nu r}^{J^\pi T}\rangle \, . \tag{3}$$

The channel states $|\Phi_{\nu r}^{J^\pi T}\rangle$ contain $(A-a)$- and a-nucleon clusters (with $a<A$) of total angular momentum, parity, isospin and additional quantum number $I_1, \pi_1, T_1, \alpha_1$ and $I_2, \pi_2, T_2, \alpha_2$, respectively, and are characterized by the relative orbital angular

momentum ℓ and channel spin $\vec{s} = \vec{I}_1 + \vec{I}_2$:

$$|\Phi^{J^\pi T}_{\nu r}\rangle = \Big[\big(|A-a\ \alpha_1 I_1^{\pi_1} T_1\rangle\, |a\ \alpha_2 I_2^{\pi_2} T_2\rangle\big)^{(sT)}\, Y_\ell(\hat{r}_{A-a,a})\Big]^{(J^\pi T)}\, \frac{\delta(r - r_{A-a,a})}{r r_{A-a,a}}. \quad (4)$$

The channel index ν collects the quantum numbers $\{A-a\ \alpha_1 I_1^{\pi_1} T_1; a\ \alpha_2 I_2^{\pi_2} T_2; s\ell\}$. The intercluster relative vector $\vec{r}_{A-a,a}$ is the displacement between the clusters' centers of mass and is given in terms of the single-particle coordinates $\vec{r}_i$ by:

$$\vec{r}_{A-a,a} = r_{A-a,a}\,\hat{r}_{A-a,a} = \frac{1}{A-a}\sum_{i=1}^{A-a}\vec{r}_i - \frac{1}{a}\sum_{j=A-a+1}^{A}\vec{r}_j. \quad (5)$$

The cluster wave functions depend on translationally invariant internal coordinates and are antisymmetric under exchange of internal nucleons, while the intercluster antisymmetrizer $\hat{\mathcal{A}}_\nu$ takes care of the exchange of nucleons belonging to different clusters.

With appropriate boundary conditions imposed on the wave functions of the relative motion $\gamma_\nu(r)$, the expansion of Eq. (3) is suitable for describing bound states, resonances and scattering states between clusters. For bound states, expansions (1) and (3) are equivalent, although for well-bound systems where short-range A-body correlations play a dominant role, the convergence of the eigenenergy would typically be more efficient within the NCSM model space defined by Eq. (1).

The unknown relative-motion wave functions $\gamma_\nu(r)$ are determined by solving the many-body Schrödinger equation in the Hilbert space spanned by the basis states $\hat{\mathcal{A}}_\nu\,|\Phi^{J^\pi T}_{\nu r}\rangle$:

$$\sum_\nu \int dr\, r^2 \Big[\mathcal{H}^{J^\pi T}_{\nu'\nu}(r',r) - E\,\mathcal{N}^{J^\pi T}_{\nu'\nu}(r',r)\Big]\,\frac{\gamma_\nu(r)}{r} = 0, \quad (6)$$

where

$$\mathcal{H}^{J^\pi T}_{\nu'\nu}(r',r) = \Big\langle \Phi^{J^\pi T}_{\nu' r'}\Big|\, \hat{\mathcal{A}}_{\nu'}\hat{H}\hat{\mathcal{A}}_\nu\, \Big|\Phi^{J^\pi T}_{\nu r}\Big\rangle, \quad (7)$$

$$\mathcal{N}^{J^\pi T}_{\nu'\nu}(r',r) = \Big\langle \Phi^{J^\pi T}_{\nu' r'}\Big|\, \hat{\mathcal{A}}_{\nu'}\hat{\mathcal{A}}_\nu\, \Big|\Phi^{J^\pi T}_{\nu r}\Big\rangle, \quad (8)$$

are the Hamiltonian and norm kernels, respectively, and E is the total energy in the c.m. frame.

3.3 NCSMC

The NCSMC ansatz for the many-body wave function includes both A-body square-integrable and $(A-a,a)$ binary-cluster continuous basis states according to:

$$|\Psi^{J^\pi T}_A\rangle = \sum_\lambda c_\lambda\,|A\lambda J^\pi T\rangle + \sum_\nu \int dr\, r^2 \frac{\gamma_\nu(r)}{r}\hat{\mathcal{A}}_\nu |\Phi^{J^\pi T}_{\nu r}\rangle. \quad (9)$$

The resulting wave function (9) is capable of describing efficiently both bound and unbound states. Indeed, the NCSM sector of the basis (eigenstates $|A\lambda J^\pi T\rangle$) provides an effective description of the short- to medium-range A-body structure, while the NCSM/RGM cluster states make the theory able to handle the scattering physics of the system. In other words, with the expansion (9) one obtains the coupling of the NCSM with the continuum. Clearly, the NCSMC model space is overcomplete, but this is not a concern. We also note that, in principle, the expansion (9) can be further generalized to include a three-cluster component suitable for the description of, e. g., Borromean halo nuclei and reactions with final three-body states [42].

The discrete (c_λ) and continuous ($\gamma_\nu(r)$) unknowns of the NCSMC wave function are obtained as solutions of the coupled equations

$$\begin{pmatrix} H_{NCSM} & \bar{h} \\ \bar{h} & \overline{\mathcal{H}} \end{pmatrix} \begin{pmatrix} c \\ \chi \end{pmatrix} = E \begin{pmatrix} 1 & \bar{g} \\ \bar{g} & 1 \end{pmatrix} \begin{pmatrix} c \\ \chi \end{pmatrix}, \tag{10}$$

where $\chi_\nu(r)$ are the relative wave functions in the NCSM/RGM sector when working with the orthogonalized cluster channel states [41]. These are related to the original wave functions $\gamma_\nu(r)$ of Eq. (9) by the relationship given in Eq. (20) of Ref. [40].

The NCSM sector of the Hamiltonian kernel is a diagonal matrix of the NCSM energy eigenvalues E_λ (2),

$$(H_{NCSM})_{\lambda\lambda'} = \langle A\lambda J^\pi T|\hat{H}|A\lambda' J^\pi T\rangle = E_\lambda\,\delta_{\lambda\lambda'}\,, \tag{11}$$

while $\overline{\mathcal{H}}$ is the orthogonalized NCSM/RGM kernel of Eq. (17) in Ref. [40]. Because of the orthogonalization procedure, both diagonal blocks in the NCSMC norm kernel are identities in their respective spaces. The coupling between square-integrable and binary-cluster sectors of the model space is described by the cluster form factor

$$\bar{g}_{\lambda\nu}(r) = \sum_{\nu'} \int dr'\, r'^2 \langle A\lambda J^\pi T|\hat{\mathcal{A}}_{\nu'}\Phi^{J^\pi T}_{\nu' r'}\rangle\, \mathcal{N}^{-\frac{1}{2}}_{\nu'\nu}(r', r) \tag{12}$$

in the norm kernel, and by the coupling form factor

$$\bar{h}_{\lambda\nu}(r) = \sum_{\nu'} \int dr'\, r'^2 \langle A\lambda J^\pi T|\hat{H}\hat{\mathcal{A}}_{\nu'}|\Phi^{J^\pi T}_{\nu' r'}\rangle\, \mathcal{N}^{-\frac{1}{2}}_{\nu'\nu}(r', r). \tag{13}$$

in the Hamiltonian kernel.

4 NCSM/RGM and NCSMC applications

4.1 ^{7}He resonances

The first demonstration of the power of the NCSMC approach was shown in an investigation of ^{7}He resonances [39,40]. The ^{7}He nucleus is a particle-unstable system with a $J^\pi T = 3/2^-\ 3/2$ ground state lying at 0.430(3) MeV [43,44] above the ^{6}He+n threshold and an excited $5/2^-$ resonance centered at 3.35 MeV, which mainly decays to α+3n (as discovered in the pioneering work of Ref. [45]). While there is a general consensus on the $5/2^-$ state, discussions are still open for the other excited states. In particular, the existence of a low-lying ($E_R \sim 1$ MeV) narrow ($\Gamma \leq 1$ MeV) $1/2^-$ state has been advocated by many experiments [46–50] while it was not confirmed in several others [51–56]. The presence of a low-lying $1/2^-$ state has been excluded by a study on the isobaric analog states of ^{7}He in ^{7}Li [57]. According to this work, a broad $1/2^-$ resonance at ∼3.5 MeV with a width $\Gamma \sim 10$ MeV fits the data the best. Neutron pick-up and proton-removal reactions [53, 54] suggest instead a $1/2^-$ resonance at about 3 MeV with a width $\Gamma \approx 2$ MeV.

From a theoretical point of view, ^{7}He is an ideal system to showcase achievements made possible by a unified *ab initio* approach to nuclear bound and continuum states such as the NCSMC. Since ^{7}He is unbound, it cannot be reasonably described within the NCSM. One could calculate its properties using the NCSM/RGM within an ^{6}He+n binary-cluster expansion. However, the ^{6}He nucleus is weakly bound and all its excited states are unbound. Consequently, a limitation to just a few lowest ^{6}He eigenstates in the NCSM/RGM expansion would be questionable especially because, except for the lowest 2^+ state, all other ^{6}He excited states are either broad resonances or simply states in the continuum. With the NCSMC these challenges are overcome.

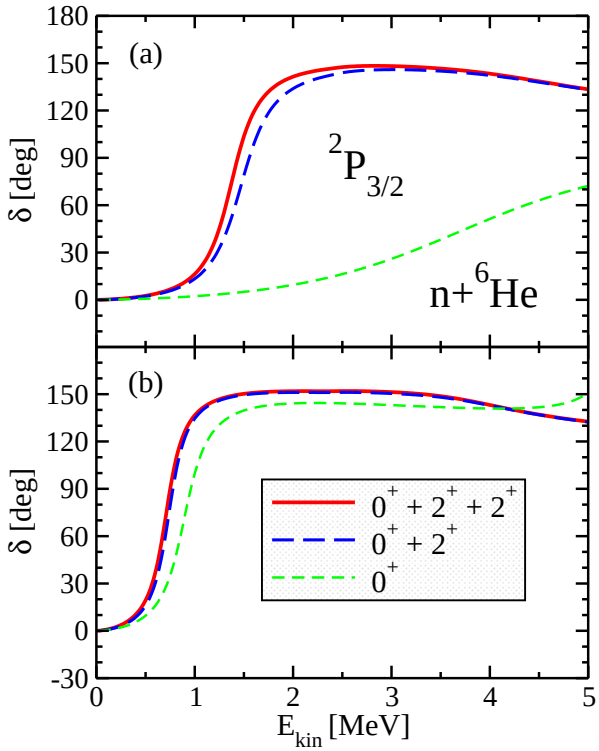

Figure 1: Dependence of the NCSM/RGM (a) and NCSMC (b) ^{6}He+n phase shifts of the ^{7}He $3/2^-$ ground state on the number of ^{6}He states included in the binary-cluster basis. The short-dashed green curve, the dashed blue curve and the solid red curve correspond to calculations with ^{6}He 0^+ ground state only, $0^+, 2^+$ states and $0^+, 2^+, 2^+$ states, respectively. The similarity-renormalization-group (SRG) [58–61] N^{3}LO [62,63] NN potential with $\Lambda = 2.02$ fm^{-1}, the $N_{\max}$=12 basis size and the HO frequency of $\hbar\Omega$=16 MeV were used.

This is seen by studying the dependence of the $3/2^-$ ground state (g.s.) phase shifts on the number of ^{6}He eigenstates included in the NCSM/RGM [panel (a)] and NCSMC [panel (b)] calculations, shown in Fig. 1. Here, the channels are denoted using the standard notation $^{2s+1}\ell_J$, e. g., $^2P_{3/2}$ for the g.s. resonance, with the quantum numbers s, ℓ and J defined as in Section 3.2, Eq. (4). We observe that the NCSM/RGM calculation with the ^{6}He target restricted to its ground state does not produce a ^{7}He $3/2^-$ resonance (the phase shift does not reach 90 degrees and is less than 70 degrees up to 5 MeV). A $^2P_{3/2}$ resonance does appear once n+^{6}He(2^+_1) channel states are coupled to the basis, and the resonance position further moves to lower energy with the inclusion of the second 2^+ state of ^{6}He. On the contrary, the NCSMC calculation with only the ground state of ^{6}He already produces the $^2P_{3/2}$ resonance. In fact, this NCSMC model space is sufficient to obtain the ^{7}He $3/2^-$ g.s. resonance at about 1 MeV above threshold, which is lower than the NCSM/RGM prediction of 1.39 MeV when three ^{6}He states are included. Adding the first 2^+ state of ^{6}He generates a modest shift of the resonance to a still lower energy while the 2^+_2 state of ^{6}He has no significant influence [see Fig. 1, panel (b)]. We further observe that the difference of about 0.7 MeV between the NCSM/RGM and NCSMC results for the resonance position is due to additional correlations in the wave function brought about by the ^{7}He eigenstates that are coupled to the neutron-^{6}He binary-cluster states in the NCSMC. Indeed, such $A = 7$ eigenstates (in the present calculation four $3/2^-$ states, of which only the $3/2^-_1$ produces a substantial effect on the $^2P_{3/2}$ resonance) have the practical effect of compensating for higher excited states of the ^{6}He target

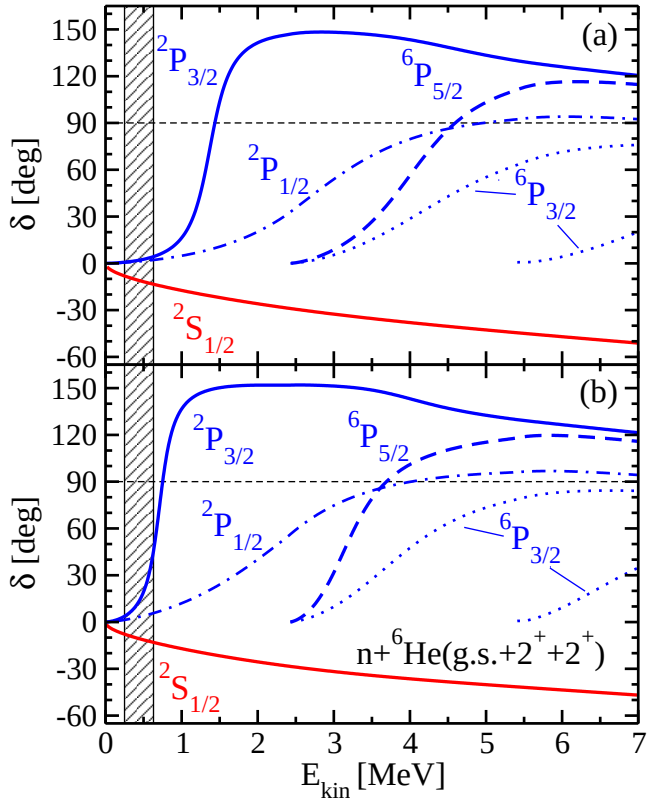

Figure 2: NCSM/RGM (a) and NCSMC (b) ^{6}He+n diagonal phase shifts (except $^6P_{3/2}$, which are eigenphase shifts) as a function of the kinetic energy in the center of mass. The dashed vertical area centered at 0.43 MeV indicates the experimental centroid and width of the ^{7}He ground state [43, 44]. In all calculations the lowest three ^{6}He states have been included in the binary-cluster basis.

omitted in the NCSM/RGM sector of the basis.

The NCSM/RGM and NCSMC phase shifts for the n+^{6}He five P-wave and the $^2S_{1/2}$ channels are shown in Fig. 2. All curves have been obtained including the three lowest ^{6}He states (i. e., the 0^+ ground state and the two lowest 2^+ excited states) within the $N_{\max} = 12$ HO basis. The model space of the NCSMC calculations [panel (b)] additionally includes ten ^{7}He NCSM eigenstates. The dashed vertical area centered at 0.43 MeV indicates the experimental centroid and width of the ^{7}He ground state [43, 44]. As expected from a variational calculation, the introduction of the additional square-integrable A-body basis states $|A\lambda J^\pi T\rangle$ [i. e., going from panel (a) to panel (b) of Fig. 2] lowers the centroid values of all ^{7}He resonances. In particular, the $3/2^-$ ground and $5/2^-$ excited states of ^{7}He are pushed toward the ^{6}He+n threshold, closer to their respective experimental positions. The resonance widths also shrink toward the observed data as we discuss below.

Computed widths Γ and resonance energies E_R are reported in Table 1, together with the available experimental data. From an experimental standpoint, the situation concerning the $1/2^-$ resonance is not clear as discussed in the beginning of this section and documented in Table 1. While the centroid energies determined in the experiments of Refs. [53, 54] and [57] are comparable, the widths are very different. Within the present determination of E_R and Γ, the NCSMC results are in fair agreement with the $1/2^-$ properties measured in the neutron pick-up and proton-removal reactions experiments of Refs. [53] and [54]. Our calculations definitely do not support the hypothesis of a low-lying ($E_R \sim 1$ MeV) narrow ($\Gamma \leq 1$ MeV) $1/2^-$ resonance [46–50].

Table 1: Experimental and theoretical values for the resonance centroids and widths in MeV for the $3/2^-$ ground state and the $5/2^-$ and $1/2^-$ excited states of ^{7}He. Calculations are carried out as described in Fig. 2 and in the text.

J^π	experiment			NCSMC		NCSM/RGM		NCSM
	E_R	Γ	Ref.	E_R	Γ	E_R	Γ	E_R
$3/2^-$	0.430(3)	0.182(5)	[44]	0.71	0.30	1.39	0.46	1.30
$5/2^-$	3.35(10)	1.99(17)	[64]	3.13	1.07	4.00	1.75	4.56
$1/2^-$	3.03(10)	2	[53]	2.39	2.89	2.66	3.02	3.26
	3.53	10	[57]					
	1.0(1)	0.75(8)	[47]					

4.2 Nucleon-^{4}He scattering with chiral NN+$3N$ interactions

The *ab initio* no-core shell model/resonating-group method has now been extended to include $3N$ interactions for the description of nucleon-nucleus collisions [65]. The extended framework was then applied to nucleon-^{4}He elastic scattering using similarity-renormalization-group evolved nucleon-nucleon plus three-nucleon potentials derived from chiral effective field theory. Up to six excited states of the ^{4}He target were included in the NCSM/RGM calculations. Significant effects from the inclusion of the chiral $3N$ force were found, e. g., it enhances the spin-orbit splitting between the $3/2^-$and $1/2^-$ resonances and leads to an improved agreement with the phase shifts obtained from an accurate R-matrix analysis of the five-nucleon experimental data. Calculated phase shifts compared to the R-matrix analysis of experimental data in the energy range up to the d-^{3}H threshold are shown in Fig. 3. The $^2P_{3/2}$ resonance position is overestimated. The probably reason is the omition of higher excited states of ^{4}He and of the other closed channels, e. g., d-^{3}H, in the calculations. The omitted states and channels can be effectively included by the NCSMC coupling to the ^{5}He eigenstates (obtained within the NCSM). Work in this direction is under way.

4.3 ^{6}He as a ^{4}He+n+n three-body cluster

The NCSM/RGM technique has also been generalized to the three-body cluster dynamics [42]. The solution of the three-cluster Schrödinger equation was obtained by means of hyperspherical harmonic expansions on a Lagrange mesh [67,68]. In Ref. [42], the first ^{4}He+n+n investigation of the g.s. of the ^{6}He nucleus was presented based on a NN potential that yields a high-precision fit of the NN phase shifts and *ab initio* four-body wave functions for the ^{4}He cluster obtained consistently from the same Hamiltonian. Within this approach, one gets the appropriate asymptotic behavior of the wave functions. This is demonstrated in Fig. 4 showing the ground-state wave function of ^{6}He. A two-peak shape distribution is found in the ground-state probability distribution. One peak corresponds to a "di-neutron" configuration in which the neutrons are close together (about 2 fm apart from each other) while the ^{4}He core is separated from their c.m. at a distance of about 3 fm. Whereas the second peak, corresponding to the "cigar" configuration, represents an almost linear structure in which the two neutrons are far from each other (about 5 fm apart) and the alpha particle lies almost in between them at $\sim$1 fm from their center of mass. Moreover, the present formalism combined with the appropriate scattering boundary conditions gives access to the *ab initio* study of resonant states of two-neutron halo nuclei (such as the excited states of ^{6}He) as well as to scattering problems involving channels with three fragments. Three-cluster NCSM/RGM ^{4}He+n+n scattering calculations with the aim to study the ^{6}He low-lying resonances are currently under way. Further, a generalization to include the NCSMC coupling is also under way.

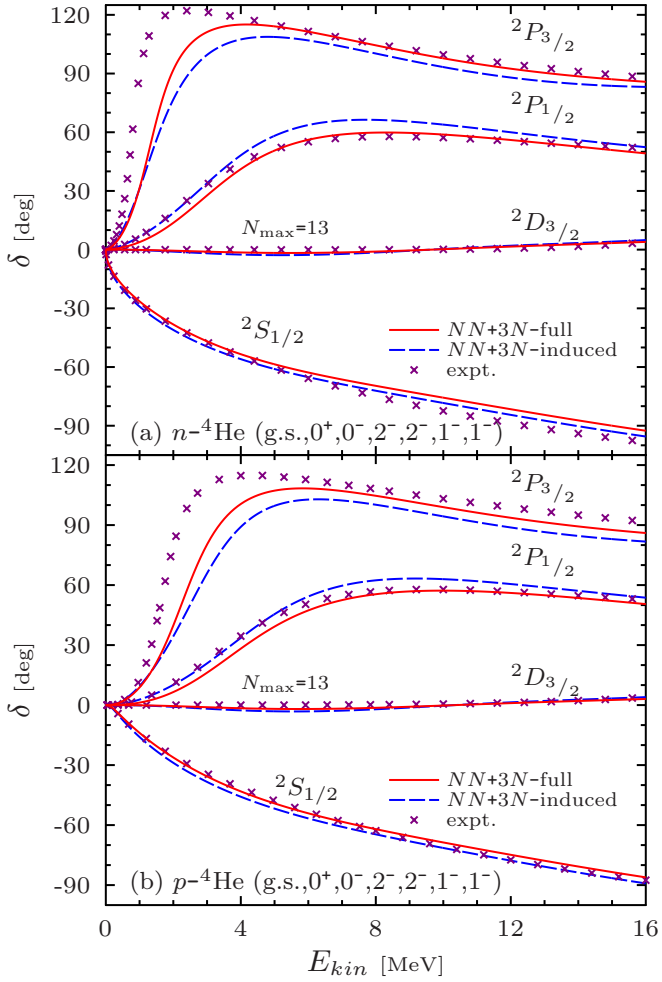

Figure 3: Comparison of the n-^{4}He (a) and p-^{4}He (b) phase-shifts ($^1S_{1/2}$, $^2P_{1/2}$, $^2P_{3/2}$ and $^2D_{3/2}$ waves) within the largest considered model space including the first six low-lying resonant states of the ^{4}He (g.s., 0^+0, 0^-0, 2^-0, 2^-1, 1^-1, 1^-0) at $N_{\max} = 13$ to the experimental phase-shifts (purple crosses) obtained from an R-matrix analysis [66]. Results for the NN+3N-full Hamiltonian are shown as red solid lines, those for the $NN + 3N$-induced Hamiltonian as blue dashed lines. For further details see Ref. [65]

4.4 Structure of ^{9}Be

The structure of ^{9}Be nucleus poses a challenge to *ab initio* approaches based on bound-state techniques such as the NCSM. The positive parity resonances are in general found too high compared to experiment and the splitting between the lowest $5/2^-$ and $1/2^-$ resonances tends to be overestimated when $3N$ effects are included [69]. A question is to which extend the continuum affects the ^{9}Be resonances and the above observations. NCSMC calculations with the chiral NN+3N interactions are now under way to answer these questions. Here we discuss preliminary results obtained using only a two-nucleon SRG-evolved NN interaction. The ^{9}Be is studied as a system of ^{8}Be+n with g.s. and the 2^+ state of ^{8}Be included. The NCSMC coupling to the ^{9}Be NCSM eigenstates is taken into account. The n-^{8}Be P-wave phaseshifts are shown in Fig. 5. A good convergence with respect to the HO basis size is found. The ^{9}Be separation energy is overestimated by 1 MeV with the used NN potential, which then

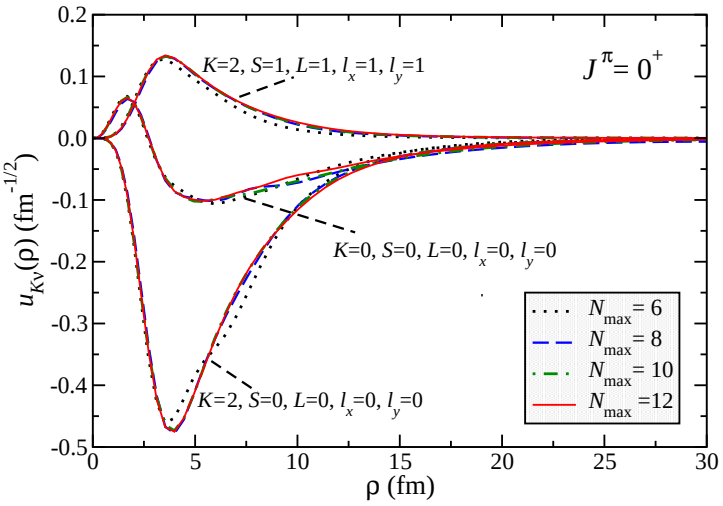

Figure 4: Three main components of the radial part of the ^{6}He g.s. wave functions as a dependence on the hyper-radius ρ for $N_{\max} = 6$, 8, 10, and 12. Further details can be found in Ref. [42]

also results in a shift of the resonances to a lower energy compared to experiment and even in a ∼100 keV binding of the $5/2^-$ state. Still, some interesting conclusions can be drawn even from these calculations. The splitting between the $5/2^-$ and the $1/2^-$ resonance is reduced substantially when the continuum is included due to the shift of the $1/2^-$ P-wave resonance with the $5/2^-$ F-wave state position unaffected. The positive-parity resonances, especially the $1/2^+_1$ and the $3/2^+_1$ S-wave resonances, are dramatically lowered in energy when the continuum is taken into account.

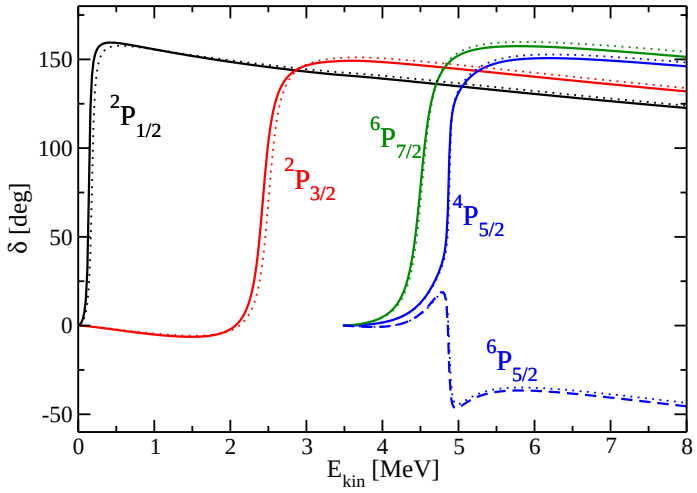

Figure 5: Preliminary results of n-^{8}Be phase shifts showing ^{9}Be P-wave resonances. The SRG-N^{3}LO NN potential with the evolution parameter $\Lambda = 2$ fm^{-1} was used. The full (dotted) lines correspond to the $N_{\max} = 10$ (8) model space, respectively. The HO frequency of 20 MeV was used.

5 Conclusions

Great progress has been made in the development of *ab initio* approaches to nuclear scattering, reactions and the description of weakly bound states. The accuracy of few-body methods improved and their ability to treat non-local and three-nucleon interactions has been extended. Nuclear reaction calculations with chiral forces are now possible. The four-nucleon scattering calculations are now feasible even above the breakup threshold. There are promising developments in methods applicable to systems of more than four nucleons. Continuum effects can now even be investigated in semi-magic nuclei beyond the p-shell.

We discussed in more details a new unified approach to nuclear bound and continuum states, the NCSMC, based on the coupling of a square-integrable basis (A-body NCSM eigenstates), suitable for the description of many-body correlations, and a continuous basis (NCSM/RGM cluster states) suitable for a description of long-range correlations, cluster correlations and scattering. This approach allows us to study weakly bound systems as well as narrow and broad resonances. The inclusion of $3N$ interactions in this formalism is under way. This opens new possibilities to perform realistic calculations for p- and light sd-shell nuclei starting from chiral NN+$3N$ interactions.

Acknowledgements

Computing support for this work came from the LLNL institutional Computing Grand Challenge program, the Jülich supercomputer Centre and Oak Ridge Leadership Computing Facility at ORNL [70]. Support from the NSERC Grant No. 401945-2011 is acknowledged. TRIUMF receives funding via a contribution through the Canadian National Research Council.

References

[1] B. S. Pudliner, V. R. Pandharipande, J. Carlson, S. C. Pieper and R. B. Wiringa, Phys. Rev. C **56**, 1720 (1997); R. B. Wiringa, S. C. Pieper, J. Carlson and V. R. Pandharipande, *ibid.* **62**, 014001 (2000); S. C. Pieper and R. B. Wiringa, Ann. Rev. Nucl. Part. Sci. **51**, 53 (2001); S. C. Pieper, K. Varga and R. B. Wiringa, Phys. Rev. C **66**, 044310 (2002).

[2] P. Navrátil, V. G. Gueorguiev, J. P. Vary, W. E. Ormand and A. Nogga, Phys. Rev. Lett. **99**, 042501 (2007).

[3] G. Hagen, T. Papenbrock, D. J. Dean and M. Hjorth-Jensen, Phys. Rev. Lett. **101**, 092502 (2008).

[4] G. Hagen, M. Hjorth-Jensen, G. R. Jansen, R. Machleidt and T. Papenbrock, Phys. Rev. Lett. **108**, 242501 (2012).

[5] R. Roth, S. Binder, K. Vobig, A. Calci, J. Langhammer and P. Navrátil, Phys. Rev. Lett. **109**, 052501 (2012).

[6] E. Epelbaum, H. Krebs, D. Lee and U.-G. Meissner, Phys. Rev. Lett. **106**, 192501 (2011).

[7] K. Wildermuth and Y. C. Tang, *A unified theory of the nucleus*. Vieweg, Braunschweig, 1977.

[8] P. Navrátil, J. P. Vary and B. R. Barrett, Phys. Rev. Lett. **84**, 5728 (2000); Phys. Rev. C **62**, 054311 (2000).

[9] H. Witała, W. Glöckle, J. Golak, A. Nogga, H. Kamada,R. Skibiński and J. Kuroś-Żołnierczuk, Phys. Rev. C **63**, 024007 (2001).

[10] R. Lazauskas and J. Carbonell, Phys. Rev. C **70**, 044002 (2004).

[11] R. Lazauskas, Phys. Rev. C **79**, 054007 (2009).

[12] A. Deltuva and A. C. Fonseca, Phys. Rev. C **75**, 014005 (2007).

[13] A. Deltuva and A. C. Fonseca, Phys. Rev. Lett. **98**, 162502 (2007).

[14] L. E. Marcucci, A. Kievsky, L. Girlanda, S. Rosati and M. Viviani, Phys. Rev. C **80**, 034003 (2009).

[15] D. Gazit, S. Bacca, N. Barnea, W. Leidemann and G. Orlandini, Phys. Rev. Lett. **96**, 112301 (2006).

[16] S. Quaglioni and P. Navrátil, Phys. Lett. B **652**, 370 (2007).

[17] S. Bacca, N. Barnea, W. Leidemann and G. Orlandini, Phys. Rev. Lett. **102**, 162501 (2009).

[18] H. M. Hofmann and G. M. Hale, Phys. Rev. C **77**, 044002 (2008).

[19] K. M. Nollett, S. C. Pieper, R. B. Wiringa, J. Carlson and G. M. Hale, Phys. Rev. Lett. **99**, 022502 (2007).

[20] S. Quaglioni and P. Navrátil, Phys. Rev. Lett. **101**, 092501 (2008).

[21] S. Quaglioni and P. Navrátil, Phys. Rev. C **79**, 044606 (2009).

[22] M. Chernykh, H. Feldmeier, T. Neff, P. von Neumann-Cosel and A. Richter, Phys. Rev. Lett **98**, 032501 (2007).

[23] R. Lazauskas, J. Carbonell, A. C. Fonseca, M. Viviani, A. Kievsky and S. Rosati, Phys. Rev. C **71**, 034004 (2005).

[24] M. Viviani, L. Girlanda, A. Kievsky, L. E. Marcucci and S. Rosati, EPJ Web Conf. **3**, 05011 (2010).

[25] M. Viviani, A. Kievski, L. Girlanda and L. E. Marcucci, Few-Body Syst. **45**, 119 (2009).

[26] A. Deltuva and A. C. Fonseca, Phys. Rev. C **86**, 011001(R) (2012).

[27] I. Brida, S. C. Pieper and R. B. Wiringa, Phys. Rev. C **84**, 024319 (2011).

[28] K. M. Nollett and R. B. Wiringa, Phys. Rev. C **83**, 041001(R) (2011).

[29] T. Neff, Phys. Rev. Lett. **106**, 04502 (2011).

[30] A. Kievsky, M. Viviani, P. Barletta, C. Romero-Redondo and E. Garrido, Phys. Rev. C **81**, 034002 (2010).

[31] Y. Suzuki, W. Horiuchi and K. Arai, Nucl. Phys. A **823**, 1 (2009).

[32] T. Luu, M. J. Savage, A. Schwenk and J. P. Vary, Phys. Rev. C **82**, 034003 (2010).

[33] J. Kirscher, H. G. Griesshammer, D. Shukla and H. M. Hofmann, Eur. Phys. J. A **44**, 239 (2010).

[34] G. Hagen, T. Papenbrock and M. Hjorth-Jensen, Phys. Rev. Lett. **104**, 182501 (2010).

[35] S. Bacca, N. Barnea, G. Hagen, G. Orlandini and T. Papenbrock, Phys. Rev. Lett. **111**, 122502 (2013).

[36] G. Hagen and N. Michel, Phys. Rev. C **86**, 021602 (2012).

[37] M. Pine, D. Lee and G. Rupak, arXiv:1309.2616 [nucl-th] (2013).

[38] S. Quaglioni and P. Navrátil, Phys. Rev. Lett. **101**, 092501 (2008).

[39] S. Baroni, P. Navrátil and S. Quaglioni, Phys. Rev. Lett. **110**, 022505 (2013).

[40] S. Baroni, P. Navratil and S. Quaglioni, Phys. Rev. C **87**, 034326 (2013), arXiv:1301.3450 [nucl-th] (2013).

[41] S. Quaglioni and P. Navrátil, Phys. Rev. C **79**, 044606 (2009).

[42] S. Quaglioni, C. Romero-Redondo and P. Navrátil, Phys. Rev. C **88**, 034320 (2013).

[43] R. H. Stokes and P. G. Young, Phys. Rev. Lett. **18**, 611 (1967); Phys. Rev. **178**, 2024 (1969).

[44] Z. X. Cao *et al.*, Phys. Lett. B **707**, 46 (2012).

[45] A. A. Korsheninnikov *et al.*, Phys. Rev. Lett. **82**, 3581 (1999).

[46] K. Markenroth *et al.*, Nucl. Phys. A **679**, 462 (2001).

[47] M. Meister *et al.*, Phys. Rev. Lett. **88**, 102501 (2002).

[48] F. Skaza *et al.*, Phys. Rev. C **73**, 044301 (2006).

[49] N. Ryezayeva *et al.*, Phys. Lett. B **639**, 623 (2006).

[50] V. Lapoux *et al.*, J. Phys. Conf. Ser. **49**, 161 (2006).

[51] H. G. Bohlen *et al.*, Phys. Rev. C **64**, 024312 (2001).

[52] G. V. Rogachev *et al.*, Phys. Rev. Lett. **92**, 232502 (2004).

[53] A. H. Wuosmaa *et al.*, Phys. Rev. C **72**, 061301 (2005).

[54] A. H. Wuosmaa *et al.*, Phys. Rev. C **78**, 041302 (2008).

[55] D. H. Denby *et al.*, Phys. Rev. C **78**, (2008) 044303.

[56] Yu. Aksyutina *et al.*, Phys. Lett. B **679**, 191 (2009).

[57] P. Boutachkov *et al.*, Phys. Rev. Lett. **95**, 132502 (2005).

[58] S. K. Bogner, R. J. Furnstahl and R. J. Perry, Phys. Rev. C **75**, 061001 (2007).

[59] R. Roth, S. Reinhardt and H. Hergert, Phys. Rev. C **77**, 064003 (2008).

[60] R. Roth, T. Neff and H. Feldmeier, Progr. Part. Nucl. Phys. **65**, 50 (2010).

[61] S. K. Bogner, R. J. Furnstahl and A. Schwenk, Progr. Part. Nucl. Phys. **65**, 94 (2010).

[62] D. R. Entem and R. Machleidt, Phys. Rev. C **68**, 041001 (2003).

[63] R. Machleidt and D. R. Entem, Phys. Rept. **503**, 1 (2011).

[64] D. R. Tilley *et al.*, Nucl. Phys. A **708**, 3 (2002).

[65] G. Hupin, J. Langhammer, P. Navrátil, S. Quaglioni, A. Calci and R. Roth, arXiv:1308.2700 [nucl-th] (2013).

[66] G. M. Hale, *private communication.*

[67] P. Descouvemont, C. Daniel and D. Baye, Phys. Rev. C **67**, 044309 (2003).

[68] P. Descouvemont, E. Tursunov and D. Baye, Nucl. Phys. A **765**, 370 (2006).

[69] C. Forssén, P. Navrátil, W. E. Ormand and E. Caurier, Phys. Rev. C **71**, 044312 (2005).

[70] Information on Titan can be found at the URL http://www.nccs.gov.

Recent Results with the Lorentz Integral Transform (LIT) Method for Inclusive Electron Scattering

Winfried Leidemann

Dipartimento di Fisica, Università di Trento, Via Sommarive 14, I-38123 Trento, Italy
Istituto Nazionale di Fisica Nucleare, Gruppo Collegato di Trento, I-38123 Trento, Italy

Abstract

A brief outline of the Lorentz Integral Transform method is given. Recent results for the inclusive electrodisintegration of ^{3}He and ^{4}He are discussed. The energy resolution that can be obtained with the LIT approach is studied and it is shown that the LIT method is a method with a controlled resolution. The final part discusses the role of the isoscalar monopole resonance of ^{4}He in (e, e') scattering.

Keywords: *Lorentz Integral Transform; inclusive electron scattering; few-body nuclei; three-nucleon force, isoscalar monopole resonance*

1 Introduction

Integral transforms are of common use in physics. In general they have the following form

$$\Phi(\sigma) = \int dE\, \mathcal{K}(E,\sigma)\, R(E), \tag{1}$$

where $\mathcal{K}(E,\sigma)$ is a well defined kernel and where $R(E)$ is an energy dependent response function of the system under consideration. Often it is very difficult or even impossible to determine $R(E)$ in a direct calculation, in particular when a many-body continuum wave function should be calculated. In such cases one may consider to determine directly the integral transform $\Phi(\sigma)$, i. e. without knowledge of $R(E)$. Then, the response function $R(E)$ can be obtained from the inversion of the integral transform.

In the following we will discuss the Lorentz integral transform (LIT) $L(\sigma)$ [1, 2]. In the past the LIT approach has been applied to a variety of inelastic electroweak reactions [2, 3]. Because of the specific form of the kernel and different from many other integral transforms, the LIT is an integral transform with a controlled resolution. The kernel $\mathcal{L}(E,\sigma)$ of the LIT is of Lorentzian shape:

$$\mathcal{L}(E,\sigma) = \frac{1}{(E-\sigma_R)^2 + \sigma_I^2} \tag{2}$$

($\sigma = \sigma_R + i\sigma_I$). It is evident that the parameter σ_I controls the width of the Lorentzian. A reduced value for σ_I leads to a higher energy resolution, however, at the same time one has also to increase the precision of the calculation. This point will be discussed in greater detail in Sect. 3.

The LIT $L(\sigma)$ is calculated by solving an equation of the form

$$(H-\sigma)\,\tilde{\Psi} = S, \tag{3}$$

Proceedings of International Conference 'Nuclear Theory in the Supercomputing Era — 2013' (NTSE-2013), Ames, IA, USA, May 13–17, 2013. Eds. A. M. Shirokov and A. I. Mazur. Pacific National University, Khabarovsk, Russia, 2014, p. 226.
http://www.ntse-2013.khb.ru/Proc/Leidemann.pdf.

where H is the Hamiltonian of the system under consideration and S is an asymptotically vanishing source term. The solution $\tilde{\Psi}$ is localized. This a very important property, since it allows to determine $\tilde{\Psi}$ with bound-state methods, even in case that the direct calculation of the response function $R(E)$ constitutes a continuum state problem. Having calculated $\tilde{\Psi}$ one obtains the LIT from the following expression:

$$L(\sigma) = \langle \tilde{\Psi} | \tilde{\Psi} \rangle. \tag{4}$$

The response function $R(E)$ is determined from the calculated $L(\sigma)$ by inverting the equation

$$L(\sigma) = \int dE \, \frac{R(E)}{(E - \sigma_R)^2 + \sigma_I^2} \, . \tag{5}$$

A general discussion of the inversion and details about various inversion methods are given in Refs. [2, 4, 5].

An alternative way to write the LIT is given by

$$L(\sigma) = -\frac{1}{\sigma_I} \, Im \Big(\Big\langle S \Big| \frac{1}{\sigma_R + i\sigma_I - H} \Big| S \Big\rangle \Big). \tag{6}$$

This reformulation is useful since it allows a direct application of the Lanczos algorithm for the determination of $L(\sigma)$ [6]. In fact the calculations discussed in the following sections are performed in this way by using expansions in hyperspherical harmonics (HH). The convergence is accelerated by introducing additional two-body correlations in case of three-nucleon applications (CHH), while for the four-body system an effective interaction approach is used (EIHH [7]).

2 Electron scattering off ^{3,4}He

In order to calculate a specific reaction one has to specify the source term S in Eqs. (3) and (6). In case of unpolarized inclusive electron scattering one has a longitudinal response function $R_L(q, \omega)$ and a transverse response function $R_T(q, \omega)$, where q and ω describe momentum and energy transfer of the electron to the nucleus. The source term S takes the following form:

$$|S\rangle = \theta |0\rangle, \tag{7}$$

where θ is a specific transition operator and $|0\rangle$ is the ground-state wave function of the nucleus. For the response functions $R_L(q, \omega)$ and $R_T(q, \omega)$ the transition operator θ corresponds to the nuclear charge and current operator, respectively.

2.1 Transverse response function $R_T(q, \omega)$ of ^{3}He in the quasi-elastic region

The inclusive transverse response function $R_T(q, \omega)$ of ^{3}He in inelastic electron scattering has recently been considered with the LIT method at momentum transfers ranging from 500 to 700 MeV/c [8]. Besides the usual non-relativistic nucleon one-body currents various additional current operators have been taken into account: meson exchange currents (MEC) [9, 10], isobar currents involving the Δ resonance (IC) [11], and relativistic corrections to the non-relativistic nucleon one-body currents [12]. In order to circumvent problems with special relativity the calculation is performed in the so-called active nucleon Breit (ANB) frame which moves with $-3\mathbf{q}/2$ with respect to the laboratory frame. In order to compare with experimental data the R_T result is then transformed to the laboratory system. As nuclear force a realistic nuclear interaction has been considered, which consists in the AV18 NN potential [13] and the UIX three-nucleon force [14].

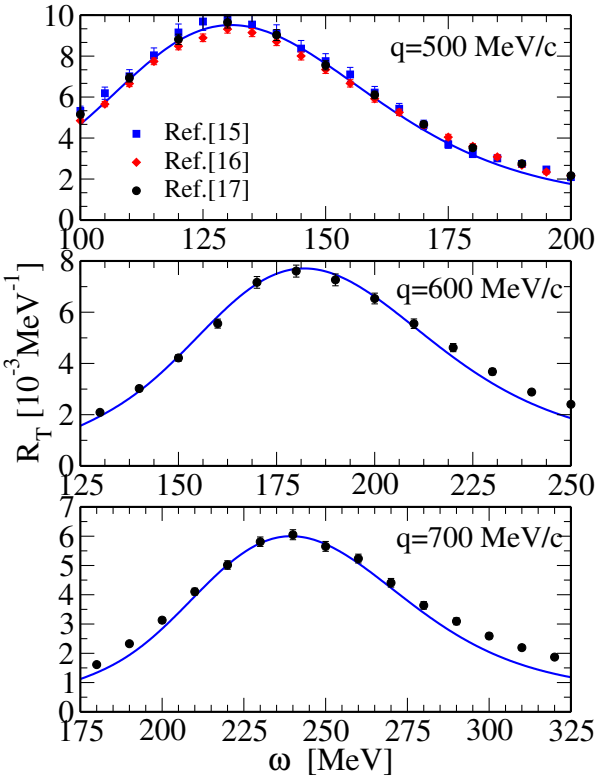

Figure 1: Transverse response function $R_T(q,\omega)$ of ^{3}He at q = 500, 600, and 700 MeV/c with force model AV18+UIX; experimental data from [15–17].

In Fig. 1 the resulting response function $R_T(q,\omega)$ is shown. One observes an excellent agreement with experimental data in the whole quasi-elastic peak region for all three considered momentum transfers. It should be pointed out that for the good agreement with experiment it is necessary to control, to some extent, problems due to special relativity (ANB frame) and to include both IC and relativistic corrections of the nucleon one-body current, whereas MEC are of less importance in the ^{3}He quasi-elastic peak region. The IC contribution is particularly interesting: (i) it cancels the effect of the three-nucleon force (3NF) in the peak region and (ii) in the isospin $T = 3/2$ channel of the disintegrated nucleus one finds an important IC contribution beyond the peak region; this isospin channel contributes exclusively to the three-body break-up of ^{3}He and thus IC should be included in the calculation of such reactions.

From the results in Fig. 1 it is evident that the LIT approach allows calculations of reactions up into the far many-body continuum. This is quite remarkable since no continuum wave functions are calculated and only bound-state methods are applied.

2.2 Longitudinal response function $R_L(q,\omega)$ of ^{4}He at lower momentum transfer

Up to present realistic LIT calculations for the ^{4}He electrodisintegration have been performed for R_L [18, 19] only, whereas for R_T a LIT calculation [20] with the central NN potential MTI/III [21] exists. The results for the longitudinal response are particularly interesting at lower momentum transfer since 3NF effects become quite important. Also at higher momentum transfer 3NF effects are non-negligible, but less important (below 10%). In Fig. 2 the ^{4}He $R_L(q,\omega)$ of [18] is shown at various

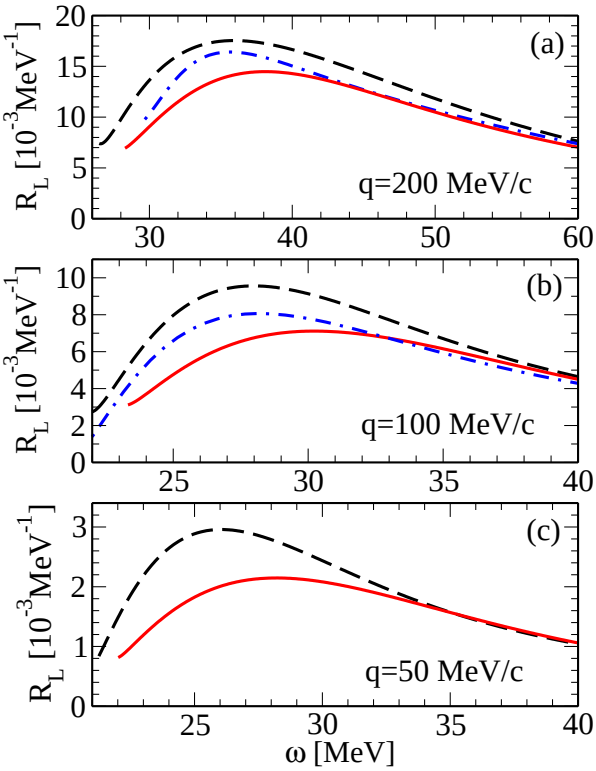

Figure 2: $R_L(q,\omega)$ of ^{4}He with force models AV18 (dashed), MTI/III (dash-dotted), and AV18+UIX (solid).

low momentum transfers for nuclear force models AV18 and AV18+UIX. In the low-energy region one finds a considerable decrease due 3NF which reaches almost 50% at $q = 50$ MeV/c. In Fig. 2 also a result with the MTI/III potential is depicted. Different from the realistic nuclear force models the MTI/III potential overestimates the ^{4}He binding energy by a few MeV. Nonetheless the MTI/III R_L lies between the AV18 and AV18+UIX results. This shows that the large 3NF effect cannot be caused just by a 3NF effect on the ^{4}He ground state, but that 3NF effects on the nuclear continuum wave function lead to essential contributions. In Ref. [19] also R_L results for force model AV18+TM' are included (TM' 3NF from Ref. [22]). In Fig. 3 we illustrate results from this reference for $q = 50$ MeV. Relatively large differences can be seen between the AV18+UIX and the AV18+TM' results, although both force models lead to almost equal ^{4}He binding energies.

3 Energy resolution with the LIT approach

It was already mentioned in the introduction that the LIT approach is a method with a controlled resolution. Here this aspect is illustrated in greater detail. A solution of the LIT equation (6) via an expansion on a basis with N basis functions can be understood as follows. One determines the spectrum of the Hamiltonian on this basis thus finding N eigenenergies E_n. Furthermore, the solution assigns to any eigenenergy a strength in form of a Lorentzian with height L_n and width σ_I. It should be noticed that the source term $|S\rangle$ affects only the height L_n. The LIT result then reads

$$L(\sigma) = \sum_{i=1}^{N} \frac{L_n}{(\sigma_R - E_n)^2 + \sigma_I^2} \,. \tag{8}$$

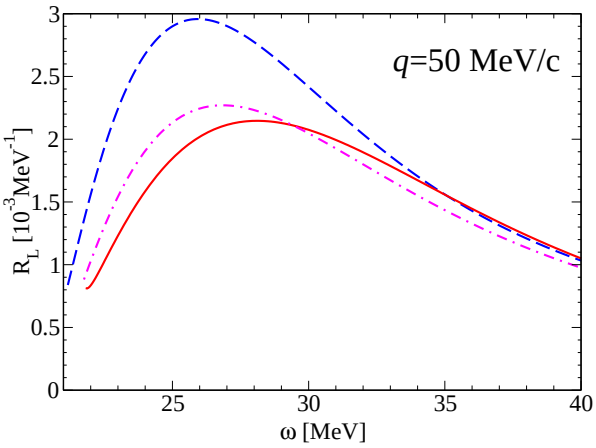

Figure 3: As Fig. 2 but for force models AV18 (dashed), AV18+TM' (dash-dotted), and AV18+UIX (solid).

Note that this result is related to the so-called Lanczos response $R_{\rm Lnczs}$ by

$$R_{\rm Lnczs}(E,\sigma_I) = \frac{\sigma_I}{\pi} L(E,\sigma_I). \tag{9}$$

In the limit $\sigma_I \to 0$ the Lanczos response is equal to the true response function $R(E)$. However, one often calculates $R_{\rm Lnczs}$ for a small but finite σ_I value and identifies the Lanczos response with the true response, which in general is an uncontrolled approximation. In the LIT approach one does not make such an identification of transform and response function. A proper treatment requires an inversion. From a practical point of view such a correct treatment is even advantageous, since the computational effort is much less. In fact, it allows to work with a not too small σ_I, thus with a relatively small number of basis functions N. Only in case of structures, which change rapidly with energy, e. g. resonances, one might need σ_I values of the order of the resonance width. To give a better understanding of the energy resolution with the Lorentz integral transform method also here deuteron photodisintegration in unretarded dipole approximation is considered as a simple example. The corresponding cross section is given by

$$\sigma_{\rm unret}(\omega) = 4\pi^2 \alpha \omega R_{\rm unret}(\omega), \tag{10}$$

where ω denotes the photon energy and α is the fine structure constant. The relevant transition operator for the calculation of $R_{\rm unret}(\omega)$ is the dipole operator $\theta = \sum_i z_i(1+\tau_{i,z})/2$, where z_i and $\tau_{i,z}$ are the z-components of the position vector and of the isospin operator of the ith nucleon, respectively. For the deuteron case the dipole operator allows only transitions to the following np final states: $^3P_0$, $^3P_1$, and $^3P_2$-$^3F_2$. For simplicity in the following example only transitions to $^3P_1$ are considered. The following ansatz for the corresponding $\tilde{\Psi}$ is made:

$$|\tilde{\Psi}\rangle = \tilde{\psi}(r)\,|(l=1,S=1)j=1\rangle\,|T=1\rangle, \tag{11}$$

where r ($T=1$) is the relative distance (isospin) of the np pair. The resulting LIT equation can be easily solved by direct numerical methods or by expansions of $\tilde{\psi}(r)$ on a complete set. Since in case of nuclei with $A>2$ we are generally using expansions on hyperspherical harmonics, where the hyperradial part is expanded in Laguerre polynomials $L_n^{m+\frac{1}{2}}$ times an exponential fall-off, here a corresponding ansatz is made:

$$\tilde{\psi}(r) = \sum_{n=1}^{N} c_n\, r\, L_n^{1+\frac{1}{2}}(r/b)\, exp(-r/2b), \tag{12}$$

where c_n is a normalization factor and b a constant.

A comparison of results with the Lanczos response and inversion results was made in Ref. [2] for the simple example of deuteron photodisintegration in unretarded dipole approximation. In this case one can check the quality of the results by comparing with a conventional calculation, where np continuum wave function are calculated. The study of Ref. [2] has shown that within the LIT approach it is sufficient to use a rather large value of 10 MeV for σ_I and hence a basis with a rather low N. On the contrary for the Lanczos response, even when using $\sigma_I = 0.25$ MeV with a quite high number of basis states, it was not possible to reproduce the $R(E)$ sufficiently correctly.

In Figs. 4–6 LIT results for the $^3P_1$ channel are shown for various values of N and σ_I. To obtain the $^3P_1$ part of the unretarded deuteron photodisintegration cross section one has to invert these transforms. However, in order to make a reliable inversion $L(\sigma)$ should be sufficiently converged for a given σ_I. In particular isolated peaks of single Lorentzians should not appear, i. e. for any σ_R value one should have a significant contribution from various Lorentzians. The results of Figs. 4–6 show that the convergence pattern is quite different for the various σ_I. For the case with the lowest resolution ($\sigma_I = 2.5$ MeV) one obtains a sufficiently converged $L(\sigma)$ already with 30 basis functions ($N = 30$). For the case with $\sigma_I = 1$ MeV one is close to convergence with $N = 50$, whereas the LIT for the highest requested resolution ($\sigma_I = 0.1$ MeV) is quite far from convergence even with $N = 50$. For the latter case the number of basis functions should be increased considerably to obtain a converged $L(\sigma)$. It is evident that a higher resolution requires a higher computational effort. In an actual calculation one should check what is the lowest σ_I value with a sufficiently converged LIT. Structures which are considerably smaller than such a σ_I value cannot be resolved by the inversion. A helpful criterion is given in Ref. [23] (see discussion of Fig. 7 in Ref. [23]).

From the discussion above it is evident that the LIT approach is a method with a controlled resolution.

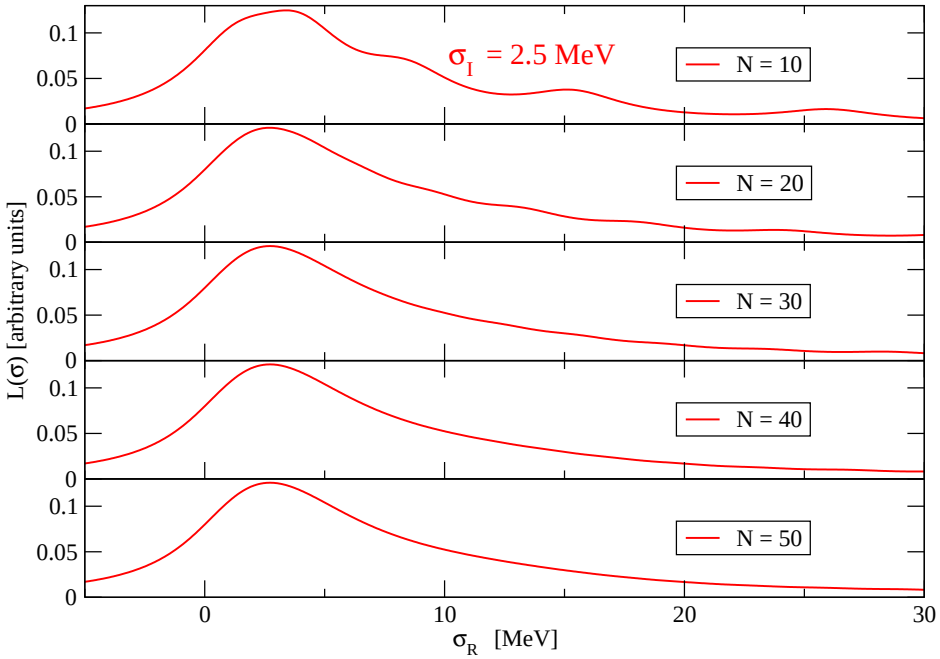

Figure 4: Deuteron photodisintegration in unretarded dipole approximation: LIT result for np channel $^3P_1$ with $\sigma_I = 2.5$ MeV.

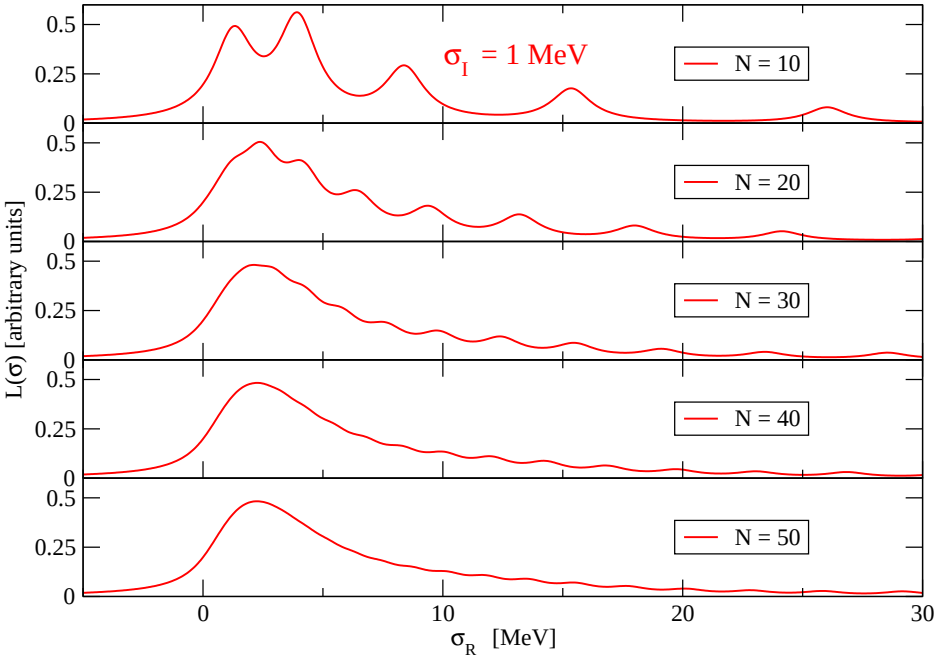

Figure 5: As Fig. 4 but with $\sigma_I = 1$ MeV.

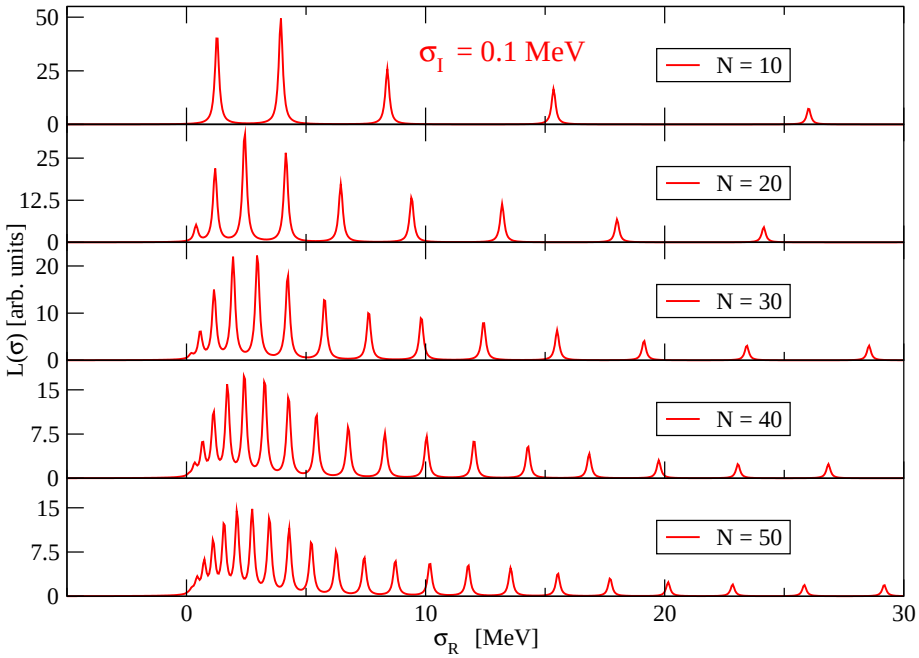

Figure 6: As Fig. 4 but with $\sigma_I = 0.1$ MeV.

4 Isoscalar monopole resonance of ^{4}He

The 0^+ resonance of ^{4}He can be studied in hadronic and electron scattering reactions. The signal of the resonance is much more pronounced in the latter case and thus electron scattering experiments of ^{4}He are the proper tool to study the resonance. In fact the pronounced cross section peak has been studied in various (e, e')

experiments [24–26]. There it has been found that the resonance is located between the two thresholds for the break-up in ^{3}H-p and ^{3}He-n and that the width is about 300 keV. In addition, the resonance strength has been measured over a rather large momentum transfer range.

In Ref. [27] a LIT calculation of the isoscalar monopole part of $R_L(q,\omega)$ of ^{4}He(e,e') has been performed using the nuclear force model AV18+UIX and a chiral nuclear force model with the Idaho N3LO NN potential [28] supplemented by a 3NF in N2LO in two different parameterizations. The calculation shows that both interaction models overestimate the resonance position by about 700 keV and sufficiently convergent LIT results could only be obtained for $\sigma_I \geq 5$ MeV. Such a resolution, much larger than the experimental width of 300 keV, is of course not sufficient to determine the detailed resonance structure. On the other hand it has been possible to separate the background strength from the resonance strength. For details of this separation I refer to Ref. [27]. Here it should only be mentioned that this is not a trivial task and that it has been achieved by an appropriate inversion procedure, which gave the energy distribution of the background strength and the total resonance strength.

In Fig. 7 the calculated resonance strength is compared to the above mentioned experimental data. One sees that the two realistic interaction models exhibit rather different results: the AV18+UIX force leads to a resonance strength which is about 20 % lower than that of the chiral force model. Thus the ^{4}He resonance strength turns out to be an observable which is very selective concerning force models. In Fig. 7 it can also be seen that even with force model AV18+UIX the experimental resonance strength is overestimated considerably. As discussed in detail in Ref. [27] it is not easy to understand what causes the difference of theoretical and experimental results (e. g., the calculated elastic ^{4}He form factor agree well with experimental data up to about $q^2 = 4$ fm^{-2} for both potential models). In Fig. 7 an additional theoretical result [29] is shown for a force model consisting in the AV8' NN potential and a simplistic 3NF. One observes a nice agreement with the experimental data. However, the calculation cannot be considered to be fully realistic (the not completely realistic potential model has led to a second 0^+ bound state and not to a resonance in the continuum).

One might ask how the width of the ^{4}He 0^+ resonance can be resolved with the

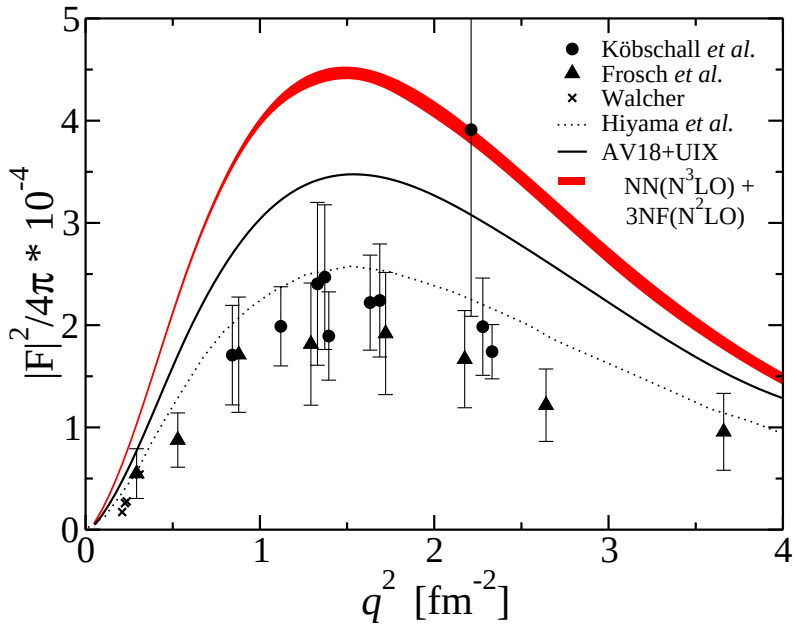

Figure 7: ^{4}He isoscalar monopole resonance strength $|F(q^2)|^2$.

LIT method. That the method is in principle capable to resolve a resonance with such a small width has been shown in Ref. [23] in a model study. In the present case one could increase the HH basis or increase the size of the box, but this might not lead to a much improved result. Probably it is better to describe the four-body system as 3+1 system with an HH expansion for the three-body part and a separate expansion for the relative motion of nucleon and residual system, of course, always with bound-state methods. Such an approach would be in close analogy to a scattering calculation for a two-body break-up.

5 Summary

An overview has been given on recent LIT applications for the inclusive electrodisintegration of ^{3}He and ^{4}He with realistic nuclear force models. The results for the transverse response function $R_T(q,\omega)$ of ^{3}He show (i) that an excellent agreement with experimental data is obtained in the quasi-elastic peak region at higher momentum transfers and (ii) that the LIT method can be applied also to reactions with energies far into the many-body continuum. For ^{4}He, results of the longitudinal response function $R_L(q,\omega)$ of ^{3}He have been reported. They exhibit strong 3NF effects at lower momentum transfers. In addition it has been discussed that a theoretical study for the isoscalar monopole part of the R_L of ^{4}He reveals (i) a strong dependence of the resonance strength on the nuclear force model and (ii) a considerable overestimation of the experimental resonance strength.

The energy resolution that can be obtained with the LIT method has also been discussed in greater detail. The discussion shows that the LIT approach is a method with a controlled resolution.

References

[1] V. D. Efros, W. Leidemann and G. Orlandini, Phys. Lett. B **338**, 130 (1994).

[2] V. D. Efros, W. Leidemann G. Orlandini and N. Barnea, J. Phys. G **34**, R459 (2007).

[3] W. Leidemann and G. Orlandini, Progr. Part. Nucl. Phys. **68**, 158 (2013).

[4] D. Andreasi, W. Leidemann, Ch. Reiss and M. Schwamb, Eur. Phys. J. A **24**, 361 (2005).

[5] N. Barnea, V. D. Efros, W. Leidemann and G. Orlandini, Few-Body Syst. **47**, 201 (2010).

[6] M. A. Marchisio, N. Barnea, W. Leidemann and G. Orlandini, Few-Body Syst. **33**, 259 (2003).

[7] N. Barnea, W. Leidemann and G. Orlandini, Phys. Rev. C **61**, 54001 (2000); Nucl. Phys. A **693**, 565 (2001).

[8] L. Yuan, W. Leidemann, V. D. Efros, G. Orlandini and E. L. Tomusiak, Phys. Lett. B **706**, 90 (2011).

[9] S. Della Monaca, V. D. Efros, A. Khugaev, W. Leidemann, G. Orlandini, E. L. Tomusiak and L. P. Yuan, Phys. Rev. C **77**, 044007 (2008).

[10] W. Leidemann, V. D. Efros, G. Orlandini and E. L. Tomusiak, Few-Body Syst. **47**, 157 (2010).

[11] L. Yuan, V. D. Efros, W. Leidemann and E. L. Tomusiak, Phys. Rev. C **82**, 054003 (2010).

[12] V. D. Efros, W. Leidemann, G. Orlandini and E. L. Tomusiak, Phys. Rev. C **81**, 034001 (2010).

[13] R. B. Wiringa, V. G. J. Stoks and R. Schiavilla, Phys. Rev. C **51**, 38 (1995).

[14] B. S. Pudliner, V. R. Pandharipande, J. Carlson, S. C. Pieper and R. B. Wiringa, Phys. Rev. C **56**, 1720 (1997).

[15] C. Marchand *et al.*, Phys. Lett. B **153**, 29 (1985).

[16] K. Dow *et al.*, Phys. Rev. Lett. **61**, 1706 (1988).

[17] J. Carlson, J. Jourdan, R. Schiavilla and I. Sick, Phys. Rev. C **65**, 024002 (2002).

[18] S. Bacca, N. Barnea, W. Leidemann and G. Orlandini, Phys. Rev. Lett. **102**, 162501 (2009).

[19] S. Bacca, N. Barnea, W. Leidemann and G. Orlandini, Phys. Rev. C **80**, 064001 (2009).

[20] S. Bacca, H. Arenhövel, N. Barnea, W. Leidemann and G. Orlandini, Phys. Rev. C **76**, 014003 (2007).

[21] R. A. Malfliet and J. Tjon, Nucl. Phys. A **127**, 161 (1969).

[22] S. A. Coon and H. K. Hahn, Few-Body Syst. **30**, 131 (2001).

[23] W. Leidemann, Few-Body Syst. **42**, 139 (2008).

[24] Th. Walcher, Phys. Lett. B, **31**, 442 (1970).

[25] R. F. Frosch *et al.*, Phys. Lett. **19**, 155 (1965); Nucl. Phys. A **110**, 657 (1968).

[26] G. Köbschall *et al.*, Nucl. Phys. A **405**, 648 (1983).

[27] S. Bacca, N. Barnea, W. Leidemann and G. Orlandini, Phys. Rev. Lett. **110**, 042503 (2013).

[28] D. R. Entem and R. Machleidt, Phys. Rev. C **68**, 041001 (2003).

[29] E. Hiyama, B. F. Gibson and M. Kamimura, Phys. Rev. C **70**, 031001 (2004).

Ab Initio Description of Light Nuclei in the Berggren Basis

J. Rotureau

Fundamental Physics, Chalmers University of Technology, 412 96 Göteborg, Sweden

Abstract

In this work we report on the first application of the No-Core Gamow Shell Model to study *ab initio* bound and unbound states in light nuclei. This model is formulated in the complex energy plane by using a complete Berggren ensemble which treats bound, resonant, and scattering states on equal footing. The resolution of the many-body Schrödinger equation is performed with the technique of the Density Matrix Renormalization Group.

Keywords: *Ab initio method; coupling with the continuum; Density Matrix Renormalization Group*

1 Introduction

In the last decade our knowledge of nuclei far from the valley of stability has radically improved. This improvement has been a by-product of advances in both experiment and theory. New experimental facilities that have already been built (RIBF at RIKEN) or are being constructed (SPIRAL2 at GANIL, FAIR, FRIB at MSU) will give us a better insight of areas in the nuclear chart that have never been explored, pushing even further our knowledge at the limits of nuclear existence. At the same time, the increase in computing power has made it possible to calculate properties of nuclei in an *ab initio* fashion, using realistic interactions which reproduce nucleon-nucleon scattering data. For few-body systems ($A \leq 4$) methods such as Faddeev [1] and Faddeev–Yakubovsky (FY) [2] provide an exact solution to the many-body problem. Methods such as the Green's Function Monte Carlo (GFMC) [3], the Hyperspherical Harmonics [4], the No-Core Shell Model (NCSM) [5], the Coupled-Cluster (CC) approach [6] and more recently, the In-Medium Similarity Renormalization Group method [7] and Dyson Self-Consistent Green's Function method [8] have been applied successfully for the *ab initio* description of light and medium mass nuclei.

Nuclei with large isospin which can be found in these remote regions, have attracted a great deal of interest. They belong to the category of Open Quantum Systems, inter-connected via the decay and reaction channels. These are very fragile objects with small separation energies and very large spatial dimensions. The proximity of the continuum affects their bulk properties (matter and charge distributions) and their spectra. Phenomena such as the anomalous behavior of elastic cross-sections and the associated overlap integral near threshold states in multi-channel coupling (Wigner-cusps) [9] and the appearance of cluster correlations in the vicinity of the respective cluster emission threshold [10], to mention a few, are all unique manifestations of the continuum coupling.

From the theoretical perspective, existing many-body methods have had to be generalized in order to construct approaches where both structure and reactions are unified to describe these exotic systems. Examples of these attempts are the Shell Model

Proceedings of International Conference 'Nuclear Theory in the Supercomputing Era — 2013' (NTSE-2013), Ames, IA, USA, May 13–17, 2013. Eds. A. M. Shirokov and A. I. Mazur. Pacific National University, Khabarovsk, Russia, 2014, p. 236.

http://www.ntse-2013.khb.ru/Proc/Rotureau.pdf.

Embedded in the Continuum (SMEC) [11] and the Gamow Shell Model (GSM) [12,13] in which nuclei are described as systems with a core above which valence nucleons interact. The GSM, which is the most recent of these two approaches, is a generalization of the Harmonic Oscillator (HO) shell model in the complex energy plane using the Berggren ensemble [14]. Recent *ab initio* approaches such as the NCSM coupled with the Resonating Group Method [15], the CC approach generalized in the complex-energy plane using the Berggren basis [16] and the GFMC [17], have allowed an *ab initio* description of bound and unbound states of nuclei.

In this work we introduce the No-Core Gamow Shell Model (NCGSM) [18] as an alternative for *ab initio* calculations of weakly-bound and unbound states of light nuclei using realistic interactions. We will show the basic ingredients of the NCGSM and describe the many-body method namely, the Density Matrix Renormalization Group (DMRG) technique, used to solve the many-body problem. We will then present selected results obtained in this approach.

2 Formalism

The intrinsic Hamiltonian H for a nucleus with A nucleons is given by

$$H = \frac{1}{A}\sum_{i<j}^{A}\frac{(\vec{p}_i - \vec{p}_j)^2}{2m} + \sum_{i<j}^{A} V_{ij}^{NN}, \tag{1}$$

where m is the nucleon mass, $\vec{p}_i$ is the momentum of the nucleon i and V^{NN} is a two-body nuclear potential. In the NCGSM [18], the weakly-bound/unbound eigenstates of H are obtained by using an expansion in the Berggren basis which allows to treats bound, resonant and scattering states on equal footing. Let us consider a finite-depth single-particle (s.p.) potential. Its eigenstates fulfill the Berggren completeness relation which can be written as

$$\sum_{n=b,d} |u_n\rangle\langle\widetilde{u_n}| + \int_{L_+} |u_k\rangle\langle\widetilde{u_k}|\, dk = 1, \tag{2}$$

where b are bound states, d are decaying resonant states and the integral along a contour L_+ represents the contribution from the non-resonant scattering continuum, see Fig. 1. By discretizing the integral in (2), a discrete set of s.p. states can be obtained from which one constructs the many-body basis in which the Hamiltonian H is diagonalized. Due to the inclusion of resonant states and complex-continuum states, the representation of H in the (many-body) Berggren basis is complex-symmetric. The dimension of the Hamiltonian matrix grows rapidly with the number of discretized continuum states and nucleons and as a consequence, advanced numerical methods that can handle large non-Hermitian matrices must be used. In the context of the GSM, it has been shown that the DMRG method is an efficient way to compute the low-lying spectrum of the Hamiltonian at a low computational cost [13, 19]. In the following, we describe the main features of DMRG applied to the NCGSM.

The DMRG method was first introduced to overcome the limitations of the Wilson-type renormalization group to describe strongly correlated systems with short-range interactions [20]. More recently, the DMRG has been reformulated and applied to finite Fermi systems [21], nuclear shell model [22–24], and open systems [19]. While most of the DMRG studies have been focused on properties in strongly correlated closed quantum systems characterized by Hermitian density matrices, systems involving non-Hermitian and non-symmetric density matrices can also be treated [19, 25].

Let us consider the application of the J-scheme DMRG in the context of the NCGSM. The objective is to calculate an eigenstate $|J^\pi\rangle$ of the Hamiltonian $\hat{H}$ with angular momentum J and parity π. As $|J^\pi\rangle$ is a many-body pole of the scattering

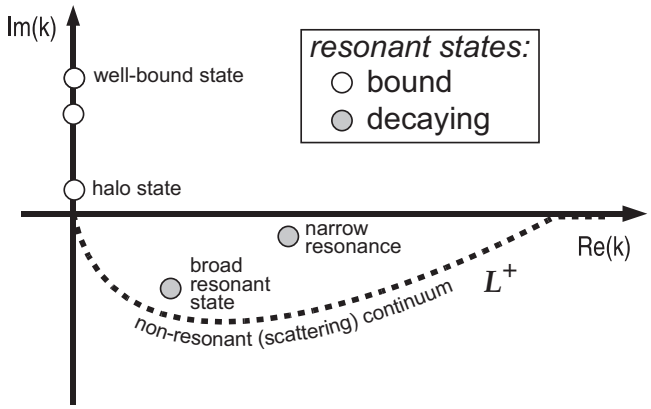

Figure 1: Illustration of the Berggren completeness relation (2) in the complex k-plane. The bound states are located on the positive imaginary axis. The weakly bound halo states lie close to the origin. The positive-energy resonant states are located in the fourth quadrant. Those with a small imaginary part can be interpreted as resonances. The complex-k contour L^+ represents the non-resonant scattering continuum.

matrix of $\hat{H}$, the contribution from non-resonant scattering shells along the continuum contour L^+ to the many-body wave function is usually smaller than the contribution from the resonant orbits [12]. Based on this observation, the following separation is usually performed [19]: the many-body states constructed from the single-particle poles form a subspace A (the so-called 'reference subspace'), and the remaining states containing contributions from non-resonant shells form a complement subspace B (see Fig. 2).

One begins by constructing states $|k\rangle_A$ forming the reference subspace A. All possible matrix elements of suboperators of the GSM Hamiltonian $\hat{H}$ acting in A, expressed in the second quantization form, are then calculated and stored and the Hamiltonian is diagonalized in the reference space to provide the zeroth-order approximation $|\Psi_J\rangle^{(0)}$ to $|J^\pi\rangle$. The scattering shells (lj), belonging to the discretized contour L^+, are then gradually added to the reference subspace to create the subspace B. This first stage of the NCGSM+DMRG procedure is referred to as the 'warm-up phase'. For each new added shell, all possible many-body states denoted as $|i\rangle_B$ are constructed and matrix elements of suboperators of the Hamiltonian H acting on $|i\rangle_B$ are computed. By coupling states in A with the states $|i_B\rangle$, one constructs the set of states of a given J^π. This ensemble serves as a basis in which the NCGSM

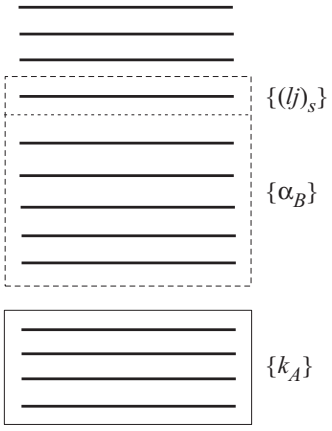

Figure 2: Schematic illustration of the NCGSM+DMRG procedure during the s^{th} step of the warm-up phase. States $\{k_A\}$ from A, previously optimized states α_B, and states $\{(lj)_s\}$ constructed by occupying the s^{th} shell with n particles are coupled to generate the new set of states $\{k_A \otimes i_B\}^J = \{k_A \otimes \{\alpha_B \otimes (lj)^n_s\}\}^J$.

Hamiltonian is diagonalized. The target state $|\Psi_J\rangle$ is selected among the eigenstates of $\hat{H}$ as the one having the largest overlap with the reference vector $|\Psi_J\rangle^{(0)}$. Then, the desired truncation is performed in B by introducing the reduced density matrix, constructed by summing over the reference subspace A [26]. In standard DMRG applications for Hermitian problems, where the eigenvalues of the density matrix are real non-negative, only the eigenvectors corresponding to the largest eigenvalues are kept during the DMRG process. Within the metric defining the Berggren ensemble, the NCGSM density matrix is complex-symmetric and its eigenvalues are, in general, complex. As a consequence, the truncation is done by keeping the eigenstates α_B (the 'optimized' states) with the largest nonzero moduli of eigenvalue [19]. The trace of the density matrix being equal to one, the truncation is done by keeping eigenstates of the density matrix with the corresponding eigenvalue w_α such that the condition

$$\left| 1 - Re\left(\sum_{\alpha=1}^{N_\rho} w_\alpha \right) \right| < \epsilon \tag{3}$$

is satisfied. The quantity ϵ in (3) can be viewed as the truncation error of the reduced density matrix. The smaller ϵ, the larger number of eigenvectors must be kept. In particular, for ϵ=0, all eigenvectors with non-zero eigenvalues are retained.

The warm-up phase is followed by the so-called sweeping phase, in which, starting from the last scattering shell $(lj)_{\text{last}}$, the procedure continues in the reverse direction (the 'sweep-down' phase) until the first scattering shell is reached. The procedure is then reversed and a sweep in the upward direction (the 'sweep-up' phase) begins. The sweeping sequences continue until convergence for target eigenvalue is achieved.

3 Selected results

We now show few results obtained with the NCGSM+DMRG approach and we start here with the ground state in ^{4}He. Obviously this system is well-bound and can be described using an expansion in a HO basis without including continuum states. Nevertheless, using an expansion in the Berggren basis in that case allows to test our approach by comparing with exact results obtained in the Faddeev–Yakubovsky approach [1]. The two-body interaction V^{NN} in (1) is chosen as the Argonne v_{18} interaction renormalized with the V_{low-k} method [27] with a sharp momentum cutoff $\Lambda = 1.9$ fm^{-1}. Using this renormalization scheme allows a decoupling between high-momentum and low-momentum degrees of freedom and as a consequence, improves the convergence of nuclear structure calculations [27]. We include $s_{1/2}$, $p_{3/2}$, $p_{1/2}$, $d_{3/2}$, $d_{5/2}$, $f_{7/2}$, $f_{5/2}$, $g_{9/2}$, $g_{7/2}$ shells for protons and neutrons. For the partial waves with angular momentum $l \leq 1$, the s.p. basis is generated by performing Gamow–Hartree–Fock (GHF) [12] calculations. In this case, the GHF potential has a neutron and proton bound state in the $s_{1/2}$ channel at respectively -26.290 MeV and -24.453 MeV. The rest of s and p shells are taken along the contour on the real k-axis which extends up to 4 fm^{-1} and is discretized with 18 points. For shells with $l \geq 2$, we take the HO basis functions given by a HO potential with a radius $b = 1.5$ fm and we include 5 d, 3 f and 3 g s.p. states for both protons and neutrons. Results for the g.s. energy in ^{4}He are shown in Fig. 3 as a function of the iteration of the NCSM+DMRG method for a truncation $\epsilon = 10^{-6}$. One can see that, as the middle of the third sweep is reached, the energy has converged and the corresponding value is

$$E_{\text{NCGSM}} = -29.15 \text{ MeV},$$

whereas the exact result in the FY approach [1] is

$$E_{\text{FY}} = -29.19 \text{ MeV}.$$

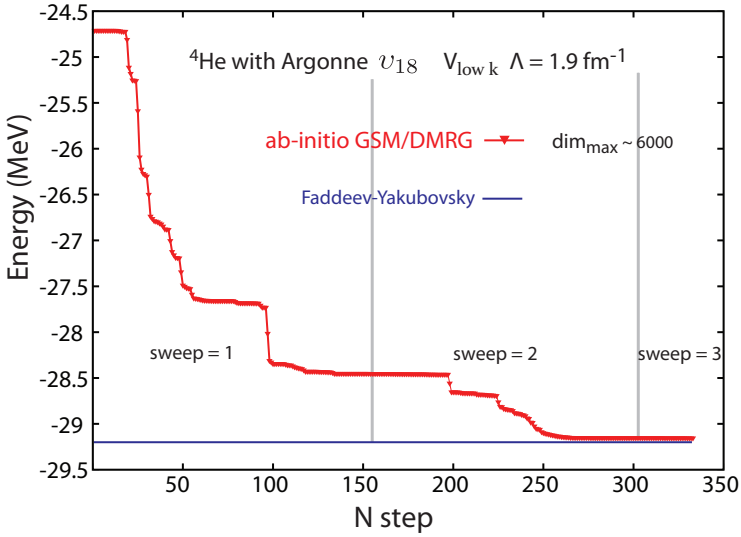

Figure 3: Energy of the ground state in ^{4}He as a function of the number of step ($N_{\rm step}$). Comparison of the NCGSM with the FY result with the V_{low-k} Argonne υ_{18} interaction.

The largest Hamiltonian matrix one has to deal with in the NCSM+DMRG has a dimension $D_{\rm max} \sim 6000$ whereas a direct resolution of the NCSM Hamiltonian matrix, that is for $\epsilon = 0$, would require to diagonalize a matrix of dimension 6,230,512 in J-scheme. The difference between our theoretical result and the experimental binding energy $E^{exp} = -28.30$ MeV, is due to higher-order terms in the nuclear interactions, such as three-nucleon forces, which are not included in the Hamiltonian (1).

We now show results for the ^{5}He nucleus which is a challenge for any many-body theory because of its unbound character. In particular, both the ground and first excited states are many-body resonances. Because of these characteristics, the complex energy formulation of the NCGSM using the Berggren ensemble is a perfect tool for its description. Indeed, in our formalism the resonance parameters (g.s. energy with respect to ^{4}He and the width) will be identified as the eigenvalues of the complex-symmetric Hamiltonian matrix. The position of the resonance will then be the real part of the energy, while the imaginary part is related to the width by the formula: $\Gamma = -2\,\Im{\rm m}(E)$. We use here the N^{3}LO interaction renormalized by V_{low-k} with a cutoff $\Lambda = 1.9$ fm^{-1}. For $l \leq 1$, the s.p. basis for protons and neutrons are generated by the GHF potential. In the $l = 0$ partial wave there are two bound states at $E = -23.290$ MeV and $E = -23.999$ MeV for respectively neutron and proton. The GHF potential has a $p_{3/2}$ s.p. resonance with a real part of energy 1.193 MeV and a width 1267 keV. In order to fulfill Berggren completeness, the $p_{3/2}$ contour is taken in the fourth-quadrant of the complex k-plane (see Fig. 1) whereas the $s_{1/2}$ and $p_{1/2}$ contours are chosen along the real-k axis. For states with $l \geq 1$, the s.p. states are given by HO basis functions as previously for ^{4}He. In Figs. 4, 5 we show the NCGSM+DMRG convergence pattern, for a truncation $\epsilon = 10^{-6}$, of the real and imaginary parts of the g.s. energy in ^{5}He. In the middle of the third sweep, the energy has converged to

$$\Re{\rm e}(E_{\rm NCGSM}) = -26.31 \text{ MeV}, \qquad \Im{\rm m}(E_{\rm NCGSM}) = -0.2 \text{ MeV}.$$

The real part lies at about 1 MeV above the experimental total binding energy [28] and as previously, the difference with the experimental binding energy is due to omitted higher-order terms in the nuclear interactions. For this truncation, the largest Hamiltonian matrix that needs to be diagonalized during the DMRG iterations has a

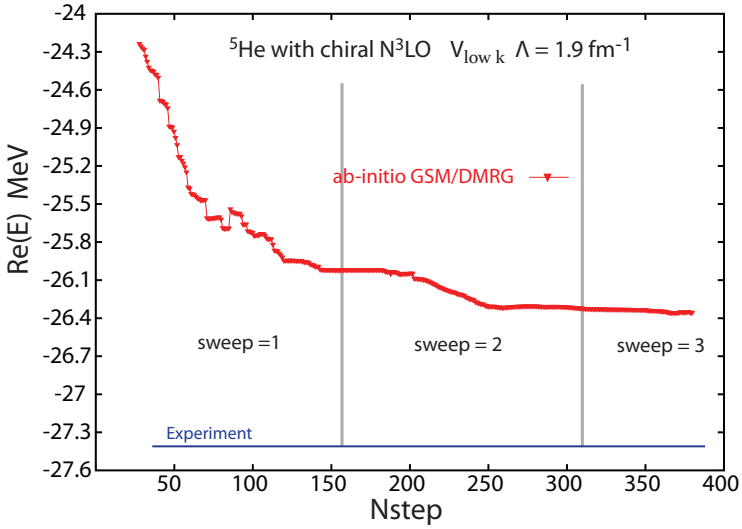

Figure 4: Real part of the energy of the ground state in ^{5}He as a function of the number of step ($N_{\rm step}$) using the chiral N^{3}LO interaction renormalized by by V_{low-k} with $\Lambda = 1.9$ fm^{-1}.

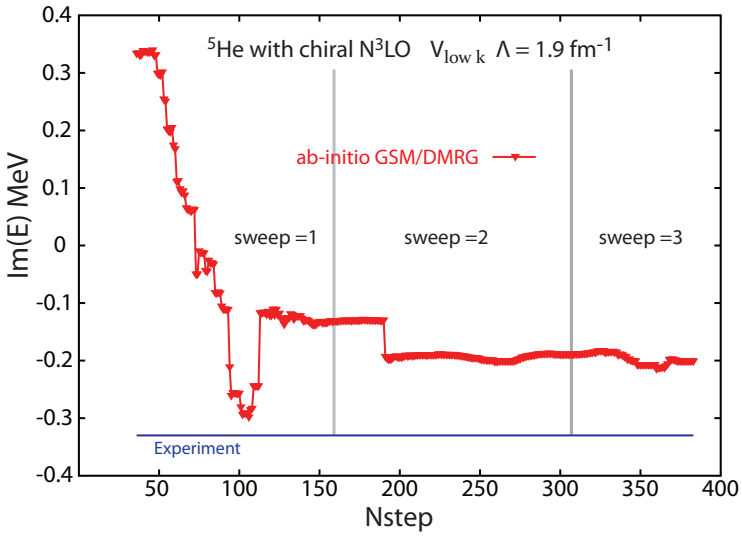

Figure 5: Imaginary part of the energy of the ground state in ^{5}He as a function of the number of step ($N_{\rm step}$) using the chiral N^{3}LO interaction renormalized by by V_{low-k} with $\Lambda = 1.9$ fm^{-1}.

dimension $D_{\rm max}$ $\sim 10^5$, whereas in the case of the full diagonalization i. e. for $\epsilon = 10^{-6}$, the Hamiltonian matrix has a dimension $\sim 3 \times 10^9$.

4 Summary

We have presented an *ab initio* approach to describe bound/unbound light nuclei using the framework of the No-Core Gamow Shell Model (NCGSM). By working in the Berggren ensemble, the NCGSM allows bound, resonant and scattering states to be treated on equal footing. The numerical solutions of the many-body Schrödinger equation are obtained by applying the Density Matrix Renormalization Group (DMRG)

method. We have shown results for the ground state in ^{4}He (bound nucleus) and the many-body ground state resonance in ^{5}He. This work serves as a proof of principle of the application of the Berggren's basis in a NCSM framework. In the future, we plan to apply the NCGSM+DMRG to study the structure of weakly bound/unbound light systems as for instance the very exotic systems in the hydrogen isotopic chain.

Acknowledgements

This talk was given during the International Conference on Nuclear Theory in the Supercomputing Era (Iowa State University, May 2013) which was in part to celebrate James Vary's birthday. Happy 70^{th} Birthday James !!

I would like to thank G. Papadimitriou, N. Michel, M. Płoszajczak and B. R. Barrett who have been collaborators in this project. This work was supported by the European Research Council under the European Community's Seventh Framework Programme (EP7/2007-2013)/ERC grant agreement no. 240603.

References

[1] A. Nogga, D. Hűber, H. Kamada and W. Gloeckle, Phys. Lett. B **409**, 19 (1997); A. Nogga, S. K.Bogner and A. Schwenk, Phys. Rev. C **70**, 061002(R) (2004).

[2] O. A. Yakubovsky, Sov. J. Nucl. Phys. **5**, 937 (1967).

[3] S. C. Pieper and R. B. Wiringa, Ann. Rev. Nucl. Part. Sci. **51**, 53 (2001).

[4] A. Kievsky, S. Rosati and M. Viviani, Nucl. Phys. A **551**, 241 (1993); N. Barnea, W. Leidemann and G. Orlandini, Phys. Rev. C **61**, 054001 (2000).

[5] P. Navrátil , J. P. Vary and B. R. Barrett, Phys. Rev. Lett. **84**, 5728 (2000); Phys. Rev. C **62**, 054311 (2000) P. Navrátil, S. Quaglioni, I. Stetcu and B. R. Barrett, J. Phys. G **36**, 083101 (2009); M. A. Caprio, P. Maris and J. P. Vary, Phys. Rev. C **86**, 034312 (2012).

[6] G. Hagen, T. Papenbrock, D. J. Dean and M. Hjorth-Jensen, Phys. Rev. C **82**, 034330 (2010).

[7] K. Tsukiyama, S. K. Bogner and A. Schwenk, Phys. Rev. Lett. **106**, 222502 (2011); H. Hergert, S. K. Bogner, S. Binder, A. Calci, J. Langhammer, R. Roth and A. Schwenk, arXiv:1212:1190 [nucl-th] (2012).

[8] V. Soma, T. Duguet and C. Barbieri, Phys. Rev. C **84**, 064317 (2011).

[9] E. P. Wigner, Phys. Rev. **73**, 1002 (1948); N. Michel, W. Nazarewicz and M. Płoszajczak, Phys. Rev. C **75**, 031301 (2007).

[10] J. Okołowicz, M. Płoszajczak and W. Nazarewicz, Progr. Theor. Phys. Suppl. **196**, 230 (2012).

[11] K. Bennaceur, F. Nowacki, J. Okołowicz and M. Płoszajczak, Nucl. Phys. A **651**, 289 (1999); J. Okołowicz, M. Płoszajczak and I. Rotter, Phys. Rept. **374**, 271 (2003); J. Rotureau, J. Okołowicz and M. Płoszajczak, Phys. Rev. Lett **95**, 042503 (2005); Nucl. Phys. A **767**, 13 (2006).

[12] N. Michel, W. Nazarewicz, M. Płoszajczak and K. Bennaceur, Phys. Rev. Lett **89**, 042502 (2002); N. Michel, W. Nazarewicz, M. Płoszajczak and J. Okołowicz, Phys. Rev. C **67**, 054311 (2003); R. Id Betan, R.J. Liotta, N. Sandulescu and T. Vertse,

Phys. Rev. Lett. **89**, 042501 (2002); N. Michel, W. Nazarewicz, M. Płoszajczak and T. Vaertse, J. Phys. G **36**, 013101 (2009).

[13] G. Papadimitriou, A.T. Kruppa, N. Michel, W. Nazarewicz, M. Płoszajczak and J. Rotureau, Phys. Rev. C **84**, 051304(R) (2011).

[14] T. Berggren, Nucl. Phys. A **109**, 265 (1968).

[15] G. Hupin, J. Langhammer, P. Navrátil, S. Quaglioni, A. Calci, R. Roth, arXiv: 1308.2700 [nucl-th] (2013); S. Quaglioni and P. Navrátil, Phys. Rev. C **79**, 044606 (2009); S. Baroni, P. Navrátil and S. Quaglioni, Phys. Rev. Lett. **110**, 022505 (2013).

[16] G. Hagen, D. J. Dean, M. Hjorth-Jensen and T. Papenbrock, Phys. Lett. B **656**, 169 (2007); G. Hagen, T. Papenbrock and M. Hjorth-Jensen, Phys. Rev. Lett. **104**, 182501 (2010); G. Hagen, M. Hjorth-Jensen, G. R. Jansen, R. Machleidt and T. Papenbrock, *ibid.* **108**, 242501 (2012).

[17] K. M. Nollett *et al.*, Phys. Rev. Lett. **99**, 022502 (2007); K. M. Nollett, Phys. Rev. C **86**, 044330 (2012).

[18] G. Papadimitriou, J. Rotureau, N. Michel, M. Płoszajczak and B. R. Barrett, arXiv:1301.7140 [nucl-th] (2013).

[19] J. Rotureau, N. Michel , W. Nazarewicz , M. Płoszajczak and J. Dukelsky, Phys. Rev. Lett **97**, 110603 (2006); Phys. Rev. C **79**, 014304 (2009).

[20] S. R. White, Phys. Rev. Lett. **69**, 2863 (1992); Phys. Rev. B **48**, 10345 (1993).

[21] J-M. Roman, G. Sierra and J. Dukelsky, Nucl. Phys. B **634**, (2002).

[22] S. Pittel and N. Sandulescu, Phys. Rev. C **73**, 014301 (2006).

[23] T. Papenbrock and D. J. Dean, J. Phys. G **31**, 1377 (2005).

[24] B. Thakur, S. Pittel and N. Sandulescu, Phys. Rev. C **78**, 041303 (2008).

[25] E. Carlon, M. Henkel and U. Schollwöck, Eur. Phys. J. B **12**, 99 (1998).

[26] I. P. McCulloch and M. Gulácsi, Europhys. Lett. **57**, 852 (2002).

[27] S. K. Bogner, T. T. S. Kuo and A. Schwenk, Phys. Rept. **386**, 1 (2003); S. K. Bogner, R. J. Furnstahl and A. Schwenk, Progr. Part. Nucl. Phys. **65**, 94 (2010).

[28] G. Audi, A. H. Wapstra and C. Thibault, Nucl. Phys. A **729**, 337 (2003).

Studies of Hot Dense Matter with the PHENIX Detector at RHIC

J. C. Hill
for the PHENIX collaboration

Department of Physics and Astronomy, Iowa State University, Ames, Iowa 50011, USA

Abstract

The PHENIX experiment at RHIC carries out studies of hot dense matter produced in heavy ion collisions and studies of the proton spin from polarized proton collisions. In this talk I concentrate on our present picture of the quark-gluon plasma as revealed in collisions of Au and other nuclei.

Keywords: *RHIC; PHENIX; QGP; perfect liquid; elliptic flow; R_{AA}; QGP temperature*

1 Introduction

The Relativistic Heavy Ion Collider (RHIC) was built at Brookhaven National Laboratory (BNL) and the first collisions of beams of 130 GeV/A Au nuclei were observed in June 2000. PHENIX and STAR are two large detector systems built to study these collisions. In the first collisions flow was observed. In the summer of 2001 experiments with collisions of Au beams at the full RHIC energy of 200 GeV/A were undertaken. After extensive analysis of the results of runs from 2000–2004 a white paper [1] was published where evidence was given for the production of a Quark–Gluon Plasma (QGP). The plasma was designated sQGP in illusion to the strong coupling observed. In addition the sQGP behaved not as a gas as many expected but like a liquid with almost zero viscosity, the so called "perfect liquid". In 2010 the first collisions of Pb nuclei were observed at the Large Hadron Collider (LHC) at a much higher energy density than at RHIC.

In this talk I will discuss the suppression of particles in the hot dense nuclear medium created at RHIC which gives evidence that the QGP is strongly coupled. Next I will discuss the evident that the QGP flows indicating that the plasma acts like a liquid rather than a gas. Finally I will discuss recent measurements at PHENIX in an attempt to measure the temperature of the QGP.

2 Suppression of particles in the sQGP

In order to produce a QGP you need not only high energies but large volumes. This is necessary to sustain high energy densities and temperatures for a sufficiently long time. Before the collision the nuclei can be pictured as two relativistically flattened "pancakes" of quarks and gluons. In the initial collision products of hard scattering are created followed by the creation of large numbers of quarks and gluons out of the vacuum to produce a dense partonic medium. This medium can initially be the QGP but as it cools and expands it evolves into a hadronic gas phase. For 200 GeV/A Au collisions of the order of 10^4 particles are created. This process is illustrated in Fig. 1.

Proceedings of International Conference 'Nuclear Theory in the Supercomputing Era — 2013' (NTSE-2013), Ames, IA, USA, May 13–17, 2013. Eds. A. M. Shirokov and A. I. Mazur. Pacific National University, Khabarovsk, Russia, 2014, p. 244.
http://www.ntse-2013.khb.ru/Proc/JHill.pdf.

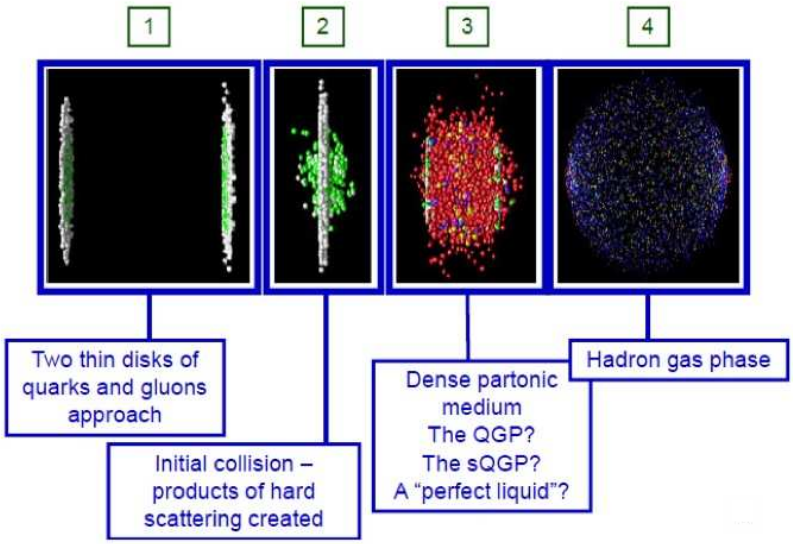

Figure 1: Stages in a relativistic heavy ion collision.

In order to study the properties of the QGP, particles that traverse the hot dense medium serve as a probe of its properties. In order to study the effects of the medium we introduce a Nuclear Modification Factor

$$R_{AA} = \frac{dN_{AA}^{J/\Psi}/dy}{N_{coll}\, dN_{pp}^{J/\Psi}/dy}.$$

In this factor the yield in nucleus-nucleus collisions is divided by the yield in p+p collisions but scaled by the appropriate number of binary collisions N_{coll} which is calculated using the Glauber model. We do not expect to produce the QGP in p+p collisions. Thus if the particles are not modified by the medium we expect $R_{AA} = 1$. In Fig. 2 the concept of participating nucleons is illustrated along with a plot of the number of binary collisions for Au collisions as a function of impact parameter.

A large number of measurements have been carried out at PHENIX to measure the response of various particles to passage through the hot dense medium created

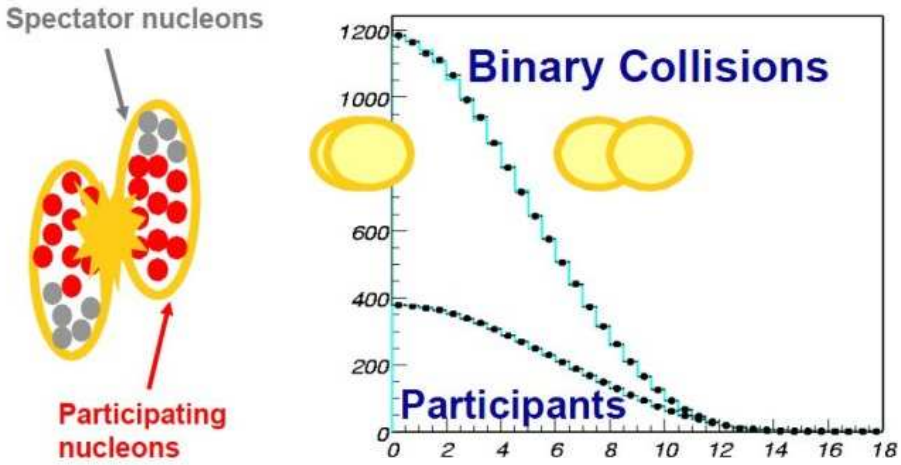

Figure 2: Concept of nuclear modification factor. On the left the concept of participant nucleons is illustrated and to the right a plot of participants and binary collisions as a function of impact parameter for Au collisions is shown.

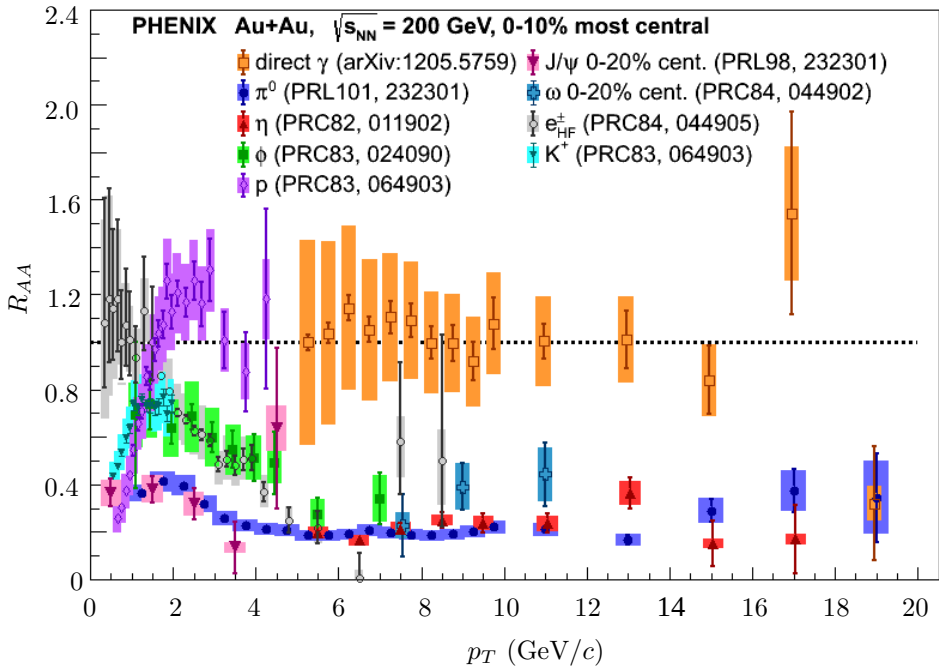

Figure 3: Plots showing R_{AA} for the 0 to 10% most central 200 GeV/A Au+Au collisions for a wide variety of mesons, protons and direct photons, and particle transverse momenta up to 19 GeV/c. Note the large suppression for hadrons but not for direct photons.

in Au+Au collisions. Using both Au+Au and p+p data measured at PHENIX R_{AA} for a number of different particles has been measured and the results are shown in Fig. 3. Particularly striking is the large suppression of π^0 mesons [2] all the way out to 19 GeV/c. In addition large suppression of η and ω mesons [3, 4] were observed. This is evidence for strong suppression of mesons composed of the light u and d quarks in the sQGP.

We also measured the suppression of ϕ and K^+ mesons that contain a heavy s quark. It is interesting to note that for these mesons the suppression was less but still [5, 6] significantly below an R_{AA} of 1.0. It might be expected that photons produced in direct interactions with the colliding quarks and gluons would not be suppressed by the sQGP since they only interact electromagnetically with the hot dense medium. This can be seen in the results in Fig. 3 for direct photons [7] where their R_{AA} is 1.0 within the error. We conclude that the sQGP strongly suppresses mesons made up of light u and d quarks but still significant suppression occurs when the meson is composed of a heavier s quark. As expected direct photons are little effected by the sQGP.

An important question is how does suppression in the QGP change if we reduce the collision energy or the centrality of the collision. We would thus expect less suppression both for lower collision energy and more peripheral collisions. Au+Au collisions were studied at 39 and 62.4 GeV/A and the results are compared with those at 200 GeV/A in Fig. 4.

The suppression for a collision energy of 62.4 GeV/A is very similar to that for 200 GeV/A except that the suppression is slightly lower at 62.4 GeV/A for π^0 momenta below 6 GeV/c. By contrast when the collision energy is lowered to 39 GeV/A the π^0 is still suppressed but to a lesser extent than at 62.4 GeV/A. It would be of interest to determine how far can we go down in collision energy and still see significant suppression. The data in Fig. 4 also shows that π^0 suppression is still

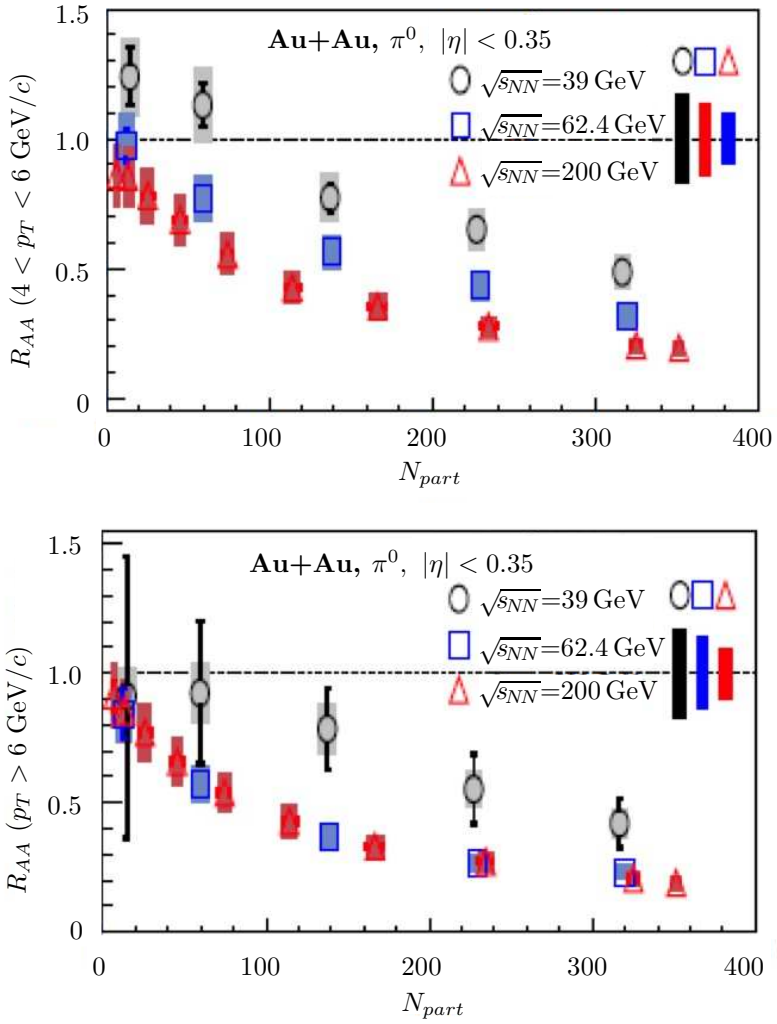

Figure 4: R_{AA} results for π^0 mesons for collision energies of 62.4 and 39 GeV/A. Particle numbers from 0 to 400 indicate a range from the most central to the most peripheral collisions.

significant at all three collision energies [8] down to peripheral collisions where of the order of 50 particles are emitted.

The LHC has produced Pb+Pb interactions with a collision energy of 2.76 TeV/A. R_{AA} for the production of π^0 and + and − charged hadrons was measured. These results for R_{AA} are compared with those from Au+Au collisions at PHENIX [9] at a collision energy of 200 GeV/A in Fig. 5.

From Fig. 5 it is observed that there is very little difference in the suppression of the π^0 even though the collision energies at ALICE are much greater. One might expect a higher suppression due to the greater energy densities at ALICE but many more particles are produced so the effects of recombination must be taken into account.

The suppression of u, d and s quarks in the sQGP is significant so it is interesting to test to what extent the much heavier c and b quarks are suppressed. To study this the R_{AA} for Au+Au collisions at 200 GeV/A were measured for electrons and positrons from decay of open charm and beauty. The R_{AA} for these particles is shown in the top part of Fig. 6 and compared [10] with results from π^0. For the most central collisions electrons with p_T greater than 2.0 GeV/c are significantly suppressed.

From the study of the suppression of various particles emitted in Au+Au collisions

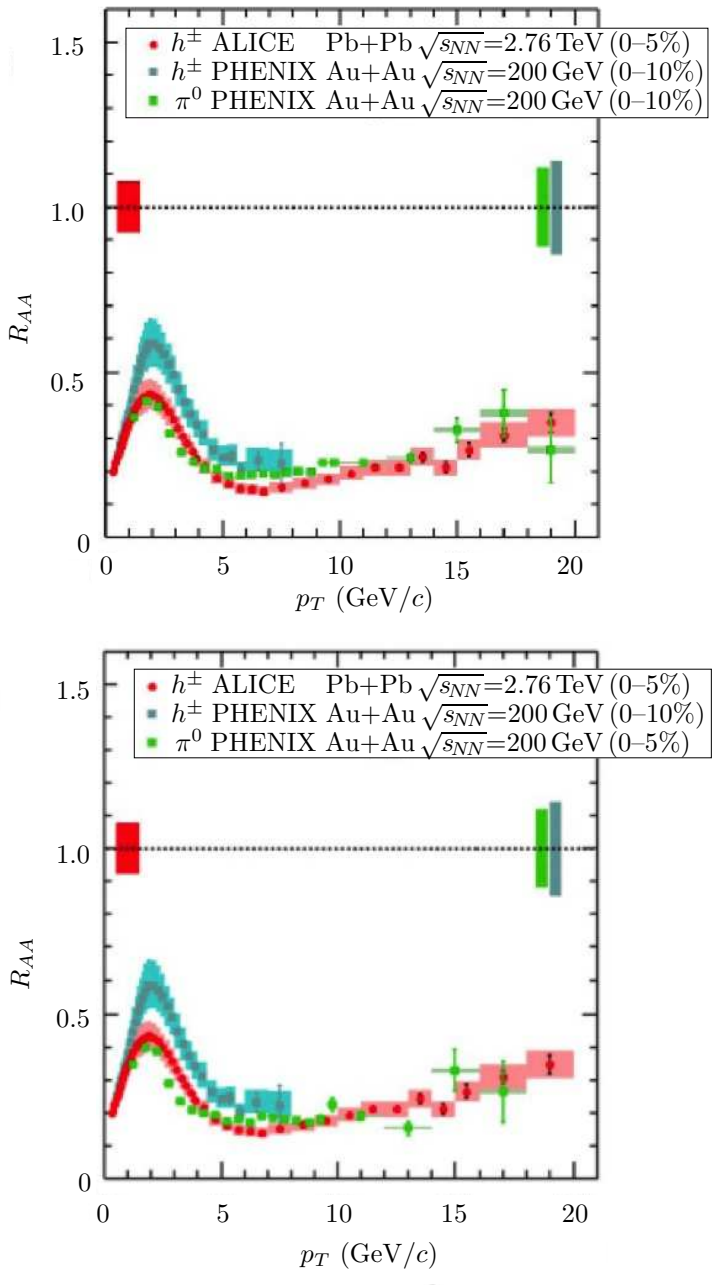

Figure 5: Plots showing R_{AA} for 200 GeV/A collisions at PHENIX and 2.76 TeV/A Pb+Pb collisions at ALICE.

we have reached the following conclusions:

A. In Au+Au collisions we have created a color opaque medium called the sQGP.

B. Suppression of particles in the medium is prominent for collision energies down to 39 GeV/A.

C. The level of suppression at the higher energy densities at the LHC is similar to that at RHIC.

D. The level of suppression is still very significant for the heavy c and b quarks.

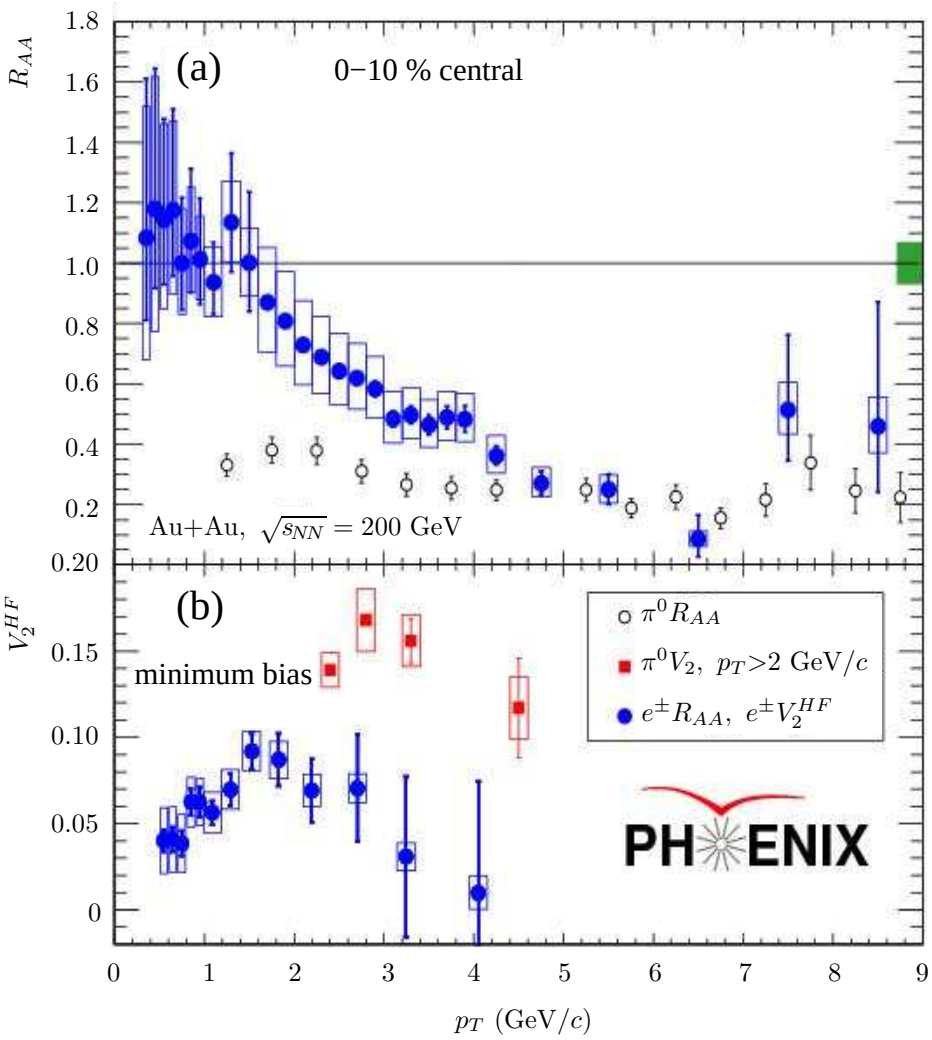

Figure 6: Plots of R_{AA} and v_2 in parts (a) and (b), respectively, for electrons from the decay of open charm and beauty. The data is for Au+Au collisions at 200 GeV and the 10% most central collisions.

3 Flow and evidence for a liquid sQGP

Early in experiments at RHIC it was observed that particles were not emitted isotropically in Au+Au collisions. This effect is shown in Fig. 7.

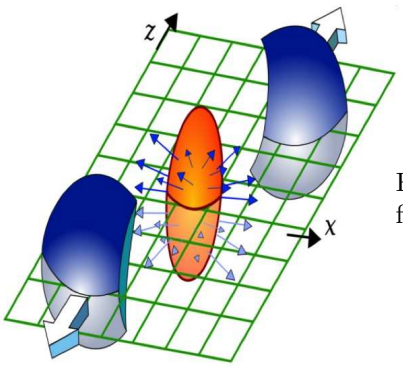

Figure 7: Figure illustrating the concept of elliptic flow.

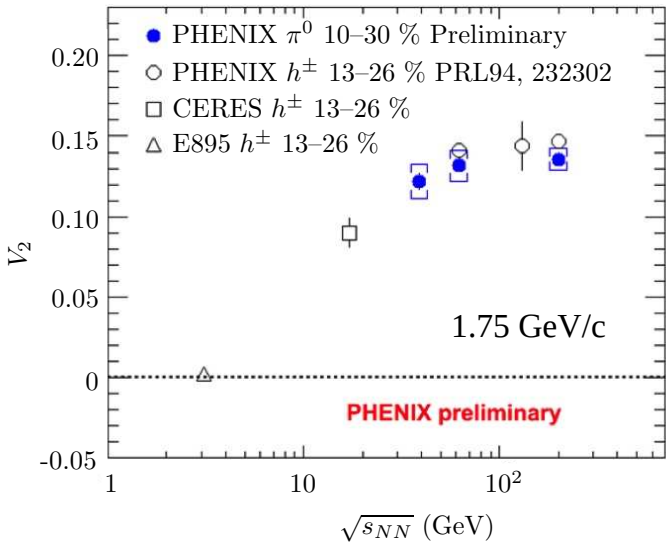

Figure 8: v_2 as a function of collision energy.

It was observed in RHIC experiments that when two heavy ions collided hot matter flowed. The colliding region is almond shaped due to the overlap of the colliding nuclei that have been flattened to "pancake" shapes due to relativistic effects. The regions of high density in the center exert a greater pressure resulting in the expansion of an elliptically shaped region (elliptic flow). The particle angular distribution can be described as:

$$\frac{dN}{d\phi} \sim 1 + 2v_2 \cos(2\phi).$$

For a spherically symmetric distribution v_2 is 0.

A plot of v_2 for Au+Au collisions at RHIC [11] is shown in Fig. 8. It is evident that the hot dense matter flows at both the lowest and highest RHIC energies. Also v_2 appears to saturate at the highest energies. There is also evidence that open charm and bottom particles flow but not as strongly as for the lighter quarks. See the (b) part of Fig. 6.

Once elliptic flow was established an important question was how did it scale with valence quark count. The v_2 was thus studied [12] for a large number of both baryons and mesons. The results are shown in Fig. 9.

The plot of v_2 on the upper part of Fig. 9 shows the results for both baryons and mesons for a number of different particle energies. If the v_2 values in the left plot are divided by the quark number the results are shown in the plot in the lower part. This result shows that v_2 scales as the quark number.

The observation of quark scaling is significant in that it establishes that collective behavior has been established during the partonic phase of the system since the degrees of freedom are partonic. This is a direct signature of deconfinement.

4 Temperature of the quark-gluon plasma

The temperature for formation of the QGP has been predicted to be around 170 MeV. It is thus important to measure the temperature of the hot hadronic matter produced at RHIC. The spectrum of photons is complex since they are generated in each stage of the collision. In the initial phase of the collision photons are emitted from the primary parton collisions. Next photons are emitted as the QGP forms, thermalizes and evolves into a mixed phase. Finally the mixed phase evolves into a hot hadron

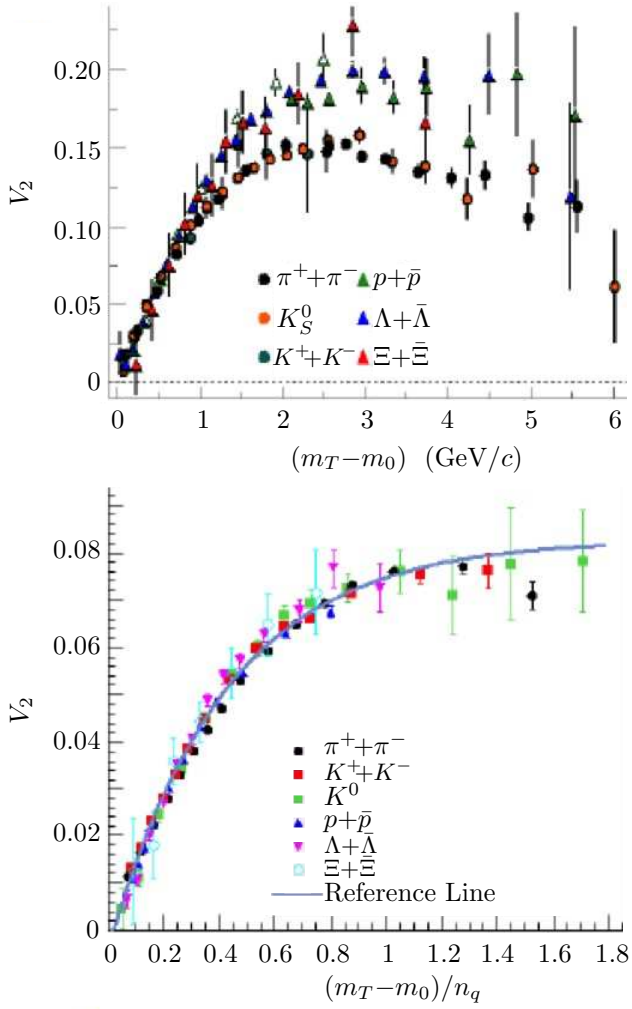

Fluid → QuasiParticles → Hadrons

Figure 9: Scaling behavior of v_2 for baryons and mesons.

gas. This process is illustrated [13] schematically in Fig. 10. Note that the photon energy spectrum becomes softer at each stage.

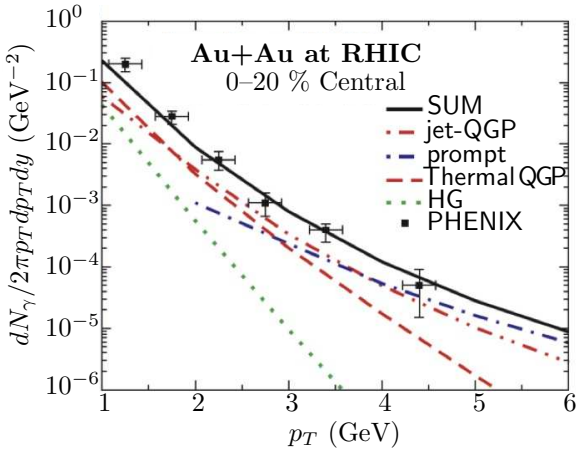

Figure 10: Photon yields from Au+Au collisions compared with calculated yields from different stages of the collision.

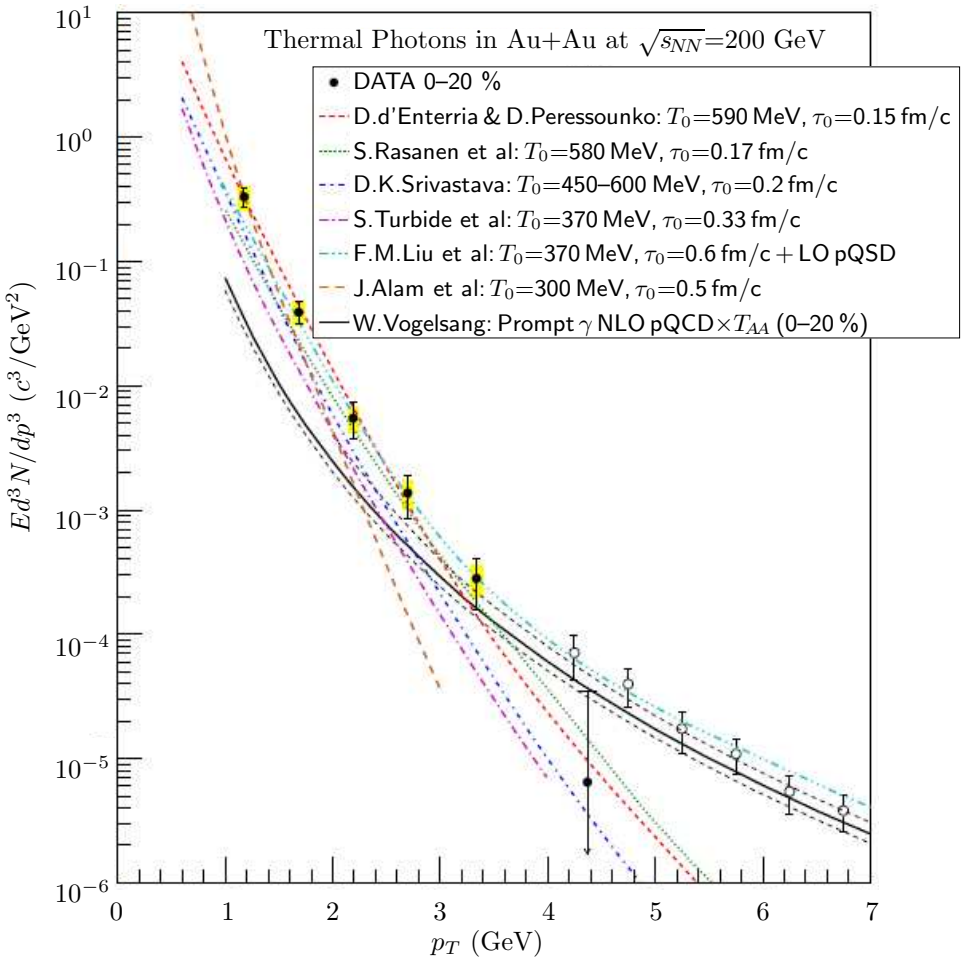

Figure 11: Spectrum of thermal photons from Au+Au collisions at 200 GeV/A compared with calculations assuming various values for formation energies and times.

In order to estimate the temperature of hot hadronic matter produced at RHIC, PHENIX measured dilepton production for 200 GeV/A Au and p collisions. This data was used to deduce the direct photon spectra shown in Fig. 11. The theoretical calculations shown in Fig. 11 assume a system with an initial temperature between 300 and 600 MeV and formation times between 0.6 and 0.15 fm/c. The PHENIX data [14] is in good agreement with calculations assuming initial temperatures above 300 MeV, which is well above the predicted formation temperature for the QGP of 170 MeV.

5 Summary and conclusions

Since the first collisions occurred at RHIC in 2000, the QGP has been produced using Au beams at RHIC and Pb beams at the LHC. This resulted in the formation of a very strongly interacting low viscosity liquid called the sQGP. Even heavy c and b quarks were stopped in the sQGP. At RHIC the temperature of the sQGP was deduced to be in the range of 300–600 MeV which is well above the proposed limit of 170 MeV for plasma formation. The transition from sQGP to hot hadronic matter is continuous rather than through a phase transition. The sQGP produced at the LHC has properties very similar to that produced at RHIC at a much lower energy density.

Acknowledgments

The author would like to thank the members of the PHENIX collaboration for their help in this project and explicitly to Gabor David for his consultations concerning this paper. The Iowa State nuclear physics group acknowledges the support of the U.S. Department of Energy under grant number DE-FG02-92ER40692.

Since this symposium is a celebration of the 70th birthday of James Vary I would like to point out that it has been almost 40 years since both James and I came to Iowa State in 1975. For many years I have valued James both as a colleague and especially as a friend. Happy 70th birthday, James.

References

[1] K. Adcox *et al.*, Nucl. Phys. A **757**, 184 (2005).

[2] A. Adare *et al.*, Phys. Rev. Lett. **101**, 232301 (2008).

[3] A. Adare, *et al.*, Phys. Rev. C **82**, 011902 (2010).

[4] A. Adare *et al.*, Phys. Rev. C **84**, 044902 (2011).

[5] A. Adare *et al.*, Phys. Rev. C **83**, 024909 (2011).

[6] A. Adare *et al.*, Phys. Rev. C **83**, 064903 (2011).

[7] S. Afanasiev *et al.*, Phys. Rev. Lett. **109**, 152302 (2012).

[8] A. Adare *et al.*, Phys. Rev. Lett. **109**, 152301 (2012).

[9] M. L. Purschke *el al.*, J. Phys. G **38**, 124016 (2011).

[10] A. Adare *et al.*, Phys. Rev. C **84**, 044905 (2011).

[11] S. S. Adler *et al.*, Phys. Rev. Lett. **94**, 232302 (2005).

[12] A. Adare *et al.*, Phys. Rev. Lett. **98**, 162301 (2007).

[13] H. van Hees, C. Gale and R. Rapp, Phys. Rev. C **84**, 054906 (2011).

[14] G. David, R. Rapp and Z. Xu, Phys. Rept. **462**, 176 (2008).

Relativistic Symmetry in Nuclei

Joseph N. Ginocchio

MS 283, Los Alamos National Laboratory, Los Alamos, NM 87545,USA

Abstract

Pseudospin symmetry has been useful in understanding atomic nuclei. We review the arguments that this symmetry is a relativistic symmetry. The condition for this symmetry is that the sum of the vector and scalar potentials in the Dirac Hamiltonian is a constant. We give the generators of pseudospin symmetry. We review predictions that follow from this insight in the origin of pseudospin symmetry. We propose non-relativistic shell model Hamiltonians that have a pseudospin dynamical symmetry. We also derive the exact solutions of the Dirac Hamiltonian for harmonic oscillator potentials in the spin and pseudospin symmetry limits. We also show that there is a higher U(3) or pseudo-U(3) symmetry in each limit, respectively.

Keywords: *Relativistic symmetry; pseudospin symmetry; shell model*

1 Introduction

When I was invited to talk at this meeting celebrating James 70th birthday I was shocked. Shocked because I could not believe that a student of mine was 70 years old and because James looks so young and vital so it was hard to believe he is 70. I arrived at Yale University in 1968 as a young professor. At that time Jim Vary was a graduate student. Jim was ready to do a thesis and he asked me if I could be his advisor. We decided on the topic of two body correlations in lead nuclei. We used a random phase approximation that used two-particle and two hole modes as well as particle-hole modes. We tested the calculations using two nucleon transfer reactions that were being measured at the time at the Yale tandem accelerator and other accelerators around the world [1,2]. Jim received his Ph.D. in 1970. He became a post doc at MIT and his career blossomed ever since and he became a leader in large shell model calculations of nuclear properties.

About the same time a quasi-degeneracy in the one nucleon states of spherical nuclei with quantum numbers $(n\ell_j, n'\ell'_{j'})$ was discovered [3, 4], where $n' = n - 1$, $\ell' = \ell + 2$, $j' = j + \frac{1}{2}$ and n, ℓ, j are the radial, orbital angular momentum, and total angular momentum quantum numbers, respectively. These quasi-degeneracies persist in recent measurements in nuclei far from stability [5]. The authors realized that, if they define the average of the orbital angular momenta as a pseudo-orbital angular momentum ($\tilde{\ell}$) and then couple a pseudospin ($\tilde{s} = \frac{1}{2}$) to the pseudo-orbital angular momentum, they will get the total angular momenta ($j = \tilde{\ell} \pm \frac{1}{2}$). For example, for the $(1s_{\frac{1}{2}}, 0d_{\frac{3}{2}})$ orbits, $\tilde{\ell} = 1$, which gives the total angular momenta $j = \frac{1}{2}, \frac{3}{2}$. Subsequently pseudospin doublets in deformed nuclei were discovered [6]. Pseudospin symmetry was later revealed to be a symmetry of the Dirac Hamiltonian [7, 8].

Proceedings of International Conference 'Nuclear Theory in the Supercomputing Era — 2013' (NTSE-2013), Ames, IA, USA, May 13–17, 2013. Eds. A. M. Shirokov and A. I. Mazur. Pacific National University, Khabarovsk, Russia, 2014, p. 254.

http://www.ntse-2013.khb.ru/Proc/Ginocchio.pdf.

2 Symmetries of the Dirac Hamiltonian

The Dirac Hamiltonian with a Lorentz scalar potential, $V_S(\vec{r})$, and a potential which is the fourth component of a Lorentz vector potential, $V_V(\vec{r})$, is

$$H = \vec{\alpha} \cdot \vec{p} + \beta\big(V_S(\vec{r}) + M\big) + V_V(\vec{r}), \tag{1}$$

where $\vec{\alpha}$, β are the Dirac matrices, $\vec{p}$ is the momentum, M is the mass, $\vec{r}$ is the radial coordinate, and the velocity of light is set equal to unity, c =1.

2.1 Spin symmetry: A symmetry of the Dirac Hamiltonian

The Dirac Hamiltonian has spin symmetry when the difference of the vector and scalar potentials in the Dirac Hamiltonian is a constant, $V_S(\vec{r}) - V_V(\vec{r}) = C_s$ [9]. Hadrons [10] and anti-nucleons in a nuclear environment have spin symmetry [11]. These are relativistic systems and normally, in such systems, we would expect large spin-orbit splittings, but, in this limit, spin doublets are degenerate. The generators for this SU(2) spin algebra, $\vec{S}$, which commute with the Dirac Hamiltonian with any potential $V(\vec{r})$, spherical or deformed, $[\,H\,,\,\vec{S}\,] = 0$, are given by [12]

$$\vec{S} = \begin{pmatrix} \vec{s} & 0 \\ 0 & U_p\,\vec{s}\,U_p \end{pmatrix}, \tag{2}$$

where $\vec{s} = \vec{\sigma}/2$ are the usual spin generators, $\vec{\sigma}$ are the Pauli matrices, and $U_p = \dfrac{\vec{\sigma}\cdot\vec{p}}{p}$ is the helicity unitary operator introduced in [13]. The generators are four by four matrices as appropriate for the Dirac Hamiltonian.

2.2 Pseudospin Symmetry: A Symmetry of the Dirac Hamiltonian

Another SU(2) symmetry of the Dirac Hamiltonian occurs when the sum of the vector and scalar potentials in the Dirac Hamiltonian is a constant, $V_S(\vec{r}) + V_V(\vec{r}) = C_{ps}$ [9]. The generators for this SU(2) algebra $\tilde{\vec{S}}$, which commute with the Dirac Hamiltonian with any potential $V(\vec{r})$, spherical or deformed, $[H, \tilde{\vec{S}}] = 0$, are given by [12]

$$\tilde{\vec{S}} = \begin{pmatrix} U_p\,\vec{s}\,U_p & 0 \\ 0 & \vec{s} \end{pmatrix}. \tag{3}$$

This symmetry was shown to be pseudospin symmetry [7]. The eigenfunctions of the Dirac Hamiltonian in this limit will have degenerate doublets of states, one of which has pseudospin aligned and the other with pseudospin unaligned. The "upper" matrix of the pseudospin generators in Eq. (3), $U_p\,\vec{s}\,U_p$, have the spin intertwined with the momentum which enables the generators to connect the states in the doublet, which differ by two units of angular momentum. The approximate equality in magnitude of the vector and scalar fields in nuclei and their opposite sign have been confirmed in relativistic mean field theories [8] and in QCD sum rules [8, 14].

3 Consequences of relativistic pseudospin symmetry

One immediate consequence of pseudospin symmetry as a relativistic symmetry is that the "lower" matrix of the pseudospin generators in Eq. (3), $\vec{s}$, does not change the radial wavefunction of the "lower" component of the Dirac eigenfunctions. Hence this symmetry predicts that the radial wavefunctions of the "lower" component is the

same for the two states in the doublet. Previous to this discovery many relativistic mean field calculations of nuclear properties had been made. Hence this prediction was tested with existing calculations and, indeed, these wavefunctions are very similar for both spherical [15, 16] and deformed nuclei [17, 18]. Because of the momentum dependence of the "upper" matrix of the generators the relationship between the "upper" components involves a differential equation and these have also been tested in spherical [19] and deformed nuclei [18] with success.

Magnetic dipole and Gamow–Teller transitions between the two states in pseudospin doublets are forbidden non-relativistically because the states differ by two units of angular momentum. However, they are not forbidden relativistically which means that they are proportional to the lower component of the Dirac eigenfunction. This leads to a condition between the magnetic moments of the states and the magnetic dipole transition between them because the radial amplitudes of the lower components of the two states in a pseudospin doublet are equal. Therefore the magnetic dipole transition between the two states in the doublet can be predicted if the magnetic moments of the states are known [8, 20]. Likewise pseudospin symmetry also predicts Gamow–Teller transitions between a state in a parent nucleus to the partner state in the daughter nucleus if the Gamow–Teller transition to the same states in the parent and daughter nucleus is known. We do not have space to discuss these relationships in detail but one example occurs in the mirror nuclei ${}^{39}_{19}\mathrm{K}_{20}$ and ${}^{39}_{20}\mathrm{Ca}_{19}$. The ground state and first excited state of ${}^{39}_{19}\mathrm{K}_{20}$ are interpreted as a $0d_{3/2}$ and $1s_{1/2}$ proton hole respectively, while the ground state and first excited state of ${}^{39}_{20}\mathrm{Ca}_{19}$ are interpreted as a $0d_{3/2}$ and $1s_{1/2}$ neutron hole respectively. These states are members of the $\tilde{n}_r = 1$, $\tilde{\ell} = 1$ pseudospin doublet. Using the magnetic moment of ^{39}Ca a transition rate is calculated which is only about 37 % larger than the measured. However, the two states in the doublet are not pure single-particle states. A modification of these relations has been derived which take into account the fact that these states are not pure single particle states [8, 21]. The modified relations give a transition rate that agrees with the measured value to within experimental error. Again using the mass 39 nuclei, the Gamow–Teller transitions from the ground state of ^{39}Ca to the ground and first excited state of ^{39}K are known, which is enough information to predict the transition from the ground state to the excited state. In the non-relativistic shell model an effective tensor term $g_{eff}[Y_2\sigma]^{(1)}$ is added to the magnetic dipole operator and the Gamow–Teller operator to produce a transition, where g_{eff} is a calculated effective coupling constant. However, the magnetic dipole transition calculated between the same states is an order of magnitude lower than the experimental transition [22] although the calculated Gamow–Teller agrees with the experimental value within the limits of experimental and theoretical uncertainty. This inconsistency has been a puzzle for the non-relativistic shell model. On the other hand the relativistic single-nucleon model gives a consistent description of both of these transitions. A global prediction of magnetic dipole transitions throughout the periodic table has had reasonable success as well [8, 21]. However, a global prediction of Gamow–Teller transitions have not been done yet. Pseudospin symmetry can also be used to relate quadrupole transitions between multiplets [8].

4 Anti-nucleon in a nuclear environment

Charge conjugation changes a nucleon into an anti-nucleon. Under charge conjugation the scalar potential of a nucleon remains invariant while the its vector potential changes sign. Hence the pseudospin condition $V_S(\vec{r}) + V_V(\vec{r}) \approx C_{ps}$ becomes $\bar{V}_S(\vec{r}) - \bar{V}_V(\vec{r}) \approx C_{ps} = \bar{C}_s$. Hence approximate pseudospin for nucleons predicts approximate spin symmetry for anti-nucleons in a nuclear environment. Since the potentials are also very deep we would expect approximate $U(3)$ symmetry as well (see Section 6). The sparse data on the scattering of polarized anti-nucleons on nuclei

supports this prediction [23]. Perhaps more data on the scattering of polarized antinucleons on nuclei will be forthcoming from GSI.

5 Shell model Hamiltonians with pseudospin as a dynamical symmetry

We would like to go beyond the mean field and use pseudospin symmetry in the non-relativistic shell model. To that goal, we have constructed the most general shell model Hamiltonian with two-nucleon interactions which has pseudospin symmetry and pseudo-orbital angular momentum symmetry as dynamical symmetries. Such Hamiltonians have eigenfunctions with conserved pseudospin and pseudo-orbital angular momentum, but the energy levels are not degenerate. We do not have the space to give the derivation, but we summarize the results.

These shell model Hamiltonians are given in momentum space. The single particle Hamiltonian for A nucleons, $h_{ps} = \Sigma_{k=1}^{A}\, h(\vec{p}_k)$, has the same form as the single particle Hamiltonian that has spin as a dynamical symmetry; that is,

$$h(\vec{p}_k) = h_c(p_k) + h_o(p_k)\,\vec{\ell}_k \cdot \vec{\ell}_k + h_{so}(p_k)\,\vec{s}_k \cdot \vec{\ell}_k. \tag{4}$$

For completely degenerate pseudospin doublets, there is the condition $h_{so}(p_k) = 4h_o(p_k)$ [24].

The two-nucleon interaction, $V_{ps} = \Sigma_{k>t=1}^{A} V(\vec{p}_k, \vec{p}_t)$, is composed of isospin zero and one parts,

$$V(\vec{p}_k, \vec{p}_t) = V^{(0)}(\vec{p}_k, \vec{p}_t)\frac{(1 - \tau_k \cdot \tau_t)}{4} + V^{(1)}(\vec{p}_k, \vec{p}_t)\frac{(3 + \tau_k \cdot \tau_t)}{4}, \tag{5}$$

where

$$\begin{aligned} V^{(T)}&(\vec{p}_k, \vec{p}_t) \\ &= V_c^{(T)} + V_s^{(T)} s_k \cdot s_t + V_o^{(T)} \ell_k \cdot \ell_t + V_{so}^{(T)}(s_k \cdot \ell_t + s_t \cdot \ell_k) \\ &+ V_t^{(T)}\,[s_k s_t]^{(2)} \cdot \Big([\hat{p}_k \hat{p}_k]^{(2)} + [\hat{p}_t \hat{p}_t]^{(2)}\Big) + V_{dt}^{(T)}\Big([s_k s_t]^{(2)} \cdot [\hat{p}_k \hat{p}_t]^{(2)} - [s_k s_t]^{(1)} \cdot [\hat{p}_k \hat{p}_t]^{(1)}\Big) \\ &+ V_{mso}^{(T)}\big([s_k \cdot \hat{p}_k]\,\hat{p}_k \cdot \vec{\ell}_t + [s_t \cdot \hat{p}_t]\,\hat{p}_t \cdot \vec{\ell}_k\big), \end{aligned} \tag{6}$$

and all the coefficients $V_i^{(T)}$ depend on the magnitudes of the momenta, p_k, p_t, and the angle between them, $\theta_{k,t}$. The first line has spin as a dynamical symmetry. However the second line has tensor interactions, and the third line has dipole interactions which break the spin symmetry, but conserve pseudospin symmetry. The tensor interaction has been shown to be important for shell evolution in exotic nuclei [25]. At the same time pseudospin doublets are also seen in these nuclei [5]. Perhaps these shell model Hamiltonians will be able to explain both effects in a unified way.

6 The Dirac Hamiltonian with harmonic oscillator potentials

The Dirac Hamiltonian with harmonic oscillator potentials has been solved analytically in the spin and pseudospin limits [8,26] but not in the limit of scalar and vector potentials independent of each other. In these two limits there are higher symmetries just as there are for the non-relativistic harmonic oscillators. We shall summarize the results for the spherically symmetric Dirac Hamiltonian.

6.1 The spherically symmetric Dirac Hamiltonian with spin symmetry and harmonic oscillator potentials

The Dirac Hamiltonian for a spherical harmonic oscillator with spin symmetry is

$$H = \vec{\alpha} \cdot \vec{p} + \beta M + (1+\beta)V(r), \tag{7}$$

r is the magnitude of the radial coordinate. The generators for the spin SU(2) algebra are given in Eq. (2). The generators for the orbital angular momentum SU(2) algebra, $\vec{L}$, which commute with the Dirac Hamiltonian with any spherically symmetric potential $V(r)$, $[H\,,\,\vec{L}\,] = 0$, are given by

$$\vec{L} = \begin{pmatrix} \vec{\ell} & 0 \\ 0 & U_p \vec{\ell} U_p \end{pmatrix}, \tag{8}$$

where $\vec{\ell} = \frac{(\vec{r}\times\vec{p})}{\hbar}$.

6.2 The energy spectrum

With the harmonic oscillator potential $V(r) = \frac{M\omega^2}{2}\, r^2$ the eigenvalue equation is [26]

$$\sqrt{E_N + M}\,(E_N - M) = \sqrt{2\hbar^2\omega^2 M}\left(N + \frac{3}{2}\right), \tag{9}$$

where $N = 2n + \ell$ is the total harmonic oscillator quantum number, n is the radial quantum number and ℓ is the orbital angular momentum. Hence the eigenenergies have the same degeneracies as the non-relativistic harmonic oscillator. This eigenvalue equation is solved with Mathematica,

$$E_N = \frac{M}{3}\left[3B(A_N) + 1 + \frac{4}{3B(A_{n_1,n_2,n_3})}\right], \tag{10}$$

where $B(A_N) = \left(\frac{A_N + \sqrt{A_N^2 - \frac{32}{27}}}{2}\right)^{\frac{2}{3}}$, and $A_N = \frac{\sqrt{2}\hbar\omega}{M}\left(N + \frac{3}{2}\right)$. The spectrum is non-linear in contrast to the non-relativistic harmonic oscillator; i. e., the relativistic harmonic oscillator is not harmonic. However for large M, the binding energy goes like

$$E_N - M \approx M\left(\frac{A_N}{\sqrt{2}} + \cdots\right) \approx \hbar\omega\left(N + \frac{3}{2}\right), \tag{11}$$

in agreement with the non-relativistic harmonic oscillator. For small M the spectrum goes as

$$E_N \approx M\left(A_N^{\frac{2}{3}} + \cdots\right) \approx M^{\frac{1}{3}}\left[\sqrt{2}\hbar\omega\left(N + \frac{3}{2}\right)\right]^{\frac{2}{3}}, \tag{12}$$

which, in lowest order, agrees with the spectrum for $M \to 0$. Hence the harmonic oscillator is not harmonic in the relativistic limit.

6.3 U(3) generators

The relativistic energy spectrum has the same degeneracies as the non-relativistic spectrum [27], even though the dependence on N is different. This suggests that the relativistic harmonic oscillator has a higher U(3) symmetry. The non-relativistic U(3) generators are the orbital angular momentum $\vec{\ell}$, the quadrupole

operator $q_m = \frac{1}{\hbar M\omega}\sqrt{\frac{3}{2}}\left(2M^2\omega^2[rr]^{(2)}_m + [pp]^{(2)}_m\right)$, where $[rr]^{(2)}_m$ means coupled to angular momentum rank 2 and projection m, and the total oscillator quantum number operator, $\mathcal{N}_{NR} = \frac{1}{2\sqrt{2}\hbar M\omega}\left(2M^2\omega^2r^2 + p^2\right) - \frac{3}{2}$. They form the closed U(3) algebra

$$\left[\mathcal{N}_{NR}, \vec{\ell}\,\right] = [\mathcal{N}_{NR}, q_m] = 0, \tag{13}$$

$$\left[\vec{\ell}, \vec{\ell}\,\right]^{(t)} = -\sqrt{2}\,\vec{\ell}\,\delta_{t,1}, \quad \left[\vec{\ell}, q\right]^{(t)} = -\sqrt{6}\,q_m\,\delta_{t,2}, \quad [q,q]^{(t)} = 3\sqrt{10}\,\vec{\ell}\,\delta_{t,1}, \tag{14}$$

with $\mathcal{N}_{NR}$ generating a U(1) algebra whose eigenvalues are the total number of quanta N and $\vec{\ell}$, q_m generating an SU(3) algebra. In the above we use the coupled commutation relation between two tenors, $T_1^{(t_1)}$, $T_2^{(t_2)}$ of rank t_1, t_2, which is $\left[T_1^{(t_1)}, T_2^{(t_2)}\right]^{(t)} = \left[T_1^{(t_1)}, T_2^{(t_2)}\right]^{(t)} - (-1)^{t_1+t_2-t}\left[T_2^{(t_2)}, T_1^{(t_1)}\right]^{(t)}$.

The relativistic orbital angular momentum generators $\vec{L}$ are given in Eq. (8). We shall now determine the the quadrupole operator Q_m and monopole operator $\mathcal{N}$ that commute with the Hamiltonian in Eq. (7). In order for the quadrupole generator

$$Q_m = \begin{pmatrix} (Q_m)_{11} & (Q_m)_{12}\ \vec{\sigma}\cdot\vec{p} \\ \vec{\sigma}\cdot\vec{p}\,(Q_m)_{21} & \vec{\sigma}\cdot\vec{p}\,(Q_m)_{22}\ \vec{\sigma}\cdot\vec{p} \end{pmatrix}, \tag{15}$$

to commute with the Hamiltonian, $[Q_m, H] = 0$, the matrix elements must satisfy the conditions,

$$(Q_m)_{12} = (Q_m)_{21}, \tag{16}$$

$$2[(Q_m)_{11}, V] + [(Q_m)_{12}, p^2] = 0, \tag{17}$$

$$2[(Q_m)_{12}, V] + [(Q_m)_{22}, p^2] = 0, \tag{18}$$

$$(Q_m)_{11} = (Q_m)_{12}\,2(V+M) + (Q_m)_{22}\,p^2. \tag{19}$$

One solution is

$$Q_m = \lambda_2 \begin{pmatrix} M\omega^2(M\omega^2\,r^2 + 2M)[rr]^{(2)}_m + [pp]^{(2)}_m & M\omega^2[rr]^{(2)}_m\,\vec{\sigma}\cdot\vec{p} \\ \vec{\sigma}\cdot\vec{p}\,M\omega^2[rr]^{(2)}_m & [pp]^{(2)}_m \end{pmatrix}, \tag{20}$$

where λ_2 is an overall constant undetermined by the commutation of Q_m with the Dirac Hamiltonian.

For this quadrupole operator to form a closed algebra, the commutation with itself must be the orbital angular momentum operator as in Eq. (14). This commutation relation gives

$$[Q,Q]^{(t)} = \sqrt{10}\,\lambda_2^2\,M\omega^2\hbar^2 \begin{pmatrix} (M\omega^2r^2 + 2M)\,\vec{\ell} & \vec{\ell}\ \vec{\sigma}\cdot\vec{p} \\ \vec{\sigma}\cdot\vec{p}\ \vec{\ell} & 0 \end{pmatrix}$$
$$= \sqrt{10}\,\lambda_2^2\,M\omega^2\hbar^2(H+M)\vec{L}\,\delta_{t,1}, \tag{21}$$

and we get the desired result if $\lambda_2 = \sqrt{\frac{3}{M\omega^2\hbar^2(H+M)}}$. The quadrupole operator then becomes

$$Q_m = \sqrt{\frac{3}{M\omega^2\hbar^2(H+M)}} \begin{pmatrix} M\omega^2(M\omega^2r^2 + 2M)[rr]^{(2)}_m + [pp]^{(2)}_m & M\omega^2[rr]^{(2)}_m\,\vec{\sigma}\cdot\vec{p} \\ \vec{\sigma}\cdot\vec{p}\,M\omega^2[rr]^{(2)}_m & [pp]^{(2)}_m \end{pmatrix}, \tag{22}$$

which reduces to the non-relativistic quadrupole generator for $H \to M$. In the original paper [28] that derives the quadrupole generators there are two typos. In Eq. (6) of that paper, $\frac{M\omega^2}{2}\,r^2$ should be replaced by $M\omega^2r^2$ and in the non-relativistic

quadrupole operator $M^2\omega^2[rr]^{(2)}_m$ should be replaced by $2M^2\omega^2[rr]^{(2)}_m$. Also, the expression for $B(A_N)$ in that paper has a misplaced factor of 2 in the denominator.

For the monopole generator, we can solve the same equations. But there is a simpler way. From Eq. (9) we get,

$$\mathcal{N} = \frac{\sqrt{H+M}(H-M)}{\hbar\sqrt{2M\omega^2}} - \frac{3}{2}. \tag{23}$$

In the non-relativistic limit, $H + M \to 2M$ and the non-relativistic Hamiltonian $(H - M) \to \hbar\omega\big(N + \frac{3}{2}\big)$ which gives the correct result.

The commutation relations are then those of the U(3) algebra,

$$\big[\mathcal{N}, \vec{L}\,\big] = [\mathcal{N}, Q_m] = 0, \tag{24}$$

$$\big[\vec{L}, \vec{L}\,\big]^{(t)} = -\sqrt{2}\vec{L}\,\delta_{t,1}, \quad \big[\vec{L}, Q\big]^{(t)} = -\sqrt{6}Q\,\delta_{t,2}, \quad [Q, Q]^{(t)} = 3\sqrt{10}\vec{L}\,\delta_{t,1}. \tag{25}$$

The spin generators in Eq. (2), $\vec{S}$, commute with the U(3) generators as well as the Dirac Hamiltonian, and so the invariance group is U(3)×SU(2), where the SU(2) is generated by the spin generators, $\big[\vec{S}, \vec{S}\,\big]^{(t)} = -\sqrt{2}\vec{S}\,\delta_{t,1}$.

6.4 The spherically symmetric Dirac Hamiltonian with pseudospin symmetry and harmonic oscillator potential

The Dirac Hamiltonian with pseudospin symmetry is [7]

$$\tilde{H} = \vec{\alpha}\cdot\vec{p} + \beta M + (1-\beta)V(r), \tag{26}$$

which explains the pseudospin doublets observed in nuclei [8]. This pseudospin Hamiltonian can be obtained from the spin Hamiltonian with a transformation

$$\gamma_5 = \begin{pmatrix} 0 & 1 \\ 1 & 0 \end{pmatrix} \quad \text{and} \quad M \to -M, \tag{27}$$

which gives the pseudospin and pseudo-orbital angular momentum generators [12]

$$\tilde{\vec{S}} = \begin{pmatrix} U_p\,\vec{s}\,U_p & 0 \\ 0 & \vec{s} \end{pmatrix}, \quad \tilde{\vec{L}} = \begin{pmatrix} U_p\,\vec{\ell}\,U_p & 0 \\ 0 & \vec{\ell} \end{pmatrix}. \tag{28}$$

6.5 Energy spectrum

With the harmonic oscillator potential $V(r) = \frac{M\omega^2}{2}\,r^2$ the eigenvalue equation in the pseudospin limit is [18]

$$\sqrt{E_{\tilde{N}} - M}\,(E_{\tilde{N}} + M) = \sqrt{2\hbar^2\omega^2 M}\left(\tilde{N} + \frac{3}{2}\right), \tag{29}$$

where $\tilde{N} = 2\tilde{n} + \tilde{\ell}$ is the pseudo total harmonic oscillator quantum number, $\tilde{n}$ is the pseudo radial quantum number and $\tilde{\ell}$ is the pseudo-orbital angular momentum. While n is the number of radial nodes and ℓ the rank of the spherical harmonic of the upper Dirac radial amplitude, $\tilde{n}$ is the number of radial nodes and $\tilde{\ell}$ the rank of the spherical harmonic of the lower Dirac radial amplitude. Again the eigenenergies have the same degeneracy pattern as the non-relativistic harmonic oscillator in the spin symmetry limit. This eigenvalue equation is solved on Mathematica,

$$E_{\tilde{N}} = \frac{M}{3}\left[3B(A_{\tilde{N}}) - 1 + \frac{4}{3\;B(A_{\tilde{N}})}\right], \tag{30}$$

where $B(A_N) = \left(\frac{A_{\tilde{N}}+\sqrt{A_{\tilde{N}}^2+\frac{32}{27}}}{2}\right)^{\frac{2}{3}}$, and $A_{\tilde{N}} = \frac{\sqrt{2}\hbar\omega}{M}\left(\tilde{N}+\frac{3}{2}\right)$. The spectrum is non-linear in contrast to the non-relativistic harmonic oscillator; i. e., the relativistic harmonic oscillator is not harmonic in either limit. Even for small $A_{\tilde{N}}$ (large M), the binding energy

$$E_{\tilde{N}} - M \approx M\left(\frac{A_{\tilde{N}}^2}{4} + \cdots\right), \tag{31}$$

and hence goes quadratically with the the total pseudo-number of quanta and is non-linear even for large M. For large $A_{\tilde{N}}$ (small M) the spectrum goes as

$$E_{\tilde{N}} \approx M\left(A_{\tilde{N}}^{\frac{2}{3}} - \frac{1}{3} + \cdots\right), \tag{32}$$

which, in the lowest order, agrees with the spectrum for spin symmetry.

6.6 Pseudo-U(3) generators

The pseudo-U(3) generators which commute with the Dirac Hamiltonian, $\left[\tilde{H}, \vec{\tilde{S}}\right] = \left[\tilde{H}, \vec{\tilde{L}}\right] = \left[\tilde{H}, \tilde{Q}_m\right] = \left[\tilde{H}, \tilde{\mathcal{N}}\right] = 0$, are then obtained by the transformation in Eq. (27) and are given by

$$\tilde{Q}_m = \sqrt{\frac{3}{M\omega^2\hbar^2(H-M)}} \begin{pmatrix} M\omega^2(M\omega^2 r^2 - 2M)[rr]_m^{(2)} + [pp]_m^{(2)} & M\omega^2[rr]_m^{(2)}\, \vec{\sigma}\cdot\vec{p} \\ \vec{\sigma}\cdot\vec{p}\; M\omega^2[rr]_m^{(2)} & [pp]_m^{(2)} \end{pmatrix}. \tag{33}$$

The commutation relations are then those of a U(3) algebra,

$$\left[\tilde{\mathcal{N}}, \vec{\tilde{L}}\right] = \left[\tilde{\mathcal{N}}, \tilde{Q}_m\right] = 0, \tag{34}$$

$$\left[\vec{\tilde{L}}, \vec{\tilde{L}}\right]^{(t)} = -\sqrt{2}\vec{\tilde{L}}\,\delta_{t,1}, \quad \left[\vec{\tilde{L}}, \tilde{Q}\right]^{(t)} = -\sqrt{6}\,\tilde{Q}\,\delta_{t,2}, \quad \left[\tilde{Q}, \tilde{Q}\right]^{(t)} = 3\sqrt{10}\vec{\tilde{L}}\,\delta_{t,1}. \tag{35}$$

However there are no bound Dirac valence states in the pseudospin limit.

Acknowledgments

This research was supported by the US Department of Energy, Contract No. W-7405-ENG-36.

References

[1] J. Vary and J. N. Ginocchio, Nucl. Phys. A **166**, 479 (1971).

[2] J. Vary, R. J. Ascuitto and J. N. Ginocchio, Nucl. Phys. A **185**, 349 (1972).

[3] A. Arima, M. Harvey and K. Shimizu, Phys. Lett. B **30**, 517 (1969).

[4] K. T. Hecht and A. Adler, Nucl. Phys. A **137**, 129 (1969).

[5] O. Sorlin and M. G. Porquet, Progr. Part. Nucl. Phys. **61**, 602 (2008).

[6] A. Bohr, I. Hamamoto and B. R. Mottelson, Phys. Scr. **26**, 267 (1982).

[7] J. N. Ginocchio, Phys. Rev. Lett. **78**, 436 (1997).

[8] J. N. Ginocchio, Phys. Rept. **414**, 165 (2005).

[9] J. S. Bell and H. Ruegg, Nucl. Phys. B **98**, 151 (1997).

[10] P. R. Page, T. Goldman and J. N. Ginocchio, Phys. Rev. Lett. **86**, 204 (2001).

[11] J. N. Ginocchio, Phys. Rept. **315**, 231 (1999).

[12] J. N. Ginocchio and A. Leviatan, Phys. Lett. B **425**, 1 (1998).

[13] A. L. Blokhin, C. Bahri and J. P. Draayer, Phys. Rev. Lett. **74**, 4149 (1995).

[14] T. D. Cohen *et al.*, Progr. Part. Nucl. Phys. **35**, 221 (1995).

[15] J. N. Ginocchio and D. G. Madland, Phys. Rev. C **57**, 1167 (1998).

[16] J. Meng, K. Sugawara-Tanabe, S. Yamaji, P. Ring and A. Arima, Phys. Rev. C **58**, R628 (1998).

[17] K. Sugawara-Tanabe, S. Yamaji and A. Arima, Phys. Rev. C **65**, 054313 (2002).

[18] J. N. Ginocchio, A. Leviatan, J. Meng and S.-G. Zhou, Phys. Rev. C **69**, 03430 (2004).

[19] J. N. Ginocchio, Phys. Rev. C **66**, 064312 (2002).

[20] J. N. Ginocchio, Phys. Rev. C **59**, 2487 (1999).

[21] P. von Neumann-Cosel and J. N. Ginocchio, Phys. Rev. C **62**, 014308 (2000).

[22] E. Hagberg *et al.*, Nucl. Phys. A **571**, 555 (1994).

[23] D. Garetta *et al.*, Phys. Lett. B **151**, 473 (1985).

[24] C. Bahri, J. P. Draayer and S. A. Moszkowski, Phys. Rev. Lett. **68**, 2133 (1992).

[25] T. Otsuka and D. Abe, Progr. Part. Nucl. Phys. **59**, 425 (2007).

[26] J. N. Ginocchio, Phys. Rev. C **69**, 034318 (2004).

[27] J. P. Elliott, Proc. R. Soc. London, Ser. A **245**, 128 (1958).

[28] J. N. Ginocchio, Phys. Rev. Lett. **95**, 252501 (2005).

Accelerating *Ab Initio* Nuclear Physics Calculations with GPUs

Hugh Potter[a], Dossay Oryspayev[b,c], Pieter Maris[a], Masha Sosonkina[c,d] James Vary[a], Sven Binder[e], Angelo Calci[e], Joachim Langhammer[e], Robert Roth[e], Ümit Çatalyürek[f] and Erik Saule[g]

[a] *Department of Physics and Astronomy, Iowa State University, Ames, IA 50011, USA*
[b] *Department of Electrical and Computer Engineering, Iowa State University, Ames, IA 50011, USA*
[c] *Ames Laboratory, Ames, IA 50011, USA*
[d] *Department of Modeling, Simulation and Visualization Engineering, Old Dominion University, Norfolk, VA 23529, USA*
[e] *Institut für Kernphysik — Theoriezentrum, Technische Universität Darmstadt, 64289, Darmstadt, Germany*
[f] *Departments of Biomedical Informatics, Electrical and Computer Engineering, and Computer Science and Engineering, Ohio State University, Columbus, OH 43210, USA*
[g] *Department of Computer Science, University of North Carolina at Charlotte, Charlotte, NC 28223, USA*

Abstract

This paper describes some applications of GPU acceleration in *ab initio* nuclear structure calculations. Specifically, we discuss GPU acceleration of the software package MFDn, a parallel nuclear structure eigensolver. We modify the matrix construction stage to run partly on the GPU. On the Titan supercomputer at the Oak Ridge Leadership Computing Facility, this produces a speedup of approximately 2.2x–2.7x for the matrix construction stage and 1.2x–1.4x for the entire run.

Keywords: *Configuration Interaction; no-core shell model; ab initio nuclear structure; GPU acceleration; Titan supercomputer*

1 Introduction

The Configuration Interaction approach to computational nuclear physics casts the Schrödinger equation for the nuclear many-body bound state problem as a matrix eigenvalue problem [1, 2]. The many-body Hamiltonian is approximated by a finite matrix whose eigenvalues and eigenvectors correspond to the bound state energies and wavefunctions. The wavefunctions can then be used to calculate other observables. Typically only the lowest eigenvalues and eigenvectors of this matrix are of interest.

The Hamiltonian matrices required to accurately calculate nuclear properties can be very large, with dimension in excess of 10^9, and 10^{13} or more nonzero matrix elements [2, 3]. Calculations of this magnitude can only be performed on supercomputers, with parallel codes like Many-Fermion Dynamics for nuclei (MFDn) [4–8], a hybrid MPI/OpenMP software package written in Fortran and C.

Proceedings of International Conference 'Nuclear Theory in the Supercomputing Era — 2013' (NTSE-2013), Ames, IA, USA, May 13–17, 2013. Eds. A. M. Shirokov and A. I. Mazur. Pacific National University, Khabarovsk, Russia, 2014, p. 263.
http://www.ntse-2013.khb.ru/Proc/Sosonkina.pdf.

The Hamiltonian matrices are very sparse, but their sparsity structure is nontrivial; locating and calculating the nonzero matrix elements takes a significant fraction of the overall runtime in MFDn, on the order of 25−45 % for some representative cases. The matrix construction stage contains a number of parallelizable steps, however, each nonzero element can be calculated independently. This problem structure is a promising target for acceleration on SIMD-style coprocessors like GPUs. We present an investigation of GPU acceleration in the matrix construction stage of MFDn.

GPU accelerators pair a large number of cores with a communal block of memory. They have much less memory per core and cannot easily handle more complex program logic, but are capable of running many calculations in parallel. The CUDA framework [9] from NVIDIA provides a high-level API for accessing GPU functionality, allowing GPUs to be programmed in languages like C and Fortran.

Code to be executed on the GPU is written in a function called the kernel. The CPU code can then invoke the kernel, specifying a number of cores on which to run simultaneously. The kernel invocation specifies thread count in a two-level hierarchy: threads are grouped together into blocks, and blocks are grouped into a grid. Each thread has its own small, private, local memory, and each thread in a block can access the shared memory of that block. Every thread in the grid has access to the global memory, which can be in the 1−6 GB range. The user calls CUDA allocation and copy functions to move data to the global memory of the GPU, invokes the kernel and waits for completion, and then uses copy functions to retrieve the results of the calculation. The kernel invocation will often request more threads than the GPU has cores. In this case, the GPU has a scheduler to stream blocks to cores as they become available.

2 Overview of MFDn

MFDn is a hybrid MPI/OpenMP parallel software package written in Fortran and C for *ab initio* nuclear physics calculations. MFDn generates a many-body nuclear Hamiltonian matrix for the nucleus in question and uses the Lanczos algorithm to extract the lowest eigenvalues and eigenvectors. The many-body matrix is stored in memory on core; this strategy limits the sizes of the matrices that can be used, but is much faster than accessing the matrix from disk. The matrix is symmetric, so only half of it is generated and stored [7, 8].

MFDn runs in several stages. After the various indexing systems are set up to specify the many-body basis, the many-body Hamiltonian matrix is constructed. The nonzero elements are then located, calculated, and stored. Elements in the many-body matrix are built up as linear combinations of kinetic energy and nuclear interaction terms. MFDn reads the kinetic energy and 2-body and 3-body potentials from file, and uses them to calculate elements of the many-body Hamiltonian. The many-body matrix is distributed among MPI processes in a way that produces a roughly uniform distribution of nonzero elements.

Once the matrix is generated, MFDn obtains the lowest eigenvalues and eigenvectors with the Lanczos algorithm, an iterative algorithm that relies on successive matrix-vector multiplications and orthogonalizations. The Lanczos algorithm requires many iterations, and is the most computationally-intensive stage. Efficient multicore approaches have been implemented in Refs. [6–8]. Performance with respect to non-uniform memory access (NUMA) architecture in supercomputer nodes has been studied in Ref. [10]. When the Lanczos algorithm has completed, MFDn uses the eigenvalues and eigenvectors to calculate other observables, which can then be compared to experiment.

Despite being computationally intensive, the Lanczos algorithm stage is not an easy target for GPU acceleration; it is memory-bound, and also cannot be easily broken down into GPU-parallelizable pieces. In the matrix construction stage, however,

each many-body matrix element can be calculated independently. Furthermore, in the current implementation of MFDn, each 3-body matrix element that is needed in the many-body matrix must be obtained by performing a change of basis on the input 3-body potential. This part of the code is very computationally intensive, and we implement GPU acceleration at the level of this basis transformation.

3 Standalone basis transformation on the GPU

3.1 Basis transformation algorithm

One method for storing the 3-body input interaction matrix is to use the coupled-JT basis, which adds, or "couples" the angular momenta of the three single-particle states (SPSs) together into one total angular momentum for the 3-body state. Isospin, a quantum number that has to do with whether a nucleon is a proton or a neutron, is similarly coupled. This basis exploits the rotational symmetry of the interaction to reduce the amount of information that must be stored. However, for constructing the many-body matrix elements, we need 3-body interaction matrix elements in an m-scheme basis; that is, we need to "decouple" these coupled-JT matrix elements every time we need a 3-body matrix element in the construction of the many-body matrix. Storing the 3-body interaction matrix in m-scheme would be more efficient for the calculations, but requires much more memory: in one representative case, a 3-body interaction is 33 GB in the m-scheme basis, but only 1 GB in the coupled-JT basis. Substantial memory savings can thus be achieved by storing the input matrix in-core in the coupled-JT basis, and calculating m-scheme elements individually as they are required by MFDn [5, 11, 12].

When MFDn requires a 3-body input interaction matrix element, then, it must convert that element from the coupled-JT basis. From linear algebra, basis transformations of matrices are of the form $A' = D^T A D$, where D is a matrix of projections from one basis to the other. Figure 1 shows a high-level illustration of this transformation. As in any basis transformation, an element in the new basis is a linear combination of elements from the old basis, weighted by the projections in D.

In the coupled-JT to m-scheme transformation, D is developed from a series of angular momentum and isospin coupling coefficients. The matrices A, D, and D^T are never actually constructed in their entirety. MFDn requests 3-body elements from A one-at-a-time, and elements of D are developed as needed for each request; Fig. 2 illustrates the calculation of a single element from A'.

In principle an element of A' is a linear combination of all elements from A. Many elements from A do not contribute, however, because of orthogonality relations that

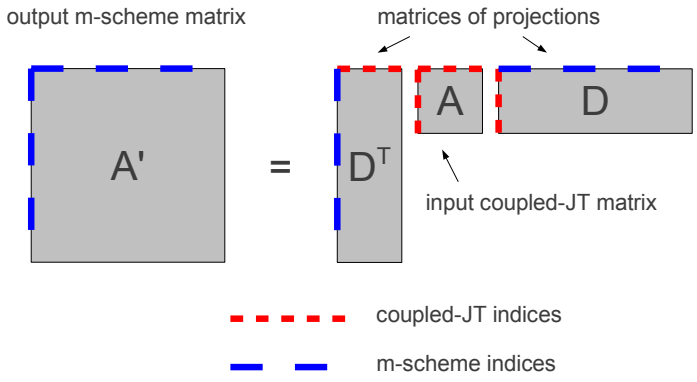

Figure 1: Matrix A is transformed from the coupled-JT basis to the m-scheme basis through multiplication with D and D^T.

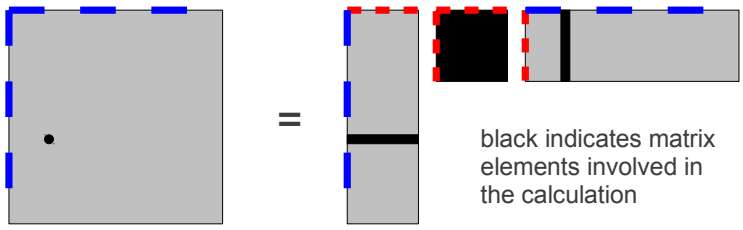

Figure 2: MFDn requests one 3-body element at a time. The single indicated element in A' can be calculated from the indicated elements in A, D, and D^T. In practice, not all the indicated elements are used, as orthogonality relations dictate that many of them are zeroes.

manifest as zeroes in A and D. This sparsity structure is highly predictable and can be exploited. A and A' can be divided into blocks in a way that allows any element in a block in A to be constructed entirely from elements in the corresponding block in A'. Furthermore, all the nonzero elements within that block can be iterated over with a set of nested loops over coupled angular momentum and isospin values.

Only these potentially-nonzero elements are stored, and they are arranged in the order that the nested loops will reference them. The basis conversion routine, then, consists of locating the start of the correct block, going through the nested angular momentum and isospin loops, and adding the elements of A one after the other, each weighted by coupling coefficients calculated from the corresponding angular momentum and isospin values. In practice, because the relevant isospin space is so small, the isospin coupling coefficients are precalculated with several conditionals, and the isospin loops are unrolled into a single weighted summation. The core of the calculation, then, is a set of three nested loops over coupled angular momentum values.

3.2 GPU implementation

The bounds of the inner angular momentum decoupling loop depend on the positions in the outer loops, and the bounds of the outer loops depend on which 3-body element is being calculated. The loop structure is thus irregular. This irregularity makes it difficult to map GPU threads to parts of the problem when dedicating more than one thread to the calculation of a single 3-body element. We parallelized with one 3-body element calculation per GPU thread, invoking the kernel across many 3-body element calculations at once.

We used CUDA to interface with the GPU. We put the nested loop structure into the kernel without modifying it significantly, and added a wrapper function to transfer a chunk of 3-body element requests to the GPU, invoke the kernel, and transfer the results back. MFDn and the decoupling code flatten the SPS quantum numbers into a single linear SPS index, so a 3-body element request takes the form of a set of six SPS indices. We also flattened several arrays that were multidimensional in the CPU-only code so that they could be transferred to and referenced on the GPU more quickly.

Before integrating this GPU acceleration strategy into MFDn, we applied it to a standalone version of the basis transformation code to test performance and act as an intermediate step; we observed a 4x to 10x speedup compared to a multithreaded CPU implementation running on eight cores [13].

4 Integration into MFDn

4.1 A closer look at matrix construction

In the matrix construction stage of MFDn, the many-body Hamiltonian is divided into chunks of elements with similar quantum numbers, and these chunks are apportioned across MPI processes. Each process then splits into OpenMP threads to count, locate, and calculate the nonzero many-body elements. Elements are stored per MPI process in a single array, with a list of column pointers to split them into columns and a secondary array to denote their locations in their columns (compressed row format, or CSR).

The nonzero elements are located in one of two ways. If a block is denser, all elements in it are iterated through and tested for being nonzero. If the block is sparser, all combinations of quantum numbers that could yield nonzero elements are iterated through. MFDn runs through nonzero elements twice during the many-body matrix generation: once to count the nonzero matrix elements so the appropriate arrays can be allocated, and once to calculate them.

4.2 Integration with standalone GPU code

During the construction of the many-body matrix, MFDn uses a recursive loop to calculate the nonzero many-body matrix elements, frequently requesting 3-body matrix elements in m-scheme. In the CPU-only version of MFDn, the decoupling code calculates 3-body elements one-by-one, as they are requested. The GPU version of the decoupling code requires a large block of simultaneous requests to be efficient, so the sequential requests in the CPU code are not ideal. To bridge the gap between MFDn and the GPU decoupling code, we use buffers to store lists of 3-body element requests so large "chunks" of requests can be sent to the GPU at once.

Each OpenMP thread has its own buffer allocated to store requests. On receiving a request, the CPU part of the decoupling subroutine stores the request in the buffer and returns 0. In the CPU-only version, the returned value is added directly to the many-body element under calculation; we must thus also store which many-body element the request pertains to so that it can be added to the correct many-body element when the calculation finishes on the GPU. Furthermore, the 3-body element is added with a specific phase, which must also be stored with the request. Larger buffers are more efficient because the overhead associated with the single CUDA memory copy and kernel invocation is split over more elements. Tests with the standalone code indicate diminishing returns after around 20,000 elements [13] on the supercomputer Dirac at the National Energy Research Scientific Computing Center. Hence, we use here buffers of approximately this size, although further testing may be required to optimize buffer size for the integrated code and for different hardware.

Each OpenMP thread starts in the so-called "accumulating mode" while passing element requests to its buffer until it is full. Then, the thread sends the buffer to the GPU and switches into the so-called "non-accumulating mode". In this mode, the decoupling code runs as in the CPU-only version of MFDn, calculating 3-body elements on the CPU at request and returning them; this allows the CPU to continue work while the GPU, which may be shared among many OpenMP threads, is busy. The thread checks periodically for a completed chunk from the GPU. When it receives the chunk, it iterates through the returned three-body elements in the chunk, multiplies them by the stored phases, and adds them to the array of many-body elements at the stored locations. It then switches back into accumulating mode, and the cycle begins again. At the end of the many-body matrix construction phase, all the 3-body contributions have been added in, either from the GPU calculations or directly from the CPU decoupling code.

5 Technical concerns

5.1 MPI and OpenMP structure of GPU access

We allow the GPU to decide which requests to calculate first. Each OpenMP thread is given its own stream to access the GPU, so at any given time the GPU will have a number of requests open. With this scheme, a single GPU may end up being accessed by multiple MPI processes. This is not possible on all systems, and incurs a performance penalty when it is possible.

One alternative is to restrict the number of MPI processes to the number of nodes used (one per node). The resulting MPI/OpenMP divisions, however, may not be ideal for the NUMA structure of the node, which may incur a performance penalty due to data locality and thread contention issues [10]. Another alternative is to GPU-accelerate only some MPI processes, leaving the others to run as in the CPU-only version. However, using this alternative would derange the almost perfect load-balancing, which is a prominent design feature of the CPU-only version of MFDn, and thus, diminish the benefit of the acceleration. Given these considerations, we opt to accept the performance penalty from multiple MPI processes per GPU on systems where that is possible, and restrict the number of MPI processes to the number of nodes on other systems.

5.2 Indexing the input interaction

The decoupling code requires the use of a six-dimensional index array, which relates quantum numbers to locations in the input coupled-JT interaction matrix. This array is highly jagged: the length along any particular dimension is not constant, but rather depends on the position along the other dimensions. In C, jagged arrays are represented as trees of pointers, wherein the "root" pointer points to an array of pointers, each of which point to further arrays of pointers, and thus until the "leaves", which hold the actual data of the array.

Generating such a structure requires a prodigious number of allocations, as each array at each level must be allocated. On the CPU this is not an issue, but allocations on the GPU must first be requested from the CPU, adding a significant transfer time penalty. Our first attempt did not take this inefficiency into account, and over 90% of the matrix construction time was spent generating the index array on the GPU.

To address this problem, we generated the entire index array in a contiguous block on the CPU, producing a structure wherein the pointers were correct relative to each other. We then applied a constant offset to all the pointers in the index array so that their absolute coordinates would be correct for a contiguous block allocated on the GPU. The entire pointer structure could then be copied into that block with one copy, allowing the index structure to be created on the GPU with a single GPU allocate and GPU copy. With this improvement the index array creation time becomes negligible in the overall matrix construction.

6 Initial experiments

We present results from the DOE supercomputer Titan at the Oak Ridge National Laboratory. Titan is a Cray XK7 supercomputer with 18,688 physical compute nodes, each of which has one 16-core 2.2 GHz AMD Opteron 6274 processor and 32 GB of RAM. Each node is divided into two NUMA domains, and nodes are served in groups of two by Gemini high-speed interconnect routers. Additionally, each node has one NVIDIA K20 Tesla GPU accelerator with 6 GB of memory.

We use the number of non-zeroes in the many-body matrix as a measure of problem size, and test at a variety of problem sizes. The number of nonzeroes is determined by

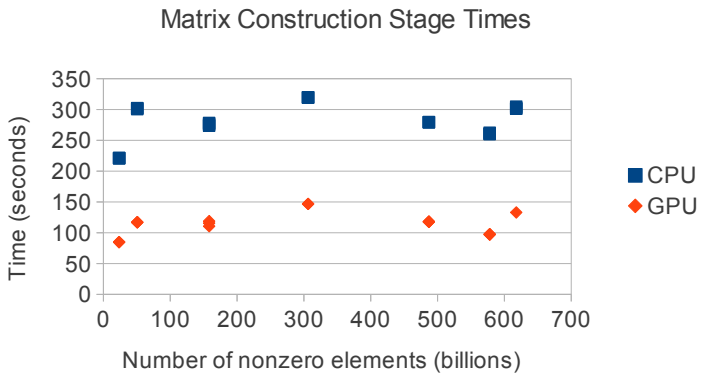

Figure 3: Matrix construction times with CPU-only and GPU-accelerated code.

the choice of nucleus and truncation, so it is difficult to provide a smooth spectrum. Different problem sizes can require vastly different numbers of cores to store the many-body matrix, so we do not test all problems sizes on the same configuration; for each problem size, we allow the many-body matrix to take up half of the total memory, and choose the smallest configuration that satisfies that requirement. We implement and test GPU acceleration in MFDn version 14, and compare against CPU performance using an unmodified build of version 14.

Our primary results are summarized in Figs. 3 and 4: We see a speedup of 2.2x–2.7x in the matrix construction stage. There is no immediately apparent pattern in the dependence of speedup on problem size. The choices of nuclei and truncation parameters required to generate the spectrum of problem sizes are somewhat haphazard, so it is possible that any problem size dependence has become entangled with dependence on those parameters. Despite the individually varying speedup, the range of speedups appears to stay roughly the same; thus the GPU acceleration appears to scale well for the problem sizes investigated.

The speedup over the entire run is a more ambiguous quantity. The time taken in the MFDn diagonalization stage depends on how many eigenvalues are required and the accuracy to which they are required to converge. The speedup over the entire run, which depends on the relative times of the matrix construction and diagonalization stages, therefore depends on these parameters also. For the representative parameter choices used in the matrix construction speedup calculations, the overall speedup is in the 1.2x–1.4x range.

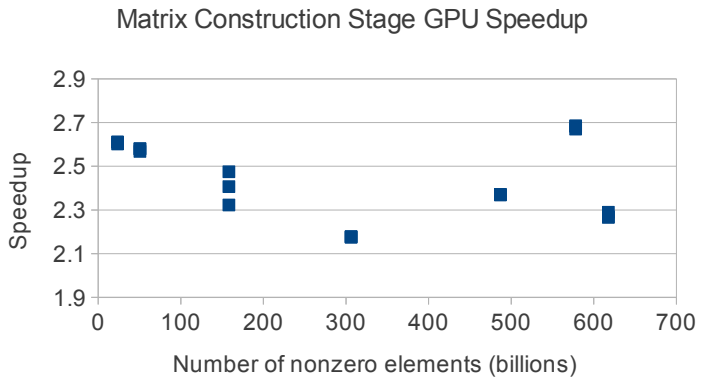

Figure 4: Matrix construction stage speedup with GPU acceleration.

7 Conclusion

We have modified the matrix construction stage of MFDn to run partly on the GPU. The current MFDn implementation stores the matrix elements of the 3-body input interaction in the compressed coupled-JT basis in-core. The conversion of these elements back to m-scheme for use with MFDn is highly parallelizable; we implement this basis transformation on the GPU.

Initial timing results with the GPU-accelerated MFDn code are promising. We have achieved a consistent speedup in the two- to three-fold range for the matrix construction stage, and our speedup scales smoothly to larger problem sizes, at least for those investigated in this paper. It may be possible, though more difficult, to leverage GPU acceleration in the diagonalization stage, or at a higher level in the matrix construction stage; such improvements are left for future consideration.

8 Acknowledgements

This work was supported in part by Iowa State University under the contract DE-AC02-07CH11358 with the U.S. Department of Energy (DOE), by the U.S. DOE under the grants DESC0008485 (SciDAC/NUCLEI), and DE-FG02-87ER40371 (Division of Nuclear Physics), by the Director, Office of Science, Division of Mathematical, Information, and Computational Sciences of the U.S. Department of Energy under contract number DE-AC02-05CH11231, and in part by the National Science Foundation grant NSF/OCI-0941434, 0904782, 1047772. This research was also supported (in part) by the DFG through SFB 634 and by HIC for FAIR.

This research used resources of the Oak Ridge Leadership Computing Facility at the Oak Ridge National Laboratory, which is supported by the Office of Science of the U.S. Department of Energy under Contract No. DE-AC05-00OR22725, and resources of the National Energy Research Scientific Computing Center, which is supported by the Office of Science of the U.S. Department of Energy under Contract No. DE-AC02-05CH11231.

References

[1] P. Navrátil, J. P. Vary and B. R. Barrett, Phys. Rev. Lett. **84**, 5728 (2000).

[2] J. P. Vary, P. Maris, E. Ng, C. Yang, M. Sosonkina, J. Phys. Conf. Ser. **180**, 012083 (2009).

[3] P. Maris *et al.*, J. Phys. Conf. Ser. **403**, 012019 (2012).

[4] P. Sternberg *et al.*, *Accelerating configuration interaction calculations for nuclear structure*, in *Proc. 2008 ACM/IEEE Conf. on Supercomputing*. IEEE Press, Piscataway, NJ, 2008, p. 15:1.

[5] P. Maris *et al.*, J. Phys. Conf. Ser. **454**, 012063 (2013).

[6] P. Maris, M. Sosonkina, J. P. Vary, E. G. Ng and C. Yang, Proc. Comput. Sci. **1**, 97 (2010).

[7] H. M. Aktulga, C. Yang, E. G. Ng, P. Maris and J. P. Vary, *Topology-aware mappings for large-scale eigenvalue problems*, in *Euro-Par 2012 Parallel Processing*, eds. C. Kaklamanis, T. S. Papatheodorou and P. G. Spirakis. Lecture Notes Comput. Sci. **7484**, 830 (2012).

[8] H. M. Aktulga, C. Yang, E. G. Ng, P. Maris and J. P. Vary, *Improving the scalability of a symmetric iterative eigensolver for multi-core platforms*, Concurrency Computat.: Pract. Exper. (2013), DOI: 10.1002/cpe.3129.

[9] NVIDIA, *CUDA C Programming Guide*. http://docs.nvidia.com/cuda/cuda-c-programming-guide/index.html, 2012.

[10] A. Srinivasa, M. Sosonkina, P. Maris and J. P. Vary, Proc. Comput. Sci. **9**, 256 (2012).

[11] R. Roth, J. Langhammer, A. Calci, S. Binder and P. Navrátil, Phys. Rev. Lett. **107**, 072501 (2011).

[12] R. Roth, A. Calci, J. Langhammer and S. Binder, arXiv:1311.3563 [nucl-th] (2013).

[13] D. Oryspayev *et al.*, in *Proc. IEEE 27th Int. Parallel and Distrib. Processing Symp. Workshops & PhD Forum, Boston, Massachusetts, US, 20–24 May, 2013*. 2013, p. 1365.

Recent Advances in MFDn

Chao Yang[a], Hasan Metin Aktulga[a], Pieter Maris[b], Esmond Ng[a] and James Vary[b]

[a] *Computational Research Division, Lawrence Berkeley National Lab, Berkeley, CA 94720*
[b] *Department of Physics and Astronomy, Iowa State University, Ames, IA 50011*

Abstract

The Many-body Fermion Dynamics for nuclear physics (MFDn) code was originally developed by James Vary and his colleagues for performing nuclear configuration interaction (CI) calculations. We describe a number of recent algorithmic and implementation advances in MFDn that enabled it to achieve high performance, and allowed scientists to study properties of light nuclei with high accuracy on modern high performance computers.

Keywords: *High-performance computing; configuration interaction method; matrix diagonalization*

1 Introduction

The MFDn (Many Fermion Dynamics for nuclear structure) software was developed by James Vary and his collaborators at Iowa State University [1, 2]. It is a computational tool for studying nuclear structure.

In MFDn, the nuclear Hamiltonian is evaluated in a large harmonic oscillator single-particle basis and diagonalized by iterative techniques to obtain the low-lying eigenvalues and eigenvectors. The eigenvectors are then used to evaluate a suite of experimental quantities to test accuracy and convergence issues. In several respects, the approach is similar to the Full Configuration Interaction (FCI) method in other fields [3, 4]. We often obtain convergence, either by direct diagonalization or simple extrapolation, and we then claim we have the result of an exact calculation.

In this paper, we describe a number of recent algorithmic and implementation advances that made MFDn highly efficient on modern high performance computers.

The paper is organized as follows. In Section 2, we will review the general formulation of the nuclear many-body problem and the nuclear CI methodology used in MFDn for computing a few lowest energy states of a nuclear structure. The implementation details of several key components of MFDn are presented in Sections 3 to 7.

2 Background

The structure of an atomic nucleus with k nucleons is described by a many-body wavefunction $\Psi(\mathbf{r}_1, \mathbf{r}_2, \ldots, \mathbf{r}_k)$, where $\mathbf{r}_j \in \mathbb{R}^3$, $j = 1, 2, \ldots, k$. The wavefunction satisfies the many-body Schrödinger equation

$$H\Psi(\mathbf{r}_1, \mathbf{r}_2, \ldots, \mathbf{r}_k) = \lambda\Psi(\mathbf{r}_1, \mathbf{r}_2, \ldots, \mathbf{r}_k), \tag{1}$$

Proceedings of International Conference 'Nuclear Theory in the Supercomputing Era — 2013' (NTSE-2013), Ames, IA, USA, May 13–17, 2013. Eds. A. M. Shirokov and A. I. Mazur. Pacific National University, Khabarovsk, Russia, 2014, p. 272.
http://www.ntse-2013.khb.ru/Proc/Yang.pdf.

where H is a many-body Hamiltonian that relates a nucleus configuration defined by Ψ to the energy of the system. We denote the energy of the system by λ. The many-body Hamiltonian H is defined as

$$H = \frac{1}{k} \sum_{i<j} \frac{(\mathbf{p}_i - \mathbf{p}_j)^2}{2m} + \sum_{i<j=1}^{k} V_n(\mathbf{r}_i - \mathbf{r}_j), \tag{2}$$

where m is the nucleon mass, $\mathbf{p}_i$ is a momentum operator, and $V_n(\mathbf{r}_i - \mathbf{r}_j)$ is a two-body potential operator that describes the interaction between the ith and jth nucleons. A more accurate treatment of the problem may include three-body potentials. Clearly, the wavefunction Ψ is an eigenfunction of H associated with the eigenvalue λ.

For nuclei that consist of a few nucleons (less than five), there are several methods to solve (1) directly. However, as k becomes larger, the size of the problem will become so large that approximate methods are necessary. One way to overcome the dimensionality explosion is to project the many-body Hamiltonian into a lower dimensional subspace $\mathcal{S}$ spanned by a set of *Slater determinants* defined as

$$\Phi_a(\mathbf{r}_1, \mathbf{r}_2, \dots, \mathbf{r}_k) = \frac{1}{\sqrt{k!}} \begin{vmatrix} \phi_{a_1}(\mathbf{r}_1) & \phi_{a_2}(\mathbf{r}_1) & \dots & \phi_{a_k}(\mathbf{r}_1) \\ \phi_{a_1}(\mathbf{r}_2) & \phi_{a_2}(\mathbf{r}_2) & \dots & \phi_{a_k}(\mathbf{r}_2) \\ \vdots & \vdots & & \vdots \\ \phi_{a_1}(\mathbf{r}_k) & \phi_{a_2}(\mathbf{r}_k) & \dots & \phi_{a_k}(\mathbf{r}_k) \end{vmatrix}, \tag{3}$$

where ϕ_{a_i} is the eigenfunction associated with the a_i-th eigenvalue of a (single-particle) Hamiltonian $h = \mathbf{p}^2/2m + v(\mathbf{r})$. Conventionally, one uses a harmonic oscillator potential, which is quadratic in $\mathbf{r}$. The use of Slater determinants is a standard technique employed in quantum mechanics.

In this paper, we define the index of $\Phi_a(\mathbf{r}_1, \mathbf{r}_2, \dots, \mathbf{r}_k)$ by a strictly increasing k-tuple of integers, i. e. $a = (a_1, a_2, \dots, a_k)$, where a_i is simply the index of the single-particle eigenfunction that appears in the ith column of the Slater determinant. We will refer to $\Phi_a(\mathbf{r}_1, \mathbf{r}_2, \dots, \mathbf{r}_k)$ or simply a as a *many-body basis state*. We will call each component of a a *single-particle state*. Not all many-body basis states are valid because each has to satisfy a set of conditions to be defined later. We denote the set of all valid many-body basis states $\{a\}$ by $\mathcal{A}$. The size of $\mathcal{A}$ will be denoted by $n = |\mathcal{A}|$.

Suppose the desired many-body wavefunction can be well represented by a linear combination of the basis functions Φ_a ($a \in \mathcal{A}$), i. e.,

$$\Psi = \sum_{a \in \mathcal{A}} c_a \Phi_a, \tag{4}$$

where $c_a \in \mathbb{R}$, we can then solve (1) by computing eigenpairs of a projected Hamiltonian $\hat{H}$, where

$$\hat{H}_{a,b} = \int_{\Omega} (\Phi_a^* H \Phi_b)\, d\mathbf{r}_1 d\mathbf{r}_2 \dots d\mathbf{r}_k. \tag{5}$$

Because H is self-adjoint, $\hat{H}$ is real symmetric. The eigenvector of $\hat{H}$ associated with the desired eigenvalue (energy) gives the coefficients c_a in (4).

Clearly, the dimension of $\hat{H}$, which is the total number of valid many-body basis states $|\mathcal{A}|$, depends on the total number of nucleons (k) contained in the nucleus of interest and the largest single-particle state ($a_{\max}$) allowed in $\Phi_a(\mathbf{r}_1, \mathbf{r}_2, \dots, \mathbf{r}_k)$, which is implicitly determined by a constraint imposed on the total oscillator quanta ($N_{\max}$). For a large nucleus with many nucleons and large $a_{\max}$ value, n can be extremely large. However, the number of nonzero elements in $\hat{H}$ is typically very small, as we will show below.

It follows from the mutual orthogonality of all single-particle eigenfunctions ϕ_ℓ ($\ell = 1, 2, \dots, a_{\max}$) that a one-body integral in (5) becomes zero when a and b differ

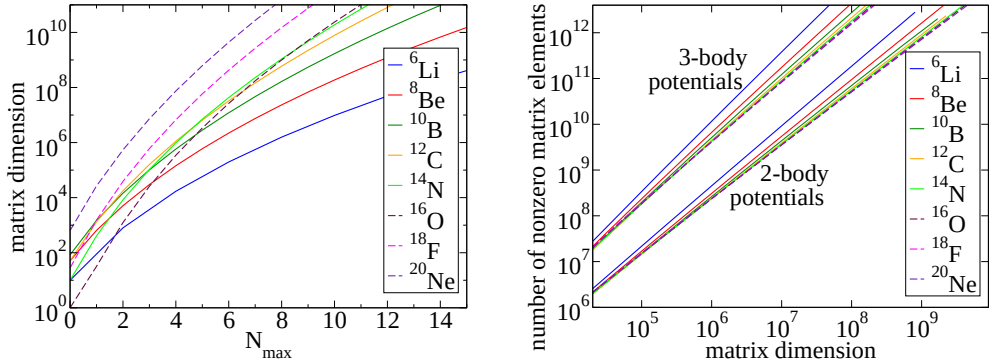

(a) The growth of the matrix dimension ($|\mathcal{A}|$) with respect to $N_{\max}$

(b) The growth of number of nonzero matrix elements in $\hat{H}$ with respect to $|\mathcal{A}|$

Figure 1: The characteristics of the CI projected Hamiltonian $\hat{H}$ for a variety of nuclei.

by more than one single-particle state, and a two-body integral becomes zero when a and b differ by more than two single-particle states, etc. This observation allows us to determine many of the zero entries of $\hat{H}$ without evaluating the numerical integral in (5).

Empirical evidence suggests that the probability of two randomly chosen but valid many-body basis states sharing more than $k-2$ single-particle states is relatively low. As a result, $\hat{H}$ is extremely sparse. Figure 1 shows both the growth of the matrix dimension ($|\mathcal{A}|$) with respect to $N_{\max}$ and the growth of the number of nonzero elements in $\hat{H}$ with respect to $|\mathcal{A}|$ for a variety of nuclei for both two-body and two- plus three-body potentials. In practice, we observe that the number of non-zeros in $\hat{H}$ is proportional to $|\mathcal{A}|^{3/2}$.

To compute the eigenvalues of $\hat{H}$ efficiently on a high performance parallel computer, the following three issues must be addressed carefully:

1. The generation and distribution of the many-body basis states — This step essentially determines how the matrix Hamiltonian $\hat{H}$ or $\hat{H}_Z$ is partitioned and distributed in subsequent calculations.

2. The construction of the sparse matrix Hamiltonian $\hat{H}$ — This step is performed simultaneously on all processors. Each processor will construct its portion of $\hat{H}$ defined by the many-body basis states assigned to it. Because the positions of the nonzero elements of the Hamiltonian is not known a priori, the key to achieving good performance during this step is to quickly identify the locations of these elements without evaluating them numerically first.

3. The calculation of the eigenvalues and eigenvectors using the Lanczos iteration — The major cost of the Lanczos iteration is the computation required to perform sparse matrix-vector multiplications of the form $y \leftarrow \hat{H}x$, where x, y are both vectors. Performing efficient orthogonalizations of the Lanczos basis vectors is also an important issue to consider.

3 Parallel basis generation

Because the rows and columns of $\hat{H}$ are indexed by valid many-body basis states, the first step of the nuclear CI calculation is to generate these states so that they can be used to construct and manipulate matrix elements of $\hat{H}$ in subsequent calculations. It

is desirable to generate the valid many-body basis states in parallel on different processors to 1) reduce the basis generation time, 2) allow Hamiltonian to be distributed and constructed in parallel in subsequent computation.

Because the set of valid many-body states cannot be described by a simple expression, the strategy we adopt is to enumerate all possible many-body basis states in some order and pick out the ones that satisfy a set of constraints to be defined below.

When single-particle wave functions ϕ's in (3) are chosen to be eigenfunctions of a harmonic oscillator, each a_i corresponds to a set of quantum numbers (n, l, j, m_j), where $n \geq 0$ is the quantum number that is associated with the radial component of the eigenfunction, $l \geq 0$ is the angular momentum of the single-particle, j, which is either $|l - 1/2|$ or $l + 1/2$, is the coupled spin-angular momentum, and m_j, which can assume the values of $-j, j + 1, \ldots, j - 1, j$ is the projection of the spin-angular momentum to a particular spatial axis, often chosen to be the z axis. Single-particle states are typically ordered by their energy levels (i. e., the corresponding eigenvalues of the harmonic oscillator Hamiltonian). The energy of the single particle associated with (n, l, j, m_j) can be labeled by $N = 2n + l$, which is degenerate. Single-particle states associated with each degenerate energy level are typically ordered by their m_j values.

If the maximum index of the allowed single-particle state is $a_{\max}$, the total number of different $\Phi_a(\mathbf{r}_1, \mathbf{r}_2, \ldots, \mathbf{r}_k)$ is $\begin{pmatrix} a_{\max} \\ k \end{pmatrix}$, which can be extremely large. However, in many cases, interesting physics of a nucleus can be ascertained from a much smaller model (or configuration) space that contains far fewer $\Phi_a(\mathbf{r}_1, \mathbf{r}_2, \ldots, \mathbf{r}_k)$'s that satisfy additional constraints. In MFDn, these constraints include

1. Oscillator excitation quanta constraint: $\sum_{i=1}^{k} N(a_i) \leq N_{\max}$, where $N(a_i)$ is the oscillator quanta with the ith single-particle, and $N_{\max}$ is known as the maximum oscillator excitation quanta chosen in advance. Clearly, the larger the $N_{\max}$ value, the larger the model space is.

2. Magnetic projection constraint: $\sum_{i=1}^{k} m_j(a_i) = m$, where $m_j(a_i)$ is the m_j value associated with the ith single-particle and m is a total magnetic projection constant chosen in advance

3. Parity constraint.

After imposing these constraints, a majority of the enumerated many-body basis states can be eliminated. A many-body basis state satisfying all three conditions above is a *valid* state. The easiest way to generate all many-body basis states is to enumerate them in a lexicographical order defined below. A many-body basis state $a = (a_1, a_2, \ldots, a_k)$ is said to be *lexicographically less than* another many-body basis state $b = (b_1, b_2, \ldots, b_k)$ if and only if there is a j for which $a_j < b_j$ and $a_i = b_i$ for all $i < j$. For example, if $a_{max} = 9$, then $(1, 3, 4, 8)$ is succeeded by $(1, 3, 4, 9)$, which is in turn succeeded by $(1, 3, 5, 6)$, and $(1, 3, 8, 9)$ is succeeded by $(1, 4, 5, 6)$. The details on how valid many-body states are enumerated can be found in [5].

To carry out nuclear CI calculation on a distributed-memory parallel computer, the projected Hamiltonian $\hat{H}$ must be partitioned and distributed among different processors. Associated with this partition is a partition and distribution of the many-body basis states.

Because $\hat{H}$ is symmetric, we generate and store only the lower triangular part of the matrix to minimize memory usage. To create the matrix and processor mapping, we first partition $\hat{H}$ into rectangular blocks of roughly the same size and map the matrix blocks in the lower triangular part of the 2D partition to different processors. Figure 2 illustrates one way to map matrix blocks to 6 processors. We label each distributed block by a processor identification (pid) number that ranges from 1 to n_p, where n_p is the total number of processors in use. Due to the particular distribution

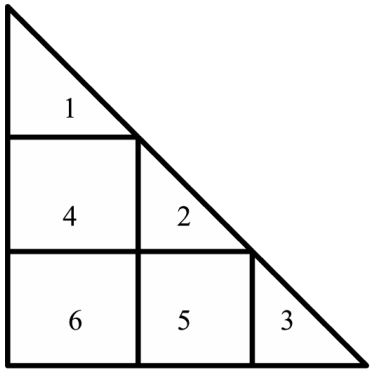

Figure 2: The projected Hamiltonian $\hat{H}$ is partitioned and distributed among 6 processors.

pattern shown in Fig. 2, the choice of n_p is not arbitrary. If we let n_d be the number of diagonal blocks in the partition, then $n_p = n_d(n_d + 1)/2$. For reasons that we will explain later n_d is typically chosen to be an odd integer. In the following, we will refer to the processors to which the diagonal blocks of $\hat{H}$ are assigned as the diagonal processors. They are labeled by 1 through n_d in Fig. 2. In MFDn, row and column communication groups are created to allow information to be passed among processors associated with row or column blocks of $\hat{H}$. As we will explain later, the matrix block to processor mapping shown in Fig. 2 is not the most efficient.

To avoid moving the matrix elements of $\hat{H}$ among different processors and to speed up the construction of $\hat{H}$, we generate the each submatrix block in (2) simultaneously. Each processor must have two sets of many-body basis states (one corresponding to the row indices and the other corresponding to the column indices except when the submatrix block is one the diagonal. In that case, the row many-body basis states are identical to the column many-body basis states.)

In MFDn, these many-body states are generated in parallel on the diagonal processors only. The ith diagonal processor is responsible for enumerating $n_d \cdot m + i$th many-body state and checking its validity. The invalid ones are simply discarded. This generation scheme naturally leads to a nearly cyclic distribution of the valid many-body states. Once a set of valid many-body basis states generated on the ith diagonal processor, they are broadcast to all processors that belong to same column and row processor groups that contain the ith diagonal processor.

The nearly cyclic distribution of the valid many-body states leads to balance load among different processors because both the sizes of the blocks assigned to different processors and the number of nonzero matrix elements of $\hat{H}$ are approximately the same [5].

Sometimes, it is convenient to partition or group valid many-body states in some way so that they can be generated one group at a time. One way to perform such a partition is to use the $\{n, l, j\}$ quantum numbers associated with all single-particle states in Φ_a as guidance. In this case, a group of many-body basis states associated with a particular sequence of (n, l, j) quantum numbers $\{\bar{n}_i, \bar{l}_i, \bar{j}_i\}$ $(i = 1, 2, ..., k)$ is defined to be

$$\mathcal{G}(\{\bar{n}_i, \bar{l}_i, \bar{j}_i\}) \equiv \{\Phi_a | n(a_i) = \bar{n}_i, l(a_i) = \bar{l}_i, j(a_i) = \bar{j}_i), \quad \text{for} \quad i = 1, 2, ..., k\}. \tag{6}$$

This particular choice of grouping is useful because the set of many-body states that belong to the same $\mathcal{G}(\{\bar{n}_i, \bar{l}_i, \bar{j}_i\})$ is invariant under the magnitude square of the total spin-angular momentum operator $\hat{\mathbf{J}}$, which is often denoted by J^2.

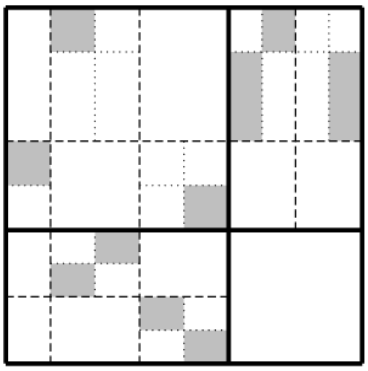

Figure 3: A three-level blocking of a portion of the Hamiltonian matrix $\hat{H}$ distributed to an off-diagonal processor. The first (coarsest) level blocks are bordered by solid lines. The second level of blocks are bordered by thinner dashed lines. The finest level blocks are bordered by dotted lines, and those blocks containing non-zeros are shaded.

4 Hamiltonian construction

A pair of many-body states that differ by no more than K single-particle states with respect to a Hamiltonian that contains at most K-body interactions is called an interacting pair. A non-interacting pair corresponds to a zero matrix element indexed by these two states. Such a matrix entry does not need to be evaluated or stored.

Once all many-body basis states have been generated, we can determine the nonzero structure of the Hamiltonian matrix by comparing each pair of many-body basis states. However, this brute-force approach of exhaustive comparison requires time proportional to the square of the number of many-body states. Even though each such pairwise test is very simple, the sheer number of them renders this process prohibitively expensive.

A more efficient way to determine the nonzero structure of the Hamiltonian was developed in [5]. It is based on the observation that the Hamiltonian matrix typically contains large blocks of zeros. The basic idea is to identify these large blocks of zeros by separating many-body basis states into different groups and assigning a group identification (id) to each group. Instead of performing pairwise comparisons of many-body basis states, we can first perform pairwise comparisons of group id's. Such comparison allows us to identify a block that contains zeros only with a single comparison. Pairwise comparisons of individual many-body basis states only need to be performed for blocks that are identified to contain nonzero matrix elements. Furthermore, this approach can be implemented recursively, which leads to a hierarchical scheme for identifying zero matrix blocks. Figure 3 gives a schematic illustration of what a three-level blocking of a Hamiltonian will look like. The shaded blocks represent the finest level blocks that contain nonzero matrix elements. In this particular case, a large block of zeros, the (2,2)-block bordered by solid lines, is identified at the coarsest level. Nine intermediate-sized zero blocks can be found at the second level. Sixteen small zero blocks can be seen at the finest level.

5 Algorithms for computing a few eigenvalues

A natural algorithm for computing a selected few eigenvalues and their corresponding eigenvectors of $\hat{H}$ is an iterative method that does not require storing all $|\mathcal{A}| \times |\mathcal{A}|$ matrix elements. In nuclear physics, the eigenvalues of interest are those at the low end

of the spectrum of $\hat{H}$ because they describe the ground and the first few excited states of the nucleus. In MFDn, these eigenvalues are computed by the Lanczos method, which projects $\hat{H}$ into a *Krylov* subspace $\mathcal{K}(\hat{H}, v_0) = \text{span}\{v_0, \hat{H}v_0, \ldots, \hat{H}^{\ell-1}v_0\}$ of dimension $\ell \ll n$, where $v_0 \in \mathbb{R}^n$ is an arbitrarily chosen starting vector. If $V = (v_1, v_2, \ldots, v_\ell)$ consists of an orthonormal basis of $\mathcal{K}(\hat{H}, v_0)$, the Lanczos method can be described by

$$\hat{H}V = VT + fe_\ell^T, \tag{7}$$

where $T = V^T\hat{H}V$ is an $\ell \times \ell$ tridiagonal matrix that represents the projection of $\hat{H}$ into $\mathcal{K}(\hat{H}, v_0)$, f is a residual vector that satisfies $V^T f = 0$, and e_ℓ is the ℓ-th column of the identity matrix. Approximations to eigenvalues of $\hat{H}$ can be obtained by computing eigenvalues of the much smaller matrix T. If q is an eigenvector of T associated with the eigenvalue θ, then $z = Vq$ is the approximation to an eigenvector of $\hat{H}$.

It is well known that well separated extremal eigenvalues converge rapidly in the Lanczos iteration [6]. Convergence can be further improved by carefully choosing the starting vector v_0 and refining it using the implicitly restarted Lanczos algorithm developed in [7] and implemented in [8]. The major cost of the algorithm is the matrix-vector multiplication $w \leftarrow \hat{H}v$ required at each iteration.

An alternative way to compute the k algebraically smallest eigenvalues is to formulate the eigenvalue problem as the following constrained minimization problem

$$\min_{Z^TZ=I} \text{trace}(Z^T\hat{H}Z), \tag{8}$$

where $Z \in \mathbb{R}^{|\mathcal{A}|\times k}$. This constrained minimization problem can be solved by preconditioned Davidson–Liu method [9] or the locally optimal block preconditioned conjugate gradient method [10]. Without a preconditioner, the convergence properties of these methods are similar to that of the Lanczos algorithm. However, when a good preconditioner is available, these methods can be much faster. Sparse matrix vector multiplication constitutes the major cost of this algorithm also.

Because it is not yet clear how to construct a good preconditioner for this type of problem, we will focus on the Lanczos algorithm in the subsequent discussion.

6 Scalable implementation

We now describe some techniques for implementing the Lanczos algorithm efficiently on large-scale distributed memory parallel high performance computers. The computational cost of the Lanczos iteration is dominated by the sparse matrix vector multiplications (SpMV) $w \leftarrow \hat{H}v$ required to expand the Krylov subspace, as well as dense matrix vector multiplications required to maintain orthonormality among columns of V.

6.1 Topology aware task-to-processor mapping for SpMV

To perform the SpMV operations efficiently on a lower triangular processor grid laid out as in Fig. 2, each input vector is partitioned among the diagonal processors.

A natural way to distribute a vector v to be multiplied by the distributed A matrix is to partition it conformally with the column partition of A into n_d subvectors $\{v_i\}$, $i = 1, 2, \ldots, n_d$ as shown in Fig. 4. Row and column communication groups are set up to allow v_i to be broadcast among processing units that lie on the ith row or column of the triangular grid. If we denote the submatrix of A assigned to the (i, j)th processing unit by $A_{i,j}$, each processing unit performs two SpMVs of the form $w_i = A_{i,j}v_j$ and $w_j = A_{i,j}^T v_i$. As depicted in Fig. 4, two reductions are required (one along the row communication groups and one along the column communication groups) to merge local products w_i and w_j to form the global result vector w.

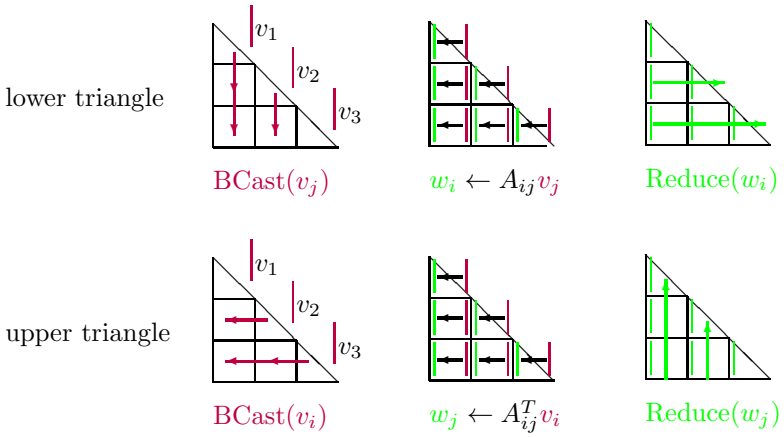

Figure 4: The decomposition of a symmetric matrix over a 2D triangular processing grid and the communication operations required during the parallel SpMV phase. Little triangular blocks along the matrix diagonal correspond to diagonal processors, and little squares correspond to off-diagonal processors. Each processor is responsible for communications and computations associated with the submatrix assigned to it.

The simple parallel SpMV scheme described above has a serious pitfall. Since different communication groups contain different number of processing units, the communication volume is not balanced among different communication groups. For example, the first column group contains n_d processing units, whereas the n_dth column group consists of a single processing unit only. This imbalance may cause significant load imbalances in large-scale computations. To address this, we extend the triangular grid on the left in Fig. 5 to a square grid on the right and place $n_d(n_d+1)/2$ processing units on this grid in such a way that each row or column of the square grid contains exactly $(n_d+1)/2$ processing units. (This is why we require n_d to be an odd integer.) We require that the processing unit that receives the $A_{i,j}$ submatrix to be placed on either the (i,j)th or the (j,i)th grid point, but not both. In particular, if the condition $i-j \leq (n_d+1)/2$ is satisfied, then the processing unit $P_{i,j}$ is placed on the (i,j)th grid point, otherwise it is placed onto the (j,i)th grid point. As a result, we can then create row and column communication groups with equal number of processing units based on the location of each processing unit on the square grid.

Although the above strategy ensures that the communication volume among different communication groups is balanced, the actual performance of the program will

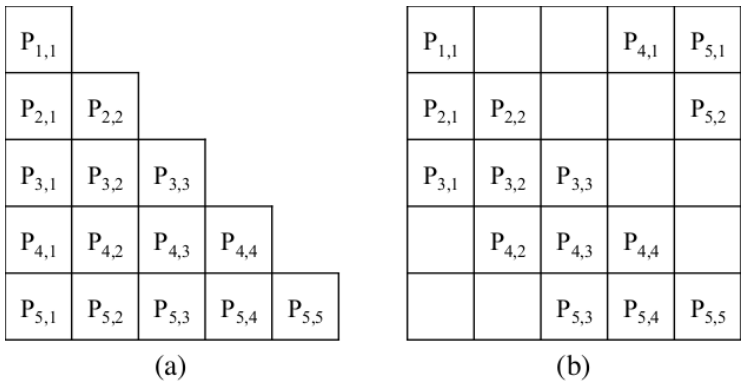

Figure 5: The layout of fifteen processing units (a) on a 2D lower triangular grid topology and (b) on a 5×5 square grid to balance row and column communication groups.

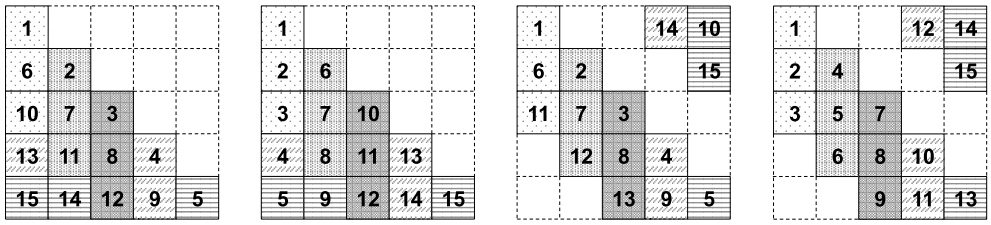

Figure 6: A schematic illustration of several different mapping schemes for a 5×5 grid, from left to right: DM, CM, BDM and BCM. Tasks mapped to the same column (row) of the grid belong to the same column (row) communication groups. Tasks with the same fill patterns belong to the same groups created for basis orthogonalization.

depend on other factors. The mapping between computational tasks and physical processing units has a strong influence, too.

There are many ways to map task blocks defined in Fig. 5 to different processors, see Fig. 6. The performance of different mapping schemes can be predicted from several metrics associated with a network load model that depends on the topology of the processor layout [11,12]. The task-to-process mapping should be defined in a way to minimize the effective load on the network measured in addition to communication volume imbalance. In particular, if we assign $1, 2, \ldots, n_{\mathrm{d}}$ to the diagonal processors first, and continue the assignment for each of the subdiagonals until all processors on the triangular grid are labeled, a scheme which we refer to as the diagonal-major (DM) ordering of processors, the measured performance of the parallel SpMV is relatively poor. On the other hand, if we go through the triangular processor grid column by column, and assign $1, 2, \ldots, n_{\mathrm{d}}$ along the way, which gives the column-major (CM) ordering, the performance of SpMV is much better.

6.2 Basis orthogonalization

To eliminate spurious eigenvalues [6], MFDn performs full orthogonalization among the columns of V in (7). As the number of columns in V increases, orthogonalization can become a computational bottleneck if it is not effectively parallelized.

For basis orthogonalization, we reconfigure the 2D triangular grid used for parallel SpMV into a $n_d \times (n_d + 1)/2$ rectangular processing grid as shown in Fig. 7(a). In an earlier version of MFDn [5], we used a 2D cyclic distribution of the columns of V, Fig. 7(b). In this scheme, communicating the local pieces of w, which we denote by w_i, among row communication groups of the 2D rectangular grid require expensive broadcast and reduction operations. We estimate the total communication volume to be $\mathcal{O}(n_d \times n)$ in this case. When the dimension of A is extremely large and the number of processing units used in the computation is large, this communication overhead significantly hinders the scalability of MFDn.

It turns out that we can reduce the communication overhead associated with basis orthogonalization by using a hierarchical 1D distribution of the basis vectors among all processing units. Note that each basis vector v was already divided into n_d subvectors v_j, $j = 1, 2, \ldots, n_d$ for SpMV computations, where each v_j is associated with the jth column group in the 2D square grid (Fig. 5). Each subvector v_j can then be partitioned further into $(n_d + 1)/2$ subvectors and distributed among processing units within the same column communication group, as shown in Fig. 7. In this case, the expensive broadcast operation required with the 2D cyclic distribution is replaced with a gathering operation (by `MPI_Gatherv`), which involves a communication volume of $\mathcal{O}(n)$. Similarly, the reduce operation after orthogonalization is replaced with a scattering operation (by `MPI_Scatterv`). The scattering operation involves $\mathcal{O}(n)$ data transfer, as well. As a result, when the basis vectors are partitioned hierarchically

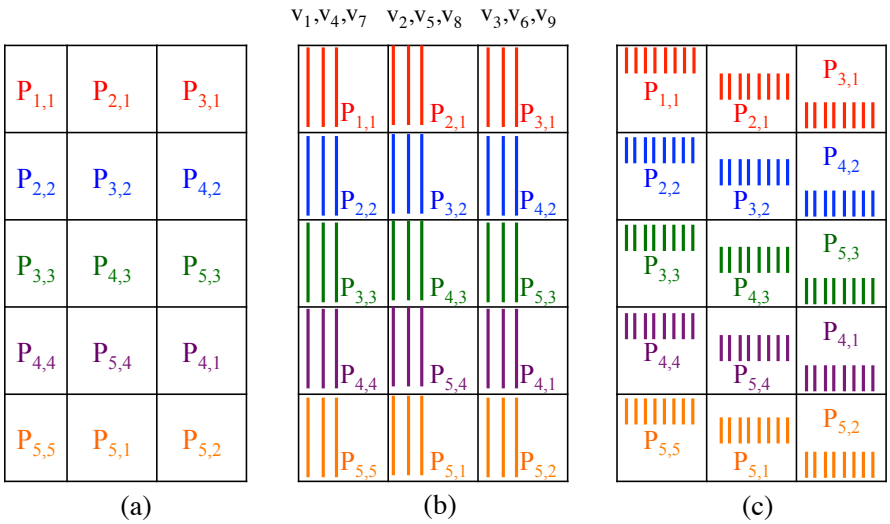

Figure 7: (a) 2D rectangular grid for 15 processors. (b) 2D cyclic distribution of the first 9 basis vectors in V over the 5×3 rectangular grid. (c) Hierarchical 1D distribution of the basis vectors in V. With this distribution, the vector w is first partitioned into 5 subvectors $\{w_i\}$, $i = 1, 2, \ldots, 5$, conformally with the column partitioning of A. Each subvector w_i is further partitioned into 3 shorter vectors, to be scattered to the processing units with matching labels.

in 1D, the total communication volume is $\mathcal{O}(n)$ instead of the $\mathcal{O}(n_d \times n)$ volume associated with the 2D cyclic distribution discussed earlier.

6.3 A hybrid MPI/OpenMP implementation

In recent years, distributed memory multi-core machines have become widely available for high performance computing. This trend is likely to continue in the foreseeable future. On such type of machine, a number of compute nodes are connected via a high speed communication network. Within each node, several processing units (or cores) share a common pool of memory. Such architecture allows us to reduce communication overhead and improve the throughput of computation by combining message passing based parallelization with thread based concurrency.

An effective technique for reducing communication volume is to restrict MPI communication among nodes that do not share a common pool of memory. This can be achieved through a hybrid programming paradigm, where local computations are performed in parallel using a thread based programming model such as OpenMP, and communication among nodes is done through MPI primitives. To perform a multi-threaded SpMV on a single node, we use the well-known compressed sparse column (CSC) method. The OpenMP parallelization for SpMV computations is performed at the outer-loop level. The columns of the sparse submatrix are assigned to OpenMP threads dynamically in chunks. The chunk size is chosen large enough to minimize the dynamic load distribution overheads, while maintaining a good load balance among threads.

The main benefit of a hybrid parallel implementation is the reduction in the memory footprint of large-scale computations [13]. Another important benefit is the reduced communication volume during the broadcast of v and reduction of w vectors, which is $\mathcal{O}(n \times n_d)$. This implies that for the same computation (so n is fixed), reducing the number of diagonal processing units n_d would lead to reduced communication overheads. Since $n_d \approx \sqrt{2n_p}$, by defining a processing unit to be a single CPU with t cores while fixing the total number of cores used at n_p, we effectively reduce the number of MPI processes by a factor of $\sqrt{t}$. Consequently, using hybrid MPI/OpenMP

parallelization, the overall communication volume is reduced by a factor of $\sqrt{t}$ compared to a pure MPI implementation.

In the case of basis orthogonalization, the dense matrix vector multiplication performed on each node can be performed by simply calling a thread-enabled BLAS subroutine `dgemv`, which is now standard in the math libraries of multi-core platforms. Since the amount of data transfer required in a hierarchical 1D distributed basis orthogonalization scheme is $\mathcal{O}(n)$ and independent of the number of processing units, there is no reduction in the communication volume in this phase.

In addition to reducing communication volume, a hybrid OpenMP/MPI implementation on a distributed multi-core system also provides opportunities for hiding communication overhead by overlapping communication with computation. It is possible to implement a symmetric SpMV with a single pass over the elements of the sparse matrix where both the lower triangular and upper triangular calculations are performed together. The key observation that allows us to hide communication during the SpMV phase is that the symmetric SpMV computations can be divided into two subtasks: $w_i = A_{ij}v_j$ (which corresponds to the lower triangular part in Fig. 4) and $w_j = A_{ij}^T v_i$ (the upper triangular part). Such a separation breaks certain data dependencies during SpMV computations. Now the input for the second subtask, v_i, is not required by the first subtask and the output of the first subtask, w_i, can be reduced independently of the second subtask. We should note that going over the matrix elements twice by dividing the SpMV into two subtasks will induce a performance penalty. But since the matrix elements are streamed sequentially from memory, the additional burden on the memory subsystem is low compared to the irregular accesses to vector elements during SpMV.

In a pure MPI implementation of the symmetric SpMV, each processing unit is responsible for both communication and computation. As shown in Fig. 8, in the absence of non-blocking collective MPI primitives, effective overlapping of communication and computation in a pure MPI implementation is not trivial.

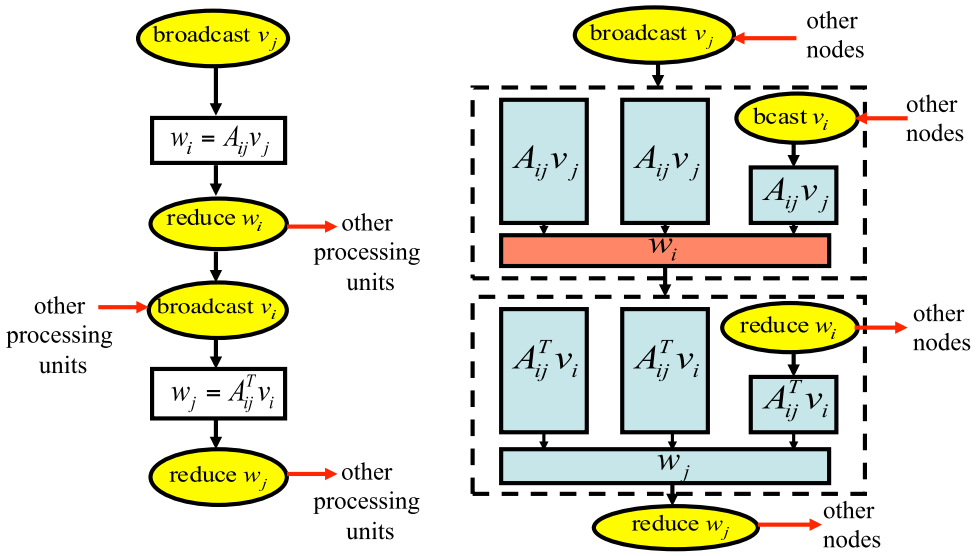

Figure 8: In a pure MPI implementation of a parallel symmetric SpMV on an off-diagonal processing unit (left subfigure), the communication blocks (yellow) separates the computational blocks (light blue). No communication/computation overlapping is possible. However, in a hybrid OpenMP-MPI implementation (right subfigure), the broadcast of v_i can be overlapped with the $w_i = A_{ij}v_j$ computation, and the reduction of w_j can be overlapped with the $w_j = A_{ij}^T v_i$ computation. The red blocks indicates where thread synchronization, which has very little overhead, is required.

However, in the hybrid OpenMP/MPI programming model where a processing unit runs on multiple cores, we may delegate one core (and the thread mapped to this core) to perform the communication, while other cores (and their corresponding threads) perform computations in parallel. As a result, the broadcast of v_i can be overlapped with the computations of the first subtask. Similarly, the reduction on w_i can be done while the computations of the second subtask are being still being carried out.

The hybrid OpenMP/MPI implementation of SpMV illustrated on the right in Fig. 8 hides the collective communications performed within row groups. When communication groups are created by using a column major ordering as discussed in section 6.1, communications along row groups tend to be the costliest ones because processing units that belong to the same row communication group are likely to be far apart from each other, as opposed to consecutively rank processing units within a column communication group [14]. Hence hiding communications within row groups is expected to have a large impact on the overall performance of the computation.

Note that in our scheme, there is no rigid designation of threads such as a communication thread or a computation thread. Since we dynamically schedule the computations among threads during SpMV, once the thread responsible for broadcasting v_i completes this communication task, it can join other threads in the multi-threaded computations of $w_i = A_{ij}v_j$. In addition, the reduction of w_i can be efficiently overlapped with the calculations of $w_j = A_{ij}^T v_i$ using the same technique, as shown in Fig. 8.

7 Computational example

In this section, we report performance gains achieved by incorporating the techniques discussed above in MFDn. We use one particular example to demonstrate performance gain. More performance results can be found in [11,12]. The test problem we selected is the ^{10}B nucleus. We are interested in computing 10 algebraically smallest eigenvalues of the Hamiltonian matrix $\hat{H}$ constructed by setting $N_{\max} = 8$ and $M_j = 1$. A 2-body interaction potential is used. The dimension of the matrix is roughly 4.8×10^8 and it contains roughly 1.2×10^{12} nonzero matrix elements in the lower triangular part of the matrix.

Table 1 lists five different implementations of a parallel Lanczos algorithm. They correspond to progressive improvements we made in terms of task to processor mapping, the way the Lanczos basis vectors are distributed, and whether there is any overlap between computation and communication. The pure MPI implementation where processes are arranged on a triangular grid in a diagonal major (DM) order

Table 1: Five versions of parallel implementations of the Lanczos algorithm. They differ by task to processing mapping, which is related to process ordering, the way the Lanczos basis vectors are distributed and whether there is any overlap between computation and communication.

Version	Parallelization Strategy	Process Ordering	Ortho. Scheme	Comm Overlapping
*ver*1	MPI only	DM	2D Cyclic	none
*ver*2	MPI/OpenMP	DM	2D Cyclic	none
*ver*3	MPI only	BCM	1D Hierarchical	none
*ver*4	MPI/OpenMP	BCM	1D Hierarchical	none
*ver*5	MPI/OpenMP	BCM	1D Hierarchical	row only

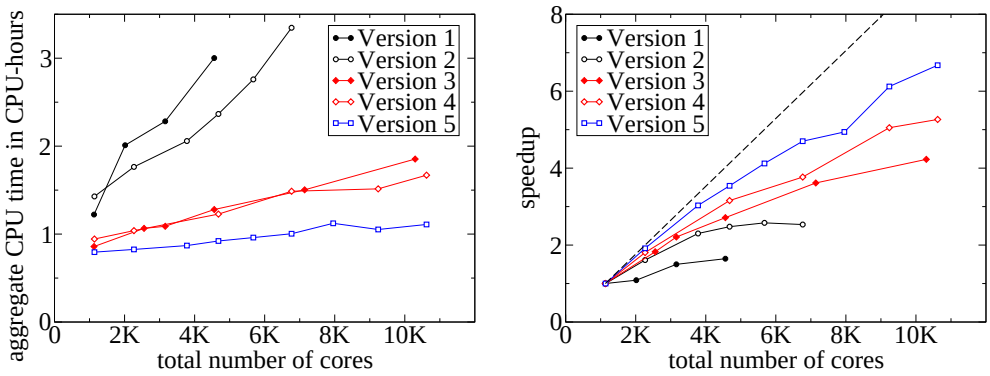

Figure 9: Strong scaling (left subfigure) and speed-ups (right subfigure) achieved by different versions on the ^{10}B, $N_{\max}$=8, M_j=1 testcase starting from 1,140 cores on up to 10,560 cores.

and the Lanczos vectors are distributed on a 2D rectangular grid in a cyclic fashion [5] is defined as *ver*1. On the other extreme, *ver*5 contains all techniques we discussed above. In particular, it allows the SpMV computations to be overlapped with communication.

The left subfigure in Fig. 9 shows the scalability of each version in Table 1 for this test problem. We define the CPU-hour cost of a single Lanczos iteration as the wall-clock time (in hours) required for an iteration times the number of cores used in that run. So in Fig. 9, the CPU-hour cost plot of an implementation with perfect strong-scaling properties would follow a horizontal line. As seen in Fig. 9, *ver*5 follow a nearly horizontal line, meaning that it has very good strong-scaling properties.

The right subfigure in Fig. 9 shows the speed-up achieved by each version for the same testcase. The speed-up measurements from *ver*1 and *ver*2 plateau after about 4,000 cores. Similarly, the gains from *ver*3 and *ver*4 start increasing only slightly after 7,000 and 9,000 cores, respectively. However, we are still able to achieve significant speed-up beyond 10,000 cores in *ver*5.

Acknowledgements

This work was supported in part by the National Science Foundation under Grant No. PHY-0904782 and the Department of Energy under Grant Nos. DE-FG02-87ER40371 and DESC0008485 (SciDAC-3/NUCLEI). The computational resources were provided by the National Energy Research Scientific Computing Center (NERSC), which is supported by the DOE Office of Science under Contract No. DE-AC02-05CH11231.

References

[1] J.P. Vary, *The many-fermion dynamics shell-model code*. 1992 (*unpublished*).

[2] J.P. Vary and D.C. Zheng, *The many-fermion dynamics shell-model code*. 1994 (*unpublished*).

[3] Z. Gan, Y. Alexeev, M. S. Gordon and R. A. Kendall, J. Chem. Phys. **119**, 47–59 (2003).

[4] E. Rossi, G. L. Bendazzoli and S. Evangelisti, J. Comp. Chem. **19(6)**, 658–672 (1998).

[5] P. Sternberg, E. G. Ng, C. Yang, P. Maris, J. P. Vary, M. Sosonkina and H. V. Le, *Accelerating configuration interaction calculations for nuclear structure*, in *Proc. 2008 ACM/IEEE Conf. on Supercomputing*. IEEE Press, Piscataway, NJ, 2008, p. 15:1.

[6] B. N. Parlett, *The Symmetric Eigenvalue Problem*. Prentice-Hall, 1980.

[7] D. C. Sorensen, SIAM J. Matrix Anal. Appl. **13(1)**, 357–385 (1992).

[8] R. B. Lehoucq, D. C. Sorensen and C. Yang, *ARPACK users guide: Solution of large scale eigenvalue problems by implicitly restarted Arnoldi methods*. SIAM, Philadelphia, PA, 1998.

[9] E. R. Davidson, J. Comput. Phys. **17**, 87–94 (1975).

[10] A. Knyazev, SIAM J. Sci. Comput. **22(2)**, 517–541 (2001).

[11] H. M. Aktulga, C. Yang, E. G. Ng, P. Maris and J. P. Vary, *Topology-aware mappings for large-scale eigenvalue problems*, in *Euro-Par*, eds. C. Kaklamanis, T. S. Papatheodorou and P. G. Spirakis. Lecture Notes Comput. Sci. **7484**, 830 (2012).

[12] H. M. Aktulga, C. Yang, E. G. Ng, P. Maris and J. P. Vary, *Improving the scalability of symmetric iterative Eigensolver for multi-core platforms*, Concurrency Computat.: Pract. Exper. (2013), DOI: 10.1002/cpe.3129.

[13] P. Maris, M. Sosonkina, J. P. Vary, E. G. Ng and C. Yang, Proc. Comput. Sci. **1**, 97–106 (2010).

[14] C. Albing, N. Troullier, S. Whalen, R. Olson, J. Glenski, H. Pritchard and H. Mills, *Scalable node allocation for improved performance in regular and anisotropic 3d torus supercomputers*, in *Recent Advances in the Message Passing Interface*. LNCS **6960**, 61–70 (2011).

Monte Carlo Shell Model and Shape Phase Transitions in Exotic Nuclei

Takaharu Otsuka[a,b,c], Yusuke Tsunoda[a], Noritaka Shimizu[b], Michio Honma[d] and Yutaka Utsuno[e]

[a] *Department of Physics, the University of Tokyo, Hongo, Tokyo 113-0033, Japan*
[b] *Center for Nuclear Study, the University of Tokyo, Hongo, Tokyo 113-0033, Japan*
[c] *National Superconducting Cyclotron Laboratory, Michigan State University, East Lansing, MI 48824, USA*
[d] *Center for Mathematical Sciences, University of Aizu, Ikki-machi, Aizu-Wakamatsu, Fukushima 965-8580, Japan*
[e] *Advanced Science Research Center, Japan Atomic Energy Agency, Tokai, Ibaraki 319-1195, Japan*

Abstract

The shapes of neutron-rich exotic Ni isotopes are studied in terms of large-scale shell model calculations performed by advanced Monte Carlo Shell Model (MCSM) for the pf-$g_{9/2}$-$d_{5/2}$ model space. Experimental energy levels are reproduced well by a single fixed Hamiltonian based on A3DA. Intrinsic shapes are analyzed for MCSM eigenstates including fluctuations. Intriguing interplays among spherical, oblate, prolate and γ-unstable shapes are seen including shape fluctuations, $E(5)$-like situation, the magicity of doubly-magic ^{56,68,78}Ni, and the coexistence of spherical and strongly deformed shapes.

Keywords: *Monte Carlo Shell Model; Ni isotopes; shape coexistence*

1 James and us

It is a great pleasure for me to give this talk in the conference celebrating the 70th birthday of James P. Vary. James has given great supports not only to the development of Monte Carlo Shell Model by our group but also to computational nuclear physics activities in Japan. We are very much grateful to his efforts, enthusiasm and actual collaborations. In fact, the nuclear structure theory group in the University of Tokyo (Tokyo group) has enjoyed many collaborations with James and his colleagues in Ames. We visited Ames many times, while James and Pieter Maris visited Japan also many times. Figure 1 shows several of Japanese members with colleagues in Ames at one of such occasions on the 28th of February, 2010.

2 Introduction

The Monte Carlo Shell Model has been explained to a good detail by Abe with co-authors in this proceedings [1]. We then skip the description of the method, and discuss what have been and can be obtained. We further restrict ourselves to calculations for heavier nuclei such as Ni isotopes. The size of the calculation is quite huge, though. We start with the motivations of such studies.

Proceedings of International Conference 'Nuclear Theory in the Supercomputing Era — 2013' (NTSE-2013), Ames, IA, USA, May 13–17, 2013. Eds. A. M. Shirokov and A. I. Mazur. Pacific National University, Khabarovsk, Russia, 2014, p. 286.
http://www.ntse-2013.khb.ru/Proc/Otsuka.pdf.

Figure 1: Photo taken in front of the Department of Physics, the Iowa State University on the 28th of February, 2010.

Atomic nuclei exhibit simple and robust regularities in their structure comprised of Z protons and N neutrons. A very early example is the (spherical) magic numbers conceived by Mayer and Jensen [2]. These magic numbers dominate low-energy dynamics of stable nuclei and their neighbors on the Segré chart. Another basic feature is nuclear shape, which has been one of the central issues of nuclear physics since Rainwater [3] and Bohr and Mottelson [4]. The shape varies as Z or N changes in such a way that it tends to be spherical near magic numbers, while becomes more deformed towards the middle of the shell. Thus, Z and N, in connection to the magic numbers, are known to be key variables in determining the shape of stable nuclei. Rare isotope beam technology developed since [5] has made experiments on exotic nuclei feasible, casting challenges to the pictures mentioned above. Even magic numbers are not exception: the changes of the shell structure due to nuclear forces, referred to as *shell evolution* [6], have been seen including disappearance of traditional magic numbers and appearance of new ones. A recent example is the discovery of $N = 34$ magic number [7] after its prediction a decade ago [8], while many other cases have been discussed [6, 9–11].

It is then of much interest to explore shapes of exotic nuclei and to look for relations to the shell evolution. In this talk, we report results of state-of-the-art large-scale shell model calculations for a wide range of Ni isotopes, focusing on these points. While the ground state turns out to be spherical basically, a strongly prolate deformed band appears at low excitation energy in some nuclei, similarly to shape coexistence known as a distinct phenomenon over decades [12–14]. The formation of this band is discussed in relation to reduced shell gaps brought about by the proton-neutron tensor force in major configurations (of single-particle orbits) of deformed states. (We introduced, after the conference, a new type of shell evolution due to configuration changes within the same nucleus, calling it *Type II shell evolution*. The shell evolution by the change of N or Z [6] is then referred to as *Type I*.) We shall

discuss other interesting features, e. g., magicity of doubly-magic ^{56,68,78}Ni, shape fluctuations including γ instability, and $E(5)$-like case [15].

We discuss, in this talk, the structure of Ni isotopes with even $N = 28-50$, utilizing results obtained by the advanced Monte Carlo Shell Model (MCSM) calculation [16–18] run on K computer for $\sim 2 \times 10^{10}$ core seconds in total. The model space consists of the full pf shell, $0g_{9/2}$ and $1d_{5/2}$ orbits for both protons and neutrons. There is no truncation within this space as an advantage of MCSM. The Hamiltonian is based on the A3DA Hamiltonian with minor revisions [16, 19]. The spurious center-of-mass motion is removed by the Lawson method [20].

3 Results for Ni isotopes

Figure 2 shows yrast and yrare levels by the present calculation compared to experiment [21]. Systematic behaviors are visible in experimental yrast levels as well as $J^\pi = 0_2^+$ and 2_2^+ yrare levels, with a remarkable agreement to the theoretical trends. Such good agreement has been obtained with a single fixed Hamiltonian, and suggests that the structure of Ni isotopes can be studied with it. The $B(E2; 0_1^+ \to 2_1^+)$ values with neutron and proton effective charges, 0.5 and 1.5, respectively, are shown in Fig. 2 compared to experiment [23] with certain discrepancies for heavier isotopes,

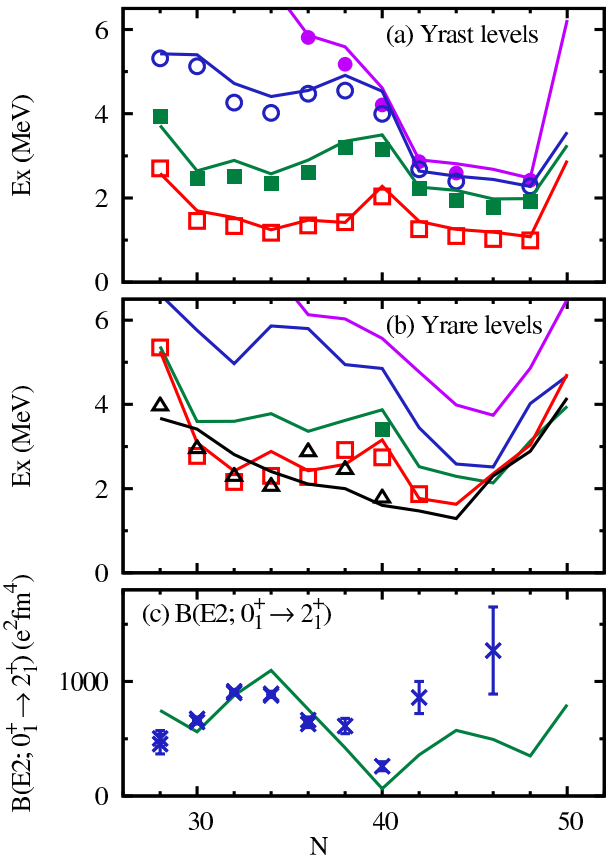

Figure 2: Energy levels for (a) yrast and (b) yrare states of Ni isotopes with even N. Symbols are experimental data for J^π=0^+ (black triangle), 2^+ (open red square), 4^+ (green filled square), 6^+ (open blue circle) and 8^+ (filled purple circle) [21,22]. Lines are present MCSM calculations with the same color code. (c) $B(E2; 0_1^+ \to 2_1^+)$ values by experiment [23] and by the present calculation.

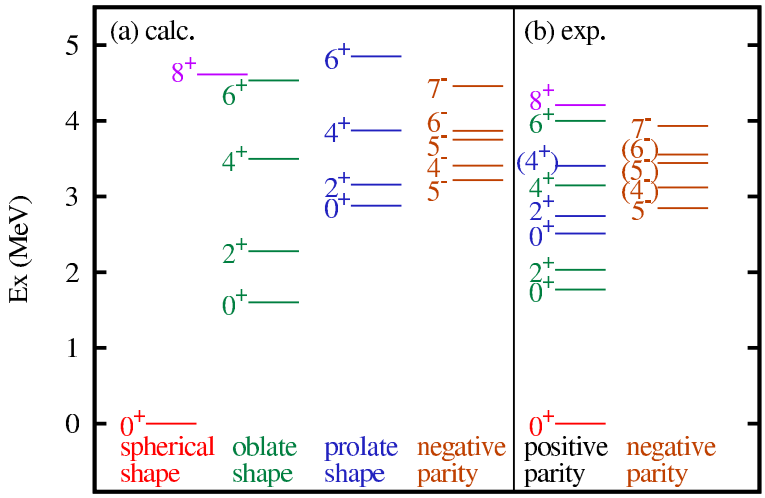

Figure 3: Energy levels of ^{68}Ni by present calculation (left panel) and by experiment (right panel) [21].

where uncertainties are larger and (p, p') data is converted ($N = 46$) [24,25]. A more systematic comparison with precise data is desired. Relevant shell model calculations have been reported [26,27]. In particular, those of [26] are remarkable achievement of large-scale conventional shell-model approach, with good agreement to experiment. Many experimental data are, however, to be obtained, and it is not the purpose of this work to compare different calculations. The primary objective here is to predict novel systematic change of band structures in $^{68-78}$Ni isotopes.

We show, in Fig. 3, a more detailed level scheme for ^{68}Ni, including negative-parity states. This nucleus has attracted much attention [22, 27–34] from theoretical and experimental sides. The positive-parity levels are classified according to their shape categories: spherical, oblate and prolate. We shall come to this point later. The correspondence between theoretical and experimental levels can be made with rather good agreement. Note that this is the first report of calculated levels beyond 2^+ and those of negative-parity.

4 Intrinsic shapes and wave functions

Figure 4 depicts, for selected states of ^{68,70,74,78}Ni isotopes, potential energy surface (PES) for the present Hamiltonian obtained by the Constraint Hartree–Fock (CHF) method with usual constraints on quadrupole moments Q_0 and Q_2. We can see many features: for instance, for ^{68}Ni, there is a spherical minimum stretched towards modest oblate region, as well as a prolate local minimum.

The MCSM wave function is expressed by a superposition of Slater determinants with the angular-momentum and parity projector $P[J^\pi]$,

$$\Psi = \sum_i c_i P[J^\pi]\, \Phi_i \,. \tag{1}$$

Here, c_i denotes an amplitude, Φ_i stands for the Slater determinant consisting of one-nucleon wave functions $\phi_1^{(i)}, \phi_2^{(i)}, \ldots, \phi_n^{(i)}$ with

$$\phi_k^{(i)} = \sum_l D_{k,l}^{(i)}\, u_l, \tag{2}$$

where u_l is the l-th single-particle state in the original model space in m-scheme,

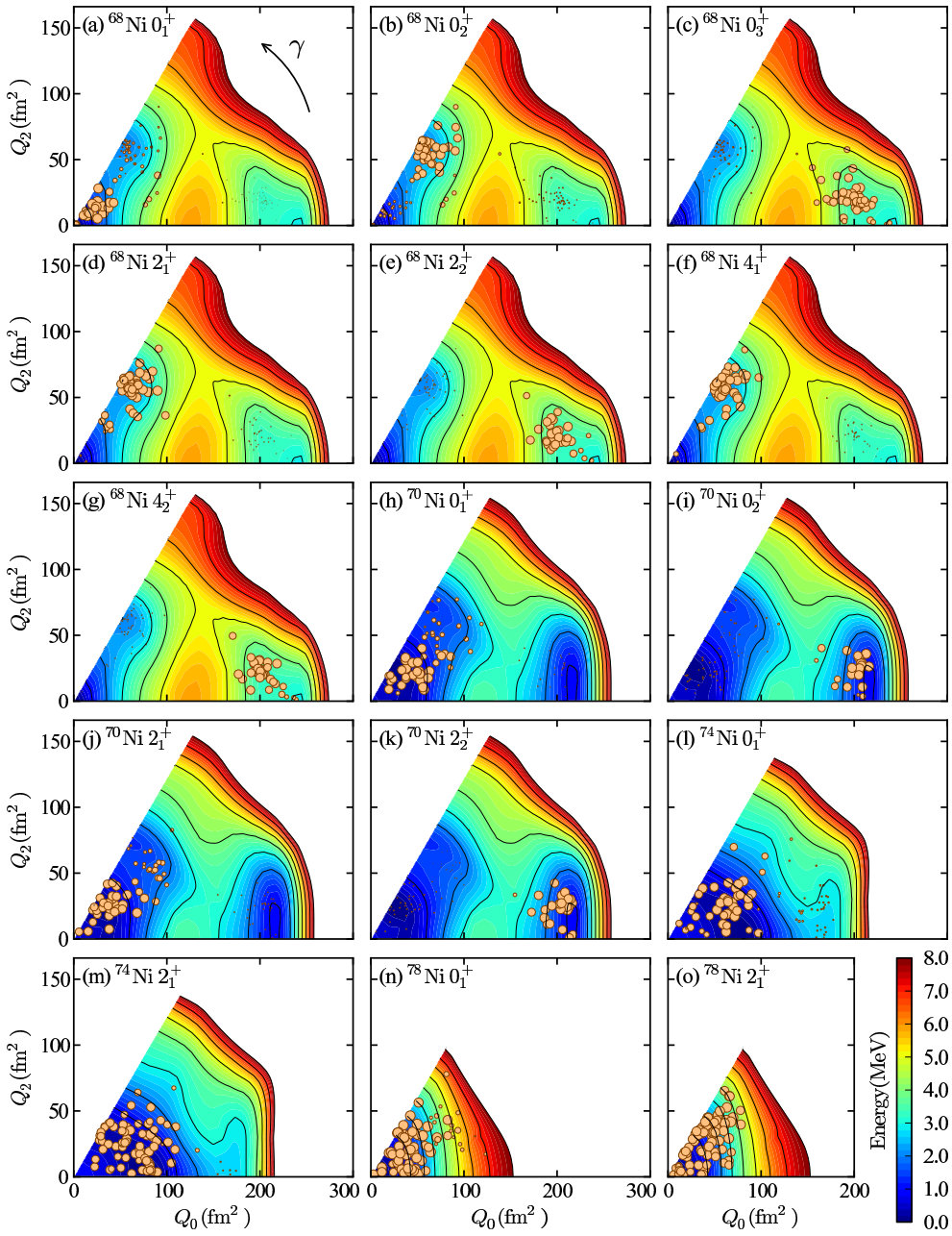

Figure 4: Potential energy surfaces (PES) of Ni isotopes, coordinated by usual Q_0 and Q_2 (or γ). The energy relative to the minimum is shown by contour plots. Circles on the PES represent shapes of MCSM basis vectors (see the text).

and D implies amplitude determined by MCSM process. Φ_i is the product of proton and neutron sectors, with n being the number of valence protons or neutrons.

For each Φ_i, we take the following process. We calculate its quadrupole moment matrix, and diagonalize. Three axes are obtained with Q_0 and Q_2 values. We then place a circle on the PES at the point corresponding to these Q_0 and Q_2 values. The size (i. e. area) of the circle is set to be proportional to the overlap probability between Ψ and the normalized $P[J^\pi]\,\Phi_i$. Thus, the location of the circle implies the intrinsic shape of Φ_i, and its size the importance of it in the eigenstate, Ψ. Note

that the states $P[J^\pi]\,\Phi_i$ $(i = 1, 2, ...)$ are not orthogonal each other in general, but the distribution pattern of the circles provides unique and clear message on intrinsic shape of the shell-model eigenstate as we shall see.

Figure 4(a) shows such circles for the ground state of ^{68}Ni. We see many large circles near the spherical point, $Q_0 = Q_2 = 0$. In general, there can be many points close to one another partly because each circle represents a Slater determinant and a two-body interaction, particularly its pairing components, mixes different Slater determinants. Those Slater determinants should have similar shapes so that the mixing between them can occur. We see also notable spreading of circle distribution from the spherical point. This implies the extent of the shape fluctuation. The 0^+_2 state in Fig. 4(b) shows similar spreading but the locations are shifted to moderately oblate region ($\beta_2 \sim -0.2$). Although there is no clear potential barrier between the spherical and oblate regions of the PES, the antisymmetrization pushes the 0^+_2 state away from the 0^+_1 state. Figure 4(c) exhibits many circles in a profound prolate minimum with $Q_0 \sim$200 fm^2 ($\beta_2 \sim 0.4$). We emphasize that we can analyze, in this way, the intrinsic shape even for 0^+ states without referring to E2 properties.

Figures 4(d, e) show the same plots for the $2^+_{1,2}$ states, while Figs. 4(f, g) the same plots for the $4^+_{1,2}$ states. The 2^+_1 and 4^+_1 states exhibit patterns almost identical to that of the 0^+_2 state, which suggests the formation of the modestly-oblate band. We would like to emphasize that the present analysis is very useful to identify the band structure buried in many-body calculations. Such striking similarity is found also among the 0^+_3, 2^+_2 and 4^+_2 states with a strong-prolate-band assignment. We mention that a band similar to this prolate band has been pointed out by a shell-model calculation in [33]. The band structure is thus clarified, with further verification by $E2$ matrix elements, and is presented in Fig. 3 including 4^+ and 6^+ members.

The prolate band being discussed comes down to the 0^+_2 and 2^+_2 states as N increases from 40 to 42 or 44 [see Figs. 4(h, k)]. Observed 2^+_2 level of ^{70}Ni is as low as 2 MeV, which is reproduced well by the present calculation as shown in Fig. 2(b), whereas this level has not been reproduced by calculations with limited configurations [35, 36]. In addition, Fig. 2(a) depicts the 2^+_1 levels in good agreement to experiment, while strong fluctuation is seen towards oblate shape in Figs. 4(h, k). This work is the first report from theory for this low-lying 2^+_2 state.

In moving to ^{74}Ni, Figs. 4(l, m) exhibit another interesting pattern. The distribution of the circles becomes wide in both magnitude and γ direction, i. e., triaxiality. A similar distribution is obtained also for the 2^+_2 states, and the situation is the same for ^{76}Ni. It is of interest that this resembles the critical point symmetry $E(5)$ [15].

Finally, we come to ^{78}Ni. This is supposed to be a doubly closed shell nucleus. Figures 4(n, o) show the PES and wave function distribution for the 0^+_1 and 2^+_1 states. The PES goes up rapidly, but to be surprising, the wave functions are spread on the bottom fully, in a almost identical ways between the 0^+_1 and 2^+_1 states, which clearly differs from what we can expect from a closed shell. The distribution is much wider than that of ^{68}Ni. It is of much interest that comparing to ^{56}Ni and ^{78}Ni, ^{68}Ni is the closest to the doubly closed picture among the three doubly magic isotopes of Ni.

5 Summary

In summary, the advanced MCSM calculations present intriguing variations of shapes analyzed in terms of intrinsic shapes. Thus, the shapes of exotic nuclei provide us with many new features. In stable nuclei, the shape has been often discussed as functions of N and Z, for instance, shape evolution from vibrational to rotational nuclei as N increases. Such simple classification may no longer be appropriate in exotic nuclei. The role of large-scale shell-model calculations is quite significant, and will become even more important in future.

Acknowledgments

This work was in part supported by MEXT Grant-in-Aid for Scientific Research (A) 20244022. This work has been supported by HPCI (hp120284 and hp130024), and is a part of the RIKEN-CNS joint research project on large-scale nuclear-structure calculations. Y.T. acknowledges JSPS for Research Fellow (No. 258994).

References

[1] T. Abe, P. Maris, T. Otsuka, N. Shimizu, Y. Tsunoda, Y. Utsuno and J. P. Vary, *see these Proceedings*, p. 294, http://www.ntse-2013.khb.ru/Proc/Abe.pdf.

[2] M. G. Mayer, Phys. Rev. **75**, 1969 (1949); O. Haxel, J. H. D. Jensen and H. E. Suess, Phys. Rev. **75**, 1766 (1949).

[3] J. Rainwater, Phys. Rev. **79**, 432 (1950).

[4] A. Bohr and B. R. Mottelson, *Nuclear Structure, vol. II.* Benjamin, Reading, Mass., 1975, and World Scientific, Singapore, 1998.

[5] I. Tanihata *et al.*, Phys. Rev. Lett. **55**, 2676 (1985).

[6] For a brief review see T. Otsuka, Phys. Scr. T **152**, 014007 (2013).

[7] D. Steppenbeck *et al.*, Nature **502**, 207 (2013).

[8] T. Otsuka *et al.*, Phys. Rev. Lett. **87**, 082502 (2001).

[9] For reviews from experimental side see A. Gade and T. Glasmacher, Progr. Part. Nucl. Phys. **60**, 161 (2008); O. Sorlin and M.-G. Porquet, Progr. Part. Nucl. Phys. **61**, 602 (2008).

[10] T. Otsuka *et al.*, Phys. Rev. Lett. **95**, 232502 (2005).

[11] T. Otsuka *et al.*, Phys. Rev. Lett. **104**, 012501 (2010).

[12] H. Morinaga, Phys. Rev. **101**, 254 (1956).

[13] K. Heyde and J. L. Wood, Rev. Mod. Phys. **83**, 1467 (2011).

[14] A. N. Andreyev *et al.*, Nature **405**, 430 (2000).

[15] F. Iachello, Phys. Rev. Lett. **85**, 3580 (2000).

[16] N. Shimizu, T. Abe, Y. Tsunoda, Y. Utsuno, T. Yoshida, T. Mizusaki, M. Honma and T. Otsuka, Progr. Theor. Exp. Phys. 01A205 (2012).

[17] N. Shimizu, Y. Utsuno, T. Mizusaki, T. Otsuka, T. Abe and M. Honma, Phys. Rev. C **82**, 061305(R) (2010).

[18] T. Otsuka, M. Honma, T. Mizusaki, N. Shimizu and Y. Utsuno, Progr. Part. Nucl. Phys. **47**, 319 (2001).

[19] Details available upon request to the corresponding authors.

[20] D. H. Gloeckner and R. D. Lawson, Phys. Lett. B **53**, 313 (1974).

[21] Evaluated Nuclear Structure Data File (ENSDF), http://www.nndc.bnl.gov/ensdf/.

[22] R. Broda *et al.*, Phys. Rev. C **86**, 064312 (2012); R. Broda, B. Fornal, W. Królas, T. Pawłat, D. Bazzacco, S. Lunardi, C. Rossi-Alvarez, R. Menegazzo, G. de Angelis, P. Bednarczyk, J. Rico, D. De Acuna, P. J. Daly, R. H. Mayer, M. Sferrazza, H. Grawe, K. H. Maier and R. Schubart, Phys. Rev. Lett. **74**, 868 (1995).

[23] B. Pritychenko, J. Choquette, M. Horoi, B. Karamy and B. Singh, At. Data Nucl. Data Tables **98**, 798 (2012).

[24] O. Perru *et al.*, Phys. Rev. Lett. **96**, 232501 (2006).

[25] N. Aoi *et al.*, Phys. Lett. B **692**, 302 (2010).

[26] S. M. Lenzi, F. Nowacki, A. Poves and K. Sieja, Phys. Rev. C **82**, 054301 (2010); references therein.

[27] K. Kaneko, M. Hasegawa, T. Mizusaki and Y. Sun, Phys. Rev. C **74**, 024321 (2006)

[28] M. Girod, P. Dessagne, M. Bernas, M. Langevin, F. Pougheon and P. Roussel, Phys. Rev. C **37**, 2600 (1988).

[29] T. Ishii *et al.*, Phys. Rev. Lett. **84**, 39 (2000).

[30] O. Sorlin *et al.*, Phys. Rev. Lett. **88**, 092501 (2002).

[31] K. Langanke, J. Terasaki, F. Nowacki, D. J. Dean and W. Nazarewicz, Phys. Rev. C **67**, 044314 (2003).

[32] D. Pauwels, J. L. Wood, K. Heyde, M. Huyse, R. Julin and P. Van Duppen, Phys. Rev. C **82**, 027304 (2010).

[33] A. Dijon *et al.*, Phys. Rev. C **85**, 031301(R) (2012).

[34] C. J. Chiara *et al.*, Phys. Rev. C **86**, 041304(R) (2012).

[35] M. Honma, T. Otsuka, T. Mizusaki and M. Hjorth-Jensen, Phys. Rev. C **80**, 064323 (2009).

[36] B. Cheal *et al.*, Phys. Rev. Lett. **104**, 252502 (2010).

Monte Carlo Shell Model Towards Ab Initio Calculations

T. Abe[a], P. Maris[b], T. Otsuka[a,c,d], N. Shimizu[c], Y. Tsunoda[a], Y. Utsuno[e] and J. P. Vary[b]

[a] *Department of Physics, the University of Tokyo, Hongo, Tokyo 113-0033, Japan*
[b] *Department of Physics and Astronomy, Iowa State University, Ames, IA 50011, USA*
[c] *Center for Nuclear Study, the University of Tokyo, Hongo, Tokyo 113-0033, Japan*
[d] *National Superconducting Cyclotron Laboratory, Michigan State University, East Lansing, MI 48824, USA*
[e] *Advanced Science Research Center, Japan Atomic Energy Agency, Tokai, Ibaraki 319-1195, Japan*

Abstract

We report on our recent application of the Monte Carlo Shell Model (MCSM) to no-core calculations. After the brief introduction, the performance of the MCSM on the K computer is discussed. At the initial stage of the application, we have performed benchmark calculations in the p-shell region. Results are compared with those in the Full Configuration Interaction and No-Core Full Configuration methods. These are found to be consistent with each other within quoted uncertainties when they could be quantified. The preliminary results in $N_{\rm shell} = 5$ reveal the onset of systematic convergence pattern.

Keywords: *Monte Carlo Shell Model; No-Core Shell Model; ab initio approach*

1 Introduction

One of the major challenges in nuclear theory is to reproduce and to predict nuclear structure and reactions from *ab initio* calculations with realistic nuclear forces. Among the *ab initio* nuclear many-body approaches for $A \geq 4$ [1], the No-Core Shell Model (NCSM) is one of the powerful methods for the study of nuclear structure and reactions in the p-shell nuclei [2].

As the NCSM treats all the nucleons on an equal footing, computational demands for the calculations explode exponentially as the number of nucleons increases. Current computational resources limit the direct diagonalization of the Hamiltonian matrix using the Lanczos algorithm to basis spaces with a dimension of around 10^{10}. Shell-model calculations in the $N_{\rm shell}$ truncation is limited in the lower p-shell region (Fig. 1). In order to access heavier nuclei beyond the p-shell region with larger basis dimensions, many efforts have been devoted to the NCSM calculations. One of these approaches is the Importance–Truncated NCSM (IT-NCSM) [3] where the basis spaces are extended by using an importance measure evaluated using perturbation theory. Another approach is the Symmetry–Adapted NCSM (SA-NCSM) [4] where the basis spaces are truncated by the selected symmetry groups. Similar to these attempts, the Monte Carlo NCSM (MC-NCSM) [5, 6] is one of the promising candidates to go beyond the Full Configuration Interaction (FCI) method which is a different truncation of the basis states that commonly used in the NCSM. Shell-model

Proceedings of International Conference 'Nuclear Theory in the Supercomputing Era — 2013' (NTSE-2013), Ames, IA, USA, May 13–17, 2013. Eds. A. M. Shirokov and A. I. Mazur. Pacific National University, Khabarovsk, Russia, 2014, p. 294.
http://www.ntse-2013.khb.ru/Proc/Abe.pdf.

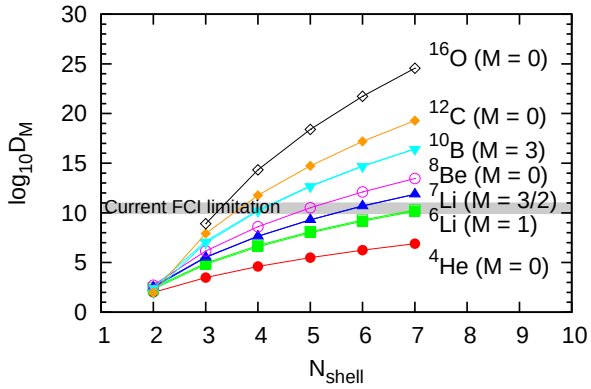

Figure 1: M-scheme dimension for light nuclei as a function of basis space cutoff, $N_{\rm shell}$.

calculations with an assumed inert core by the MCSM have succeeded in obtaining the approximated solutions where the direct diagonalization is difficult due to large dimensionalities as described in Fig. 2.

In these proceedings, we focus on the latest application of the MCSM toward the *ab initio* no-core calculations, which has become feasible recently with the aid of the major developments in the MCSM algorithm [7] and also a remarkable growth in the computational power of the state-of-the-art supercomputers, such as the K computer. Most of the benchmark results in the MC-NCSM presented here are summarized in Ref. [6].

2 Monte Carlo Shell Model

2.1 Brief overview

The MCSM has been developed mainly for conventional shell-model calculations with an assumed inert core [8]. Recently the algorithm and code itself have been heavily revised and rewritten so as to accommodate massively parallel computing environments [7]. Now we can apply the MCSM not only to conventional shell-model

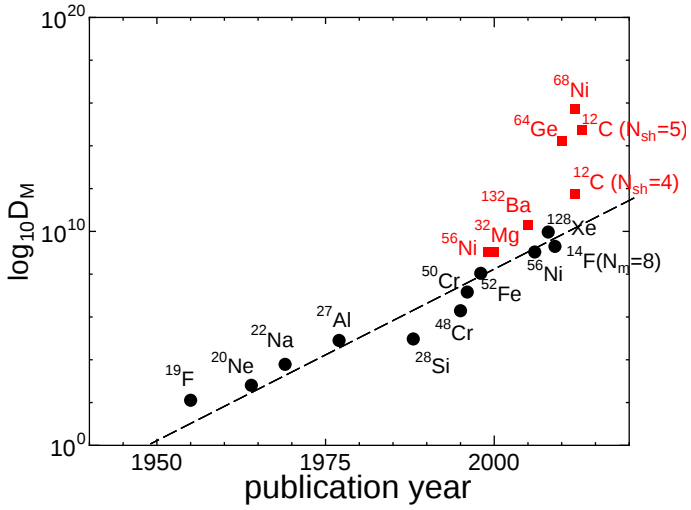

Figure 2: M-scheme dimension for conventional shell-model calculations with an assumed inert core as a function of publication year (right). Red squares are for the MCSM results, and black circles are for the conventional shell-model results by the direct diagonalization with the Lanczos technique.

calculations but also to no-core calculations.

The MCSM approach proceeds through a sequence of diagonalization steps within the Hilbert subspace spanned by the deformed Slater determinants in the HO single-particle basis. The many-body basis state $|\Psi^{J^\pi M}\rangle$ is approximated as a linear combination of non-orthogonal angular-momentum (J) and parity (π) projected deformed Slater determinants with good total angular momentum projection (M),

$$|\Psi^{J^\pi M}\rangle = \sum_{n=1}^{N_b} f_n \sum_{K=-J}^{J} g_{nK}\, P^J_{MK}\, P^\pi |\phi_n\rangle, \tag{1}$$

where N_b is the number of Slater determinants. P^J_{MK} is the projection operator for the total angular momentum J with its z-projection in the laboratory (body-fixed) frame, M (K). P^π is the projection operator for the parity. The coefficients f and g are determined by the diagonalization of Hamiltonian matrix. The deformed Slater determinant $|\phi\rangle$ in Eq. (1) is described as

$$|\phi\rangle = \prod_{i=1}^{A} a_i^\dagger |-\rangle, \tag{2}$$

with the vacuum $|-\rangle$ and the creation operator, $a_i^\dagger = \sum_{\alpha=1}^{N_{\rm sp}} c_\alpha^\dagger\, D_{\alpha i}$. $N_{\rm sp}$ is specified by the cutoff of the single particle basis space, $N_{\rm shell}$. The transformation coefficients D form the complex $N_{\rm sp} \times A$ matrix with the normalization condition, $D^\dagger D = 1$. Importance-truncated bases $|\phi\rangle$ are stochastically sampled so as to minimize the energy variationally. With increasing the number of importance-truncated basis states, the computed energy converges from above to the exact value and gives the variational upper bound. An exploratory no-core MCSM investigation of the proof-of-principle type has been done for the low-lying states of the Be isotopes by applying the existing MCSM algorithm with a core to a no-core problem [5].

Recent improvements on the MCSM algorithm have enabled significantly larger calculations [7]. The crucial developments for no-core calculations achieve (1) the efficient computation of matrix products for the most time-consuming part in the MCSM calculations, (2) the conjugate gradient method in the basis-search process, and (3) the energy-variance extrapolation for our MCSM (approximated) results into the FCI (exact) ones in the finite basis spaces. Because of space limitations, we refer for the details of these improvements to Ref. [7].

As a typical example of the implementation, the behavior of the ground-state energies of ^{4}He (0^+) and ^{12}C (0^+) with respect to the number of basis states and to the energy variance are shown in Fig. 3. From Fig. 3, one can see that the MCSM results can be extrapolated into the FCI ones by using the quadratic fit function with respect to the energy variance ΔE_2 of $E(\Delta E_2) = E(\Delta E_2 = 0) + c_1 \Delta E_2 + c_2 (\Delta E_2)^2$ with the fit parameters, $E(\Delta E_2 = 0)$, c_1, and c_2.

2.2 Tests on the K computer

At the initial stage of the implementation of K computer, we have performed some test calculations to measure our code performance. In this subsection, we show some of the test calculations: the ratio to the peak performance and the parallel efficiency of our code.

In order to measure our code performance on K computer, we have chosen the optimization of 15th basis dimension of the wave function in $N_{\rm shell} = 5$ with 100 CG iterations without the preprocessing as a test case. The code has run on K computer by using MPI/OpenMP with 8 threads.

Figure 4 illustrate our recent MCSM code performance. The left panel of Fig. 4 shows the ratio to the peak performance in the calculation of the ^{4}He 0^+ ground

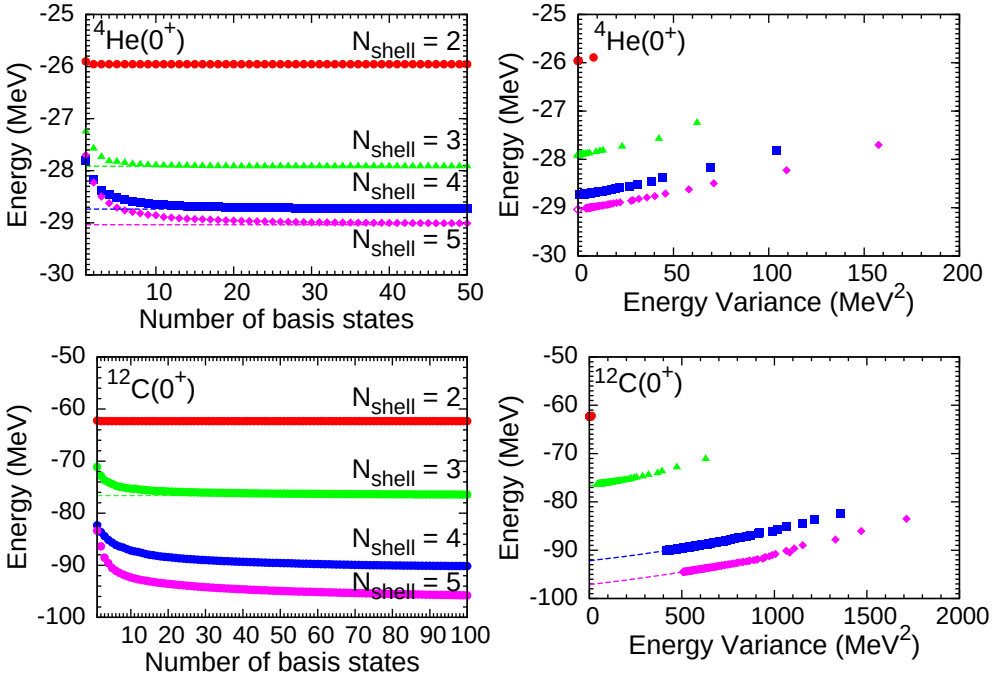

Figure 3: ^{4}He and ^{12}C 0^+ ground-state energies as functions of number of basis states (left) and energy variance (right). From the above to the bottom, the symbols (horizontal dashed lines in the left figure and open symbols at the zero energy variance in the right figure) are the MCSM (FCI) results in $N_{\rm shell} = 2$, 3, 4 and 5, respectively. Note that the results of ^{12}C in $N_{\rm shell} = 4$ and 5 are obtained only by the MCSM. See Ref. [6] for the details.

state. Although the performance decreases as the number of CPU cores increases, it is around 30–40% up to 30720 cores (8 cores per node). The right panel of Fig. 4 shows the ratio to the peak performance as a function of the atomic numbers. The nuclear states listed in the figure are for the ground state of each nucleus. From the figure, the dependence of the performance on atomic number A is relatively weak for

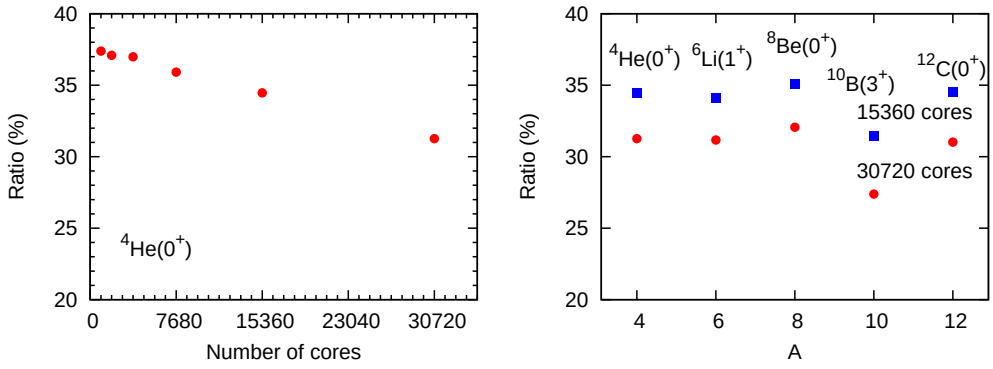

Figure 4: Ratio to the peak performance of the MCSM test calculations. Peak ratio of the calculation for the ^{4}He (0^+) ground state as a function of the number of cores (left). Peak ratio of the calculation for the ground states as a function of the number of nucleons (right). Red circles denotes the results with 30720 cores, and blue squares are with 15360 cores.

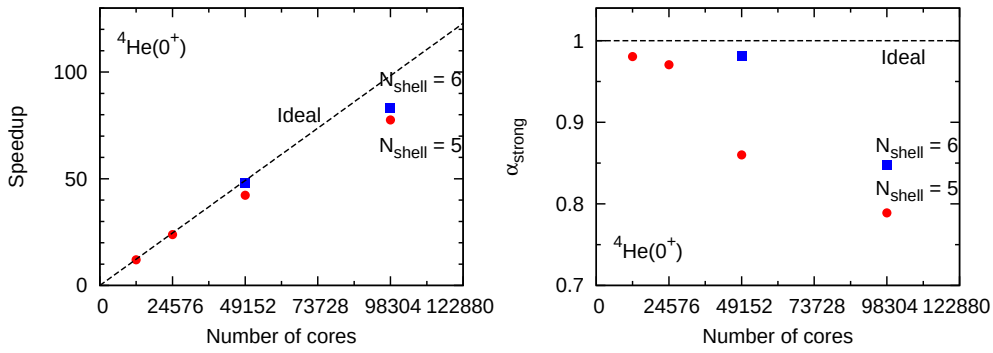

Figure 5: Speedup of the parallel computation with arbitrary unit (left), and the strong scaling (right).

the number of nucleons at least up to $A = 12$.

For testing the parallel efficiency, we have measured the dependence on the number of CPU cores. Figure 5 demonstrates the speedup (left) and the strong scaling (right) of our MCSM code on K computer as a function of the cores. The test case is the optimization of the 15th (48th) basis for ^{4}He (0^+) ground state in $N_{\rm shell} = 5$ (6) with 100 CG iterations without the preprocessing. Each setup has been chosen so that the number of MPI tasks is divisible by $N_{\rm procs}$, for simplicity. $32 \times 32 \times 30$ mesh points are used for the angular momentum projection, and 2 for the parity projection.

The left panel describes the speedup with arbitrary unit. In Fig. 5, the dotted line describes the perfect (ideal) scaling. The right panel of Fig. 5 is about the strong scaling. Here $\alpha_{\rm strong}$ is defined by the ratio of the time T with the number of CPU cores $N_{\rm procs}$ as $\alpha_{\rm strong} \equiv T(N_{\rm procs})/(T(N_{\rm procs}/2) \times 2)$. In this definition, $\alpha_{\rm strong} = 1$ describes the perfect strong scaling. As seen in Fig. 5, the strong scaling is nearly perfect up to 98304 cores both in $N_{\rm shell} = 5$ and 6.

3 Benchmarks

The recent development of the MCSM algorithm [7] , together with significant computational resources, enables us to perform a benchmark of no-core MCSM calculations [6]. Figure 6 is the recent comparison of the energies for each state and basis space in the selected p-shell nuclei between the MCSM and FCI methods. The FCI gives the exact energies in the finite basis spaces, while the MCSM provides approximate energies. Thus the comparisons between them show how well the MCSM works in no-core calculations. Furthermore, we also plot the No-Core Full Configuration (NCFC) [9] results for the states of $4 \leq A \leq 10$ as the fully converged energies in the infinite basis space.

For this benchmark comparison, the JISP16 two-nucleon interaction [10] is adopted and the Coulomb force is turned off. The energies are evaluated for the optimal harmonic oscillator frequencies where the calculated energies are minimized for each state and basis space. Here the contributions from the spurious center-of-mass motion are ignored for simplicity. The basis space ranges from $N_{\rm shell} = 2$ to 5 where $N_{\rm shell}$ is the number of the major shell included in the basis space. Some energies in $N_{\rm shell} = 4$ and 5 are available only from the MCSM results, as the M-scheme dimensions for these states are already close to or above the current computational limitation in the FCI approach. We took 100 importance-truncated basis states and extrapolated the results by the energy variance.

As seen in Fig. 6, the energies are consistent with each other to within ~ 100 keV where both results are available. Furthermore the $N_{\rm shell} = 5$ results begin to show

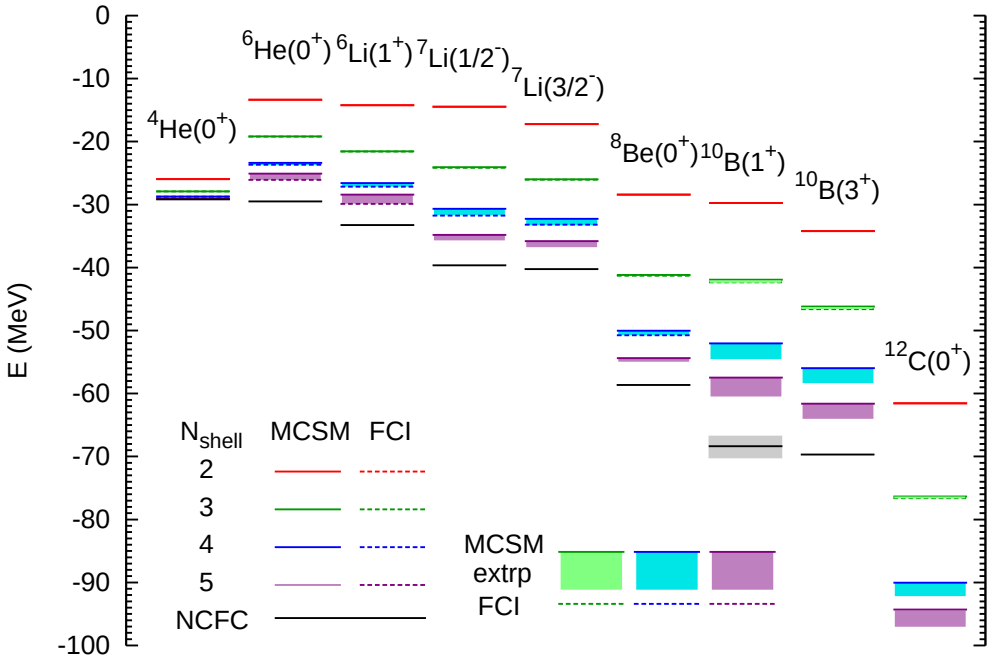

Figure 6: Comparisons of the energies between the MCSM and FCI along with the fully converged NCFC results where available. The NCFC result for the ^{10}B(1^+) state has a large uncertainty indicated by the grey band. The MCSM (FCI) results are shown as the solid (dashed) lines that nearly coincide where both are available. The extrapolated MCSM results are illustrated by bands. From top to bottom, the truncation of the basis space is $N_{\rm shell} = 2$ (red), 3 (green), 4 (blue), and 5 (purple). Note that the MCSM results are extrapolated by the energy variance with the second-order polynomials. Also note that the FCI results in $N_{\rm shell} = 2$ (red dotted lines) and 3 (green dotted lines) are almost overlapped with the MCSM results (red and green solid lines), which means that the MCSM results are converged well to the FCI results. Some results in $N_{\rm shell} = 4$ and 5 were obtained only with MCSM.

the trend of the convergence to the NCFC results obtained by extrapolating the $N_{\rm max}$ truncated results to the infinite basis space. The next step is to extrapolate the $N_{\rm shell}$ results to the infinite basis space by using the extrapolation techniques in the $N_{\rm max}$ truncation [9, 11, 12]. In principle, the results extrapolated to the infinite basis space should be consistent with each other in spite of how the basis spaces are truncated. It is interesting to examine whether the extrapolated results in the $N_{\rm shell}$ and $N_{\rm max}$ truncations converge to the same value within quantified uncertainties. The detailed comparisons among the MCSM, FCI, and NCFC methods are discussed in Ref. [6].

4 Summary

By exploiting the recent development in the MCSM algorithm, no-core calculations with the MCSM algorithm can be achieved on massively parallel supercomputers. As a test on such environments, we have discussed the performance of the MCSM on the K computer. From the benchmark calculations, the observables give good agreement between the MCSM and FCI results in the p-shell nuclei. The $N_{\rm shell} = 5$ results reveal the onset of systematic convergence pattern. Further work is needed to investigate the extrapolation to the infinite basis space in the $N_{\rm shell}$ truncation.

Acknowledgments

This work was supported in part by the SPIRE Field 5 from MEXT, Japan. We also acknowledge Grants-in-Aid for Young Scientists (Nos. 20740127 and 21740204), for Scientific Research (Nos. 20244022 and 23244049), and for Scientific Research on Innovative Areas (No. 20105003) from JSPS, and the CNS-RIKEN joint project for large-scale nuclear structure calculations. This work was also supported in part by the US DOE Grants No. DESC0008485 (SciDAC-3/NUCLEI), and DE-FG02-87ER40371, by US NSF Grant No. PHY-0904782, and through JUSTIPEN under grant No. DE-FG02-06ER41407. A part of the MCSM calculations was performed on the K computer at AICS, the T2K Open Supercomputer at the University of Tokyo and University of Tsukuba, and the BX900 Supercomputer at JAEA. Computational resources for the FCI and NCFC calculations were provided by the National Energy Research Supercomputer Center (NERSC), which is supported by the Office of Science of the U.S. Department of Energy under Contract No. DE-AC02-05CH11231, and by the Oak Ridge Leadership Computing Facility at the Oak Ridge National Laboratory, which is supported by the Office of Science of the U.S. Department of Energy under Contract No. DE-AC05-00OR22725.

References

[1] For a recent review, see, e. g., W. Leidemann and G. Orlandini, Progr. Part. Nucl. Phys. **68**, 158 (2013).

[2] P. Navrátil, J. P. Vary and B. R. Barrett, Phys. Rev. Lett. **84**, 5728 (2000); Phys. Rev. C **62**, 054311 (2000); S. Quaglioni and P. Navrátil, Phys. Rev. Lett. **101**, 092501 (2008); Phys. Rev. C **79**, 044606 (2009). For a recent review, see, e. g., B. R. Barrett, P. Navratil and J. P. Vary, Progr. Part. Nucl. Phys. **69**, 131 (2013).

[3] R. Roth and P. Navrátil, Phys. Rev. Lett. **99**, 092501 (2007); R. Roth, Phys. Rev. C **79** 064324 (2009); R. Roth, J. Langhammer, A. Calci, S. Binder and P. Navrátil, Phys. Rev. Lett. **107**, 072501 (2011); R. Roth, S. Binder, K. Vobig, A. Calci, J. Langhammer and P. Navrátil, *ibid.* **109**, 052501 (2012).

[4] T. Dytrych, K. D. Sviratcheva, C. Bahri, J. P. Draayer and J. P. Vary, Phys. Rev. Lett. **98**, 162503 (2007); Phys. Rev. C **76**, 014315 (2007); J. Phys. G **35**, 095101 (2008). For a review, see T. Dytrych, K. D. Sviratcheva, J. P. Draayer, C. Bahri and J. P. Vary, *ibid.* **35**, 123101 (2008).

[5] L. Liu, T. Otsuka, N. Shimizu, Y. Utsuno and R. Roth, Phys. Rev. C **86**, 014304 (2012).

[6] T. Abe, P. Maris, T. Otsuka, N. Shimizu, Y. Utsuno and J. P. Vary, Phys. Rev. C **86**, 054301 (2012).

[7] N. Shimizu, Y. Utsuno, T. Mizusaki, T. Otsuka, T. Abe and M. Honma, Phys. Rev. C **82**, 061305(R) (2010); N. Shimizu, Y. Utsuno, T. Mizusaki, M. Honma, Y. Tsunoda and T. Otsuka, *ibid.* **85**, 054301 (2012); Y. Utsuno, N. Shimizu, T. Otsuka and T. Abe, Comput. Phys. Commun. **184**, 102 (2013); N. Shimizu, T. Abe, Y. Tsunoda, Y. Utsuno, T. Yoshida, T. Mizusaki, M. Honma and T. Otsuka, Progr. Theor. Exp. Phys. 01A205 (2012).

[8] M. Honma, T. Mizusaki and T. Otsuka, Phys. Rev. Lett. **75**, 1284 (1995); **77**, 3315 (1996); T. Otsuka, M. Honma and T. Mizusaki, *ibid.* **81**, 1588 (1998), For a review, see T. Otsuka, M. Honma, T. Mizusaki, N. Shimizu and Y. Utsuno, Progr. Part. Nucl. Phys. **47**, 319 (2001).

[9] P. Maris, J. P. Vary and A. M. Shirokov, Phys. Rev. C **79**, 14308 (2009); P. Maris, A. M. Shirokov and J. P. Vary, *ibid.* **81**, 021301 (2010); C. Cockrell, J. P. Vary and P. Maris, *ibid.* **86**, 034325 (2012).

[10] A. M. Shirokov, J. P. Vary, A. I. Mazur and T. A. Weber, Phys. Lett. B **644**, 33 (2007); A. M. Shirokov, J. P. Vary, A. I. Mazur, S. A. Zaytsev and T. A. Weber, *ibid.* **621**, 96 (2005).

[11] R. J. Furnstahl, G. Hagen and T. Papenbrock, Phys. Rev. C **86**, 031301 (2012); S. N. More, A. Ekstrom, R. J. Furnstahl, G. Hagen and T. Papenbrock, *ibid.* **87**, 044326 (2013).

[12] S. A. Coon, M. I. Avetian, M. K. G. Kruse, U. van Kolck, P. Maris and J. P. Vary, Phys. Rev. C **86**, 054002 (2012); S. A. Coon, in *Proc. Int. Workshop Nucl. Theor. Supercomputing Era (NTSE-2012), Khabarovsk, Russia, June 18–22, 2012*, eds. A. M. Shirokov and A. I. Mazur. Pacific National University, Khabarovsk, 2013, p. 171, arXiv:1303.6358 [nucl-th] (2013).

Neutron matter with chiral EFT interactions: Perturbative and first QMC calculations

I. Tews[a,b], T. Krüger[a,b], A. Gezerlis[c,a,b], K. Hebeler[a,b] and A. Schwenk[b,a]

[a] *Institut für Kernphysik, Technische Universität Darmstadt, 64289 Darmstadt, Germany*
[b] *ExtreMe Matter Institute EMMI, GSI Helmholtzzentrum für Schwerionenforschung GmbH, 64291 Darmstadt, Germany*
[c] *Department of Physics, University of Guelph, Guelph, Ontario N1G 2W1, Canada*

Abstract

Neutron matter presents a unique system in chiral effective field theory (EFT), because all many-body forces among neutrons are predicted to next-to-next-to-next-to-leading order (N^3LO). We discuss perturbative and first Quantum Monte Carlo (QMC) calculations of neutron matter with chiral EFT interactions and their astrophysical impact for the equation of state and neutron stars.

Keywords: *Chiral EFT; three-body forces; QMC; neutron matter; neutron stars*

1 Chiral EFT and many-body forces

Chiral EFT describes the interactions between nucleons at momentum scales of the order of the pion mass $Q \sim m_\pi$ based on the symmetries of QCD [1, 2]. The resulting nuclear forces are organized in a systematic expansion in powers of Q/Λ_b, where $\Lambda_b \sim 500\,\mathrm{MeV}$ denotes the breakdown scale, leading to a typical expansion parameter $Q/\Lambda_b \sim 1/3$ for nuclei. At a given order this includes contributions from one- or multi-pion exchanges that govern the long- and intermediate-range parts and from short-range contact interactions. The short-range couplings are fit to few-body data and thus capture all short-range effects relevant at low energies.

In particular, chiral EFT provides a systematic basis to investigate many-body forces and their impact on few- and many-body systems [3]. In addition, it is possible to estimate theoretical uncertainties in the EFT. An important feature of chiral EFT is the consistency of two-nucleon (NN) and three-nucleon ($3N$) interactions. This predicts the two-pion-exchange parts of the leading (N^2LO) $3N$ forces, leaving only two low-energy couplings c_D, c_E that encode pion interactions with short-range NN pairs and short-range three-body physics. At the next-order, all many-body interactions are predicted parameter-free with many new structures [1]. This makes the application of N^3LO $3N$ and $4N$ forces very exciting. This is especially the case, because $3N$ forces have been found to be key for neutron matter [4] and for neutron-rich nuclei [3, 5], see, e.g., the recent work on the calcium isotopes [6–10].

2 Neutron matter from chiral EFT interactions

The physics of neutron matter ranges from universal properties at low densities [11,12] to the densest matter in neutron stars. For neutrons, the c_D, c_E parts of N^2LO $3N$ forces do not contribute due to the Pauli principle and the pion coupling to the

Proceedings of International Conference 'Nuclear Theory in the Supercomputing Era — 2013' (NTSE-2013), Ames, IA, USA, May 13–17, 2013. Eds. A. M. Shirokov and A. I. Mazur. Pacific National University, Khabarovsk, Russia, 2014, p. 302.
http://www.ntse-2013.khb.ru/Proc/Schwenk.pdf.

nucleon spin (also the c_4 two-pion-exchange part does not contribute due to the isospin structure) [4]. Therefore, all three- and four-neutron forces are predicted to N^{3}LO. To study these, we recently presented the first calculation of the neutron-matter energy that includes all NN, $3N$, and $4N$ interactions consistently to N^{3}LO [13, 14].

The largest contributions to the neutron-matter energy arise from NN interactions. In Refs. [13,14] we studied the perturbative convergence of all existing NN potentials at N^{2}LO and at N^{3}LO of Epelbaum, Glöckle, and Meißner (EGM) [15,16] with cutoffs $\Lambda/\tilde{\Lambda} = 450/500, 450/700, 550/600, 600/600$, and $600/700$ MeV, where Λ and $\tilde{\Lambda}$ denote the cutoff in the Lippmann–Schwinger equation and in the two-pion-exchange spectral-function regularization, respectively; as well as the available N^{3}LO NN potentials of Entem and Machleidt (EM) [2, 17] with cutoffs $\Lambda = 500$ and 600 MeV.

To study the perturbative convergence of the different NN potentials, we calculated the Hartree–Fock as well as second- and third-order energies, only including particle-particle diagrams, with both free and Hartree–Fock single-particle energies. The results for NN and N^{2}LO $3N$ forces are shown in Fig. 1 for the perturbative NN

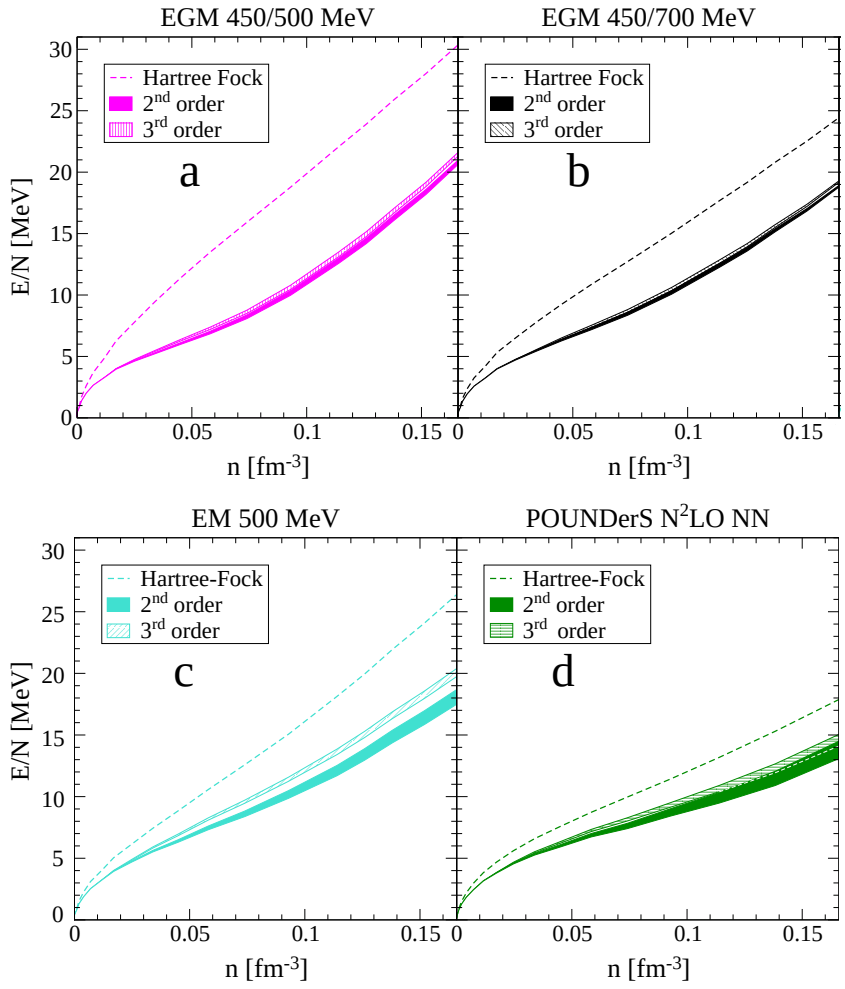

Figure 1: Panels a–c: Neutron-matter energy per particle E/N as a function of density n for the N^{3}LO NN potentials that exhibit a perturbative convergence. The dashed lines are Hartree–Fock results. The filled and shaded bands are second- and third-order results, where at each order the band ranges from using a free to a Hartree–Fock spectrum. All calculations include N^{2}LO $3N$ forces with a $3N$ cutoff $\Lambda = 2.0\,\mathrm{fm}^{-1}$ and low-energy couplings $c_1 = 0.75\,\mathrm{GeV}^{-1}$ and $c_3 = 4.77\,\mathrm{GeV}^{-1}$. For details see Ref. [14]. Panel d: Same for the POUNDerS N^{2}LO NN potential (without $3N$ forces).

interactions for a $3N$ cutoff $\Lambda = 2.0\,\mathrm{fm}^{-1}$ and a particular choice of $c_1 = 0.75\,\mathrm{GeV}^{-1}$, $c_3 = 4.77\,\mathrm{GeV}^{-1}$, although the general picture is unchanged for other coupling values. The bands result from using a free to a Hartree–Fock single-particle spectrum. The N^{3}LO EGM potentials with cutoffs 450/500 MeV and 450/700 MeV exhibit only small energy changes from second to third order. This indicates that these potentials are perturbative for neutron matter. For the EM 500 MeV potential the difference between second and third order is larger compared to the EGM potentials. Since this potential is most commonly used in nuclear structure calculations, we include it in our complete N^{3}LO calculation. The perturbative convergence for these potentials in neutron matter is similar to renormalization-group-evolved interactions in nuclear matter [18]. We have also studied in Fig. 1 the POUNDerS N^{2}LO NN potential [19], which is found to be perturbative as well. In addition, there are in-medium chiral perturbation theory schemes that treat the Fermi momentum as an explicit scale [20,21].

The larger-cutoff N^{3}LO EGM 550/600 MeV and 600/600 MeV potentials as well as the EM 600 MeV potential are not used in our calculations because they show large changes from second to third order [14]. This demonstrates that these interactions are nonperturbative. The N^{3}LO EGM 600/600 MeV potential is not used because it breaks Wigner symmetry ($C_T = 0$) at the interaction level (as discussed in Ref. [14]).

The subleading N^{3}LO $3N$ forces have been derived recently [22, 23]. They can be grouped into five topologies, where the latter two depend on the NN contacts $C_{T/S}$:

$$V_{3N}^{\mathrm{N^3LO}} = V^{2\pi} + V^{2\pi\text{-}1\pi} + V^{\mathrm{ring}} + V^{2\pi\text{-cont}} + V^{1/m}. \tag{1}$$

$V^{2\pi}$, $V^{2\pi\text{-}1\pi}$, and V^{ring} denote the long-range two-pion-exchange, the two-pion–one-pion-exchange, and the pion-ring $3N$ interactions, respectively [22]. The terms $V^{2\pi\text{-cont}}$ and $V^{1/m}$ are the short-range two-pion-exchange–contact $3N$ interaction and $3N$ relativistic corrections [23]. The N^{3}LO $4N$ forces have been derived in Refs. [24, 25] and in general depend on the contact C_T, but in neutron matter the C_T-dependent parts do not contribute. There are seven $4N$ topologies that lead to non-vanishing contributions. In neutron matter only two three-pion-exchange diagrams (in Ref. [24] named V^a and V^e) and the pion-pion-interaction diagram (V^f) contribute [13].

The N^{3}LO many-body interactions are evaluated in the Hartree–Fock approximation, which is expected to be reliable for neutron matter [4]. We show the individual contributions of the $3N$ and $4N$ forces in Fig. 2, where the bands correspond to the $3N/4N$ cutoff variation $\Lambda = 2\text{–}2.5\,\mathrm{fm}^{-1}$. The N^{3}LO two-pion-exchange expectation value (panel 1) sets the expected scale of N^{3}LO $3N$ interactions. Compared to this, we find relatively large expectation values in the $V^{2\pi\text{-}1\pi}$, V^{ring}, and $V^{2\pi\text{-cont}}$ topologies. This could indicate that in these topologies Δ contributions shifted to N^{4}LO are expected to be important [14, 26]. The $3N$ relativistic corrections and the contributions from N^{3}LO $4N$ forces are small (see also Ref. [27]). However, also for $4N$ forces additional larger contributions from Δ excitations may arise at N^{4}LO [28].

The complete N^{3}LO result for neutron matter is shown in the left panel of Fig. 3, which includes all NN, $3N$, and $4N$ interactions to N^{3}LO [13]. At saturation density, we obtain for the energy per particle $E/N = 14.1\text{–}21.0\,\mathrm{MeV}$. This range is based on different NN potentials, a variation of the couplings $c_1 = -(0.75\text{–}1.13)\,\mathrm{GeV}^{-1}$, $c_3 = -(4.77\text{–}5.51)\,\mathrm{GeV}^{-1}$ [26], which dominates the total uncertainty, a $3N/4N$-cutoff variation $\Lambda = 2\text{–}2.5\,\mathrm{fm}^{-1}$, and the uncertainty in the many-body calculation.

The neutron-matter energy in Fig. 3 is in very good agreement with NLO lattice results [29] and QMC simulations [12] at very low densities (see also the inset). At nuclear densities, we compare our N^{3}LO results with variational calculations based on phenomenological potentials (APR) [30], which are within the N^{3}LO band, but do not provide theoretical uncertainties. In addition, we compare the density dependence with results from Auxiliary Field Diffusion MC (AFDMC) calculations (GCR) [31] based on nuclear force models adjusted to a symmetry energy of 32 MeV.

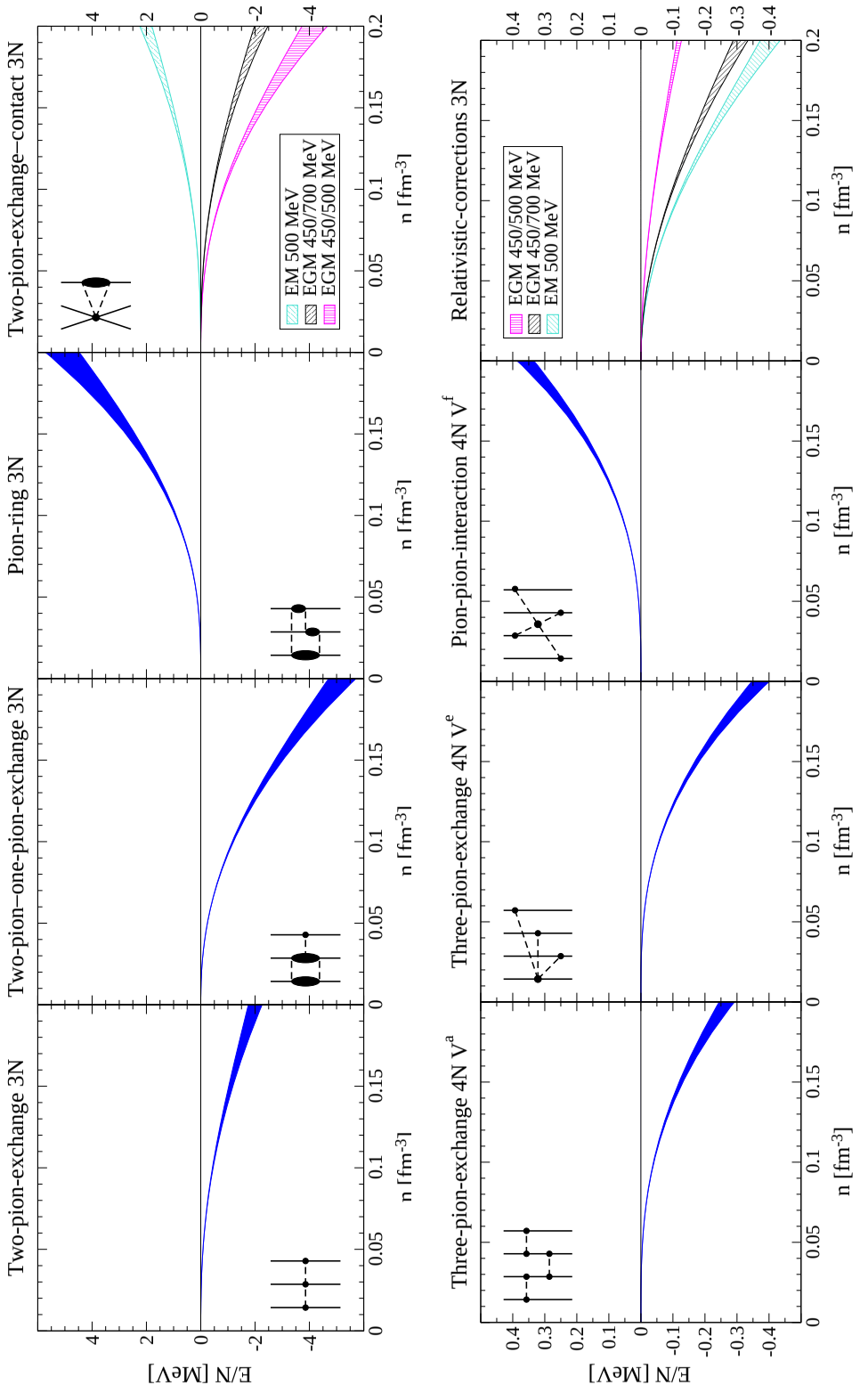

Figure 2: Energy per particle E/N as a function of density n for all individual N^{3}LO $3N$- and $4N$-force contributions to neutron matter at the Hartree–Fock level [13]. All bands are obtained by varying the $3N/4N$ cutoffs $\Lambda = 2.0{-}2.5\,\mathrm{fm}^{-1}$. For the $3N$ two-pion-exchange–contact forces and the $3N$ relativistic corrections, the different bands correspond to the different NN contacts, C_T and C_S, determined consistently for the N^{3}LO EM/EGM potentials. The diagrams illustrate the $3N/4N$ force topology.

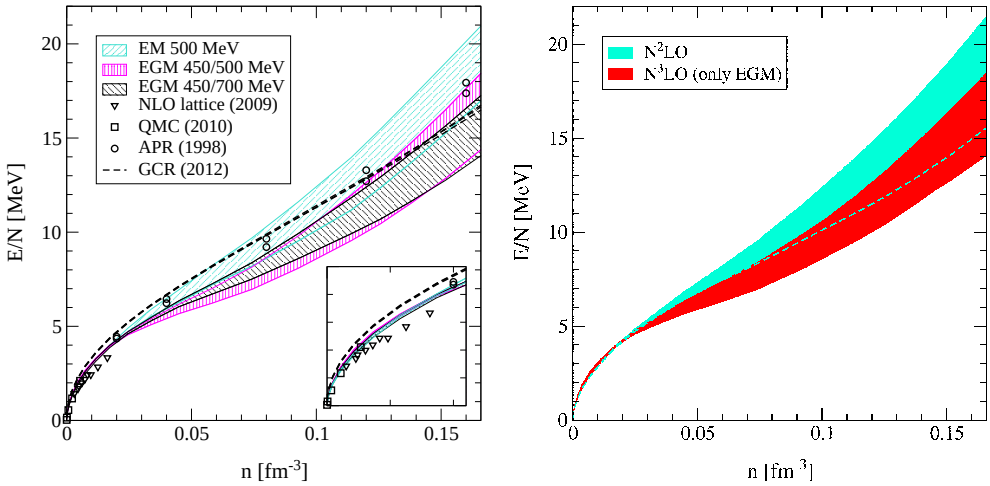

Figure 3: Left panel: Neutron-matter energy per particle E/N as a function of density n including NN, $3N$ and $4N$ forces to N^{3}LO for the given EM/EGM NN potentials [13]. The bands include uncertainty estimates due to the many-body calculation, the low-energy c_i couplings, and by varying the $3N/4N$ cutoffs. For comparison, results are shown at low densities (see also the inset) from NLO lattice [29] and QMC simulations [12], and at nuclear densities from variational [30] and Auxiliary Field Diffusion MC calculations (GCR) [31] based on phenomenological potentials. Right panel: Neutron-matter energy per particle at N^{2}LO (upper cyan band that extends to the dashed line) and N^{3}LO (lower red band) [13]. The bands are based on the EGM NN potentials and include the same uncertainty estimates.

We also compare the convergence from N^{2}LO to N^{3}LO in the same calculational setup. For this comparison, we only consider the EGM potentials with cutoffs 450/500 MeV and 450/700 MeV. This leads to an N^{3}LO energy range of 14.1−18.4 MeV per particle at n_0. For the N^{2}LO band in the right panel of Fig. 3, we have estimated the theoretical uncertainties in the same way, and find an energy of 15.5−21.4 MeV per particle at n_0. The two bands overlap but the range of the band is only reduced by a factor of 2/3 in contrast to the 1/3 expected from the EFT power counting. We attribute this to Δ effects (see the discussion in Refs. [13, 14]).

3 QMC calculations with chiral EFT interactions

Quantum Monte Carlo methods have not been used with chiral EFT interactions due to nonlocalities in their present implementation in momentum space. Nonlocalities are difficult to handle in QMC [32]. In the momentum-space interactions, there are two sources of nonlocalities: first, due to regulator functions that lead to nonlocal interactions upon Fourier transformation, and second, due to contact interactions that depend on the momentum transfer in the exchange channel $\mathbf{k}$ and from $\mathbf{k}$-dependent parts in pion-exchange contributions beyond N^{2}LO. For applications in QMC, we have developed local chiral EFT interactions in Ref. [32].

To avoid regulator-generated nonlocalities for the long-range pion-exchange parts, we use the local coordinate-space expressions for the LO one-pion-exchange as well as NLO and N^{2}LO two-pion-exchange interactions [33,34] and regulate them directly in coordinate space using the function $f_{\rm long}(r) = 1 - e^{-(r/R_0)^4}$, which smoothly cuts off interactions at short distances $r < R_0$ while leaving the long-range parts unchanged [32]. So, R_0 takes over the role of the cutoff Λ in momentum space.

To remove the $\mathbf{k}$-dependent contact interactions to N^{2}LO, we make use of the

freedom to choose a basis of short-range operators in chiral EFT interactions (similar to Fierz ambiguities). At LO, one usually considers the two momentum-independent contact interactions $C_S + C_T\,\boldsymbol{\sigma}_1 \cdot \boldsymbol{\sigma}_2$. However, it is equivalent to choose any two of the four operators $\mathbb{1}$, $\boldsymbol{\sigma}_1 \cdot \boldsymbol{\sigma}_2$, $\boldsymbol{\tau}_1 \cdot \boldsymbol{\tau}_2$, and $\boldsymbol{\sigma}_1 \cdot \boldsymbol{\sigma}_2\, \boldsymbol{\tau}_1 \cdot \boldsymbol{\tau}_2$, with spin and isospin operators $\boldsymbol{\sigma}_i, \boldsymbol{\tau}_i$, because there are only two S-wave channels due to the Pauli principle. It is a convention in present chiral EFT interactions to neglect the isospin dependence, which is then generated from the exchange terms [15–17].

We use this freedom to keep at NLO (order Q^2) an isospin-dependent q^2 contact interaction and an isospin-dependent $(\boldsymbol{\sigma}_1 \cdot \mathbf{q})(\boldsymbol{\sigma}_2 \cdot \mathbf{q})$ tensor part in favor of a nonlocal k^2 contact interaction and a nonlocal $(\boldsymbol{\sigma}_1 \cdot \mathbf{k})(\boldsymbol{\sigma}_2 \cdot \mathbf{k})$ tensor part. This leads to the following seven linearly independent contact interactions at NLO that are local [32],

$$V_{\rm short}^{\rm NLO} = C_1\, q^2 + C_2\, q^2\, \boldsymbol{\tau}_1 \cdot \boldsymbol{\tau}_2 + \big(C_3\, q^2 + C_4\, q^2\, \boldsymbol{\tau}_1 \cdot \boldsymbol{\tau}_2\big)\, \boldsymbol{\sigma}_1 \cdot \boldsymbol{\sigma}_2 + i\, \frac{C_5}{2}\, (\boldsymbol{\sigma}_1 + \boldsymbol{\sigma}_2) \cdot \mathbf{q} \times \mathbf{k} + C_6\, (\boldsymbol{\sigma}_1 \cdot \mathbf{q})(\boldsymbol{\sigma}_2 \cdot \mathbf{q}) + C_7\, (\boldsymbol{\sigma}_1 \cdot \mathbf{q})(\boldsymbol{\sigma}_2 \cdot \mathbf{q})\, \boldsymbol{\tau}_1 \cdot \boldsymbol{\tau}_2, \quad (2)$$

where the only $\mathbf{k}$-dependent contact interaction (C_5) is a spin-orbit potential.

The low-energy couplings $C_{S/T}$ at LO plus C_{1-7} at NLO and N^{2}LO are fitted in Ref. [36] for different R_0 to the NN phase shifts of the Nijmegen partial-wave analysis [35] at laboratory energies $E_{\rm lab} = 1, 5, 10, 25, 50$, and 100 MeV, using a local regulator. The reproduction of the isospin $T = 1$ S- and P-waves is shown order by order in Fig. 4, where the bands are obtained by varying R_0 between 0.8−1.2 fm and provide a measure of the theoretical uncertainty. At N^{2}LO, an isospin-symmetry-breaking contact interaction (C_{nn} for neutrons) is added, which is fitted to $a_{nn} = -18.8$ fm. As shown in Fig. 4, the comparison with NN phase shifts is very good for $E_{\rm lab} \lesssim 150$ MeV. This is similar for higher partial waves and isospin $T = 0$ channels. In cases where there are deviations for higher energies (such as in the $^3P_2$), the width of the band signals significant theoretical uncertainties due to the chiral EFT truncation at N^{2}LO. The NLO and N^{2}LO bands nicely overlap or are very close, but it is also apparent that the bands at N^{2}LO are of a similar size as at NLO. This is because the width of the bands at both NLO and N^{2}LO shows effects of the neglected order-Q^4 contact interactions.

Since nuclear forces contain quadratic spin, isospin, and tensor operators (of the form $\boldsymbol{\sigma}_i^\alpha\, A_{ij}^{\alpha\beta}\, \boldsymbol{\sigma}_j^\beta$), the many-body wave function cannot be expressed as a product of single-particle spin-isospin states. All possible spin-isospin nucleon-pair states need to be explicitly accounted for, leading to an exponential increase in the number of possible states. However, the AFDMC method [37] is capable of efficiently handling spin-dependent Hamiltonians. AFDMC rewrites the Green's function by applying a Hubbard–Stratonovich transformation using auxiliary fields to change the quadratic spin-isospin operator dependences to linear. For the case of neutrons, it is also possible to include spin-orbit interactions and $3N$ forces in AFDMC nonperturbatively [38,39].

In the upper panel of Fig. 5 we show first AFDMC calculations for the neutron-matter energy with local chiral EFT NN interactions at LO, NLO, and N^{2}LO [32]. At each order, the full interaction is used both in the propagator and when evaluating observables. The bands in Fig. 5 give the range of the energy obtained by varying R_0 between 0.8−1.2 fm, where the softer $R_0 = 1.2$ fm interactions yield the lower energies. At LO, the energy has a large uncertainty. The overlap of the bands at different orders in Fig. 5 is very systematic. In addition, the result that the NLO and N^{2}LO bands are comparable is expected from the discussion of the phase-shift bands in Fig. 4 and from the large c_i entering at N^{2}LO.

Our AFDMC results provide first nonperturbative benchmarks for chiral EFT interactions at nuclear densities. We have performed perturbative calculations as in the previous section based on the same local N^{2}LO NN interactions. The perturbative energies are compared in the lower panel of Fig. 5 to the AFDMC N^{2}LO results. For the softer $R_0 = 1.2$ fm ($\Lambda \sim 400$ MeV) interaction, the third-order corrections

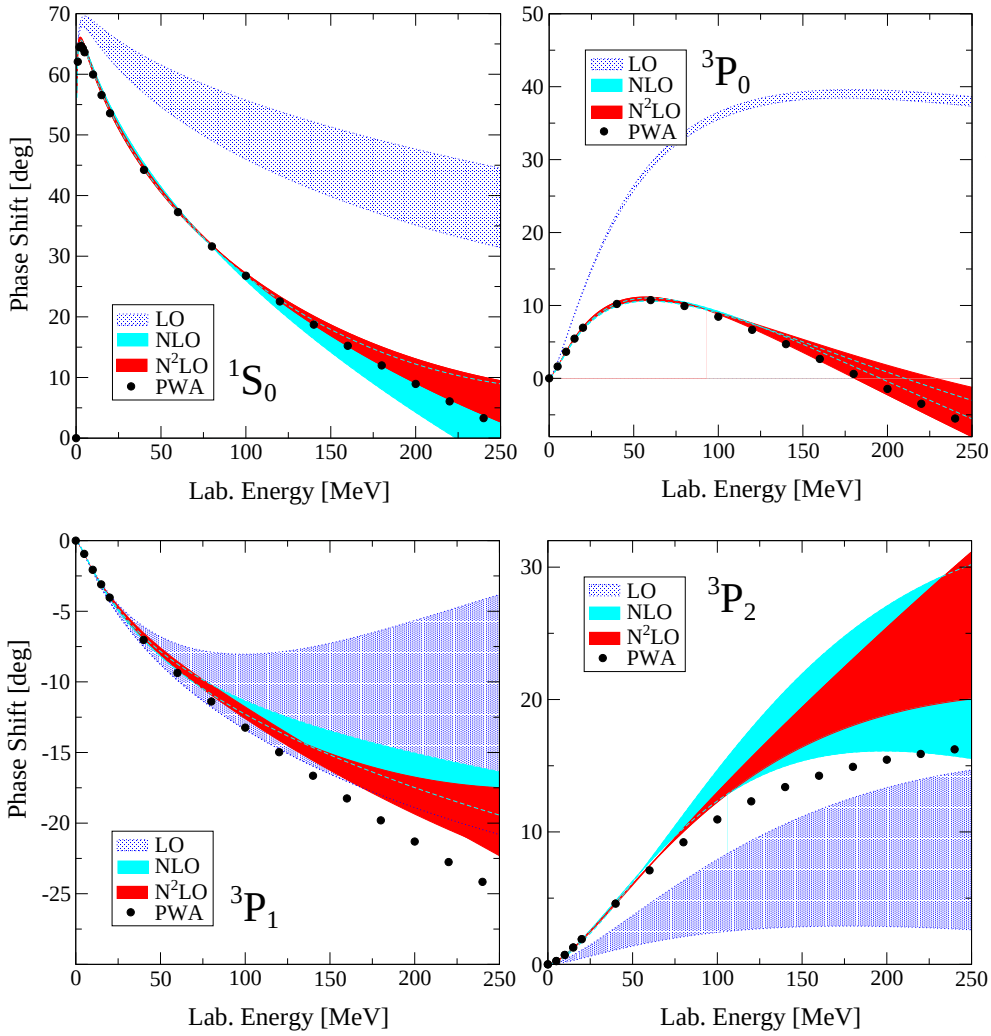

Figure 4: Neutron-proton phase shifts as a function of laboratory energy in the ${}^1S_0$, ${}^3P_0$, ${}^3P_1$, and ${}^3P_2$ partial waves in comparison to the Nijmegen partial-wave analysis (PWA) [35]. The LO, NLO, and N^{2}LO local chiral potential bands are obtained by varying R_0 between 0.8−1.2 fm (with a spectral-function cutoff $\widetilde{\Lambda} = 800$ MeV) [32,36].

are small and the perturbative third-order energy is in excellent agreement with the AFDMC results, while for the harder $R_0 = 0.8$ fm ($\Lambda \sim 600$ MeV) interaction, the convergence is clearly slow. This is the first nonperturbative validation for neutron matter of the possible perturbativeness of low-cutoff $\Lambda \sim 400$ MeV interactions [40].

4 Astrophysical applications

The symmetry energy S_v and its density derivative L provide important input for astrophysics [41]. To calculate these, we follow Ref. [42]. The predicted ranges for S_v and L at saturation density are $S_v = 28.9-34.9$ MeV and $L = 43.0-66.6$ MeV. The S_v and L ranges are in very good agreement with experimental constraints from nuclear masses [43] and from the dipole polarizability of ^{208}Pb [44], see the left panel of Fig. 6. In addition, they also overlap with the results for RG-evolved NN interactions with N^{2}LO $3N$ forces [41, 42], but due to the additional density dependences from N^{3}LO

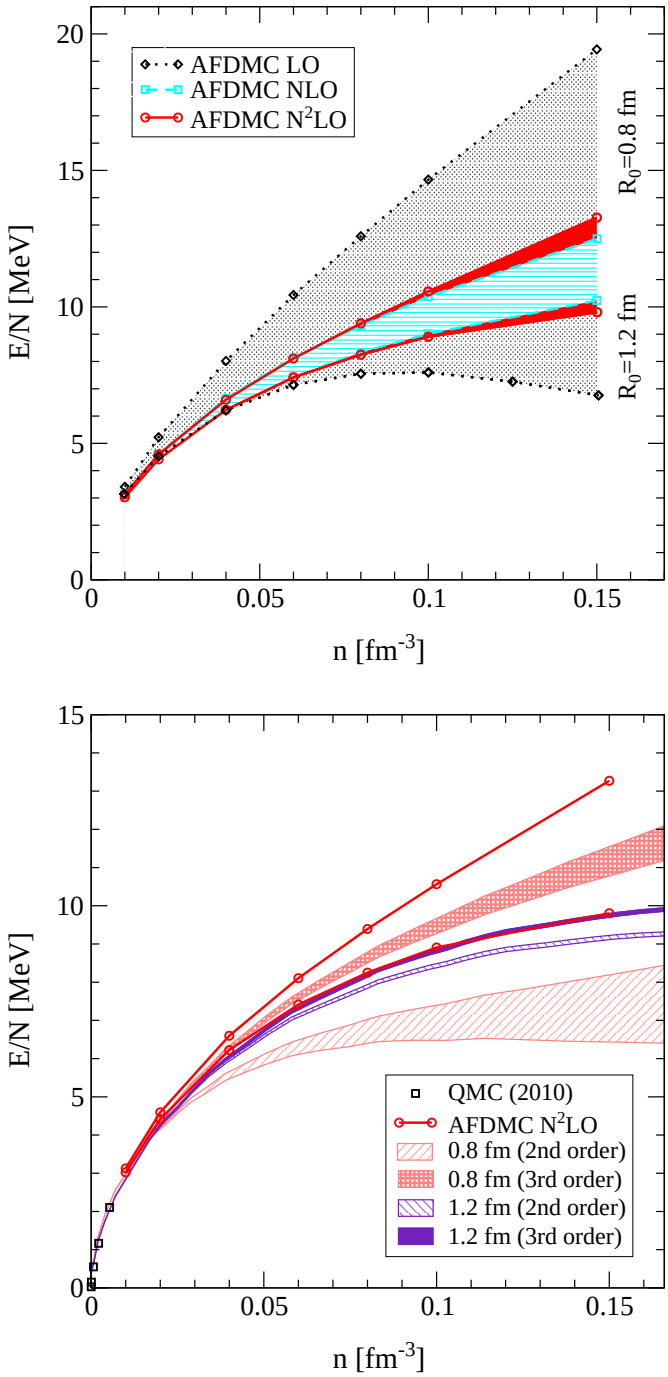

Figure 5: Upper panel: Neutron-matter energy per particle E/N as a function of density n calculated using AFDMC with chiral EFT NN interactions at LO, NLO, and N^{2}LO [32]. The statistical errors are smaller than the points shown. The lines give the range obtained by varying R_0 between 0.8−1.2 fm. Lower panel: The AFDMC N^{2}LO band in comparison to perturbative calculations using the same N^{2}LO NN interactions. The lower (upper) limit of the AFDMC N^{2}LO band is for $R_0 = 1.2$ fm ($R_0 = 0.8$ fm), corresponding to a momentum cutoff $\Lambda \sim 400$ MeV ($\Lambda \sim 600$ MeV). Perturbative results are shown at second and third order. For the softer $R_0 = 1.2$ fm interaction (narrow purple bands), third-order corrections are small and the third-order energy is in excellent agreement with the AFDMC results, while for the harder $R_0 = 0.8$ fm interaction (light red bands), the convergence is clearly slow.

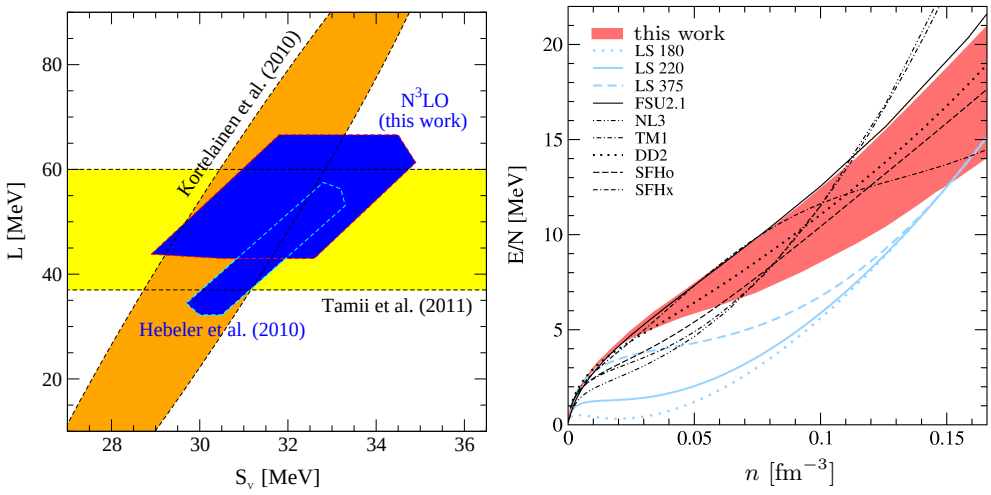

Figure 6: Left panel: Range for the symmetry energy S_v and its density dependence L obtained at N^{3}LO [13] versus including $3N$ forces at N^{2}LO (Hebeler *et al.* [42]). For comparison, see Ref. [41], we show constraints obtained from energy-density functionals for nuclear masses (Kortelainen *et al.* [43]) and from the ^{208}Pb dipole polarizability (Tamii *et al.* [44]). Right panel: Comparison of the N^{3}LO neutron-matter energy of the left panel of Fig. 3 (red band) with equations of state for core-collapse supernova simulations provided by Lattimer–Swesty (LS with different incompressibilities 180, 220, and 375 MeV), G. Shen (FSU2.1, NL3), Hempel (TM1, SFHo, SFHx), and Typel (DD2). For details see Ref. [14].

many-body forces, the correlation between S_v and L is not as tight.

The neutron-matter results also provide constraints for equations of state for core-collapse-supernova simulations. In the right panel of Fig. 6, we compare the N^{3}LO neutron-matter band (red band) to the Lattimer–Swesty (LS) equation of state [45] (with different incompressibilities 180, 220, and 375 MeV), which is most commonly used in simulations, and to different relativistic mean-field-theory equations of state based on the density functionals DD2 [46], FSU2.1 [47], NL3 [48], SFHo, SFHx [49], and TM1 [50]. At low densities only the DD2, FSU2.1 and SFHx equations of state are consistent with the N^{3}LO neutron-matter band. The NL3 and TM1 equations of state have a too strong density dependence, which leads to unnaturally large S_v and L values. In addition, Fig. 6 exhibits a strange density dependence of SFHx.

Next, we use the N^{3}LO neutron-matter results to provide constraints for the structure of neutron stars. We follow Refs. [42, 51] for incorporating beta equilibrium and for the extension to high densities using piecewise polytropes that are constrained by causality and by the requirement to support a $1.97 \pm 0.04\,M_\odot$ neutron star [52] (see also the recent $2.01 \pm 0.04\,M_\odot$ discovery [53]). In addition, we consider the case, if a $2.4\,M_\odot$ neutron star were to be observed. The resulting constraints on the neutron star mass-radius diagram are shown in Fig. 7 by the red bands. The bands represent an envelope of a large number of individual equations of state reflecting the uncertainties in the N^{3}LO neutron-matter calculation and in the polytropic extensions to high densities [42, 51]. The combination with the $2\,M_\odot$ neutron star (left panel) predicts a radius range of 9.7−13.9 km for a $1.4\,M_\odot$ star [14, 42]. The maximal neutron star mass is found to be $3.1\,M_\odot$, with a corresponding radius of about 14 km. We also find very good agreement with the mass-radius constraints from the neutron-matter calculations based on RG-evolved NN interactions with N^{2}LO $3N$ forces [42], which are shown by the thick dashed blue lines in the left panel of Fig. 7.

In addition, we show in Fig. 7 the mass-radius relations obtained from equations

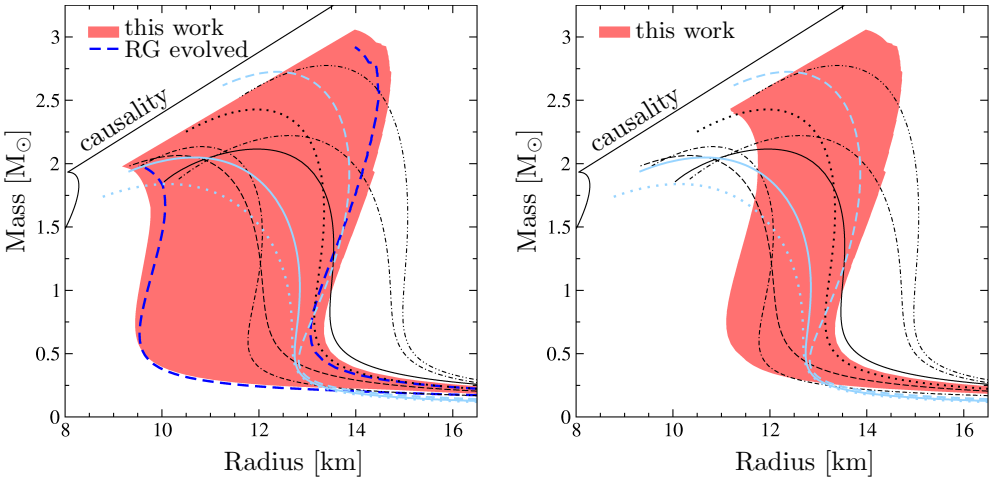

Figure 7: Constraints on the mass-radius diagram of neutron stars based on our neutron-matter results at N^{3}LO following Ref. [42, 51] for the extension to neutron-star matter and to high densities (red band), in comparison to the constraints from calculations based on RG-evolved NN interactions (thick dashed blue lines) [42]. We also show the mass-radius relations obtained from the equations of state for core-collapse supernova simulations shown in Fig. 6. Left panel: Band obtained with the constraint of a 1.97 $M_\odot$ neutron star [14]. Right panel: Same for a 2.4 $M_\odot$ star.

of state for core-collapse supernova simulations [45, 47–50, 54, 55]. The inconsistency in Fig. 6 of many of the equations of state with the N^{3}LO neutron-matter band at low densities results in a large spread of very low mass/large radius neutron stars, where the red band is considerably narrower in Fig. 7. For typical neutron stars, our calculations rule out the NL3 and TM1 equations of state, which produce too large radii. Finally, we have also explored the constraints from N^{3}LO calculations for the chiral condensate in neutron matter [56].

All the very best for your 70th birthday, James, lots of good health and energy for fun in life and physics (and many days like the one we enjoyed in Capri)! We would like to thank E. Epelbaum, S. Gandolfi, J. M. Lattimer, A. Nogga, and C. J. Pethick, who contributed to the results presented in this talk. This work was supported by the DFG through Grant SFB 634, the ERC Grant No. 307986 STRONGINT, the Helmholtz Alliance HA216/EMMI, and NSERC. Computations were performed at the Jülich Supercomputing Center and at NERSC.

References

[1] E. Epelbaum, H.-W. Hammer and U.-G. Meißner, Rev. Mod. Phys. **81**, 1773 (2009).

[2] R. Machleidt and D. R. Entem, Phys. Rept. **503**, 1 (2011).

[3] H.-W. Hammer, A. Nogga and A. Schwenk, Rev. Mod. Phys. **85**, 197 (2013).

[4] K. Hebeler and A. Schwenk, Phys. Rev. C **82**, 014314 (2010).

[5] T. Otsuka, T. Suzuki, J. D. Holt, A. Schwenk and Y. Akaishi, Phys. Rev. Lett. **105**, 032501 (2010).

[6] J. D. Holt, T. Otsuka, A. Schwenk and T. Suzuki, J. Phys. G **39**, 085111 (2012).

[7] G. Hagen, M. Hjorth-Jensen, G. R. Jansen, R. Machleidt and T. Papenbrock, Phys. Rev. Lett. **109**, 032502 (2012).

[8] A. T. Gallant *et al.*, Phys. Rev. Lett. **109**, 032506 (2012).

[9] J. D. Holt, J. Menéndez and A. Schwenk, J. Phys. G **40**, 075105 (2013).

[10] F. Wienholtz *et al.*, Nature **498**, 346 (2013).

[11] A. Schwenk and C. J. Pethick, Phys. Rev. Lett. **95**, 160401 (2005).

[12] A. Gezerlis and J. Carlson, Phys. Rev. C **81**, 025803 (2010); A. Gezerlis and R. Sharma, *ibid.* **85**, 015806 (2012).

[13] I. Tews, T. Krüger, K. Hebeler and A. Schwenk, Phys. Rev. Lett. **110**, 032504 (2013).

[14] T. Krüger, I. Tews, K. Hebeler and A. Schwenk, Phys. Rev. C **88**, 025802 (2013).

[15] E. Epelbaum, W. Glöckle and U.-G. Meißner, Eur. Phys. J. A **19**, 401 (2004).

[16] E. Epelbaum, W. Glöckle and U.-G. Meißner, Nucl. Phys. A **747**, 362 (2005).

[17] D. R. Entem and R. Machleidt, Phys. Rev. C **68**, 041001(R) (2003).

[18] S. K. Bogner, A. Schwenk, R. J. Furnstahl and A. Nogga, Nucl. Phys. A **763**, 59 (2005); K. Hebeler, S. K. Bogner, R. J. Furnstahl, A. Nogga and A. Schwenk, Phys. Rev. C **83**, 031301(R) (2011).

[19] A. Ekström, G. Baardsen, C. Forssén, G. Hagen, M. Hjorth-Jensen, G. R. Jansen, R. Machleidt, W. Nazarewicz, T. Papenbrock, J. Sarich and S. M. Wild, Phys. Rev. Lett. **110**, 192502 (2013).

[20] N. Kaiser, S. Fritsch and W. Weise, Nucl. Phys. A **697**, 255 (2002); J. W. Holt, N. Kaiser and W. Weise, arXiv:1304.6350 (2013).

[21] A. Lacour, J. A. Oller and U.-G. Meißner, Ann. Phys. (NY) **326**, 241 (2011).

[22] V. Bernard, E. Epelbaum, H. Krebs and U.-G. Meißner, Phys. Rev. C **77**, 064004 (2008).

[23] V. Bernard, E. Epelbaum, H. Krebs and U.-G. Meißner, Phys. Rev. C **84**, 054001 (2011).

[24] E. Epelbaum, Phys. Lett. B **639**, 456 (2006).

[25] E. Epelbaum, Eur. Phys. J. A **34**, 197 (2007).

[26] H. Krebs, A. Gasparyan and E. Epelbaum, Phys. Rev. C **85**, 054006 (2012).

[27] S. Fiorilla, N. Kaiser and W. Weise, Nucl. Phys. A **880**, 65 (2012).

[28] N. Kaiser, Eur. Phys. J. A **48**, 135 (2012).

[29] E. Epelbaum, H. Krebs, D. Lee and U.-G. Meißner, Eur. Phys. J. A **40**, 199 (2009).

[30] A. Akmal, V. R. Pandharipande and D. G. Ravenhall, Phys. Rev. C **58**, 1804 (1998).

[31] S. Gandolfi, J. Carlson and S. Reddy, Phys. Rev. C **85**, 032801(R) (2012).

[32] A. Gezerlis, I. Tews, E. Epelbaum, S. Gandolfi, K. Hebeler, A. Nogga and A. Schwenk, Phys. Rev. Lett. **111**, 032501 (2013).

[33] N. Kaiser, R. Brockmann and W. Weise, Nucl. Phys. A **625**, 758 (1997).

[34] E. Epelbaum, W. Glöckle and U.-G. Meißner, Eur. Phys. J. A **19**, 125 (2004).

[35] V. G. J. Stoks, R. A. M. Klomp, M. C. M. Rentmeester and J. J. de Swart, Phys. Rev. C **48**, 792 (1993).

[36] M. Freunek, *Diploma thesis.* Universität Bonn and Forschungszentrum Jülich, 2007.

[37] K. E. Schmidt and S. Fantoni, Phys. Lett. B **446**, 99 (1999).

[38] A. Sarsa, S. Fantoni, K. E. Schmidt and F. Pederiva, Phys. Rev. C **68**, 024308 (2003).

[39] S. Gandolfi, A. Yu. Illarionov, K. E. Schmidt, F. Pederiva and S. Fantoni, Phys. Rev. C **79**, 054005 (2009).

[40] S. K. Bogner, R. J. Furnstahl and A. Schwenk, Progr. Part. Nucl. Phys. **65**, 94 (2010).

[41] J. M. Lattimer and Y. Lim, Astrophys. J. **771**, 51 (2013).

[42] K. Hebeler, J. M. Lattimer, C. J. Pethick and A. Schwenk, Astrophys. J. **773**, 11 (2013).

[43] M. Kortelainen, T. Lesinski, J. Moré, W. Nazarewicz, J. Sarich, N. Schunck, M. Stoitsov and S. Wild, Phys. Rev. C **82**, 024313 (2010).

[44] A. Tamii *et al.*, Phys. Rev. Lett. **107**, 062502 (2011).

[45] J. M. Lattimer and F. D. Swesty, Nucl. Phys. A **535**, 331 (1991).

[46] S. Typel, *private communication.*

[47] G. Shen, C. J. Horowitz and E. O'Connor, Phys. Rev. C **83**, 065808 (2011).

[48] G. Shen, C. J. Horowitz and S. Teige, Phys. Rev. C **83**, 035802 (2011).

[49] A. W. Steiner, M. Hempel and T. Fischer, arXiv:1207.2184 (2012).

[50] H. Shen, H. Toki, K. Oyamatsu and K. Sumiyoshi, Astrophys. J. Suppl. **197**, 20 (2011).

[51] K. Hebeler, J. M. Lattimer, C. J. Pethick and A. Schwenk, Phys. Rev. Lett. **105**, 161102 (2010).

[52] P. B. Demorest, T. Pennucci, S. M. Ransom, M. S. E. Roberts and J. W. T. Hessels, Nature **467**, 1081 (2010).

[53] J. Antoniadis *et al.*, Science **340**, 448 (2013).

[54] M. Hempel, T. Fischer, J. Schaffner-Bielich and M. Liebendörfer, Astrophys. J. **748**, 70 (2012).

[55] E. O'Connor, *private communication*; A. Kleiner, *B. Sc. Thesis.* Technische Universität Darmstadt, 2012.

[56] T. Krüger, I. Tews, B. Friman, K. Hebeler and A. Schwenk, Phys. Lett. B **726**, 412 (2013).

Universal Properties of Infrared Extrapolations in a Harmonic Oscillator Basis

Sidney A. Coon[a], **Michael K. G. Kruse**[b]

[a] *Department of Physics, University of Arizona, Tucson, Arizona USA*
[b] *Lawrence Livermore National Laboratory, P.O. Box 808, L-414, Livermore, California 94551, USA*

Abstract

We continue our studies of infrared (ir) and ultraviolet (uv) regulators of no-core shell model calculations. We extend our results that an extrapolation in the ir cutoff with the uv cutoff above the intrinsic uv scale of the interaction is quite successful, not only for the eigenstates of the Hamiltonian but also for expectation values of operators considered long range. The latter results are obtained with Hamiltonians transformed by the similarity renormalization group (SRG) evolution. On the other hand, a suggested extrapolation in the uv cutoff when the ir cutoff is below the intrinsic ir scale is neither robust nor reliable.

Keywords: *No-core shell model; convergence of expansion in harmonic oscillator functions; ultraviolet regulator; infrared regulator*

1 Introduction

Variational calculations based upon a harmonic oscillator (HO) basis expansion have a long history in nuclear structure physics. If one views a shell-model calculation as a variational calculation, expanding the configuration space merely serves to improve the trial wave function [1]. A parallel program uses the HO eigenfunctions as a basis of a finite linear expansion to make a straightforward variational calculation of the properties of light nuclei [2]. Theorems based upon functional analysis established the asymptotic convergence rate of these calculations as a function of the counting number ($\mathcal{N}$) which characterizes the size of the expansion basis (or model space) [3,4]. The convergence rates of these theorems (inverse power laws in $\mathcal{N}$ for "non smooth" potentials such as Yukawa's with strong short range correlations and exponential in $\mathcal{N}$ for "smooth" potentials such as gaussians) were demonstrated numerically in Ref. [3] for the HO expansion and in Ref. [5] for the analogous expansion in hyperspherical harmonics. These convergence theorems are used to extrapolate to the "infinite" basis in few-body studies [6] and in "*ab initio*" "no-core shell model" (NCSM) calculations of *s*- and *p*-shell nuclei [7]. However, the HO expansion basis has an intrinsic scale parameter $\hbar\omega$ which does not naturally fit into an extrapolation scheme based upon $\mathcal{N}$ as discussed in Refs. [3,4,8]. Indeed the model spaces of these NCSM approaches are characterized by the ordered pair $(\mathcal{N}, \hbar\omega)$. Here the basis truncation parameter $\mathcal{N}$ and the HO energy parameter $\hbar\omega$ are variational parameters [7,9,10]. With the HO basis in the nuclear structure problem, convergence has been discussed, in practice, with an emphasis on obtaining those parameters which appear linearly in the trial function (i. e. convergence with $\mathcal{N}$). In an early example, $\hbar\omega$ is simply fixed at a value which gives the fastest convergence in $\mathcal{N}$ [6]. Later, for each $\mathcal{N}$ the non-linear parameter $\hbar\omega$ is varied to obtain the minimal energy [9,11] for a fixed $\mathcal{N}$ and then

Proceedings of International Conference 'Nuclear Theory in the Supercomputing Era — 2013' (NTSE-2013), Ames, IA, USA, May 13–17, 2013. Eds. A. M. Shirokov and A. I. Mazur. Pacific National University, Khabarovsk, Russia, 2014, p. 314.
http://www.ntse-2013.khb.ru/Proc/Coon.pdf.

the convergence with $\mathcal{N}$ is examined at that fixed value of $\hbar\omega$. Other extrapolation schemes have been proposed and used [10, 12].

It is the purpose of this contribution to continue an investigation of the extrapolation tools introduced in Ref. [13] which use $\mathcal{N}$ and $\hbar\omega$ on an equal footing. These tools are based upon the pair of ultraviolet (uv) and infrared (ir) cutoffs (each a function of both $\mathcal{N}$ and $\hbar\omega$) of the model space. These regulators were first introduced to the NCSM by Ref. [14] in the context of an effective field theory (EFT) approach. For a recent review of this program see Ref. [15].

The early *ab initio* calculations, both of the "no-core" shell model in which all nucleons are active [1] and of the Moshinsky program attempted to overcome the challenges posed by "non-smooth" two-body potentials by including Jastrow type two-body correlations in the trial wave function. Nowadays, the NN potentials are tamed by unitary transformations within the model space [16] or in free space by either the similarity renormalization group (SRG) evolution [17] or the $V_{low\,k}$ truncation [18, 19]. In all three cases, this procedure generates effective many-body interactions in the new Hamiltonian. Neglecting these destroys the variational aspect of the calculation (and changes the physics contained in the calculation, of course). We retain the variational nature of our NCSM investigation by choosing a realistic smooth nucleon-nucleon (NN) interaction Idaho N^{3}LO [20] which has been used previously without renormalization within the model space for light nuclei ($A \leq 6$) [9]. The Idaho N^{3}LO potential is a rather soft one, with heavily reduced high-momentum components ("super-Gaussian falloff in momentum space") as compared to earlier realistic NN potentials with a strongly repulsive core. Alternatively, in coordinate space, the contact interaction and the Yukawa singularity at the origin are regulated away so that this potential would be considered "smooth" by Delves and Schneider and the convergence in $\mathcal{N}$ would be expected to be exponential [3, 4]. Even without the construction of an effective interaction, convergence with the Idaho N^{3}LO NN potential is exponential in $\mathcal{N}$, as numerous studies have shown [9, 17].

We refer the reader to a comprehensive review article [7] on the no-core shell model (NCSM) for details and references to the literature. Inspired by EFT, one uses a truncation parameter $\mathcal{N}$ which refers, not to the many-body system, but to the properties of the HO single-particle states. The many-body truncation parameter N_{max} is the maximum number of oscillator quanta shared by all nucleons above the lowest HO configuration for the chosen nucleus. One unit of oscillator quanta is one unit of the quantity $(2n+l)$ where n is the principle quantum number and l is the angular quantum number. If the highest HO single-particle state of this lowest HO configuration has N_0 HO quanta, then $N_{max} + N_0 = N$ identifies the highest HO single-particle states that can be occupied within this many-body basis. Since N_{max} is the maximum of the *total* HO quanta above the minimal HO configuration, we can have at most one nucleon in such a highest HO single-particle state with N quanta. Note that N_{max} characterizes the many-body basis space, whereas N is a label of the corresponding single particle space. Let us illustrate this distinction with two examples. ^{6}He is an open shell nucleus with $N_0 = 1$ since the valence neutron occupies the $0p$ shell in the lowest many-body configuration. Thus if $N_{max} = 4$ the single particle truncation N is 5. On the other hand, the highest occupied orbital of the closed shell nucleus ^{4}He has $N_0 = 0$ so that $N = N_{max}$.

2 Ultraviolet and infrared cutoffs inherent to the finite HO basis

We begin by thinking of the finite single-particle basis space defined by N and $\hbar\omega$ as a model space characterized by two momenta associated with the basis functions themselves. We follow Ref. [14] and define $\Lambda = \sqrt{m_N(N+3/2)\hbar\omega}$ as the momentum

(in units of MeV/c) associated with the energy of the highest HO level. The nucleon mass is $m_N = 938.92$ MeV. To arrive at this definition one applies the virial theorem to this highest HO level to establish kinetic energy as one half the total energy [i. e., $(N + 3/2)\hbar\omega$] and solves the non-relativistic dispersion relation for Λ. Thus, the usual definition of an ultraviolet cutoff Λ in the continuum has been extended to discrete HO states. It is then quite natural to interpret the behavior of the variational energy of the system with addition of more basis states as the behavior of this observable with the variation of the ultraviolet cutoff Λ. Because the energy levels of a particle in a HO potential are quantized in units of $\hbar\omega$, the momentum difference between single-particle orbitals is $\lambda = \sqrt{m_N \hbar\omega}$ and that has been taken to be an infrared cutoff [14]. That is, there is a low-momentum cutoff $\lambda = \hbar/b$ where $b = \sqrt{\frac{\hbar}{m_N \omega}}$ plays the role of a characteristic length of the HO potential and basis functions. Note however that there is *no* external confining HO potential in place. Instead the only $\hbar\omega$ dependence is due to the scale parameter of the underlying HO basis. In Ref. [14] the influence of the infrared cutoff is removed by extrapolating to the continuum limit, where $\hbar\omega \to 0$ with $N \to \infty$ so that Λ is fixed. Clearly, one cannot achieve both the ultraviolet limit and the infrared limit by taking $\hbar\omega$ to zero in a fixed-Nmodel space as this procedure takes the ultraviolet cutoff to zero. Other studies define the ir cutoff as the infrared momentum which corresponds to the maximal radial extent needed to encompass the many-body system we are attempting to describe by the finite basis space (or model space). These studies find it natural to define the ir cutoff by $\lambda_{sc} = \sqrt{(m_N \hbar\omega)/(N + 3/2)}$ [17, 21]. Note that λ_{sc} is the inverse of the root-mean-square (rms) radius of the highest single-particle state in the basis; $\langle r^2 \rangle^{1/2} = b\sqrt{N + 3/2}$. We distinguish the two definitions by denoting the first (historically) definition by λ and the second definition by λ_{sc} because of its scaling properties demonstrated in the next Section.

3 Running of variational energies with cutoffs and establishment of intrinsic regulator scales

We display in the next two figures the running of the ground-state eigenvalue of the nucleus, ^{2}H, on the truncated HO basis by holding one cutoff of (Λ, λ_{ir}) fixed and letting the other vary. In Fig. 1 and the following figures, $|\Delta E/E|$ is defined as $|(E(\Lambda, \lambda_{ir}) - E)/E|$ where E reflects a consensus ground-state energy from benchmark calculations with this NN potential, this nucleus, and different few-body methods.

In Fig. 1 we hold fixed the uv cutoff of (Λ, λ_{ir}) to display the running of $|\Delta E/E|$ upon the suggested ir cutoff λ_{sc}. For fixed λ_{sc}, a larger Λ implies a smaller $|\Delta E/E|$ since more of the uv region is included in the calculation. But we immediately see a qualitative change in the curves between the transition $\Lambda = 700$ MeV and $\Lambda = 900$ MeV; for smaller Λ, $|\Delta E/E|$ does not go to zero as the ir cutoff is lowered and more of the infrared region is included in the calculation. This behavior suggests that $|\Delta E/E|$ does not go to zero unless $\Lambda \geq \Lambda^{NN}$, where Λ^{NN} is some uv regulator scale of the NN interaction itself. From this figure one estimates $\Lambda^{NN} \sim 900$ MeV/c for the Idaho N^{3}LO interaction. For $\Lambda < \Lambda^{NN}$ there will be missing contributions so "plateaus" develop as $\lambda_{ir} \to 0$, revealing this missing contribution to $|\Delta E/E|$. The "plateaus" that we do see are not flat as $\lambda_{ir} \to 0$ and, indeed, rise significantly with decreasing $\Lambda < \Lambda^{NN}$. This suggests that corrections are needed to Λ and λ_{ir} which are presently defined only to leading order in λ_{ir}/Λ.

Around $\Lambda \sim 700$ MeV/c and above the plot of $|\Delta E/E|$ versus λ_{sc} in Fig. 1 begins to suggest a universal pattern, especially at large λ_{sc}. For $\Lambda \sim 900$ MeV/c and above the pattern defines a universal curve for all values of λ_{sc}. This is the region where $\Lambda \geq \Lambda^{NN}$ indicating that nearly all of the ultraviolet physics set by the potential

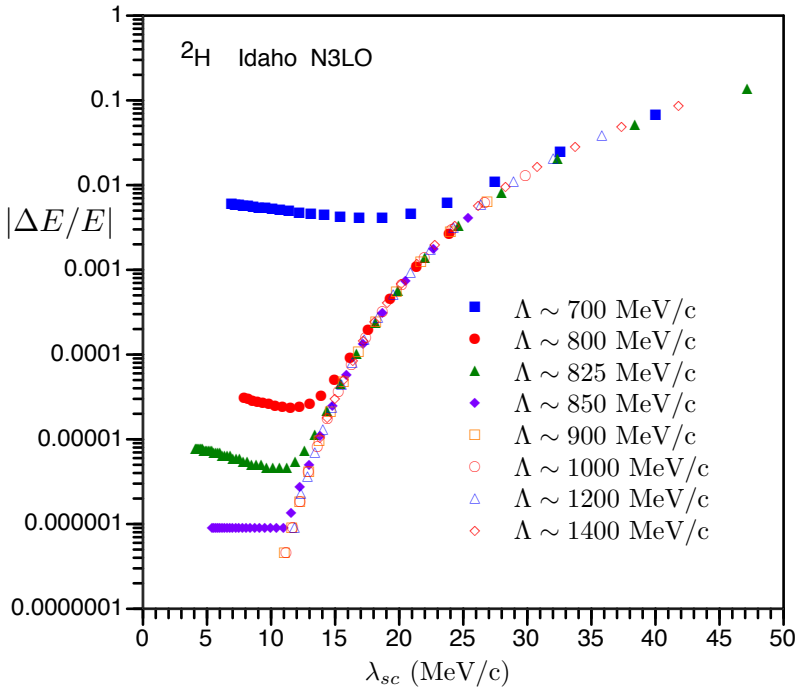

Figure 1: Dependence of the ground-state energy of ^{2}H (compared to a converged value; see text) upon the ir momentum cutoff $\lambda_{sc} = \sqrt{(m_N\hbar\omega)/(N+3/2)}$ for fixed $\Lambda = \sqrt{m_N(N+3/2)\hbar\omega}$.

has been captured. The universal curve can be fit by the $|\Delta E/E| = a\exp(-b/\lambda_{sc})$ which suggests immediately that λ_{sc} could be used for extrapolation to the ir limit, provided that Λ is kept large enough to capture the uv region of the calculation, i. e. $\Lambda \geq \Lambda^{NN}$. Figure 1 is also the motivation for our appellation λ_{sc}, which we read as "lambda scaling", since this figure exhibits the attractive scaling properties of this regulator.

The originally suggested ir cutoff $\lambda = \sqrt{m_N\hbar\omega}$, corresponding to the non-zero energy spacing between HO levels, gives not a universal curve for $\Lambda \geq \Lambda^{NN}$ but instead a set of curves fit by $|\Delta E/E| = a\exp(-B(\Lambda)/\lambda)$ (see Fig. 3 of Ref. [13]). That is, B is not a constant and independent of the uv cutoff Λ, as it should be in an EFT framework. One can remove the dependence of B upon Λ to a large extent by noting that $\lambda = \sqrt{\Lambda\lambda_{sc}}$ so that $\exp(-B/\lambda)$ becomes $\exp\left(\frac{-B/\sqrt{\Lambda}}{\sqrt{\lambda_{sc}}}\right)$ and this multiplier of $1/\sqrt{\lambda_{sc}}$ is constant to within a few per cent. This trivial manipulation demonstrates that the ir regulator which is independent of the uv cutoff is a function of λ_{sc}. The point is not that the ir regulator λ cannot be used to remove ir effects by extrapolating it to zero; indeed it works equally well to remove ir artifacts from a calculation as does λ_{sc} [13]. Indeed, any momentum cutoff $\lambda_{sc} \leq \lambda_{ir} \leq \Lambda$ will remove ir artifacts, but the ir regulator which is independent of the uv cutoff is some function of λ_{sc}. It is λ_{sc} which causes the ir effects and one does not need to decrease an ir cutoff below that of λ_{sc} to remove ir effects (i. e. extrapolate to zero).

In Fig. 2 we hold fixed the ir cutoff of (Λ, λ_{ir}) to display the running of $|\Delta E/E|$ upon the cutoff Λ. Again plateaus are evident. Such a plateau-like behavior was attributed in Fig. 1 to a uv regulator scale characteristic of the NN interaction. Another "missing contributions" argument leads to a universal behavior at low Λ only if $\lambda_{sc} \leq \lambda_{sc}^{NN}$ where λ_{sc}^{NN} is a second characteristic ir regulator scale implicit in the NN interaction itself. One can envisage such an ir cutoff as related to the lowest

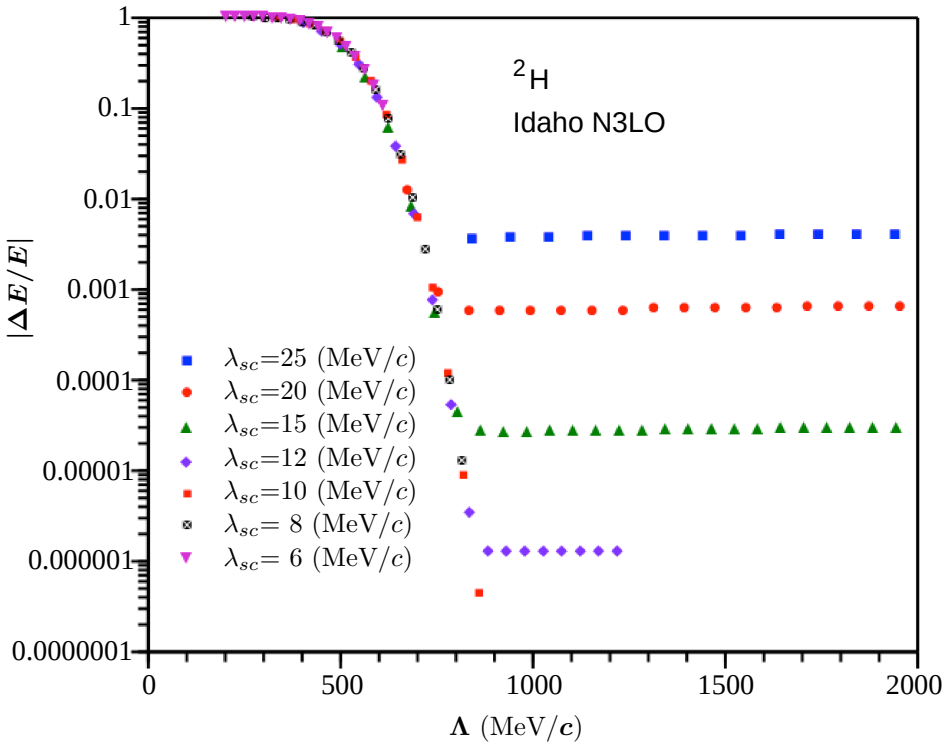

Figure 2: Dependence of the ground-state energy of ^{2}H (compared to a converged value; see text) upon the uv momentum cutoff Λ for different values of the ir momentum cutoff λ_{sc}.

energy configuration that the NN potential could be expected to describe. This would be in the range of the deuteron binding momentum $Q = 45$ MeV/c down to about 16 MeV/c which is the average of the four inverse scattering lengths. However the behavior of the running as $\Lambda \geq \Lambda^{NN}$ again suggests that corrections are needed to Λ and λ_{ir} which are presently defined only to leading order in λ_{ir}/Λ.

Can one make an estimate of the uv and ir regulator scales of the NN interactions used in nuclear structure calculations? It is easy with the JISP16 potential [22]. The S wave parts of JISP16 potential are fit to data in a HO space of $N = 8$ and $\hbar\omega = 40$ MeV. Nucleon-nucleon interactions are defined in the relative coordinates of the two-body system so one should calculate $\Lambda^{NN} = \sqrt{m(N + 3/2)\hbar\omega}$ with the *reduced* mass m rather than the nucleon mass m_N appropriate for the single-particle states of the model space. Taking this factor into account, one finds $\Lambda^{\rm JISP16} \sim 600$ MeV/c and $\lambda_{sc}^{\rm JISP16} \sim 63$ MeV/c. In practice, the uv region seems already captured at $\Lambda > 500{-}550$ MeV/c [13]. The Idaho N^{3}LO interaction was fit to data with a high-momentum cutoff of the "super-Gaussian" regulator set at $\Lambda_{\rm N3LO} = 500$ MeV/c [20]. What is the uv regulator scale of the Idaho N^{3}LO interaction appropriate to the discrete HO basis of this study? A published emulation of this interaction in a harmonic oscillator basis uses $\hbar\omega = 30$ MeV and $N_{max} \approx 2n = 40$. A more systematic study of emulations gave a few more sets of $(N, \hbar\omega)$ which described ^{3}He ground state energy equally well [23]. The successful emulation of the Idaho N^{3}LO interaction in a HO basis suggests that $\Lambda^{\rm N3LO} \sim 900{-}1100$ MeV/c and $\lambda_{sc}^{\rm N3LO} \sim 21{-}42$ MeV/c, consistent with Figs. 2 and 3. In practice from calculations of a variety of light nuclei the uv region seems already captured at $\Lambda > 800$ MeV/c [13].

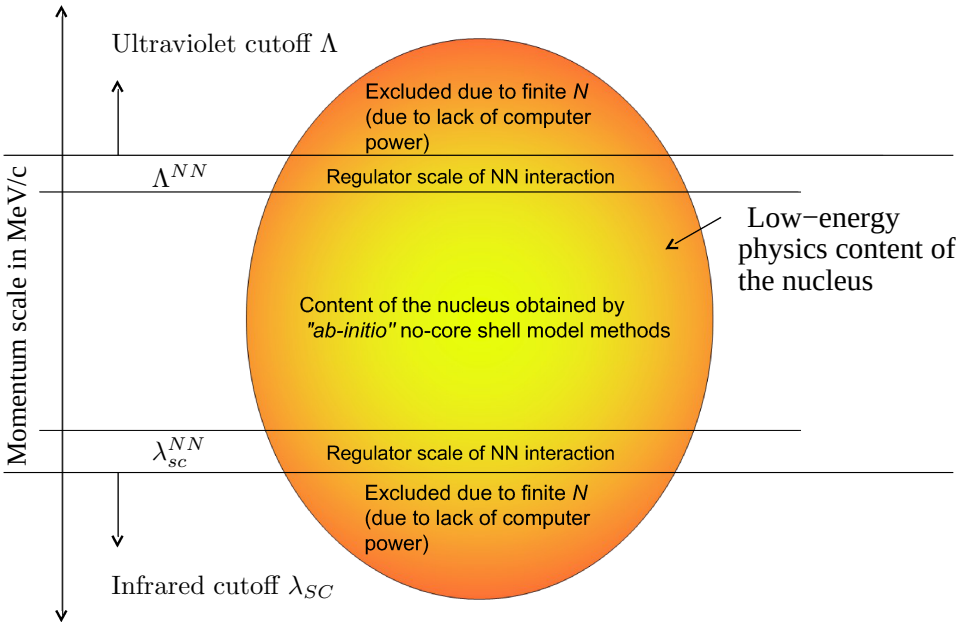

Figure 3: Schematic view of a finite model space (limited by the basis truncation parameter N as described in the text), in which the uv and ir momentum cutoffs are arbitrary. To reach the full many-body Hilbert space, symbolized by the complete oval, one expects to let the uv cutoff $\to \infty$ and the ir cutoff $\to 0$.

4 Extrapolations

The extrapolation scheme proposed in [13] gives N and $\hbar\omega$ equal roles by employing uv and ir cutoffs which should be taken to infinity and to zero, respectively to achieve a converged result (see Fig. 3).

From Fig. 1 we conclude uv cutoff $\Lambda = \sqrt{m_N(N+3/2)\hbar\omega}$ should be greater than the intrinsic Λ^{NN} of the NN interaction. Figure 2 suggests that the ir cutoff $\lambda_{sc} = \sqrt{(m_N\hbar\omega)/(N+3/2)}$ should be less than the intrinsic λ_{sc}^{NN} of the chosen NN interaction. Noting that $N = \Lambda/\lambda_{sc} - 3/2$ and $\hbar\omega = (\Lambda\lambda_{sc})/m_N$, one can establish the minimum values of N and $\hbar\omega$ needed for a converged result (see Table 1). The intrinsic λ_{sc}^{NN} corresponding to the lowest energy configuration of two nucleons is not well determined by numerical investigations (see Figs. 4 and 8 of Ref. [13]) so we include a range of values in Table 1. It is a computational challenge to increase N which gets harder the more particles there are in the nucleus. From this Table one

Table 1: Intrinsic regulator scales determine N and $\hbar\omega$ for a converged result.

$\Lambda \geq \Lambda^{NN} = 800$ MeV/c

$\lambda_{sc}^{NN} \approx 10$ MeV/c	$\lambda_{sc}^{NN} \approx 20$ MeV/c	$\lambda_{sc}^{NN} \approx 40$ MeV/c
$N \geq 80$ $\hbar\omega \geq 8$ MeV	$N \geq 40$ $\hbar\omega \geq 16$ MeV	$N \geq 20$ $\hbar\omega \geq 32$ MeV

$\Lambda \geq \Lambda^{NN} = 500$ MeV/c

$\lambda_{sc}^{NN} \approx 10$ MeV/c	$\lambda_{sc}^{NN} \approx 20$ MeV/c	$\lambda_{sc}^{NN} \approx 40$ MeV/c
$N \geq 50$ $\hbar\omega \geq 5$ MeV	$N \geq 25$ $\hbar\omega \geq 10$ MeV	$N \geq 12$ $\hbar\omega \geq 20$ MeV

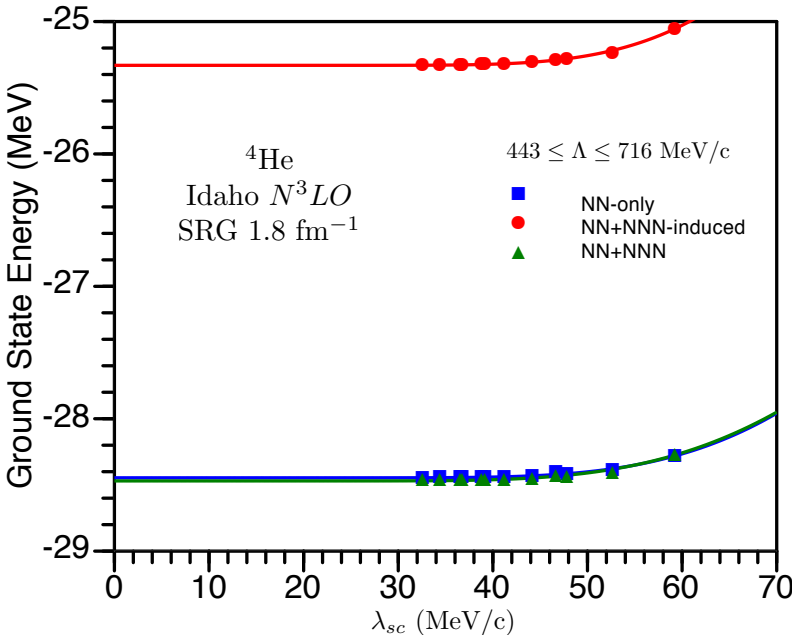

Figure 4: The ground state energy of ^{4}He calculated at values of $\Lambda \geq 443$ MeV/c and variable λ_{sc}. The curves are a fit to the points and the function fitted is used to extrapolate to the ir limit $\lambda_{sc} = 0$. The three SRG transformed Hamiltonians are described in the text.

concludes that one must extrapolate for all but the lightest nuclei and the softest of interactions.

We now utilize the scaling behavior displayed on Fig. 1 to suggest an extrapolation procedure which we illustrate in Figs. 4, 5, and 6. We plot the ground state energy eigenvalue, the root mean square radius, and the total dipole strength of ^{4}He obtained by a NCSM calculation [24], done in a translationally invariant basis which depends only on Jacobi coordinates [25]. The NN interaction is the Idaho N^{3}LO [20] softened by the similarity renormalization group (SRG) evolution according to the method described in Ref. [17]. Transforming the Hamiltonian induces the appearance of higher order many-body forces which should be kept to preserve the unitary nature of the transformation. If they are not kept results become dependent on the SRG flow parameter. It is of interest to learn if the scaling behavior apparent in Fig. 1 and the many examples in Ref. [13] is also true for the induced many-body forces and the three-body forces added to the Hamiltonian (see Refs. [17, 24] for a full description of the SRG scheme and nomenclature). For this exercise, we utilized calculations with $\hbar\omega = 22$ and 28 MeV and $N \leq 18$. The SRG parameter was 1.8 fm^{-1} and our own study of the results suggest that the intrinsic uv cutoff of this SRG transformed interaction is less than 440 MeV/c (see Figures). Then according to Table 1, the calculations should be fully converged with this model space.

The extrapolation is performed by a fit of an exponential plus a constant to each set of results at fixed Λ. That is, we fit the ground state energy with three adjustable parameters using the relation $E_{gs}(\lambda_{sc}) = a\exp(-b/\lambda_{sc}) + E_{gs}(\lambda_{sc} = 0)$. The rms radius and the total dipole strength are obtained by similar fits: $r(\lambda_{sc}) = a\exp(-b/\lambda_{sc}) + r(\lambda_{sc} = 0)$ and $D^2(\lambda_{sc}) = a\exp(-b/\lambda_{sc}) + D^2(\lambda_{sc} = 0)$. The extrapolation formulae work equally well for the induced three-body forces and the added three-body forces. It should be noted that our extrapolations in these figures employ an exponential function whose argument $1/\lambda_{sc} = \sqrt{(N + 3/2)/(m_N\hbar\omega)}$ is proportional to $\sqrt{N/(\hbar\omega)}$. This extrapolation procedure of taking λ_{sc} downward from the

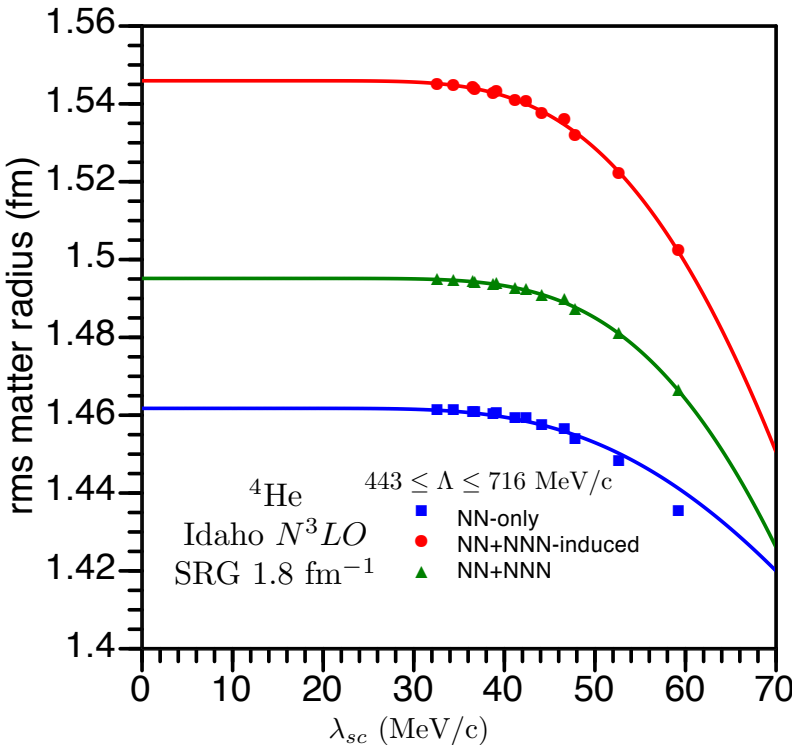

Figure 5: The rms radius $\langle 0|r^2|0\rangle^{1/2}$ of ^{4}He calculated as in Fig. 4.

smallest value allowed by computational limitations treats both N and $\hbar\omega$ on an equal basis. The exponential extrapolation in $\sqrt{N/(\hbar\omega)}$ is therefore distinct from the popular extrapolation which employes an exponential in N_{max} ($= N$ for this s-shell

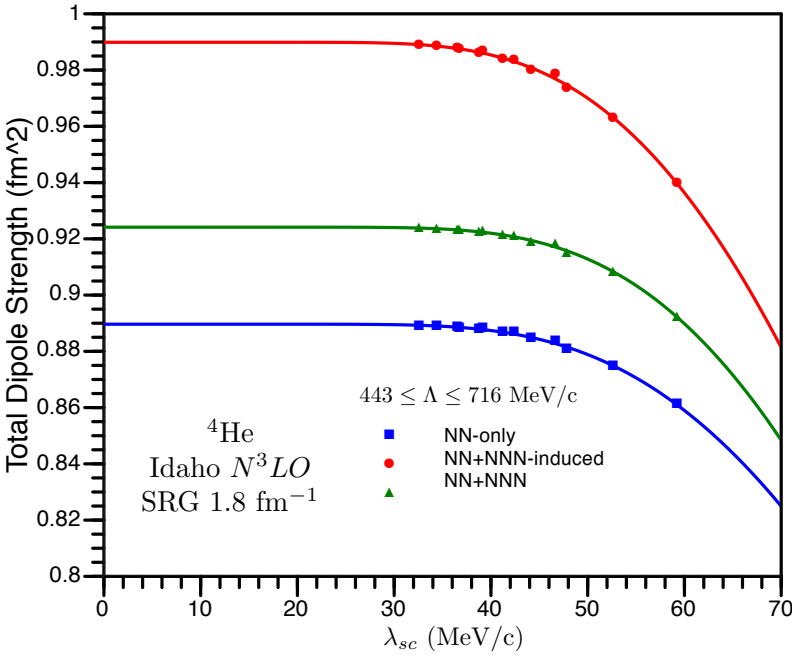

Figure 6: (Color online) The total dipole strength $\langle 0|\mathbf{D}\cdot\mathbf{D}|0\rangle$ of ^{4}He calculated as in Fig. 4. Here $\mathbf{D}$ is the unretarded dipole operator defined in Ref. [24].

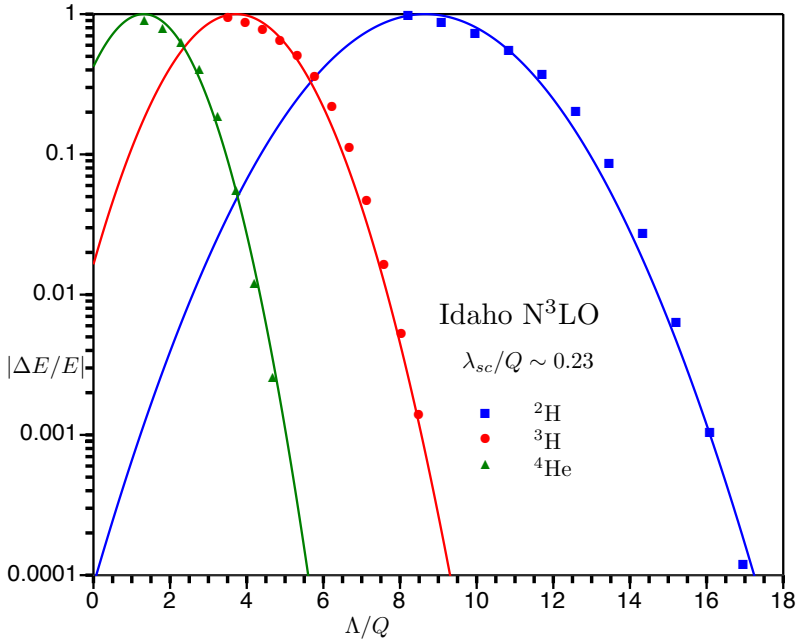

Figure 7: Dependence of the ground-state energy of three s-shell nuclei (compared to a converged value; see text) upon the uv momentum cutoff $\Lambda \leq \Lambda^{\rm N3LO}$. The data are fit to Gaussians. Both uv and ir cutoffs are scaled to Q, the binding momentum of each nucleus, so that the s-state nuclei can be fit on a single plot. The unscaled values are $\lambda_{sc} = 10$ MeV/c for ^{2}H, $\lambda_{sc} = 20$ MeV/c for ^{3}H and $\lambda_{sc} = 40$ MeV/c for ^{4}He.

case) [7, 9, 10, 17]. The convergence of all three operators is the same with the λ_{sc} extrapolation, in contrast to the traditional extrapolation for the same data which found slower and slower convergence for the ground state energy eigenvalue, the root mean square radius, and the total dipole strength [24]. As the model space is large and the intrinsic uv cutoff is small, the extrapolated results obtained here agree with those of the traditional extrapolation of Ref. [24].

Finally, we return to Fig. 2 and restrict our attention to the sector $\Lambda \leq \Lambda^{NN}$. The universal curve in that sector is generalized to three s-shell nuclei in Fig. 7 where all momenta are scaled by the binding momentum Q of the considered nucleus in order to put them on the same plot. For such low fixed momenta λ_{sc}, $|\Delta E/E|$ does go to zero with increasing Λ because $\lambda_{sc} \leq \lambda_{sc}^{NN}$. The "high" Λ tails of these curves were fit by Gaussians (shifted from the origin) in the variable Λ/Q in Ref. [13]. This behavior suggests another possible extrapolation scheme; fixing the ir physics first and then extrapolating in the uv cutoff. A later paper did advocate such an extrapolation with Λ^2 in the exponential fit function [26]. We have tried to fit our data with the ansatz, $E_{gs}(\Lambda) = A\exp(-2\Lambda^2/\Lambda^{NN^2}) + E(\Lambda = \infty)$, of that paper and failed. Because the Gaussians are shifted from the origin, a fit requires $E_{gs}(\Lambda/Q) = a\exp\left[-(\Lambda/Q - b)^2/2c^2\right] + E(\Lambda/Q{=}\infty)$, provided that one restricts to values of $\Lambda/Q \leq \Lambda^{NN}/Q$. Such fits are shown in Fig. 8.

Unfortunately, the extrapolated energies of Fig. 8 do not agree with those obtained from independent calculations. The extrapolated energies are always lower: 2 keV for the deuteron, 300 keV (or 4%) for the triton and 20 keV(or 2.4 %) for the alpha particle. It is difficult to achieve consistent extrapolations with different values of fixed (low) λ_{sc}. For example, if one takes $\lambda_{sc} = 12$ MeV/c, seemingly closer to the ir limit so that even more of the ir physics is captured, the extrapolated triton energy is -10.149 MeV; 2.3 MeV below the accepted value. Only with the SRG transformed potentials does the extrapolation illustrated in Fig. 8 agree with other independent

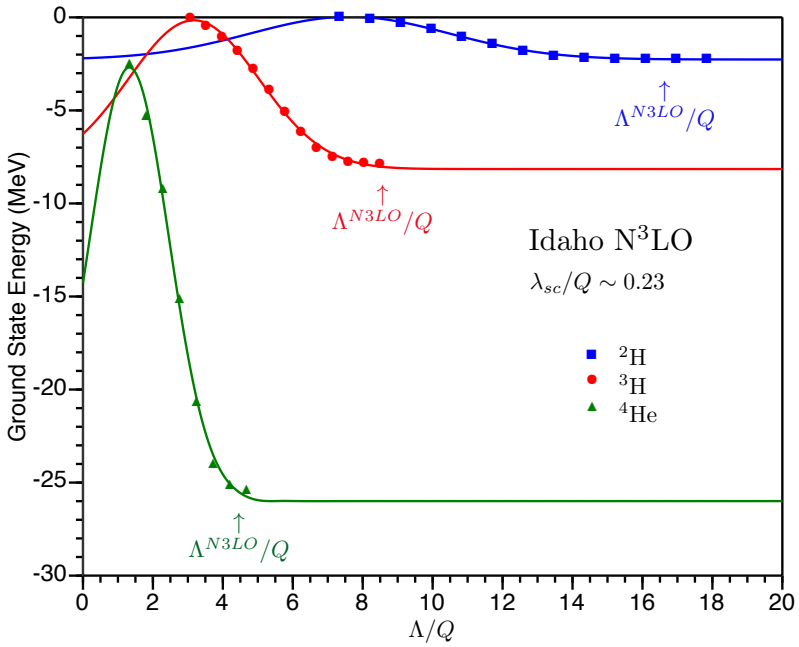

Figure 8: Extrapolation at fixed $\lambda_{sc} \leq \lambda_{sc}^{\rm N3LO}$. Both uv and ir cutoffs are scaled to Q, the binding momentum of each nucleus, so that the s-state nuclei can be fit on a single plot. The unscaled values are $\lambda_{sc} = 10$ MeV/c for ^{2}H, $\lambda_{sc} = 20$ MeV/c for ^{3}H and $\lambda_{sc} = 40$ MeV/c for ^{4}He. The arrows indicate that the UV extrapolation uses only points for which $\Lambda \leq \Lambda^{\rm N3LO}$.

calculations.

In conclusion, we have established that an extrapolation in the ir cutoff with the uv cutoff above the intrinsic uv scale of the interaction is quite successful, not only for the eigenstates of the Hamiltonian but also for expectation values of operators considered long range. On the other hand, the suggested extrapolation [26] in the uv cutoff when the ir cutoff is below the intrinsic ir scale is neither robust nor reliable.

5 Acknowledgements

Extremely useful conversations with Sean Fleming are acknowledged. We thank the authors of [24] for sharing with us their results before publication. We are grateful to Petr Navrátil for generously allowing us to use his `manyeff` code [25] for our calculations. Numerical calculations have been performed in part at the LLNL LC facilities supported by LLNL under Contract No. DE-AC52-07NA27344. This contribution was supported in part by USDOE Division of Nuclear Physics grant DE-FG02-04ER41338 (Effective Theories of the Strong Interaction).

References

[1] J. M. Irvine, G. S. Mani, V. F. E. Pucknell, M. Vallieres and F. Yazici, Ann. Phys. (NY) **102**, 129 (1976).

[2] M. Moshinsky, *The harmonic oscillator in modern physics: from atoms to quarks*. Gordon and Breach, New York, 1969.

[3] I. M. Delves, in in *Advances in Nuclear Physics, vol. 5*, eds. M. Baranger and E. Vogt. Plenum Press, New York, 1972, p. 1.

[4] T. R. Schneider, J. Math. Phys. **12**, 1508 (1971); Phys. Lett. B **40**, 439 (1972).

[5] M. Fabre de la Ripelle, Ann. Phys. (NY) **147**, 281 (1983).

[6] A. D. Jackson, A. Lande and P. U. Sauer, Nucl. Phys. A **156**, 43 (1970); Phys. Lett. B **35**, 365 (1971); M. R. Strayer and P. U. Sauer, Nucl. Phys. A **231**, 1 (1974).

[7] P. Navrátil, S. Quaglioni, I. Stetcu and B. R. Barrett, J. Phys. G **36**, 083101 (2009).

[8] S. Kvaal, Phys. Rev. B **80**, 045321 (2009).

[9] P. Navrátil and E. Caurier, Phys. Rev C **69**, 014311 (2004).

[10] P. Maris, J. P. Vary and A. M. Shirokov, Phys. Rev. C **79**, 014308 (2009).

[11] S. A. Coon and O. Portilho, Lecture Notes Phys. **273**, 219 (1987).

[12] C. Forssen, J. P. Vary, E. Caurier and P. Navrátil, Phys. Rev. C **77**, 024301 (2008).

[13] S. A. Coon, M. I. Avetian, M. K. G. Kruse, U. van Kolck, P. Maris and J. P. Vary, Phys. Rev. **C** 86, 054002 (2012), arXiv:1205.3230 [nucl.th] (2012).

[14] I. Stetcu, B. R. Barrett and U. van Kolck, Phys. Lett. B **653**, 358 (2007).

[15] I. Stetcu and J. Rotureau, Progr. Part. Nucl. Phys. **69**, 182 (2013).

[16] S. Okubo, Progr. Theor. Phys. **12**, 603 (1954); K. Suzuki and S. Y. Lee, *ibid.* **64**, 2091(1980).

[17] E. D. Jurgenson, P. Navrátil and R. J. Furnstahl, Phys. Rev C **83**, 034301 (2011).

[18] S. Fujji, E. Epelbaum, H. Kamada, R. Okamoto, K. Suzuki and W. Gloeckle, Phys. Rev. C **70**, 024003 (2004).

[19] A. Nogga, S. K. Bogner and A. Schwenk, Phys. Rev. C **70**, 0611002(R) (2004).

[20] D. R. Entem and R. Machleidt, Phys. Rev C **68**, 041001(R) (2003).

[21] G. Hagen, T. Papenbrock, D. J. Dean and M. Hjorth-Jensen, Phys. Rev. C **82**, 034330 (2010).

[22] A. M. Shirokov, J. P. Vary, A. I. Mazur and T. A. Weber, Phys. Lett. B **644**, 33 (2007).

[23] N. Barnea, W. Leidemann and G. Orlandini, Phys. Rev. C **81**, 064001 (2010); N. Barnea, *private communication.*

[24] M. D. Schuster, S. Quaglioni, C. W. Johnson, E. D. Jurgenson and P. Navrátil, arXiv:1304.5491 [nucl.th] (2013).

[25] P. Navrátil, G. P. Kamuntavičius and B. R. Barrett, Phys. Rev. C **61**, 044001 (2000).

[26] R. J. Furnstahl, G. Hagen and T. Papenbrock, Phys. Rev. C **86**, 031301(R) (2012).

Halo Nuclei with the Coulomb–Sturmian Basis

M. A. Caprio[a], P. Maris[b] and J. P. Vary[b]

[a] *Department of Physics, University of Notre Dame, Notre Dame, Indiana 46556, USA*
[b] *Department of Physics and Astronomy, Iowa State University, Ames, Iowa 50011, USA*

Abstract

The rapid falloff of the oscillator functions at large radius (Gaussian asymptotics) makes them poorly suited for the description of the asymptotic properties of the nuclear wave function, a problem which becomes particularly acute for halo nuclei. We consider an alternative basis for *ab initio* no-core configuration interaction (NCCI) calculations, built from Coulomb–Sturmian radial functions, allowing for realistic (exponential) radial falloff. NCCI calculations are carried out for the neutron-rich He isotopes, and estimates are made for the RMS radii of the proton and neutron distributions.

Keywords: *No-core configuration interaction; Coulomb–Sturmian basis; neutron halo; nuclear radii*

1 Introduction

The *ab initio* theoretical description of light nuclei is based on direct solution of the nuclear many-body problem given realistic nucleon-nucleon interactions. In no-core configuration interaction (NCCI) calculations [1, 2], the nuclear many-body problem is formulated as a matrix eigenproblem. The Hamiltonian is represented in terms of basis states which are antisymmetrized products of single-particle states for the full A-body system of nucleons, i. e., with no assumption of an inert core.

In practice, the nuclear many-body calculation must be carried out in a truncated space. The dimension of the problem grows combinatorially with the size of the included single-particle space and with the number of nucleons in the system. Computational restrictions therefore limit the extent to which converged results can be obtained, for energies or for other properties of the wave functions. Except for the very lightest systems ($A \lesssim 4$), convergence is generally beyond reach. Instead, we seek to approach convergence as closely as possible. Based on the still-unconverged calculations which are computationally feasible, we would then ideally be able to obtain a reliable estimate of the true values of observables which would be obtained in the full, untruncated space. Therefore, progress may be pursued both by seeking accelerated convergence, e. g., through the choice of basis, as considered here, and by developing means by which robust extrapolations can be made [3–7].

NCCI calculations have so far been based almost exclusively upon bases constructed from harmonic oscillator single-particle wave functions. The harmonic oscillator radial functions have the significant limitation that their asymptotic behavior is Gaussian, i. e., falling as $e^{-\alpha r^2}$ for large r. The actual asymptotics for nucleons bound by a finite-range force are instead expected to be exponential, i. e., falling as $e^{-\beta r}$.

The problem encountered in using an oscillator basis to describe a system with exponential asymptotics may be illustrated through the simple one-dimensional example of the Schrödinger equation with a Woods–Saxon potential. In Fig. 1, we see

Proceedings of International Conference 'Nuclear Theory in the Supercomputing Era — 2013' (NTSE-2013), Ames, IA, USA, May 13–17, 2013. Eds. A. M. Shirokov and A. I. Mazur. Pacific National University, Khabarovsk, Russia, 2014, p. 325.
http://www.ntse-2013.khb.ru/Proc/Caprio.pdf.

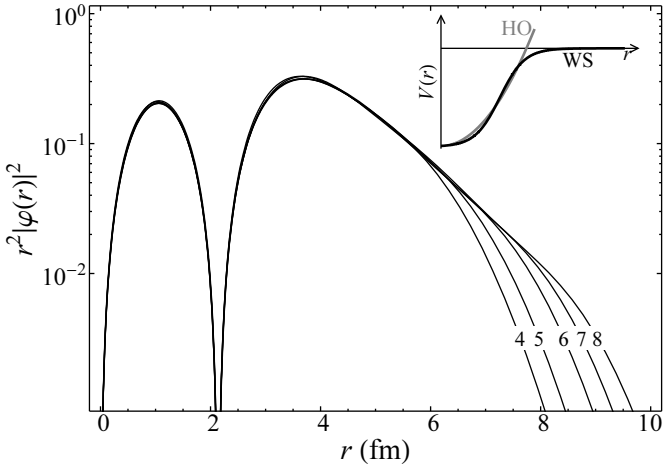

Figure 1: The calculated wavefunction obtained when a problem with exponential asymptotics — here, the Woods–Saxon problem is taken for illustration — is solved in a finite basis of oscillator functions. The radial probability density $r^2|\varphi(r)|^2$ is shown on a logarithmic scale, so that exponential asymptotics would appear as a straight line. The Woods–Saxon and oscillator potentials are shown in the inset. (Solutions are for the Woods–Saxon $1s_{1/2}$ function, with potential parameters appropriate to neutrons in ^{16}O [8], with maximal basis radial quantum numbers n as indicated.)

the results of solving for a particular eigenfunction in terms of successively larger bases of oscillator radial functions. In the classically forbidden region, where the potential is nearly flat, the tail of the wave function should be exponential. It should thus appear as a straight line on the logarithmic scale in Fig. 1. Inclusion of each additional basis function yields a small extension to the region in which the expected straight-line behavior is reproduced, but, for any finite number of oscillator functions, there is a radius beyond which the calculated tail is seen to sharply fall below the true asymptotics.

Observables which are sensitive to the large-radius asymptotic portions of the nuclear wave function therefore present a special challenge to convergence in NCCI calculations with a conventional oscillator basis. Such "long-range" observables include the RMS radius and $E2$ moments and transitions, since the r^2 dependence of the relevant operators in both cases preferentially weight the larger-r portions of the wave-function. The results for these observables in NCCI calculations are in general highly basis-dependent [9, 10].

Furthermore, a prominent feature in light nuclei is the emergence of halo structure [11], in which one or more loosely-bound nucleons surround a compact core, spending much of their time in the classically-forbidden region. A realistic treatment of the long-range properties of the wave function is essential for an accurate reproduction of the halo structure [12].

We are therefore motivated to consider alternative bases which might be better suited for expanding the nuclear wave function in its asymptotic region. The framework for carrying out NCCI calculations with a general radial basis is developed in Ref. [13]. We explore the use of the Coulomb–Sturmian functions [14–16], which form a complete set of square-integrable functions and have exponential asymptotics.

In the present work, we apply the Coulomb–Sturmian basis to NCCI calculations for the neutron halo nuclei ^{6,8}He — as well as to the baseline case ^{4}He, for which converged results can be obtained. We examine the possibility of extracting RMS radii for the proton and neutron distributions based on a relatively straightforward estimate, the "crossover point" [9,10], pending further development of more sophisticated

extrapolation schemes [5]. Motivated by the disparity between proton and neutron radial distributions in the neutron-rich halo nuclei, we also explore the use of proton-neutron asymmetric bases, with different length scales for the proton and neutron radial basis functions. The basis and methods are first reviewed (Section 2), after which the results for ^{4,6,8}He are discussed (Section 3).

2 Basis and methods

The harmonic oscillator basis functions, as used in conventional NCCI calculations, constitute a complete, discrete, orthogonal set of square-integrable functions and are given by $\Psi_{nlm}(b;\mathbf{r}) = R_{nl}(b;r)\,Y_{lm}(\hat{\mathbf{r}})/r$, with radial wave functions

$$R_{nl}(b;r) \propto (r/b)^{l+1} L_n^{l+1/2}\big[(r/b)^2\big] e^{-\frac{1}{2}(r/b)^2}, \tag{1}$$

where the L_n^α are generalized Laguerre polynomials, the Y_{lm} are spherical harmonics, n is the radial quantum number, l and m are the orbital angular momentum and its z-projection, and b is the oscillator length. The Coulomb–Sturmian functions likewise constitute a complete, discrete, orthogonal set of square-integrable functions, while also possessing exponential asymptotics more appropriate to the nuclear problem. They are given by $\Lambda_{nlm}(b;\mathbf{r}) = S_{nl}(b;r)\,Y_{lm}(\hat{\mathbf{r}})/r$, with radial wave functions

$$S_{nl}(b;r) \propto (2r/b)^{l+1} L_n^{2l+2}(2r/b) e^{-r/b}, \tag{2}$$

where b again represents a length scale. Further details may be found in Ref. [13]. Both sets of radial functions are shown in Fig. 2, for comparison.

For either basis, the single-particle basis states $|nljm\rangle$ are then defined by coupling of the orbital angular momentum with the spin, to give total angular momentum j, and the many-body basis is defined by taking antisymmetrized products of these single-particle states. Thus, the structure of the many-body calculation is independent of the details of the radial basis. The choice of radial basis only enters the calculation through the values of the Hamiltonian two-body matrix elements (or higher-body matrix elements, if present), which we must first generate as the input to the many-body calculation.

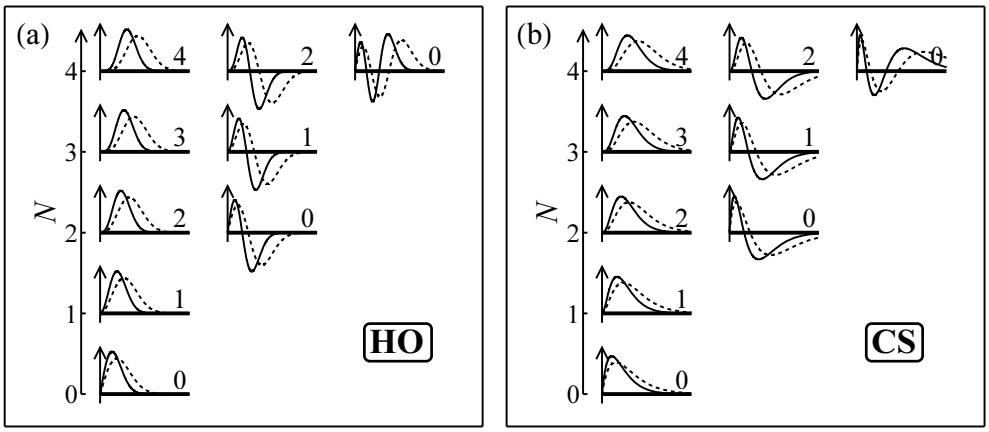

Figure 2: Radial functions (a) $R_{nl}(b;r)$ of the harmonic oscillator basis and (b) $S_{nl}(b_l;r)$ of the Coulomb–Sturmian basis, with b_l given by the node-matching prescription (see text). These functions are shown arranged according to the harmonic oscillator principal quantum number $N \equiv 2n + l$, and are labeled by l. The dotted curves show the same functions dilated outward by a factor of $\sqrt{2} \approx 1.414$.

The nuclear Hamiltonian for NCCI calculations has the form $H = T_{\rm rel} + V$, where $T_{\rm rel}$ is the Galilean-invariant, two-body relative kinetic energy operator, and V is the nucleon-nucleon interaction.[1] The relative kinetic energy decomposes into one-body and two-body terms as

$$T_{\rm rel} \equiv \frac{1}{4Am_N} \sum_{ij}{}' (\mathbf{p}_i - \mathbf{p}_j)^2 = \frac{1}{2Am_N} \left[(A-1) \sum_i \mathbf{p}_i^2 - \sum_{ij}{}' \mathbf{p}_i \cdot \mathbf{p}_j \right]. \tag{3}$$

Since the two-body term is separable, matrix elements of $T_{\rm rel}$ may be calculated in a straightforward fashion for any radial basis, in terms of one-dimensional radial integrals of the operators p and p^2 [13].

Calculation of the interaction two-body matrix elements becomes more involved if one moves to a general radial basis. The nucleon-nucleon interaction is defined in relative coordinates. The oscillator basis is special, in that matrix elements in a relative oscillator basis, consisting of functions $\Psi_{nl}(\mathbf{r}_1 - \mathbf{r}_2)$, can readily be transformed to the two-body oscillator basis, consisting of functions $\Psi_{n_1 l_1}(\mathbf{r}_1)\Psi_{n_2 l_2}(\mathbf{r}_2)$, by the Moshinsky transformation. We therefore still begin by carrying out the transformation to two-body matrix elements $\langle cd; J|V|ab; J\rangle$ with respect to the oscillator basis, and only then carry out a change of basis to the Coulomb–Sturmian basis in the two-body space, as [13]

$$\langle \bar{c}\bar{d}; J|V|\bar{a}\bar{b}; J\rangle = \sum_{abcd} \langle a|\bar{a}\rangle \langle b|\bar{b}\rangle \langle c|\bar{c}\rangle \langle d|\bar{d}\rangle \, \langle cd; J|V|ab; J\rangle, \tag{4}$$

where we label single-particle orbitals for the oscillator basis by unbarred symbols $a = (n_a l_a j_a)$ and those for the Coulomb–Sturmian basis by barred symbols $\bar{a} = (\bar{n}_a \bar{l}_a \bar{j}_a)$. The coefficients $\langle a|\bar{a}\rangle$ required for the transformation are obtained from straightforward one-dimensional overlaps of the harmonic oscillator and Coulomb–Sturmian radial functions, $\langle R_{nl}|S_{\bar{n}l}\rangle = \int_0^\infty dr\, R_{nl}(b_{\rm int}; r)\, S_{\bar{n}l}(b; r)$. The oscillator length $b_{\rm int}$ with respect to which the interaction two-body matrix elements are defined and the length scale b of the final Coulomb–Sturmian basis functions may in general be different. The change-of-basis transformation in (4) is, in practice, limited to a finite sum, e. g., with a shell cutoff $N_a, N_b, N_c, N_d \leq N_{\rm cut}$. The cutoff $N_{\rm cut}$ must be chosen high enough to insure that the results of the subsequent many-body calculation are cutoff-independent, which may in general depend upon the oscillator and Coulomb–Sturmian length parameters, interaction, nucleus, and observable at hand.

Any single particle basis, including (1) or (2), has a free length scale b. For the oscillator basis, this is traditionally quoted as the oscillator energy $\hbar\Omega$, where

$$b(\hbar\Omega) = \frac{(\hbar c)}{[(m_N c^2)(\hbar\Omega)]^{1/2}}. \tag{5}$$

In deference to the convention of presenting NCCI results as a function of the basis "$\hbar\Omega$", we nominally carry over this relation to define an $\hbar\Omega$ parameter for general radial bases, although $\hbar\Omega$ no longer has any direct physical meaning as an energy scale. Regardless, the inverse square-root dependence remains, so that a factor of two change in $\hbar\Omega$ describes a factor of $\sqrt{2}$ change in radial scale, as illustrated for both harmonic oscillator and Coulomb–Sturmian bases by the dotted curves in Fig. 2.

Furthermore, there is much additional freedom in the basis, since the many-body basis states (antisymmetrized product states) constructed from a single-particle basis are orthonormal so long as the single-particle states are orthonormal. Orthogonality for single-particle states of different l or j follows entirely from the angular and

[1] A Lawson term proportional the number $N_{\rm c.m.}$ of center-of-mass oscillator quanta can also be included, to shift center-of-mass excitations out of the low-lying spectrum, but it is not essential for the ground-state properties considered here. The implications of center-of-mass dynamics for general bases are addressed in Ref. [13].

spin parts of the wave function. Only orthogonality *within* the space of a given l and j follows from the radial functions, e. g., for the Coulomb–Sturmian functions, $\langle n'l'j'|nlj\rangle = \left[\int dr\, S_{n'l}(b;r)\, S_{nl}(b;r)\right] \delta_{l'l}\delta_{j'j}$. We are therefore free to choose b independently, firstly, for each l space (or j space), as b_l (or b_{lj}), and, secondly, for protons and neutrons, as b_p and b_n.

The first observation raises the possibility, still to be explored, of obtaining significant improvements in the efficacy of the basis by optimizing the l-dependence of the length parameter. In Ref. [13], the radial scale of the Coulomb–Sturmian functions, for each l, was fixed by matching the first node of the $n = 1$ Coulomb–Sturmian function to the first node of the $n = 1$ oscillator function, at that l, yielding the prescription $b_l = [2/(2l+3)]^{1/2} b(\hbar\Omega)$ [13].

The second observation raises the possibility of proton-neutron asymmetric length scales, which might be advantageous for nuclei with significant disparities between the proton and neutron distributions, in particular, halo nuclei. Therefore, in the present work, we adopt

$$b_{l,p} = \sqrt{\frac{2}{2l+3}}\, b(\hbar\Omega), \qquad b_{l,n} = \beta \sqrt{\frac{2}{2l+3}}\, b(\hbar\Omega), \tag{6}$$

where β sets an overall relative scale b_n/b_p. For example, if the solid and dotted curves in Fig. 2(b) are taken to represent the proton and neutron radial functions, respectively, then the figure illustrates the case in which $b_n/b_p = \sqrt{2} \approx 1.414$.

3 Results for the He isotopes

We carry out calculations for the isotopes ^{4,6,8}He using both the harmonic oscillator and Coulomb–Sturmian bases. These calculations are based on the JISP16 nucleon-nucleon interaction [17], plus Coulomb interaction. The bare interaction is used, i. e., without renormalization. The proton-neutron M-scheme code MFDn [18, 19] is employed for the many-body calculations. Results are calculated with basis truncations up to $N_{\max} = 14$ for ^{4}He, $N_{\max} = 12$ for ^{6}He, and $N_{\max} = 10$ for ^{8}He.[2]

The last neutrons in ^{6}He and ^{8}He are only weakly bound, with two-neutron separation energies of 0.97 MeV and 2.14 MeV, respectively. These isotopes are interpreted as consisting of neutron halos surrounding an α core [11]. The basic observables indicating halo properties are the RMS radii of the proton and neutron distributions, r_p and r_n, respectively.[3] Moving from ^{4}He to ^{6}He, r_p increases by ∼32%. This may be understood as resulting from the recoil of the α core against the halo neutrons, and potentially core polarization, as well. In turn, r_n is larger than r_p by ∼42%, reflecting the extended halo neutron distribution. The radii for ^{8}He are comparable to those for ^{6}He.

We first consider calculations for ^{4}He as a baseline. Results are shown over two doublings in $\hbar\Omega$, i. e., representing a doubling in basis length scale, in Fig. 3. Energy convergence is reached for the harmonic oscillator basis, as evidenced by approximate $N_{\max}$ and $\hbar\Omega$ independence of the higher $N_{\max}$ results over a range of $\hbar\Omega$ values, in Fig. 3(a, b). Convergence is obtained at the ∼10 keV level by $N_{\max} = 14$. The

[2]The harmonic oscillator many-body basis is normally truncated according to the $N_{\max}$ scheme, based on the total number of oscillator quanta. That is, the many-body basis states are characterized by a total number of oscillator quanta $N_{\rm tot} \equiv \sum_i N_i$, where $N_i \equiv 2n_i + l_i$. If $N_{\rm tot}$ is written as $N_{\rm tot} = N_0 + N_{\rm ex}$, where N_0 in the lowest Pauli-allowed number of quanta, then the basis is subject to the restriction $N_{\rm ex} \le N_{\max}$. We formally carry this truncation over to the Coulomb–Sturmian basis, although $N \equiv 2n + l$ no longer has significance as an oscillator principal quantum number.

[3]Specifically, r_p and r_n are the RMS radii of the point-proton and point-neutron distributions, measured relative to the center of mass. See Ref. [20] for definitions, and Ref. [13] for evaluation of the two-body relative RMS radius observable with a general radial basis. From the analysis of experimental charge and matter radii in Ref. [11], ^{4}He has $r_p = 1.457(10)$ fm ($\approx r_n$), ^{6}He has $r_p = 1.925(12)$ fm and $r_n = 2.74(7)$ fm, and ^{8}He has $r_p = 1.807(28)$ fm and $r_n = 2.72(4)$ fm.

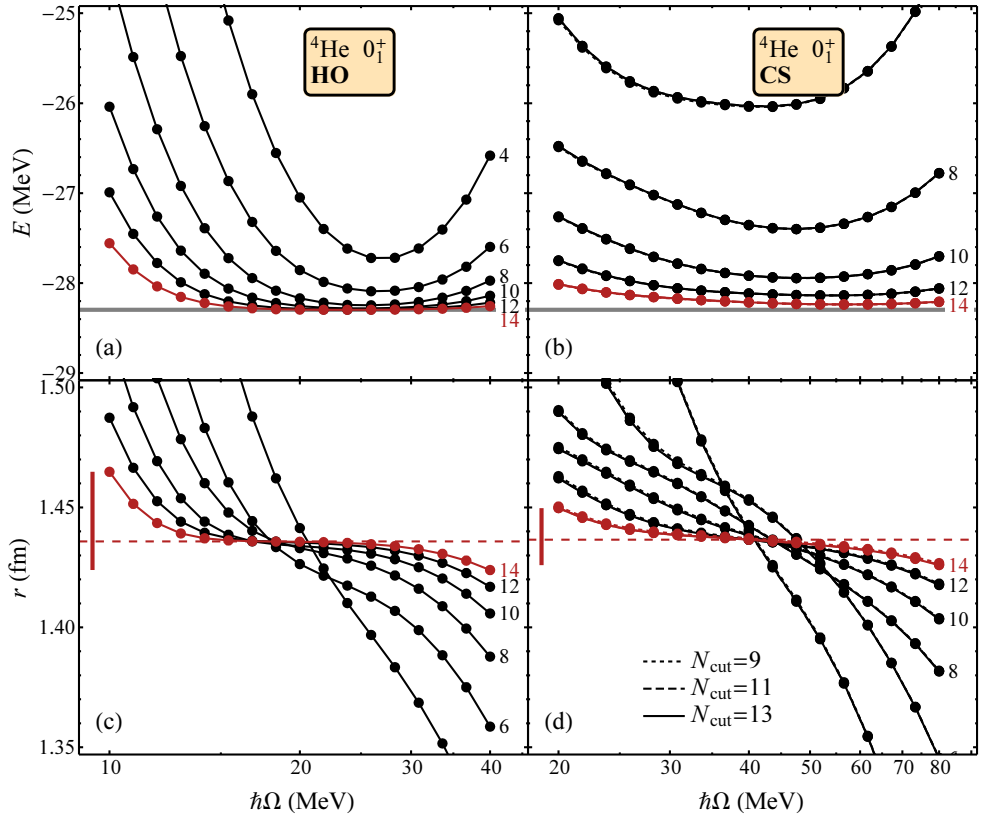

Figure 3: The calculated ^{4}He ground state energy (top) and RMS point-proton radius r_p (bottom), using the conventional oscillator (left) and Coulomb–Sturmian (right) bases. These are shown as functions of the basis $\hbar\Omega$ parameter, for $N_{\rm max} = 4$ to 14 (as labeled), and for transformation cutoffs $N_{\rm cut} = 9$, 11, and 13 (Coulomb–Sturmian basis only, indicated by dashing, curves nearly indistinguishable). The converged energy is indicated by the horizontal line (at top), the crossover radii by dashed horizontal lines (at bottom), and the spread in radius values by vertical bars (again at bottom).

binding energies for ^{4}He computed with the Coulomb–Sturmian basis lag significantly behind those obtained with the oscillator basis, by about two steps in $N_{\rm max}$. This should perhaps not be surprising, given that ^{4}He is tightly bound, and the structure can thus be expected to be driven by short-range correlations rather than asymptotic properties. Incidentally, it may be seen from Fig. 3(b, d) that stability with respect to the cutoff in the change-of-basis transformation (4) has been obtained — calculations with $N_{\rm cut} = 9$, 11, and 13 are virtually indistinguishable (the transformation has been carried out from oscillator basis interaction matrix elements at $\hbar\Omega_{\rm int} = 40\,$MeV).

Convergence of the computed RMS radii, for both the oscillator and Coulomb–Sturmian bases, is again indicated by approximate $N_{\rm max}$ and $\hbar\Omega$ independence over a range of $\hbar\Omega$ values, which appears as a shoulder in the curves of Fig. 3(c, d). The $\hbar\Omega$ dependence for the Coulomb–Sturmian calculations appears to be moderately shallower, over the range (two doublings) of $\hbar\Omega$ shown, than for the harmonic oscillator calculations [see vertical bars in Fig. 3(c, d)].

It was proposed in Refs. [9, 10] that the radius can be estimated — even before convergence is well-developed — by the crossover point between the curves obtained for successive $N_{\rm max}$ values. This is an admittedly *ad hoc* prescription, rather than a theoretically motivated extrapolation. However, we can test it — for both oscillator

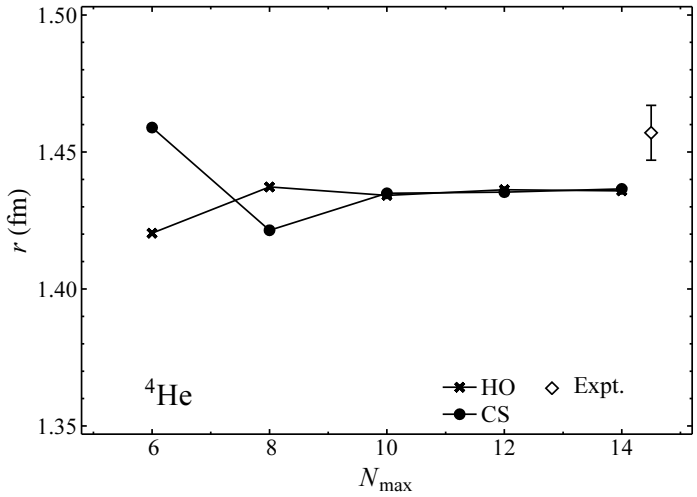

Figure 4: The ^{4}He ground state RMS point-proton radius r_p, as estimated from the crossover point (see text), calculated for the harmonic oscillator and Coulomb–Sturmian bases. The experimental value is from Ref. [11].

and Coulomb–Sturmian bases — in this case of ^{4}He, where the final converged value is known. The crossover radii are shown as a function of $N_{\max}$, for both bases, in Fig. 4. The curves used in deducing these crossovers are computed by cubic interpolation of the calculated data points at different $\hbar\Omega$. The crossovers already serve to estimate the final converged value to within $\sim$0.05 fm at $N_{\max} = 6$. It may be noted, from Fig. 4, that the converged radius obtained with the JISP16 interaction agrees with experiment to within $\sim$0.03 fm.

Let us now consider the calculations for the halo nuclei ^{6,8}He. The computed ground state energies, proton radii, and neutron radii are shown in Figs. 5 and 7. Results are included (at right in each figure) for a Coulomb–Sturmian basis with proton-neutron asymmetric length scales in the ratio $b_n/b_p = 1.414$, which is comparable to the ratio r_n/r_p of neutron and proton distribution radii for these nuclei. Energy convergence in the Coulomb–Sturmian basis lags that of the harmonic oscillator basis, but less dramatically than seen above for ^{4}He. A basic three-point exponential extrapolation of the energy with respect to $N_{\max}$, at each $\hbar\Omega$ value, is indicated by the dashed curves in Figs. 5 and 7. The extrapolated energy is remarkably $\hbar\Omega$-independent in the $b_n/b_p = 1.414$ calculations, still with some $N_{\max}$ dependence. It appears to be approximately consistent with the harmonic oscillator extrapolations as well. However, such extrapolations must be viewed with caution, as both theoretical arguments and empirical studies suggest that other functional forms may be more appropriate, over at least portions of the $\hbar\Omega$ range [4–6].

Comparing the results for radii obtained with the various bases, for ^{6,8}He, we see that the Coulomb–Sturmian results (for either $b_n/b_p = 1$ or $b_n/b_p = 1.414$) again have a moderately shallower $\hbar\Omega$ dependence than obtained with the harmonic oscillator basis. Well-defined and stable crossover points are visible in Figs. 5 and 7, especially for the $b_n/b_p = 1.414$ calculations (at right). The extracted crossover radii are shown, as functions of $N_{\max}$, in Figs. 6 and 8. The radii obtained for the Coulomb–Sturmian calculations with different ratios of neutron and proton length scales ($b_n/b_p = 1$, 1.189, and 1.414) track each other closely from $N_{\max} \approx 8$ onward, agreeing with each other to within $\sim$0.1 fm. For r_p, the values are stable with respect to $N_{\max}$ and agree with the values obtained from the harmonic oscillator basis crossover as well. For r_n, it appears that the values might be drifting systematically with $N_{\max}$, although they do remain within an $\sim$0.2 fm range from $N_{\max} = 6$ onward. (The

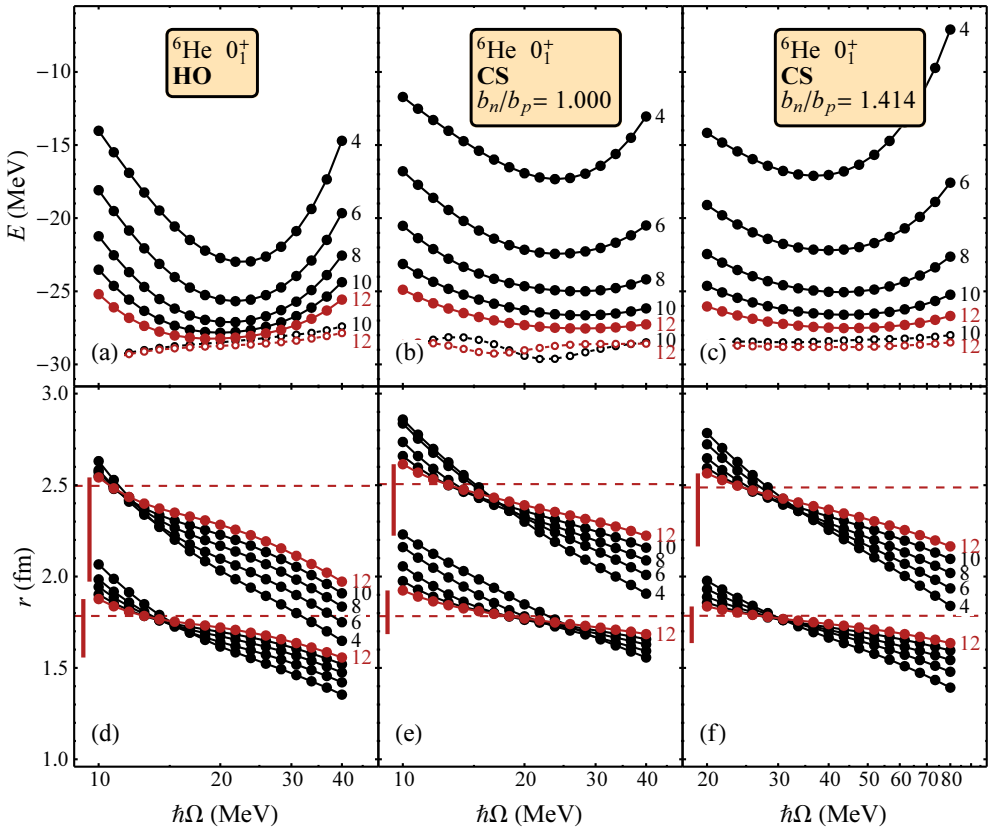

Figure 5: The calculated ^{6}He ground state energy (top) and RMS point-proton radius r_p and point-neutron radius r_n (bottom), using the conventional oscillator basis (left), Coulomb–Sturmian basis (center), and Coulomb–Sturmian basis with $b_n/b_p = 1.414$ (right). Exponentially extrapolated energies are indicated by dashed curves (at top), and crossover radii by dashed horizontal lines (at bottom).

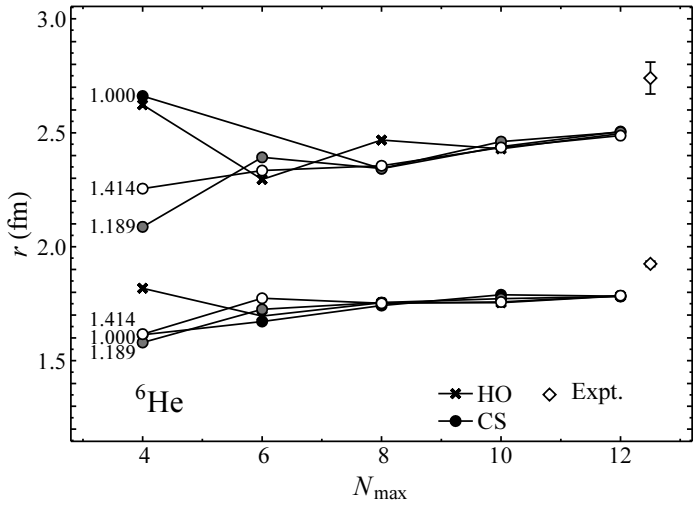

Figure 6: The ^{6}He ground state RMS point-proton radius r_p (lower curves) and point-neutron radius r_n (upper curves), as estimated from the crossover point (see text), calculated for the harmonic oscillator basis and for Coulomb–Sturmian bases with $b_n/b_p = 1$, 1.189, and 1.414 (as indicated). Experimental values are from Ref. [11].

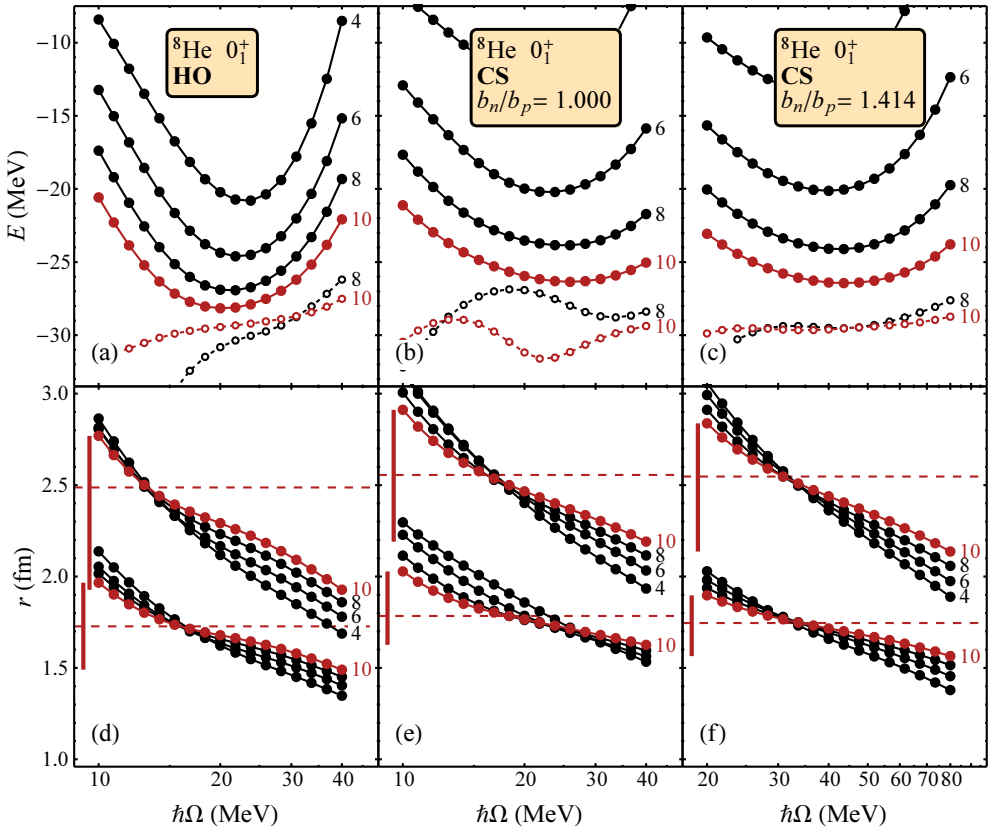

Figure 7: The calculated ^{8}He ground state energy (top) and RMS point-proton radius r_p and point-neutron radius r_n (bottom), using the conventional oscillator basis (left), Coulomb–Sturmian basis (center), and Coulomb–Sturmian basis with $b_n/b_p = 1.414$ (right). Exponentially extrapolated energies are indicated by dashed curves (at top), and crossover radii by dashed horizontal lines (at bottom).

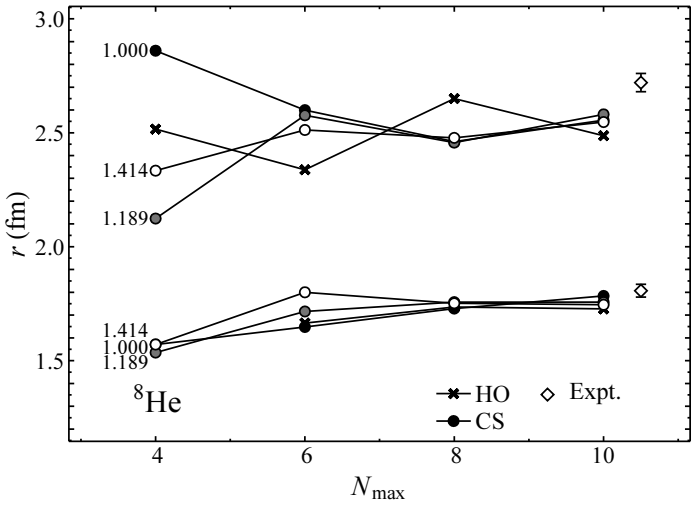

Figure 8: The ^{8}He ground state RMS point-proton radius r_p (lower curves) and point-neutron radius r_n (upper curves), as estimated from the crossover point (see text), calculated for the harmonic oscillator basis and for Coulomb–Sturmian bases with $b_n/b_p = 1$, 1.189, and 1.414 (as indicated). Experimental values are from Ref. [11].

crossover radii obtained from the harmonic oscillator calculations are fluctuating over a wider range.) Therefore, it is not possible to give a definitive value, but an estimate of $r_n \approx 2.5$–$2.6\,\mathrm{fm}$ can reasonably be made, for both ^{6,8}He.

Thus, *ab initio* NCCI calculations for ^{6,8}He with the JISP16 interaction, using both conventional and Coulomb–Sturmian bases, yield consistent estimates of the RMS point-proton and point-neutron radii, when these are extracted by the crossover prescription. The results qualitatively reproduce the trend in proton and neutron radii across the He isotopes, while quantitatively suggesting that the JISP16 interaction may yield radii which are smaller than experimentally observed, by as much as $\sim$0.2–0.3 fm for the ^{6,8}He neutron radii.

Acknowledgements

We thank S. Quaglioni, S. Bacca, and M. Brodeur for valuable discussions and A. E. McCoy for comments on the manuscript. This work was supported by the Research Corporation for Science Advancement through the Cottrell Scholar program, by the US Department of Energy under Grants No. DE-FG02-95ER-40934, DESC0008485 (SciDAC/NUCLEI), and DE-FG02-87ER40371, and by the US National Science Foundation under Grant No. 0904782. Computational resources were provided by the National Energy Research Supercomputer Center (NERSC), which is supported by the Office of Science of the U.S. Department of Energy under Contract No. DE-AC02-05CH11231.

References

[1] P. Navrátil, J. P. Vary and B. R. Barrett, Phys. Rev. Lett. **84**, 5728 (2000); Phys. Rev. C **62**, 054311 (2000).

[2] B. R. Barrett, P. Navrátil and J. P. Vary, Progr. Part. Nucl. Phys. **69**, 131 (2013).

[3] P. Maris, J. P. Vary and A. M. Shirokov, Phys. Rev. C **79**, 014308 (2009).

[4] S. A. Coon, M. I. Avetian, M. K. G. Kruse, U. van Kolck, P. Maris and J. P. Vary, Phys. Rev. C **86**, 054002 (2012).

[5] R. J. Furnstahl, G. Hagen and T. Papenbrock, Phys. Rev. C **86**, 031301 (2012).

[6] S. N. More, A. Ekstrom, R. J. Furnstahl, G. Hagen and T. Papenbrock, Phys. Rev. C **87**, 044326 (2013).

[7] E. D. Jurgenson, P. Maris, R. J. Furnstahl, P. Navratil, W. E. Ormand and J. P. Vary, Phys. Rev. C **87**, 054312 (2013).

[8] J. Suhonen, *From nucleons to nucleus*. Springer-Verlag, Berlin, 2007.

[9] S. K. Bogner, R. J. Furnstahl, P. Maris, R. J. Perry, A. Schwenk and J. Vary, Nucl. Phys. A **801**, 21 (2008).

[10] C. Cockrell, J. P. Vary and P. Maris, Phys. Rev. C **86**, 034325 (2012).

[11] I. Tanihata, H. Savajols and R. Kanungo, Progr. Part. Nucl. Phys. **68**, 215 (2013).

[12] S. Quaglioni and P. Navrátil, Phys. Rev. C **79**, 044606 (2009).

[13] M. A. Caprio, P. Maris and J. P. Vary, Phys. Rev. C **86**, 034312 (2012).

[14] M. Rotenberg, Ann. Phys. (NY) **19**, 262 (1962).

[15] E. J. Weniger, J. Math. Phys. **26**, 276 (1985).

[16] B. D. Keister and W. N. Polyzou, J. Comput. Phys. **134**, 231 (1997).

[17] A. M. Shirokov, J. P. Vary, A. I. Mazur and T. A. Weber, Phys. Lett. B **644**, 33 (2007).

[18] P. Maris, M. Sosonkina, J. P. Vary, E. Ng and C. Yang, Proc. Comput. Sci. **1**, 97 (2010).

[19] H. M. Aktulga, C. Yang, E. G. Ng, P. Maris and J. P. Vary, Concurrency Computat.: Pract. Exper. (2013), DOI: 10.1002/cpe.3129.

[20] S. Bacca, N. Barnea and A. Schwenk, Phys. Rev. C **86**, 034321 (2012).

NTSE-2013 Keynote Talk:

Origin and Properties of Strong Inter-Nucleon Interactions[1]

R. Machleidt

Department of Physics, University of Idaho, Moscow, Idaho 83844, USA

Abstract

I start with a historical review of the attempts to construct theories for the origin of nuclear forces, for which I also summaries the most important properties. The review then shifts to its main focus, which is the chiral effective field theory approach to nuclear forces. I summarize the current status of this approach and discuss the most important open issues: the proper renormalization of the chiral two-nucleon potential and sub-leading three-nucleon forces.

Keywords: *Nuclear forces; nucleon-nucleon scattering; low-energy QCD; effective field theory; renormalization; few-nucleon forces*

1 Introduction and overview

The nuclear force problem is as old as *James Vary*, namely seven decades. What a coincidence!

The development of a proper theory of nuclear forces has occupied the minds of some of the brightest physicists and has been one of the main topics of physics research in the 20th century. The original idea was that the force is caused by the exchange of lighter particles (than nucleons) known as mesons, and this idea gave rise to the birth of a new sub-field of modern physics, namely, (elementary) particle physics. The modern perception of the nuclear force is that it is a residual interaction (similar to the van der Waals force between neutral atoms) of the even stronger force between quarks, which is mediated by the exchange of gluons and holds the quarks together inside a nucleon.

1.1 Early history

After the discovery of the neutron in 1932, it was clear that the atomic nucleus is made up from protons and neutrons. In such a system, electromagnetic forces cannot be the reason why the constituents of the nucleus are sticking together. Therefore, the concept of a new strong nuclear interaction was introduced. In 1935, the first theory for this new force was developed by the Japanese physicist Yukawa [1], who suggested that the nucleons would exchange particles between each other and this mechanism would create the force. Yukawa constructed his theory in analogy to the theory of the electromagnetic interaction where the exchange of a (massless) photon is the cause of the force. However, in the case of the nuclear force, Yukawa assumed that the

[1]Dedicated to James Vary on the occasion of his 70th birthday.

Proceedings of International Conference 'Nuclear Theory in the Supercomputing Era — 2013' (NTSE-2013), Ames, IA, USA, May 13–17, 2013. Eds. A. M. Shirokov and A. I. Mazur. Pacific National University, Khabarovsk, Russia, 2014, p. 336.

http://www.ntse-2013.khb.ru/Proc/Machleidt.pdf.

"force-makers" (which were eventually called "mesons") carry a mass of a fraction of the nucleon mass. This would limit the effect of the force to a finite range, since the uncertainty principal allows massive particles to travel only a finite distance. The meson predicted by Yukawa was finally found in 1947 in cosmic ray and in 1948 in the laboratory and called the pion. Yukawa was awarded the Nobel Prize in 1949. In the 1950's and 60's more mesons were found in accelerator experiments and the meson theory of nuclear forces was extended to include many mesons. These models became know as one-boson-exchange models, which is a reference to the fact that the different mesons are exchanged singly in this model. The one-boson-exchange model is very successful in explaining essentially all properties of the nucleon-nucleon interaction at low energies [2–6]. In the 1970's and 80's, also meson models were developed that went beyond the simple single-particle exchange mechanism. These models included, in particular, the explicit exchange of two pions with all its complications. Well-known representatives of the latter kind are the Paris [7] and the Bonn potential [8].

Since these meson models were quantitatively very successful, it appeared that they were the solution of the nuclear force problem. However, with the discovery (in the 1970's) that the fundamental theory of strong interactions is quantum chromodynamics (QCD) and not meson theory, all "meson theories" had to be viewed as models, and the attempts to derive a proper theory of the nuclear force had to start all over again.

1.2 QCD and the nuclear force

The problem with a derivation of nuclear forces from QCD is two-fold. First, each nucleon consists of three quarks such that the system of two nucleons is already a six-body problem. Second, the force between quarks, which is created by the exchange of gluons, has the feature of being very strong at the low energy-scale that is characteristic of nuclear physics. This extraordinary strength makes it difficult to find "converging" mathematical solutions. Therefore, during the first round of new attempts, QCD-inspired quark models became popular. The positive aspect of these models is that they try to explain nucleon structure (which consists of three quarks) and nucleon-nucleon interactions (six-quark systems) on an equal footing. Some of the gross features of the two-nucleon force, like the "hard core" are explained successfully in such models. However, from a critical point of view, it must be noted that these quark-based approaches are yet another set of models and not a theory. Alternatively, one may try to solve the six-quark problem with brute computing power, by putting the six-quark system on a four dimensional lattice of discrete points which represents the three dimensions of space and one dimension of time. This method has become known as lattice QCD and is making progress. However, such calculations are computationally very expensive and cannot be used as a standard nuclear physics tool.

1.3 Chiral effective field theory

Around 1990, a major breakthrough occurred when the nobel laureate Steven Weinberg applied the concept of an effective field theory (EFT) to low-energy QCD [9,10]. He simply wrote down the most general theory that is consistent with all the properties of low-energy QCD, since that would make this theory identical to low-energy QCD. A particularly important property is the so-called chiral symmetry, which is "spontaneously" broken. Massless particles observe chiral symmetry, which means that their spin and momentum are either parallel ("right-handed") or anti-parallel ("left-handed") and remain so forever. Since the quarks, which nucleons are made of ("up" and "down" quarks), are almost mass-less, approximate chiral symmetry is a given. Naively, this symmetry should have the consequence that one finds in nature mesons of the same mass, but with positive and negative parity. However, this is

not the case and such failure is termed a "spontaneous" breaking of the symmetry. According to a theorem first proven by Goldstone, the spontaneous breaking of a symmetry creates a particle, here, the pion. Thus, the pion becomes the main player in the production of the nuclear force. The interaction of pions with nucleons is weak as compared to the interaction of gluons with quarks. Therefore, pion-nucleon processes can be calculated without problem. Moreover, this effective field theory can be expanded in powers of momentum/scale, where "scale" denotes the "chiral symmetry breaking scale" which is about 1 GeV. This scheme is also known as chiral perturbation theory (ChPT) and allows to calculate the various terms that make up the nuclear force systematically power by power, or order by order. Another advantage of the chiral EFT approach is its ability to generate not only the force between two nucleons, but also many-nucleon forces, on the same footing [11]. In modern theoretical nuclear physics, the chiral EFT approach is becoming increasingly popular and is applied with great success [12, 13].

1.4 Main properties of the nuclear force and phenomenological potentials

Some properties of nuclear interactions can be deduced from the properties of nuclei. The property of saturation suggests that nuclear forces are of short range (a few fm) and strongly attractive at that range, which explains nuclear binding. But the nuclear force has also a very complex spin-dependence. First evidence came from the observation that the deuteron (proton-neutron bound state, smallest atomic nucleus) deviates slightly from a spherical shape. This suggests a force that depends on the orientation of the spins of the nucleons with regard to the line connecting the two nucleons (tensor force). In heavier nuclei, a shell structure has been observed which according to a suggestion by Mayer and Jensen can be explained by a strong force between the spin of the nucleon and its orbital motion (spin-orbit force). More clear-cut evidence for the spin-dependence is extracted from scattering experiments where one nucleon is scattered off another nucleon. In such experiments, the existence of the nuclear spin-orbit and tensor forces has clearly been established. Scattering experiments at higher energies (more than 200 MeV) show indications that the nucleon-nucleon interaction at very short distances (smaller than 0.5 fm) becomes repulsive ("hard core"). Besides the force between two nucleons (2NF), there are also three-nucleon forces (3NF), four-nucleon forces (4NF), etc. However, the 2NF is much stronger than the 3NF, which in turn is much stronger than the 4NF, etc. In exact calculations of the properties of light nuclei based upon the bare nuclear forces, it has been shown that 3NFs are important. Their contribution is small, but crucial. The need for 4NF for explaining nuclear properties has not (yet) been clearly established.

Phenomenological nucleon-nucleon (NN) potentials are constructed in close relationship to the empirical facts. In this regard, the most faithful method of construction is inverse scattering theory, which the so-called JISP-16 potentials are based upon [14].

In the following sections, I will elaborate more on the theory of nuclear forces with particular emphasis on the view according to which the forces between nucleons emerge from low-energy QCD via an effective field theory.

2 Effective field theory for low-energy QCD

Quantum chromodynamics (QCD) is the theory of strong interactions. It deals with quarks, gluons and their interactions and is a part of the Standard Model of Particle Physics. QCD is a non-Abelian gauge field theory with color SU(3) as the underlying gauge group. The non-Abelian nature of the theory has dramatic consequences. While

the interaction between colored objects is weak at short distances or high momentum transfer ("asymptotic freedom"); it is strong at long distances ($\gtrsim 1$ fm) or low energies, leading to the confinement of quarks into colorless objects, the hadrons. Consequently, QCD allows for a perturbative analysis at large energies, whereas it is highly non-perturbative in the low-energy regime. Nuclear physics resides at low energies and the force between nucleons is a residual color interaction similar to the van der Waals force between neutral molecules. Therefore, in terms of quarks and gluons, the nuclear force is a very complicated problem that, nevertheless, can be attacked with brute computing power on a discretized, Euclidean space-time lattice (known as lattice QCD). In a recent study [15], the neutron-proton scattering lengths in the singlet and triplet S-waves have been determined in fully dynamical lattice QCD. This result is then extrapolated to the physical pion mass with the help of chiral perturbation theory. The pion mass of 354 MeV is still too large to allow for reliable extrapolations, but the feasibility has been demonstrated and more progress can be expected for the near future. In a lattice calculation of a very different kind, the NN potential was studied [16]. The central part of the potential shows a repulsive core plus attraction of intermediate range. This is a very promising result, but it must be noted that also in this investigation still rather large pion masses are being used. In any case, advanced lattice QCD calculations are under way and continuously improved. However, since these calculations are very time-consuming and expensive, they can only be used to check a few representative key-issues. For everyday nuclear structure physics, a more efficient approach is needed.

The efficient approach is an effective field theory. For the development of an EFT, it is crucial to identify a separation of scales. In the hadron spectrum, a large gap between the masses of the pions and the masses of the vector mesons, like $\rho(770)$ and $\omega(782)$, can clearly be identified. Thus, it is natural to assume that the pion mass sets the soft scale, $Q \sim m_\pi$, and the rho mass is associated with the hard scale, $\Lambda_\chi \sim m_\rho$, also known as the chiral-symmetry breaking scale. This is suggestive of considering an expansion in terms of the soft scale over the hard scale, Q/Λ_χ. Concerning the relevant degrees of freedom, we noticed already that, for the ground state and the low-energy excitation spectrum of an atomic nucleus as well as for conventional nuclear reactions, quarks and gluons are ineffective degrees of freedom, while nucleons and pions are the appropriate ones. To make sure that this EFT is not just another phenomenology, it must have a firm link with QCD. The link is established by having the EFT to observe all relevant symmetries of the underlying theory. This requirement is based upon a 'folk theorem' by Weinberg [9]:

> If one writes down the most general possible Lagrangian, including *all* terms consistent with assumed symmetry principles, and then calculates matrix elements with this Lagrangian to any given order of perturbation theory, the result will simply be the most general possible S-matrix consistent with analyticity, perturbative unitarity, cluster decomposition, and the assumed symmetry principles.

In summary, the EFT program consists of the following steps:

1. Identify the soft and hard scales, and the degrees of freedom (DOF) appropriate for (low-energy) nuclear physics. Soft scale: $Q \sim m_\pi$, hard scale: $\Lambda_\chi \sim m_\rho \sim 1$ GeV; DOF: pions and nucleons.

2. Identify the relevant symmetries of low-energy QCD and investigate if and how they are broken: explicitly and spontaneously broken chiral symmetry (spontaneous symmetry breaking generates the pions as Goldstone bosons).

3. Construct the most general Lagrangian consistent with those symmetries and symmetry breakings, see Ref. [13].

4. Design an organizational scheme that can distinguish between more and less important contributions: a low-momentum expansion, $(Q/\Lambda_\chi)^\nu$, with ν determined by 'power counting'. For an irreducible diagram that involves A nucleons, we have:

$$\nu = -2 + 2A - 2C + 2L + \sum_i \Delta_i \,. \tag{1}$$

where

$$\Delta_i \equiv d_i + \frac{n_i}{2} - 2 \,, \tag{2}$$

with C being the number of separately connected pieces and L being the number of loops in the diagram; d_i is the number of derivatives or pion-mass insertions and n_i is the number of nucleon fields (nucleon legs) involved in vertex i; the sum runs over all vertices i contained in the diagram under consideration. Note that for an irreducible NN diagram ($A = 2$, $C = 1$), the power formula collapses to the very simple expression

$$\nu = 2L + \sum_i \Delta_i \,. \tag{3}$$

5. Guided by the expansion, calculate Feynman diagrams for the problem under consideration to the desired accuracy (see next Section).

3 The hierarchy of nuclear forces in chiral EFT

Chiral perturbation theory and power counting imply that nuclear forces emerge as a hierarchy controlled by the power ν, Fig. 1.

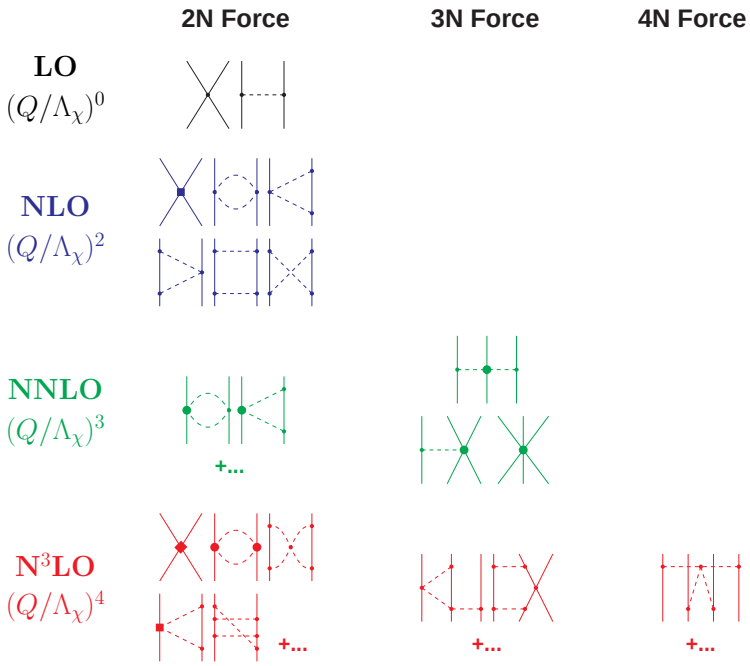

Figure 1: Hierarchy of nuclear forces in ChPT. Solid lines represent nucleons and dashed lines pions. Small dots, large solid dots, solid squares, and solid diamonds denote vertices of index $\Delta_i = 0$, 1, 2, and 4, respectively. Further explanations are given in the text.

In the lowest order, better known as leading order (LO, $\nu = 0$), the NN amplitude is made up by two momentum-independent contact terms ($\sim Q^0$), represented by the four-nucleon-leg graph with a small-dot vertex shown in the first row of Fig. 1, and static one-pion exchange (1PE), the second diagram in the first row of the figure. This is, of course, a rather rough approximation to the two-nucleon force (2NF), but it accounts already for some important features. The 1PE provides the tensor force, necessary to describe the deuteron, and it explains NN scattering in peripheral partial waves of very high orbital angular momentum. At this order, the two contacts which contribute only in S-waves provide the short- and intermediate-range interaction which is somewhat crude.

In the next order, $\nu = 1$, all contributions vanish due to parity and time-reversal invariance.

Therefore, the next-to-leading order (NLO) is $\nu = 2$. Two-pion exchange (2PE) occurs for the first time ("leading 2PE") and, thus, the creation of a more sophisticated description of the intermediate-range interaction is starting here. Since the loop involved in each pion-diagram implies already $\nu = 2$ [cf. Eq. (3)], the vertices must have $\Delta_i = 0$. Therefore, at this order, only the lowest order πNN and $\pi\pi NN$ vertices are allowed which is why the leading 2PE is rather weak. Furthermore, there are seven contact terms of $\mathcal{O}(Q^2)$, shown by the four-nucleon-leg graph with a solid square, which contribute in S and P waves. The operator structure of these contacts include a spin-orbit term besides central, spin-spin, and tensor terms. Thus, essentially all spin-isospin structures necessary to describe the two-nucleon force phenomenologically have been generated at this order. The main deficiency at this stage of development is an insufficient intermediate-range attraction.

This problem is finally fixed at order three ($\nu = 3$), next-to-next-to-leading order (NNLO). The 2PE involves now the two-derivative $\pi\pi NN$ seagull vertices (proportional to the c_i LECs) denoted by a large solid dot in Fig. 1. These vertices represent correlated 2PE as well as intermediate $\Delta(1232)$-isobar contributions. It is well-known from the meson phenomenology of nuclear forces [7, 8] that these two contributions are crucial for a realistic and quantitative 2PE model. Consequently, the 2PE now assumes a realistic size and describes the intermediate-range attraction of the nuclear force about right. Moreover, first relativistic corrections come into play at this order. There are no new contacts.

The reason why we talk of a hierarchy of nuclear forces is that two- and many-nucleon forces are created on an equal footing and emerge in increasing number as we go to higher and higher orders. At NNLO, the first set of nonvanishing three-nucleon forces (3NF) occur [17, 18], cf. column '3N Force' of Fig. 1. In fact, at the previous order, NLO, irreducible 3N graphs appear already, however, it has been shown by Weinberg [11] that these diagrams all cancel. Since nonvanishing 3NF contributions happen first at order $(Q/\Lambda_\chi)^3$, they are very weak as compared to 2NF which start at $(Q/\Lambda_\chi)^0$.

More 2PE is produced at $\nu = 4$, next-to-next-to-next-to-leading order ($\mathrm{N^3LO}$), of which we show only a few symbolic diagrams in Fig. 1. Two-loop 2PE graphs show up for the first time and so does three-pion exchange (3PE) which necessarily involves two loops. 3PE was found to be negligible at this order [19, 20]. Most importantly, 15 new contact terms $\sim Q^4$ arise and are represented by the four-nucleon-leg graph with a solid diamond. They include a quadratic spin-orbit term and contribute up to D-waves. Mainly due to the increased number of contact terms, a quantitative description of the two-nucleon interaction up to about 300 MeV lab. energy is possible, at $\mathrm{N^3LO}$ (see red solid line in Fig. 2 and cf. Table 1). Besides further 3NF, four-nucleon forces (4NF) start at this order. Since the leading 4NF come into existence one order higher than the leading 3NF, 4NF are weaker than 3NF. Thus, ChPT provides a straightforward explanation for the empirically known fact that 2NF $\gg$ 3NF $\gg$ 4NF ... .

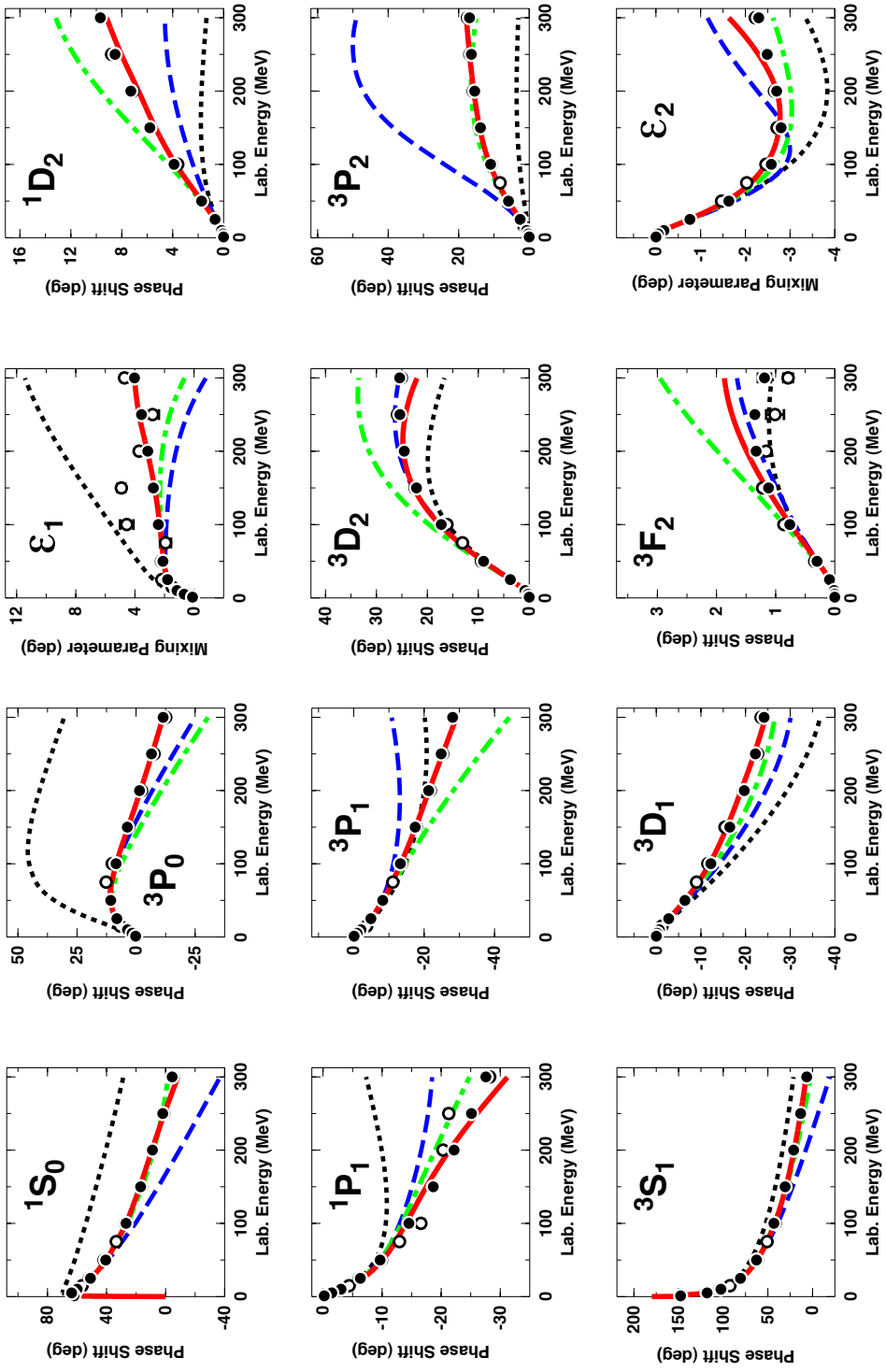

Figure 2: Phase shifts of np scattering as calculated from NN potentials at different orders of ChPT. The black dotted line is LO(500), the blue dashed is NLO(550/700) [21], the green dash-dotted NNLO(600/700) [21], and the red solid N^{3}LO(500) [22], where the numbers in parentheses denote the cutoffs in MeV. Partial waves with total angular momentum $J \leq 2$ are displayed. The solid dots and open circles are the results from the Nijmegen multi-energy np phase shift analysis [23] and the VPI/GWU single-energy np analysis SM99 [24], respectively.

Table 1: χ^2/datum for the reproduction of the 1999 *np* database [25] below 290 MeV by various *np* potentials. $T_{\rm lab}$ denotes the kinetic energy of the incident neutron in the laboratory system.

$T_{\rm lab}$ bin (MeV)	# of *np* data	N^{3}LO [22]	NNLO [21]	NLO [21]	AV18 [26]
0–100	1058	1.05	1.7	4.5	0.95
100–190	501	1.08	22	100	1.10
190–290	843	1.15	47	180	1.11
0–290	2402	1.10	20	86	1.04

During the past decade or so, chiral two-nucleon forces have been used in many microscopic calculations of nuclear reactions and structure [27–33] and the combination of chiral two- and three-nucleon forces has been applied in few-nucleon reactions [18, 34–37], structure of light- and medium-mass nuclei [38–46], and nuclear and neutron matter [47–50] — with a great deal of success. The majority of nuclear structure calculations is nowadays based upon chiral forces.

However, in spite of this progress, we are not done. Due to the complexity of the nuclear force issue, there are still many subtle and not so subtle open problems. We will not list and discuss all of them, but instead just focus on the two open issues, which we perceive as the most important ones:

- The proper renormalization of chiral nuclear potentials and
- Subleading chiral few-nucleon forces.

4 Renormalization of chiral nuclear forces

4.1 The chiral NN potential

In mathematical terms, the various orders of the irreducible graphs in Fig. 1, which define the chiral NN potential, are given by:

$$V_{\rm LO} = V_{\rm ct}^{(0)} + V_{1\pi}^{(0)}, \tag{4}$$

$$V_{\rm NLO} = V_{\rm LO} + V_{\rm ct}^{(2)} + V_{1\pi}^{(2)} + V_{2\pi}^{(2)}, \tag{5}$$

$$V_{\rm NNLO} = V_{\rm NLO} + V_{1\pi}^{(3)} + V_{2\pi}^{(3)}, \tag{6}$$

$$V_{\rm N^3LO} = V_{\rm NNLO} + V_{\rm ct}^{(4)} + V_{1\pi}^{(4)} + V_{2\pi}^{(4)} + V_{3\pi}^{(4)}, \tag{7}$$

where the superscript denotes the order ν of the low-momentum expansion. Contact potentials carry the subscript "ct" and pion-exchange potentials can be identified by an obvious subscript.

Multi-pion exchange, which starts at NLO and continues through all higher orders, involves divergent loop integrals that need to be regularized. An elegant way to do this is dimensional regularization which (besides the main nonpolynomial result) typically generates polynomial terms with coefficients that are, in part, infinite or scale dependent. One purpose of the contacts is to absorb all infinities and scale dependencies and make sure that the final result is finite and scale independent. This is the renormalization of the perturbatively calculated NN amplitude (which, by definition, is the "NN potential"). It is very similar to what is done in the ChPT calculations of $\pi\pi$ and πN scattering, namely, a renormalization order by order, which is the method of choice for any EFT. Thus, up to this point, the calculation fully meets the standards of an EFT and there are no problems. The perturbative NN amplitude can be used to make model independent predictions for peripheral partial waves.

4.2 Nonperturbative renormalization of the NN potential

For calculations of the structure of nuclear few and many-body systems, the lower partial waves are the most important ones. The fact that in S waves we have large scattering lengths and shallow (quasi) bound states indicates that these waves need to be treated nonperturbatively. Following Weinberg's prescription [10], this is accomplished by inserting the potential V into the Lippmann-Schwinger (LS) equation:

$$T(\vec{p}\,',\vec{p}) = V(\vec{p}\,',\vec{p}) + \int d^3p''\, V(\vec{p}\,',\vec{p}\,'')\, \frac{M_N}{p^2 - p''^2 + i\epsilon}\, T(\vec{p}\,'',\vec{p})\,, \tag{8}$$

where M_N denotes the nucleon mass.

In general, the integral in the LS equation is divergent and needs to be regularized. One way to do this is by multiplying V with a regulator function

$$V(\vec{p}\,',\vec{p}) \longmapsto V(\vec{p}\,',\vec{p})\, e^{-(p'/\Lambda)^{2n}}\, e^{-(p/\Lambda)^{2n}}\,. \tag{9}$$

Typical choices for the cutoff parameter Λ that appears in the regulator are $\Lambda \approx 0.5$ GeV $< \Lambda_\chi \approx 1$ GeV.

It is pretty obvious that results for the T-matrix may depend sensitively on the regulator and its cutoff parameter. This is acceptable if one wishes to build models. For example, the meson models of the past [4] always depended sensitively on the choices for the cutoff parameters which, in fact, were important for the fit of the NN data. However, the EFT approach wishes to be fundamental in nature and not just another model.

In field theories, divergent integrals are not uncommon and methods have been developed for how to deal with them. One regulates the integrals and then removes the dependence on the regularization parameters (scales, cutoffs) by renormalization. In the end, the theory and its predictions do not depend on cutoffs or renormalization scales. So-called renormalizable quantum field theories, like QED, have essentially one set of prescriptions that takes care of renormalization through all orders. In contrast, EFTs are renormalized order by order.

Weinberg's implicit assumption [10, 51] was that the counterterms introduced to renormalize the perturbatively calculated potential, based upon naive dimensional analysis ("Weinberg counting"), are also sufficient to renormalize the nonperturbative resummation of the potential in the LS equation. In 1996, Kaplan, Savage, and Wise (KSW) [52] pointed out that there are problems with the Weinberg scheme if the LS equation is renormalized by minimally-subtracted dimensional regularization. This criticism resulted in a flurry of publications on the renormalization of the nonperturbative NN problem. The literature is too comprehensive to elaborate on all contributions. Therefore, we will restrict ourselves, here, to discussing just a few aspects that we perceive as particularly important. A more comprehensive consideration can be found in Ref. [13]

Naively, the most perfect renormalization procedure is the one where the cutoff parameter Λ is carried to infinity while stable results are maintained. This was done successfully at LO in the work by Nogga *et al.* [53]. At NNLO, the infinite-cutoff renormalization procedure has been investigated in [54] for partial waves with total angular momentum $J \leq 1$ and in [55] for all partial waves with $J \leq 5$. At N^{3}LO, the $^1S_0$ state was considered in Ref. [56], and all states up to $J = 6$ were investigated in Ref. [57]. From all of these works, it is evident that no counter term is effective in partial-waves with short-range repulsion and only a single counter term can effectively be used in partial-waves with short-range attraction. Thus, for the $\Lambda \to \infty$ renormalization prescription, even at N^{3}LO, there exists either one or no counter term per partial-wave state. This is inconsistent with any reasonable power-counting scheme and prevents an order-by-order improvement of the predictions.

To summarize: In the infinite-cutoff renormalization scheme, the potential is admitted up to unlimited momenta. However, within the EFT, this potential is derived from has validity only for momenta smaller than the chiral symmetry breaking scale $\Lambda_\chi \approx 1$ GeV. The lack of order-by-order convergence and discrepancies in lower partial-waves demonstrate that the potential should not be used beyond the limits of the effective theory [57] (see Ref. [58] for a related discussion). The conclusion then is that cutoffs should be limited to $\Lambda \lesssim \Lambda_\chi$ (but see also Ref. [59]).

A possible solution of this problem was proposed already in [53] and reiterated in a paper by Long and van Kolck [60]. A calculation of the proposed kind has been performed by Valderrama [61] for the S, P, and D waves. The author renormalizes the LO interaction nonperturbatively and then uses the LO distorted wave to calculate the 2PE contributions at NLO and NNLO perturbatively. It turns out that perturbative renormalizability requires the introduction of about twice as many counter terms as compared to Weinberg counting, which reduces the predictive power. The order-by-order convergence of the NN phase shifts appears to be reasonable.

However, even if one considers the above method as successful for NN scattering, there is doubt if the interaction generated in this approach is of any use for applications in nuclear few- and many-body problems. In applications, one would first have to solve the many-body problem with the re-summed LO interaction, and then add higher order corrections in perturbation theory. It was shown in a recent paper [62] that the renormalized LO interaction is characterized by a very large tensor force from 1PE. This is no surprise since LO is renormalized with $\Lambda \to \infty$ implying that the 1PE, particulary its tensor force, is totally uncut. As a consequence of this, the wound integral in nuclear matter, κ, comes out to be about 40%. The hole-line and coupled cluster expansions are known to converge $\propto \kappa^{n-1}$ with n the number of hole-lines or particles per cluster. For conventional nuclear forces, the wound integral is typically between 5 and 10% and the inclusion of three-body clusters (or three hole-lines) are needed to obtain converged results in the many-body system. Thus, if the wound integral is 40%, probably, up to six hole-lines need to be included for approximate convergence. Such calculations are not feasible even with the most powerful computers of today and will not be feasible any time soon. Therefore, even if the renormalization procedure proposed in [60] will work for NN scattering, the interaction produced will be highly impractical (to say the least) in applications in few- and many-body problems because of convergence problems with the many-body energy and wave functions.

Crucial for an EFT are regulator independence (within the range of validity of the EFT) and a power counting scheme that allows for order-by-order improvement with decreasing truncation error. The purpose of renormalization is to achieve this regulator independence while maintaining a functional power counting scheme.

Thus, in the spirit of Lepage [63], the cutoff independence should be examined for cutoffs below the hard scale and not beyond. Ranges of cutoff independence within the theoretical error are to be identified using Lepage plots [63]. Recently, we have started a systematic investigation of this kind. In our work, we quantify the error of the predictions by calculating the χ^2/datum for the reproduction of the neutron-proton (np) elastic scattering data as a function of the cutoff parameter Λ of the regulator function Eq. (9). We have investigated the predictions by chiral np potentials at order NLO and NNLO applying Weinberg counting for the counter terms (NN contact terms). We show our results for the energy range 35–125 MeV in the upper frame of Fig. 3 and for 125–183 MeV in the lower frame. It is seen that the reproduction of the np data at these energies is generally poor at NLO, while at NNLO the χ^2/datum assumes acceptable values (a clear demonstration of order-by-order improvement). Moreover, at NNLO one observes "plateaus" of constant low χ^2 for cutoff parameters ranging from about 450 to 850 MeV. This may be perceived as cutoff independence (and, thus, successful renormalization) for the relevant range of

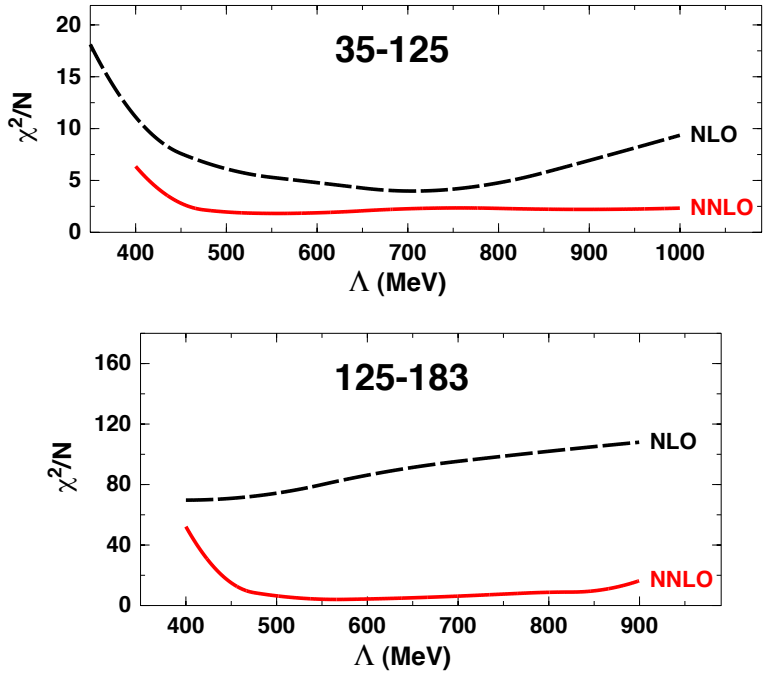

Figure 3: χ^2/datum for the reproduction of the *np* data in the energy range 35–125 MeV (upper frame) and 125–183 MeV (lower frame) as a function of the cutoff parameter Λ of the regulator function Eq. (9). The (black) dashed curves show the χ^2/datum achieved with *np* potentials constructed at order NLO and the (red) solid curves are for NNLO.

cutoff parameters.

5 Few-nucleon forces and what is missing

We will now discuss the other issue we perceive as unfinished and important, namely, subleading chiral few-nucleon forces.

Nuclear three-body forces in ChPT were initially discussed by Weinberg [11]. The 3NF at NNLO, was derived by van Kolck [17] and applied, for the first time, in nucleon-deuteron scattering by Epelbaum *et al.* [18]. The leading 4NF (at N^{3}LO) was constructed by Epelbaum [64] and found to contribute in the order of 0.1 MeV to the ^{4}He binding energy (total ^{4}He binding energy: 28.3 MeV) in a preliminary calculation [65], confirming the traditional assumption that 4NF are essentially negligible. Therefore, the focus is on 3NFs.

For a 3NF, we have $A = 3$ and $C = 1$ and, thus, Eq. (1) implies

$$\nu = 2 + 2L + \sum_i \Delta_i \,. \tag{10}$$

We will use this equation to analyze 3NF contributions order by order. The first non-vanishing 3NF occurs at $\nu = 3$ (NNLO), which is obtained when there are no loops ($L = 0$) and $\sum_i \Delta_i = 1$, i.e., $\Delta_i = 1$ for one vertex while $\Delta_i = 0$ for all other vertices. There are three topologies which fulfill this condition, known as the two-pion exchange (2PE), one-pion exchange (1PE), and contact graphs (cf. Fig. 1).

The 3NF at NNLO has been applied in calculations of few-nucleon reactions [35], structure of light- and medium-mass nuclei [38–46], and nuclear and neutron matter [47–50] with a great deal of success. However, the famous 'A_y puzzle' of nucleon-

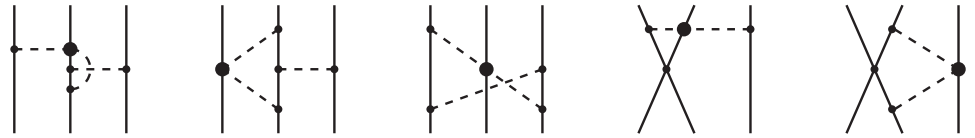

(a) (b) (c) (d) (e)

Figure 4: 3NF one-loop contributions at N^{4}LO ($\nu = 5$). We show one representative diagram for each of five topologies, which are: (a) 2PE, (b) 2PE-1PE, (c) ring, (d) 1PE-contact, and (e) 2PE-contact. Notation as in Fig. 1.

deuteron scattering [18] and the analogous problem with the analyzing power in p-^{3}He scattering [37] is not resolved. Furthermore, the spectra of light nuclei leave room for improvement [39]. Since we are dealing with a perturbation theory, it is natural to turn to the next order when looking for improvements.

The next order is N^{3}LO, where we have loop and tree diagrams. For the loops, we have $L = 1$ and, therefore, all Δ_i have to be zero to ensure $\nu = 4$. Thus, these one-loop 3NF diagrams can include only leading order vertices, the parameters of which are fixed from πN and NN analysis. One sub-group of these diagrams (the 2PE graphs) has been calculated by Ishikawa and Robilotta [66], and the other topologies have been evaluated by the Bochum–Bonn group [67, 68]. The N^{3}LO 2PE 3NF has been applied in the calculation of nucleon-deuteron observables in Ref. [66] causing little impact. Very recently, the long-range part of the chiral N^{3}LO 3NF has been tested in the triton [69] and in three-nucleon scattering [70] yielding only moderate effects. The long- and short-range parts of this force have been used in neutron matter calculations (together with the N^{3}LO 4NF) producing relatively large contributions from the 3NF [71]. Thus, the ultimate assessment of the N^{3}LO 3NF is still outstanding and will require more few- and many-body applications.

In the meantime, it is of interest to take already a look at the next order of 3NFs, which is N^{4}LO or $\nu = 5$ (of the Δ-less theory to which the present discussion is restricted because of lack of space). The loop contributions that occur at this order are obtained by replacing one vertex in the N^{3}LO loops by a $\Delta_i = 1$ vertex (with LEC c_i), Fig. 4, which is why these loops may be more sizable than the N^{3}LO loops. The 2PE topology turns out to be of modest size [72]; moreover, it can be handled in a practical way by summing it up together with the 2PE topologies at NNLO and N^{3}LO [72]. The 2PE-1PE and ring topologies have also been derived [73]. Finally, there are also tree topologies at N^{4}LO (Fig. 5) which include a new set of 3N contact interactions (graph (c)). These 3N contacts have recently been derived by the Pisa group [74]. Contact terms are typically simple (as compared to loop diagrams) and their coefficients are unconstrained (except for naturalness). Therefore, it would be an attractive project to test some terms (in particular, the spin-orbit terms) of the N^{4}LO contact 3NF [74] in calculations of few-body reactions (specifically, the p-d and p-^{3}He A_y) and spectra of light nuclei.

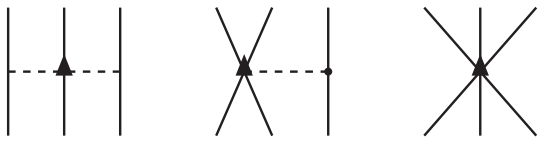

(a) (b) (c)

Figure 5: 3NF tree graphs at N^{4}LO ($\nu = 5$) denoted by: (a) 2PE, (b) 1PE-contact, and (c) contact. Solid triangles represent vertices of index $\Delta_i = 3$.

6 Conclusions and Outlook

The past 15 years have seen great progress in our understanding of nuclear forces in terms of low-energy QCD. A key to this development was the realization that the low-energy QCD is equivalent to an effective field theory which allows for a perturbative expansion that has become known as chiral perturbation theory. In this framework, two- and many-body forces emerge on an equal footing and the empirical fact that nuclear many-body forces are substantially weaker then the two-nucleon force is explained automatically.

In spite of the great progress and success of the past 15 years, there are still some unresolved issues. One problem is the proper renormalization of the chiral two- and many-nucleon potentials, where systematic investigations are already under way (cf. Sec. 4).

The other unfinished business is the few-nucleon forces beyond NNLO ("subleading few-nucleon forces") which are needed to hopefully resolve some important outstanding nuclear structure problems. At orders N^3LO and N^4LO very many new 3NF structures appear, some of which have already been tested. However, in view of the multitude of 3NF topologies it will take a while until we will have a proper overview of impact and convergence of these contributions.

If the open issues discussed in this paper will be resolved within the next few years, then, after 70 years of desperate struggle, we may finally claim that the nuclear force problem is essentially under control. The greatest beneficiaries of such progress will be the *ab initio* nuclear structure physicists, including *James Vary*. May this be a birthday present for him.

This work was supported in part by the U.S. Department of Energy under Grant No. DE-FG02-03ER41270.

References

[1] H. Yukawa, Proc. Phys. Math. Soc. Japan **17**, 48 (1935).

[2] R. A. Bryan and B. L. Scott, Phys. Rev. **135**, B434 (1964); **177**, 1435 (1969).

[3] K. Holinde and R. Machleidt, Nucl. Phys. A **247**, 495 (1975); *ibid.* **256**, 479 (1976); *ibid.* **256**, 497 (1976).

[4] For a thorough and pedagogical introduction into the meson theory of nuclear forces, see: R. Machleidt, Adv. Nucl. Phys. **19**, 189 (1989).

[5] R. Machleidt, Phys. Rev. C **63**, 024001 (2001).

[6] A. Deltuva, R. Machleidt and P. U. Sauer, Phys. Rev. C **68**, 024005 (2003).

[7] M. Lacombe, B. Loiseau, J. M. Richard, R. Vinh Mau, J. Côté, P. Pires and R. de Tourreil, Phys. Rev. C **21**, 861 (1980).

[8] R. Machleidt, K. Holinde and Ch. Elster, Phys. Rept. **149**, 1 (1987).

[9] S. Weinberg, Physica A **96**, 327 (1979).

[10] S. Weinberg, Nucl. Phys. B **363**, 3 (1991).

[11] S. Weinberg, Phys. Lett. B **295**, 114 (1992).

[12] E. Epelbaum, H.-W. Hammer and U.-G. Meißner, Rev. Mod. Phys. **81**, 1773 (2009).

[13] A comprehensive and accessible presentation of the chiral effective field theory approach to nuclear forces can be found in: R. Machleidt and D. R. Entem, Phys. Rept. **503**, 1 (2011).

[14] A. M. Shirokov, V. A. Kulikov, P. Maris, A. I. Mazur, E. A. Mazur and J. P. Vary, EPJ Web Conf. **3**, 05015 (2010).

[15] S. R. Beane *et al.*, Phys. Rev. Lett. **97**, 012001 (2006).

[16] T. Hatsuda, J. Phys. Conf. Ser. **381**, 012020 (2012).

[17] U. van Kolck, Phys. Rev. C **49**, 2932 (1994).

[18] E. Epelbaum, A. Nogga, W. Glöckle, H. Kamada, U.-G. Meißner and H. Witala, Phys. Rev. C **66**, 064001 (2002).

[19] N. Kaiser, Phys. Rev. C **61**, 014003 (2000).

[20] N. Kaiser, Phys. Rev. C **62**, 024001 (2000).

[21] E. Epelbaum, W. Glöckle and U.-G. Meißner, Eur. Phys. J. A **19**, 401 (2004).

[22] D. R. Entem and R. Machleidt, Phys. Rev. C **68**, 041001 (2003).

[23] V. G. J. Stoks, R. A. M. Klomp, M. C. M. Rentmeester and J. J. de Swart, Phys. Rev. C **48**, 792 (1993).

[24] R. A. Arndt, I. I. Strakovsky and R. L. Workman, SAID, Scattering Analysis Interactive Dial-in computer facility, George Washington University (formerly Virginia Polytechnic Institute), solution SM99 (Summer 1999); for more information see, e. g., R. A. Arndt, I. I. Strakovsky and R. L. Workman, Phys. Rev. C **50**, 2731 (1994).

[25] The 1999 NN data base is defined in Ref. [5].

[26] R. B. Wiringa, V. G. J. Stoks and R. Schiavilla, Phys. Rev. C **51**, 38 (1995).

[27] A. Deltuva and A. C. Fonseca, Phys. Rev. Lett. **98**, 162502 (2007); Phys. Rev. C **76**, 021001 (2007); arXiv:1005.1308 [nucl-th] (2010).

[28] L. Coraggio, A. Covello, A. Gargano, N. Itaco, T. T. S. Kuo, D. R. Entem and R. Machleidt, Phys. Rev. C **66**, 021303 (2002).

[29] L. Coraggio, A. Covello, A. Gargano, N. Itaco, T. T. S. Kuo and R. Machleidt, Phys. Rev. C **71**, 014307 (2005).

[30] L. Coraggio, A. Covello, A. Gargano and N. Itaco, Phys. Rev. C **81**, 064303 (2010).

[31] P. Navrátil and E. Caurier, Phys. Rev. C **69**, 014311 (2004).

[32] G. Hagen, T. Papenbrock, D. J. Dean and M. Hjorth-Jensen, Phys. Rev. Lett. **101**, 092502 (2008).

[33] S. Fujii, R. Okamoto and K. Suzuki, Phys. Rev. Lett. **103**, 182501 (2009).

[34] H. Witala, J. Golak, R. Skibinski, W. Glöckle, A. Nogga, E. Epelbaum, H. Kamada, A. Kievsky and M. Viviani, Phys. Rev. C **73**, 044004 (2006).

[35] N. Kalantar-Nayestanaki, E. Epelbaum, E. Messchendorp and A. Nogga, Rep. Progr. Phys. **75**, 016301 (2012).

[36] A. Kievsky, M. Viviani, L. Girlanda and L. E. Marcucci, Phys. Rev. C **81**, 044003 (2010).

[37] M. Viviani, L. Giarlanda, A. Kievsky, L. E. Marcucci and S. Rosati, arXiv:1004.1306 [nucl-th] (2010).

[38] A. Nogga, P. Navratil, B. R. Barrett and J. P. Vary, Phys. Rev. C **73**, 064002 (2006).

[39] P. Navratil, V. G. Gueorguiev, J. P. Vary, W. E. Ormand and A. Nogga, Phys. Rev. Lett. **99**, 042501 (2007).

[40] T. Otsuka, T. Susuki, J. D. Holt, A. Schwenk and Y. Akaishi, Phys. Rev. Lett. **105**, 03250 (2010).

[41] J. W. Holt, N. Kaiser and W. Weise, Phys. Rev. C **79**, 054331 (2009).

[42] R. Roth, S. Binder, K. Vobig, A. Calci, J. Langhammer and P. Navrátil, Phys. Rev. Lett. **109**, 052501 (2012).

[43] H. Hergert, S. K. Bogner, S. Binder, A. Calci, J. Langhammer, R. Roth and A. Schwenk, Phys. Rev. C **87**, 034307 (2013).

[44] G. Hagen, M. Hjorth-Jensen, G. R. Jansen, R. Machleidt and T. Papenbrock, Phys. Rev. Lett. **108**, 242501 (2012).

[45] G. Hagen, M. Hjorth-Jensen, G. R. Jansen, R. Machleidt and T. Papenbrock, Phys. Rev. Lett. **109**, 032502 (2012).

[46] A. Ekström *et al.*, Phys. Rev. Lett. **110**, 192502 (2013).

[47] K. Hebeler and A. Schwenk, Phys. Rev. C **82**, 014314 (2010).

[48] K. Hebeler, S.K. Bogner, R. J. Furnstahl, A. Nogga and A. Schwenk, Phys. Rev. C **83**, 031301(R) (2011).

[49] F. Sammarruca, B. Chen, L. Coraggio, N. Itaco and R. Machleidt, Phys. Rev. C **86**, 054317 (2013).

[50] L. Coraggio, J. W. Holt, N. Itaco, R. Machleidt and F. Sammarruca, Phys. Rev. C **87**, 014322 (2013).

[51] S. Weinberg, *Effective Field Theory, Past and Future*, arXiv:0908.1964 [hep-th] (2009).

[52] D. B. Kaplan, M. J. Savage and M. B. Wise, Nucl. Phys. B **478**, 629 (1996).

[53] A. Nogga, R. G. E. Timmermans and U. van Kolck, Phys. Rev. C **72**, 054006 (2005).

[54] C.-J. Yang, Ch. Elster and D. R. Phillips, Phys. Rev. C **80**, 044002 (2009).

[55] M. Pavón Valderrama and E. Ruiz Arriola, Phys. Rev. C **74**, 064004 (2006).

[56] D. R. Entem, E. Ruiz Arriola, M. Pavón Valderrama and R. Machleidt, Phys. Rev. C **77**, 044006 (2008).

[57] Ch. Zeoli, R. Machleidt and D. R. Entem, Few-Body Syst. DOI 10.1007/s00601-012-0481-4 (2012); arXiv:1208.2657 [nucl-th] (2012).

[58] E. Epelbaum and J. Gegelia, Eur. Phys. J. A **41**, 341 (2009).

[59] E. Epelbaum and J. Gegelia, Phys. Lett. B **716**, 338 (2012).

[60] B. Long and U. van Kolck, Ann. Phys. (NY) **323**, 1304 (2008).

[61] M. P. Valderrama, Phys. Rev. C **84**, 064002 (2011).

[62] R. Machleidt, P. Liu, D. R. Entem and E. R. Arriola, Phys. Rev. C **81**, 024001 (2010).

[63] G. P. Lepage, *How to Renormalize the Schrödinger Equation*, arXiv:nucl-th/9706029 (1997).

[64] E. Epelbaum, Eur. Phys. J. A **34**, 197 (2007).

[65] D. Rozpedzik *et al.*, Acta Phys. Polon. B **37**, 2889 (2006).

[66] S. Ishikawa and M. R. Robilotta, Phys. Rev. C **76**, 014006 (2007).

[67] V. Bernard, E. Epelbaum, H. Krebs and U.-G. Meißner, Phys. Rev. C **77**, 064004 (2008).

[68] V. Bernard, E. Epelbaum, H. Krebs and U.-G. Meißner, Phys. Rev. C **84**, 054001 (2011).

[69] R. Skibinski *et al.*, Phys. Rev. C **84**, 054005 (2011).

[70] H. Witała, *private communication.*

[71] I. Tews, T. Krüger, K. Hebeler and A. Schwenk, Phys. Rev. Lett. **110**, 032504 (2013).

[72] H. Krebs, A. Gasparyan and E. Epelbaum, Phys. Rev. C **85**, 054006 (2012).

[73] H. Krebs, A. Gasparyan and E. Epelbaum, Phys. Rev. C **87**, 054007 (2013).

[74] L. Girlanda, A. Kievsky and M. Viviani, Phys. Rev. C **84**, 014001 (2011).

Computational Challenges in the Relativistic Few-Nucleon Problem

Wayne Polyzou

The University of Iowa, Department of Physics and Astronomy, Iowa City, IA

Abstract

I discuss computational challenges in the relativistic few-nucleon problem and the resolution of some of these challenges. I also discuss the outlook for the future.

Keywords: *Relativistic quantum mechanics, few-nucleon problems, Faddeev equations*

1 Introduction

Studying nuclear physics at distance scales that are potentially sensitive to sub-nucleon physics requires a relativistic treatment of the dynamics. This scale is interesting because QCD is non-perturbative at this scale; of particular concern is that it is not yet known how to compute mathematical error bounds, even for non-perturbative methods, making the accuracy of calculations based directly on QCD difficult to assess. This is also the scale where transition from meson-nucleon to sub-nucleon degrees of freedom is poorly understood.

Relativistic quantum mechanics provides a means for studying few-body problems at this scale. It provides a quantum mechanical description of the dynamics of the relevant degrees of freedom consistent with the exact Poincaré symmetry of underlying theory. Because few-body models can be solved exactly, comparison of these computations to experiment provides the direct feedback needed to construct realistic models based on a given set of degrees of freedom.

Normally the relevant degrees of freedom are the experimental degrees of freedom which are the particle spins and momenta that are observed in reactions at this scale. A suitable model Hilbert space is the direct sum of tensor products of the single-nucleon spaces,

$$\mathcal{H} = \oplus(\otimes\mathcal{H}_{m_i\, j_i}), \tag{1}$$

which are irreducible representation spaces for the Poincaré group.

Any relativistic model formulated on this space is necessarily characterized by a unitary representation of the Poincaré group [1]

$$U(\Lambda, a) : \mathcal{H} \to \mathcal{H}. \tag{2}$$

The dynamical unitary representation $U(\Lambda, a)$ of the Poincaré group necessarily differs from the natural free-particle representation, $U_0(\Lambda, a)$, given by the direct sum of tensor products free-particle irreducible representations on $\mathcal{H}$.

The ability to perform local tests of special relativity requires that the unitary representations of the Poincaré group corresponding to different subsystems be related

Proceedings of International Conference 'Nuclear Theory in the Supercomputing Era — 2013' (NTSE-2013), Ames, IA, USA, May 13–17, 2013. Eds. A. M. Shirokov and A. I. Mazur. Pacific National University, Khabarovsk, Russia, 2014, p. 352.

http://www.ntse-2013.khb.ru/Proc/Polyzou.pdf.

to $U(\Lambda, a)$ by cluster properties

$$\lim_{|r_{ij}-r_k|\to\infty} \|\big(U(\Lambda,a) - U_{ij}(\Lambda,a)\otimes U_k(\Lambda,a)\big)|\psi\rangle\| = 0. \tag{3}$$

The problem of relativistic few-body physics is to construct mathematical models $U(\Lambda, a)$ with the above properties that provide a realistic quantitative and consistent description of few-GeV scale structure and reactions for few-hadron systems. This problem is a natural extension of the corresponding non-relativistic problem; but the relativistic treatment leads to a number of computational issues that do not arise in the non-relativistic formulation of the same problem.

In the non-relativistic case it is useful to work in a frame where the total momentum $\mathbf{P}$ is zero. In that frame the Hamiltonian is replaced by the center of mass Hamiltonian, $h = H - \mathbf{P}^2/2M$, where M is the Galilean mass of the system. In the relativistic case the corresponding operator is the invariant mass operator, which is the rest energy of the system. We denote the mass operator by M.

The first complication in formulation of a relativistic few-body dynamics arises because the Hamiltonian appears on the *right-hand side* of three different commutators. As a consequence, the Poincaré commutation relations require that at least three of the Poincaré generators have an interaction dependence. The commutation relations impose a set of non-linear constraints on these interactions. One way to satisfy these constraints is to notice that all ten generators can be expressed in terms of the two Casimir operators (mass and spin), four commuting functions of the generators, and four functions of the generators that are conjugate to the four commuting functions of the generators. If interactions are added to the non-interacting mass operator, keeping these other nine operators free of interactions, and the ten generators are expressed as functions of these nine operators and the interacting invariant mass, the resulting generators will satisfy the Poincaré commutation relations provided the interaction terms commute with these nine-non-interacting operators. This is the assumption that defines the Bakamjian–Thomas [2] method. These nine commutators with the relativistic interaction are the relativistic equivalent of the nine constraints on the non-relativistic interactions that result from the requirements that the interactions be translationally invariant, rotationally invariant, and independent of the total momentum.

Solving for the mass eigenvalue problem in a suitable irreducible free-particle basis leads to an explicit dynamical unitary representation of the Poincaré group, $\bar{U}_{ij}(\Lambda, a)$, on the two particle Hilbert space.

If this method is applied to the three-nucleon system, the resulting three-nucleon mass operator [3] has the form

$$\bar{M} := \bar{M}_{12,3} + \bar{M}_{23,1} + \bar{M}_{31,2} - 2M_0, \tag{4}$$

$$\bar{M}_{ij,k} = M_0 + \bar{V}_{ij}, \tag{5}$$

$$M_0 = \sqrt{\mathbf{q}_k^2 + \Big(\sqrt{\mathbf{k}_{ij}^2 + m_i^2} + \sqrt{\mathbf{k}_{ij}^2 + m_j^2}\Big)^2} + \sqrt{\mathbf{q}_k^2 + m_k^2}\,, \tag{6}$$

where the relativistic Jacobi momenta

$$\mathbf{q}_i := \mathbf{\Lambda}(P/M_0)^{-1} p_i, \qquad \mathbf{k}_{ij} := \mathbf{\Lambda}\Big(\frac{q_i + q_j}{m_{0ij}}\Big)^{-1} q_i \tag{7}$$

are obtained by Lorentz transforming single-particle momenta to the two and three-body rest frames with non-interacting Lorentz transformations. We call these variables relativistic Jacobi momenta because the usual Jacobi momenta can be constructed in the same manner by replacing the Lorentz boost by a Galilean boost.

Because all three of the interactions commute with the same nine functions of the three-nucleon Poincaré generators, the interactions can be combined algebraically in

the three-nucleon mass operator and the result will commute with these same nine operators. Poincaré generators can then be expressed in terms of the interacting mass operator and the nine-other three-body kinematic operators. Again, diagonalizing $\bar{M}$ in a suitable irreducible free-particle basis gives a dynamical unitary representation of the Poincaré group, $\bar{U}(\Lambda, a)$, for a system of three interacting particles.

The commutator of the interaction with the free spin operator, $\mathbf{j}_0^2$,

$$[\bar{V}_{ij}, \mathbf{j}_0^2] = 0, \tag{8}$$

is incompatible with cluster properties of the three-body Poincaré generators. The problem is that the *relative orbital* angular momentum, which contributes to the total spin, gets modified as a consequence of the interactions. Here the failure means that

$$\bar{U}(\Lambda, a) \to \bar{U}_{ij,k}(\Lambda, a) \neq \bar{U}_{ij} \otimes U_k(\Lambda, a), \tag{9}$$

where $\bar{U}_{ij,k}(\Lambda, a)$ is obtained from $\bar{U}(\Lambda, a)$ by turning off the interactions involving particle k. The way that cluster properties fail at the operator level is that interactions that should survive in the cluster limit actually vanish.

While cluster properties of $\bar{U}(\Lambda, a)$ in the sense the equation (3) do not hold, it turns our that the S matrices associated with the $2+1$ representations of $\bar{U}_{ij,k}(\Lambda, a)$ and $\bar{U}_{ij} \otimes U_k(\Lambda, a)$ are identical.

The equivalence of the 2+1 S matrices to the corresponding S matrices for the tensor product dynamics

$$\bar{S}_{ij,k} = \bar{S}_{ij} \otimes I_k \tag{10}$$

implies the existence [4] of an S-matrix preserving unitary transformation, $A_{ij,k}$, satisfying

$$A_{ij,k}\, \bar{U}_{ij,k}(\Lambda, a)\, A_{ij,k}^\dagger = \bar{U}_{ij} \otimes U_k(\Lambda, a), \tag{11}$$

$$A_{ij,k}\, \bar{M}_{ij,k}\, A_{ij,k}^\dagger = M_{ij\otimes k}, \tag{12}$$

$$A_{ij,k}\, \mathbf{j}_0^2\, A_{ij,k}^\dagger = \mathbf{j}_{ij\otimes k}^2 \neq \mathbf{j}_0^2. \tag{13}$$

Using these unitary operators for each pair of interacting particles we construct their Cayely transforms, add the Cayley transforms, and inverse Cayley transform the sum of the individual Cayley transforms to get a new unitary operator A [5]:

$$C_{ij,k} := i(A_{ij,k} - I)(A_{ij,k} + I)^{-1}, \tag{14}$$

$$C := C_{12,3} + C_{23,1} + C_{31,2}, \tag{15}$$

$$A := (I - iC)(I + iC)^{-1}, \qquad A \to A_{ij,k} \to I. \tag{16}$$

The resulting transformation A is an S-matrix preserving unitary transformation. Using it to transform $\bar{U}(\Lambda, a)$ gives a new unitary representation [6] of the Poincaré group

$$U(\Lambda, a) := A^\dagger \bar{U}(\Lambda, a) A$$

satisfying cluster properties (3) of the unitary representation of the Poincaré group

$$U(\Lambda, a) \to \bar{U}_{ij}(\Lambda, a) \otimes U_k(\Lambda, a). \tag{17}$$

The Poincaré generators for this representation include sums of the different pairwise interactions. The operators A and $A_{ij,k}$ also generate additional three-nucleon forces that are needed to satisfy the commutation relations. These three-nucleon forces are different from standard three-nucleon forces because they are frame-dependent *and* are explicit functions of the underlying two-nucleon forces.

The resulting invariant mass operator has the form

$$M = A\Big(\sum A_{ij,k}^\dagger M_{ij\otimes k} A_{ij,k} - 2M_0\Big) A^\dagger = A\bar{M}A^\dagger. \tag{18}$$

The important property is that because A is S-matrix preserving it means that $\bar{M}$ leads to the same S matrix as M, so even though the representation $\bar{U}(\Lambda, a)$ fails to satisfy (3), it has the same S matrix as the model satisfying cluster properties. This means that for scattering and bound state calculations, *it is sufficient to solve the Faddeev equations for* $\bar{M}$.

This avoids that complications of computing the additional three-nucleon interaction that appears in M in the three-body case, however it is important to remark that this equivalence does not extend to the four-nucleon case unless the corresponding generated three-body interactions appear in the four-body mass operator. We also remark that two-body interactions $\bar{V}_\gamma$ are really three-body operators due to the role of the spectator momentum — one can think of them as frame-dependent two-body interactions.

The next set of complications is more technical. In order to formulate relativistic Faddeev equations for the dynamics given by the mass operator $\bar{M}$ we define the operators

$$\bar{M} = M_0 + \bar{V}, \qquad \bar{V} = \sum_\alpha \bar{V}_\alpha, \qquad \alpha \in \{(12,3),(23,1),(31,2)\}, \tag{19}$$

$$\bar{V}_\alpha = \bar{M}_\alpha - M_0, \qquad \bar{V}^\alpha = \bar{M} - \bar{M}_\alpha. \tag{20}$$

Using time-dependent methods [7] it is possible to show that the S matrix can be expressed in terms of the following relativistic transition operator:

$$\bar{T}^{\alpha\beta}(m) := \bar{V}^\beta + \bar{V}^\alpha (m - \bar{M} + i0^+)^{-1} \bar{V}^\beta, \tag{21}$$

$$\langle a_0 | S^{\alpha\beta} | b_0 \rangle = \langle a_0 | b_0 \rangle - 2\pi i \langle a_0 | \delta(m_a - m_b) \bar{T}^{\alpha\beta}(m_a + i0^+) | b_0 \rangle. \tag{22}$$

The different components of $\bar{T}^{\alpha\beta}(m)$ satisfy the relativistic Faddeev equation

$$\bar{T}^{\alpha\beta}(z) = \bar{V}^\beta + \sum_{\gamma \neq \alpha} \bar{T}_\gamma (z - M_0)^{-1} \bar{T}^{\gamma\beta}(z). \tag{23}$$

The input to (23) equation is the $2+1$ transition operators

$$\bar{T}_\gamma(z) = \bar{V}_\gamma + \bar{V}_\gamma (z - M_0)^{-1} \bar{T}_\gamma(z). \tag{24}$$

As in the non-relativistic case the Faddeev equation can be solved with mathematically controlled errors because the iterated kernel is compact and can be uniformly approximated by a finite dimensional matrix:

$$\bar{T}(z) = \bar{D}(z) + \bar{K}(z)\bar{T}(z), \qquad \bar{K}(z)^2 \ \ \textbf{compact}, \tag{25}$$

$$\bar{T}(z) = (I - \bar{K}(z)^2)^{-1} (\bar{D}(z) + \bar{K}(z)\bar{T}(z)). \tag{26}$$

The first technical problem is to construct realistic two-nucleon interactions. Repeating what was done for the non-relativistic problem, by carefully fitting models to two-nucleon phase shifts, can also be done in the relativistic case, but because both the relativistic and non-relativistic interactions are fit to the same data, refitting is not necessary. The trick was first given by Coester, Pieper and Serduke [8].

The mass operator in the Bakamjian–Thomas representation has the form

$$\bar{M} := M_0 + \bar{V}_{12} + \bar{V}_{23} + \bar{V}_{31}, \tag{27}$$

where

$$\bar{V}_{ij} := \sqrt{\mathbf{q}_k^2 + \left(\sqrt{\mathbf{k}_{ij}^2 + m_i^2 + 2\mu_{ij} v_{nr\,ij}} + \sqrt{\mathbf{k}_{ij}^2 + m_j^2 + \mu_{ij} v_{nr\,ij}}\right)^2} - \sqrt{\mathbf{q}_k^2 + \left(\sqrt{\mathbf{k}_{ij}^2 + m_i^2} + \sqrt{\mathbf{k}_{ij}^2 + m_j^2}\right)^2},$$

$$\bar{M}_{ij,k} = M_{ij,k}(h_{nr\,ij}), \tag{28}$$

and μ_{ij} is the two-nucleon reduced mass. The important property of this interaction is that the corresponding $2+1$ mass operator is a function of the non-relativistic nucleon-nucleon rest Hamiltonian, $h_{ij} = H_{ij} - \frac{(\mathbf{p}_i+\mathbf{p}_j)^2}{2(m_i+m_j)}$. This means that the S matrix in both the relativistic and non-relativistic models have the same internal wave functions and phase shifts as a function of the center of mass momentum $\mathbf{k}$:

$$\langle \mathbf{p}, \mathbf{q}_r, \mathbf{k}_r | S_{ij,k\,r} | \mathbf{p}', \mathbf{q}'_r, \mathbf{k}'_r \rangle = \delta(\mathbf{p}-\mathbf{p}')\delta(\mathbf{q}_r - \mathbf{q}'_r)\langle \mathbf{k}_r | s_{ij} | \mathbf{k}'_r \rangle, \tag{29}$$

$$\langle \mathbf{p}, \mathbf{q}_{nr}, \mathbf{k}_{nr} | S_{ij,k\,nr} | \mathbf{p}', \mathbf{q}'_{nr}, \mathbf{k}'_{nr} \rangle = \delta(\mathbf{p}-\mathbf{p}')\delta(\mathbf{q}_{nr} - \mathbf{q}'_{nr})\langle \mathbf{k}_{nr} | s_{ij} | \mathbf{k}'_{nr} \rangle. \tag{30}$$

In order to take advantage of this relationship we recall that the two-body input to the relativistic Faddeev equation can be expressed in the following ways:

$$\langle \mathbf{p}, \mathbf{q}_r, \mathbf{k}_r | \bar{T}_\alpha | \mathbf{p}', \mathbf{q}'_r, \mathbf{k}'_r \rangle = \langle \mathbf{p}, \mathbf{q}_r, \mathbf{k}_r | \bar{V}_\alpha | \mathbf{p}', \mathbf{q}'_r, \mathbf{k}'^-_r \rangle = \langle \mathbf{p}, \mathbf{q}_r, \mathbf{k}_r | (\bar{M}_\alpha - M_0) | \mathbf{p}', \mathbf{q}'_r, \mathbf{k}'^-_r \rangle. \tag{31}$$

Since for the above choice of interaction the internal relativistic and non-relativistic wave functions are identical we get the identifications

$$\langle \mathbf{k} | \mathbf{k}'^-_{nr} \rangle = \langle \mathbf{k} | \mathbf{k}'^-_r \rangle. \tag{32}$$

Using this it follows that the Faddeev kernel can be written as

$$\begin{aligned} &\langle \mathbf{q}_\alpha, \mathbf{k}_\alpha | T_\alpha(z)(z-\bar{M}_0)^{-1} | \mathbf{q}'_\alpha, \mathbf{k}'_\alpha \rangle \\ &\qquad = \delta(\mathbf{q}_\alpha - \mathbf{q}'_\alpha)\, \frac{m_{0\alpha}(\mathbf{k}) + m_{0\alpha}(\mathbf{k}')}{\sqrt{\mathbf{q}_\alpha^2 + m_{0\alpha}^2(\mathbf{k}_\alpha)} + \sqrt{\mathbf{q}_\alpha^2 + m_{0\alpha}^2(\mathbf{k}'_\alpha)}} \\ &\qquad\qquad \times \langle \mathbf{k}_\alpha | t_r(z) | \mathbf{k}'_\alpha \rangle \frac{1}{M_0(\mathbf{q}_\alpha, \mathbf{k}_\alpha) - M_0(\mathbf{q}_\alpha, \mathbf{k}'_\alpha) + i0^+}, \end{aligned} \tag{33}$$

where

$$m_{0\alpha}(\mathbf{k}_\alpha) := \sqrt{\mathbf{k}_\alpha^2 + m_i^2} + \sqrt{\mathbf{k}_\alpha^2 + m_j^2} \tag{34}$$

and

$$z = M_0(\mathbf{q}_\alpha \mathbf{k}_\alpha) + i0^+,$$

$$\begin{aligned} &\langle \mathbf{k}_\alpha | t_r(z) | \mathbf{k}'_\alpha \rangle \\ &= \left(\frac{2\mu}{\sqrt{\mathbf{k}_\alpha^2 + m_i^2} + \sqrt{\mathbf{k}_\alpha'^2 + m_j^2}} + \frac{2\mu}{\sqrt{\mathbf{k}_\alpha^2 + m_i^2} + \sqrt{\mathbf{k}_\alpha'^2 + m_j^2}} \right) \langle \mathbf{k}_\alpha | t_{nr}(\mathbf{k}_\alpha^2/2\mu + i0^+) | \mathbf{k}'_\alpha \rangle. \end{aligned} \tag{35}$$

These relations express the Faddeev kernel in terms of the *non-relativistic transition* matrix elements. The identity of the wave functions, which was used to derive the result, is limited to the case that the transition matrix elements are half-on shell. This relation does not extend to the off-shell transition matrix elements which appear in the Faddeev kernel.

The fully off-shell two-body $\bar{T}_\alpha(z)$ embedded in the three-nucleon Hilbert space can be computed by solving the first resolvent equation [9]:

$$\bar{T}_\alpha(z) = \bar{T}_\alpha(z') + \bar{T}_\alpha(z)\, \frac{z'-z}{(z-M_0)(z'-M_0)}\, \bar{T}_\alpha(z'). \tag{36}$$

Finally we note that while it is natural to use variables to label two-nucleon interactions to be associated with the two-nucleon rest frames, with theses variables the permutation operators involve Wigner rotations. The Wigner rotations can be

removed from the permutation operators by expressing everything in terms of variables associated with the three-nucleon rest frame. In this representation the Wigner rotations appear in the elementary nucleon-nucleon interactions:

$$\langle \mathbf{q}_i,\mu_i,\mathbf{q}_j,\mu_j|t_r(z)|\mathbf{q}'_i,\mu'_i,\mathbf{q}'_j,\mu'_j\rangle = \left(\frac{\omega_i(\mathbf{q}_i)+\omega_j(\mathbf{q}_j)}{\omega_i(\mathbf{k}_{ij})+\omega_j(\mathbf{k}_{ji})}\frac{\omega_i(\mathbf{k}_{ij})}{\omega_i(\mathbf{q}_i)}\frac{\omega_j(\mathbf{k}_{ji})}{\omega_j(\mathbf{q}_j)}\right)^{1/2}$$
$$\times\sum D^{j_i}_{\mu_i\nu_i}\big[R_{wc}(B_c(q_{ij}),k_{ij})\big]D^{j_j}_{\mu_j\nu_j}\big[R_{wc}(B_c(q_{ij}),k_{ji})\big]\langle \mathbf{k}_{ij},\nu_i,\nu_j|t_r(z)|\mathbf{k}'_{ij},\nu'_i,\nu'_j\rangle$$
$$\times D^{j_i}_{\nu'_i\mu'_i}\big[R_{wc}(B_c^{-1}(q_{ij}),q_i)\big]D^{j_j}_{\nu'_j\mu'_j}\big[R_{wc}(B_c^{-1}(q_{ij}),q_j)\big]$$
$$\times\left(\frac{\omega_i(\mathbf{q}'_i)+\omega_j(\mathbf{q}'_j)}{\omega_i(\mathbf{k}'_{ij})+\omega_j(\mathbf{k}'_{ji})}\frac{\omega_i(\mathbf{k}'_{ij})}{\omega_i(\mathbf{q}'_i)}\frac{\omega_j(\mathbf{k}'_{ji})}{\omega_j(\mathbf{q}'_j)}\right)^{1/2}. \quad (37)$$

The final technical challenge is that at the few-hundred MeV scale partial-wave projections begin to loose their underlying advantage. This is in part because the transition operator is a relatively smooth operator, so there is necessarily a lot of cancellations involved in the partial wave expansions, especially at large angles. As a practical matter double precision three-nucleon calculations based on partial wave methods are limited to about 300 MeV. Direct integration calculations are stable over a wider range of energies [9], extending to the few-GeV scale.

The final computational challenge is that the natural input to direct-interaction three-nucleon calculations is a momentum-space interaction in operator form. One of the few realistic interactions in operator form is the Argonne V18 interaction which is given in a configuration-space representation. It has been Fourier transformed [10] in an operator form. The resulting interaction can be expanded in terms of 24 spin-isospin operators.

It is possible to reduce the number of required operators using symmetry properties. The most general nucleon-nucleon interactions can be expanded in terms of the following spin operators:

$$\langle \mathbf{k}|v_{nr}|\mathbf{k}'\rangle = \sum V_n W_n, \quad (38)$$

$$W_1 := I, \quad (39)$$

$$W_2 := \mathbf{j}_1\cdot\mathbf{j}_2, \quad (40)$$

$$W_3 := (\mathbf{j}_1\cdot\hat{\mathbf{K}})\otimes(\mathbf{j}_2\cdot\hat{\mathbf{K}}), \quad (41)$$

$$W_4 := (\mathbf{j}_1\cdot\hat{\mathbf{Q}})\otimes(\mathbf{j}_2\cdot\hat{\mathbf{Q}}), \quad (42)$$

$$W_5 := (\mathbf{j}_1\cdot\hat{\mathbf{N}})\otimes I_2 + I_1\otimes(\mathbf{j}_2\cdot\hat{\mathbf{N}}), \quad (43)$$

$$W_6 := (\mathbf{j}_1\cdot\hat{\mathbf{K}})\otimes(\mathbf{j}_2\cdot\hat{\mathbf{Q}}) + (\mathbf{j}_1\cdot\hat{\mathbf{Q}})\otimes(\mathbf{j}_2\cdot\hat{\mathbf{K}}), \quad (44)$$

where

$$\mathbf{K} := \mathbf{k}'-\mathbf{k}, \qquad \mathbf{Q} := \mathbf{k}'+\mathbf{k}, \qquad \mathbf{N} := \mathbf{k}'\times\mathbf{k}. \quad (45)$$

The coefficients of these operator expansions are simply related to the Wolfenstein parameters [11], which facilitates the computation of spin observables. The remaining computational difficulty is related to the observation that there are five independent operators on shell, and one more off shell.

Numerical instabilities can arise when the independent on-shell and off-shell operators are not simply related [12]. For the choice above five of the off-shell operators become the five on-shell operators in the on-shell limit.

The last dynamical consideration is the computation of current matrix elements, which are needed to study few-nucleon systems with few-GeV scale hadronic probes.

The important observation is that any change of representation of the Poincaré generators requires a corresponding change of representation of the current operator in order to leave the physical observables unchanged. In principle one expects both the strong dynamics and electromagnetic current to satisfy cluster properties. This suggests that currents that have well-behaved cluster expansions should not be used in Bakamjian–Thomas representation of the dynamics. In general one expects that one must first transform either the current operator or the dynamics with an operator like (16):

$$\langle\Psi_f|J^\mu(0)|\Psi_i\rangle = \langle\bar{\Psi}_f|A^\dagger J^\mu(0)A|\bar{\Psi}_i\rangle \approx \langle\bar{\Psi}_f|J^\mu(0)|\bar{\Psi}_i\rangle. \tag{46}$$

When A is close to the identity, which appears to be the case for nuclear physics scales [7], this operator can be ignored, resulting in a significant increase in computational efficiency.

As a result of these various simplifications and tricks it has been possible to perform three-nucleon calculations with realistic interactions [13]. Figure 1 show the differential cross section for p-d elastic scattering for relativistic and non-relativistic three-nucleon models with realistic two- (CD Bonn) and three-nucleon (TM99) interactions. The calculations show that for elastic scattering the relativistic effects are small, except at back angles, where there is some enhancement due to relativity for the 250 MeV curves. Comparison of these calculations with measurements from [14] shows that there is missing physics that is not explained by the combination of the TM99 three-nucleon force and relativity. Elastic spin observables also show a weak dependence on relativistic effects. The comparison that we show is only sensitive to the difference in how the two-nucleon subsystem is embedded in the three nucleon system. Breakup calculations, on the other hand, exhibit strong relativistic effects in certain observables. The calculations in Fig. 2 [15] provide a beautiful illustration of some of these effects. These calculations were at a much higher energy than the calculations of Fig. 1 however they use the spin-independent Malfliet–Tjon interaction. Figure 2

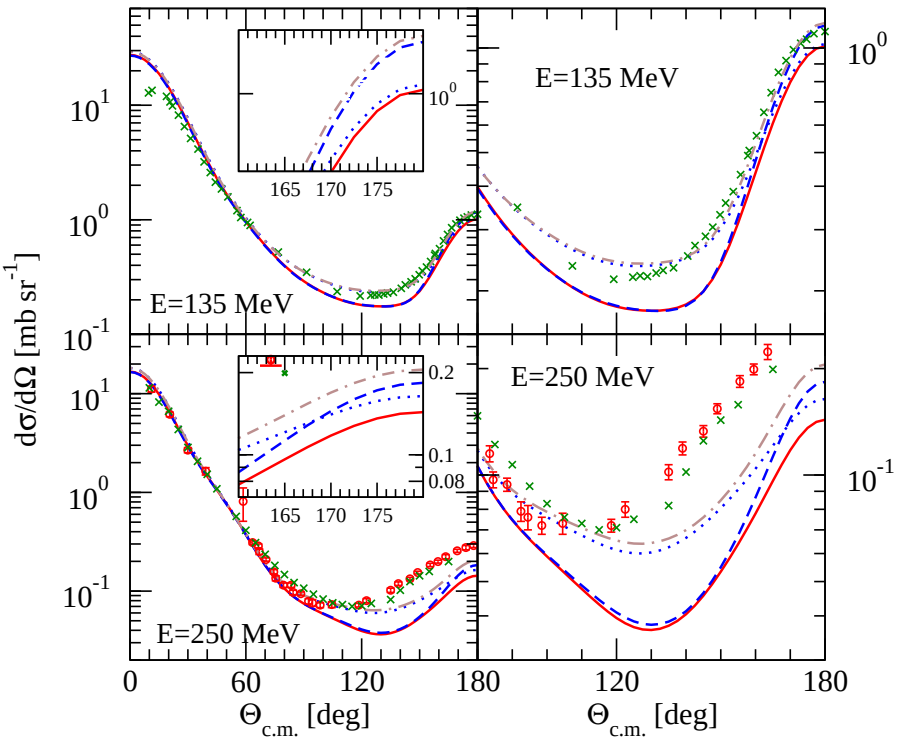

Figure 1: Relativistic effects in elastic p-d scattering.

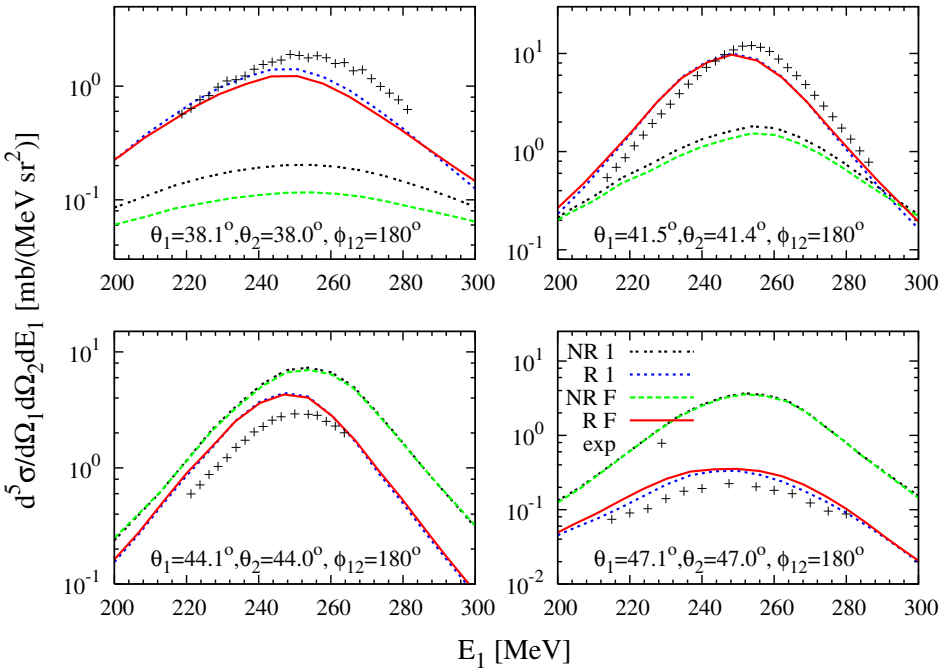

Figure 2: Relativistic effects in n-d breakup reactions.

shows the fivefold differential cross section where the scattered protons emerge symmetric at different angles relative to the beam line. These are plotted against the energy of one of the scattered protons. This figure shows a dramatic crossing of the non-relativistic and relativistic results as the angle is changed. The data is from [16].

In this manuscript we have discussed many of the complications involved in making realistic relativistic three-nucleon calculations. We have discussed tricks that make realistic calculations possible at relativistic energies. The calculations suggest that the relativistic effects are small for nucleon-meson degrees of freedom, except in certain areas of breakup phase space, however realistic relativistic calculations have not been performed at the few-GeV scale. The discrepancy of the calculated large-angle elastic scattering cross section with data suggests some missing short distance physics in the three-nucleon forces.

We anticipate that relativistic few-body methods will be an important tool for understanding physics at scales between the chiral perturbation theory and perturbative QCD scales. Modern computers have made realistic few-GeV scale few-body calculations feasible. The approach that we advocate, using models with the dominant degrees of freedom and symmetries is similar to the approach used in condensed mater physics. It is far easier than attempting to get mathematical convergent approximations of QCD at the few GeV scale.

This research supported by the U.S. Department of Energy Office of Science.

References

[1] E. P. Wigner, Ann. Math, **40**, 149 (1939).

[2] B. Bakamjian and L. H. Thomas, Phys. Rev. **92**, 1300 (1953).

[3] F. Coester, Helv. Phys. Acta **38**, 7 (1965).

[4] H. Ekstein, Phys. Rev. **117**, 1590 (1960).

[5] F. Coester and W. N. Polyzou, Phys. Rev. D **26**,1348(1982).

[6] S. N. Sokolov, Dokl. Akad. Nauk SSSR **233**, 575 (1977).

[7] B. Keister and W. N. Polyzou, Phys. Rev. C **86**, 014002 (2012).

[8] F. Coester, S. C. Pieper and F. J. D. Serduke, Phys. Rev. C **11**, 1 (1975).

[9] T. Lin, Ch. Elster, W. N. Polyzou, H. Witała and W. Glöckle, Phys. Rev. C **78**, 024002 (2008).

[10] S. Veerasamy and W. N. Polyzou, Phys. Rev. C **84**, 034003 (2011).

[11] W. Glöckle, *The quantum mechanical few-body problem.* Springer-Verlag, Berlin, 1983.

[12] S. Veerasamy, Ch. Elster and W. N. Polyzou, Few-Body Syst. DOI: 10.1007/s00601-012-0476-1 (2012).

[13] H. Witała, J. Golak, R. Skibínski, W. Glöckle, H. Kamada and W.N. Polyzou, Phys. Rev. C **83**, 044001 (2011).

[14] K. Sekiguchi *et al.*, Phys. Rev. C **65**, 034003 (2002).

[15] T. Lin, Ch. Elster, W. N. Polyzou and W. Glöckle, Phys. Lett. B **660**, 345 (2008).

[16] V. Punjabi *et al.*, Phys. Rev. C **38**, 2728 (1988).

Three-Nucleon Forces Revisited — Some Historical Thoughts

Peter U. Sauer

Institute for Theoretical Physics, Leibniz University, D-30167 Hannover, Germany

Abstract

Historic steps in the emergence, the derivation and the use of three-nucleon forces, genuine and effective, for calculations of few-nucleon systems and of the structure of heavier nuclei are recalled. The research focus is on few-nucleon systems. The need of three-nucleon forces for a successful description of some data and the remaining puzzles of other data, not explainable despite the inclusion of three-nucleon forces, are discussed.

Keywords: *Nuclear forces; shell model; few-nucleon systems*

1 Introduction

The shell-model theme of this conference is not my current research territory. I would not have attended, would the conference not also celebrate James Vary with whom I shared early stages of my carrier. I decided against a standard talk on actual research. Instead, I want first to reflect on what drove our research then, before coming to the *Here and Now*, which is the nuclear shell model for James and few-nucleon systems for me.

I got to know James in 1970/71, when we were both postdocs in the nuclear theory group of MIT. We started to collaborate on the challenge of that time, the derivation of nuclear properties from the interaction between free nucleons. And that challenge is still with us today, as this conference proves.

2 My personal view on the nuclear shell model, then and now

Doing microscopic nuclear structure in 1970/71, i. e., calculating the properties of nuclear matter, of doubly closed-shell nuclei and of simple shell-model systems in terms of a realistic two-nucleon ($2N$) interaction, was a courageous enterprise: The suggested $2N$ potentials were scary beasts, their short-ranged core was conceptually unknown and, furthermore, it was parametrized in form of a strong repulsion which had to be smoothened into the in-medium reaction matrix of Brueckner theory [1].

At that time, James's and my common nuclear-structure playground was the shell-model of ^{18}O, described by an inert ^{16}O core with two active neutrons outside the core. The latter nucleons formed the active Hilbert space, the model space, consisting of $2s$-$1d$ states only, the corresponding effective interaction being the $2N$ reaction matrix, modified by core-polarization, shown in Fig. 1(a); core polarization acts technically as an effective interaction between the two active nucleons, though, physically, it involves three nucleons. Kuo and Brown [2] had initiated this game and appeared to

Proceedings of International Conference 'Nuclear Theory in the Supercomputing Era — 2013' (NTSE-2013), Ames, IA, USA, May 13–17, 2013. Eds. A. M. Shirokov and A. I. Mazur. Pacific National University, Khabarovsk, Russia, 2014, p. 361.

http://www.ntse-2013.khb.ru/Proc/Sauer.pdf.

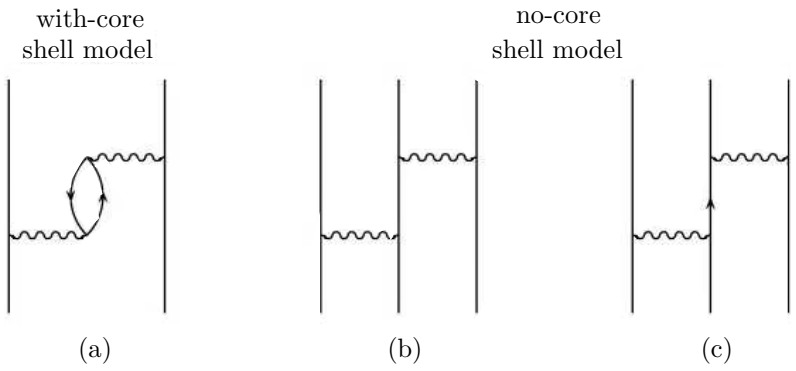

Figure 1: Strategies describing the contribution of core polarization to the effective shell-model interaction. Plot (a) represents the contribution in calculations with an inert core; plots (b) and (c) represent the same process when resolved in no-core calculations. The vertical lines without an arrow stand for nucleons in the model space, the horizontal wavy lines for the $2N$ Brueckner reaction matrix derived from the $2N$ potential. In plot (a), the backward arrow indicates a hole state in the inert core, the forward arrow is a particle state outside the core; plot (a) is an irreducible $2N$ contribution to the effective interaction, irrespectively, if the particle state is within or outside the model space. However, if the particle state is inside the model space of a no-core calculation, the process is reducible into two subsequent interactions within the model space, as plot (b) shows. In contrast, if the particle state is outside the model space as in plot (c), the process remains irreducible within the model space and is a part of an effective $3N$ contribution to the shell-model interaction.

have also closed the issue by their impressive achievement in describing data. But our revolutionary minds were challenged. We improved the calculation by better numerics [3] and found the numerical inadequacy of the effective interaction in use, therefore the distortion of our names Vary, Sauer and Wong in the author list by the community to *Very sorry, wrong!*; others [4, 5] challenged the whole shell-model strategy of that time on more fundamental grounds than we did. This was the dark moment of the early microscopic shell model.

Increasing computational capability of theoretical physics allowed a novel, more physical shell-model strategy, e. g., the description of ^{18}O without an inert ^{16}O core [6, 7]: Use a model space, numerically manageable and physically large enough for accommodating the considered physics phenomena realistically, accompanied by a corresponding effective interaction, which should stay as simple as possible. This fact is illustrated in Figs. 1(b) and 1(c) for the core-polarization contribution to the effective shell-model interaction in the no-core description. Of course, in the search for balance between model space and effective interaction the truncation of the full Hilbert space to the active model space generally remains necessary in shell-model calculations: The usually employed oscillator basis is advantageous for the symmetry and geometry of finite nuclei, but awkward when having to build up the tail behavior of single-particle states and when having to punch the correlation hole into the $2N$ wave function. Thus, the truncation of Hilbert space remains physically severe and makes effective many-body contributions to the interaction important. Even without *genuine* $3N$ forces, *effective* ones arise as from core polarization, shown in Fig. 1(c). This search for an efficient balance between Hilbert space and interaction is a basic nuclear-structure problem also in a broader context outside the shell model; it is my theme throughout this talk.

At this special occasion, another paper with James and Pradhan of that early time [8] comes to my mind, a paper whose idea still echos in modern shell-model ap-

proaches: The core region of the $2N$ force — now in meson theory the realm of omega- and rho-meson exchanges, in chiral effective field theory (EFT) the realm of two- and many-nucleon contact contributions — was for us *terra incognita* which we wanted to explore by the technique of short-ranged phase-equivalent off-shell variations, hoping to stumble on a novel, more pleasing parametrization of the $2N$ potential. In retrospect, we did not learn anything about that unknown part of the $2N$ force, since we were searching rather randomly in that paper. Our hope for information on the force from nuclear structure was a naive illusion at that time. But that hope is still behind the so-called *ab exitu* approach to the effective interaction [9] in no-core shell-model calculations, and it is still behind the modern and really clever use of phase-equivalent variations [10], in fact a smoothening procedure of the $2N$ potential — a similar strategy as Brueckner theory used with its reaction matrix by the ladder summation of highly excited states, — the prize to be payed being the rise of *effective* many-nucleon interactions even without a proper truncation of Hilbert space.

The basic assumption of nuclear theory, before the advent of quantum chromodynamics and still now, is: *Rigid nucleons, the only active degrees of freedom in nuclei, interact through genuine two-, three- and possibly many-nucleon forces according to the rules of non-relativistic quantum mechanics.* That assumption confronts us with two distinct problems which in 1970/71 also defined different fields of research: First, assuming a parametrization of nuclear dynamics, how can we solve the many-nucleon problem throughout the periodic table? This is still the challenge for present-day *shell-model* calculations. But second, more basic, how can we learn details about those forces from some nuclear properties, if they are really reliably described theoretically? Our paper on phase-equivalent off-shell variations [8] mixed up both fields of research, and therefore hopelessly dealt with too complex problems. The second question is the field of *few-nucleon systems*. I chose that path of few-body physics for my later research which I discuss next, but I shall remember, how my early research with James influenced what I am doing today.

3 Few-nucleon systems

The many-body problem is for few-nucleon bound and scattering states conceptually under control due to Faddeev [11] and Alt, Grassberger and Sandhas [12], and it is getting, step-by-step, also calculationally under control by various numerical techniques. My collaborators and me adopted integral equations in momentum space as our numerical technique; compared to shell-model calculations of bound-state systems, the calculations are quite tricky for few-nucleon scattering due to singularities, though the singularities are integrable; they arise from open inelastic channels. Results shown later on are obtained by that technique. The latest important technical achievements were the inclusion of the Coulomb interaction between protons (p) in the scattering equations [13], a stumbling block for the theoretical description during decades, and the description of $4N$ scattering above the four-particle breakup threshold [14]. On the experimental side, there is a multitude of data, especially now data of reactions with polarized particles. From those data one can hope to get more and more information on nuclear forces. I describe that project in its important steps.

3.1 Choice of dynamics

The form of the nuclear dynamics to be tested has to be specified. We had to decide on our form, when pion factories were en vogue; the inclusion of pion production and absorption was necessary: Thus, the important active degrees of freedom to be considered were, besides the nucleon (N), the pion (π) and the Delta-isobar (Δ), which strongly mediates π production in the $2N$ isospin-triplet partial waves; experimentally, the Δ isobar is observed as P_{33} πN resonance; single-π production dominates well

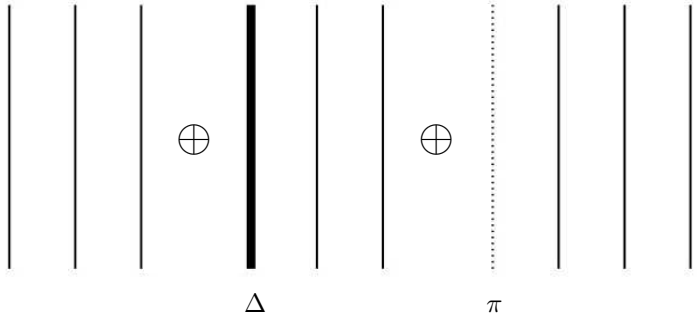

Figure 2: Hilbert space for the description of nuclear phenomena at low and intermediate energies. Compared with the purely nucleonic one, it is expanded by sectors, in which one N is turned into a Δ isobar and one π is added to the N's. πN scattering is described in the corresponding Hilbert space of baryon number one. The $2N$ reactions without and with a single π are described in the corresponding Hilbert space of baryon number two.

above 2π- and 3π-production thresholds. The chosen Hilbert space is shown in Fig. 2; in fact, the choice of an expanded Hilbert space is conceptually based on the same strategy which the no-core shell model took when including the physically important core degrees explicitly in the active model space: *Active degrees of freedom belong to the Hilbert space, they cannot be simulated well by a complicated Hamiltonian.* That strategy [15] allows a unified description of nuclear phenomena at low and at intermediate energies, e. g., the simultaneous description of $2N$ reactions, elastic and inelastic with single-π production and absorption.

The Hamiltonian corresponding to the chosen Hilbert space was taken from meson theory which was without alternative at that time. It is illustrated in Fig. 3, it consists of a one-baryon piece, mediating πN scattering in the P_{33} partial waves — a πN potential is to be added for the non-resonant partial waves — and mediating π production and absorption, and it consists of two-baryon potentials derived from all possible meson exchanges. That Hamiltonian has a particular characteristic for the Δ isobar [16]; it cannot be produced experimentally; the corresponding S-matrix element is exactly zero; observables are the coupled πN states. For that ambitious Hamiltonian we were able to do calculations in most of its aspects [15], e. g., for all reactions in the two-baryon sector $NN \to NN$, $NN \to d\pi$, $NN \to NN\pi$, $d\pi \to d\pi$, $d\pi \to NN\pi$ and $d\pi \to NN$ up to 0.5 GeV c. m. energy — d standing for the deuteron. But the Hamiltonian was not well tuned to low-energy $2N$ data and therefore was not reliable enough for the description of few-nucleon systems at low energies, my more recent research focus.

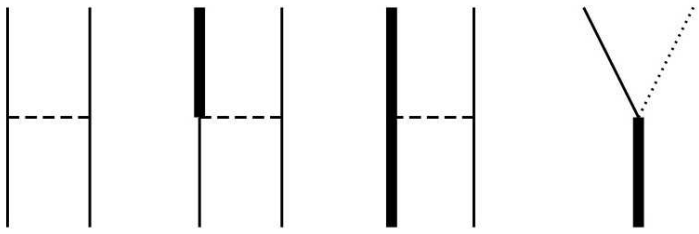

Figure 3: Hamiltonian describing the nuclear dynamics in the Hilbert space of Fig. 2. The interactions are of two-baryon nature, coupling purely nucleonic channels with those containing a Δ isobar; the latter ones are coupled to the pionic channels by a single-baryon vertex.

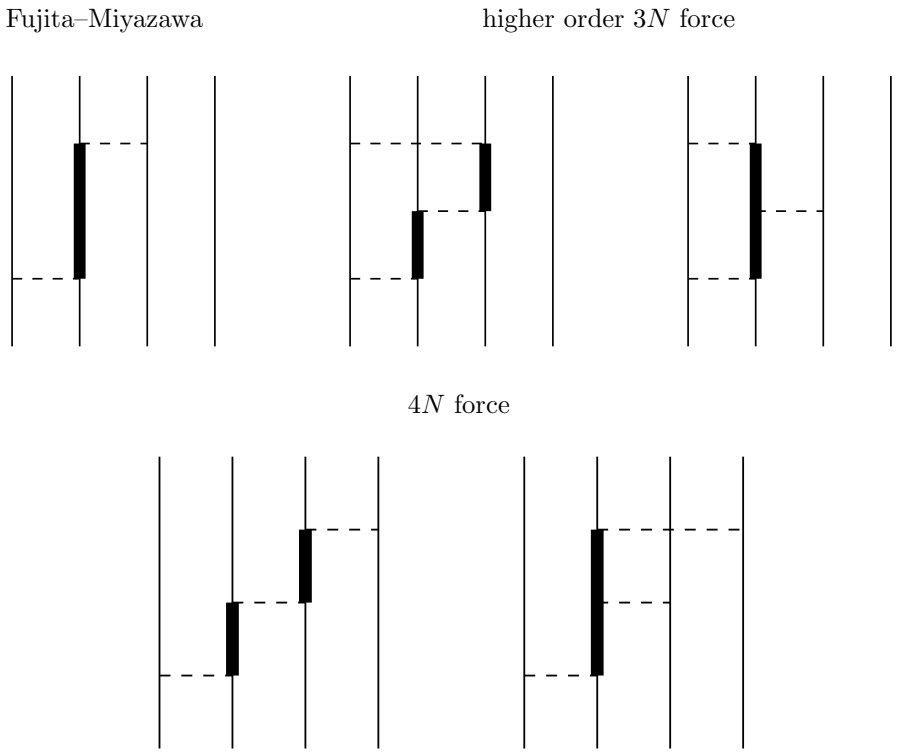

Figure 4: Δ-mediated $3N$ and $4N$ forces, consistent with each other and with the $2N$ interaction. The upper row shows examples for the arising $3N$ force, the Fujita-Miyazawa process being the one of lowest order [18]. The lower row shows examples for the arising $4N$ force. All possible meson exchanges are considered.

The explicit treatment of the Δ isobar has an important and wanted effect; it yields effective $3N$, $4N$ and many-N forces; they are irreducible in the purely nucleonic Hilbert sector, but are resolved into two-baryon pieces in the expanded Hilbert space of Fig. 2. In standard meson theory and in standard EFT, $2N$, $3N$ and many-N potentials arise from freezing non-nucleonic degrees of freedom; but vice versa, as done in the present approach, an important contribution to *genuine* $3N$ and many-N forces can be resolved, when keeping the Δ-isobar degree of freedom explicitly. And without active pions, i. e., without the one-baryon piece of Fig. 3, the Hamiltonian is tuned well for the purposes of low energies [17], i. e., below π-production threshold. The coupled two-baryon potential will be referred to as CD Bonn + Δ; its purely nucleonic reference potential is CD Bonn, whose extension it is. Even that truncated Hamiltonian provides consistent $2N$, $3N$ and $4N$ forces, in general many-N forces, for what Fig. 4 shows examples; their forms and strengths are fixed, they do not allow any further tuning to $3N$ and $4N$ data; physicswise, those arising forces are still incomplete, since other mechanisms leading to irreducible many-N forces besides the Δ-mechanism are left out.

I have discussed $3N$ and many-N forces from various angles. It is now appropriate to come to a conclusive summary: There are *genuine* and *effective* nuclear forces.

The *genuine* forces are derived in the form of instantaneous potentials of a many-N Hamiltonian in a complete Hilbert space for the quantum-mechanical description of many-N systems; they incorporate accepted knowledge of the nuclear forces as the one-π exchange tail; the remainder of the genuine $2N$ potential was phenomenological in the early days, was later on derived from meson theory and is now usually derived from EFT, i. e., from field theories with non-nucleonic degrees of freedom; in the

step to the potential all non-nucleonic degrees are frozen; this step is non-unique. In the same way, $3N$ and many-N potentials are not made by God, they are babies of theoreticians and therefore in principle non-observable. When we loosely speak that some experimental data signal the dynamic need of a contribution from the $3N$ potential, we mean that in a chosen dynamic description the use of a $2N$ potential alone is insufficient.

The *effective* forces are by-products of particular solution techniques for the nuclear many-nucleon problem in the frame work of non-relativistic quantum mechanics. They arise when the complete Hilbert space has to be truncated, the arising $2N$, $3N$ and many-N forces then correct for that truncation; those forces are often energy-dependent, i. e., time-delayed; the $2N$ reaction matrix of Brueckner theory is such an energy-dependent $2N$ force, it is also dependent on the amount of truncation. The *effective* forces also arise when the Hamiltonian is transformed to act dominantly in a particular and convenient subspace, even without truncation, most conveniently in a subspace of low momenta; they are by-products of a particular smoothing technique. *Effective* $3N$ and many-N forces arise, even if the underlying Hamiltonian consists of $2N$ *genuine* forces only.

In structure calculations of heavier nuclei *effective* many-N forces arise in the process of solving the nuclear many-body problem. In the description of few-nucleon systems at low and intermediate energies *genuine* many-N forces can be simulated as in Fig. 4 by keeping non-nucleonic degrees of freedom explicitly in the active Hilbert space.

3.2 Results for few-nucleon bound states

Hadronic and electromagnetic properties of ^{3}H, ^{3}He and ^{4}He are calculated. The effect of the $3N$ force on binding is sizable according to Ref. [19], its Fujita–Miyazawa part [18] being the dominant contribution, usually twice the other $3N$-force contributions. In contrast, the effect of the $4N$ force on binding is small, in fact, an order of magnitude smaller than the $3N$-force effect. This observation is the first solid confirmation of the general folklore on the hierarchy in many-N forces. Since the chosen dynamics cannot be tuned anymore, the resulting binding energies still fail the experimental values slightly. That miss of binding is therefore carried to the thresholds of reactions, a disadvantage for the description of $4N$ scattering close to thresholds. In contrast, the experimental binding-energy difference between ^{3}H and ^{3}He is well accounted for.

3.3 Results for few-nucleon reactions

The few-nucleon community is able to account for a very large amount of experimental $3N$ and $4N$ data at low energies, i. e., at energies up to the π-production threshold. This is quite satisfying. The inclusion of Coulomb and of a $3N$ interaction is often needed; I give an example for both effects. Besides those successes which are in the overwhelming majority, there are, however, puzzles, i. e., there is a persistent disagreement between theoretical prediction and data without any hint for a solution; in fact that is the much more interesting situation, since we hope to learn from such cases; I shall also give an example for such a puzzle. In the presented figures, the predictions derived from the coupled-channel potential CD Bonn + Δ with Coulomb, indicated by Δ+Coulomb and by the red curves, are the most complete ones, including the effect of Coulomb and of many-N forces mediated by the Δ isobar simultaneously. The predictions derived from the purely nucleonic reference potential CD Bonn with Coulomb, indicated by N + Coulomb and by the green curves, include the effect of Coulomb, but leave out the effect of many-N forces mediated by the Δ isobar; the difference between red and green curves indicate the effect of many-N forces on the considered observable. The predictions derived from the coupled-channel potential

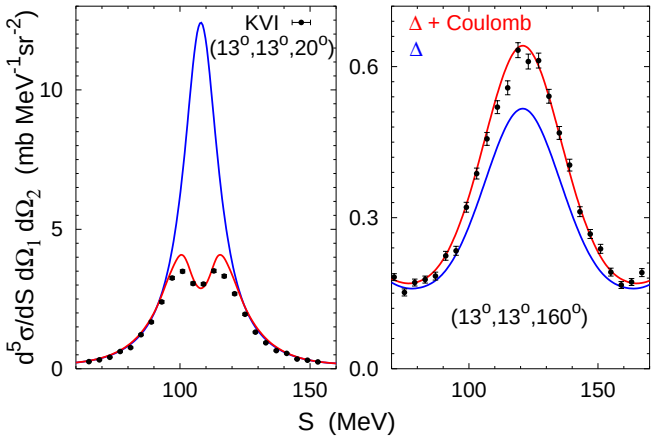

Figure 5: *dp* breakup at 130 MeV *d* energy. The Coulomb effect is quite pronounced due to the correlation between the two protons in the final state. The angles of the two outgoing *p*'s are fixed; their energies are constrained by the kinematical locus S. There is no evidence for the need of a $3N$ force. The experimental data and the theoretical predictions are from Ref. [20].

CD Bonn + Δ without Coulomb, indicated by Δ and by blue curves, leave out the effect of Coulomb, but include the effect of many-N forces mediated by the Δ isobar; the difference between red and blue curves indicate the effect of Coulomb on the considered observable.

The inclusion of the Coulomb repulsion between the two *p*'s is necessary for the successful description of $3N$ and $4N$ elastic scattering at low energies. But Fig. 5 shows that Coulomb can be quite important also at much higher beam energies, when, in the breakup situation, the two outgoing *p*'s are strongly correlated at rather low relative energies. Signals for the working of the $3N$ force in the considered dynamic model are shown in Fig. 6.

A very long-standing puzzle is the spin observable A_y in elastic *pd*, but also in elastic p^3He scattering in a particular low-energy window. Another observable which is extremely hard to describe is the total elastic neutron-^{3}H (n^3H) cross section. I like to discuss a further puzzle arising at low-energy *pd* breakup in the space-star kinematics. Data and the theoretical predictions are shown in Fig. 7. That space-star kinematics was believed by experimentalists to show the effect of the $3N$ force most strongly; in fact, that effect is not seen at all. At 13 MeV N lab energy there are *pd* and *nd* data; since the *nd* experiments are especially difficult, the data were twice remeasured, but appear now to be confirmed; the *pd* data were taken only once. There is a sizable difference between *pd* and *nd* data; theory is unable to account for that difference; the Coulomb effect is minor; if the data were true beyond any doubt, an extremely large nuclear charge-asymmetry effect shows up. Such an effect appears, however, conceptually rather unlikely.

3.4 Summary

In the past, the theoretical fields of nuclear structure and few-nucleon systems were entirely disjoint with respect to research goals, to employed dynamics and to numerical techniques used for solving the nuclear many-body problems. Research settled on different banks of the river "nuclear theory". That situation passed; there are now interesting cross-overs between those fields as this conference in Iowa is witness for, and the beautiful bridges of Iowa as the one of Fig. 8 are pictures for those cross-overs. The talk discussed *genuine* and *effective* $2N$ and many-N forces, their appearance and their different roles in nuclear-structure and in few-nucleon calculations. The

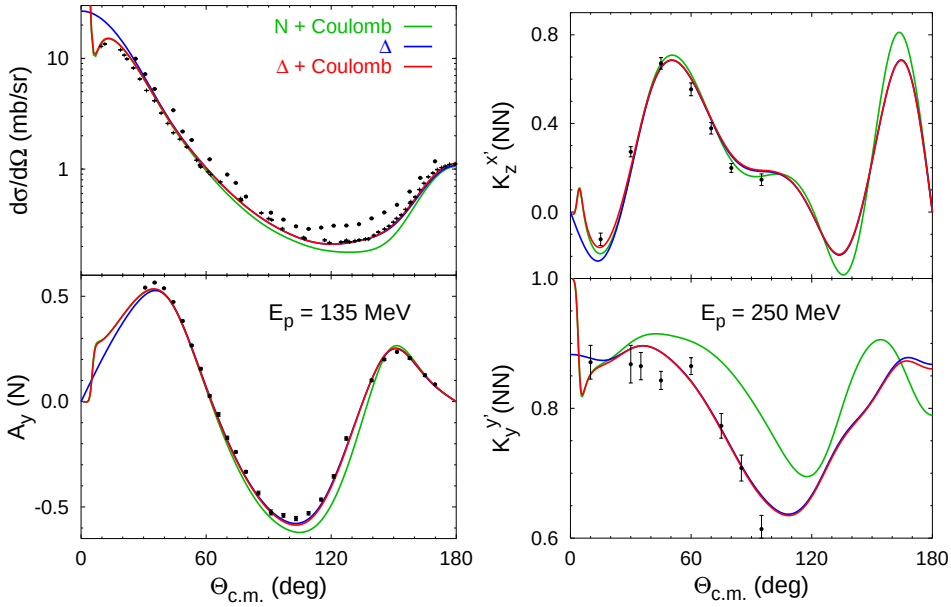

Figure 6: Selected observables of pd elastic scattering at higher energies. The effect of the $3N$ force is quite pronounced. In contrast, an effect of the Coulomb repulsion between the protons is only seen in the extreme forward direction. At 135 MeV p energy, the experimental data are from Ref. [21], the lower data in the differential cross section from Ref. [22], an example for conflicting experimental data; the theoretical predictions are from Ref. [23]. At 250 MeV p energy, the experimental data are from Ref. [24], the theoretical predictions from Ref. [25].

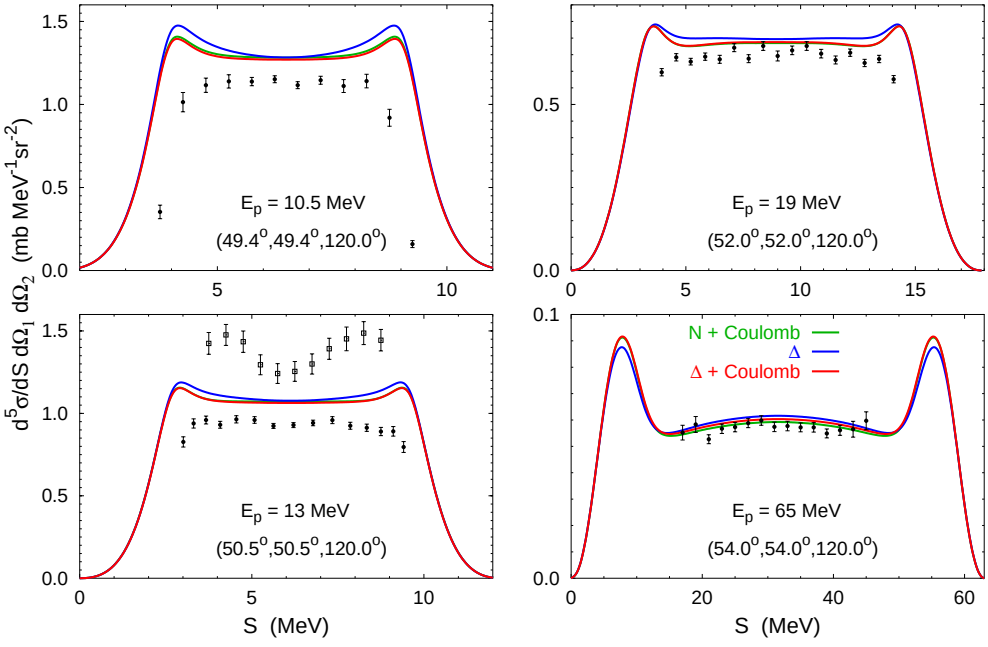

Figure 7: Nd breakup in the space-star kinematics. Neither the Coulomb force between the two p's nor the $3N$ force show up in any significant way. The angles of two outgoing N's are fixed; their energies are constrained by the kinematical locus S. The data refer to pd breakup with the exception of the upper data at 13 MeV N beam energy which are nd data. The theoretical predictions are from Ref. [26] which also gives the references to the experimental data.

Figure 8: One of the covered bridges of Iowa.

talk presented some examples for the achievements of few-nucleon theory, but also for outstanding puzzles in the description of data.

At the end, I wish the man of honor at this conference, James Vary, further success in his admirable engagement for the advancement of nuclear physics, which has been and will be stimulating to others.

The shown results for few-nucleon systems were obtained in a long successful collaboration with A. Deltuva and A. C. Fonseca, University of Lisbon, for which I am very grateful.

References

[1] K. A. Brueckner, Phys. Rev. **97**, 1353 (1955); *ibid.* **100**, 36 (1955).

[2] T. T. S. Kuo and G. E. Brown, Nucl. Phys. **85**, 40 (1966).

[3] J. P. Vary, P. U. Sauer and C. W. Wong, Phys. Rev. C **7**, 1776 (1973).

[4] B. R. Barrett and M. W. Kirson, Phys. Lett. B **27**, 544 (1968).

[5] T. H. Schucan and H. A. Weidenmüller, Ann. Phys. (NY) **73**, 108 (1972).

[6] D. C. Zheng *et al.*, Phys. Rev. C **48**, 1083 (1993).

[7] P. Navrátil and B. R. Barrett, Phys. Rev. C **54**, 2986 (1996).

[8] H. C. Pradhan, P. U. Sauer and J. P. Vary, Phys. Rev. C **6**, 407 (1972).

[9] A. M. Shirokov, J. P. Vary, A. I. Mazur and T. A. Weber, Phys. Lett. B **644**, 33 (2007).

[10] S. K. Bogner *et al.*, Phys. Lett. B **576**, 265 (2003).

[11] L. D. Faddeev, Sov. Phys. JETP **12**, 1014 (1961).

[12] E. O. Alt, P. Grassberger and W. Sandhas, Nucl. Phys. B **2**, 167 (1967).

[13] A. Deltuva, A. C. Fonseca and P. U. Sauer, Ann. Rev. Nuc. Part. Sci. **58**, 27 (2008).

[14] A. Deltuva and A. C. Fonseca, Phys. Rev. C **86**, 011001(R) (2012).

[15] P. U. Sauer, Progr. Part. Nucl. Phys. **16**, 35 (1986).

[16] H. Poepping, P. U. Sauer and Zhang Xi-Zhen, Nucl. Phys. A **474**, 557 (1987) [*Erratum: ibid.* A **550**, 563 (1992)].

[17] A. Deltuva, R. Machleidt and P. U. Sauer, Phys. Rev. C **68**, 024005 (2003).

[18] J. Fujita and H. Miyazawa, Progr. Theor. Phys. **17**, 360 (1957).

[19] A. Deltuva, A. C. Fonseca and P. U. Sauer, Phys. Lett. B **660**, 471 (2008).

[20] St. Kistryn *et al.*, Phys. Lett. B **641**, 23 (2006).

[21] K. Ermisch *et al.*, Phys. Rev. C **71**, 064004 (2005).

[22] K. Sekiguchi *et al.*, Phys. Rev. C **65**, 034003 (2002).

[23] A. Deltuva, A. C. Fonseca and P. U. Sauer, Phys. Rev. C **71**, 054005 (2005).

[24] K. Hatanaka *et al.*, Phys. Rev. C **66**, 044002 (2002).

[25] A. Deltuva, A. C. Fonseca and P. U. Sauer, Few-Body Syst. **49**, 27 (2011).

[26] A. Deltuva, A. C. Fonseca and P. U. Sauer, Phys. Rev. C **72**, 054004 (2005).

High-Resolution Probes of Low-Resolution Nuclei

R. J. Furnstahl

Department of Physics, Ohio State University, Columbus, OH 43085

Abstract

Renormalization group (RG) methods used to soften Hamiltonians allow large-scale computational resources to be used to greater advantage in calculations of nuclear structure and reactions. These RG transformations lower the effective resolution of the nuclei, which raises questions about how to calculate and interpret high-momentum transfer probes of nuclear structure. Such experiments are conventionally explained in terms of short-range correlations, but these disappear with the evolution to low-momentum scales. We highlight the important issues and prospects in the context of recent developments in RG technology, with guidance from the analogous extraction of parton distributions.

Keywords: *Renormalization group; nuclear structure*

1 Introduction

Recent electron scattering experiments on nuclei that use large four-momentum transfers to knock out nucleons have been interpreted in terms of short-range correlations (SRCs) in the nuclear wave function [1,2]. As indicated schematically in Fig. 1 (top), the dominant source of ejected back-to-back nucleons is identified as the break-up of an SRC formed by low-momentum nucleons being coupled to high-momentum by the nucleon-nucleon (NN) interaction. At the same time, the use of softened ("low-momentum") Hamiltonians has had great success in pushing the limits of microscopic calculations of nuclear structure and reactions [3–5]. This success is in large part due to the *absence* of SRCs in the corresponding nuclear wave functions. We seek to reconcile these results by applying a renormalization group (RG) viewpoint, which manifests the scale (and scheme) dependence of nuclear Hamiltonians and operators by continuous changes in the *resolution*. RG transformations shift the physics between structure and reaction mechanism so that the same data can have apparently different explanations. We use the RG perspective to discuss implications in light of the current and future possibilities of applying new RG technology.

The RG is a powerful and versatile tool for this purpose. The common features of the RG for critical phenomena and high-energy scattering are discussed by Steven Weinberg in an essay in Ref. [6]. He summarizes:

> "The method in its most general form can I think be understood as a way to arrange in various theories that the degrees of freedom that you're talking about are the relevant degrees of freedom for the problem at hand."

This is the essence of what we do by evolving to low-momentum interactions: we arrange for the degrees of freedom to be the relevant ones for nuclear structure (and reactions). This does not mean that other degrees of freedom cannot be used (including SRCs from high-momentum interactions), but we need to be mindful of Weinberg's

Proceedings of International Conference 'Nuclear Theory in the Supercomputing Era — 2013' (NTSE-2013), Ames, IA, USA, May 13–17, 2013. Eds. A. M. Shirokov and A. I. Mazur. Pacific National University, Khabarovsk, Russia, 2014, p. 371.

http://www.ntse-2013.khb.ru/Proc/Furnstahl.pdf.

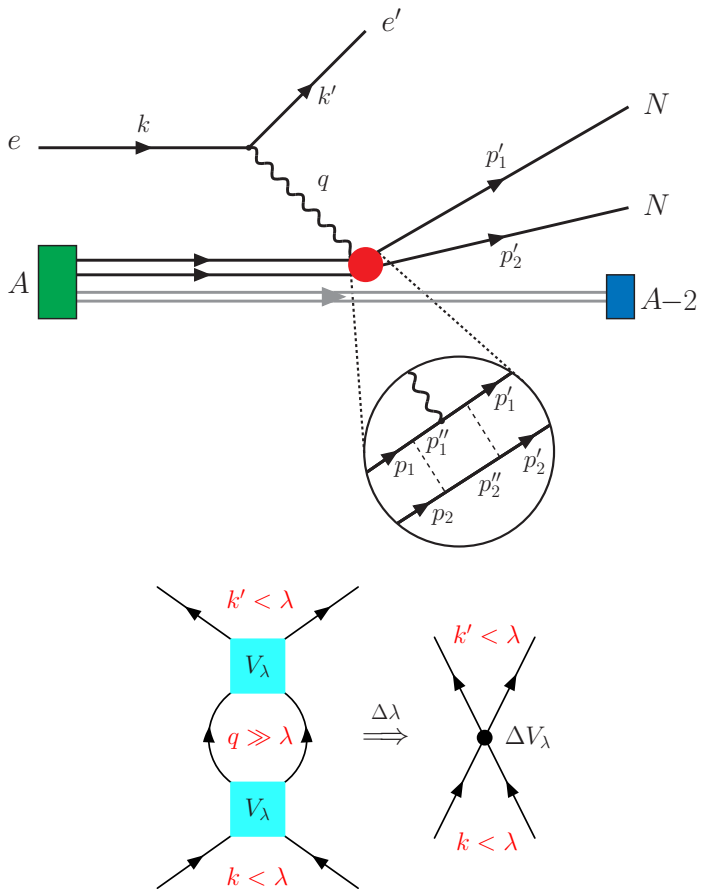

Figure 1: Schematic two-nucleon knock-out experiment with SRC interpretation (top) and diagrammatic illustration that the contribution of decoupled high-momentum modes in intermediate states is replaced by (regularized) contact interactions (bottom).

adage [6]:

> "You can use any degrees of freedom you want, but if you use the wrong ones, you'll be sorry."

The benefits of applying RG to high-energy (particle) physics include improving perturbation theory, e. g., in QCD. A mismatch of energy scales can generate large logarithms that ruins perturbative convergence even when couplings by themselves are small. The RG shifts strength between loop integrals and coupling constants to reduce these logs. For critical phenomena in condensed matter systems, the RG reveals the nature of observed universal behavior by filtering out short-distance degrees of freedom.

Both these aspects are seen in applications of RG to nuclear structure and reactions. As the resolution is lowered, nuclear calculations become more perturbative, implying that scales are more appropriately matched. In addition, the potentials flow toward universal form (e. g., see Fig. 3) as model dependent short-distance details are suppressed. The end result might be said to make nuclear physics look more like quantum chemistry calculationally, opening the door to a wider variety of techniques (such as many-body perturbation theory) and simplifying calculations (e. g., by improving convergence of basis expansions). However, maintaining RG-induced three-nucleon (NNN) forces (and possibly four-nucleon forces) has been found to be essential for

accurate and scale-independent results. Recently developed RG technology to handle three-body evolution [4,7,8] will be critical to realize the power of the RG.

2 Similarity renormalization group flow

Renormalization group methods and applications to nuclear systems are well documented in the literature (see Refs. [3,5] and references therein) and in contributions to these proceedings. A popular approach, which we focus on here, is the similarity renormalization group (SRG). In most implementations of the SRG, an initial Hamiltonian (typically with both NN and NNN interactions) is driven by a series of continuous unitary transformations toward more diagonal form in momentum representation. This flow toward the diagonal is illustrated for both NN and NNN matrix elements in Fig. 2 [8]. More diagonal means greater decoupling of low- and high-momentum modes, making interactions more perturbative. The changes in many-body interactions highlight the need to be able to control this part of the evolution.

Where does the physics of the decoupled high-momentum modes go? It flows to modifications of the low-momentum parts of both the two- and three-nucleon interactions, which effective field theory (EFT) tells us can be absorbed into regulated contact interactions (as indicated schematically in the bottom in Fig. 1). That the leading change in the NN potential induced by the SRG does have this form can be shown using the operator product expansion (see Section 3 and Refs. [10,11]) but it is implicit in the NN $^1S_0$ partial wave in Fig. 3, where the off-diagonal matrix elements of a set of chiral EFT NN potentials with different regularization schemes (left) are evolved to low resolution (right). We directly see the suppression of off-diagonal strength for $k > \lambda$ and a flow to universal values when the high-momentum model dependence is suppressed (evidence for universal flow has also been observed in three-body evolution [7,8]). The dominant change in the potential at low momentum is a constant shift, as would be expected from changing the strength of a regulated (smeared) delta function in coordinate space.

A visualization of how two-nucleon interactions evolve in coordinate representation is given for two potentials in the $^1S_0$ partial wave in Fig. 4, where local projections are applied to the intrinsically non-local SRG evolved potentials [12]. The melting

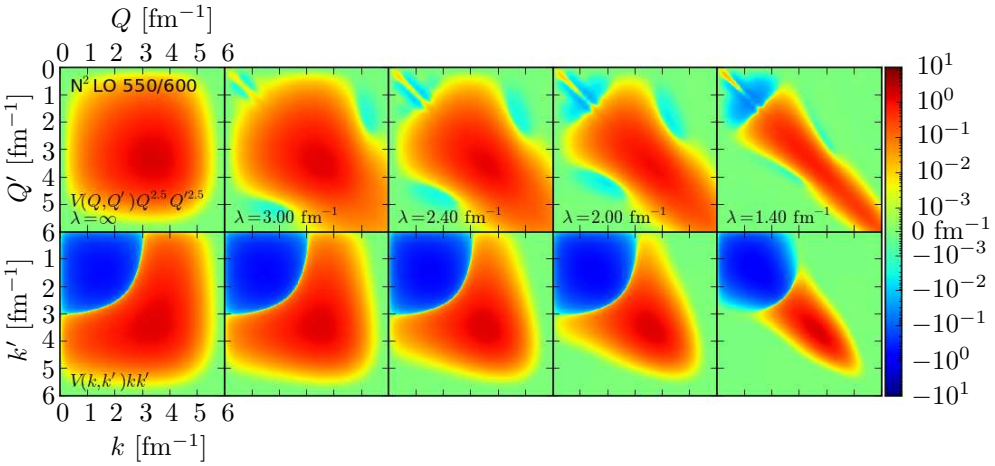

Figure 2: Evolution by the SRG showing flow toward the momentum diagonal for both NN (bottom) and NNN (top) interactions [8]. The initial potential is an $NN + NNN$ chiral EFT interaction at next-to-next-to-leading order (see Ref. [9] for background). λ is a flow parameter with $\hbar^2\lambda^2/M$ roughly equal to the energy decoupling scale.

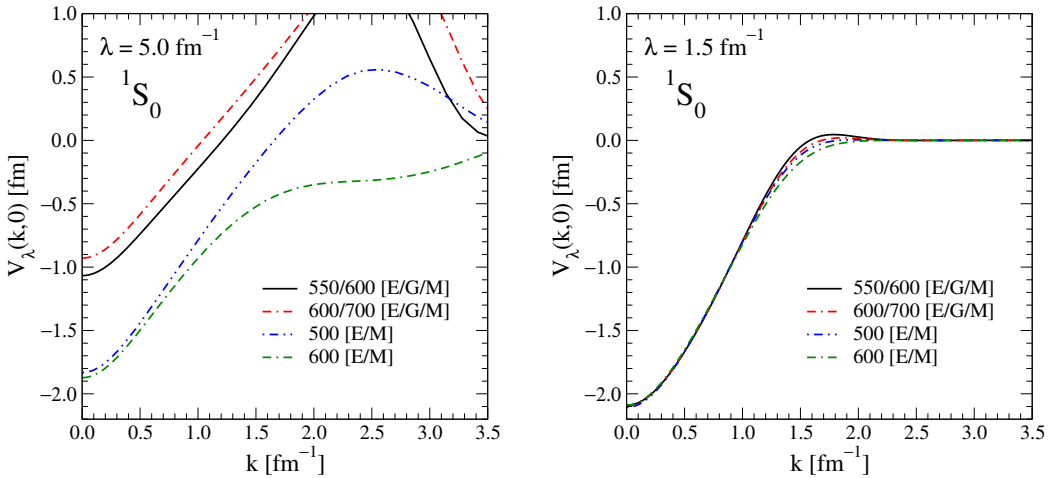

Figure 3: Off-diagonal matrix elements of different chiral EFT potentials evolved by the SRG slightly to $\lambda = 5\ \mathrm{fm}^{-1}$ (left) and much further to $\lambda = 1.5\ \mathrm{fm}^{-1}$ (right) [3].

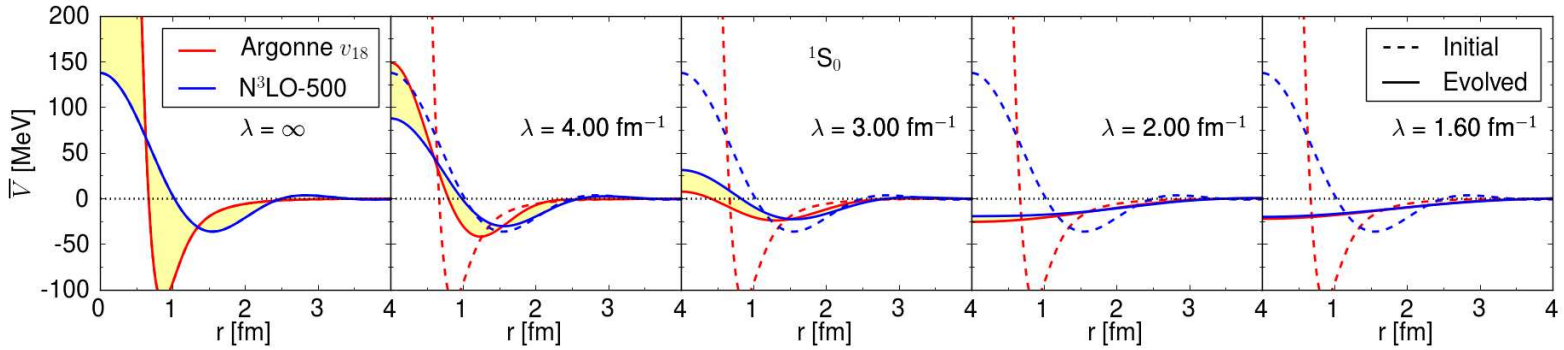

Figure 4: Evolution by the SRG of two NN interactions in coordinate space as visualized by local projections (see Ref. [12] for definitions and details).

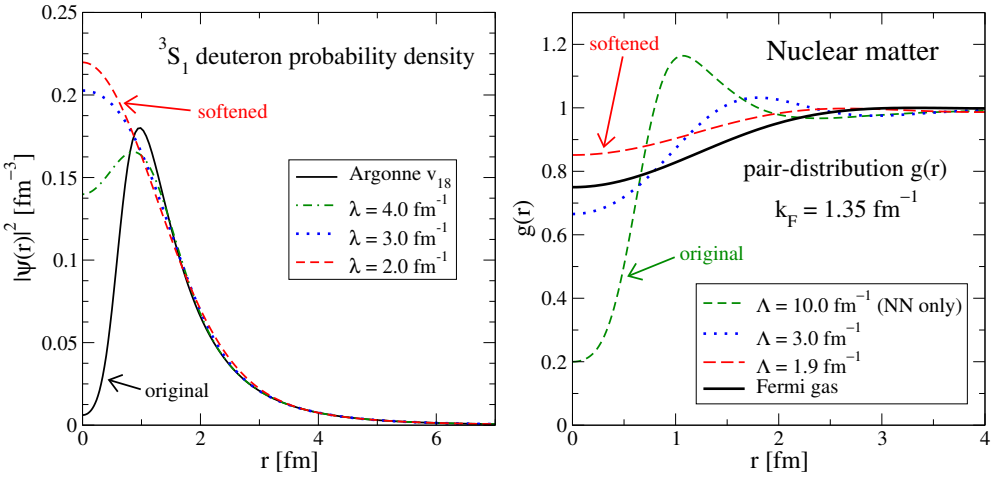

Figure 5: Short-range correlations induced in the $L = 0$ part of the deuteron wave function by the Argonne v_{18} potential [13], seen as a suppression at short distances, is removed with SRG evolution to $\lambda = 2$ fm^{-1} (left). Short-range correlations in nuclear matter, which are manifested by the "wound" in the pair distribution function compared to the Fermi gas, are largely removed by $V_{\mathrm{low}\,k}$ RG evolution to $\Lambda = 1.9$ fm^{-1} [3].

of the hard repulsive core is manifest as well as the flow to universal form. The soft NN (and NNN) potentials after evolution are much more amenable to many-body methods that use basis expansions, such as the no-core shell model, coupled cluster, and the in-medium SRG (see Ref. [5] for recent results). Indeed, nuclear structure and low-energy reactions are more natural with low-momentum interactions, because the Fermi momentum sets the scale rather than a repulsive core. The successes of this approach with the SRG and other RG methods (e. g., which enable many-body perturbation theory for the shell model) are reviewed elsewhere [3,5]. But because the repulsive core is the dominant source of SRCs, the nuclear wave functions have variable SRCs as the resolution is changed (i. e., as λ is lowered). This is illustrated in Fig. 5 for the deuteron (left) and nuclear matter (right). What then are the implications for RG evolution for the high-resolution (that is, high four-momentum transfer) electron scattering experiments? How does the resolution of the nuclear states even enter the analysis? To address these questions, we must ask about the evolution of operators other than the Hamiltonian.

3 Operator evolution by the SRG

To gain insight into how RG changes in scale should enter the analysis of nuclear knock-out experiments, we can use the extraction of parton distribution functions from deep inelastic scattering (DIS) as a paradigm. The key property that make parton distributions well defined is the controlled factorization of the cross section into structure and reaction parts at hard scales (meaning sufficiently large Q^2) [14]. By this means, a structure function such as $F_2(x, Q^2)$ is decomposed into short-distance physics from the electron-quark scattering that is captured in Wilson coefficients in $\widehat{F}_2^a\big(x, \frac{Q}{\mu_f}\big)$ and the remainder, which is the soft, long-distance physics defining the parton distribution $f_a(x, \mu_f)$ (where a labels quarks):

$$F_2(x, Q^2) \sim \sum_a f_a(x, \mu_f) \otimes \widehat{F}_2^a\Big(x, \frac{Q}{\mu_f}\Big). \tag{1}$$

The *choice* of the factorization scale μ_f defines the border between the long- and short-distance contributions. It is not unique! But because the observable F_2 must be independent of μ_f, knowing how the short-distance part changes with μ_f determines the RG running of the parton distribution. A typical choice is $\mu_f = Q$ (to minimize logarithmic contributions to the Wilson coefficient for the optimal extraction of PDFs from experiment), so this running translates into a Q^2 dependence in the parton distribution [14].

An example of this RG running is shown for the u-quark PDF in a proton as a function of x and Q^2 in Fig. 6. In the top panel, the combination $xu(x, Q^2)$

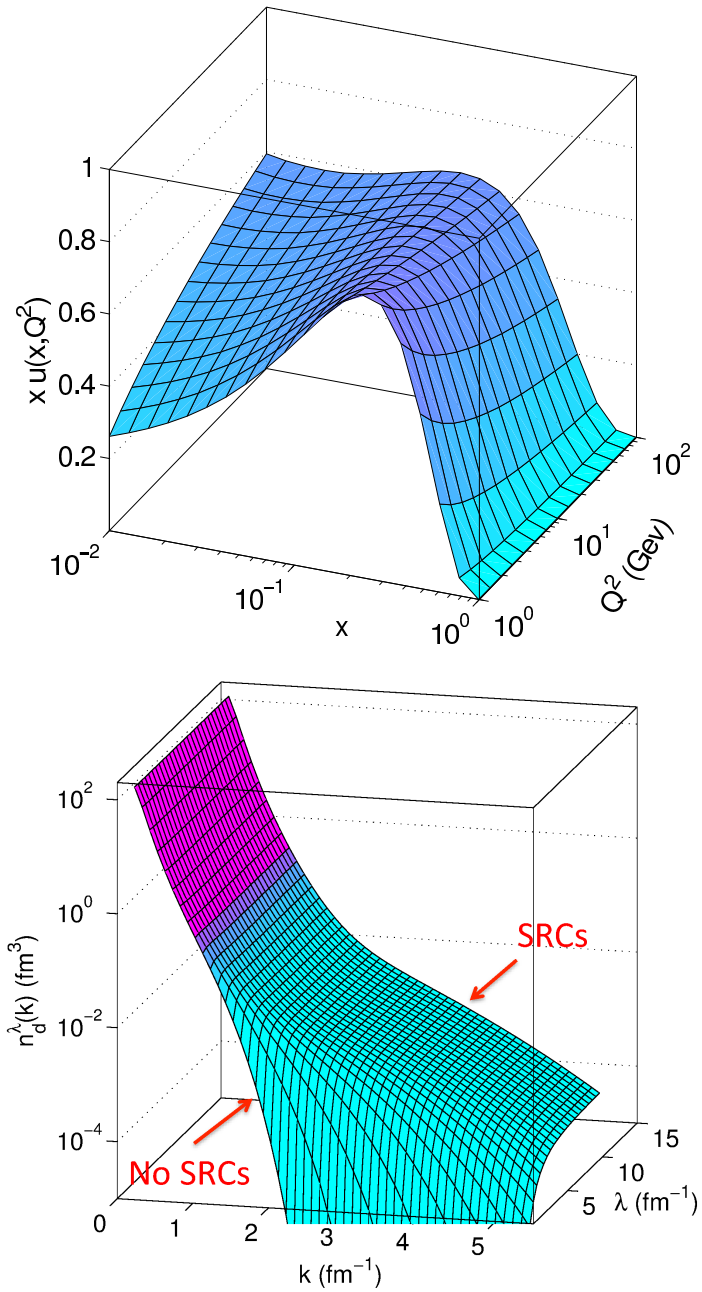

Figure 6: Parton distribution $xu(x, Q^2)$ for the u-quarks in the proton as a function of x and Q^2 (top, calculated from [16]) and deuteron momentum distribution $n_d^\lambda(k)$ at different SRG resolutions λ (bottom).

measures the share of momentum carried by u-quarks in a proton within a particular x-interval [15, 16]. This momentum distribution changes as a function of the resolution scale Q^2 according to RG evolution equations. Thus $u(x, Q^2)$ is scale dependent (as well as scheme dependent, see Ref. [14]). In the bottom panel, we see that the deuteron momentum distribution $n_d^\lambda(k)$ is also scale and scheme dependent. Plotted is $n_d^\lambda(k)$ for an initial AV18 potential [13] (the choice of potential is a *scheme* dependence), which is SRG-evolved from $\lambda = \infty$ (corresponding to the initial potential and high resolution) down to $\lambda = 1.5$ fm^{-1} (lowest resolution). It is evident that the high-momentum tail, which is identified with SRC physics, is highly scale dependent and is essentially eliminated at lower resolution.

The extraction of momentum distributions or quantities such as spectroscopic factors from nuclear experiments is also predicated on factorization assumptions just as in DIS. That is, the observable cross sections are separated into the structure and reaction parts according to some assumptions, which is once again not a unique decomposition but depends on the factorization scale. If the impulse approximation is accurate for some scale, then the separation is clean. But this is rarely true in nuclear physics (at least not to the precision we hope to reach). Therefore we should ask for the nucleon knock-out experiments the same questions that are carefully addressed in DIS: Is the factorization robust? Is it process dependent? What is necessary for consistency between structure and reaction models? What are the trade-offs between using different scales (and schemes)?

Let's see how the scale dependence like in DIS works out in the language of SRG unitary transformations. The measured cross section is a convolution: reaction $\otimes$ structure, but the separate parts are not unique, only the combination. A (short-range) unitary transformation $\widehat{U}$ leaves matrix elements of an operator $\widehat{O}$ invariant:

$$O_{mn} \equiv \langle \Psi_m | \widehat{O} | \Psi_n \rangle = \left(\langle \Psi_m | \widehat{U}^\dagger \right) \widehat{U} \widehat{O} \widehat{U}^\dagger \left(\widehat{U} | \Psi_n \rangle \right) = \langle \widetilde{\Psi}_m | \widetilde{O} | \widetilde{\Psi}_n \rangle \equiv \widetilde{O}_{\tilde{m}\tilde{n}} \,. \qquad (2)$$

RG unitary transformations change the decoupling scale, which means that the effective factorization scale (which determines what goes into the operator and what into the wave function) is changed. Note that matrix elements of the operator $\widehat{O}$ itself between the transformed states are in general modified:

$$O_{\tilde{m}\tilde{n}} \equiv \langle \widetilde{\Psi}_m | \widehat{O} | \widetilde{\Psi}_n \rangle \neq O_{mn} \quad \Longrightarrow \quad \text{e. g., } \langle \Psi_n^{A-1} | a_\alpha | \Psi_0^A \rangle \text{ changes,} \qquad (3)$$

where the latter is a spectroscopic factor. In a low-energy effective theory, transformations that modify short-range unresolved physics yield equally valid states, so matrix elements such as spectroscopic factors (SFs) or momentum distributions (see Fig. 6) are scale/scheme dependent observables.

All ingredients for the analysis of an experimental cross section mix under a unitary transformation that changes the resolution. A one-body current becomes a many-body current:

$\widehat{U}\widehat{\rho}(\mathbf{q})\widehat{U}^\dagger$ =

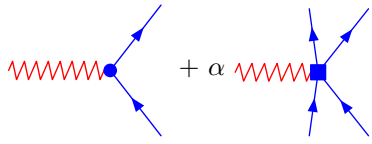

$+ \alpha$

$+ \cdots ,$

final-state interactions are modified, and new wave function correlations appear (or disappear in the case of short-range calculations at lower resolution):

$\widehat{U}|\Psi_0^A\rangle = \widehat{U}$

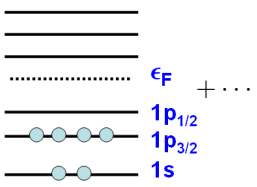

$+ \cdots \Longrightarrow Z$

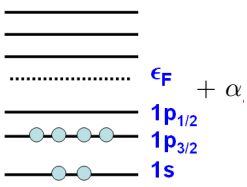

$+ \alpha$

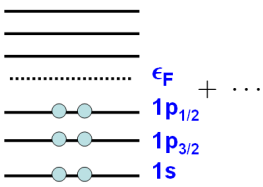

$+ \cdots$

Again, this means that quantities such as SFs are scale dependent. The bottom line is that the cross section is unchanged only if all pieces are included with the same U: the Hamiltonian, the current operator, and the final state interactions.

Now consider again the high resolution experiment from Fig. 1 and what happens when RG unitary transformations act to change the resolution. In particular, how does the SRC explanation of nuclear scaling, which accounts for plateaus in inclusive cross section ratios, evolve with the resolution scale? This explanation is based on the dominant role played by the one-body current, the two-body interaction, and SRCs.

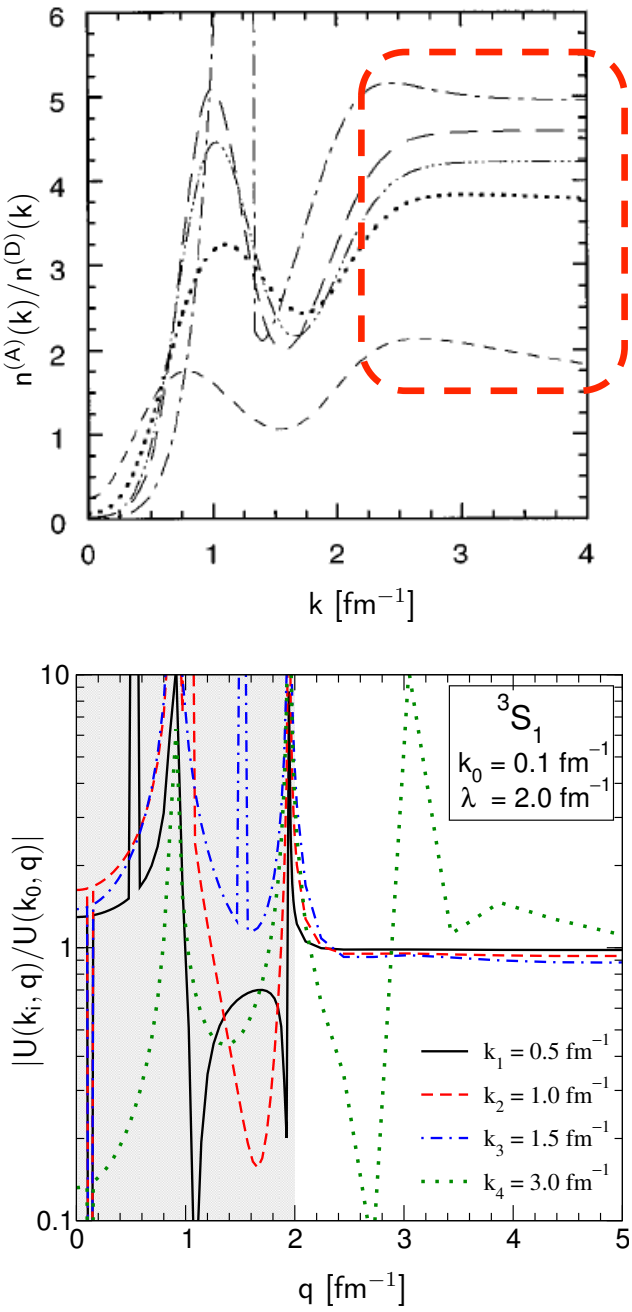

Figure 7: Ratio of momentum distributions in nuclei to the deuteron (denoted n_A and n_d in the text) with a high-resolution potential [17] (top) and U_λ-factorization test for the $^3S_1$ channel [10] (bottom).

The underlying physics is most simply isolated by considering the high-resolution momentum distributions in nuclei. In Fig. 7 on top, we see that ratios of the these momentum distributions in various nuclei to that in the deuteron are almost flat in the high momentum region associated with SRCs (i. e., above $k = 2\ \mathrm{fm}^{-1}$). The contribution highlighted in the circle in Fig. 1 yields a k dependence largely independent of the nuclear environment, so $n_A(k)$ simply scales with A. If we now evolve to lower momentum through unitary transformations, this can no longer explain the cross section, because the softening of the interaction and therefore the wave function means the momentum distribution has no support at these high momenta (e. g., as in Fig. 6 for the deuteron).

But the cross section *must* be unchanged, because it is a unitary transformation. With RG evolution, the probability of high momentum in a nucleus decreases, but if we transform the wave functions *and* operators:

$$n(k) \equiv \langle A|a^\dagger_{\mathbf{k}}a_{\mathbf{k}}|A\rangle = \left(\langle A|\widehat{U}^\dagger\right)\widehat{U}a^\dagger_{\mathbf{k}}a_{\mathbf{k}}\widehat{U}^\dagger\left(\widehat{U}|\Psi_n\rangle\right) = \langle\widetilde{A}|\widehat{U}a^\dagger_{\mathbf{k}}a_{\mathbf{k}}\widehat{U}^\dagger|\widetilde{A}\rangle, \tag{4}$$

then the original momentum distribution is unchanged! We know that the transformed state $|\widetilde{A}\rangle$ is easier to calculate, but is the new operator too difficult to calculate or even pathological (e. g., does it explode to compensate for the super-exponential suppression of the low-resolution momentum distribution)?

Let us consider the SRG operator flow for the momentum distribution graphically. The evolution with λ of any operator $\widehat{O}$ is given by:

$$\widehat{O}_\lambda = \widehat{U}_\lambda\,\widehat{O}\,\widehat{U}^\dagger_\lambda\,, \tag{5}$$

which can be carried out by a flow equation similar to that used to evolve the Hamiltonian. In practice it is more efficient to construct the unitary transformation from $\widehat{U}_\lambda = \sum_i |\psi_i(\lambda)\rangle\langle\psi_i(0)|$ or by solving the $dU_\lambda/d\lambda$ flow equation. In any case, matrix elements of evolved operators are unchanged by construction (for the deuteron) *but the distribution of strength flows*. The integrand of the momentum distribution $\langle\psi_d|a^\dagger_q a_q|\psi_d\rangle$ in the deuteron at $q \approx 3.0\ \mathrm{fm}^{-1}$ is shown in Fig. 8. In the top figure, the initial integrand of $\widehat{U}_\lambda a^\dagger_q a_q \widehat{U}^\dagger_\lambda$ at $\lambda = \infty$ has a delta function at $k = k' = q$. In the

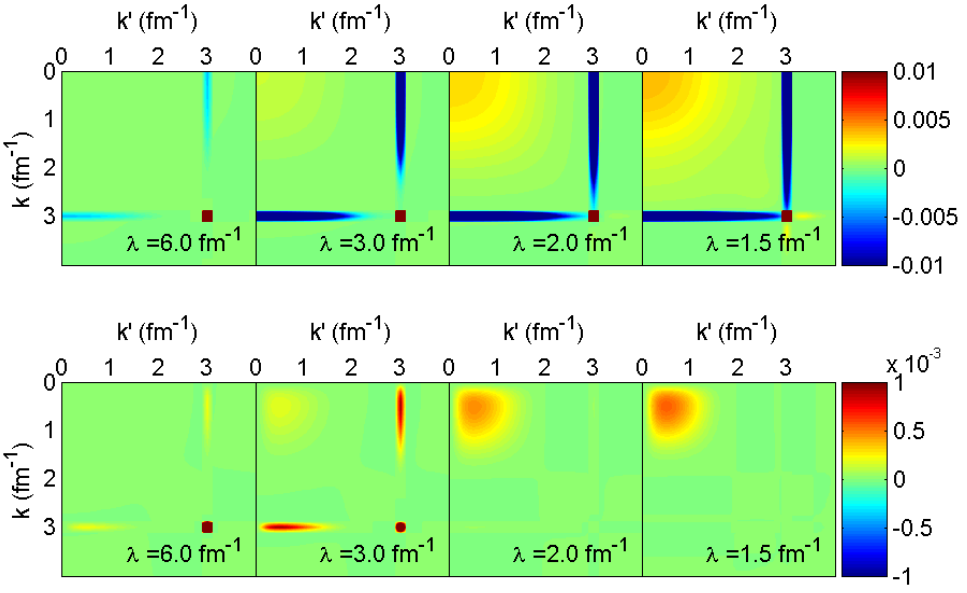

Figure 8: Integrand of the deuteron momentum distribution at $q \approx 3\ \mathrm{fm}^{-1}$ without (top) and with (bottom) the deuteron wave functions included [10].

SRG flow, one-body operators such as $a_q^\dagger a_q$ do not evolve, and their contribution is in fact unchanged with λ. However, there is a clear flow to lower momentum, which must be entirely due to a two-body operator. In the bottom figure, the deuteron wave functions are folded in (such that the integrated area is the invariant value of the original momentum distribution at $q = 3$ fm^{-1}). We see there is negligible amplitude at small λ from the original one-body operator (nothing explodes!), but instead a smooth contribution at low momenta from the induced two-body operator, which is reminiscent of a regularized delta function.

We might wish to conclude that this operator flow implies a type of "conservation of difficulty" with the simplification of the wave function countered by the complication of the operator. But in this situation the separation of momentum scales leads to an important generic factorization of the unitary transformation operator U_λ. In particular, U_λ-factorization says that the two-body unitary transformation becomes a simple product (in each partial wave): $U_\lambda(k,q) \to K_\lambda(k)\, Q_\lambda(q)$ whenever $k < \lambda$ and $q \gg \lambda$. This result follows from applying effective interaction methods or the operator product expansion (OPE) for nonrelativistic wavefunctions; we refer the reader to Refs. [10, 11] for the technical details. Here we rely on a visual demonstration. In particular, we test U_λ-factorization by considering the ratio of $U_\lambda(k,q)$ at fixed q but variable k. In the factorization region:

$$\frac{U_\lambda(k_i,q)}{U_\lambda(k_0,q)} \xrightarrow[q\gg\lambda]{k<\lambda} \frac{K_\lambda(k_i)\, Q_\lambda(q)}{K_\lambda(k_0)\, Q_\lambda(q)} = \frac{K_\lambda(k_i)}{K_\lambda(k_0)} \approx 1, \tag{6}$$

so for $q \gg \lambda$ we expect the ratio to go to a constant, which is in fact unity because $K_\lambda(k)$ becomes independent of k to leading order in the OPE. In Fig. 7 (bottom), we plot this ratio in the $^3S_1$ channel and see clear plateaus close to one (at the 10–15% level) for those curves with $k_i < \lambda$ in the $q > \lambda$ region, just as expected. It works similarly in other channels [10].

We emphasize that because the leading order for $K_\lambda(k)$ is constant for $k < \lambda$, the factors $K_\lambda(k)\, K_\lambda(k')$ to good approximation play the role of a contact term. Then the contribution from large λ in the diagram in Fig. 1 (bottom) with an implied integration over q and q' has the simplification:

$$\begin{aligned}\Delta V_\lambda(k,k') &= \int_{q,q'} U_\lambda(k,q)\, V_\lambda(q,q')\, U_\lambda^\dagger(q',k') \quad \text{for} \quad k,k' < \lambda, \quad q,q' \gg \lambda \\ &\xrightarrow{U_\lambda \to K\cdot Q} K(k) \left[\int_{q,q'} Q(q)\, V_\lambda(q,q')\, Q(q') \right] K(k') \quad \text{with} \quad K(k) \approx 1, \end{aligned} \tag{7}$$

which is a constant times a smeared delta function, as advertised. Further, we can understand why nuclear scaling is expected directly from U_λ-factorization, if we can argue that the deuteron channel dominates (as in the SRC argument [1,2]). When $k < \lambda$ and $q \gg \lambda$, the ratio of original momentum distributions becomes (in a schematic notation):

$$\begin{aligned}\frac{n_A(q)}{n_d(q)} &= \frac{\langle \widetilde{A}|\widehat{U} a_{\mathbf{q}}^\dagger a_{\mathbf{q}} \widehat{U}^\dagger|\widetilde{A}\rangle}{\langle \widetilde{d}|\widehat{U} a_{\mathbf{q}}^\dagger a_{\mathbf{q}} \widehat{U}^\dagger|\widetilde{d}\rangle} = \frac{\langle \widetilde{A}|\int U_\lambda(k',q')\, \delta_{q'q}\, U_\lambda^\dagger(q,k)|\widetilde{A}\rangle}{\langle \widetilde{d}|\int U_\lambda(k',q')\, \delta_{q'q}\, U_\lambda^\dagger(q,k)|\widetilde{d}\rangle} \\ &= \frac{\langle \widetilde{A}|\int K_\lambda(k')[\int Q_\lambda(q')\, \delta_{q'q}\, Q_\lambda(q)] K_\lambda(k)|\widetilde{A}\rangle}{\langle \widetilde{d}|\int K_\lambda(k')[\int Q_\lambda(q')\, \delta_{q'q}\, Q_\lambda(q)] K_\lambda(k)|\widetilde{d}\rangle} = \frac{\langle \widetilde{A}|\int K_\lambda(k')\, K_\lambda(k)|\widetilde{A}\rangle}{\langle \widetilde{d}|\int K_\lambda(k')\, K_\lambda(k)|\widetilde{d}\rangle} \\ &\equiv C_A, \end{aligned} \tag{8}$$

where C_A is the scaling ratio. A proof of principle test in a toy one-dimensional model verified that this scenario can work [10]. For the realistic nuclear case, we need to examine all contributions quantitatively, including from three-body operators, but the pattern in Eq. (8) is promising.

We might further speculate that the recent observation that the A dependences of scaling ratios and the slope of the EMC effect $dR_A(x)/dx$ (where $R_A(x)$ is the large Q^2 ratio of nuclear cross sections for $0.7 < x < 1.0$) are linearly correlated [1] could be understood by U_λ-factorization and subsequent cancellations in cross section ratios. The EFT treatment of Chen and Detmold [18] predict an analogous factorization in the EMC ratio. In particular, they assert:

> "The x dependence of $R_A(x)$ is governed by short-distance physics, while the overall magnitude (the A dependence) of the EMC effect is governed by long distance matrix elements calculable using traditional nuclear physics."

If the same leading operators dominate in the two types of processes (i. e., two-body contact operators with deuteron quantum numbers), then we would expect precisely this sort of linear A dependence. Quantitative calculations are needed!

To do such calculations, we need many-body operator contributions, as shown by Neff for ^{4}He relative momentum distributions [19]. Fortunately, the recently developed technology for evolution of three-body forces can be adopted for more general operator evolution. This will enable direct calculations by *ab initio* methods in lighter nuclei and many-body perturbation theory for operators in heavier nuclei.

4 Summary and outlook

We have presented a brief overview of high-resolution probes of low-resolution nuclei based on the RG/EFT perspective. Some summary observations:

- Lower resolution means more natural nuclear structure.
- While scale and scheme-dependent observables can be (to good approximation) unambiguous for *some* systems, they are often (generally?) not so for nuclei. And while cross sections are invariant, the physics interpretation can change with resolution!
- Working with scale and scheme dependence requires *consistent* Hamiltonian and operators. Be wary of treating experimental analysis in independent pieces (as is often done).
- Unitary transformations can be used to reveal *natural* scheme dependence.

The RG/EFT perspective and associated tools can help to address whether we can have controlled factorization at low energies, to identify the roles of short-range versus long-range correlations, and to quantitatively assess the scheme-dependence of spectroscopic factors and related quantities.

An overreaching question is how should one choose the appropriate scale in different situations (with the RG to evolve the scale as needed). One general motivation is to make calculations easier or more convergent, such as using the QCD running-coupling scale to improve perturbation theory. For nuclear structure and low-energy reactions, low-momentum potentials are chosen to improve convergence in configuration interaction or coupled cluster calculations or to make a microscopic connection to the shell model. Conversely, local potentials (which until recently were only high resolution) are favored for quantum Monte Carlo. The scale could also be chosen for interpretation or intuition; the SRC phenomenology is such an example. But the most important issue for knock-out experiments is to have the cleanest and most controlled extraction of quantities analogous to PDFs from experiment; this might mean optimizing the validity of the impulse approximation but there are other possibilities (e. g., optimizing U_λ-factorization). To make progress, the plan is to make test calculations

with a range of scales starting from initial Hamiltonians and operators matched in an EFT framework, with the RG used to consistently relate scales and quantitatively probe ambiguities (e. g., in spectroscopic factors). A priority calculation in the short term is deuteron electrodisintegration, which is well controlled because of the absence of three-body forces and operators.

I thank my collaborators E. Anderson, S. Bogner, B. Dainton, K. Hebeler, H. Hergert, S. More, R. Perry, A. Schwenk, and K. Wendt. This work was supported in part by the National Science Foundation under Grant No. PHY–1002478 and the U.S. Department of Energy under Grant No. DE-SC0008533 (SciDAC-3/NUCLEI project).

References

[1] J. Arrington, D. Higinbotham, G. Rosner and M. Sargsian, Prog. Part. Nucl. Phys. **67**, 898 (2012).

[2] M. Alvioli, C. Ciofi degli Atti, L. Kaptari, C. Mezzetti and H. Morita, Phys. Rev. C **87**, 034603 (2013).

[3] S. K. Bogner, R. J. Furnstahl and A. Schwenk, Prog. Part. Nucl. Phys. **65**, 94 (2010).

[4] R. Roth, J. Langhammer, S. Binder and A. Calci, J. Phys. Conf. Ser. **403**, 012020 (2012).

[5] R. Furnstahl and K. Hebeler, Rep. Prog. Phys. (*in press*); [arXiv:1305.3800].

[6] A. H. Guth, K. Huang and R. L. Jaffe, editors, *Asymptotic Realms of Physics.* MIT Press, Cambridge, MA, 1983.

[7] K. Hebeler, Phys. Rev. C **85**, 021002 (2012).

[8] K. A. Wendt, Phys. Rev. C **87**, 061001 (2013).

[9] E. Epelbaum, H.-W. Hammer and U.-G. Meißner, Rev. Mod. Phys. **81**, 1773 (2009).

[10] E. Anderson, S. Bogner, R. Furnstahl and R. Perry, Phys. Rev. C **82**, 054001 (2010).

[11] S. Bogner and D. Roscher, Phys. Rev. C **86**, 064304 (2012).

[12] K. Wendt, R. Furnstahl and S. Ramanan, Phys. Rev. C **86**, 014003 (2012).

[13] R. B. Wiringa, V. G. J. Stoks and R. Schiavilla, Phys. Rev. C **51**, 38 (1995).

[14] CTEQ Collaboration, R. Brock *et al.*, Rev. Mod. Phys. **67**, 157 (1995).

[15] B. Povh, K. Rith, C. Scholz and F. Zetsche, *Particles and nuclei: an introduction to the physical concepts, 4th ed.* Springer, Berlin, 2004.

[16] CTEQ Collaboration, H. Lai *et al.*, Eur. Phys. J. C **12**, 375 (2000).

[17] C. Ciofi degli Atti and S. Simula, Phys. Rev. C **53**, 1689 (1996).

[18] J.-W. Chen and W. Detmold, Phys. Lett. B **625**, 165 (2005).

[19] T. Neff, *private communication.*

NTSE-2013 Summary Talk:

Conference Summary

Bruce R. Barrett

Department of Physics, PO Box 210081, University of Arizona, Tucson, AZ 85721-0081

Abstract

The conference summary observes how the presented talks reflect the diverse research interests of Professor James P. Vary and how, as a whole, they lead to the underlying goals of the International Conference on Nuclear Theory in the Supercomputing Era — 2013.

Keywords: *Conference summary; goals; high performance computing; light front quantization; ab initio nuclear theory*

1 Introduction

As the schedule for the International Conference on Nuclear Theory in the Supercomputing Era — 2013 (NTSE-2013) clearly shows, this was an exciting, diverse and highly informative conference, reflecting, appropriately, the research interests of Professor James P. Vary, the meeting honoree, on his 70th birthday. (See the conference schedule of presented talks, appearing earlier in these proceedings.) Looking back on the 50 talks presented over the last five days, I see the synthesis of the three major themes of this meeting, i. e., 1) High Performance Computing, 2) from Quantum Chromodynamics (QCD) to Nuclear Structure, and 3) *ab initio* Nuclear Structure and Reaction Theory, into one underlying goal, or *physics driver*, as James would say. I would state this goal as "the collaboration of computer scientists and nuclear physicists (both theorists and experimentalists) to determine the nucleon-nucleon (NN) and higher-nucleon interactions, based on QCD, and to use these interactions in microscopic calculations of nuclear properties for structure and reactions with predictive power and error quantification," i. e., we want a reliable, predictive theory of nuclei with proper error estimates.

One could say that James' research program is like a three-legged stool, in which all three legs are necessary in order to have a stable, final entity. I will consider these three legs in the order given in the previous paragraph, instead of the order of the talks, as given during the conference.

2 High performance computing: Large scale computational science in support of nuclear physics

Speakers: {Ng, Çatalyürek, Fann, Nam, Sosonkina, Yang}

Performing calculations at the forefront of computing technology has always been a priority for James Vary, so it is no surprise that he quickly adapted to the new

Proceedings of International Conference 'Nuclear Theory in the Supercomputing Era — 2013' (NTSE-2013), Ames, IA, USA, May 13–17, 2013. Eds. A. M. Shirokov and A. I. Mazur. Pacific National University, Khabarovsk, Russia, 2014, p. 383.

http://www.ntse-2013.khb.ru/Proc/Barrett.pdf.

paradigm that physical scientists will need to collaborate with computer scientists, if the former want to take full advantage of the new developments in computer hardware and software.

Exascale computing is coming, roughly between 2016 and 2020. When it does arrive, it will produce a time of disruptive change. Although it will be difficult and challenging, it will also be a *perfect storm* of opportunities for new investigations. As the speakers in this section made clear, collaborations between nuclear theorists and computer scientists will be crucial in the exascale era. Or as one slide in the keynote talk by Esmond Ng indicted — in the form of a demonstrator with a sign reading "Collaborate or Die!".

Even though there is much to do to get ready for the exascale era, we should remember that high performance computers, such as Titan, currently exist, as well as Graphics Processing Units (GPUs). These tools should be used now for training and preparation for the exascale era.

3 From Quantum Chromodynamics to nuclear structure

The scales of nuclear physics go from the quark and gluon degrees of freedom to those of the nucleons, the interactions among the nucleons and nuclear structure. One of the principal goals of nuclear physics is to unite the physics of quarks and gluons, i. e., Quantum Chromodynamics in the form of the QCD Lagrangian, with nuclear structure, i. e., the physics of nucleons and mesons in nuclei. Two approaches to achieving this goal were discussed during NTSE-2013: 1) Lattice Gauge Theory (or Lattice QCD) and 2) Light Front QCD.

3.1 Lattice QCD

Speakers: {Savage, Qiu}

In recent years, significant progress and advances have been made in Lattice QCD. As the keynote talk by Martin Savage made clear, everything that is required to do calculations at the physical quark masses now exists. What is required are *more* resources in order to perform these calculations. Doing this will allow Lattice QCD, combined with chiral Effective Field Theory and nuclear many-body techniques, to provide first principles, predictive capabilities for nuclear physics with quantifiable uncertainties. Consequently, the main, outstanding problem for nuclear physicists is to determine how to optimally match the results of Lattice QCD calculations, namely, well-calculated energy eigenvalues, to the nuclear many-body machinery. This is a current, major problem of interest in nuclear physics and rapid progress is being made in attacking it.

3.2 Light front QCD

Speakers: {Brodsky, Chakrabarti, Honkanen, Karmanov, D. S. Kulshreshtha, U. Kulshreshtha, Li, Vary, Wiecki, Zhao}

The second approach, Light Front QCD, is the method being investigated by James Vary and his collaborators. The keynote talk on this topic by Stanley Brodsky emphasized the fact that AdS + Light Front Holography yields an analytic first approximation to QCD, which is as simple as Schrödinger theory in atomic physics. This talk was then followed by a number of presentations by Iowa State University physicists and other collaborators on numerous applications of this Basic Light Front Quantization.

4 *Ab initio* nuclear structure and reaction theory

I will divide this section into three major parts: 1) the efforts to determine the fundamental interactions among the nucleons, 2) many-body nuclear-structure theory and experiment, and 3) nuclear-reaction theory and experiment: scattering, reactions, loosely bound/unbound nuclei.

4.1 *NN*, *NNN*, and higher-*N* interactions

Speakers: {Machleidt, Epelbaum, Polyzou, Sauer}

The keynote talk by Ruprecht Machleidt gave a comprehensive overview of the origin and properties of strong inter-nucleon interactions, both historically and theoretically. One of the facts, which was clearly brought forward at this conference, is that the field of nuclear physics is still waiting for QCD based strong interactions, i. e., based on lattice QCD and/or Light Front QCD. Until then, one will need to use the best-fit NN and NNN interactions to the scattering data. Fortunately, the new POUNDerS (Practical Optimization Using No Derivatives) routine is now providing truly high quality fits to the experimental data.

Talks at this meeting also pointed out that NN and NNN interactions derived from Effective Field Theory and Chiral Perturbation Theory (CPT) still have some unresolved problems, which need to be addressed. In this regard, the important role of NNN interactions in understanding nuclear structure microscopically has become apparent. Consequently, CPT NN interactions need consistent NNN interactions at the same order, e. g., next-to-next-to-next-lowest order (N3LO). There is also the problem of whether or not to include deltas into the CPT expansion.

4.2 Many-body nuclear-structure theory and experiment

Speakers: {Hagen, Draayer, Abe, Bogner, Caprio, Carlson, Coon, Dean, Dytrych, Furnstahl, Ginocchio, Hjorth-Jensen, Kim, Maris, Miller, Otsuka, Pieper, Papenbrock, Roth, Rotureau, Schwenk, Sosonkina, Tuchin, Vary, Weidenmüller, Wiringa}

As pointed out in the keynote presentation by Gaute Hagen, many excellent *ab initio* nuclear many-body approaches now exist, such as, Quantum Monte Carlo, Lattice EFT, NCSM (both Effective Interaction and Configuration Interaction), Monte Carlo NCSM, NCSM with the Continuum (NCSMC), NCSM with a Core, NC-Gamow-SM (NCGSM), Coupled Cluster method (CCM), In-Medium Similarity Renormalization Group (SRG), Self-Consistent Green's Functions, Effective Interaction Hyperspherical Harmonics method, etc. All these methods compete with each other and at the same time complement each other. As such, it is definitely time to start new benchmark calculations among these different approaches, such as between the In-Medium SRG and the NCSM with a Core and among the NCSMC, the NCGSM and the CCM with the Berggren basis.

The important role of symmetry in understanding nuclear structure and the strong interaction was emphasized in the keynote talk by Jerry Draayer. Nuclear shell models and nuclear collective models were shown to be complementary methods. This led to the application of symmetry approaches to the NCSM, in what is known as the Symmetry Adapted NCSM (SA-NCSM), which builds on the exact and approximate symmetries of nuclei.

These improved many-body techniques along with the latest high-performance computers have made much more accurate calculations possible. These results coupled with theory-guided extrapolation methods have made possible theoretical predictions with quantified error estimates. Consequently, it is now possible to perform

calculations to guide future experiments and to make meaningful predictions in *terra incognita*.

As mentioned earlier, collaborations between nuclear theorists and computer scientists play a crucial role in these calculations and have proven to be most beneficial. Indeed, supercomputing has become an essential part of nuclear theory.

4.3 Nuclear-reaction theory and experiment: Scattering, reactions, loosely bound/unbound nuclei

Speakers: {Navrátil, Hill, Leidemann, Polyzou, Rotureau, Shirokov}

The keynote address by Petr Navrátil presented an overview of some of the numerous *ab initio* approaches that now exist for studying nuclear reactions, such as the NCSM + Resonating Group Method (NCSM/RGM), the NCSMC, the QMC/GFMC, the CCM with Berggren basis, the Fermionic Molecular Dynamics (FMD) approach, etc., while other talks discussed approaches, such as the Lorentz Integral Transform + Effective Interaction Hyperspherical Harmonics (LIT/EIHH) method, the LIT/NCSM, the Gamow Shell + NCSM (NCGSM), etc. Significant progress has been made with the NCSM/RGM and NCSMC approaches, which can now include NNN forces and can handle three-body clusters. The LIT approach has the advantage of having a controlled resolution, and it can also be used for *ab initio* calculations far into the continuum. The NCGSM and the CCM methods have demonstrated the usefulness of the Berggren basis for including the continuum into nuclear structure and reaction calculations.

5 Summary of recent advances

I list below a few of the numerous recent advances in *ab initio* microscopic nuclear structure and reaction theory. Although it is an impressive list, it is far from being a complete list.

1. Petascale computers and GPUs
2. Increasing collaborations among nuclear theorists and computers scientists
3. First basis Light Front Quantization applications
4. Lattice QCD calculations with physical masses
5. Best fit (POUNDerS) NN interactions
6. Many excellent *ab initio* many-body methods
7. In-Medium SRG approach and results
8. UV and IR limits and extrapolations of results
9. NCSM/RGM and NCSMC with three-body clusters
10. New *ab initio* methods for nuclear-reaction theory

6 Some remaining challenges

As in Section 5, I will simply list a few of the remaining challenges that are faced in *ab initio* nuclear structure and reaction theory. As before, this is only a partial list of such challenges.

1. Making the transition to exascale computers, GPUs, etc.
2. Finding the resources for Lattice QCD calculations with the physical pion mass
3. Determining how to link Lattice QCD and LFQCD with the nuclear many-body machinery
4. Obtaining consistent NN and NNN interactions for all current potential approaches (AV18, EFT/CPT interactions, etc.)
5. Extending successful *ab initio* approaches for $0p$-shell nuclei to heavier mass nuclei
6. Developing error quantification for theoretical results
7. Establishing new collaborations, especially with computer scientists
8. And most important of all, recruiting more young physicists into nuclear-physics research

7 Conclusions

The talks at this conference, along with the honoring of James Vary on his 70th birthday, have reminded me of the closing statement by my *Thesis Grandfather*, Victor F. Weisskopf, i. e., the thesis advisor of my thesis advisor, in his summary talk for the International Conference on Nuclear Structure, held in Kingston, Canada, August 29 to September 3, 1960.

"But don't let yourself be talked into believing that the nucleus is not interesting. It is so small and it has so few parts and still it shows a tremendous variety of phenomena. Its investigation requires the whole arsenal of presently available experimental techniques and its understanding makes use of almost all branches of theoretical physics. What a marvelous invention! It is worth devoting a lifetime to it." [1].

James Vary has, indeed, devoted his professional life to this challenging system. We all wish him many more years of excellent health and excitement, as he continues this task. Happy 70th birthday, James!

References

[1] V. F. Weisskopf, in *Proc. Int. Conf. Nuclear Structure, Kingston, Canada, August 29 — September 3, 1960*, edited by D. A. Bromley and E. W. Vogt. University of Toronto Press, Toronto, 1960, p. 905.

List of participants

- **Takashi Abe**, University of Tokyo, Japan
- **H. Metin Aktulga**, Lawrence Berkeley National Laboratory, USA
- **Bruce Barrett**, University of Arizona, USA
- **Scott Bogner**, Michigan State University, USA
- **Stan Brodsky**, SLAC, Stanford University, USA
- **Mark Caprio**, University of Notre Dame, USA
- **Joe Carlson**, Los Alamos National Laboratory, USA
- **Ümit Çatalyürek**, The Ohio State University, USA
- **Dipankar Chakrabarti**, Indian Institute of Technology, India
- **Sidney A. Coon**, University of Arizona, USA
- **David Dean**, Oak Ridge National Laboratory, USA
- **Jerry Draayer**, Louisiana State University, USA
- **Tomáš Dytrych**, Louisiana State University, USA
- **Evgeny Epelbaum**, University of Bochum, Germany
- **George Fai**, U.S. Department of Energy, USA
- **George Fann**, Oak Ridge National Laboratory, USA
- **Dick Furnstahl**, The Ohio State University, USA
- **Joe Ginocchio**, Los Alamos National Laboratory, USA
- **Gaute Hagen**, Oak Ridge National Laboratory, USA
- **John Hill**, Iowa State University, USA
- **Morten Hjorth-Jensen**, University of Oslo, Norway and Michigan State University, USA
- **Heli Honkanen**, Pennsylvania State University, USA
- **Vladimir Karmanov**, Lebedev Physical Institute, Russia
- **Youngman Kim**, Institute for Basic Science, South Korea
- **Daya Shankar Kulshreshtha**, University of Delhi, India
- **Usha Kulshreshtha**, University of Delhi, India
- **Winfried Leidemann**, University of Trento, Italy
- **Yang Li**, Iowa State University, USA
- **Ruprecht Machleidt**, University of Idaho, USA
- **Pieter Maris**, Iowa State University, USA

- **Alexander Mazur**, Pacific National University, Russia
- **Anna McCoy**, University of Notre Dame, USA
- **Gerald Miller**, University of Washington, USA
- **Hai Ah Nam**, Oak Ridge National Laboratory, USA
- **Petr Navrátil**, TRIUMF, Canada
- **Esmond Ng**, Lawrence Berkeley National Laboratory, USA
- **Takaharu Otsuka**, University of Tokyo, Japan
- **Dossay Oryspayev**, Iowa State University, USA
- **Thomas Papenbrock**, University of Tennessee, USA
- **Steve Pieper**, Argonne National Laboratory, USA
- **Wayne Polyzou**, University of Iowa, USA
- **Hugh Potter**, Iowa State University, USA
- **Jianwei Qiu**, Brookhaven National Laboratory, USA
- **Robert Roth**, Technical University Darmstadt, Germany
- **Jimmy Rotureau**, Chalmers University of Technology, Sweden
- **Peter Sauer**, University of Hannover, Germany
- **Martin Savage**, University of Washington, USA
- **Achim Schwenk**, Technical University Darmstadt, Germany
- **Andrey Shirokov**, Moscow State University, Russia
- **Masha Sosonkina**, Old Dominion University, USA
- **John Spence**, Iowa State University, USA
- **Ionel Stetcu**, Los Alamos National Laboratory, USA
- **Kirill Tuchin**, Iowa State University, USA
- **James Vary**, Iowa State University, USA
- **Hans Weidenmüller**, Max Planck Institute for Nuclear Physics, Heidelberg, Germany
- **Paul Wiecki**, Iowa State University, USA
- **Bob Wiringa**, Argonne National Laboratory, USA
- **Chao Yang**, Lawrence Berkeley National Laboratory, USA
- **Xingbo Zhao**, Iowa State University, USA

NUCLEAR THEORY IN THE SUPERCOMPUTING ERA – 2013 (NTSE-2013)

International Conference Proceedings

Ames, Iowa, USA
May 13–17, 2013

Printing date: Febriary 7, 2014. Format 70x108 1/16.
Writing paper. "Computer modern" font. Digital printing.
Quire 34.1. Number of copies 150. Order number 11.

Publisher: Pacific National University,
136 Tikhookeanskaya street, Khabarovsk 680035, Russia.